ADDIS ABABA UNIVERSITY

COLLEGE OF NATURAL AND COMPUTATIONAL SCIENCES

DEPARTMENT OF CHEMISTRY

ADVANCED ELECTROCHEMICAL SENSORS FOR THE DETERMINATION OF SELECTED ANTIBIOTIC DRUG RESIDUES IN FOOD AND WATER SAMPLES

BY

WONDIMENEH DUBALE ADANE

June 2024

Addis Ababa, Ethiopia

ADVANCED ELECTROCHEMICAL SENSORS FOR THE DETERMINATION OF SELECTED ANTIBIOTIC DRUG RESIDUES IN FOOD AND WATER SAMPLES

By

Wondimeneh Dubale Adane

A Thesis Submitted to the Department of Chemistry, College of Natural and Computational Sciences, Addis Ababa University in Partial Fulfilment of the Requirements for the Degree of Doctor of Philosophy in Chemistry (Analytical)

Supervisors:

Dr. Merid Tessema

Prof. B. S. Chandravanshi

June 2024

Addis Ababa, Ethiopia

Approval Sheet

Addis Ababa University

College of Natural and Computational Sciences

Department of Chemistry

This is to certify that the thesis prepared by ***Wondimeneh Dubale Adane***, entitled: **"*Advanced Electrochemical Sensors for the Determination of Selected Antibiotic Drug Residues in Food and Water Samples,"*** submitted in partial fulfilment of the requirements of the degree of Doctor of Philosophy in Chemistry (Analytical), complies with the regulations of the university and meets the standards with respect to quality and originality.

Approved by the examining committee:

Name	Signature	Date
Prof. Hailemichael Alemu **External examiner**	_____	_____
Dr. Weldegebriel Yohannes **Internal examiner**	_____	_____
Dr. Solomon Mehretie **Internal examiner**	_____	_____
Dr. Merid Tessema	_____	_____
Prof. B. S. Chandravanshi **Supervisors**	_____	_____
Prof. Ahmed Mustefa **Chairman of the Department**	_____	_____

Dedication

I dedicate this work to my entire family.

Declaration

I hereby declare that this thesis submitted for the degree of Doctor of Philosophy (Ph.D.) in Chemistry (Analytical) at Addis Ababa University, College of Natural and Computational Sciences, Addis Ababa, Ethiopia, is my own original work and has not been submitted previously to any other institution. All sources of materials used in this work have been duly acknowledged.

Table of Contents

Acknowledgements

Above all, I am grateful to the Almighty God. His unwavering guidance and constant presence have been the cornerstone of my journey so. I give Him all the credit, adoration, and reverence for granting me the fortitude and discernment required to navigate this path. With the divine assistance of the Holy Spirit, I am emboldened to pursue this endeavor with certainty and purpose.

I would like to express my heartfelt gratitude to my esteemed supervisors, Dr. Merid Tessema and Prof. B. S. Chandravanshi, for their unwavering guidance, benevolent supervision, and invaluable support throughout my journey. Their insightful advice, scientific expertise, and inspiring discussions have been instrumental in shaping my work. Their warm demeanors and caring approach have made every interaction a delight. Their generous provision of resources and unwavering encouragement has been monumental. I extend my heartfelt thanks for their constructive criticisms during courses, seminars, manuscript preparation, and thesis writing. Their mentorship has been a beacon of inspiration and guidance for which I am forever grateful.

I am deeply thankful to my wife, Tigist Mulugeta, and our Kids *Ema*, *Nani*, and *Fiker*, whose unwavering love, firm support, boundless patience, and selfless sacrifices have been the cornerstone of my journey. Your endless encouragement has fueled my determination, and your presence has been my greatest source of strength. Thank you for standing by my side throughout this arduous journey; your unwavering belief in me has been my guiding light. Moreover, I want to express my deepest gratitude to my precious family members: my father, Dubale Adane, your wisdom and steadfast support have served as my guiding light; my mother, Kassech Kebede, your boundless love, prayers, and encouragement have inspired me beyond measure; and my brother, Liyouneh Dubale, sister, Bezawork Mekonnen, and brother, Andualem Engida, your unwavering support and encouragement have been an endless source of motivation and invaluable energy to me. Without your strong support, this accomplishment would not have been possible. To all my family members and friends, whose names are not mentioned here, I extend my deepest appreciation for your strong support in every possible way. Your encouragement, prayers, and unwavering belief in me have been instrumental in reaching this milestone. I would also like to express my gratitude to Rahwa Michael (Canada), Mimisho (London), China (USA), and Mesay Taye (USA) for their assistance in delivering electrode materials and chemicals from abroad. May God bless each of you abundantly.

I extend my heartfelt gratitude to Dr. Woldegebriel Yohannes and Dr. Negussie Negash for their insightful and constructive feedback during my seminar presentations. Their valuable comments have greatly enriched my work and helped me refine my ideas. I am deeply grateful to Prof. Ahmed Mustefa for his generous support in providing the necessary facilities and administrative cooperation. I would like to express my sincere appreciation to Prof. Yonas Chebude and Dr. Negash Getachew for their expertise in conducting FT-IR and XRD analyses. Their contributions have provided invaluable insights into my research findings. The Mechanical Engineering Department of Haramaya University and the Biology Department of Adama Science and Technology University (ASTU) should be acknowledged for SEM and EDX analysis. Their collaboration has been instrumental in advancing my research. I am thankful to the Ethiopian Pharmaceutical Manufacturing S.C., Addis Ababa, Ethiopia, for generously providing antibiotic standards. I would like to express my sincere gratitude to Dr. Mekonen Ababayehu for his unwavering support throughout this journey.

My special thanks goes to Prof. Wondimagegn Mammo for his genuine inspiration, invaluable guidance, warm and nurturing approach throughout my research work. His willingness to engage in discussions and provide constructive feedback has greatly enriched my research experience, and I am deeply grateful for that.

I extend my sincere appreciation to my seniors, Dr. Tesfu Hailu, Dr. Gizaw Tesfaye, and Dr. Endale Tesfaye, for their generous provision of laboratory materials, guidance in instrument operation, invaluable discussions, cooperation, and encouragement throughout my laboratory activities. Additionally, I am profoundly grateful to my friends, Desalegn Nigatu, Getachew Denbela, Asmamaw Taye, and Tadele Tamenu, for their unwavering support, insightful ideas, and constructive comments, which have been instrumental in shaping this work. Their special assistance and encouragement have truly made a significant difference. Finally, I extend my gratitude to the Department of Chemistry, Addis Ababa University for generously providing the necessary laboratory facilities and instruments essential for the completion of this work.

Abstract

The presence of antibiotic drug residues in food and water sources poses a critical challenge to the public health and environmental sustainability. Addressing this challenge requires the development of highly sensitive and selective detection methods capable of accurately quantifying trace levels of the residues in complex sample matrices. The aim of this study was to contribute to this vital area of research by focusing on the designing, fabrication, characterization, and application of advanced electrochemical sensors for the detection of antibiotic residues in various matrices. In this study, eight cutting-edge electrochemical sensors were developed, characterized, and successfully applied for the individual and simultaneous determination of selected antibiotic drug residues in food and water samples. Through thorough experimentation and optimization, novel electrochemical sensor architectures have been developed using innovative materials, including gold-silver alloy nanocoral clusters (Au-Ag-ANCCs), thermally annealed gold–silver alloy nanoporous matrices (TA-Au-Ag-ANpM), iron-doped polyaniline (Fe-dop-PANI), nickel oxide nanoparticles (NiO-NPs), zinc oxide nanoparticles (ZnO-NPs), functionalized multi-walled carbon nanotubes (*f*-MWCNTs), reduced graphene oxide (*r*-GO), poly(L-histidine), poly(L-serine), poly(glycine), polyethylene oxide (PEO), and choline chloride (ChCl), to improve sensitivity, selectivity, and stability. The surface morphology, elemental composition, and electrochemical properties of the developed sensors were characterized using an array of analytical techniques, including UV–Vis spectroscopy, Fourier transform infrared spectroscopy (FT-IR), X-ray diffraction spectroscopy (XRD), energy dispersive X-ray spectroscopy (EDX), scanning electron microscopy (SEM), electrochemical impedance spectroscopy (EIS), and cyclic voltammetry (CV). Among the developed sensors, ChCl/CPE was designed for the determination of ciprofloxacin (CPRO) in eye drops, river water, and egg samples. It exhibited outstanding performance with a wide linear range (0.005–200 μM), and impressive detection and quantification limits of 0.36 nM and 1.2 nM, respectively. ChCl/GCE was prepared for the simultaneous determination of tinidazole (TIN) and chloramphenicol (CAP) in egg, honey, and milk samples. It showed exceptional detection capability with a wide linear range of 0.010–170 μM and 0.005–300 μM for TIN and CAP, respectively. The limit of detection (LOD) and limit of quantification (LOQ) were 0.90 nM and 3.0 nM for TIN, and 0.27 nM and 0.89 nM for CAP, respectively. TA-Au-Ag-ANpM/*r*-GO/poly(glycine)/GCE was developed for the detection of life-threatening residues of metronidazole (MTZ) in milk powder, pork, and chicken meat samples. It

performed exceptionally in the detection of MTZ with a wide linear range from 2.0 pM to 410 μM. The LOD and LOQ were determined to be 0.0312 pM and 0.104 pM, respectively. Au-Ag-ANCCs/*r*-GO/poly(L-histidine)/GCE was used for the simultaneous determination of vancomycin (VAN) and ceftriaxone (CFT) residues in chicken meat, fish, and milk samples. The sensor demonstrated outstanding performance in the determination of the analytes over a wide dynamic range, from 1.0 pM to 120 μM for VAN and from 1.0 pM to 290 μM for CFT. The LOD and LOQ values were determined to be 0.11 pM and 0.36 pM for VAN and 0.017 pM and 0.057 pM for CFT, respectively. TA-Au-Ag-ANpM/*f*-MWCNTs-CPE/poly(L-serine) was prepared for the simultaneous detection of sulfathiazole (SFT) and sulfamethoxazole (SFM) residues in honey, beef, and egg samples. It showed exceptional performance in a wide linear range (4.0 pM to 490 μM for SFT and 4.0 pM to 520 μM for SFM), with picomolar detection and quantification limits (0.53 pM and 1.75 pM for SFT, 0.41 pM and 1.35 pM for SFM). Au-Ag-ANCCs/f-MWCNTs-CPE/ChCl was developed for the simultaneous determination of rifampicin (RAMP) and norfloxacin (NFX) residues in water samples. It exhibited outstanding performance in a broad linear range, from 14 pM to 115 μM for RAMP and from 0.9 nM to 200 μM for NFX, with LOD and LOQ values of 2.7 pM and 8.85 pM for RAMP and 0.14 nM and 0.47 nM for NFX, respectively. Au-Ag-ANCCs/ZnO-NPs-CPE/PEO was prepared for the simultaneous detection of nitrofurantoin (NFT) and furazolidone (FZD) in poultry, fish, honey, dairy products, and municipal wastewater samples. The sensor demonstrated exceptional performance over a wide linear range, from 1.0 pM to 250 μM for NFT and 0.9 nM to 360 μM for FZD. The LOD and LOQ were found to be 0.26 pM and 0.88 pM for NFT and 0.023 pM and 0.076 pM for FZD, respectively. Finally, TA-Au-Ag-ANpM/Fe-dop-PANI/NiONPs/GCE was developed for simultaneously determining azithromycin (AZM) and enrofloxacin (ENF) residues in food and water samples. The sensor exhibited exceptional performance in a broad dynamic range from 0.8 pM to 250 μM for AZM and 0.1 pM to 550 μM for ENF, with LOD and LOQ values of 0.053 pM and 0.18 pM for AZM and 0.013 pM and 0.042 pM for ENF, respectively. In order to maximize the efficiency of the proposed sensors, an extensive optimization of various experimental parameters was performed. The optimization process included the selection of the appropriate supporting electrolytes, choice of the pH of the electrolyte solutions, determination of the number of electropolymerization cycles, optimization of the mixing ratio of the nanocomposites, adjustment of the volume of the drop-casting species, and selection of the square wave voltammetry (SWV) parameters, such as amplitude, frequency, and step potential, as

well as other instrumental parameters. Under these optimized experimental conditions, the developed sensors exhibited remarkable selectivity and effectively discriminated between the target analytes and interferents present in complex sample matrices. In addition, the developed sensors exhibited exceptional reproducibility, repeatability, and long-term stability. Subsequently, the developed sensors were validated using real food and water samples that were suspected to contain antimicrobial drug residues. The results revealed impressive recoveries ranging from 95.6 to 103%, with relative standard deviations below 5%. In general, the results presented in this paper represent a significant advance in the field of electrochemical sensor technology, particularly in the vital area of identifying antibiotic residues in food and water samples. The introduction of these state-of-the-art sensors heralds a new era characterized by increased sensitivity, selectivity, and reliability. This advancement will change the landscape of monitoring, regulating, and controlling antibiotic residues in food chains and water sources. Beyond enriching scientific knowledge, this breakthrough offers tangible benefits for public health and environmental sustainability, and embodies the laudable pursuit of advancing knowledge for the benefit of society.

Keywords: Antibiotic resides; Electrochemical sensors; Nanocomposite modifiers; Food samples; Water samples

List of Publications

1. A simple, ultrasensitive and cost-effective electrochemical sensor for the determination of ciprofloxacin in various types of samples. *Sensing and Bio-Sensing Research 39 (2023) 100547.* https://doi.org/10.1016/j.sbsr.2022.100547.

2. Highly sensitive and selective electrochemical sensor for the simultaneous determination of tinidazole and chloramphenicol in food samples (egg, honey and milk). *Sensors & Actuators: B. Chemical 390 (2023) 134023.* https://doi.org/10.1016/j.snb.2023.134023.

3. A novel electrochemical sensor for the detection of metronidazole residues in food samples. *Chemosphere 359 (2024) 142279.* https://doi.org/10.1016/j.chemosphere.2024.142279.

4. A cutting-edge electrochemical sensing platform for the simultaneous determination of the residues of antimicrobial drugs, rifampicin and norfloxacin, in water samples. *Analytica Chimica Acta 1312 (2024) 342746.* https://doi.org/10.1016/j.aca.2024.342746.

5. Hypersensitive electrochemical sensor based on thermally annealed gold–silver alloy nanoporous matrices for the simultaneous determination of sulfathiazole and sulfamethoxazole residues in food samples. *Food Chemistry 457 (2024) 140071.* https://doi.org/10.1016/j.foodchem.2024.140071.

6. A novel hypersensitive electrochemical sensor (Au-Ag-ANCCs/r-GO/poly(L-histidine)/GCE) for the simultaneous determination of vancomycin and ceftriaxone residues in chicken meat, fish, and milk samples. *Chemical Engineering Journal* ***(Revised Manuscript under Review).***

7. Ultra-performance multi-elemental nanocomposite electrochemical sensor architecture: Designed for simultaneously detecting residues of antimicrobial drugs, nitrofurantoin and furazolidone, in poultry, fish, honey, dairy products and municipal wastewater. *Sensing and Bio-Sensing Research.* ***(Under Review).***

8. Pioneering electrochemical sensing platform of multi-elemental nanocomposites for simultaneously determining azithromycin and enrofloxacin residues in food and water samples**.** *Electrochemica Acta* ***(Under Review).***

List of Figures

List of Abbreviations

AC	Alternating Current
Ag/AgCl	Silver/Silver Chloride Electrode
AIDS	Acquired Immunodeficiency Syndrome
AMR	Antimicrobial Resistance
AZM	Azithromycin
BSED	Backscattered Electron Detectors
CAP	Chloramphenicol
C_{dl}	Double Layer Capacitance
CE	Capillary Electrophoresis
CF	Cystic Fibrosis
CFT	Ceftriaxone
ChCl	Choline Chloride
CNTs	Carbon Nanotubes
COPD	Chronic Obstructive Pulmonary Disease
CPE	Carbon Paste Electrode
CPRO	Ciprofloxacin
CT	Computed Tomography
CV	Cyclic voltammetry
DPV	Differential Pulse Voltammetry
EDX	Energy-Dispersive X-Ray
EIS	Electrochemical Impedance Spectroscopy
ELISA	Enzyme-Linked Immunosorbent Assay
ENF	Enrofloxacin
FT-IR	Fourier-Transform Infrared
FWHM	Full Width at Half Maximum
FZD	Furazolidone
GC	Gas Chromatography

GCE	Glassy Carbon Electrode
GC-MS	Gas Chromatography-Mass Spectrometry
GO	Graphene Oxide
HIV	Human Immunodeficiency Virus
HPLC	High-Performance Liquid Chromatography
LC-MS	Liquid Chromatography-Mass Spectrometry
LC-MS/MS	Liquid Chromatography-Tandem Mass Spectrometry
LSV	Linear Sweep Voltammetry
MALD/IMS	Matrix-Assisted Laser Desorption/Ionization Mass Spectrometry
MCA	Multichannel Analyzer
MRI	Magnetic Resonance Imaging
MTZ	Metronidazole
MWCNTs	Multi-Walled Carbon Nanotubes
NFT	Nitrofurantoin
NFX	Norfloxacin
NPV	Normal Pulse Voltammetry
PANI	Polyaniline
PCR	Polymerase Chain Reaction
PEO	Poly ethylene oxide
RAMP	Rifampicin
R_{ct}	Charge Transfer Resistance
r-GO	Reduced Graphene Oxide
R_s	Solution Resistance
SAMs	Self-Assembled Monolayers
SCE	Saturated Calomel Electrode
SED	Secondary Electron Detectors
SEM	Scanning Electron Microscopy
SERS	Surface-Enhanced Raman Spectroscopy

SFM	Sulfamethoxazole
SFT	Sulfathiazole
STIs	Sexually Transmitted Infections
SWCNTs	Single-Walled Carbon Nanotubes
SWV	Square Wave Voltammetry
TA	Thermally Annealed
TB	Tuberculosis
TEM	Transmission Electron Microscopy
TIN	Tinidazole
TLC	Thin-Layer Chromatography
UHPLC	Ultra-High Performance Liquid Chromatography
UTIs	Urinary Tract Infections
UV-Vis	Ultraviolet-visible
VAN	Vancomycin
XRD	X-Ray Diffraction
Z_w	Warburg Impedance

Chapter One

1.1. Introduction

1.1.1. Antibiotics

The word "antibiotics" originally used to describe substances naturally produced by microorganisms, like bacteria or fungi, which could inhibit the growth of other microbes or disrupt their cellular integrity. However, with the advent of semi-synthetic derivatives, a new terminology was used. Now, "antimicrobials" encompasses a broader category that includes synthetic, semi-synthetic, and natural compounds, all of which are effective in hindering microbial proliferation and inducing apoptosis [1]. Before the discovery of antibiotics, humanity was highly vulnerable to various infectious diseases like pneumonia, meningitis, and tuberculosis presenting significant challenges in treatment, often with limited or no effective options. Major epidemics threatened public health, and medical specialties such as surgery, pediatrics, and hematology faced elevated mortality rates due to infectious complications [2]. The emergence of antibiotics brought a significant transformations in the medical field. Physicians were freed from the fear of infection, allowing them to expand and enhance their research efforts. Specialized areas like surgery and hematology saw a remarkable growth and advancement. Consequently, humanity has been spared from major pandemics and effectively managed afflictions like tuberculosis. Antibiotics became synonymous with medical salvation in public perception [3]. Over time, numerous novel antimicrobial agents with diverse mechanisms of action have been discovered, resulting in an extensive armamentarium that offers broad protection against almost all pathogens [4].

The use of antibiotics dates back over 2,500 years to ancient Chinese civilization, where the therapeutic properties of moldy soybeans were discovered and utilized to treat various infections, such as furuncles and carbuncles. Similarly, other ancient civilizations, such as the Egyptians and Greeks, resorted to molds and plants to combat infections, although the understanding of compounds that displayed antibiotic properties was limited at the time [5]. In 1665, Robert Hooke made significant advancements in microbial observation by utilizing a simple microscope to study small organisms, plants, microbes, and fungi, marking the initiation of cell theory “the concept that all living organisms are composed of cells”. Notably, in 1674, Anton van Leeuwenhoek further

enhanced the field by constructing powerful microscopes, enabling him to observe live microorganisms, leading to the recognition of bacteria and protozoa [6]. It wasn't until the late 19th century that the history of antimicrobial drugs began to unfold. In the 1890s, German researchers Rudolf Emmerich and Oscar Löw discovered the first antibiotic pyocyanase [7]. Subsequently, in 1909, Paul Ehrlich introduced Salvarsan, an arsenic-based drug that is effective against syphilis, laying the groundwork for further antimicrobial development. The milestone in this evolution came in 1928 with the discovery of penicillin by Alexander Fleming, which revolutionized clinical therapies [8,9]. The mid-20th century saw the rise of streptomycin and tetracycline in the late 1940s and the early 1950s, ushering in an era of antibiotic chemotherapy in clinical medicine. These antibiotics have demonstrated efficacy against various pathogenic bacteria, including Bacillus tuberculosis. Additionally, the evolving interest in pharmaceuticals and environmental substances, such as heavy metals, pesticides, and antibiotics, has become a focal point of research in recent decades, highlighting the ongoing exploration of antimicrobial agents and environmental factors [5].

Antibiotics can be classified based on their route of administration, origin, spectrum of activity, molecular structure, and mode of action. Antibiotics belonging to the same structural group generally demonstrate comparable efficacy, similar side effects, and toxicity [10-12]. Classification by mode of action divides antibiotics into four main groups (Figure 1). The first group involves the inhibition of cell wall synthesis, mainly effective against gram-positive bacterial infections due to their ability to interfere with cell wall formation, leading to cell lysis and death. The second group disrupts cell membranes and includes polycationic peptide antibiotics such as polymyxins. These antibiotics target gram-negative bacteria by interacting with their cell membranes, causing changes in permeability and cell death. Polymyxins are often reserved for use as a last resort against multi-drug-resistant strains because of their potency and potential toxicity. The third group inhibits nucleic acid synthesis, with notable examples being quinolones, rifampicin, and sulfonamides. Fluoroquinolones, a subclass of quinolones, are synthetic antimicrobial agents widely used in clinical settings due to their broad-spectrum activity and effectiveness in treating various infections by interfering with DNA replication and transcription. The fourth group focuses on the inhibition of protein synthesis and includes antibiotics, such as tetracycline, aminoglycosides, chloramphenicol, and macrolides. These antibiotics target

ribosomal RNA-rich regions of ribosomes, disrupting the protein synthesis necessary for bacterial growth and replication. Some of these antibiotics, such as aminoglycosides, have shown efficacy against specific infections, including tuberculosis, making them vital tools for the treatment of severe bacterial diseases [13,14].

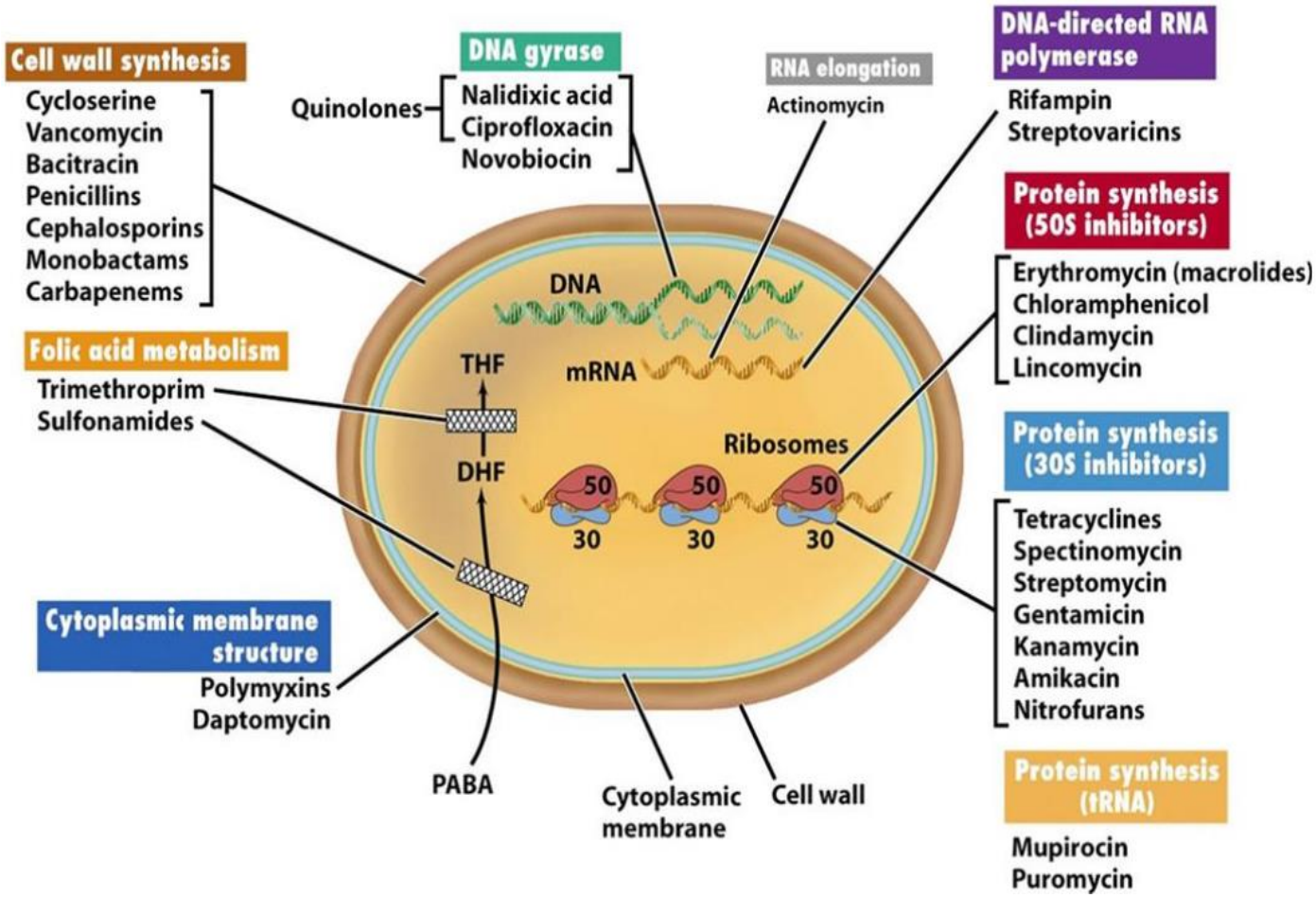

Figure 1. Classification of antibiotics.

1.1.2. The role of antibiotics in human health and animal husbandry

Antibiotics have dramatically transformed healthcare, revolutionizing the infectious diseases treatment and significantly lowering mortality and morbidity rates across the globe. They are essential for treating a wide range of bacterial infections, from common issues, like respiratory and urinary tract infections, to more serious conditions, including skin abscesses and sexually transmitted infections (STIs) [8,15]. For instance, antibiotics such as penicillin and amoxicillin

effectively combat streptococcal throat infections, whereas azithromycin and ciprofloxacin are frontline treatments for bronchitis and sinusitis [16]. In surgical practice, antibiotics administered before procedures, such as prophylaxis, significantly mitigate the risk of postoperative infections, crucially averting surgical site infections and associated complications. Antibiotics such as cefazolin and clindamycin are commonly employed for this purpose, and are selected based on their efficacy against pathogens relevant to specific surgeries [17]. In managing severe infections like tuberculosis (TB), meningitis, and sepsis, timely antibiotic therapy is paramount for reducing morbidity and mortality. TB necessitates prolonged antibiotic regimens for the cure and prevention of relapse, whereas prompt antibiotic treatment is imperative in meningitis to prevent serious complications [18]. In sepsis, early administration of broad-spectrum antibiotics is vital to halt the progression of systemic infection and forestall organ dysfunction. Chronic diseases like chronic obstructive pulmonary disease (COPD) and cystic fibrosis (CF) often feature recurrent bacterial infections, warranting antibiotic therapy to suppress bacterial growth and minimize exacerbations [19]. Prophylactic antibiotics, such as azithromycin and tobramycin, are utilized in CF to prevent Pseudomonas aeruginosa lung infections, while antibiotics like doxycycline and ciprofloxacin, mitigate exacerbation symptoms in COPD [20]. Immunocompromised individuals, such as those with HIV/AIDS or those undergoing chemotherapy, are particularly vulnerable to opportunistic infections, necessitating antibiotic treatment for both therapeutic and prophylactic purposes. For instance, trimethoprim-sulfamethoxazole is widely used to prevent pneumocystis pneumonia in HIV/AIDS patients, whereas invasive fungal infections may require antifungal antibiotics such as fluconazole and itraconazole for effective management [21].

Antibiotics play a critical role in animal husbandry and agriculture, used for various purposes from therapeutic interventions to non-therapeutic applications. In animal healthcare, therapeutic antibiotic use is essential to combat bacterial infections, ensure livestock well-being, and maintain productivity. This targeted approach involves administering antibiotics under veterinary guidance, effectively managing diseases, and preventing their spread within the herds [22]. Similarly, antibiotics are crucial in agriculture to prevent and treat bacterial diseases in crops and to safeguard agricultural productivity [23]. However, concerns have arisen regarding the non-therapeutic use of antibiotics, particularly their historical application at sub-therapeutic doses to boost growth rates, improve feed efficiency, and prevent diseases in high-density and stressful environments

[24]. While initially beneficial, these practices are now under scrutiny because of their potential contribution to antimicrobial resistance (AMR) and environmental contamination. To address these concerns, concerted efforts have been made to reduce and regulate non-therapeutic antibiotic use in animal agriculture [25]. This shift involves promoting alternative strategies such as enhanced biosecurity, vaccination, and probiotic integration into animal diets. The overarching objective is to promote sustainable animal production practices that balance disease prevention with responsible antibiotic stewardship to mitigate the risks associated with antibiotic misuse in agriculture [26].

1.1.3. Antibiotic resistance

Antibiotic resistance is an escalating global issue, where bacteria evolve to resist the effects of antibiotics, rendering the treatments inefficient against infections they were once treated successfully. Key contributors to antibiotic resistance include the misuse and overuse of antimicrobials in animal husbandries and human medications, incomplete treatment procedures, agricultural practices such as the non-therapeutic use of antibiotics in livestock, poor infection control measures, and worldwide dissemination of resistant bacteria [23,27]. The phenomenon has a profound effect on human health, economy, and the environment. The rise in resistant infections has made the treatment more challenging, resulting in longer illnesses, increased healthcare expenses, treatment failures, and higher mortality rates [28]. Economically, antibiotic resistance places a substantial burden on healthcare systems and productivity owing to longer hospital stays, elevated medication costs, and lost workdays. The uncontrolled discharge of antibiotics to the surrounding contributes to antibiotic pollution, affects ecosystems, and potentially pollutes food and water sources [29]. Therefore, combating antibiotic resistance requires multifaceted strategies. These include promoting prudent antibiotic use through improved stewardship practices, enhancing infection prevention and control measures to reduce the spread of resistant bacteria, developing new antibiotics and alternative treatments, investing in research and development of novel antimicrobial agents, and fostering global collaboration to tackle this critical issue comprehensively [30,31]. By implementing these strategies, stakeholders can preserve the effectiveness of antibiotics, protect public health, sustain economies, and safeguard the environmental integrity.

1.1.4. Antibiotic residue pollution

Antibiotic residue pollution is a global problem arising from various sources, such as agricultural practices and pharmaceutical waste disposal. This pollution causes extensive contamination of soil, water, and food, and severely affects the environment and public health [32,33]. Livestock farming and aquaculture are responsible for a considerable amount of this pollution because antibiotics are administered to animals for various purposes. Moreover, improper disposal of medications and inadequate wastewater treatment worsen the issue, leading to long-lasting antibiotic residues in the environment [22,34]. These residues pose significant risks to ecosystems and public health by promoting the development and spread of antibiotic resistant bacteria. This, in turn, compromises the effectiveness of antibiotic treatments in both human and veterinary medicine. Antibiotic residue pollution has far-reaching consequences that extend beyond environmental harm, including economic and social effects [35,36]. For instance, the rise of antibiotic-resistant bacteria elevates healthcare costs, necessitating alternative treatments and prolonged hospitalization. In agriculture, antibiotic residues can decrease livestock productivity and result in trade restrictions on contaminated food products, thereby impacting food security and economic stability. Furthermore, antibiotic residue pollution exacerbates existing health disparities and socioeconomic inequalities, especially affecting vulnerable populations with limited access to clean water and healthcare services [37,38]. Addressing this complex issue demands collaborative efforts across sectors to enact sustainable agricultural practices, enhance wastewater management, and endorse responsible antibiotic use to mitigate adverse impacts on human health, the environment, and the global economy.

1.1.5. Overview of antibiotic residues in food and water

Antibiotics are widely used in animal husbandry for treating infectious diseases and as growth promoters. The overuse and abuse of veterinary antibiotics resulted in the presence of their residues in animal organs, body tissues, and milk [39]. It was found that animals cannot absorb all antibiotics and approximately, 30–90% were extracted to the aquatic environment through urine, faces, and wastewater effluent [40]. Recently, antibiotic residues from animal husbandry are one of the major hazardous pollutants of aquatic ecosystems including aquatic animals. Among several antibiotics used in the livestock farms, tetracycline, quinolones, streptomycin, and lincomycin are

the most common in milk, tissue, and marine animals [41]. The residues are relatively stable in the environment, and even latest wastewater treatment plants cannot remove the residues completely. As a result, they can be easily ingested by humans through the food chain. Therefore, antibiotic residues from food-producing animals are a growing public health concern across the whole world. The residues in foods mainly results in allergic problems, carcinogenic risk, toxicity, and the development of antibiotic-resistant bacteria [39]. On the other hand, multi-drug resistant bacteria are health risk issues that can spread from various environmental settings, like livestock farm waste, sewage treatment effluent, and aquatic environment to the human body [42]. Considering the emerging health risk issues with antibiotic residues in food-producing animals, researchers are devoted to finding alternatives for antibiotics to use in livestock farms. Recently, plants and their extract having bioactive compounds, organic acids, probiotics, prebiotics, and other natural materials have been studied to replace antibiotics in animal husbandry [43].

The presence of antibiotic residues in aquatic ecosystems is a global concern. In addition to the direct use of antibiotics in aquaculture, several other pathways also contribute to the discharge of these residues into the environment. Figure 2 shows the various routes through which antibiotics enter aquatic environments [44]. The introduction of human-used antibiotics into aquatic environments poses a significant threat to water quality and ecosystem health through various pathways. A major route is through the excretion of antibiotics in the urine and feces following human consumption. Antibiotics can also enter water bodies through sources such as direct effluent discharge from sewage treatment plants, leachate from landfills, leaks from sewers and manure storage tanks, runoff from fields fertilized with contaminated manure, and leaching from polluted soils. Consequently, antibiotic residues have the potential to contaminate surface, groundwater, and drinking water sources, illustrating the complex and multifaceted nature of antibiotic pollution in aquatic ecosystems [45,46]. The highest concentrations of antibiotic residues are typically found in water bodies contaminated with effluents from hospitals, sewage treatment plants, and manure with antibiotic contamination [47]. Several studies have confirmed the presence of various antibiotics in animal manures. For instance, oxy-tetracycline showed the highest concentrations, reaching 416.8 mg/kg in chicken manure, while chlortetracycline had the highest concentrations, peaking at 764.4 mg/kg in swine manure. In addition, another study has indicated that the presences of chloramphenicol, sulfonamide, and tetracycline in animal manure

at concentrations ranging from 3.27 to 17.85 mg/kg, 5.85 to 33.37 mg/kg, and 4.54 to 24.66 mg/kg, respectively [48,49]. Furthermore, through extensive monitoring, a range of antibiotic residues have been identified in surface water and river sediments. Sulfamethoxazole, oxytetracycline, ciprofloxacin, norfloxacin, ofloxacin, clarithromycin, and erythromycin are among the most commonly detected antibiotics [50]. Sabri et al. [51] shows the presence of antibiotics in the water and sediment samples obtained from a river located within 20 km downstream of the effluent discharge points. Generally, these findings emphasize the widespread existence of antibiotic residues, the complex pathways by which antibiotic pollutants can affect both aquatic ecosystems and human health, and the need for effective strategies to mitigate this global challenge.

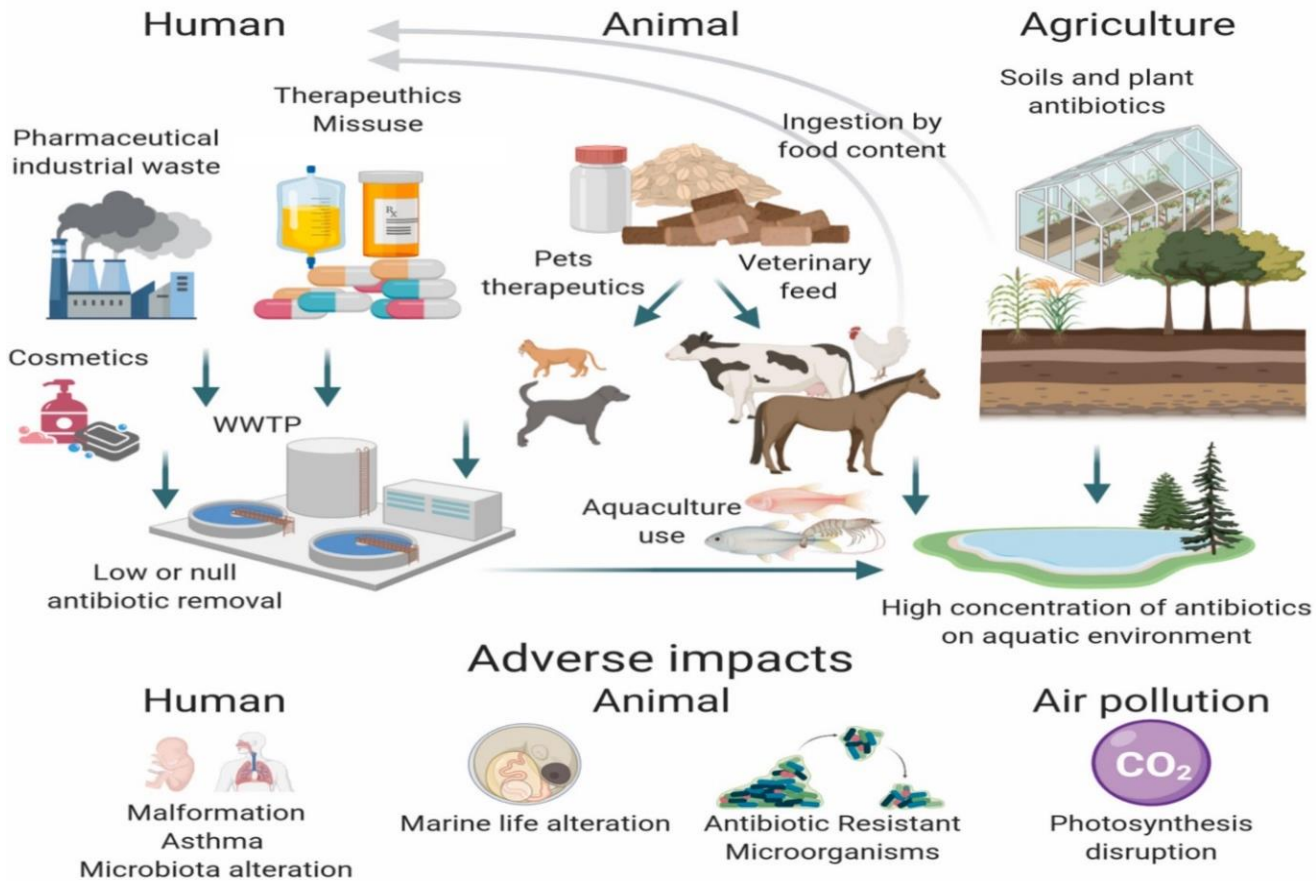

Figure 2. The pathway through which antibiotic residues pollute the aquatic environment.

1.2. Chemically modified electrodes

Electrochemical reactions play a crucial role in analytical chemistry, involving the intricate exchange of electrons between the working electrode and analyte at the interfacial boundary. To determine the full potential of electrochemical analysis, it is essential to understand and optimize the properties of the electrode surface. This interfacial complexity is influenced by various factors, such as the detailed microstructural features of electrode materials, inherent characteristics of the electrode, pristine cleanliness of the electrode surface, and diverse array of functional groups present on its surface [52]. A significant challenge arises from the heterogeneous nature of these reactions, which are often characterized by slow electron transfer kinetics when bare electrode surfaces are used. This limitation not only impedes sensitivity but also affects selectivity and sets stringent constraints on the detection limits. Consequently, the direct application of bare electrodes for trace-level quantification remains a challenging endeavor in electrochemical analysis [53]. In addition, it is difficult to distinguish analytes with closely spaced electrochemical oxidation and reduction potentials. The sluggish electron transfer kinetics at the bare electrode surface further complicates this issue, leading to the merging of redox peaks and hindering precise analyte identification and quantification [54]. To improve the electron transfer kinetics, enhance sensitivity, and achieve better differentiation among analytes, electrode surfaces can be modified using a range of enhancement techniques, from surface functionalization to nanomaterial deposition. This pursuit not only broadens the scope of analytical prospects but also enriches the capabilities of electrochemical analysis with exceptional sensitivity and selectivity, marking a new era of advanced electrochemical methodologies.

Chemically modified electrodes refer to electrodes intentionally modified by immobilizing various modifiers such as polymers, organic ligands, nanocomposites, lipids, ion exchangers, surfactants, organic and inorganic compounds, organometallic or inorganic catalysts, clays, biological materials, zeolites, and silicates onto the electrode surface. Selecting an appropriate modifier for electrode modification can effectively reduce the overpotential, prevent surface fouling, and enhance the sensitivity, selectivity, stability, and reproducibility of electrodes [55]. The most common modification techniques are surface functionalization, polymer coatings, nanomaterial deposition, enzyme immobilization, and molecular monolayer formation.

Surface functionalization involves attaching specific functional groups or molecules to the electrode surface through self-assembly, chemical reactions, or physical adsorption. This technique offers enhanced stability, as functional groups form strong chemical bonds with the electrode surface, improving its durability. It also improves the electron transfer kinetics, as certain functional groups can facilitate faster electron transfer reactions, leading to better electrochemical performance. Additionally, functionalized surfaces can selectively interact with target analytes, enhancing selectivity in sensing applications [56].

Polymer coatings are applied to electrode surfaces through techniques such as electropolymerization, drop-coating, or spin coating using conducting polymers such as polypyrrole, polyaniline, and polythiophene. The advantages of polymer coatings include high surface area, which increases analyte accessibility and sensitivity. They also offer enhanced conductivity, which facilitates rapid electron transfer kinetics. Furthermore, polymer coatings are versatile and can be tailored by incorporating functional groups or dopants, allowing diverse applications in sensing and electrocatalysis [57].

Nanomaterial deposition involves placing nanomaterials, such as nanoparticles, nanotubes, or graphene sheets, on electrode surfaces through methods such as electrodeposition, drop-casting, or chemical vapor deposition. The benefits of this technique include a high surface-area-to-volume ratio, which increases the number of active sites available for electrochemical reactions. Nanomaterials also exhibit enhanced catalytic activity, which improves the efficiency of the electrocatalytic reactions. In addition, the presence of nanomaterials increases the sensitivity of the electrode, enabling the detection of trace analytes with high precision [58].

Enzyme immobilization involves attaching enzymes to electrode surfaces using techniques such as physical adsorption, covalent attachment, or encapsulation within matrices, such as hydrogels or nanomaterials. This approach offers high substrate specificity, enabling the selective detection of target analytes in complex samples. Immobilization also protects enzymes from denaturation and degradation, thereby enhancing their stability and shelf-life. Moreover, enzyme-based electrodes can be regenerated by replenishing the enzyme, allowing multiple uses and long-term stability [59].

Molecular monolayer formation involves the creation of self-assembled monolayers (SAMs) of organic molecules on electrode surfaces using techniques such as immersion, vapor deposition, or Langmuir-Blodgett deposition. SAMs provide controlled surface properties, allowing precise control over surface chemistry and tailored functionalities. They also offer reproducibility, providing uniform and consistent surface modification across multiple electrodes. Additionally, certain SAMs mimic biological membranes or receptor sites, enabling the development of biomimetic sensors with enhanced affinity and specificity [60].

These modification techniques are crucial for enhancing the electrode properties tailored for specific applications, ranging from environmental monitoring to biomedical diagnostics. By harnessing the benefits of chemically modified electrodes, researchers can improve performance metrics, such as sensitivity, selectivity, stability, and reproducibility, advancing the field of electrochemical sensing and analysis. A wide range of materials, including graphene, carbon nanotubes, polymers, metal oxide nanoparticles, metal nanoparticles, and nanocomposites have been extensively used to modify electrode surfaces.

1.3. Materials used for electrode modification

In this study, various materials were used to prepare modified electrodes, which were then used to detect antibiotic residues in different samples. Below, we explore the different types of modifiers employed in this work.

1.3.1. Choline chloride

Choline chloride, (ChCl), ($(CH_3)_3N(CH_2)_2OH)^+Cl^-$), is a versatile organic compound with multifaceted applications. It is a cheap, environmentally friendly and non-toxic quaternary ammonium salt, consisting of choline cation ($(CH_3)_3N(CH_2)_2OH)^+$ and chloride anion (Cl^-). It is a bifunctional compound, containing both a quaternary ammonium ($–N^+(CH_3)_3$) and a hydroxyl (–OH) functional groups (Figure 3). ChCl is a white, water-soluble salt that is primarily utilized in animal feed formulations. Its significance extends across various fields, including fundamental biological processes, industrial uses, and applications in analytical chemistry [61].

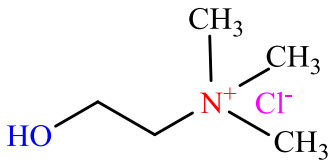

Figure 3. Structure of choline chloride.

In biological systems, ChCl serves as a precursor for the synthesis of the neurotransmitter acetylcholine, which is crucial for the transmission of signals between neurons. Additionally, it is a crucial component of cell membranes and contributes to membrane integrity and fluidity. ChCl is also involved in lipid metabolism and serves as a methyl donor in phospholipid synthesis, which is vital for cell structure and signaling. Moreover, ChCl serves as a methyl donor in the synthesis of other important molecules such as betaine, which involves in homocysteine metabolism [62]. ChCl is widely used in the industrial sector, particularly in the agricultural and food industries. As a feed additive for livestock, it plays a crucial role in promoting animal growth, improving feed efficiency, and preventing disorders, such as fatty liver syndrome in poultry. ChCl supplementation in animal diets also enhances reproductive performance and overall health [63]. Furthermore, it is employed in the formulation of dietary supplements for humans to address deficiencies associated with inadequate dietary intake [64]. In addition to its role in nutrition, ChCl is utilized in the production of pharmaceuticals, where it serves as a precursor for various drugs that target neurological disorders, liver diseases, and other health conditions. Additionally, ChCl has applications in cosmetics, where it functions as a skin conditioning agent in skincare products [65].

ChCl plays a vital role in analytical chemistry, particularly in electrochemical analysis. It serves as an outstanding electrode modifier, enhancing the performance of electrodes used in electrochemical techniques. Upon incorporation onto electrode surfaces, ChCl enhances conductivity and promotes electrochemical activity [66]. The modification process involves the utilization of the –OH group to immobilize ChCl at the electrode surface through covalent bonding. Additionally, the cationic polar group ($–N^+(CH_3)_3$) enhances electrostatic interactions, leading to a uniformly positively charged surface that facilitates electron transfer between the analyte and electrode (Figure 4) [67]. This modification enhances electron transfer kinetics, resulting in increased sensitivity and selectivity for analyte detection.

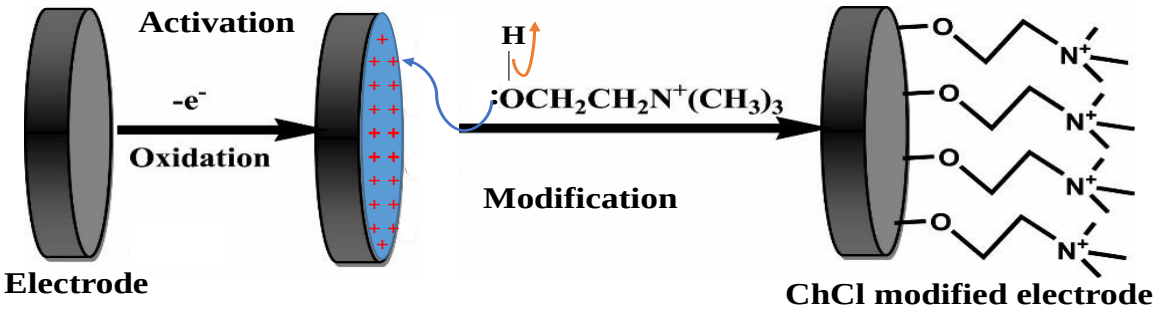

Figure 4. Schematic representation for the preparation of a ChCl modified electrode.

ChCl-modified electrodes play a significant role in a wide range of electrochemical methods for quantifying analytes in complex matrices. Several studies have been reported the versatility of ChCl as an electrode modifier for electrochemical determination of various analytes in environmental monitoring, pharmaceutical analysis, and biomedical diagnostics. A notable study by Bahrani et al. [67] introduced the ultrasonically accelerated synthesis of AuNP-ChCl-GO for the detection of meloxicam in human plasma samples. Shahamirifard et al. [68] developed a zirconia-ChCl-AuNP/CPE sensor for the simultaneous detection of gallic acid and uric acid in human urine. Parsaee et al. [66] fabricated Ag-ChCl-GO/CPE for electrochemical detection of celecoxib in human plasma. Biya et al. [69] reported voltammetric sensor for the determination of brucine in artificial urine sample based on ChCl/GCE. Moreover, Hung et al. [70] engineered a Pd/Ag hollow structure-modified electrode using galvanic replacement reactions in deep eutectic ChCl-based solvents to detect hydrazine in ponds and tap water. These innovative initiatives emphasize the fundamental role of ChCl-modified electrodes in advancing electrochemical sensing techniques in diverse domains.

1.3.2. Carbon-based modifiers

Carbon-based modifiers such as graphene and carbon nanotubes (CNTs) have attracted a significant attention and extensive exploration in electrochemical sensor development. This intense interest stems from their exceptional properties, including outstanding electrical conductivity, impressive mechanical strength, durable chemical stability, inherent biocompatibility, and a notably high surface-to-volume ratio. These characteristics make carbon-based materials highly attractive for electrode modification, leading to enhanced electrochemical

performance [71]. Furthermore, carbon-based materials offer an opportunity for synergistic integration with other nanomaterials, presenting avenues for improving the electron transfer kinetics of electrodes. The synergistic effects stemming from the combination of various nanomaterials resulted in significant enhancements in both the sensitivity and selectivity of the modified electrode [72]. Among carbon-based materials, derivatives of graphene and CNTs have emerged as attractive candidates for electrode modification. This is primarily due to their exceptional characteristics, including large surface area, excellent conductivity, and robust thermal and mechanical stability. These unique properties place carbon-based materials at the forefront of research efforts, highlighting their crucial role in advancing electrochemical sensing applications [73].

1.3.2.1. Graphene oxide

Graphene, a single atomic layer of carbon atoms arranged in a hexagonal lattice, represents one of the most intriguing materials in modern science. Its structure consists of carbon atoms bonded in a two-dimensional honeycomb lattice, forming a planar sheet that is only one atom thick [74,75]. Graphene serves as the foundational building block for a vast array of graphitic materials of different dimensions, ranging from zero-dimensional fullerenes to one-dimensional carbon nanotubes and three-dimensional graphite [76]. Graphene-based nanomaterials, including graphene, graphene oxide (GO), and reduced graphene oxide (*r*-GO), exhibit remarkable structural versatility and functional diversity. Graphene comprises pristine, unmodified sheets of carbon atoms, while GO features oxygen-containing functional groups such as hydroxyl, epoxy, and carboxyl groups, imparting it with increased hydrophilicity and chemical reactivity. Reduced graphene oxide, obtained through the chemical or thermal reduction of GO, exhibits a partially restored graphene structure, retaining some oxygen functionalities but with improved electrical conductivity compared to GO [77]. The structures of graphene, GO, and *r*-GO are shown in Figure 5 [78].

The unique properties of graphene and its derivatives have sparked immense interest and exploration since their discovery. These properties include an exceptionally high specific surface area, which provides abundant active sites for chemical interactions; high electrocatalytic activity facilitating efficient electrochemical reactions; remarkable mechanical flexibility allowing for

bending and deformation without breaking; facile functionalization enabling tailored surface modifications; exemplary electrical and thermal conductivity facilitating rapid charge and heat transfer; strong adsorptive capability for capturing molecules and ions from the surrounding environment; facile synthesis methods ranging from mechanical exfoliation to chemical vapor deposition; low production cost due to abundant carbon sources; and non-toxicity, making them suitable for various biomedical and environmental applications [79,80].

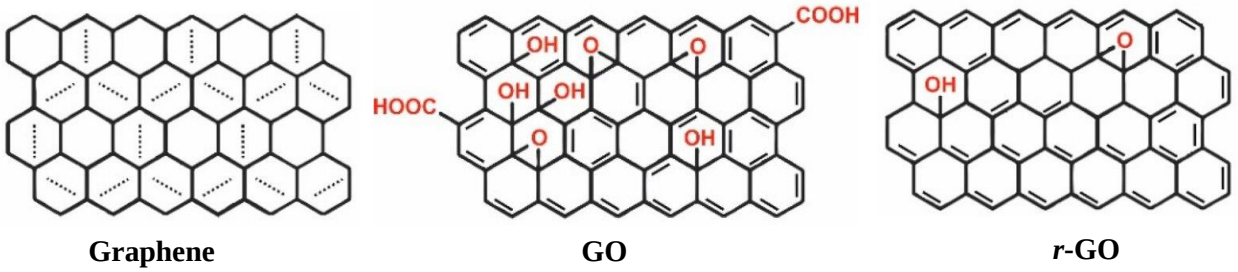

Figure 5. Structures of graphene, GO, and *r*-GO.

One of the primary challenges in utilizing graphene directly as an electrode modifier is its poor solubility and dispersion in aqueous solutions, which can be attributed to van der Waals forces and strong π–π stacking interactions between aromatic rings [74,81]. Consequently, graphene tends to aggregate in aqueous environments, which impedes its effective utilization. To address this issue, efforts have been focused on converting the hydrophobic surface of graphene to a hydrophilic one, thereby resolving the dispersion problem in aqueous media.

Graphene oxide (GO) is synthesized via the chemical oxidation of graphite, resulting in a material rich in oxygen-containing functional groups such as hydroxyl, carboxyl, carbonyl, and epoxy moieties [82]. The presence of these polar functional groups imparts hydrophilicity and biocompatibility to GO, facilitating its dispersion in polar solvents, such as water. This characteristic allows for the easy deposition of dispersed GO onto various substrates using techniques such as dip coating, drop casting, or spin coating, making it an ideal candidate for electrode material applications. However, the electrical conductivity of GO is lower than that of pristine graphene because of the disruption of the sp^2 bonding network during the oxidation process [79]. Therefore, the reduction of GO is essential for enhancing its conductivity by reducing the abundance of oxygen-containing functional groups and increasing the degree of conjugation [83]. Various reduction methods, including thermal, chemical, and electrochemical techniques,

have been employed to achieve this transformation [79]. These reduction processes are pivotal for optimizing the electrical properties of GO, thereby broadening its utility across a wide range of applications, including electronics and energy storage.

Chemical reduction is a highly efficient and extensively used method for reducing GO due to its cost-effectiveness and suitability for large-scale production. However, it involves the use of strong acids, multiple reduction steps, and is time-consuming [81,82]. Furthermore, chemical reduction often results in the incomplete removal of oxygen functionalities. The thermal reduction method relies on high temperatures to eliminate oxygen-containing functional groups from the GO. Although it is considered environmentally friendly and yields graphene with a high surface area, drawbacks such as structural damage to graphene, mass loss, high production costs, and the need for meticulous control of experimental conditions are notable [84,85]. On the other hand, the electrochemical reduction process, which employs various voltammetric techniques, such as LSV, CV, and amperometry, offers a viable alternative. Electrochemical reduction effectively removes the oxygen functionalities from GO by directly attaching the *r*-GO to the electrode surface. Compared to thermal and chemical reduction, electrochemical reduction is relatively cost-effective, simple, rapid, allows for precise control of the film thickness, enables the formation of stable films, and is environmentally friendly; however, it is not suitable for large-scale production [74,84]. In general, *r*-GO exhibits enhanced interactions with polymers and diverse nanoparticles, forming composites owing to its defect sites and fewer oxygen-containing functional groups. These properties make it an ideal material for electrode modifications.

1.3.2.2. Carbon nanotubes

Carbon nanotubes (CNTs) are cylindrical nanostructures composed entirely of carbon atoms arranged in a hexagonal lattice, similar to graphene, but rolled up into a tube. They exhibit extraordinary mechanical, electrical, and thermal properties owing to their unique structure. CNTs can be single-walled (SWCNTs), consisting of a single layer of carbon atoms, or multi-walled (MWCNTs), comprising several concentric layers of graphene (Figure 6) [86,87]. The discovery of carbon nanotubes dates back to 1991, when Sumio Iijima observed needle-like carbon structures while studying the carbon arc evaporation of graphite. These structures, later identified as CNTs, sparked significant interest in the scientific community due to their remarkable properties [88].

Since their discovery, extensive research has been conducted to understanding their synthesis, properties, and potential applications, leading to significant advancements in nanotechnology and materials science. SWCNTs and MWCNTs differ in their electrical and mechanical properties. SWCNTs typically exhibit a higher electrical conductivity and are more flexible than MWCNTs. However, MWCNTs are generally more robust and exhibit superior mechanical properties. The choice between SWCNTs and MWCNTs depends on specific application requirements, such as the desired conductivity, mechanical strength, and surface area [89].

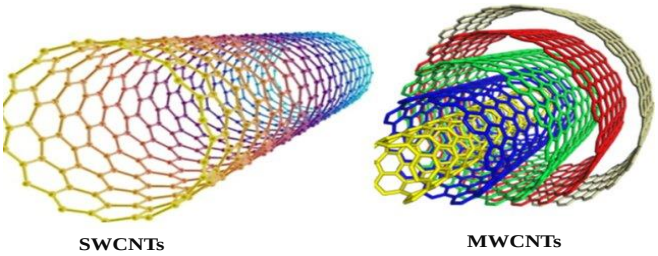

Figure 6. Stractural view of SWCNTs and MWCNTs.

CNTs are widely used in electronics, materials science, aerospace, and medicine owing to their exceptional properties, such as high surface area, chemical stability, mechanical strength, electrocatalytic activity, biocompatibility, and resistance to surface fouling [90,91]. In electrochemical sensors development, CNTs are valuable electrode modifiers that enhance the electrical conductivity, surface area, and electron transfer kinetics when incorporated onto electrode surfaces. CNT-modified electrodes play a critical role in electrochemical applications in detecting and quantifying various analytes, ranging from environmental pollutants to biomolecules and pharmaceuticals, in electrochemical applications [92]. Their superior surface area, conductivity, and biocompatibility make them ideal for sensing applications. Furthermore, CNT-modified electrodes offer several benefits such as enhanced stability, reproducibility, and lower detection limits than conventional electrodes, highlighting their importance in advancing electrochemical sensing technologies [93].

The development of CNTs-based devices faces challenges related to poor solubility, hydrophobicity, and dispersibility, which hinders their progress [94]. CNTs tend to aggregate in aqueous solutions due to strong π–π interactions and strong van der Waals forces between their aromatic rings, making it difficult to disperse them in common solvents [90]. Overcoming this

limitation necessitates the modification of CNTs surfaces to be hydrophilic through functionalization. Functionalization involves attaching chemical groups or molecules to the nanotube surface to enhance their compatibility with different matrices and to improve their solubility in solvents. This process not only enhances solubility and biocompatibility, but also enables specific molecular recognition, making CNTs suitable for sensing applications and biomedical devices. Furthermore, it enhances the interaction of CNTs with solvents, polymers, and organic molecules, thereby expanding their potential applications [95,96].

The two main functionalization techniques are covalent and non-covalent modifications. Covalent functionalization involves the chemical bonding of functional groups or molecules at the surface of CNTs through strong covalent bonds. This technique mainly results in stable attachment and significant changes in the surface chemistry of the CNTs. The most common method of covalent functionalization is the oxidation of CNTs using strong oxidizing acids, such as H_2SO_4 and HNO_3, due to its efficiency and ease of preparation [97]. This oxidation method results in the opening of CNT tips and the introduction of oxygen-containing functional groups, such as carboxyl, hydroxyl, ketone, and epoxy groups, as well as amine groups [98]. Covalent modification can enhance the dispersibility of CNTs in different solvents, improve their compatibility with polymers or other materials, and introduce specific chemical functionalities for targeted applications. However, covalent functionalization may degrade the mechanical properties of CNTs, disrupts the delocalize π-electron systems, and alter their intrinsic properties [97].

Non-covalent functionalization involves the adsorption or physical attachment of molecules or polymers onto the surface of CNTs through weak non-covalent interactions, such as π-π stacking, Van der Waals forces, hydrogen bonding, or electrostatic interactions [99]. Unlike covalent modification, non-covalent functionalization does not alter the structure of CNTs and generally preserves their intrinsic properties. Common non-covalent modifiers include surfactants, polymers, proteins, and DNA [100]. Non-covalent functionalization can improve the dispersibility of CNTs in solvents, enhance their compatibility with other materials, and introduce specific functionalities without significantly affecting their structure. However, non-covalent interactions may be less stable than covalent bonds, due to the leaching of modifiers over time [101]. Generally, the choice between covalent and non-covalent functionalization depends on the specific

requirements of the application, including the desired stability, compatibility, and functionality of the modified carbon nanotubes, because both methods offer unique advantages and challenges.

1.3.3. Amino acid polymers

Amino acids stand as key components in electrochemistry, serving as electroactive substances crucial for modifying electrode surfaces in the development of advanced electrochemical sensors. Their unique chemical composition makes them ideal for electrode modification. Amino acids contains electron-donating amino functional groups (-NH_2), a characteristic part for their role in electropolymerization [102]. Their electropolymerization involves the oxidation of amino functional groups, generating free cation radicals capable of forming stable covalent bonds with the carbon atoms at the electrode surface [103]. Subsequently, these monomeric units undergo condensation reactions between amino and carboxylic groups, resulting in the formation of peptide linkages. This results in the polymerization of amino acids, thereby yielding amino acid polymers, which characterized by a diverse array of interconnected monomeric units via peptide bonds [104]. The incorporation of amino acids into electrode modification utilizes their inherent electrochemical properties to impart unique functionalities to the electrode surface. For example, amino groups facilitate the formation of stable covalent bonds with electrodes, ensuring robust and durable modifications [105]. In addition, amino acid polymers enhance electron transfer kinetics and stability, which are critical attributes for developing high-performance electrochemical sensing platforms. Furthermore, the incorporation of amino acids into electrode surfaces enables the formation of customized molecular architectures capable of recognizing specific molecules, thereby improving the selectivity and sensitivity of electrochemical sensors and biosensors [106].

Amino acid polymer-modified electrodes represent a versatile approach in electrochemical sensor development, offering a range of advantages that contribute to their widespread use in various applications. One significant advantage is their ability to form stable covalent bonds with electrode surfaces, ensuring robust and long-lasting modifications. This feature is particularly advantageous, as it provides a solid foundation for the attachment of the polymer to the electrode, enhancing the stability and durability of the modified electrode [107]. Additionally, amino acid polymers enhance electron transfer kinetics, facilitating rapid and efficient electron transfer

between the analyte and the electrode surface. This improved electron transfer is crucial for achieving high-performance electrochemical sensing platforms, enabling accurate and precise detection of target analytes [108].

Amino acid polymers such as poly (L-serine), poly (glycine), and poly (L-histidine) are among the widely used materials for electrode modification, each offering unique properties and functionalities that contribute to their efficacy in electrochemical sensor development. Poly(L-serine), for example, possesses a hydrophilic nature due to the presence of hydroxyl (-OH) groups in its side chain, making it suitable for enhancing the stability of the electrode [109]. Additionally, poly(glycine), being the simplest amino acid polymer, offers a high degree of flexibility and biocompatibility, making it ideal for designing a novel architectures at the electrode surfaces [110]. Furthermore, poly(L-histidine) exhibits pH-responsive behavior due to the imidazole group in its side chain, allowing for selective and sensitive sensing under different pH conditions [111].

Amino acid polymers introduce various functional groups to the electrode surface, including amino ($-NH_2$), carboxyl (-COOH), and peptide linkages (-CONH) [112]. These functional groups play critical roles in facilitating the attachment of the polymer to the electrode and providing sites for specific molecular recognition. For instance, the $-NH_2$ groups in poly(L-histidine) enable protonation and deprotonation reactions depending on the pH of the supporting electrolyte [111]. Similarly, the -COOH groups in poly(glycine) and poly(L-serine) can undergo chemical modifications to introduce additional functionalities or facilitate the immobilization of biomolecules or nanoparticles, enhancing the selectivity and sensitivity of the modified electrode [109,110].

Electrodes modified with poly(L-serine), poly(glycine), and poly(L-histidine) find diverse applications across various analytes and target molecules. Poly(L-serine)-modified electrodes are utilized for detecting heavy metal ions in environmental samples due to their capability to chelate metal ions via the carboxyl groups within the polymer backbone [109]. In biosensing, poly(glycine)-modified electrodes are employed for detecting biomolecules like proteins and enzymes, benefiting from the polymer's biocompatibility and flexibility [113]. Similarly, poly(L-histidine)-modified electrodes are applied in biomedical diagnostics for pH-responsive sensing of biological analytes such as DNA and enzymes [114]. In general, amino acid polymers like poly(L-

serine), poly(glycine), and poly(L-histidine) play a significant role in advancing electrochemical sensor technology. These polymers exhibit distinct properties such as hydrophilicity, flexibility, biocompatibility, and pH responsiveness, making them versatile materials for electrode modification. Their application spans across a range of fields, including analytical chemistry, food safety, environmental monitoring, and biomedical research, illustrating the diverse utility of amino acid polymers in enhancing sensor development.

1.3.4. Metal oxide nanoparticles

Nanoparticles, which are between 1 and 100 nm in size, have distinct properties that differentiate them from bulk materials. Their tiny size contributes to a remarkable surface area-to-volume ratio, which increases reactivity and enables applications in catalysis, sensing, and imaging [115]. In particular, nanoparticles exhibit different optical properties due to the plasmonic effect, which, in the case of metallic nanoparticles, manifests in bright colors and underpins their utility in sensing and imaging [116]. The surface chemistry of nanoparticles is crucial as it enables functionalization to improve interactions with other molecules for precise drug delivery and biosensing [117]. Magnetic nanoparticles, such as iron oxide nanoparticles, play an important role in magnetic resonance imaging (MRI), drug delivery systems, and magnetic separation techniques [118]. In addition, nanoparticles exhibit exceptional thermal properties, including high thermal conductivity and heat capacity, leading to applications in thermoregulation, thermoelectric devices, and photo-thermal therapy [119]. In voltammetry, nanoparticles have attracted much attention due to their high surface area, numerous electroactive sites, high conductivity, good adsorption performance, and strong catalytic activity. They can also be used as catalysts in electrochemical processes to speed up the transfer of electrons and catalyze electrochemical reactions [120].

Metal oxide nanoparticles, particularly zinc oxide (ZnO) and nickel oxide (NiO), have emerged as essential materials in voltammetry due to their numerous beneficial properties. These nanoparticles exhibit exceptional catalytic activity, enabling efficient catalysis of various chemical reactions relevant to electrochemical sensing. Additionally, they possess strong adsorption capacities that enhance the effective binding of target analytes to their surfaces, thereby increasing electrode sensitivity [121,122]. Their biocompatibility makes them suitable for biological and

medical applications. Furthermore, they are characterized by high stability, ensuring long-lasting and reliable performance in sensor applications [123]. Importantly, they have low toxicity, minimizing potential health and environmental hazards associated with their use. Their ability to facilitate rapid electron transfer processes further contributes to their effectiveness in electrochemical sensing, enabling fast and accurate detection of analytes. Generally, metal oxide nanoparticles offer a cost-effective solution for the development of sensors, making them ideal for widespread use in various fields [124].

Zinc oxide (ZnO) is a semiconductor material with a wide band gap of about 3.37 eV and a large exciton binding energy of 60 meV [125]. It exhibits excellent physical and chemical properties, including a large surface area, a high isoelectric point, excellent film-forming ability, easy availability, good electrical conductivity, high crystallinity, synthesis at low temperatures, strong catalytic activity, and biocompatibility. ZnO-NPs are known for their large surface-to-volume ratio, which enables high sensitivity in sensor applications [126]. They possess unique properties such as piezoelectricity, UV absorption, and photocatalytic activity, making them suitable for various applications, from gas sensing to biomedical devices. In electrochemical sensors, ZnO-NPs are widely used due to their excellent catalytic properties, fast electron transfer kinetics, and ability to improve the sensitivity and selectivity of sensors for detecting various analytes, including gases, heavy metals, and biomolecules [127]. Nickel oxide (NiO) is another metal oxide nanoparticle with a narrower band gap, typically around 3.6 eV. It exhibits special physical and chemical properties, including high electrical conductivity, chemical stability, and corrosion resistance [128]. NiO-NPs are often used in electrochemical sensors due to their unique redox properties and catalytic activity. They can facilitate electron transfer reactions, increase the stability of electrode surfaces, and improve the sensor performance for the detection of different analytes [129]. Generally, nanoparticles, including ZnO and NiO, are widely used in electrochemical applications for several reasons. First, their large surface-to-volume ratio provides a large active surface area for interactions with analytes, resulting in higher sensitivity and better detection limits. Secondly, their tunable physical and chemical properties allow them to be adapted to specific sensing requirements. They offer better stability, reproducibility, and durability compared to conventional sensor materials. In addition, the ease of synthesis and functionalization

of nanoparticles enables the development of versatile and efficient electrochemical sensors for a wide range of applications.

In addition to the metal oxide nanoparticles mentioned previously, iron-doped polyaniline (Fe-dop-PANI) and polyethylene oxide (PEO) are known for their unique properties and applications, particularly in the development of electrochemical sensor. Fe-dop-PANI represents a subclass of conductive polymers characterized by their unique electrical properties and flexibility. The doping process, in which iron atoms are introduced into the polyaniline structure, increases conductivity and sensitivity to the target analytes [130]. These materials are used in electrochemical sensor applications where the interactions between Fe-dop-PANI and the analytes lead to measurable changes in electrical properties [131]. Fe-dop-PANI layers can be tactically deposited on electrode surfaces to create sensor interfaces optimized for the detection of specific analytes. Through precise manipulation of polymer morphology and chemical composition, Fe-dop-PANI sensors provide selectivity for target molecules, enabling robust detection amidst complex sample matrices [132]. Similarly, PEO serves as a versatile binder and matrix material in the development of electrochemical sensors and offers a unique combination of mechanical stability, biocompatibility, and ionic conductivity [133]. As a binder, PEO immobilizes sensing elements such as metal oxide nanoparticles or conductive polymers within sensor architectures, preserving structural integrity and preventing material loss [134]. The high ionic conductivity of PEO, especially when complexed with certain salts, facilitates ion transport through solid-state electrolytes and thus improves sensor performance. In addition, PEO-based sensor matrices ensure compatibility with biological systems and exhibit chemical resistance that ensures long-term reliability under various operating conditions [135]. The porous nature of PEO matrices promotes the diffusion of analytes to the active sensor sites, resulting in increased sensitivity and fast response times, thus improving electrochemical sensor functions in various fields [136].

1.3.5. Gold-silver alloy nanoparticles

Gold and silver are precious metals that are known for their distinct physical and chemical properties. Gold is a dense, malleable, and ductile metal known for its bright yellow color, which makes it highly desirable for decorative and ornamental purposes. Due to its exceptional thermal and electrical conductivity, it is often used in electronics and electrical applications. Due to its

noble nature, gold does not tarnish or corrode and retains its shiny appearance for a long time. Although it is generally unreactive, it can form compounds with certain elements, such as cyanide or mercury, which are used in gold extraction processes such as cyanidation [137]. Silver, a shiny white metal known for its exceptional reflectivity and luster, is also malleable and ductile, so it can be molded into various shapes. It has high thermal and electrical conductivity, and used in mirrors, jewelry, and electrical contacts. Although it tarnishes over time when exposed to sulfur compounds and forms a dark oxide layer, silver remains relatively stable and does not react to most acids. However, it can react with sulfur, halogens, and other reactive elements to form compounds such as silver nitrate, which has antiseptic properties and is used in medicine [138,139].

Gold and silver nanoparticles are tiny particles that are typically 1 to 100 nanometers in size and have unique physical and chemical properties due to their small size. Due to their extraordinary properties, gold nanoparticles (Au-NPs) have become key players in various fields. In biomedicine, they are extensively researched for targeted drug delivery, utilizing their ability to penetrate cell membranes and deliver therapeutic agents to specific tissues [140]. In addition, they serve as contrast agents in imaging modalities such as computed tomography (CT) and photoacoustic imaging, providing high-resolution images for disease diagnosis [141]. Recent advances include the development of multifunctional gold nano-platforms that can combine therapeutic and diagnostic functions, paving the way for personalized medicine [142]. In addition, Au-NPs are being used in the field of plasmonics to enhance the interactions between light and matter, enabling advances in areas such as photo-thermal therapy and surface-enhanced Raman spectroscopy (SERS). Their applications in environmental sensing are constantly evolving. Researchers are exploring their use in the detection of pollutants, heavy metals, and pathogens in water and air [143].

Silver nanoparticles (Ag-NPs) play an important role in various fields, especially in healthcare, where their strong antimicrobial properties are used to heal wounds and fight infections. Recent research has focused on optimizing their antibacterial efficacy while minimizing potential cytotoxicity to mammalian cells to ensure their safe use in medical applications [144]. In electronics, silver nanoparticles are an integral part of conductive inks used in printed electronics, enabling the production of flexible and stretchable electronic devices. They also play a critical role

in the development of next-generation catalysts for green chemistry applications, including selective oxidation reactions and carbon dioxide reduction [145,146]. In nanotechnology, advances in the synthesis and functionalization of silver nanoparticles have led to their incorporation into advanced materials with tailored properties such as increased conductivity, mechanical strength, and optical transparency, enabling new applications in energy storage, sensing, and catalysis [147]. In general, gold and silver nanoparticles continue to drive innovation in various disciplines, with ongoing research focused on expanding their capabilities and applications. By using their unique properties at the nanoscale, scientists can revolutionize fields ranging from healthcare and electronics to environmental monitoring and sustainable chemistry, finding solutions to pressing global challenges and pushing technological boundaries.

Gold and silver alloys nanoparticles (Au-Ag-ANPs) are an emerging field of research with significant advances in recent years. These alloyed nanoparticles combine the unique properties of both metals and offer advantages such as tunable physical and chemical properties, enhanced electrochemical activity, and improved stability [148]. Recent developments in alloyed nanoparticle synthesis techniques, such as controlled colloidal synthesis and nanoscale alloying, have enabled precise control of particle size, composition, and morphology, resulting in tailored properties optimized for specific sensor applications [149]. In addition, advances in surface functionalization strategies have facilitated the integration of alloyed nanoparticles into sensor platforms with improved biocompatibility, stability, and selectivity. For example, the development of novel ligands and surface modification techniques has enabled the immobilization of alloy nanoparticles on electrode surfaces, ensuring efficient electron transfer and improving sensor performance. In addition, new strategies such as template synthesis and bottom-up assembly approaches offer new opportunities for the development of complex nanostructures with unique properties for advanced sensor applications [150].

In the development of electrochemical sensors, the alloying of Au-Ag-NPs offers several distinct advantages over single metal nanoparticles. Recent studies have shown that the synergistic effects between gold and silver atoms result in alloyed nanoparticles with enhanced catalytic activity, enabling faster electron transfer and higher sensitivity to target analytes [151]. This increased electrochemical activity has been utilized for the development of high-performance sensors capable of detecting trace amounts of analytes with unprecedented sensitivity and

selectivity. In addition, the versatility of Au-Ag-ANPs enables the development of multifunctional sensor platforms that can detect multiple analytes simultaneously or be integrated with other sensing elements to improve performance [152]. Recent advances in microfabrication technology and sensor miniaturization have enabled the integration of alloy nanoparticles into compact, portable sensor devices for on-site analysis in various fields, including environmental monitoring, biomedical diagnostics, and food safety analysis [153].

Beyond traditional electrochemical sensing applications, Au-Ag-ANPs hold promise in emerging fields such as wearable sensors, point-of-care diagnostics, and environmental monitoring. Their compatibility with flexible substrates and integration into miniaturized sensor devices facilitate the development of wearable and portable sensor platforms for real-time monitoring of physiological parameters, environmental pollutants, or food contaminants. Additionally, the biocompatibility and stability of alloy nanoparticles make them suitable for implantable biosensors and biomedical devices, offering opportunities for advanced healthcare monitoring and personalized medicine. The high sensitivity and selectivity of alloy nanoparticle-based sensors, combined with their robustness and ease of use, make them promising tools for monitoring environmental quality and safeguarding public health [154]. Furthermore, advances in nanomaterial characterization techniques, such as transmission electron microscopy (TEM), XRD, and SERS, have provided insights into the structure-property relationships of alloy nanoparticles, aiding in the rational design of sensors optimized for environmental sensing applications [155,156].

Gold-silver alloy nanocoral clusters (Au-Ag-ANCCs) represent a novel nanostructure comprising Au and Ag atoms structured in a coral-like morphology, characterized by intricate porosity and interconnectedness. The formation of these nanocoral clusters typically involves controlled synthesis techniques, such as template-assisted deposition or galvanic replacement reactions, which allow precise control over the size, shape, and composition of the clusters. This structural design results in a highly porous network with numerous active sites available for electrochemical interactions, making them advantageous for sensor applications [157]. One of the primary advantages of Au-Ag-ANCCs in electrochemical sensor development is their exceptionally high surface area-to-volume ratio. This large surface area provides a vast number of active sites for analyte adsorption and electrochemical reactions, enhancing the sensitivity of the

sensor. Additionally, the porous structure of nanocoral clusters facilitates rapid diffusion of analytes to the electrode surface, enabling faster response times and improved detection limits compared to conventional sensor materials. This enhanced mass transport is particularly beneficial for detecting low-concentration analytes in complex sample matrices [158].

The alloying of gold and silver in nanocoral clusters offers synergistic effects that further enhance their electrochemical performance. Gold is well-known for its excellent electrical conductivity and catalytic activity, while silver possesses antimicrobial properties and contributes to the overall stability of the alloy structure. By combining these properties, Au-Ag-ANCCs exhibit enhanced electrochemical activity, enabling efficient electron transfer and improved sensor response [159]. Moreover, the presence of silver in the alloy composition enhances the sensor's resistance to fouling and biofouling, ensuring reliable and robust performance in practical applications [160]. Furthermore, the three-dimensional morphology of nanocoral clusters imparts mechanical stability and durability to the sensor platform. This structural robustness enables the sensor to withstand mechanical stress and environmental factors, making it suitable for long-term monitoring applications. Additionally, the interconnected pore network of nanocoral clusters allows for efficient electrolyte penetration and ion transport, leading to stable and reproducible electrochemical responses over multiple measurement cycles. These attributes make Au-Ag-ANCCs ideal candidates for the development of high-performance electrochemical sensors for various applications, including environmental monitoring, biomedical diagnostics, and industrial process control [161].

Thermal annealed gold-silver alloy nanoporous matrices (TA-Au-Ag-ANpM) are advanced nanostructures with intricate designs that are promising for the development of electrochemical sensors. These matrices are synthesized through meticulous processes that often involve controlled thermal annealing to create a porous framework of Au and Ag atoms. The result is a three dimensional network of interconnected nanoporous structures that provide a large surface area with many active sites for electrochemical interactions [162]. Advanced techniques such as self-assembly and template synthesis are used to synthesize these matrices, allowing precise control over their composition, morphology, and pore size distribution. TA-Au-Ag-ANpMs offer numerous advantages in the development of electrochemical sensors. Firstly, their intricate nanoporous structure confers an exceptionally high surface area to volume ratio, a property that is

essential for improving sensor sensitivity. This increased surface area facilitates the adsorption of analytes to the sensor surface, resulting in improved electrochemical signal transduction. In addition, the porous nature of these matrices promotes efficient mass transport of analytes to the electrode surface, alleviating diffusion limitations and enabling fast response times. Consequently, sensors using these matrices have a higher sensitivity and allow the detection of trace analytes with remarkable precision and accuracy [163].

The composition of Au and Ag in the nanoporous alloy matrices can be precisely tuned during synthesis, which offers further advantages in the development of electrochemical sensors. By adjusting the alloy composition, the electrochemical behavior of the matrices can be modulated to meet the specific requirements of different sensor applications. For example, the ratio of gold to silver can influence the conductivity, catalytic activity, and stability of the matrices, allowing fine-tuning of sensor performance. This versatility in composition allows researchers to optimize sensor properties based on factors such as the type of analyte, detection limits, and environmental conditions, increasing the versatility and applicability of these matrices in sensor technology [164]. Mechanical stability and durability are of paramount importance in the development of electrochemical sensors, and TA-Au-Ag-ANpM excels in these aspects. The robust nanoporous structure provides the matrices with a mechanical resistance that ensures their integrity and functionality under harsh operating conditions. This resilience enables the integration of nanoporous matrices into durable sensor platforms that function reliably over long periods. In addition, the structural stability of these matrices increases the robustness of the sensors, making them suitable for use in various environments, such as field and industrial applications [165]. Furthermore, the versatility of TA-Au-Ag-ANpM also extends to their functionalization and adaptation to specific capture tasks. Researchers can incorporate additional components, such as enzyme catalysts, molecular recognition elements, or nanomaterials, into the matrices to increase sensor functionality. The functionalization of the matrices improves the selectivity and specificity of the sensor and enables the detection of target analytes amidst complex sample matrices with minimal interference from other species [166].

In general, TA-Au-Ag-ANpMs represents an innovative approach to the development of electrochemical sensors. They offer a variety of advantages, such as increased surface area, fast mass transport, tailored composition, mechanical stability, and versatile functionalization. These

matrices have immense potential to revolutionize sensor technology and enable the development of highly sensitive, reliable, and customizable sensor platforms for a variety of applications. With continued research efforts focused on refining synthesis techniques and exploring novel functionalization strategies, TA-Au-Ag-ANpM is poised to drive innovation in sensor technology and address new challenges in analytical chemistry and biosensing.

1.3.6. Nanocomposite materials

A nanocomposite material represents a sophisticated combination of different substances, each retaining its own unique chemical and physical characteristics while synergistically interacting at their interfaces to produce enhanced properties not achievable by any individual component alone [167]. Nanocomposites typically comprise two primary constituents: the reinforcement, or filler, and the matrix. The reinforcement imparts desirable traits, such as mechanical strength, electrical conductivity, thermal stability, or optical transparency, augmenting the inherent properties of the matrix material. This combination results in a material with enhanced characteristics suitable for a wide range of applications [168]. In the search for advanced materials with exceptional attributes, the development of novel nanocomposite materials has emerged as a focal point of scientific research and technological innovation. Among the countless types of nanocomposites, those based on conducting amino acid polymers have garnered significant attention in recent years. The nanocomposites offer a surplus advantages, including flexibility, facile synthesis, ease of film formation, cost-effectiveness, high electrical conductivity, a large surface area, and the ability to encapsulate biomolecules. These properties render them highly appealing for diverse applications, spanning from flexible electronics and wearable devices to energy storage systems and biosensors [169].

However, the widespread adoption of conducting polymer-based nanocomposites has been hindered by inherent challenges associated with processing and performance. The extended conjugated chain structure and tendency to agglomerate pose significant hurdles, leading to diminished electrical conductivity and solubility. To overcome these limitations, researchers have turned to the development of nanocomposite materials that leverage the complementary properties of individual components to enhance overall performance [170]. By carefully designing nanocomposite configurations, scientists aim to optimize properties such as electrical conductivity,

mechanical strength, thermal stability, and chemical resistance, thereby unlocking the full potential of conducting polymer-based nanocomposites for various applications. In recent years, significant strides have been made in the exploration of nanocomposite configurations specifically for electrochemical sensor development. These configurations aim to combine the unique advantages of individual modifier-based composites to achieve hypersensitivity, ultra-selectivity, and enhanced sensor performance. By integrating conducting polymers with suitable reinforcement materials, such as metal oxides, *r*-GO, or *f*-MWCNTs, researchers seek to develop sensor platforms capable of precisely detecting target analytes at trace levels across diverse sample matrices [171]. Furthermore, advancements in nanomaterial synthesis, characterization techniques, and sensor fabrication methods have enabled precise control over composite morphology, composition, and interface properties, resulting in the development of novel sensor architectures with superior sensitivity, stability, and reliability.

1.4. Research gap and motivation

Antibiotic residues in food and water are a pressing global issue due to their adverse effects on human health and the environment. Current detection methods, such as chromatography and mass spectrometry, although highly accurate, are often limited by their complexity, high costs, time-consuming nature, and the need for extensive sample preparation. These methods are not easily adaptable for rapid, on-site, or real-time monitoring, which is crucial for timely decision-making and intervention. Furthermore, traditional electrochemical sensors, while promising, often struggle with issues related to sensitivity, selectivity, and stability, particularly in complex matrices like food and water. Many existing electrochemical sensors fail to detect antibiotic residues at the low concentration levels required to ensure safety and compliance with regulatory standards. There is also a significant gap in the ability to simultaneously detect multiple antibiotic residues using a single sensor platform, which would greatly enhance efficiency and reliability in monitoring practices.

Given the limitations of current methodologies, there is a compelling need to develop advanced electrochemical sensors that can overcome these challenges. The motivation for this research stems from the urgent necessity to provide a more effective, reliable, and user-friendly

approach to detect antibiotic residues. The development of such sensors would have profound implications for public health, food safety, and environmental protection.

The proposed research aims to fill this gap by designing and fabricating novel electrochemical sensors that integrate cutting-edge materials and nanotechnology. Specifically, the use of Au-Ag-ANCCs, TA-Au-Ag-ANpM, poly amino acids, carbon based modifiers, and metal oxide nanocomposites offers a promising pathway to significantly enhance sensor performance. These materials are chosen for their exceptional properties, such as high surface area, excellent electrical conductivity, catalytic activity, and robust chemical stability, which are crucial for achieving high sensitivity and selectivity. By developing a sensor capable of detecting antibiotic residues at picomolar levels, this research seeks to provide a powerful tool for ensuring food and water safety. The ability to perform simultaneous detection of multiple antibiotics will streamline monitoring processes and offer more comprehensive insights into contamination levels. This advancement not only addresses a critical gap in current detection technologies but also aligns with global efforts to combat antibiotic resistance and safeguard public health.

In general, the motivation behind this study is to develop an innovative, and practical solution that enhances the detection of antibiotic residues through advanced electrochemical sensing. This research aspires to contribute significantly to the fields of analytical chemistry and environmental monitoring, ultimately leading to safer food and water supplies and a healthier population.

1.5. Objectives of the study

1.5.1. General objective

The main objective of this work is to develop novel, hypersensitive, ultraselective, and exceptionally performing electrochemical sensors for simultaneously and individually determining residues of selected antimicrobial drugs (ciprofloxacin, tinidazole, chloramphenicol, rifampicin, norfloxacin, vancomycin, ceftriaxone, sulfathiazole, sulfamethoxazole, metronidazole, azithromycin, enrofloxacin, nitrofurantoin, and furazolidone) in various food matrices and water samples.

1.5.2. Specific objectives

The specific objectives of the study include:

- To synthesize gold-silver alloy nanocoral clusters (Au-Ag-ANCCs), thermally annealed gold–silver alloy nanoporous matrices (TA-Au-Ag-ANpM), iron-doped polyaniline (Fe-dop-PANI), nickel oxide nanoparticles (NiO-NPs), and zinc oxide nanoparticles (ZnO-NPs) for the modification of different electrodes.
- To functionalize and characterize multi-walled carbon nanotubes (MWCNTs) and graphene oxide (GO).
- To develop a simple, highly sensitive and selective electrochemical sensors by modifying CPE and GCE using choline chloride (ChCl).
- To develop a novel electrochemical sensor by integrating Au-Ag-ANCCs with *f*-MWCNTCPE and ChCl.
- To develop a pioneering electrochemical sensor by incorporating Au-Ag-ANCCs with reduced graphene oxide (*r*-GO) and poly(L-histidine) composites at the surface of GCE.
- To fabricate hypersensitive voltammetric sensor by decorating TA-Au-Ag-ANpM with *f*-MWCNTs-CPE and poly(L-serine) nanocomposites.
- To fabricate ultraselective voltammetric sensor comprising TA-Au-Ag-ANpM integrated with *r*-GO and poly(glycine) at the surface of a GCE.
- To develop multi-elemental nanocomposite electrochemical sensor by integrating TA-Au-Ag-ANpM with Fe-dop-PANI and NiO-NPs at the surface of a GCE.
- To fabricate a cutting-edge electrochemical sensor by integrating Au-Ag-ANCCs with ZnO-NPs-CPE and polyethylene oxide (PEO) nanocomposites.
- To characterize the structural and electrochemical properties of the developed sensors and their constituting composite materials using CV, EIS, UV-Vis, FT-IR, XRD, SEM and EDX techniques.
- To use the developed electrochemical sensors under the optimized experimental conditions for the simultaneous and individual determination of the intended antibiotics via SWV.

Chapter Two

2.1. Electrochemical methods and instruments

2.1.1. Electrodes in voltammetry

In most voltammetric measurements, a three-electrode system is typically employed to accurately measure and facilitate the electrochemical processes. This system is crucial for providing precise control and measurement capabilities, which are essential for studying the kinetics, thermodynamics, and mechanisms of the electrochemical reactions. The three electrodes used for the voltammetric measurements were the reference, counter, and working electrodes. Each electrode plays a unique role in accurately performing the electrochemical reactions. A schematic representation of a typical three-electrode system electrochemical cell is presented in Figure 7 [172].

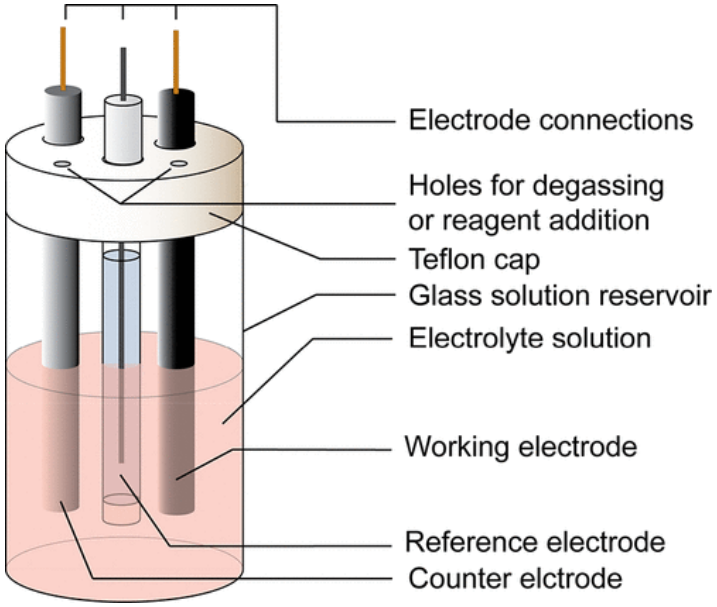

Figure 7. Schematic representation of a typical three-electrode system voltammetric cell.

2.1.1.1. Reference electrode

The reference electrode functions as a stable benchmark for controlling and measuring the potential of the working electrode without current passing through it. This maintains a consistent

and known potential against which the working electrode potential is referenced. As the name suggests, the reference electrode served as the standard for referencing the working electrode potential [173]. Importantly, the potential remained unaffected by the electrolyte composition being investigated. Reference electrodes are typically manufactured using materials that exhibit stable and reversible redox reactions. They must exhibit reversible half-reactions with potentials dictated by the Nernst equation and maintain consistent and constant potentials over time [174]. Common reference electrodes include a saturated calomel electrode (SCE) ($Hg/Hg_2Cl_2(s)$/saturated KCl) and silver/silver chloride electrode (Ag/AgCl). SCE contains liquid mercury in contact with a saturated solution of mercury (I) chloride and potassium chloride, with a Pt wire linked to the solution of interest. The Ag/AgCl electrode consisted of Ag wire coated with AgCl immersed in a saturated KCl solution [175].

2.1.1.2. Counter electrode

The counter electrode, also known as the auxiliary electrode, plays a vital role in enabling the passage of current between the working and the reference electrodes. Its primary function is to efficiently conduct the necessary current to drive electrochemical reactions at the working electrode efficiently. An ideal counter electrode should exhibit low resistance to promote unhindered current flow and should not participate in the redox processes of the target analyte [176]. Counter electrodes are typically fabricated from both electrochemically and chemically inert materials. The most common materials used as counter electrode include platinum, graphite, gold, and conductive carbon. To prevent reactions from occurring in the vicinity of the electrode by dictating the overall current flow in the system, the surface area of the auxiliary electrode must surpass that of the working electrode [177].

2.1.1.3. Working electrode

The working electrode serves as the focal point in electrochemical sensors, where the intended redox reactions and charge transfer takes place, a fundamental component influencing the performance of voltammetric devices [178]. As a result, careful selection of the working electrode material is vital for experimental success. Several factors govern the choice of working electrode for electrochemical analysis, including the potential window, redox behavior of the target

analyte, electrical conductivity, surface reproducibility, chemical inertness, cost-effectiveness, availability, and toxicity considerations [179]. The most commonly used electrode materials includes mercury, noble metals (silver, platinum and gold), and carbon-based electrodes. Mercury electrodes were predominant in earlier voltammetric techniques, notably polarography [180]. They offer distinct advantages, including renewal of the electrode surface, prevention of surface passivation, the capacity to form amalgams with different metals, and a high hydrogen overpotential [181]. However, recently the widespread use of mercury electrodes was reduced, mainly due to environmental and health concerns associated with mercury toxicity. Furthermore, the limited anodic potential range of mercury electrodes poses challenges for examining some analytes in the oxidation mode, as the mercury itself undergo oxidation at low potentials [182].

Metal-based electrodes, such as gold, silver, and platinum, are widely utilized as working electrodes in electrochemical applications due to their inherent properties. These electrodes are prized for their inertness, ease of manipulation, nontoxic nature, wide potential windows, high electrical conductivity, and minimal background currents [183]. Despite these advantages, metal electrodes have certain limitations. One notable limitation is the low overpotential for hydrogen evolution exhibited by these electrodes, which constrains the cathodic potential range that is available for electrochemical processes. Moreover, under high anodic potentials in aqueous environments, these metals may corrode to generate metal oxide layers, impeding electron transfer kinetics and compromising the reproducibility of the measurements [184].

Like that of metal electrodes, carbon based electrodes also have played a vital role in the construction of working electrode due to their numerous beneficial properties. They are known for their low background currents, wide potential range, versatile surface chemistry that can be easily modified, easy renewal of electrode surface, high hydrogen and oxygen over voltages, cost-effectiveness, and chemical inertness [185]. However, carbon-based electrodes are noted for their slower electron transfer kinetics when compared to their metal-based counterparts. There are various types of carbon electrodes, including carbon fiber, glassy carbon electrodes, carbon paste electrodes, screen-printed carbon electrodes, and pyrolytic graphite [186]. These electrodes can be classified into homogeneous types, which consist of purely carbon materials like glassy carbon electrodes, fullerenes, carbon nanotubes, diamond, and graphite, and heterogeneous types that

combine carbon with other substances, such as carbon paste and screen-printed carbon electrodes [178,187].

Recently, working electrodes based on nanocomposite materials have gained a significant attention for various electrochemical applications due to their exceptional properties and versatility. Nanocomposites, consisting of nanostructured materials incorporated within a matrix, offer unique advantages, such as enhanced electrical conductivity, increased surface area, improved mechanical strength, and tailored functionalities, making them promising candidates for diverse electrochemical applications [188]. For instance, carbon-based nanocomposites, such as graphene-based nanomaterials and carbon nanotubes incorporated into polymer matrices, have shown remarkable performance as working electrodes for electrochemical sensor development [189]. These nanocomposites exhibited high electrical conductivity and mechanical stability, enabling efficient charge transfer. Additionally, metal oxide-based nanocomposites such as titanium dioxide-graphene hybrids and zinc oxide-carbon nanotube composites have demonstrated excellent performance in electrochemical sensors and biosensors [190]. These nanocomposites exhibit enhanced sensing capabilities, rapid response times, and increased sensitivity owing to their large surface-to-volume ratios and synergistic effects between the components [191]. Moreover, nanocomposite catalysts, such as gold, platinum nanoparticles supported on carbon nanotubes or graphene, have shown remarkable catalytic activity and durability in voltammetric applications. This underscores the growing significance of nanocomposite materials in advancing various electrochemical technologies, offering tailored solutions for efficient sensing and catalytic applications [192].

2.1.2. Supporting electrolyte solutions

In voltammetry, the supporting electrolyte solution acts as a crucial component that goes beyond merely facilitating the electrochemical reactions; it is essentially the backbone of the entire process. Its primary function is to maintain a stable environment within an electrochemical cell, which is paramount for obtaining reliable and reproducible results [193]. One of its key roles is to increase the ionic strength of a solution. By providing a high concentration of electrolyte ions, the supporting electrolyte ensures that the solution maintains a consistent ionic environment, which is vital for proper functioning of the electrochemical cell. This stability prevents fluctuations that can

skew measurements and compromise the accuracy of the analysis [194]. Moreover, the presence of ions in the supporting electrolyte solution significantly increases the electrical conductivity of the solution. This heightened conductivity facilitates efficient electron transfer at the electrode-electrolyte interface, thereby enhancing the overall performance of the electrochemical system [195]. Furthermore, the supporting electrolyte solution plays a pivotal role in minimizing the background noise and interference, thus improving the signal-to-noise ratio of the measurements. This is particularly crucial for obtaining clear and accurate electrochemical signals, especially in complex samples or when dealing with low analyte concentrations [196].

Various factors must be carefully considered while selecting a supporting electrolyte solution to ensure an optimal performance. These include compatibility with the analyte and electrode material, chemical stability under experimental conditions, appropriate ionic strength for specific electrochemical measurements, maintenance of the desired pH range, and easing of background noise and interference [197]. The supporting electrolyte solution should be highly pure chemicals and resist rapid oxidation or reduction. In voltammetry, commonly used supporting electrolyte solutions are inorganic salts (potassium chloride, sodium sulfate, and potassium nitrate), mineral acids (perchloric acid and sulfuric acid), and buffer solutions, each offering unique advantages and chosen based on the specific requirements of the experiment [198]. In general, the selection of an appropriate supporting electrolyte solution is important for successful electrochemical experiments. It not only ensures the reliability, reproducibility, and accuracy of the measurements but also serves as a foundation for achieving meaningful insights in various fields ranging from analytical chemistry to environmental monitoring and beyond.

2.1.3. Modes of mass transfer in voltammetry

Voltammetry is a highly effective analytical method for investigating electrochemical reactions that quantifies the current as a function of the applied potential. Mass transfer is a critical aspect of voltammetry as it regulates the movement of electroactive species to and from the electrode surface, thereby impacting the recorded electrochemical behavior. The three primary modes of mass transfer in voltammetry are diffusion, convection and migration [172].

2.1.3.1. Convection

Convection refers to the movement of electroactive species induced by the bulk fluid flow. In voltammetry, convection can occur owing to external stirring or flow of the electrolyte solution, vibration of the electrochemical cell, and rotation of the electrode. Convection enhances mass transfer by rapidly replenishing the electroactive species at the electrode surface. However, excessive convection can disrupt the diffusion layer near the electrode surface, leading to deviations from ideal diffusion-limited behavior [199].

2.1.3.2. Migration

Migration involves movement of charged species in an electric field. In voltammetry, this occurs when an external potential is applied to the working electrode, leading to the migration of ions towards or away from the electrode surface based on their charge. For example, if the electrode carries a positive charge, the anion will move toward the electrode, and the cation will move toward the bulk solution, and vice versa. Unlike diffusion and convection, migration only affects the mass transport of charged particles [173].

2.1.3.3. Diffusion

Diffusion is the primary mode of mass transfer in voltammetry, it involves the movement of electroactive species from regions of high concentration (bulk solution) to regions of low concentration (near the electrode surface). Concentration gradients between the bulk solution and the vicinity of the electrode arise because of electro-oxidation or the reduction of electroactive species around the electrode surface. As a result, the concentration of the analyte at the electrode surface decreases, and thus, more reactants diffuse from the bulk solution towards the electrode surface at a speed proportional to the concentration gradient. In voltammetry, diffusion-limited conditions are often desired to ensure that the rate of the electrochemical reaction at the electrode surface is higher than the rate of mass transfer of the electroactive species to the electrode [172].

2.1.4. Types of electrode reactions in voltammetry

In electrochemical reactions, kinetic effects play a crucial role in determining the rate at which electrons are transferred between the electrode and electroactive species present in the solution. The rate of the electrode reaction depends on two main factors: the transport of the electroactive species to the electrode surface and the rate of electron transfer between these species and the electrode interface. Assessing the electron transfer rate at the electrode surface allows the classification of the electron transfer kinetics of a redox pair into three main categories: reversible, irreversible, or quasi-reversible, each exhibiting distinct characteristics [200].

2.1.4.1. Reversible electrode reaction

An electrochemical reaction is considered reversible when the electron transfer rate at the electrode surface surpasses the mass transport rate of electroactive species from the solution to the electrode surface [200]. In reversible systems, the current is primarily governed by mass transport. At the electrode-solution interface of reversible systems, equilibrium between the reduced and oxidized forms of the electroactive species is rapidly established, typically with a minimal overpotential [174]. The equilibrium is described quantitatively by the Nernst equation (Equation 1), where the ratio of the concentrations of the reduced species (C_R) to the oxidized species (C_O) at the interface corresponds to the electrode potential [172].

$$E = E^0 + \frac{RT}{nF} \ln \frac{C_R}{C_O} \quad (1)$$

where E = applied potential, C_R = concentration of reduced species, C_O = concentration of oxidized species, E° = standard electrode potential, n = number of electrons, F = Faraday constant, R = universal gas constant and T = temperature. The Nernst equation describes the correlation between the concentrations and the electrode potential, irrespective of the current flow. A cyclic voltammogram for a reversible process contains essential parameters such as anodic peak potential (E_{pa}), cathodic peak potential (E_{pc}), anodic peak current (I_{pa}) and cathodic peak current (I_{pc}). The peak current (Ip) of a reversible electrode reaction (at 25 °C) is related to concentration by the Randles-Sevcik equation (2) [172].

$$I_p = 2.69 \times 10^5 n^{3/2} A D^{1/2} C v^{1/2} \quad (2)$$

where I_p, n, A, D, C and υ are peak current, number of electrons transferred at the electrode surface, electroactive surface area (cm^2), diffusion coefficient (cm^2s^{-1}), concentration ($molcm^{-3}$) and scan rate (Vs^{-1}), respectively. According to equation (2), the peak current in a reversible process is directly proportional to the square root of the diffusion coefficient, the concentration of the electroactive species, and the square root of the scan rate. For a reversible electrode reactions, anodic and cathodic peak potential separation is independent of scan rate (Figure 8). Peak potential separation is equal 0.059/n (equation 3) [201].

$$\Delta E_p = \left| E_{pa} - E_{pc} \right| = \frac{2.3RT}{nF} = \frac{0.059}{n} \quad (3)$$

where ΔE_p = peak potential separation, E_{pa} = anodic peak potential and E_{pc} = cathodic peak potential, n = number of electrons transferred, F = Faraday constant, R = universal gas constant and T = absolute temperature. The formal potential (E^o) centered between E_{pa} and E_{pc} in the voltammogram is the average of the two peak potentials (equation 4) [202].

$$E^0 = E_{1/2} = \frac{E_{pa} + E_{pc}}{2} \quad (4)$$

For a reversible system, both I_{pa} and I_{pc} increase proportional to $v^{1/2}$. The ratio of the forward and reverse peak currents is independent of the scan rate and is equal to unity (equation 5) [203].

$$\frac{I_{pa}}{I_{pc}} = 1 \quad (5)$$

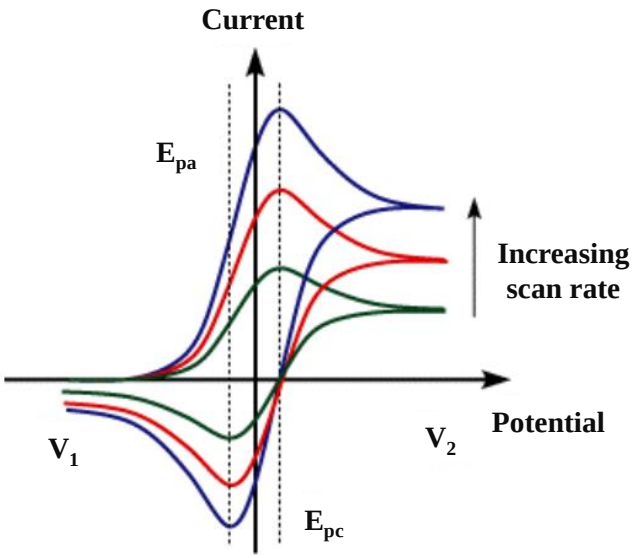

Figure 8. Cyclic voltammogram of reversible electrode reaction at different scan rates.

2.1.4.2. Irreversible electrode reaction

In an irreversible electrochemical reaction, the rate of electron transfer at the electrode surface is slower than the mass transfer, establishing electron transfer as the rate-limiting step. This scenario is characterized by a significantly low exchange current density and standard heterogeneous rate constant. Consequently, the electron transfer rate is insufficient to maintain an equilibrium; thus, the concentrations of the oxidized and reduced species are no longer related to the Nernst equation at a given scan rate. To facilitate this reaction, an irreversible electrochemical reaction requires a substantial overpotential. A distinguishing feature of an irreversible system is the absence of a reverse peak in the cyclic voltammogram, as illustrated in Figure 9. Moreover, it is known by a shift in the peak potential at varying scan rates [172]. For an irreversible electrode process, the peak potential (E_p) is given by equation 6.

$$E_p = E^0 - \frac{RT}{\alpha F}\left[0.780 + \ln\left(\frac{\sqrt{D}}{K_s}\right) + \sqrt{\frac{\alpha F v}{RT}}\right] \quad (6)$$

where α = charge-transfer coefficient, K_s = heterogeneous electron-transfer rate constant, R = universal gas constant, F = Faraday constant, T = absolute temperature, D = diffusion coefficient, and v = scan rate. In an irreversible electrode process, a substantial overpotential is necessary to

initiate the charge transfer reaction. Equation (7) describes the peak current for an irreversible system [204].

$$I_p = 2.99 \times 10^5 \alpha^{1/2} A D^{1/2} n^{3/2} v^{1/2} C \quad (7)$$

At 25°C, the peak potential and the half-peak potential differ by 47.7 mV/α (equation 8).

$$E_p - E_{\frac{1}{2}} = 1.857 \frac{RT}{\alpha F} = \frac{47.7}{\alpha} \text{ mV} \quad (8)$$

2.1.4.3. Quasi-reversible electrode reaction

Quasi-reversible systems represent an intermediate state between fully reversible and irreversible electrochemical systems and are characterized by moderate electron transfer kinetics. In these systems, the rate of electron transfer is neither extremely slow nor exceptionally high. Compared to fully reversible processes, the voltammograms of quasi-reversible systems display broader peaks with a greater separation between their peak potentials. Additionally, the voltammograms exhibit a more elongated shape and the peak intensities are reduced (Figure 9). Notably, the increase in the peak current with the square root of the scan rate ($\nu^{1/2}$) is not linear. The separation between the anodic and cathodic peak potentials (ΔE) exceeds the theoretical value of 0.059/n, and tends to increase at higher scan rates. In quasi-reversible processes, both the mass transfer and charge transfer mechanisms influence the peak current, as described by the Randles-Sevcik equation (9) [55,201].

$$I_p = 2.65 \times 10^5 A D^{1/2} n^{3/2} v^{1/2} C \quad (9)$$

In quasi-reversible systems, with increasing scan rates, both the reduction and oxidation peak potentials exhibit slight shifts in the negative and positive directions, respectively. The interrelation between the peak potentials, heterogeneous rate constant, and scan rate is described by equations (10), (11), and (12) [205,206].

$$E_{pa} = E^o + \frac{2.303RT}{(1-\alpha)nF}\left(\log v + \log \frac{(1-\alpha)nF}{RTk_s}\right. \quad (10)$$

$$E_{pc} = E^{o} - \frac{2.303RT}{\alpha nF}(\log v + \log\frac{\alpha nF}{RTk_s} \quad (11)$$

$$\log k_s = \alpha\log(1-\alpha) + (1-\alpha)\log\alpha - \log\frac{RT}{nFv} - \alpha(\frac{(1-\alpha)nF\Delta E_p}{2.3RT}) \quad (12)$$

where E^o = formal potential, T = temperature, R = universal gas constant, α = transfer coefficient, v = scan rate, n = number of electrons transferred, F = Faraday's constant, K_s = heterogeneous electron transfer rate constant and ΔE_p = peak-to-peak potential separation. The equations provided above are used to determine the electron transfer coefficient (α), number of electrons (n), and heterogeneous electron transfer rate constant (k_s) for both reversible and quasi-reversible electrode reactions. A comparison of the cyclic voltammograms obtained for the reversible, quasi-reversible, and irreversible systems at the same formal potential (E^o) is shown in Figure 9.

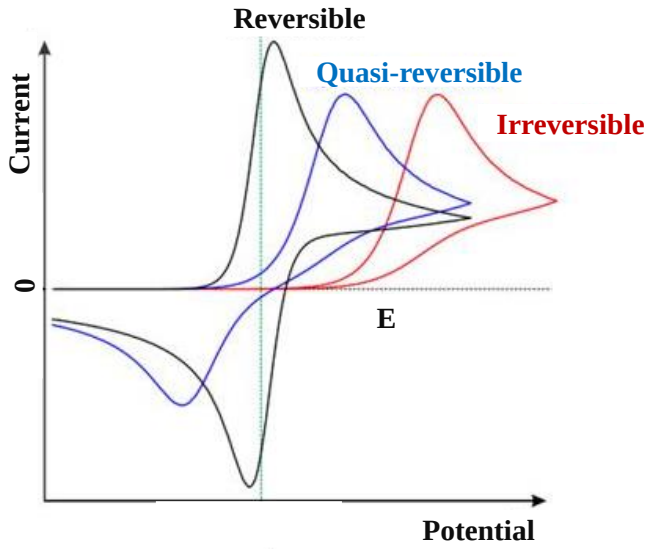

Figure 9. Comparison of cyclic voltammograms of the electron transfer processes for reversible, quasi-reversible, and irreversible electrode reactions.

Cyclic voltammetry serves as a valuable tool for investigating both the diffusion and adsorption behaviors of electroactive species, while also providing kinetic insights. The nature of the electrode reaction can be deduced from the relationship between the scan rate and peak current. When the peak current varies proportionally to the square root of the scan rate, it indicates diffusion-controlled kinetics. Conversely, if the peak current is proportional to the scan rate, then

the electrode reaction is governed by adsorption. Moreover, valuable information regarding electrode processes can be obtained from the slope of the linear plot depicting the logarithm of peak current (log I_p) *vs.* the logarithm of the scan rate (log *v*). Specifically, slope values of 0.5 and 1 correspond to diffusion and adsorption-controlled processes, respectively [207]. Intermediate slope values may indicate a "mixed" diffusion-adsorption mechanism. Furthermore, CV facilitates the determination of the quantity of electroactive species adsorbed onto the electrode surface, which is known as the surface coverage. In adsorption-controlled processes, the peak current is directly correlated with surface coverage and scan rate, as given in equation (13) [204].

$$I_p = \frac{n^2 F^2 \Gamma A v}{4RT} \quad (13)$$

where Γ = absorption capacity (mol cm^{-2}), A = electrode surface area (cm^2), n = number of electrons, F = Faraday's constant, υ = scan rate, R = universal gas constant, and T = temperature. The equation is used to calculate the surface concentration of the adsorbed species at the electrode surface for adsorption-controlled process.

2.1.5. Electrochemical methods

Voltammetry is an electrochemical method in which a specific voltage profile is applied to a working electrode as a function of time and the current produced by the system is measured. The applied potential induces the oxidation or reduction of electroactive species at the electrode surface. The resulting current is directly proportional to the analyte concentration [208]. In voltammetric techniques, the measured current comprises two components: faradaic and non-faradaic currents [209]. The faradaic current arises from the oxidation or reduction of electroactive species in the electrolyte solution at the electrode surface, which directly correlates with the concentration of the analyte. Moreover, it relies on the electron transfer rate at the electrode surface and mass transport of the electroactive species [210]. The non-faradaic current arises from the change in the structure of the electrode-solution interface owing to the movement of electrolyte ions in the electrolyte solution [211]. A charging current, or capacitive current, occurs when the electrical double layer at the working electrode is charged or discharged. This double layer arises from electrostatic interactions between the cations or anions and the electrode surface, balancing the electrode charge [212]. Voltammetric techniques are prized for their high sensitivity and

selectivity, enabling the precise quantification of analyte concentrations. Widely utilized in analytical chemistry, environmental monitoring, and biomedical research, these methods offer versatility and applicability to a broad range of analytes and sample matrices [213]. Voltammetric techniques can be classified into several categories based on the method used to apply a potential to the working electrode and to measure the resulting current. Some common classifications of voltammetric techniques are discussed below.

2.1.5.1. Sweep voltammetric techniques

Linear sweep voltammetry

Linear sweep voltammetry (LSV) is a fundamental voltammetric technique that is simple and useful for electrochemical analysis. In this method, a linearly changing potential is applied to the working electrode, starting from an initial potential and progressing to a final potential as a function of time (Figure 10A) [214]. In LSV, the working electrode undergoes a linear potential scan at a constant rate in one direction, from positive to negative or vice versa, corresponding to reduction and oxidation, respectively [215]. As the potential scan progressed, current was generated from the oxidation or reduction of electroactive species at the electrode surface upon reaching their oxidation or reduction potentials. The resultant current, measured as a function of the applied potential, yields valuable insights into redox behavior, kinetics, and analyte concentration [216]. A linear sweep voltammogram, represented by plotting the current against the applied potential (Figure 10B), reveals a characteristic trend where the current increases with potential until it reaches a maximum, after which it diminishes owing to the consumption of electroactive species near the electrode interface [217]. However, LSV is seldom employed for quantitative determination because of the increasing charging current with increasing scan rate. This phenomenon led to an amplified contribution of the charging current to the total current, thereby diminishing the signal-to-noise ratio of the LSV. Consequently, the decrease in the ratio of faradaic current to capacitive current results in reduced sensitivity and detection limits [218]. Thus, LSV primarily provides qualitative insights into the electrochemical behavior of a given analyte, rather than providing precise quantitative data. Key parameters in LSV include the peak potential (E_p), half-peak potential ($E_{p/2}$), half-peak current ($i_{p/2}$), and peak current (ip), which offer valuable information regarding the electrochemical system under investigation [219].

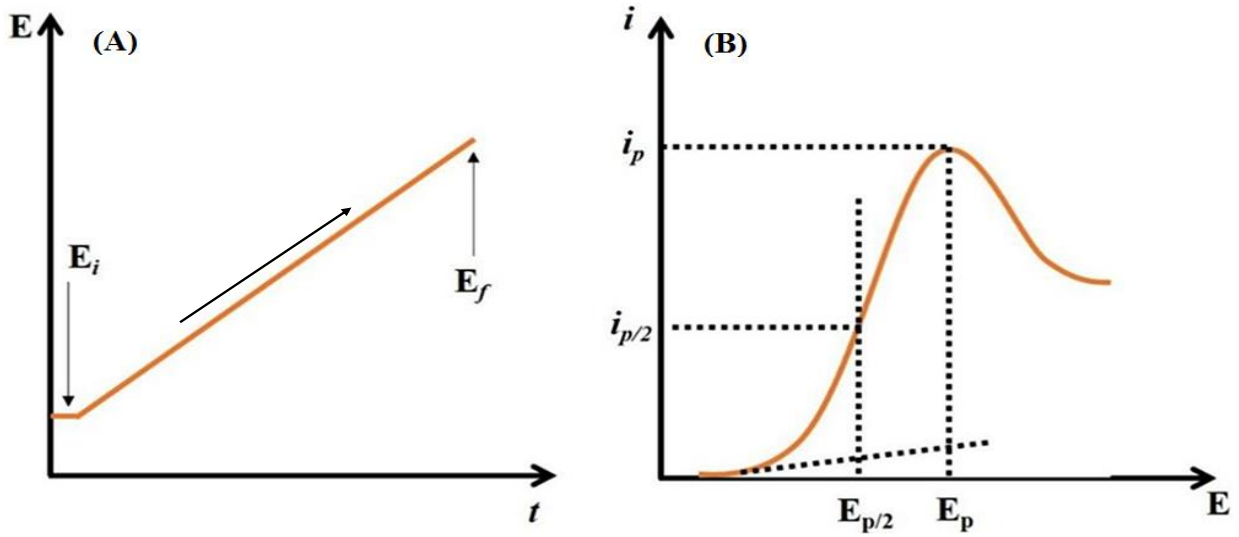

Figure 10. Excitation signal for LSV (A) and linear sweep voltammogram (B).

Cyclic voltammetry

Cyclic voltammetry (CV) is one of the most extensively employed sweep potential techniques and is primarily utilized to obtain qualitative insights into electrochemical reactions. Owing to its reliability and rapid characterization capabilities, CV offers valuable information regarding the redox behavior of analytes at the electrode surfaces [220]. It serves as a powerful tool for understanding crucial aspects of electrochemical processes, including the potential at which oxidation or reduction occurs, adsorptive or diffusive nature of electrode processes, reaction mechanisms, number of electrons, rate of electron transfer, and associated chemical processes [221,222]. In a CV experiment, the current is monitored while cycling the potential at a fixed scan rate between the initial potential (E_i) and the final potential (E_f) in both the forward and reverse directions [223]. Upon reaching the end of the first scan (E_f), the potential scan direction was reversed to E_i to obtain a cyclic scan. The potential applied to the working electrode changes over time at a certain rate, which is termed the excitation signal. For CV, the excitation signal commonly consists of a linear potential scan with a triangular waveform, as shown in Figure 11A. The selection of potential values (E_i and E_f) is crucial to ensure that the oxidation or reduction processes of electroactive species occur within the potential interval. During the experiment, the potentiostat measures the current generated in the redox process, resulting in a plot of current versus applied potential, known as a cyclic voltammogram [224]. This graphical representation offers valuable

insights into the electrochemical behavior of the system under investigation, aiding the interpretation of various electrochemical phenomena.

A characteristic cyclic voltammogram representing a reversible electrochemical process is given in Figure 11B. Consider the reversible process R ⇌ O + ne, where R is the reduced species, O is the oxidized form of the same species, and ne represents the number of electrons transferred during the electrochemical reaction. Initially, the bulk solution contains only R, resulting in no net conversion of R to O at potentials lower than the initial potential. Upon the application of a positive potential from the value where no reaction occurs during the first half of the cycle, an anodic current is observed. This current steadily increases with potential until it reaches a peak (point B). At this anodic peak (point B), the redox potential becomes sufficiently positive such that any R reaching the electrode surface is instantaneously oxidized to O. Subsequently, upon reversing the potential scan direction (point C), the electrochemically generated oxidized species (O) from the forward scan are reduced back to R, resulting in the observation of a cathodic peak (point D) [225]. Hence, the development of a diffusion layer near the electrode surface resulted in the formation of characteristic peaks in the cyclic voltammogram. The parameters typically measured from cyclic voltammograms include the anodic peak potential (E_{pa}), cathodic peak potential (E_{pc}), anodic peak current (i_{pa}), and cathodic peak current (i_{pc}). These parameters provide crucial insights into the kinetics and thermodynamics of the electrochemical reaction under investigation, aiding in the comprehensive understanding and interpretation of cyclic voltammetric data.

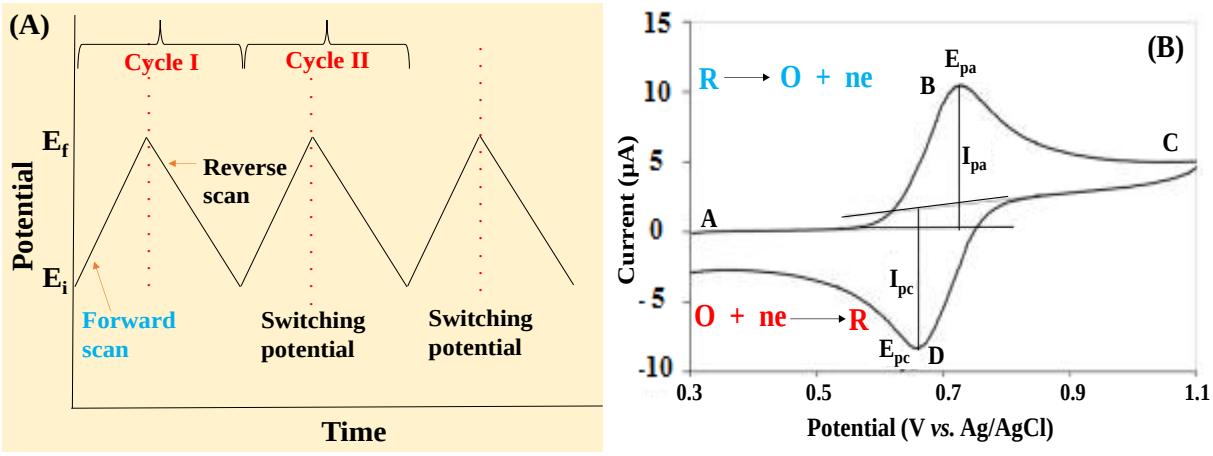

Figure 11. Excitation signal for CV (A) and cyclic voltammogram (B).

2.1.5.2. Pulse voltammetric techniques

Pulse voltammetric techniques were used to analyze the current response as a function of changes in potential and time. These methods have been developed to improve the sensitivity and lower detection limits of voltammetric analysis by addressing the challenge of charging currents [200]. The difference in potential between the working and reference electrodes initiates the oxidation or reduction of electroactive species and causes charging and discharging of the electrical double layer at the electrolyte-electrode interface [226]. Although the current generated by the electrical double layer (non-faradaic current) is typically insignificant for analytical use, it can interfere with the faradaic current. In the case of low analyte concentrations, the non-faradaic current may overshadow the faradaic current, resulting in reduced sensitivity and higher detection limits [227]. Pulse techniques address this issue by introducing pulsed current through potential variations. These techniques operate based on the difference in the decay rates of the faradaic and charging currents following a potential step or pulse. The charging current (i_c) decreases exponentially with time (e^{-kt}), whereas the faradaic current (i_f) decreases as $t^{-1/2}$ [228]. This causes the non-faradaic current to decay significantly faster than the faradaic current after the potential pulse ceases, leading to a higher ratio of faradaic to capacitive currents (i_f/i_c) when utilizing pulse techniques. Consequently, pulse techniques enhance the sensitivity and reduce the detection limits in electrochemical measurements, making them ideal for quantitative analysis. The key parameters in pulse techniques include pulse width (duration of the potential pulse), pulse amplitude (height of the potential pulse), and sampling period (time when the current is measured at the end of the potential pulse) [229]. Optimizing these parameters is crucial for maximizing the performance and efficiency of the pulse techniques in analytical applications.

Normal pulse voltammetry

Normal pulse voltammetry (NPV) is a widely employed technique for electrochemical analysis. In NPV, a series of distinct potential pulses is applied to the working electrode with a constant pulse duration and increasing amplitude, followed by return to the initial potential value after each pulse [230]. The current signal was sampled at the end of the applied potential pulse, allowing sufficient time for the decay of the non-faradaic current. Pulse durations typically range from 1 to 200 ms, while the intervals between pulses typically range from 0.1 to 5 s [231]. NPV

offers advantages such as enhanced sensitivity, selectivity, and temporal resolution compared with traditional sweep voltammetry methods because of its thinner diffusion layer, resulting in a higher faradaic current [232]. By analyzing the resulting current relative to the applied potential, the NPV provides valuable insights into the redox behavior, kinetics, and concentration of electroactive species at the electrode surface [230]. This technique is widely applied in different fields such as analytical chemistry, environmental monitoring, and biomedical research owing to its versatility and ability to deliver rapid and accurate analysis of electrochemical systems. Figure 12 illustrates a typical potential-time excitation signal and the resulting voltammogram.

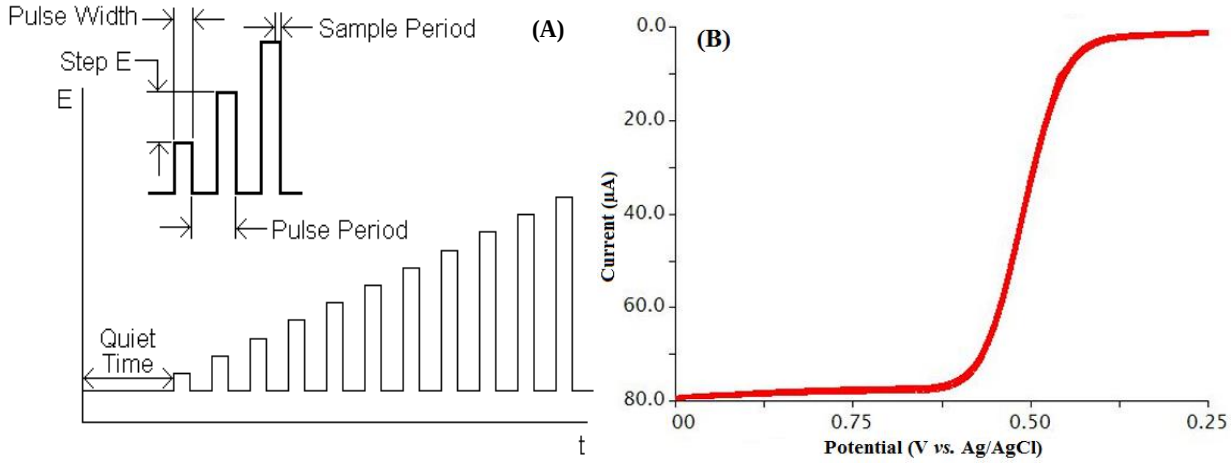

Figure 12. Potential excitation signals (A) and voltammograms for NPV (B).

Differential pulse voltammetry

Differential pulse voltammetry (DPV) is a well-established electrochemical technique known for its high sensitivity and low detection limits for the analysis of electroactive species. Unlike NPV, it involves the application of a series of pulses of constant amplitude on a linear ramp potential [233]. Each pulse consisted of a small constant amplitude superimposed on a slowly changing base potential. In DPV, the current is sampled at two key points for each pulse: first, immediately before the pulse is applied, and second, at the end of the pulse [234]. The resulting current response is obtained by subtracting the current measured during the reverse pulse from that measured during the forward pulse. This process effectively eliminates the background and capacitive currents, leading to enhanced sensitivity. The peak height in the differential pulse voltammogram is directly proportional to the concentration of the analyte [235]. DPV is

particularly useful for detecting low concentrations of analytes in complex matrices because of its high signal-to-noise ratio, which is characterized by a significant faradaic current compared to the charging current [236]. DPV is widely utilized in analytical chemistry, biochemistry, environmental monitoring, and pharmaceutical analysis owing to its advantages, such as low detection limits and minimal interference from background currents. Its robust capabilities make DPV an essential tool in electrochemical analysis, enabling the precise and reliable determination of analyte concentrations even in challenging sample matrices [237]. Figure 13 illustrates a typical potential-time excitation signal and the resulting voltammogram.

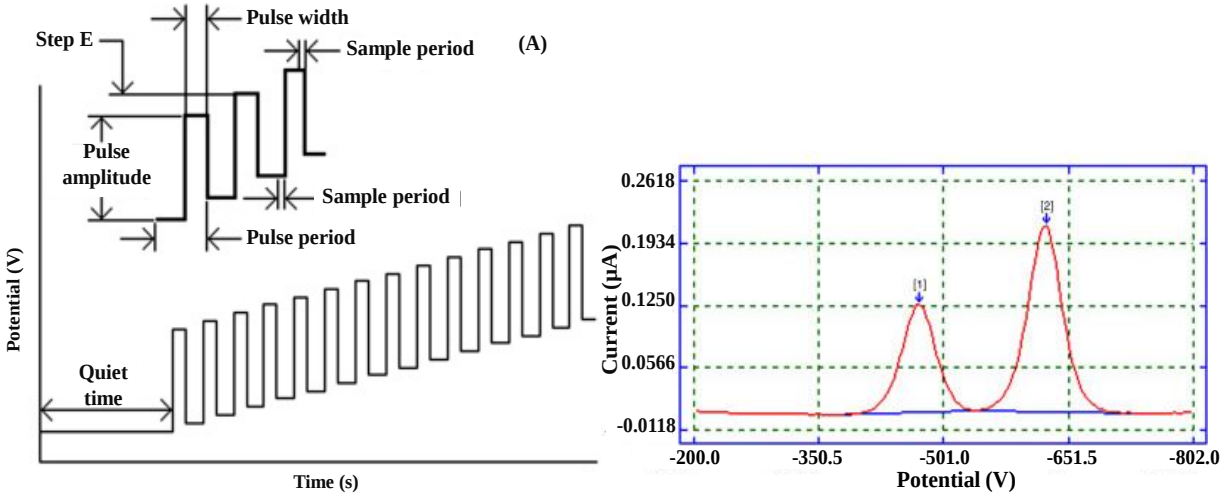

Figure 13. Potential excitation signals (A) and voltammograms for DPV (B).

Square-wave voltammetry

Square wave voltammetry (SWV) is a pulse technique that involves the application of a combined square wave and staircase potential to a working electrode. Their applications span various fields, including food, medicine, and the environment [238]. In SWV, the potential-current curve is shaped by applying potentials of height ΔE (pulse amplitude), which vary based on the potential step (E_{step}) and τ duration. On the potential-time curve, the pulse width (τ/2) is represented as t, and the pulse frequency is denoted as f (1/t). The currents were measured at the end of the forward (I_1) and reverse (I_2) pulses and the signal was obtained as the intensity of the resulting differential current (ΔI). SWV offers exceptional sensitivity and effectively rejects capacitive currents. The measurement began at the initial time (t_i) when the working electrode was polarized

at a potential where no redox reaction occurred [239,240]. Figure 14(A) provides a detailed illustration of the potential application of SWV, defining the parameters used. Figure 14(B) depicts the theoretical voltammograms for reversible (a) and irreversible (b) systems, showing the separation of the forward, reverse, and resulting currents. Because the reverse current sign is opposite to that of the forward current, the net current is the sum of the absolute values of both current components, resulting in a higher value than either the reverse or forward current alone [241]. SWV exhibits higher sensitivity compared to most voltammetric techniques because of the measurement of both forward and reverse currents, leading to a net current extent greater than that of the individual forward or reverse current components [242]. This technique offers numerous advantages, including exceptional sensitivity, low detection limit, ability to discriminate background currents, and rapid analysis capabilities. Moreover, SWV enables the elucidation of electrochemical reaction mechanisms and evaluation of fast electron transfer kinetics. Currently, SWV has emerged as a crucial analytical tool, considering the time-consuming, intricate, and costly methods of chromatography and spectrophotometry [243].

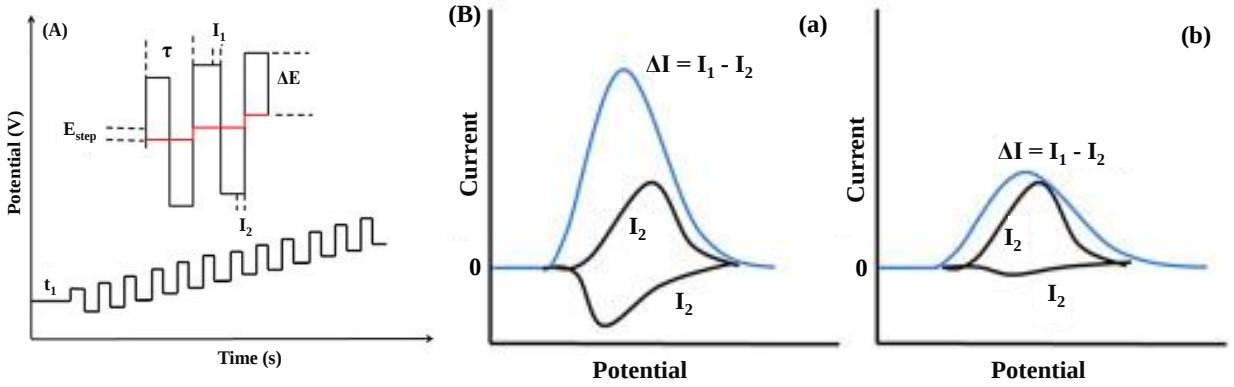

Figure 14. (A) Potential excitation signals and (B) schematics of SWV voltammogram representing a redox process for a reversible (a) and an irreversible system (b).

2.1.6. Electrochemical impedance spectroscopy

Electrochemical impedance spectroscopy (EIS) is a highly sensitive characterization technique used to establish the electrical response of chemical systems in a nondestructive manner. EIS systems characterize the time response of chemical systems using low amplitude alternating current (AC) voltages over a range of frequencies [244]. It plays a crucial role in uncovering the kinetic and mechanistic details across various electrochemical systems, with applications spanning

corrosion studies, semiconductor research, energy conversion and storage, chemical sensing, biosensing, and noninvasive diagnostics [245]. Impedance, a measure of a circuit resistance to electrical current flow, differs from resistance by not following Ohm's law, and is influenced by the frequency of the applied signal [246]. Evaluating the electrochemical impedance involves applying an AC potential to the working electrode and measuring the resulting current. When an electrochemical cell is subjected to sinusoidal potential excitation, the current response displayed a sinusoidal pattern at the corresponding frequency with a different phase. In EIS analysis, the outcomes are separated into real and imaginary components upon applying an AC potential to an electrochemical cell. The complex impedance (Z) comprises the real part Z', corresponding to resistors in line with the voltage, and the imaginary part Z", associated with capacitors that show a phase shift with respect to the applied potential. The absolute impedance |Z| is determined by the vector sum of Z' and Z", as described in equation 14 [247].

$$|\mathbf{Z}| = \left|(\mathbf{Z}')^{\mathbf{2}} + (\mathbf{Z}'')^{\mathbf{2}}\right|^{\mathbf{1/2}} \quad (14)$$

The response of EIS is typically depicted through Nyquist and Bode plots, with the Nyquist plot being the more widely utilized representation. In the Nyquist plots, the imaginary components of impedance, derived from the double-layer capacitance, are plotted against the real part of the impedance at different frequencies. The electrical circuits exhibit frequency-dependent impedance variations [244]. The Nyquist plot involves plotting the real impedance on the x-axis and the imaginary impedance on the y-axis across varying frequencies. As illustrated in Figure 15, the EIS plot contains two distinctive sections: a semicircle at high frequencies and a linear segment at low frequencies. The high frequency semicircle indicates the charge transfer resistance (R_{ct}) of the electrode, whereas the low-frequency linear line indicates a diffusion-limited process (the rate-limiting step during the transportation of reactants and products to and from the electrode surface). Moreover, a smaller semicircle diameter indicates a faster electron transfer rate, whereas a larger diameter indicates a slower electron transfer rate [248,249].

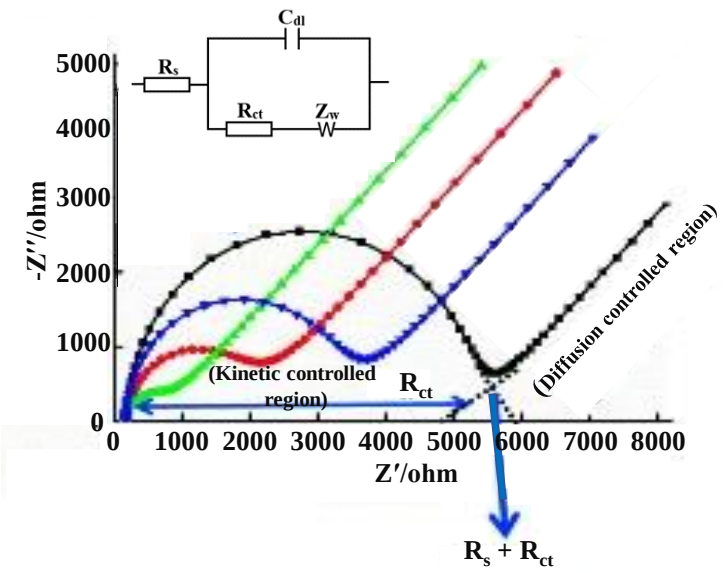

Figure 15. Nyquist plot (Insets: Randle's equivalent circuit).

The variation of impedance with frequency is a distinctive characteristic of electrical circuits. When analyzing EIS data, researchers use an equivalent electrical circuit model that is customized to represent the system being studied. One such widely used model is Randle's equivalent circuit, which is shown in the inset of Figure 15, and includes components such as the solution resistance (R_s), the double layer capacitance (C_{dl}), the charge transfer resistance (R_{ct}), and the Warburg impedance (Z_w) [250].

The solution resistance (R_s), also known as electrolyte resistance, is the resistance that appears in the electrolytic solution between the working and reference electrodes. R_s is independent of frequency and can be observed at the highest frequency interception of the real axis, marking the starting point of the semicircle in the Nyquist plot. A high R_s value will shift the semicircle to higher x-axis values. At higher frequencies, impedance is entirely dictated by Ohmic resistance, with the entire current flowing through this element. Hence, R_s is introduced as a series element in the equivalent circuit [248]. The double-layer capacitance (C_{dl}) arises from the charges accumulated at the electrode-electrolyte interface, resembling a pure capacitor. The extent of charge accumulation is influenced by factors such as the electrode surface area and ion size. Double-layer capacitance is impervious to Faradaic processes and increases with enlarging electrode surface area [251].

Warburg impedance (Z_w) indicates resistance to mass transfer or diffusion processes, and its magnitude is influenced by the perturbation frequency. The linear impedance portion at lower frequencies indicates a diffusion-limited process. High-frequency impedance indicates low Warburg impedance as the reactants require minimal diffusion. Conversely, at low frequencies, the distance traversed by diffusing reactants elevates the Warburg impedance, predominantly manifesting in the low-frequency spectrum [252]. Charge transfer resistance (R_{ct}) represents the resistance linked to charge transfer mechanisms during electrode reactions, governing electron transfer kinetics at the electrode interface. The high-frequency semicircle in the Nyquist plot corresponds to the R_{ct} at the electrode surface. The diameter of the semicircle represents the charge transfer resistance at the electrode surface, with larger semicircles indicating sluggish electron transfer kinetics. R_{ct} is mathematically related to the heterogeneous electron transfer rate constant (k^o) and exchange current density (J_o) via equations (15) and (16), respectively [253].

$$R_{ct} = \frac{RT}{n^2F^2AK^0C} \quad (15)$$

$$R_{ct} = \frac{RT}{nJ_0AF} \quad (16)$$

where R_{ct} = electron transfer resistance (Ω), R = universal gas constant (8.314 $JK^{-1}mol^{-1}$), T = temperature (298 K), F = Faraday constant (96485 C mol^{-1}), J_o = exchange current density (A/cm^2), k^o = electron transfer rate constant (cms^{-1}), A = electrode surface area (cm^2), C = concentration of the bulk species, and n = number of electrons involved in the electrode reaction.

2.2. Characterization techniques

2.2.1. Ultraviolet-visible spectroscopy

Ultraviolet-visible (UV-Vis) spectroscopy operates on the principle of molecular absorption of light in the UV and visible regions of the electromagnetic spectrum. When a beam of UV-Vis light passes through a sample, molecules within the sample absorb specific wavelengths of light based on their electronic structure. The absorption of light leads to electronic transitions within the molecules, causing electrons to move from lower to higher energy levels [254]. The working principle of UV-Vis spectroscopy involves measuring the intensity of transmitted or absorbed light as a function of wavelength. A spectrophotometer, the instrument used for UV-Vis spectroscopy,

typically consists of a UV-Vis light source, a monochromater to select specific wavelengths of light, a sample holder, and a detector to measure the intensity of light passing through the sample [239]. In a UV-Vis spectrophotometer, a beam of polychromatic light is directed through the sample. The monochromater selects a specific wavelength of light, which passes through the sample. The detector then measures the intensity of the transmitted light. By scanning across a range of wavelengths and measuring the corresponding absorbance or transmittance values, a UV-Vis spectrum can be obtained. The concentration of a sample can be determined through the absorption spectra produced at specific wavelengths using the Beer-Lambert law. The law states that for a given material, the path length and concentration of the sample are directly proportional to the absorbance of the light. Hence, UV-visible spectroscopy enables the determination of the sample concentration based on the Beer-Lambert Law given by equation (17) [255,256]:

$$A = \varepsilon c l \tag{17}$$

where A = absorbance, l = optical path length (cm) of the cell or cuvette, c = concentration of the solution (mol dm^{-3}), and ε = molar absorptivity of the compound or molecule in solution. Molar absorptivity remains constant for a specific substance at a particular wavelength ($dm^3mol^{-1}cm^{-1}$).

The absorption spectrum produced by UV-Vis spectroscopy provides information about the electronic transitions occurring in the molecules within the sample. Each compound absorbs light at characteristic wavelengths, leading to unique absorption spectra that can be used for identification and quantification purposes [257]. UV-Vis spectroscopy is particularly useful for analyzing samples containing chromophores, which are chemical groups capable of absorbing UV or visible light. Common chromophores include conjugated double bonds, aromatic rings, and transition metal complexes. By studying the absorption patterns of these chromophores, researchers can gain insights into the composition, structure, and concentration of compounds in a sample [254]. Overall, UV-Vis spectroscopy is a powerful analytical technique with broad applications in chemistry, biochemistry, environmental science, pharmaceuticals, and materials science, providing valuable information about molecular composition and electronic transitions in a wide range of samples.

2.2.2. Fourier-transform infrared spectroscopy

Fourier-transform infrared (FT-IR) spectroscopy is a powerful analytical technique widely used in various scientific fields to analyze the chemical composition of samples. Its principle relies on the interaction of infrared (IR) radiation with molecules, which causes specific chemical bonds to absorb IR radiation at characteristic frequencies. These frequencies correspond to the vibrational modes of the bonds within the molecule, providing valuable information about its structure and composition [258]. FT-IR spectroscopy is based on the Fourier transform mathematical technique that converts the time-domain interferogram signal obtained from the instrument into the frequency-domain spectrum, allowing for the identification of specific absorption peaks associated with different functional groups. The instrumentation of FT-IR spectroscopy consists of several key components, including an IR radiation source, an interferometer, a sample compartment, and a detector [259]. The IR radiation source emits a broad spectrum of IR light, typically generated by a heated filament or a ceramic source. This IR radiation is directed towards the interferometer, where it is split into two beams by a beam splitter. One beam travels through the sample, while the other serves as a reference. After passing through the sample, both beams are recombined, creating an interference pattern known as an interferogram. This interferogram contains information about the absorption of IR radiation by the sample as a function of wavenumber [260].

The interferogram obtained from the interferometer is subjected to Fourier transformation, a mathematical process that converts the signal from the time domain to the frequency domain. This transformation separates the individual frequency components of the interferogram, revealing the IR absorption spectrum of the sample. The resulting spectrum represents the intensity of absorbed IR radiation as a function of wavenumber, providing detailed information about the molecular vibrations present in the sample [261]. FT-IR spectroscopy is sensitive to various types of molecular vibrations, including stretching, bending, and combination modes of different chemical bonds. Each functional group within a molecule exhibits characteristic absorption peaks in the FTIR spectrum, allowing for the identification and quantification of specific chemical moieties within the sample. For example, the presence of functional groups such as C-H, O-H, N-H, C=O, and C-C bonds can be identified based on their unique absorption frequencies [262]. FT-IR spectroscopy finds applications in a wide range of scientific disciplines, including chemistry, material science, pharmaceuticals, environmental science, and forensics. It is commonly used for

chemical analysis, material characterization, quality control of pharmaceuticals and polymers, environmental monitoring of air and water pollutants, and forensic analysis of trace evidence. Its non-destructive nature, high sensitivity, and ability to provide detailed molecular information make it an indispensable tool in modern analytical laboratories [263].

2.2.3. X-ray diffraction

X-ray diffraction (XRD) is a versatile analytical technique based on the principle of scattering of X-rays by crystalline materials. When X-rays interact with the atoms in a crystalline sample, they undergo scattering due to the interaction with the electron cloud around each atom [264]. This scattering leads to the generation of diffracted X-rays, which can interfere constructively or destructively depending on the angles and phases of the scattered waves. The resulting diffraction pattern contains information about the arrangement of atoms within the crystal lattice [265]. The basic principle of XRD is governed by Bragg's law, which describes the relationship between the angle of incidence (θ), the wavelength of the incident X-rays (λ), and the spacing between the crystal planes (d) within the sample. Mathematically, Bragg's law is expressed as (equation 18) [266]:

$$2d\sin(\theta) = n\lambda \quad (18)$$

where n is an integer representing the order of diffraction. The law explains why certain angles of incidence produce peaks in the diffraction pattern, corresponding to constructive interference between the diffracted X-rays.

XRD instruments typically consist of three main components: an X-ray source, a sample holder, and a detector. The X-ray source emits monochromatic X-rays, usually with wavelengths in the range of 0.1 to 1 nm. These X-rays are directed towards the sample, which is mounted on a sample holder. The detector measures the intensity of the diffracted X-rays at various angles as the sample is rotated, allowing the generation of a diffraction pattern [267]. The diffraction pattern obtained from XRD experiments provides valuable information about the crystal structure of the sample. By analyzing the positions and intensities of the diffraction peaks, researchers can determine various structural parameters, such as lattice parameters, unit cell dimensions, crystal symmetry, and atomic arrangement. This information is crucial for understanding the physical and

chemical properties of the material under investigation [268]. One important application of XRD is in the determination of particle size in crystalline materials. This is often achieved using the Scherrer's equation, which relates the broadening of diffraction peaks to the size of crystalline domains within the sample. The equation (19) is given by [269]:

$$D = \frac{K\lambda}{\beta\cos(\theta)} \tag{19}$$

where D is the average crystallite size, K is a dimensionless shape factor (typically around 0.9), λ is the wavelength of the X-rays, β is the full width at half maximum (FWHM) of the diffraction peak, and θ is the Bragg angle. By measuring the FWHM of specific diffraction peaks and applying the Scherrer equation, one can estimate the average size of the crystalline domains in the sample. Generally, XRD is a powerful technique for characterizing the structure of crystalline materials and is widely used in materials science, chemistry, geology, and other fields. Its ability to provide detailed information about crystal structure, phase composition, and particle size makes it an invaluable tool for both research and industrial applications [270].

2.2.4. Scanning electron microscopy

Scanning electron microscopy (SEM) is an advanced imaging technique used to examine the surface morphology, composition, and properties of materials at high resolution. It operates on the principle of interacting a focused beam of electrons with a sample to generate various signals that provide detailed information about its surface characteristics [271]. In SEM, a beam of electrons is generated by an electron gun and accelerated towards the sample. When the electrons interact with the atoms in the sample, they undergo various interactions, including elastic scattering, inelastic scattering, and secondary electron emission. These interactions provide valuable information about the topography, composition, and other properties of the sample surface [272]. The interaction between the primary electron beam and the sample leads to various processes, each offering unique insights into the properties of the sample. Elastic scattering occurs when some electrons interact with the atomic electrons of the sample without losing energy. This process provides valuable information about the atomic structure of the material, including details about the arrangement of atoms and the crystal lattice [273]. Inelastic scattering, on the other hand, involves electrons transferring energy to the sample atoms, resulting in excitation or ionization.

This interaction can lead to the emission of characteristic X-rays or Auger electrons, which can be analyzed to determine the elemental composition of the sample [274]. Additionally, a significant portion of the primary electrons undergo secondary electron emission, where low-energy electrons are ejected from the surface of the sample due to the impact of the primary beam [275]. These secondary electrons carry essential information about the surface morphology, topography, and texture of the material, allowing for detailed characterization of surface features and structures. Together, these interactions in SEM provide comprehensive information about the composition, structure, and surface properties of a sample, making SEM a powerful tool for material characterization and analysis [276].

SEM instruments, at their core, integrate a sophisticated array of components to facilitate the intricate process of sample analysis and imaging. The electron gun, functioning as the primary electron beam source, employs advanced mechanisms such as filaments or field emission sources to generate electrons. These electrons are accelerated by an anode, preparing them for their crucial role in sample interrogation [277]. As the electron beam navigates through the instrument, it traverses a meticulously designed pathway comprising electromagnetic lenses and precision apertures. These components meticulously focus and shape the electron beam, ensuring optimal interaction with the sample surface. Meanwhile, the sample stage serves as the platform for sample mounting, offering impeccable precision in positioning and versatile movement capabilities along multiple axes [278]. Additionally, advanced SEM setups often integrate temperature control mechanisms within the sample stage, enabling meticulous investigation of sample behavior under varied thermal conditions. To capture the rich array of signals emanating from the sample, SEMs incorporate a diverse array of detectors [279]. These detectors, including secondary electron detectors (SED), backscattered electron detectors (BSED), and energy-dispersive X-ray (EDX) spectroscopy detectors, meticulously capture and analyze emitted or scattered signals, unraveling intricate details about the sample's composition and structure. This system governs every aspect of SEM operation, from beam control and image acquisition to intricate data processing and analysis, ensuring that each captured image and data point provides invaluable insights into the sample under analysis [280]. SEM is widely used in various fields, including materials science, biology, geology, and nanotechnology, for characterizing a wide range of materials such as metals, semiconductors, polymers, ceramics, and biological specimens. It helps to study surface features,

particle size and distribution, fracture surfaces, and other important characteristics of materials. Moreover, SEM can be coupled with other analytical techniques, such as EDX and BSED, to obtain additional information about the chemical composition and crystallographic structure of the sample [281].

2.2.5. Energy-dispersive X-ray spectroscopy

Energy-dispersive X-ray (EDX) spectroscopy is an indispensable analytical technique used in conjunction with SEM to offer profound insights into the elemental composition and spatial distribution of materials. EDX capitalizes on the interactions between the high-energy electrons emitted by the SEM electron beam and the atoms constituting the sample under examination. When bombarded by these energetic electrons, the atoms in the sample undergo ionization, leading to the ejection of inner-shell electrons and subsequent relaxation by outer-shell electrons, resulting in the emission of characteristic X-rays that are indicative of the elemental constituents present [282]. The intricate EDX instrumentation was designed to capture and analyze the emitted X-rays with precision and accuracy. Central to this setup is the X-ray detector, strategically positioned within the SEM chamber to intercept X-rays emanating from the sample. Detectors, often made from materials such as lithium-drifted silicon or germanium, act as sensitive receptors, converting incoming X-rays into electrical pulses proportional to their energy. These pulses are then channeled into a pulse processor for amplification and conditioning before being directed to a multichannel analyzer (MCA). MCA serves as the command center, segregating the pulses based on their energy levels and generating an energy spectrum that serves as a fingerprint of the elemental composition of the sample [283,284].

In EDX analysis, the discernment of elements hinges on the thorough comparison of the obtained energy spectrum with the established X-ray spectra of standard reference materials. Each element exhibits distinct characteristic X-ray lines at specific energy levels, facilitating the identification of constituent elements within the sample. Moreover, the intensity of these X-ray peaks correlates directly with the abundance of the corresponding elements, enabling semi-quantitative or quantitative elemental analysis. This robust analytical framework enables the elucidation of the elemental composition of diverse materials with remarkable precision and accuracy [285,286]. The advantage of EDX lies in its ability to offer elemental insights into

localized regions of interest within the sample owing to its seamless integration with SEM imaging capabilities. By connecting the exceptional spatial resolution of SEM, specific microstructures, particles, or features can be pinpointed for elemental examination. The spatial resolution not only facilitates targeted analysis, but also enables comprehensive investigations into the elemental distribution and concentration gradients across intricate material designs [287]. Furthermore, the relentless march of technological innovation has ushered in a new era of EDX systems, characterized by enhanced sensitivity, resolution, and elemental mapping capabilities. Modern EDX platforms can rapidly acquire high-resolution elemental maps, affording unprecedented insights into the intricate microstructural landscapes and elemental heterogeneities of complex materials and nanostructures. The integration of EDX with SEM imaging produces a potent analytical arsenal that has found multifarious applications across an array of disciplines. Generally, EDX is a beacon of scientific inquiry that light up the elemental tapestry of the microscopic world with unparalleled clarity and depth [288,289].

References

[1] Nicolaou, K.C., Rigol, S. A brief history of antibiotics and select advances in their synthesis. J. Antibiot. 2018, 71 (2), 153–184.

[2] Miller, K. Patient perceptions of the caring environment. J. Healthc. Commun. 2017, 02 (04).

[3] Hutchings, M.I., Truman, A.W., Wilkinson, B. Antibiotics: past, present and future. Curr. Opin. Microbiol. 2019, 51, 72–80.

[4] Sarmah, A.K., Meyer, M.T., Boxall, A.B.A. A global perspective on the use, sales, exposure pathways, occurrence, fate and effects of veterinary antibiotics (VAs) in the environment. Chemosphere 2006, 65 (5), 725–759.

[5] Aminov, R.I. A brief history of the antibiotic era: lessons learned and challenges for the future. Front. Microbiol. 2010, 1.

[6] Gest, H. The discovery of microorganisms by Robert Hooke and Antoni van Leeuwenhoek, fellows of the royal society. Notes Rec. R. Soc. Lond. 2004, 58 (2), 187–201.

[7] Selvarajan, R., Obize, C., Sibanda, T., Abia, A.L.K., Long, H. Evolution and emergence of antibiotic resistance in given ecosystems: possible strategies for addressing the challenge of antibiotic resistance. Antibiotics 2022, 12 (1), 28.

[8] Aminov, R. History of antimicrobial drug discovery: major classes and health impact. Biochem. Pharmacol. 2017, 133, 4–19.

[9] Ramalingam, A.J. History of antibiotics and evolution of resistance. Res. J. Pharm. Technol. 2015, 8 (12), 1719.

[10] Bryskier, A. Antibiotics and antibacterial agents: classifications and structure-activity relationship. Bryskier, A., Ed.; ASM Press: Washington, DC, USA, 2014, pp 13–38.

[11] Wong, W.R., Oliver, A.G., Linington, R.G. Development of antibiotic activity profile screening for the classification and discovery of natural product antibiotics. Chem. Biol. 2012, 19 (11), 1483–1495.

[12] O'Rourke, A., Beyhan, S., Choi, Y., Morales, P., Chan, A.P., Espinoza, J.L., Dupont, C.L., Meyer, K.J., Spoering, A., Lewis, K., Nierman, W.C., Nelson, K.E. Mechanism-of-action classification of antibiotics by global transcriptome profiling. Antimicrob. Agents Chemother. 2020, 64 (3), e01207-19.

[13] Li, F., Collins, J.G., Keene, F.R. Ruthenium complexes as antimicrobial agents. Chem. Soc. Rev. 2015, 44 (8), 2529–2542.

[14] Peach, K.C., Bray, W.M., Winslow, D., Linington, P.F., Linington, R.G. Mechanism of action-based classification of antibiotics using high-content bacterial image analysis. Mol. BioSyst. 2013, 9 (7), 1837.

[15] Stone, S., Gonzales, R., Maselli, J., Lowenstein, S.R. Antibiotic prescribing for patients with colds, upper respiratory tract infections, and bronchitis: a national study of hospital-based emergency departments. Ann. Emerg. Med. 2000, 36 (4), 320–327.

[16] Henry, D.C., Riffer, E., Sokol, W.N., Chaudry, N.I., Swanson, R.N. Randomized double-blind study comparing 3- and 6-day regimens of azithromycin with a 10-day amoxicillin-clavulanate regimen for treatment of acute bacterial sinusitis. Antimicrob. Agents Chemother. 2003, 47 (9), 2770–2774.

[17] Dehne, M.G., Mühling, J., Sablotzki, A., Nopens, H., Hempelmann, G. Pharmacokinetics of antibiotic prophylaxis in major orthopedic surgery and blood-saving techniques. Orthopedics 2001, 24 (7), 665–669.

[18] Cresswell, F.V., Te Brake, L., Atherton, R., Ruslami, R., Dooley, K.E., Aarnoutse, R., Van Crevel, R. Intensified antibiotic treatment of tuberculosis meningitis. Expert Rev. Clin. Pharmacol. 2019, 12 (3), 267–288.

[19] Ballmann, M., Smyth, A., Geller, D.E. Therapeutic approaches to chronic cystic fibrosis respiratory infections with available, emerging aerosolized antibiotics. Respir. Med. 2011, 105, S2–S8.

[20] Heinzl, B., Eber, E., Oberwaldner, B., Haas, G., Zach, M.S. Effects of inhaled gentamicin prophylaxis on acquisition of pseudomonas aeruginosa in children with cystic fibrosis: a pilot study. Pediatr, Pulmonol. 2002, 33 (1), 32–37.

[21] McDonald, E.G., Afshar, A., Assiri, B., Boyles, T., Hsu, J.M., Khuong, N., Prosty, C., So, M., Sohani, Z.N., Butler-Laporte, G., Lee, T.C. Pneumocystis jirovecii pneumonia in people living with HIV: a review. Clin. Microbiol. Rev. 2024, e00101-22.

[22] Manyi-Loh, C., Mamphweli, S., Meyer, E., Okoh, A. Antibiotic use in agriculture and its consequential resistance in environmental sources: potential public health implications. Molecules 2018, 23 (4), 795.

[23] Mann, A., Nehra, K., Rana, J.S., Dahiya, T. Antibiotic resistance in agriculture: perspectives on upcoming strategies to overcome upsurge in resistance. Curr. Res. Microb. Sci. 2021, 2, 100030.

[24] Ma, F., Xu, S., Tang, Z., Li, Z., Zhang, L. Use of antimicrobials in food animals and impact of transmission of antimicrobial resistance on humans. Biosaf. Health 2021, 3 (1), 32–38.

[25] Muurinen, J., Richert, J., Wickware, C.L., Richert, B., Johnson, T.A. Swine growth promotion with antibiotics or alternatives can increase antibiotic resistance gene mobility potential. Sci. Rep. 2021, 11 (1), 5485.

[26] He, Y., Yuan, Q., Mathieu, J., Stadler, L., Senehi, N., Sun, R., Alvarez, P.J.J. Antibiotic resistance genes from livestock waste: occurrence, dissemination, and treatment. Clean Water 2020, 3 (1), 4.

[27] Alanis, A.J. Resistance to antibiotics: are we in the post-antibiotic era? Arch. Med. Res. 2005, 36 (6), 697–705.

[28] Serra-Burriel, M., Keys, M., Campillo-Artero, C., Agodi, A., Barchitta, M., Gikas, A., Palos, C., López-Casasnovas, G. Impact of multi-drug resistant bacteria on economic and clinical outcomes of healthcare-associated infections in adults: systematic review and meta-analysis. PLoS One 2020, 15 (1), e0227139.

[29] Founou, R.C., Founou, L.L., Essack, S.Y. Clinical and economic impact of antibiotic resistance in developing countries: a systematic review and meta-analysis. PLoS One 2017, 12 (12), e0189621.

[30] Baym, M., Stone, L.K., Kishony, R. Multidrug evolutionary strategies to reverse antibiotic resistance. Science 2016, 351 (6268), aad3292.

[31] Lee, C.R., Cho, I., Jeong, B., Lee, S. Strategies to minimize antibiotic resistance. IJERPH 2013, 10 (9), 4274–4305.

[32] Polianciuc, S.I., Gurzău, A.E., Kiss, B., Ștefan, M.G., Loghin, F. Antibiotics in the environment: causes and consequences. Med. Pharm. Rep. 2020.

[33] Kulik, K., Lenart-Boroń, L.A., Wyrzykowska, K. Impact of antibiotic pollution on the bacterial population within surface water with special focus on mountain rivers. Water 2023, 15 (5), 975.

[34] Pinto Jimenez, C.E., Keestra, S., Tandon, P., Cumming, O., Pickering, A.J., Moodley, A., Chandler, C.I.R. Biosecurity and Water, sanitation, and hygiene (WASH) interventions in animal agricultural settings for reducing infection burden, antibiotic use, and antibiotic resistance: a one health systematic review. Lancet Planet. Health 2023, 7 (5), e418–e434.

[35] Serwecińska, L. Antimicrobials and antibiotic-resistant bacteria: a risk to the environment and to public health. Water 2020, 12 (12), 3313.

[36] Arsène, M.M.J., Davares, A.K.L., Viktorovna, P.I., Andreevna, S.L., Sarra, S., Khelifi, I., Sergueïevna, D.M. The public health issue of antibiotic residues in food and feed: causes, consequences, and potential solutions. Vet. World 2022, 662–671.

[37] Dadgostar, P. Antimicrobial resistance: implications and costs. IDR 2019, 12, 3903–3910.

[38] Tian, M., He, X., Feng, Y., Wang, W., Chen, H., Gong, M., Liu, D., Clarke, J.L., Van Eerde, A. Pollution by antibiotics and antimicrobial resistance in livestock and poultry manure in china, and countermeasures. Antibiotics 2021, 10 (5), 539.

[39] Redwan Haque, A., Sarker, M., Das, R., Azad, Md.A.K., Hasan, Md.M. A review on antibiotic residue in foodstuffs from animal source: global health risk and alternatives. Int. J. Environ. Anal. Chem. 2023, 103 (16), 3704–3721.

[40] Naquin, A., Shrestha, A., Sherpa, M., Nathaniel, R., Boopathy, R. Presence of antibiotic resistance genes in a sewage treatment plant in Thibodaux, Louisiana, USA. Bioresour. Technol. 2015, 188, 79–83.

[41] Du, B., Wen, F., Zhang, Y., Zheng, N., Li, S., Li, F., Wang, J. Presence of tetracyclines, quinolones, lincomycin and streptomycin in milk. Food Control 2019, 100, 171–175.

[42] Qiao, M., Ying, G.G., Singer, A.C., Zhu, Y.G. Review of antibiotic resistance in China and its environment. Environ. Int. 2018, 110, 160–172.

[43] Zhai, H., Liu, H., Wang, S., Wu, J., Kluenter, A.M. Potential of essential oils for poultry and pigs. Anim. Nutr. 2018, 4 (2), 179–186.

[44] Ayukekbong, J.A., Ntemgwa, M., Atabe, A.N. The threat of antimicrobial resistance in developing countries: causes and control strategies. Antimicrob. Resist. Infect. Control 2017, 6 (1), 47.

[45] Yao, L., Wang, Y., Tong, L., Deng, Y., Li, Y., Gan, Y., Guo, W., Dong, C., Duan, Y., Zhao, K. Occurrence and risk assessment of antibiotics in surface water and groundwater from different depths of aquifers: a case study at Jianghan Plain, central China. Ecotoxicol. Environ. Saf. 2017, 135, 236–242.

[46] Li, N., Ho, K.W.K., Ying, G.G., Deng, W.J. Veterinary antibiotics in food, drinking water, and the urine of preschool children in Hong Kong. Environ. Int. 2017, 108, 246–252.

[47] Verlicchi, P., Al Aukidy, M., Zambello, E. What have we learned from worldwide experiences on the management and treatment of hospital effluent? An overview and a discussion on perspectives. Sci. Total Environ. 2015, 514, 467–491.

[48] Zhang, H., Luo, Y., Wu, L., Huang, Y., Christie, P. Residues and potential ecological risks of veterinary antibiotics in manures and composts associated with protected vegetable farming. Environ. Sci. Pollut. Res. 2015, 22 (8), 5908–5918.

[49] Pan, X., Qiang, Z., Ben, W., Chen, M. Residual Veterinary antibiotics in swine manure from concentrated animal feeding operations in Shandong province, China. Chemosphere 2011, 84 (5), 695–700.

[50] Hanna, N., Sun, P., Sun, Q., Li, X., Yang, X., Ji, X., Zou, H., Ottoson, J., Nilsson, L.E., Berglund, B., Dyar, O.J., Tamhankar, A.J., Stålsby Lundborg, C. Presence of antibiotic residues in various environmental compartments of Shandong province in Eastern China: its potential for resistance development and ecological and human risk. Environ. Int. 2018, 114, 131–142.

[51] Sabri, N.A., Schmitt, H., Van Der Zaan, B., Gerritsen, H.W., Zuidema, T., Rijnaarts, H.H.M., Langenhoff, A.A.M. Prevalence of antibiotics and antibiotic resistance genes in a wastewater effluent-receiving river in the Netherlands. J. Environ. Chem. Eng. 2020, 8 (1), 102245.

[52] Kebede, M., Admassu, S. Application of antioxidants in food processing industry: options to improve the extraction yields and market value of natural products. Adv. Food Technol. Nutr. Sci. Open J. 2019, 5 (2), 38–49.

[53] Srivastava, A.K., Upadhyay, S.S., Rawool, C.R., Punde, N.S., Rajpurohit, A.S. Voltammetric techniques for the analysis of drugs using nanomaterials based chemically modified electrodes. CAC 2019, 15 (3), 249–276.

[54] Kumar, S.A., Chen, S. Nanostructured zinc oxide particles in chemically modified electrodes for biosensor applications. Anal. Lett. 2008, 41 (2), 141–158.

[55] Sajid, M., Nazal, M.K., Mansha, M., Alsharaa, A., Jillani, S.M.S., Basheer, C. Chemically modified electrodes for electrochemical detection of dopamine in the presence of uric acid and ascorbic acid: a review. TrAC Trends Anal. Chem. 2016, 76, 15–29.

[56] Alkire, R.C., Kolb, D.M., Lipkowski, J., Ross, P.N. Electrochemical surface modification: thin films, functionalization and characterization, Advances in electrochemical sciences and engineering, 1st Ed., Wiley, 2008.

[57] De With, G. Polymer coatings: a guide to chemistry, characterization, and selected applications, Wiley-VCH, Weinheim, 2018.

[58] Lin, Y. Advanced Nano Deposition Methods, Wiley-VCH Verlag GmbH and Co. KGaA, Chemical Industry Press, Weinheim, Germany, 2016.

[59] Minteer, S.D. Enzyme stabilization and immobilization: methods and protocols; methods in molecular biology, Humana Press, Totowa, NJ, 2011; Vol. 679.

[60] Sengar, R.S., Kumar, A., Chaudhary, R., Singh, A. Advances in molecular techniques, CRC Press, Boca Raton , 1st Ed., Taylor and Francis, 2018.

[61] Frauenkron, M., Melder, J., Ruider, G., Rossbacher, R., Höke, H. Ethanolamines and propanolamines. In Ullmann's encyclopedia of industrial chemistry, Wiley-VCH, Wiley, 2001.

[62] Gaioto, R.C., Dias, M.C.G.C., Ndiaye, P.M., Igarashi-Mafra, L., Mafra, M.R. Choline chloride aqueous solution: a thermophysical study. Fluid Ph. Equilibria 2023, 574, 113903.

[63] Das, S., Patra, A., Mandal, A., Mondal, N.S., Dey, S., Mondal, A.K., Dey, A.K., Ghosh, A.R. Choline chloride induces growth performance of Indian major carps and air-breathing fish species with an outcome of quality food-fish under a semi-intensive culture system: a biochemical investigation. ACS Omega 2022, 7 (17), 14579–14590.

[64] Zeisel, S.H. Choline: an essential nutrient for humans. Nutrition 2000, 16 (7–8), 669–671.

[65] Amoroso, R.; Hollmann, F., Maccallini, C. Choline chloride-based DES as solvents/catalysts/chemical donors in pharmaceutical synthesis. Molecules 2021, 26 (20), 6286.

[66] Parsaee, Z., Karachi, N., Abrishamifar, S.M., Kahkha, M.R.R., Razavi, R. Silver-choline chloride modified graphene oxide: novel nano-bioelectrochemical sensor for celecoxib detection and CCD-RSM model. Ultrason. Sonochem. 2018, 45, 106–115.

[67] Bahrani, S., Razmi, Z., Ghaedi, M., Asfaram, A., Javadian, H. Ultrasound-accelerated synthesis of gold nanoparticles modified choline chloride functionalized graphene oxide as a novel sensitive bioelectrochemical sensor: optimized meloxicam detection using CCD-RSM design and application for human plasma sample. Ultrason. Sonochem. 2018, 42, 776–786.

[68] Shahamirifard, S.A., Ghaedi, M., Razmi, Z., Hajati, S. A simple ultrasensitive electrochemical sensor for simultaneous determination of gallic acid and uric acid in human urine and fruit juices based on zirconia-choline chloride-gold nanoparticles-modified carbon paste electrode. Biosens. Bioelectron. 2018, 114, 30–36.

[69] Biya, S., Negash, N., Hailu, T., Tesfaye, G., Yaya, E.E. Highly sensitive square wave voltammetric method for determination of brucine in artificial urine samples based on choline chloride modified glassy carbon electrode. Heliyon 2023, 9 (3), e14544.

[70] Hung, T.C., Liu, Y.R., Chou, P.C., Lin, C.W., Hsieh, Y.T. Electrochemical sensing of hydrazine using hollow Pd/Ag dendrites prepared by galvanic replacement from choline chloride-based deep eutectic solvents. J. Electroanal. Chem. 2022, 922, 116791.

[71] Miron, C., Mele, P., Kaneko, S., Endo, T. Carbon-related materials: in honor of Nobel Laureate Akira Suzuki's lecture at IUMRS-ICEM 2018, Springer International Publishing, Cham, 2020.

[72] Jawaid, M., Khan, A. Carbon composite catalysts: preparation, structural and morphological property and applications; Composites science and technology, Springer Nature Singapore, Singapore, 2022.

[73] Ooi, P.C., Xie, M., Dee, C.F. Enhanced carbon-based materials and their applications, WILEY-VCH: Weinheim, Germany, 2023.

[74] Marrani, A.G., Motta, A., Amato, F., Schrebler, R., Zanoni, R., Dalchiele, E.A. Effect of electrolytic medium on the electrochemical reduction of graphene oxide on Si(111) as probed by XPS. Nanomaterials 2021, 12 (1), 43.

[75] Loryuenyong, V., Totepvimarn, K., Eimburanapravat, P., Boonchompoo, W., Buasri, A. Preparation and characterization of reduced graphene oxide sheets via water-based exfoliation and reduction methods. Adv. Mater. Sci. Eng. 2013, 2013, 1–5.

[76] Madurani, K.A., Suprapto, S., Machrita, N.I., Bahar, S.L., Illiya, W., Kurniawan, F. Progress in graphene synthesis and its application: history, challenge and the future outlook for research and industry. J. Solid State Sci. Technol. 2020, 9 (9), 093013.

[77] Utkan, G., Yumusak, G., Tunali, B.C., Ozturk, T., Turk, M. Production of reduced graphene oxide by using three different microorganisms and investigation of their cell interactions. ACS Omega 2023, 8 (34), 31188–31200.

[78] Tadyszak, K., Wychowaniec, J., Litowczenko, J. Biomedical applications of graphene-based structures. Nanomaterials 2018, 8 (11), 944.

[79] Munonde, T.S., Nomngongo, P.N. Nanocomposites for electrochemical sensors and their applications on the detection of trace metals in environmental water samples. Sensors 2020, 21 (1), 131.

[80] Alam, S.N., Sharma, N., Kumar, L. Synthesis of graphene oxide (GO) by modified hummers method and its thermal reduction to obtain reduced graphene oxide (rGO). Graphene 2017, 06 (01), 1–18.

[81] Jampasa, S., Siangproh, W., Duangmal, K., Chailapakul, O. Electrochemically reduced graphene oxide-modified screen-printed carbon electrodes for a simple and highly sensitive electrochemical detection of synthetic colorants in beverages. Talanta 2016, 160, 113–124.

[82] Yan, Y., Nashath, F.Z., Chen, S., Manickam, S., Lim, S.S., Zhao, H., Lester, E., Wu, T., Pang, C.H. Synthesis of graphene: potential carbon precursors and approaches. Nanotechnol. Rev. 2020, 9 (1), 1284–1314.

[83] Karačić, D., Gutić, S.J., Vasić, B., Mirsky, V.M., Skorodumova, N.V., Mentus, S.V., Pašti, I.A. Electrochemical reduction of thin graphene-oxide films in aqueous solutions: Restoration of Conductivity. Electrochem. Acta 2022, 140046.

[84] Palakollu, V.N., Thapliyal, N., Chiwunze, T.E., Karpoormath, R., Karunanidhi, S., Cherukupalli, S. Electrochemically reduced graphene oxide/poly-glycine composite modified electrode for sensitive determination of L-Dopa. Mater. Sci. Eng: C 2017, 77, 394–404.

[85] Toh, S.Y., Loh, K.S., Kamarudin, S.K., Daud, W.R.W. Graphene production via electrochemical reduction of graphene oxide: synthesis and characterization. Chem. Eng. J. 2014, 251, 422–434.

[86] Devi, R., Gill, S.S. A squared bossed diaphragm piezo resistive pressure sensor based on CNTs for low pressure range with enhanced sensitivity. Microsyst. Technol. 2021, 27 (8), 3225–3233.

[87] O'Connell, M. Carbon nanotubes: properties and applications, CRC/Taylor and Francis: Boca Raton, California, 2006.

[88] Endo, M., Iijima, S., Dresselhaus, M. S. Carbon nanotubes, 1st Ed., Pergamum, Oxford, Tarrytown, NewYork, 1996.

[89] Tanaka, K., Iijima, S. Carbon nanotubes and graphene, 2nd Ed., Elsevier, Amsterdam, Netherlands, 2014.

[90] Jun, L.Y., Mubarak, N.M., Yon, L.S., Bing, C.H., Khalid, M., Abdullah, E.C. Comparative study of acid functionalization of carbon nanotube via ultrasonic and reflux mechanism. J. Environ. Chem. Eng. 2018, 6 (5), 5889–5896.

[91] Yang, C., Denno, M.E., Pyakurel, P., Venton, B.J. Recent trends in carbon nanomaterial-based electrochemical sensors for biomolecules: a review. Anal. Chim. Acta 2015, 887, 17–37.

[92] Kivrak, H., Selcuk, K., Caglar, A., Aktas, N. Selective electrochemical determination of L-cysteine by a cobalt carbon nanotube (CNT)-modified glassy carbon electrode (GCE). Anal. Lett. 2024, 1–15.

[93] Morris, J.E., Iniewski, K. Graphene, carbon nanotubes, and nanostructures: techniques and applications; devices, circuits, and systems, CRC Press, Boca Raton, 2013.

[94] Brito, C.L., Ferreira, E.I., La-Scalea, M.A. Multi-walled carbon nanotube functionalization and the dispersing agents study applied for the glassy carbon electrode modification and voltammetric reduction of nitrofurazone. J. Solid State Electrochem. 2020, 24 (8), 1969–1980.

[95] Hu, J., Zhang, Z. Application of electrochemical sensors based on carbon nanomaterials for detection of flavonoids. Nanomaterials 2020, 10 (10), 2020.

[96] Rohani, T., Taher, M.A. Novel functionalized multiwalled carbon nanotube-glassy carbon electrode for simultaneous determination of ascorbic acid and uric acid. Arab. J. Chem. 2018, 11 (2), 214–220.

[97] Díez-Pascual, A.M. Chemical functionalization of carbon nanotubes with polymers: a brief overview. Macromol. 2021, 1 (2), 64–83.

[98] Rathinavel, S., Priyadharshini, K., Panda, D. A review on carbon nanotube: an overview of synthesis, properties, functionalization, characterization, and the application. Mat. Sci. Eng.: B 2021, 268, 115095.

[99] Zhang, Y., Bai, Y., Yan, B. Functionalized carbon nanotubes for potential medicinal applications. Drug Discov. Today 2010, 15 (11–12), 428–435.

[100] Ata, M.S., Poon, R., Syed, A.M., Milne, J., Zhitomirsky, I. New developments in non-covalent surface modification, dispersion and electrophoretic deposition of carbon nanotubes. Carbon 2018, 130, 584–598.

[101] Ibos, L., Schulz, E. Non-Covalent interactions in supported asymmetric catalysis: a brief account. C. R. Chim. 2024, 27 (S2), 1–27.

[102] Bui, M.P.N., Li, C.A., Seong, G.H. Electrochemical detection of dopamine with poly-glutamic acid patterned carbon nanotube electrodes. Biochip J. 2012, 6 (2), 149–156.

[103] Prinith, S.N., Manjunatha, J.G. Electrochemical analysis of l-tryptophan at highly sensitive poly (glycine) modified carbon nanotube paste sensor. Mat. Res. Innov. 2022, 26 (3), 134–143.

[104] Naik, T.S.S.K., Swamy, B.E.K., Ramamurthy, P.C., Chetankumar, K. Poly (L-leucine) modified carbon paste electrode as an electrochemical sensor for the detection of paracetamol in presence of folic acid. Mat. Sci. Energy Technol. 2020, 3, 626–632.

[105] Bauri, K., Nandi, M., De, P. Amino acid-derived stimuli-responsive polymers and their applications. Polym. Chem. 2018, 9 (11), 1257–1287.

[106] Kordasht, H.K., Hasanzadeh, M., Seidi, F., Alizadeh, P.M. Poly (amino acids) towards sensing: recent progress and challenges. TrAC Trends Anal.l Chem. 2021, 140, 116279.

[107] Zewde, B.W., Admassie, S. Electrocatalysis of oxygen reduction at poly (4-amino-3-hydroxynaphthalene sulfonic acid) and platinum loaded polymer modified glassy carbon electrodes. J. Power Sources 2012, 216, 502–507.

[108] Qiu, L., Lv, P., Zhao, C., Feng, X., Fang, G., Liu, J., Wang, S. Electrochemical detection of organophosphorus pesticides based on amino acids conjugated nanoenzyme modified electrodes. Sens. Actuators B: Chem. 2019, 286, 386–393.

[109] Nikhil, J.L., Manjunatha, J.G., Hareesha, N., Kanthappa, B., Karthik, C.S., Mallu, P., Al Othman, Z.A. Electrochemical determination of methyl orange using poly(L-serine)-modified carbon paste electrode. J. Electron. Mater. 2023, 52 (10), 7021–7029.

[110] Wang, T., Zhang, L., Zhang, C., Deng, D., Wang, D., Luo, L. Simultaneous determination of xanthine and hypoxanthine using poly glycine/rGO-modified glassy carbon electrode. Molecules 2023, 28 (3), 1458.

[111] Wang, B., Huang, J.S. Using poly-L-histidine modified glassy carbon electrode to trace hydroquinone in the sewage water. Int. J. Electrochem. 2014, 2014, 1–7.

[112] Hareesha, N., Manjunatha, J.G., Amrutha, B.M., Pushpanjali, P.A., Charithra, M M., Prinith Subbaiah, N. Electrochemical analysis of indigo carmine in food and water samples using a poly(glutamic acid) layered multi-walled carbon nanotube paste electrode. J. Elec. Mater. 2021, 50 (3), 1230–1238.

[113] Harisha, K.V., Kumara Swamy, B.E., Ebenso, E.E. Poly (glycine) modified carbon paste electrode for simultaneous determination of catechol and hydroquinone: a voltammetric study. J. Electroanal. Chem. 2018, 823, 730–736.

[114] Li, L.D., Chen, Z.B., Zhao, H.T., Guo, L. Electrochemical real-time detection of l-histidine via self-cleavage of DNA enzymes. Biosens. Bioelectron. 2011, 26 (5), 2781–2785.

[115] Dridi, F., Marrakchi, M., Gargouri, M., Saulnier, J., Jaffrezic-Renault, N., Lagarde, F. Nanomaterial-based electrochemical biosensors for food safety and quality assessment. In nano biosensors. Elsevier, 2017, pp 167–204.

[116] Aflatoonian, M.R., Tajik, S., Aflatoonian, B., Beitollahi, H., Zhang, K., Le, Q.V., Cha, J.H., Jang, H.W., Shokouhimehr, M., Peng, W. A screen-printed electrode modified with graphene/Co_3O_4 nanocomposite for electrochemical detection of tramadol. Front. Chem. 2020, 8, 562308.

[117] Zhang, J., Mou, L., Jiang, X. Surface chemistry of gold nanoparticles for health-related applications. Chem. Sci. 2020, 11 (4), 923–936.

[118] Laurent, S., Forge, D., Port, M., Roch, A., Robic, C., Vander Elst, L., Muller, R.N. Magnetic iron oxide nanoparticles: synthesis, stabilization, vectorization, physicochemical characterizations, and biological applications. Chem. Rev. 2008, 108 (6), 2064–2110.

[119] Wang, J., Xie, H., Guo, Z., Guan, L., Li, Y. Improved thermal properties of paraffin wax by the addition of TiO_2 nanoparticles. Appl. Therm. Eng. 2014, 73 (2), 1541–1547.

[120] Li, Q., Guo, J., Xu, D., Guo, J., Ou, X., Hu, Y., Qi, H., Yan, F. Electrospun N-doped porous carbon nanofibers incorporated with NiO Nanoparticles as free standing film electrodes for high performance supercapacitors and CO_2 capture. Small 2018, 14 (15), 1704203.

[121] George, J.M., Antony, A., Mathew, B. Metal oxide nanoparticles in electrochemical sensing and biosensing: a review. Microchim. Acta 2018, 185 (7), 358.

[122] Fazio, E., Spadaro, S., Corsaro, C., Neri, G., Leonardi, S.G., Neri, F., Lavanya, N., Sekar, C., Donato, N., Neri, G. Metal-oxide based nanomaterials: synthesis, characterization and their applications in electrical and electrochemical sensors. Sensors 2021, 21 (7), 2494.

[123] Augustine, R., Hasan, A. Emerging applications of biocompatible phytosynthesized metal/metal oxide nanoparticles in healthcare. J. Drug Deliv. Sci. Technol. 2020, 56, 101516.

[124] Baskar, V., Safia, N., Sree Preethy, K., Dhivya, S., Thiruvengadam, M., Sathishkumar, R. A comparative study of phytotoxic effects of metal oxide (CuO, ZnO and NiO) nanoparticles on in-vitro grown abelmoschus esculents. Plant Biosyst. 2021, 155 (2), 374–383.

[125] Sharma, D.K., Shukla, S., Sharma, K.K., Kumar, V. A review on ZnO: fundamental properties and applications. Mater. Today: Proc. 2022, 49, 3028–3035.

[126] Chikere, C., Faisal, N.H., Lin, P.K.T., Fernandez, C. Zinc oxide nanoparticles modified-carbon paste electrode used for the electrochemical determination of gallic acid. J. Phys.: Conf. Ser. 2019, 1310 (1), 012008.

[127] Tripathy, N., Kim, D.H. Metal oxide modified ZnO nanomaterials for biosensor applications. Nano Converg. 2018, 5 (1), 27.

[128] Deshpande, M.P., Patel, K.N., Gujarati, V.P., Patel, K., Chaki, S.H. Structural, thermal and optical properties of nickel oxide (NiO) nanoparticles synthesized by chemical precipitation method. AMR 2016, 1141, 65–71.

[129] Darbandi, M., Mohajer, M.F., Eynollahi, M., Asadpour-Zeynali, K. Sensitive sensing platform based on NiO and NiO-Ni nanoparticles for electrochemical determination of metronidazole. Chem. Phys. 2022, 560, 111590.

[130] Alghunaim, N.S., El-Khodary, S.A., Ibrahim, M., El-Enany, G.M. Spectroscopic analyses of iron doped protonated polyaniline/graphene oxide system. Spectrochim. Acta A: Molecular Biomol. Spectrosc. 2019, 216, 349–358.

[131] Yazar, S., Arvas, M.B., Sahin, Y. Hydrothermal synthesis of flexible Fe-doped polyaniline/dye-functionalized carbon felt electrode for supercapacitor applications. ChemistrySelect 2022, 7 (21), e202200016.

[132] Butoi, B., Ciobanu, C., Iconaru, S., Negrilă, C., Badea, M., Balas, M., Dinischiotu, A., Predoi, G., Bita, B., Groza, A., Predoi, D. Iron-oxide-nanoparticles-doped polyaniline composite thin films. Polymers 2022, 14 (9), 1821.

[133] Mo, J., Zhang, D., Sun, M., Liu, L., Hu, W., Jiang, B., Chu, L., Li, M. Polyethylene oxide as a multifunctional binder for high-performance ternary layered cathodes. Polymers 2021, 13 (22), 3992.

[134] Zhang, S.S. A concept for making poly (ethylene oxide) based composite gel polymer electrolyte lithium/sulfur battery. J. Electrochem. Soc. 2013, 160 (9), A1421–A1424.

[135] Car, A., Drioli, E., Giorno, L. Polyethylene oxide. In encyclopedia of membranes, Springer Berlin Heidelberg: Berlin, Heidelberg, 2014.

[136] Bailey, F.E., Koleske, J.V. Poly (ethylene oxide), Academic Press, New York, 1976.

[137] Schmidbaur, H. Gold chemistry is different. Interdiscipl. Sci. Rev. 1992, 17 (3), 213–220.

[138] Abrikosov, A.A., Beknazarov, A. Fundamentals of the Theory of Metals, Dover Publications, Inc., Mineola, New York, 2017.

[139] Peyret, R. Metals: properties and applications, New York, Research Press, Place of publication not identified, 2019.

[140] Majdalawieh, A., Kanan, M.C., El-Kadri, O., Kanan, S.M. Recent advances in gold and silver nanoparticles: synthesis and applications. J. Nanosci. Nanotech. 2014, 14 (7), 4757–4780.

[141] Cole, L.E., Ross, R.D., Tilley, J.M., Gogola, V.T., Roeder, R.K. Gold nanoparticles as contrast agents in X-ray imaging and computed tomography. Nanomedicine 2015, 10 (2), 321–341.

[142] Kundu, P., Singh, D., Singh, A., Sahoo, S.K. Cancer nanotheranostics: a nanomedicinal approach for cancer therapy and diagnosis. ACAMC 2020, 20 (11), 1288–1299.

[143] Das, A., Tsai, H.C., Sen, T., Moirangthem, R.S. Plasmonic nanoparticle-based surface-enhanced Raman spectroscopy-guided photothermal therapy: emerging cancer theranostics. Nanomedicine 2023, 18 (6), 555–576.

[144] Vadakkan, K., Rumjit, N.P., Ngangbam, A.K., Vijayanand, S., Nedumpillil, N.K. Novel advancements in the sustainable green synthesis approach of silver nanoparticles (AgNPs) for antibacterial therapeutic applications. Coord. Chem. Rev. 2024, 499, 215528.

[145] Shaker Ardakani, L., Surendar, A., Thangavelu, L., Mandal, T. Silver nanoparticles (Ag NPs) as catalyst in chemical reactions. Synth. Commun. 2021, 1–21.

[146] Ibrahim, N., Akindoyo, J.O., Mariatti, M. Recent development in silver-based ink for flexible electronics. J. Sci.: Adv. Mater. Devices 2022, 7 (1), 100395.

[147] Bouafia, A., Laouini, S.E., Ahmed, A.S.A., Soldatov, A.V., Algarni, H., Feng Chong, K., Ali, G.A.M. The recent progress on silver nanoparticles: synthesis and electronic applications. Nanomaterials 2021, 11 (9), 2318.

[148] Ha Pham, T.T., Dien, N.D., Vu, X.H. Facile synthesis of silver/gold alloy nanoparticles for ultra-sensitive Rhodamine B detection. RSC Adv. 2021, 11 (35), 21475–21488.

[149] Baig, N., Kammakakam, I., Falath, W. Nanomaterials: a review of synthesis methods, properties, recent progress, and challenges. Mater. Adv. 2021, 2 (6), 1821–1871.

[150] Kumar, S., Bhushan, P., Bhattacharya, S. Fabrication of nanostructures with bottom-up approach and their utility in diagnostics, therapeutics, and others. In environmental, chemical and medical sensors, Energy, Environment and Sustainability, Springer Singapore, Singapore, 2018.

[151] Islam, M.S., Banik, S., Collinson, M.M. Recent advances in bimetallic nanoporous gold electrodes for electrochemical sensing. Nanomaterials 2023, 13 (18), 2515.

[152] Malik, S., Singh, J., Goyat, R., Saharan, Y., Chaudhry, V., Umar, A., Ibrahim, A.A., Akbar, S., Ameen, S., Baskoutas, S. Nanomaterials-based biosensor and their applications: a review. Heliyon 2023, 9 (9), e19929.

[153] Ollé, E.P., Farré-Lladós, J., Casals-Terré, J. Advancements in micro fabricated gas sensors and micro-analytical tools for the sensitive and selective detection of odors. Sensors 2020, 20 (19), 5478.

[154] Jebril, S., Fredj, Z., Saeed, A.A., Gonçalves, A.M., Kaur, M., Kumar, A., Singh, B. Nanomaterial-based electrochemical chemo (bio) sensors for the detection of nano plastic residues: trends and future prospects. RSC Sustain. 2024, 10.1039.D3SU00471F.

[155] Yu, T., He, W., Zhang, Q., Ma, D. Advanced nanomaterials and characterization techniques for photovoltaic and photocatalysis applications. Acc. Mater. Res. 2023, 4 (6), 507–521.

[156] Smith, D.J. Kirkland, A. I., Haigh, S. J. Characterization of nanomaterials using transmission electron microscopy. In nano characterization, The Royal Society of Chemistry, 2015, 1–29.

[157] Cheng, H., Wang, C., Qin, D., Xia, Y. Galvanic replacement synthesis of metal nanostructures: bridging the gap between chemical and electrochemical approaches. Acc. Chem. Res. 2023, 56 (7), 900–909.

[158] Wu, T., Liu, C., Kong, B., Sun, J., Gong, Y., Liu, K., Xie, J., Pei, A., Cui, Y. Amidoxime-functionalized macro porous carbon self-refreshed electrode materials for rapid and high-capacity removal of heavy metal from water. ACS Cent. Sci. 2019, 5 (4), 719–726.

[159] Mutalik, C., Saukani, M., Khafid, M., Krisnawati, D.I., Darmayanti, W.R., Puspitasari, B., Cheng, T.M., Kuo, T.R. Gold-based nanostructures for antibacterial application. IJMS 2023, 24 (12), 10006.

[160] Cao, P., He, X., Xiao, J., Yuan, C., Bai, X. Covalent bonding of AgNPs to 304 stainless steel by reduction in situ for antifouling applications. Appl. Surf. Sci. 2018, 452, 201–209.

[161] Li, S., Ma, Y., Liu, Y., Xin, G., Wang, M., Zhang, Z., Liu, Z. Electrochemical sensor based on a three dimensional nanostructured MoS_2 nanosphere-PANI/reduced graphene oxide composite for simultaneous detection of ascorbic acid, dopamine, and uric acid. RSC Adv. 2019, 9 (6), 2997–3003.

[162] Luc, W., Jiao, F. Nanoporous metals as electrocatalysts: state-of-the-art, opportunities, and challenges. ACS Catal. 2017, 7 (9), 5856–5861.

[163] Sha, R., Basak, A., Maity, P.C., Badhulika, S. ZnO nano-structured based devices for chemical and optical sensing applications. Sens. Actuators Rep. 2022, 4, 100098.

[164] Pasparakis, G. Recent developments in the use of gold and silver nanoparticles in biomedicine. Wiley Interdiscip. Rev. Nanomed. Nanobiotechnol. 2022, 14 (5), e1817.

[165] Yang, J.W., Kwon, H.R., Seo, J.H., Ryu, S., Jang, H.W. Nanoporous oxide electrodes for energy conversion and storage devices. RSC Appl. Interfaces 2024, 1 (1), 11–42.

[166] Oliverio, M., Perotto, S., Messina, G.C., Lovato, L., De Angelis, F. Chemical functionalization of plasmonic surface biosensors: a tutorial review on issues, strategies, and costs. ACS Appl. Mater. Interfaces 2017, 9 (35), 29394–29411.

[167] Mourdikoudis, S., Kostopoulou, A., La Grow, A.P. Magnetic nanoparticle composites: synergistic effects and applications. Adv. Sci. 2021, 8 (12), 2004951.

[168] Faisal, M., Harraz, F.A., Al-Salami, A.E., Al-Sayari, S.A., Al-Hajry, A., Al-Assiri, M.S. Polythiophene/ZnO nanocomposite-modified glassy carbon electrode as efficient electrochemical hydrazine sensor. Mater. Chem. Phys. 2018, 214, 126–134.

[169] Begum, B., Bilal, S., Shah, A.U.H.A., Röse, P. Synthesis, characterization and electrochemical performance of a redox-responsive polybenzopyrrole@nickel oxide nanocomposite for robust and efficient faraday energy storage. Nanomaterials 2022, 12 (3), 513.

[170] Kausar, A. Conducting polymer-based nanocomposites: structuration, compatibilizing effect, conductivity, and physical properties. In conducting polymer-based nanocomposites. Elsevier, 2021, pp 27–56.

[171] Soloducho, J., Cabaj, J. Conducting polymers in sensor design. In conducting polymers, InTech, 2016.

[172] Bard, A.J., Faulkner, L.R., White, H.S. Electrochemical methods: fundamentals and applications, 3rd Ed., Wiley: Hoboken, NJ, 2022.

[173] Settle, F.A. Handbook of instrumental techniques for analytical chemistry, Prentice Hall PTR, Upper Saddle River, New Jersey, J. Liq. Chromatogr. Relat. Technol. 1998, 21 (19), 3072–3076.

[174] Miguel, E.A., Martin, G.M.C., Gil, L.M.Á. Agricultural and food electroanalysis, Wiley: Chichester, West Sussex, 2015.

[175] Mandler, D., Scholz F. Electroanalytical methods. Guide to experiments and applications, 2nd Ed. Anal. Bioanal. Chem. 2010, 398 (7–8), 2771–2772.

[176] Zoski, C.G. Handbook of electrochemistry, transferred to digital print. Elsevier: Amsterdam Heidelberg, 2007.

[177] Zanello, P., Nervi, C., Fabrizi de Biani, F. Inorganic electrochemistry: theory, practice and application, 2nd Ed., RSC Pub., Cambridge, GB, 2012.

[178] Rouessac, F., Rouessac, A. Chemical analysis: modern instrumentation methods and techniques, 3rd Ed., Wiley: Hoboken, NJ, 2022.

[179] Barek, J. How to improve the performance of electrochemical sensors via minimization of electrode passivation. Chemosensors 2021, 9 (1), 12.

[180] Ozkan, S.A., Kauffmann, J.M., Zuman, P. Electroanalysis in biomedical and pharmaceutical sciences: voltammetry, amperometry, biosensors, applications, monographs in electrochemistry, Springer Berlin Heidelberg : Imprint: Springer: Berlin, Heidelberg, 2015.

[181] Ariño, C., Serrano, N., Díaz-Cruz, J.M., Esteban, M. Voltammetric determination of metal ions beyond mercury electrodes. A review. Anal. Chim. Acta 2017, 990, 11–53.

[182] Zuman, P. Role of mercury electrodes in contemporary analytical chemistry. Electroanalysis 2000, 12 (15), 1187–1194.

[183] Terzi, F., Pigani, L., Zanardi, C. Unusual metals as electrode materials for electrochemical sensors. Curr. Opin. Electrochem. 2019, 16, 157–163.

[184] Łukaszewski, M., Soszko, M., Czerwiński, A. Electrochemical methods of real surface area determination of noble metal electrodes-an overview. Int. J. Electrochem. Sci. 2016, 11 (6), 4442–4469.

[185] Asadian, E., Ghalkhani, M., Shahrokhian, S. Electrochemical sensing based on carbon nanoparticles: a review. Sens. Actuators B: Chem. 2019, 293, 183–209.

[186] Malode, S.J., Sharma, P., Hasan, M.R., Shetti, N.P., Mascarenhas, R.J. Carbon and carbon paste electrodes. In electrochemical sensors. Elsevier, 2022, pp 79–114.

[187] Uslu, B., Ozkan, S. Electroanalytical application of carbon based electrodes to the pharmaceuticals. Analytical Lett. 2007, 40 (5), 817–853.

[188] Sharma, S., Sudhakara, P., Omran, A.A.B., Singh, J., Ilyas, R.A. Recent trends and developments in conducting polymer nanocomposites for multifunctional applications. Polymers 2021, 13 (17), 2898.

[189] Idumah, C.I., Hassan, A. Emerging trends in graphene carbon based polymer nanocomposites and applications. Rev. Chem. Eng. 2016, 32 (2).

[190] Immanuel, S., Aparna, T.K., Sivasubramanian, R. Graphene–metal oxide nanocomposite modified electrochemical sensors. In graphene-based electrochemical sensors for biomolecules. Elsevier, 2019, pp 113–138.

[191] Wang, Y., Liu, A., Han, Y., Li, T. Sensors based on conductive polymers and their composites: a review. Polymer Int. 2020, 69 (1), 7–17.

[192] Karczmarska, A., Adamek, M., Houbbadi, S., Kowalczyk, P., Laskowska, M. Carbon-supported noble-metal nanoparticles for catalytic applications-a review. Crystals 2022, 12 (5), 584.

[193] Tsirlina, G.A. The role of supporting electrolyte in heterogeneous electron transfer. J. Solid State Electrochem. 2017, 21 (7), 1833–1845.

[194] Dickinson, E.J.F., Limon-Petersen, J.G., Rees, N.V., Compton, R.G. How much supporting electrolyte is required to make a cyclic voltammetry experiment quantitatively “diffusional”? A theoretical and experimental investigation. J. Phys. Chem. C 2009, 113 (25), 11157–11171.

[195] Mansouri, K., Ibrik, K., Bensalah, N., Abdel-Wahab, A. Anodic dissolution of pure aluminum during electrocoagulation process: influence of supporting electrolyte, initial pH, and current density. Ind. Eng. Chem. Res. 2011, 50 (23), 13362–13372.

[196] Mugisa, J., Chukwu, R., Brogioli, D., La Mantia, F. Effect of ion-paring on the kinetics of redox systems with concentrated supporting electrolyte. Electrochim. Acta 2024, 473, 143473.

[197] Zhao, Y., Kang, Y., Du, H., Kang, F., Li, B. Considerations of advanced aqueous batteries recycling: a perspective. J. Energy Chem. 2024, 93, 46–54.

[198] Honeychurch, K. Trace voltammetric determination of lead at a recycled battery carbon rod electrode. Sensors 2019, 19 (4), 770.

[199] Chapman, C.S., Van den Berg, C.M.G. Anodic stripping voltammetry using a vibrating electrode. Electroanalysis 2007, 19 (13), 1347–1355.

[200] Scholz, F. Voltammetric techniques of analysis: the essentials. ChemTexts 2015, 1 (4), 17.

[201] Ferrari, G.M.A., Foster, C., Kelly, P., Brownson, D., Banks, C. Determination of the electrochemical area of screen-printed electrochemical sensing platforms. Biosensors 2018, 8 (2), 53.

[202] Pereira, C., Gulaboski, R. Electroanalytical techniques and instrumentation in food analysis. In handbook of food analysis instruments, Ñtle, S., Ed., CRC Press, 2008.

[203] Sandford, C., Edwards, M.A., Klunder, K.J., Hickey, D.P., Li, M., Barman, K., Sigman, M. S., White, H.S., Minteer, S.D. A synthetic chemist's guide to electroanalytical tools for studying reaction mechanisms. Chem. Sci. 2019, 10 (26), 6404–6422.

[204] Westbroek, P. Analytical electrochemistry in textiles, Textile Institute, Eds.; Woodhead publishing in textiles, CRC Press, Boca Raton, 2005.

[205] Arvand, M., Anvari, M. A graphene-based electrochemical sensor for sensitive detection of quercetin in foods. J. Iran. Chem. Soc. 2013, 10 (5), 841–849.

[206] Laviron, E. General expression of the linear potential sweep voltammogram in the case of diffusion less electrochemical systems. J. Electroanal. Chem. Interf. Electrochem. 1979, 101 (1), 19–28.

[207] Pattar, V.P., Nandibewoor, S.T. Electroanalytical method for the determination of 5-fluorouracil using a reduced graphene oxide/chitosan modified sensor. RSC Adv. 2015, 5 (43), 34292–34301.

[208] Singh, R., Gupta, R., Bansal, D., Bhateria, R., Sharma, M. A review on recent trends and future developments in electrochemical sensing. ACS Omega 2024, acsomega.3c08060.

[209] Kiniman, V., Kanokwhale, C., Boonto, P., Pholauyphon, W., Nantasaksiri, K., Charoen-amornkitt, P., Suzuki, T., Tsushima, S. Modeling cyclic voltammetry responses of porous electrodes: an approach incorporating faradaic and non-faradaic contributions through porous model and constant phase element. J. Energy Storage 2024, 83, 110804.

[210] Abdul Aziz, S.F.N., Hui, O.S., Salleh, A.B., Normi, Y.M., Yusof, N.A., Ashari, S.E., Alang Ahmad, S.A. Enhancing uric acid electrochemical detection with copper ion-activated mini protein mimicking uricase within ZIF-8: response surface methodology (RSM) optimization. Anal. Bioanal. Chem. 2024, 416 (1), 227–241.

[211] Minakshi, M., Wickramaarachchi, K. Electrochemical aspects of supercapacitors in perspective: from electrochemical configurations to electrode materials processing. Prog. Solid State Chem. 2023, 69, 100390.

[212] Sikiru, S., Dele-Afolabi, T.T., Yeganeh Ghotbi, M., Rehman, Z.U. Recent advancements in technology projection on electric double layer effect in battery recycling for energy storage. J. Power Sources 2024, 596, 234056.

[213] Liu, J., Xu, Y., Liu, S., Yu, S., Yu, Z., Low, S.S. Application and progress of chemometrics in voltammetric biosensing. Biosensors 2022, 12 (7), 494.

[214] Cetinkaya, A., Kaya, S.I., Ozkan, S.A. A collection of the best practice examples of electroanalytical applications in education: from polarography to sensors. J. Solid State Electrochem. 2024, 28 (3–4), 869–895.

[215] Jerkiewicz, G. Applicability of platinum as a counter-electrode material in electrocatalysis research. ACS Catal. 2022, 12 (4), 2661–2670

[216] Dave, S., Das, J., Dave, S., Mohanty, P., Priya, G.M., Jagtap, P., Pawar, R. Contribution of cyclic voltammetry and electrochemical impedance spectroscopy in deciphering the electron transport system in biofilm. In analytical methodologies for biofilm research; Nag, M., Lahiri, D., Eds.; Springer Protocols Handbooks; Springer US: New York, 2021.

[217] Seeber, R., Zanardi, C., Inzelt, G. The inherent coupling of charge transfer and mass transport processes: the curious electrochemical reversibility. ChemTexts 2016, 2 (2), 8.

[218] Ponce-de-León, C., Low, C.T.J., Kear, G., Walsh, F.C. Strategies for the determination of the convective-diffusion limiting current from steady state linear sweep voltammetry. J. Appl. Electrochem. 2007, 37 (11), 1261–1270.

[219] Venton, B.J., Cao, Q. Fundamentals of fast-scan cyclic voltammetry for dopamine detection. Analyst. 2020, 145 (4), 1158–1168.

[220] Hoyos-Arbeláez, J., Vázquez, M., Contreras-Calderón, J. Electrochemical methods as a tool for determining the antioxidant capacity of food and beverages: a review. Food Chem. 2017, 221, 1371–1381.

[221] Elgrishi, N., Rountree, K.J., McCarthy, B.D., Rountree, E.S., Eisenhart, T.T., Dempsey, J.L. A practical beginner's guide to cyclic voltammetry. J. Chem. Educ. 2018, 95 (2), 197–206.

[222] Qian, L., Durairaj, S., Prins, S., Chen, A. Nanomaterial-based electrochemical sensors and biosensors for the detection of pharmaceutical compounds. Biosens. Bioelectron. 2021, 175, 112836.

[223] Farghaly, O.A., Hameed, R.S.A., Abu-Nawwas, A.A.H. Analytical application using modern electrochemical techniques. Int. J. Electrochem. Sci. 2014, 9 (6), 3287–3318.

[224] Scholz, F., Bond, A.M., Compton, R.G., Fiedler, D.A., Inzelt, G., Kahlert, H., Komorsky-Lovrić, Š., Lohse, H., Lovrić, M., Marken, F., Neudeck, A., Retter, U., Scholz, F., Stojek, Z., Electroanalytical methods, Eds.; Springer Berlin Heidelberg: Berlin, Heidelberg, 2010.

[225] Thapliyal, N., Chiwunze, T.E., Karpoormath, R., Goyal, R.N., Patel, H., Cherukupalli, S. Research progress in electroanalytical techniques for determination of antimalarial drugs in pharmaceutical and biological samples. RSC Adv. 2016, 6 (62), 57580–57602.

[226] Shin, S.J., Kim, D.H., Bae, G., Ringe, S., Choi, H., Lim, H.K., Choi, C.H., Kim, H. On the importance of the electric double layer structure in aqueous electrocatalysis. Nat. Commun. 2022, 13 (1), 174.

[227] Dorledo De Faria, R.A., Dias Heneine, L.G., Matencio, T., Messaddeq, Y. Faradaic and non-faradaic electrochemical impedance spectroscopy as transduction techniques for sensing applications. IJBSBE 2019, 5 (1).

[228] Casebolt, R., Levine, K., Suntivich, J., Hanrath, T. Pulse check: potential opportunities in pulsed electrochemical CO_2 reduction. Joule 2021, 5 (8), 1987–2026.

[229] Gulaboski, R., Mirceski, V. Calculating of square-wave voltammograms-a practical on-line simulation platform. J. Solid State Electrochem. 2024, 28 (3–4), 1121–1130.

[230] Williams, T., Shum, R., Rappleye, D. Review-concentration measurements in molten chloride salts using electrochemical methods. J. Electrochem. Soc. 2021, 168 (12), 123510.

[231] Alghamdi, A.H. Applications of stripping voltammetric techniques in food analysis. Arab. J. Chem. 2010, 3 (1), 1–7.

[232] Porada, R., Jedlińska, K., Lipińska, J., Baś, B. Review-voltammetric sensors with laterally placed working electrodes: a review. J. Electrochem. Soc. 2020, 167 (3), 037536.

[233] Baluta, S., Meloni, F., Halicka, K., Szyszka, A., Zucca, A., Pilo, M.I., Cabaj, J. Differential pulse voltammetry and chronoamperometry as analytical tools for epinephrine detection using a tyrosinase-based electrochemical biosensor. RSC Adv. 2022, 12 (39), 25342–25353.

[234] Verrinder, E., Leung, K.K., Erdal, M.K., Sepunaru, L., Plaxco, K.W. Comparison of voltammetric methods used in the interrogation of electrochemical aptamer-based sensors. Sens. Diagn. 2024, 3 (1), 95–103.

[235] Barón-Jaimez, J., Joya, M.R., Barba-Ortega, J. Anodic stripping voltammetry-ASV for determination of heavy metals. J. Phys. Conf. Ser. 2013, 466, 012023.

[236] Ren, S., Zeng, J., Zheng, Z., Shi, H. Perspective and application of modified electrode material technology in electrochemical voltammetric sensors for analysis and detection of illicit drugs. Sens. Actuators A: Phys. 2021, 329, 112821.

[237] Wang, H.Y., Pan, M.L., Oliver Su, Y.L., Tsai, S.C., Kao, C.H., Sun, S.S., Lin, W.Y. Comparison of differential pulse voltammetry (DPV)-a new method of carbamazepine analysis-with fluorescence polarization immunoassay (FPIA). J. Anal. Chem. 2011, 66 (4), 415–420.

[238] Barhoum, A., Altintas, Z., Advanced sensor technology: biomedical, environmental, and construction applications, Elsevier: Amsterdam, 2023.

[239] Brett, C.M.A., Brett, A.M.O. Electrochemistry: principles, methods, and applications, Oxford science publications, Oxford University Press: Oxford, New York, 1993.

[240] Wandelt, K., Bussetti, G., Encyclopedia of solid-liquid interfaces, Elsevier: Amsterdam, 2024.

[241] Mirceski, V., Skrzypek, S., Stojanov, L. Square-wave voltammetry. ChemTexts 2018, 4 (4), 17.

[242] Mirceski, V., Komorsky-Lovric, S., Lovric, M. Square-wave voltammetry: theory and application; monographs in electrochemistry; Springer Berlin Heidelberg: Berlin, Heidelberg, 2007.

[243] Scott, K. Electrochemical principles and characterization of bioelectrochemical systems. In microbial electrochemical and fuel cells. Elsevier, 2016, pp 29–66.

[244] Magar, H.S., Hassan, R.Y.A., Mulchandani, A. Electrochemical impedance spectroscopy (EIS): principles, construction, and biosensing applications. Sensors 2021, 21 (19), 6578.

[245] Lazanas, A.C., Prodromidis, M.I. Electrochemical impedance spectroscopy-a tutorial. ACS Meas. Sci. Au 2023, 3 (3), 162–193.

[246] Lasia, A. Electrochemical impedance spectroscopy and its applications, Springer New York: New York, NY, 2014.

[247] Wang, S., Zhang, J., Gharbi, O., Vivier, V., Gao, M., Orazem, M.E. Electrochemical impedance spectroscopy. Nat. Rev. Methods Primers. 2021, 1 (1), 41.

[248] Randviir, E.P., Banks, C.E. Electrochemical impedance spectroscopy: an overview of bioanalytical applications. Anal. Methods 2013, 5 (5), 1098.

[249] Santos, M.A., Wong, A., Almeida, A.A., Fatibello-Filho, O. Simultaneous determination of paracetamol and ciprofloxacin in biological fluid samples using a glassy carbon electrode modified with graphene oxide and nickel oxide nanoparticles. Talanta 2017, 174, 610–618.

[250] Liustrovaite, V., Drobysh, M., Ratautaite, V., Ramanaviciene, A., Rimkute, A., Simanavicius, M., Dalgediene, I., Kucinskaite-Kodze, I., Plikusiene, I., Chen, C.F., Viter, R., Ramanavicius, A. Electrochemical biosensor for the evaluation of monoclonal antibodies targeting the N protein of SARS-CoV-2 virus. Sci. Total Environ. 2024, 171042.

[251] Prabha Sarangi, P., Prava Sahoo, D., Aparajita Mohanty, U., Nayak, S., Parida, K. Recent advancement in quantum dot modified layered double hydroxide towards photocatalytic, electrocatalytic, and photo electrochemical applications. ChemCatChem 2024, e202301533.

[252] Jiang, Y., Li, Y., Li, Y., Li, S. A sensitive enzyme-free hydrogen peroxide sensor based on a chitosan–graphene quantum dot/silver nanocube nanocomposite modified electrode. Anal. Methods 2016, 8 (11), 2448–2455.

[253] Randviir, E.P., Banks, C.E. A review of electrochemical impedance spectroscopy for bioanalytical sensors. Anal. Methods 2022, 14 (45), 4602–4624.

[254] Akash, M.S.H.; Rehman, K. Ultraviolet-visible (UV-VIS) spectroscopy. In essentials of pharmaceutical analysis, Springer Nature Singapore, Singapore, 2020.

[255] Ríos-Reina, R., Azcarate, S.M. How chemometrics revives the UV-Vis spectroscopy applications as an analytical sensor for spectralprint (nontargeted) analysis. Chemosensors 2022, 11 (1), 8.

[256] Picollo, M., Aceto, M., Vitorino, T. UV-Vis spectroscopy. Phys. Sci. Rev. 2019, 4 (4), 20180008.

[257] Santos, I.C., Schug, K.A. Recent advances and applications of gas chromatography vacuum ultraviolet spectroscopy. J. Sep. Sci. 2017, 40 (1), 138–151.

[258] Grosso, M. Maffettone, P.J. Fourier transform rheology: a new tool to characterize material properties. IntechOpen 2011.

[259] Larkin, P. Infrared and Raman spectroscopy: principles and spectral interpretation. Elsevier, Amsterdam, Boston, 2011.

[260] Griffiths, P.R., De Haseth, J.A. Fourier transform infrared spectrometry, 1st Ed., Wiley, 2007.

[261] Smith, B.C. Fundamentals of Fourier transform infrared spectroscopy, 1st Ed., CRC Press, 2011.

[262] Moore, E. Fourier transform infrared spectroscopy (FTIR): methods, analysis, and research insights, Ed., Chemical engineering methods and technology; Novinka, imprint of Nova Science Publishers, Inc: New York, 2017.

[263] Alvarez-Ordóñez, A., Prieto, M. Fourier transform infrared spectroscopy in food microbiology, Springer US, Boston, MA, 2012.

[264] Waseda, Y., Matsubara, E., Shinoda, K. X-ray diffraction crystallography: introduction, examples and solved problems, Springer Berlin Heidelberg: Berlin, Heidelberg, 2011.

[265] Katz, L. X-ray diffraction in crystals, imperfect crystals, and amorphous bodies (Guinier, A.). J. Chem. Educ. 1964, 41 (5), 292.

[266] Giacovazzo, C., Monaco, H.L., Artioli, G., Viterbo, D., Milanesio, M., Gilli, G., Gilli, P., Zanotti, G., Ferraris, G., Catti, M. Fundamentals of Crystallography, Ed., Oxford University Press, 2011.

[267] Hammond, C. The basics of crystallography and diffraction, 4th Ed., Oxford University Press, Oxford, 2015.

[268] Shih, K. X-ray diffraction: structure, principles, and applications, materials science and technologies, Nova Publishers, Hauppauge, New York, 2013.

[269] Zolotoyabko, E. Basic concepts of X-ray diffraction, Wiley-VCH, Verlag GmbH and Co. KGaA, Weinheim, 2014.

[270] Drenth, J. Principles of protein X-ray crystallography, Springer New York, New York, NY, 2007.

[271] Newbury, D.E., Joy, D.C., Echlin, P., Fiori, C.E., Goldstein, J.I. Advanced scanning electron microscopy and X-ray microanalysis, Springer US, Boston, MA, 1986.

[272] Goldstein, J.I., Newbury, D.E., Echlin, P., Joy, D.C., Romig, A.D., Lyman, C.E., Fiori, C., Lifshin, E. Scanning electron microscopy and X-ray microanalysis: A text for biologists, materials scientists, and geologists, Springer US, Boston, MA, 1992.

[273] Egerton, R. F. Physical principles of electron microscopy, Springer US, Boston, MA, 2005.

[274] Schatten, H. Scanning electron microscopy for the life sciences, 1st Ed., Cambridge University Press, 2012.

[275] Egerton, R.F. Electron energy-loss spectroscopy in the electron microscope, Springer US, Boston, MA, 2011.

[276] Goldstein, J.I., Yakowitz, H. Practical scanning electron microscopy: electron and ion microprobe analysis, Springer US, Boston, MA, 1975.

[277] Goldstein, J.I., Newbury, D.E., Echlin, P., Joy, D.C., Lyman, C.E., Lifshin, E., Sawyer, L., Michael, J.R. Scanning electron microscopy and X-ray microanalysis, 3rd Ed, Springer US, Boston, MA, 2003.

[278] Reimer, L. Hawkes, P.W., Lotsch, H.K.V. Scanning electron microscopy: physics of image formation and microanalysis, Springer series in optical sciences, Springer Berlin Heidelberg: Berlin, Heidelberg, 1998, vol. 45.

[279] Khursheed, A. Scanning electron microscope optics and spectrometers, World Scientific, 2010.

[280] Thomas, S., Thomas, R., Zachariah, A.K., Mishra, R.K. Microscopy methods in nanomaterials characterization; nanomaterials characterization techniques series. Elsevier, Amsterdam Oxford Cambridge, MA, 2017.

[281] Zhou, W., Wang, Z.L. Scanning microscopy for nanotechnology, Springer New York, New York, NY, 2007.

[282] Garratt-Reed, A.J., Bell, D.C. Energy-dispersive X-ray analysis in the electron microscope; Microscopy handbooks; BIOS, Oxford, 2003.

[283] Russ, J.C. Fundamentals of energy dispersive X-ray analysis; Butterworths monographs in materials, Butterworths, London Boston, 1984.

[284] Walter, A., Mannheim, J.G., Caruana, C.J. Imaging modalities for biological and preclinical research: a compendium: Part I: ex vivo biological imaging, IOP Publishing, 2021.

[285] Gruyter D. Energy dispersive X-ray spectroscopy (EDX). In Failure Analysis, 2022, 101–104.

[286] Hodoroaba, V.D. Energy-dispersive X-ray spectroscopy (EDS). In characterization of nanoparticles. Elsevier, 2020, pp 397–417.

[287] Scimeca, M., Bischetti, S., Lamsira, H.K., Bonfiglio, R., Bonanno, E. Energy dispersive X-ray (EDX) microanalysis: a powerful tool in biomedical research and diagnosis. Eur. J. Histochem. 2018.

[288] Ngo, P.D. Energy dispersive spectroscopy. In failure analysis of integrated circuits, Wagner, L.C., Ed., Springer US, Boston, MA, 1999.

[289] Huang, J., Günther, B., Achterhold, K., Cui, Y., Gleich, B., Dierolf, M., Pfeiffer, F. Energy-dispersive X-ray absorption spectroscopy with an inverse Compton source. Sci. Rep. 2020, 10 (1), 8772.

Chapter Three: Paper I

A simple, ultrasensitive and cost-effective electrochemical sensor for the determination of ciprofloxacin in various types of samples

Wondimeneh Dubale Adane, Bhagwan Singh Chandravanshi, Merid Tessema

Sensing and Bio-Sensing Research 39 (2023) 100547

https://doi.org/10.1016/j.sbsr.2022.100547

Sensing and Bio-Sensing Research 39 (2023) 100547

Contents lists available at ScienceDirect

Sensing and Bio-Sensing Research

journal homepage: www.elsevier.com/locate/sbsr

A simple, ultrasensitive and cost-effective electrochemical sensor for the determination of ciprofloxacin in various types of samples

Wondimeneh Dubale Adane, Bhagwan Singh Chandravanshi *, Merid Tessema

Department of Chemistry, Addis Ababa University, P. O. Box 1176, Addis Ababa, Ethiopia

ARTICLE INFO

Keywords:
Ciprofloxacin
Choline chloride
Carbon paste electrode
Square wave voltammetry
Electrochemical sensor

ABSTRACT

In this study, a simple, ultrasensitive, inexpensive, and environmentally friendly sensor was developed for the electrochemical determination of ciprofloxacin (CPRO) using a choline chloride-modified carbon paste electrode (ChCl/CPE). The electrochemical properties of ChCl/CPE were examined by square wave voltammetry (SWV). Cyclic voltammetry (CV), electrochemical impedance spectroscopy (EIS), scanning electron microscopy (SEM), ultraviolet-visible (UV–Vis) spectroscopy, and Fourier transform infrared (FT-IR) spectrometry were used for electrochemical and morphological characterizations. The sensor exhibits excellent conductivity and superior electrocatalytic activity, within the linear range of 0.005–200 μM, for the detection of CPRO in citrate buffer solution (CBS) at pH 5, with detection and quantification limits of 0.36 nM and 1.2 nM. The electroactive surface area of ChCl/CPE was calculated to be 0.123 cm^3, which is four times higher than that of the bare CPE (0.037 cm^2). The ChCl/CPE is not only simple, inexpensive and time-saving, but also has the lowest detection limit and widest linear range compared to the recently reported sensors for the determination of CPRO. The developed sensor also showed excellent reproducibility, repeatability, long-term stability, and exceptional selectivity against potentially interfering organic, inorganic, and antibiotic species. In addition, ChCl/CPE was successfully applied for the determination of ciprofloxacin in eye drops, river water, and egg samples with very good recoveries of 97–102% and relative standard deviations (RSD) of 0.27–3.85%. Therefore, the proposed electrochemical sensor is a potential candidate for the determination of ciprofloxacin in various matrices.

1. Introduction

Antibiotics are the most commonly used drugs to treat human and animal diseases caused by pathogenic microorganisms such as bacteria, microalgae, fungi, viruses, and protozoa. Antibiotics are also widely used in animal husbandry as growth promoters in poultry and livestock [1,2]. However, improper use and disposal of antibiotics harm the environment and ecology. Antibiotic residues seriously threaten the ecological balance and cause various human health problems, such as nausea, cardiac arrhythmia, hearing loss, acute and chronic toxicity, and allergic problems [3]. In addition, the efficiency of antibiotics against diseases decreases due to improper use and the increased occurrence of antibiotic resistant genes [4]. Antibiotic buildup in food and water is a growing food and environmental safety concern, urging researchers to develop more efficient methods to analyze antibiotic residues in water and food samples.

Fluoroquinolones are an important class of antibiotics with a broad spectrum of antibacterial activity. Ciprofloxacin (CPRO) is a second-generation fluoroquinolone antibiotic, the fifth generic antibiotic manufactured worldwide, and accounts for 24% of therapeutic prescriptions in the market. It is characterized by bactericidal activity against both gram-positive and gram-negative bacteria. CPRO is widely used to treat infectious diseases in livestock, poultry, and humans, including respiratory, urinary tract, gastrointestinal, eye, and skin infections [5,6]. However, excessive consumption of CPRO can lead to tendon rupture and chondrotoxic effects in young animals and to photo-toxicity, allergies, diarrhea, nausea, alterations in liver function, headache, and vomiting in humans [7]. Prolonged exposure to CPRO can cause several facets of effects, including immunotoxicity, carcinogenicity, hypertension, genotoxicity, and endocrine disruption [8]. Furthermore, the presence of CPRO and other antibiotic residues in the environment is of great concern due to the potential emergence of antibiotic-resistant bacteria [9]. Therefore, the development of fast, sensitive, and efficient techniques to monitor antibiotic levels in various matrices such as food, pharmaceuticals, and water samples is an active area of research.

In recent decades, analytical and electroanalytical methods have

* Corresponding author.
E-mail address: bscv2006@yahoo.com (B.S. Chandravanshi).

https://doi.org/10.1016/j.sbsr.2022.100547
Received 2 October 2022; Received in revised form 4 December 2022; Accepted 9 December 2022
Available online 10 December 2022

been widely used for the determination of inorganic, organic, pharmaceutical and neurochemical substances in biological and environmental samples [10]. CPRO has been quantified using different analytical methods in a variety of samples, such as food, animal tissue, body fluids, wastewater, pharmaceuticals, and dairy products. The most commonly used techniques for the determination of CPRO are high performance liquid chromatography (HPLC) [11], liquid chromatography-mass spectroscopy (LC-MS) [12], capillary electrophoresis [13], spectrophotometry [14], and chemiluminescence [15]. Although these techniques have proven to be sensitive and accurate, they have several disadvantages, such time-consuming, expensive and labor-intensive procedures that require tedious sample pretreatment and longer analysis times [16,17]. Electrochemical techniques have advantageous over other analytical methods due to their simplicity, small sample consumption and inexpensive equipment, higher selectivity and sensitivity, fast response times, and suitability for miniaturization and portability [10,17,18]. As a result, electrochemical methods have been widely applied for the determination of CPRO in various fields such as biomedical, pharmaceutical, environmental, and food [7].

Carbon-based electrodes are one of the most commonly used electrodes in electroanalytical methods due to their low cost, wide potential window, low electrical resistivity, and versatility of chemical modification. Many types of carbon-based electrodes, such as glassy carbon, carbon composites, and carbon pastes, have been used as modified electrodes [19]. A carbon paste electrode (CPE) is a special type of electrode, consisting of a mixture made from carbon powder and a non-conductive binder [20]. CPEs are widely used for the development of electrochemical sensor due to their characteristic properties such as low background current, wide potential window, lower detection limit, low cost, simplicity of surface renewal, and modification using different modifiers [10,21,22]. Furthermore, the feasibility of incorporating different substances during the paste preparation allows the fabrication of carbon paste electrodes with the desired composition and hence with predetermined properties [19]. The electrochemical determination of CPRO has been thoroughly studied using a variety of carbon-based electrodes, such as Nafion-MWCNTs [9], copper-zinc ferrite nanoparticles [23], reduced graphene oxide [24], $BiPO_4$/GO-MMIPs/PGE [25], and carbon nanotube V_2O_5 chitosan nanocomposites [26]. However, these methods have drawbacks such as complicated modification steps, high cost, time consumption, and chemical toxicity. Therefore, it is important to develop sensors with simple, inexpensive, and environmentally friendly modifiers such as choline chloride.

Choline chloride is a cheap, environmentally friendly and non-toxic quaternary ammonium salt with –OH and $–N^+(CH_3)_3$ groups. The –OH group facilitates the immobilization of ChCl on the carbon paste surface through covalent bonding, and the cationic polar group ($–N^+(CH_3)_3$) enhances electrostatic attraction and forms a uniform positively charged surface to promote the transfer of electrons between the analyte and the electrode surface [27]. Bahrani et al. [27] reported an ultrasonically accelerated synthesis of the AuNPs-ChCl-GO sensor for the detection of meloxicam in human plasma samples. A zirconia-ChCl-AuNPs/CPE sensor was developed by Shahamirifard et al. [28] for the simultaneous detection of gallic and uric acid in human urine. Parsaee et al. [29] prepared Ag-ChCl-GO/CPE for the detection of celecoxib in human plasma. However, to the best of our knowledge, there are no previous reports on the electrochemical determination of ciprofloxacin using ChCl modified CPE.

The objective of this study is to develop a simple, sensitive, environmentally friendly, and inexpensive electrochemical sensors for determining ciprofloxacin in various types of samples such as eye drops, river water, and egg samples, using choline chloride-modified carbon paste electrode.

2. Experimental

2.1. Chemicals and reagents

Ciprofloxacin (≥98%), amoxicillin (95.0–102.0%), chloramphenicol (≥98%), norfloxacin (≥98%), and doxycycline (≥98%) standards were obtained from Ethiopian Pharmaceutical Manufacturing S.C. (EPHARM), Addis Ababa, Ethiopia. Choline chloride (≥99%) in KCl (98%) (Wagtech International Ltd., UK) was purchased from Sigma-Aldrich, USA. Sodium citrate (98%) (BDH Chemicals Ltd., England), citric acid (99%) (Research-Lab Fine Chem. Industries, India), dipotassium hydrogen phosphate (98%) (Riedel-de Haen, Germany), potassium dihydrogen phosphate (98%) (BDH Chemicals Ltd., England), boric acid (99.5%) (Carlo Erba Reagents, Italy), acetic acid (99.8%) (Sigma-Aldrich, Germany), phosphoric acid (85%) (UniChem, China), ammonium chloride (≥99.5%) (BDH Chemicals Ltd., England) and sodium acetate (≥99%) (Sigma-Aldrich, Germany) were used to prepare buffer solutions. Graphite powder (Spectroscopic Grade, RBW) from SGL Carbon (Ringsdorff, Germany) and paraffin oil (Uvasol, Merck, Germany) were used to prepare the CPE. Potassium hexacyanoferrate(III) (99%) (BDH Chemicals Ltd., England) in KCl, magnesium sulfate (≥97%), sodium hydroxide (98%), hydrochloric acid (37%), calcium bicarbonate (99%), potassium nitrate (99%), copper carbonate (≥95%), ferric chloride (97%), ascorbic acid (≥99.7%), uric acid (99%), folic acid (≥97%), urea (98%), glucose (≥99.5%), lactose (≥99%), fructose (≥99%), and sucrose (≥99.5%) were purchased from Sigma-Aldrich, USA. Ciprofloxacin eye drops (ZOXAN) (FDC, Limited, India) were purchased from a local pharmacy in Addis Ababa, Ethiopia.

A stock standard solution of 0.01 M CPRO was prepared in 0.005 M HCl and stored at 4 °C until analysis. Citrate buffer solution (CBS) was prepared by mixing 0.1 M citric acid and 0.1 M sodium citrate, and the pH was adjusted using 0.1 M HCl and 0.1 M NaOH. The CPRO working solutions were prepared by diluting the stock solutions with 0.1 M CBS (pH 5.0). A 0.002 M ChCl solution was prepared by dissolving 75 mg of KCl and 28 mg of ChCl in 0.1 M phosphate buffer solution (PBS) (pH 7.0).

2.2. Apparatus and instruments

Electrochemical measurements were conducted with a CHI 760D electrochemical analyzer (CH Instruments, USA) in a 20 mL cell using three-electrode system, a platinum wire (counter) electrode, bare CPE or ChCl/CPE (working electrode), and silver-silver chloride (reference) electrode. A pH meter (Senses Ion™ + MM150, China) was used for measuring the pH. An electronic digital balance (Model: Scientech: ZSA 120, USA) was used for weighing solid chemicals. A centrifuge (model 800–1, China) and an ultrasonic cleaner (model YJ5120-B, China) were used during egg sample preparation. The surface morphologies of bare CPE and ChCl/CPE were examined by SEM (CX-200plus-Coxem, Korea). UV–Vis spectra were recorded in the range of 225–400 nm using a PerkinElmer (Lambda 950, USA) dual-beam UV–Vis spectrometer fitted with a standard 1 cm quartz cuvette. Infrared spectra were recorded on a Fourier transform infrared spectrometer (FT-IR, PerkinElmer, Spectrum 100, USA).

2.3. Sample preparation

2.3.1. Egg sample

Egg samples were obtained from the Elfora Agro-Industries plc poultry farm in Bishoftu, Ethiopia, and stored at 4 °C until analysis. The egg sample was prepared as described by Chullasat et al. [30] with slight modification. The egg was homogenized with continuous stirring. Then, 10 mL of acetonitrile was added to 5.0 g of egg in a 15 mL centrifuge tube. The mixture was ultrasonically extracted for 15 min and centrifuged at 2240 relative centrifugal force (RCF) for 10 min, then the supernatant was transferred to another 15 mL polypropylene centrifuge

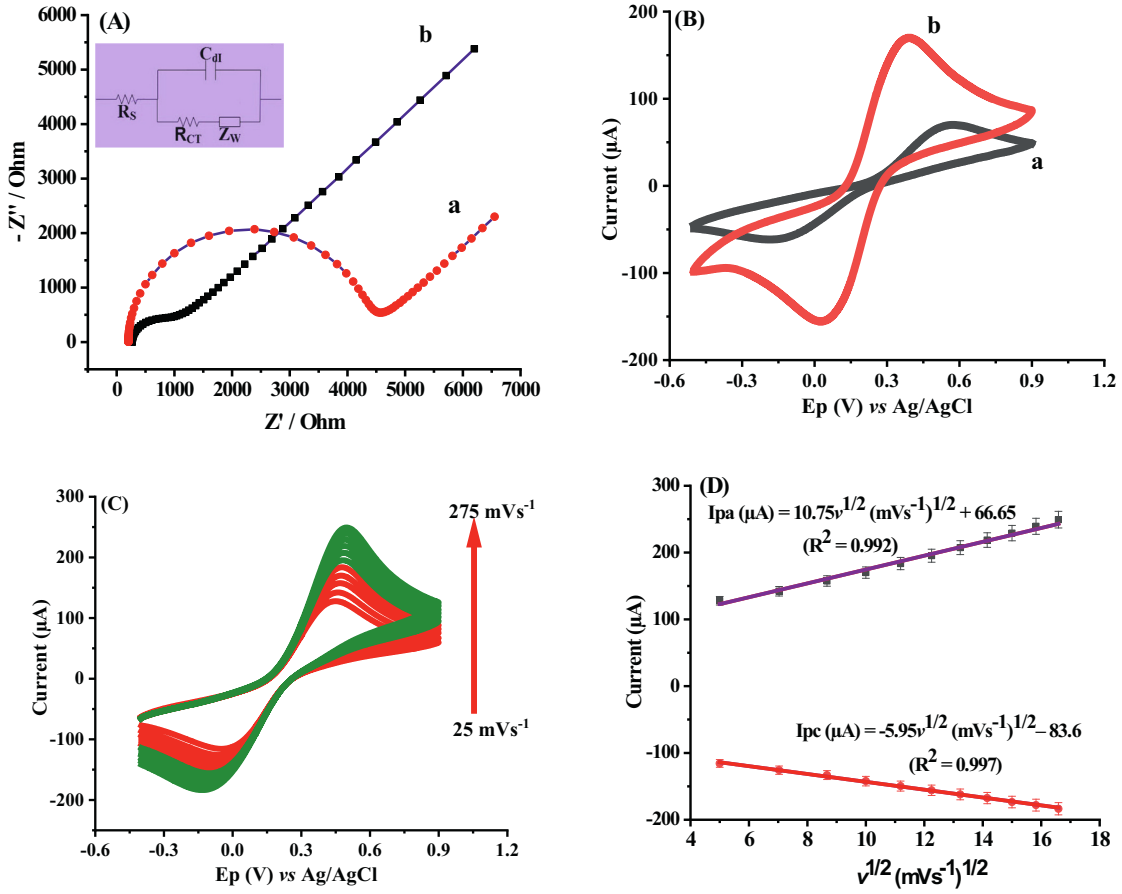

Fig. 1. (A) Nyquist plots of bare CPE (a) and ChCl/CPE (b) in 0.1 M KCl containing 5.0 mM $[Fe(CN)_6]^{3-/4-}$. (B) CV results for the bare CPE (a) and ChCl/CPE (b) in 0.1 M KCl containing 5.0 mM $[Fe(CN)_6]^{3-/4-}$ at a scan rate of 100 mVs^{-1}. (C) CVs of 5 mM $[Fe(CN)_6]^{3-/4-}$ at different scan rates using ChCl/CPE and (D) plot of Ip (μA) versus $v^{1/2}$ (mVs^{-1})$^{1/2}$.

tube. After that, 1.0 mL of 4.0 M ammonium acetate buffer (pH 6.75) was added to the mixture and vortexed. Additionally, 20 mL of dichloromethane was added to the mixture and centrifuged at 2240 RCF for 10 min. The supernatant was then collected and evaporated at 40 °C. Finally, the extract was re-dissolved in 2.0 mL of phosphate buffer (pH 7.0) and filtered through a 150 mm filter membrane before analysis.

2.3.2. River water sample

A 300 mL river water sample was collected from Akaki River in Addis Ababa, Ethiopia, and stored at 4 °C until analysis. The sample was filtered three times through a 150 mm filter membrane, a portion of the sample was taken and diluted 1:5 (*v*/*v*) in citrate buffer (pH 5.0) to a total volume of 25 mL, and spiked with 0, 5.0, 10.0, and 20.0 μM CPRO standard solutions in triplicate. After an incubation time of 30 min, the samples were analyzed without further treatment.

2.3.3. CPRO eye drops sample

A 5.5 μL portion of the CPRO eye drops sample was transferred to a 10 mL volumetric flask and diluted to the mark with 0.1 M citrate buffer, pH 5.0. The samples were spiked with 0, 5.0, 10.0, and 20.0 μM CPRO standard solutions in triplicate. The samples were stored at 4 °C until analysis and analyzed without further treatment.

2.4. Preparation of CPE

The CPE was prepared by mixing 70% (*w*/w) graphite powder and 30% paraffin oil, and homogenizing the mixture with a mortar and pestle for 25 min. Then, the paste was filled into a 1 mL syringe, electrically contacted with a copper wire, and the surface was smoothed on a clean piece of paper until it had a shiny surface. Whenever electrode renewal was required, a thin layer of the surface was carefully removed, filled with a new paste and polished.

2.5. Preparation of ChCl/CPE

Before modification, the bare CPE was rinsed with distilled water and dried at room temperature. Then, for the electrochemical deposition of ChCl at the CPE (Fig. S1), CV was performed for 14 cycles in 0.1 M PBS (pH 7.0) containing 0.002 M ChCl in 0.01 M KCl in a potential range of 0.7 V to 1.6 V at a scan rate of 25 mVs^{-1}. The electrode was then cleaned with distilled water and made ready for use.

3. Results and discussion

3.1. Electrochemical characterization

Electrochemical impedance spectroscopy was performed to study the interface properties of bare CPE and ChCl/CPE in the frequency range from 0.1 Hz to 100 kHz at an applied potential of 100 mV. The Nyquist plots of bare CPE (curve a) and ChCl/CPE (curve b) in 0.1 M KCl containing 5 mM $[Fe(CN)_6]^{3-/4-}$ couple as a redox probe are shown in Fig. 1A. The impedance data was fitted, and the corresponding Randles equivalent circuit model is given as an inset in Fig. 1A. The circuit displays, Warburg impedance (Z_w), charge transfer resistance (R_{ct}), double layer capacitance (C_{dl}), and electrolyte solution resistance (R_s). As depicted in Fig. 1A, both curves have two distinct parts: a semicircle in

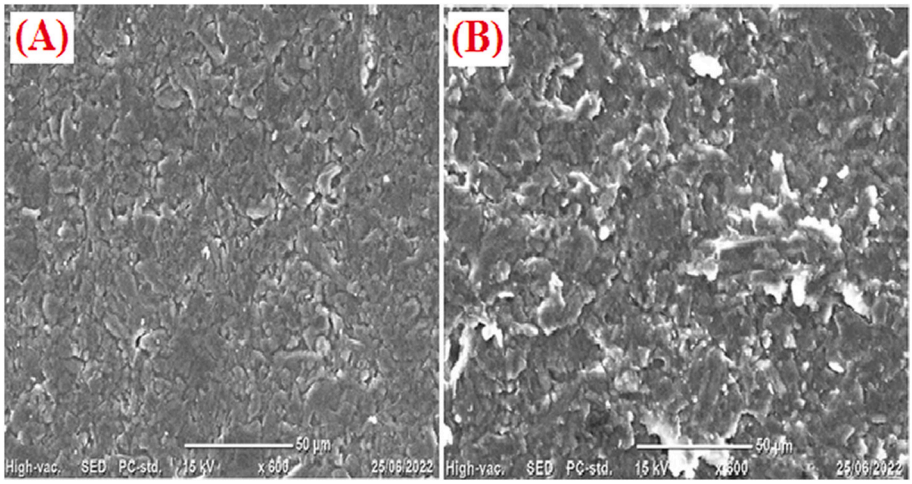

Fig. 2. SEM images of (A) bare CPE and (B) ChCl/CPE.

the high frequency range and a straight line in the low frequency range. The semicircular portion of the curve at high frequency represents the charge transfer resistance (R_{ct}) of the electrode, and the linear segment at lower frequencies indicates a diffusion-limited process. In addition, a smaller semicircle diameter indicates a rapid rate of electron transfer and a larger semicircle diameter indicates a slower electron transfer rate [31]. The calculated R_{ct} values are 4062 Ω for bare CPE and 628.1 Ω for ChCl/CPE. The enhanced electron transfer between the electrode and the electrolyte solution is made possible by the superior electrical conductivity of ChCl and higher specific surface area, which also contribute to the significantly lower charge transfer resistance of ChCl/CPE compared to bare CPE.

CV scans were performed at a scan rate of 100 mVs^{-1} for a 5 mM $[Fe(CN)_6]^{3-/4-/}$ redox probe containing 0.1 M KCl to investigate the surface areas of bare CPE and ChCl/CPE. Cathodic and anodic peak currents obtained at the ChCl/CPE were higher than that of the bare CPE, as shown in Fig. 1B. In addition, the peak-to-peak separation (ΔEp) was lower at the ChCl/CPE than that of the bare CPE, which indicates a significant increment of reversibility. The results showed that ChCl/CPE exhibited excellent conductivity and faster electron transfer capability than the bare CPE due to the increase in its electroactive surface area. Furthermore, ChCl/CPE and bare CPE were examined at various scan rates (25–275 mVs^{-1}) (Figs. 1C and S2A). As shown in Figs. 1D and S2B, the redox peak currents increased linearly with the square root of the scan rate. It indicated that the mass transfer at the electrodes was mainly diffusion controlled. The electroactive surface area of the CPE and the ChCl/CPE was also determined using the Randles-Sevcik Eq. (1) [32].

$$Ip = 2.69 \times 10^5 n^{3/2} AD^{1/2} C\nu^{1/2} \quad (1)$$

where Ip, D, C, A, n, and ν are the peak current, diffusion coefficient (cm^2/s), concentration of $[Fe(CN)_6]^{3-/4-}$ (mol cm^{-3}), surface area of electrode, number of electrons, and scan rate (Vs^{-1}), respectively. The regression equations obtained from CV analysis for the bare CPE and ChCl/CPE are $Ip = 4.38\ \nu^{1/2}\ (mVs^{-1})^{1/2} + 27.75$ ($R^2 = 0.993$) and $Ip = 10.75\ \nu^{1/2}\ (mVs^{-1})^{1/2} + 66.65$ ($R^2 = 0.992$), respectively (Fig. 1C, D and S2). The electroactive surface areas were calculated from the slopes of the plot Ip versus $\nu^{1/2}$. The calculated active surface area values are 0.037 cm^2 for the bare CPE and 0.123 cm^2 for the ChCl/CPE. This result demonstrates that ChCl is an effective modifier that enhances the electroactive surface area of the electrode. The CV results are consistent with those obtained from EIS.

Furthermore, the heterogeneous rate constant (k°) for the electrodes was calculated from the EIS and CV data using the following Eq. (2) [33].

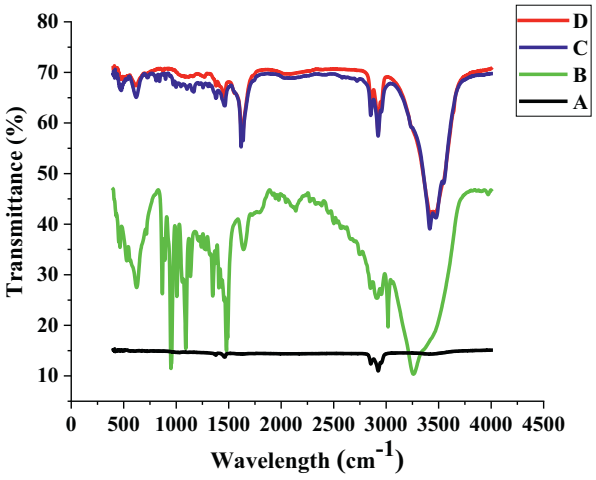

Fig. 3. (A) FT-IR spectra of bare CPE, (B) pure ChCl, (C) ChCl/CPE and (D) ChCl/CPE in 50 µM CPRO.

$$k^0 = \frac{RT}{R_{ct}ACF^2} \quad (2)$$

where k°, F, R_{ct}, T, C, A, and R, are the standard heterogeneous electron transfer rate constant (cm s^{-1}), Faraday constant (96,485C mol^{-1}), the electron transfer resistance (Ω), temperature (298 K), the concentration of $[Fe(CN)_6]^{3-/4-}$ solution (mol cm^{-3}), the electrode surface area (cm^2), and gas constant (8.314 J K^{-1} mol^{-1}), respectively. The k° values obtained for bare CPE and ChCl/CPE were 3.54×10^{-4} and 6.89×10^{-4} cm s^{-1}, respectively. The higher k° value for the ChCl/CPE shows a faster electron transfer and a higher active surface area than the bare CPE.

3.2. Surface characterization

The surface morphologies of the bare CPE and the ChCl/CPE were examined by SEM image analysis. As shown in Fig. 2, significant differences are observed between the morphologies of the two electrodes. The bare CPE surface (Fig. 2A) is characterized by evenly distributed pores and tightly curled graphite flakes. In contrast, after modification (Fig. 2B), at the surface of the modified electrode, the number of pores and their size increased, with uneven distribution and irregular shapes. The SEM image of ChCl/CPE also shows a denser film with granular and

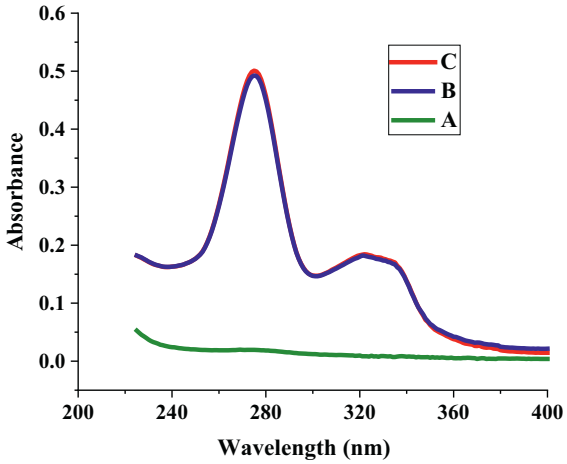

Fig. 4. UV–Vis spectra of (A) pure ChCl, (B) CPRO and ChCl mixture, and (C) CPRO in aqueous solution.

rough structures, increasing the surface area and active sites for CPRO oxidation.

The FT-IR spectra of bare CPE, pure ChCl, ChCl/CPE, and ChCl/CPE in 50 μM CPRO are given in Fig. 3. As shown in Fig. 3A, no significant bands were observed at the bare CPE surface. The C—H stretching of the alicyclic (–CH_2–) group of the paraffin oil used to prepare the bare CPE, is observed in the region between 2853 and 2923 cm^{-1}. The appearance of a very intense and broad band at the frequency of 3262 cm^{-1} corresponds to the O—H stretch of the ChCl used to modify CPE (Fig. 3B). The bands at 3000–2800 cm^{-1} are attributed to the C—H stretches of the –CH_3 and –CH_2– groups and the band at 1090 cm^{-1} is attributed C—O of ChCl. A specific set of quaternary ammonium compounds is present in the range of 900–1000 cm^{-1} and the peak at 950 cm^{-1} is believed to be the peak for the C—N group of ChCl [34]. As shown in Fig. 3C, the spectrum of ChCl/CPE shows a slight decrease in band intensity and width, and a small shift in the O—H stretch to 3415 cm^{-1} due to the decrease in hydrogen bonding. Similar to the pure ChCl, the frequencies at 480, 618, 1618, and 2924 cm^{-1} are not changed but reduced the band intensity, indicating the presence of ChCl at the surface of the modified electrode. In addition, the characteristic absorption originating from the $(CH_3)_3N^+$ group of pure ChCl is observed at 1464 cm^{-1} [27]. As a result, the above observations confirm the electrodeposition of ChCl at the surface of CPE. As illustrated in Fig. 3C and D, there is no difference between the two spectra. The result gives clear evidence for the absence of interaction between ChCl/CPE and CPRO, whereas the modifier ChCl electro-catalyzes the oxidation of CPRO at the surface of ChCl/CPE by increasing the electroactive area of the modified electrode.

The UV absorption spectrum of CPRO in water was measured in the range 225–400 nm, and showed an absorption band at $\lambda_{max\ (water)} = 275$ nm (Fig. 4C). The absorption band was attributed to the n-π^* transition of CPRO, since it is a nitrogen-containing compound [35]. From Fig. 4B, it was observed that the absorption band of CPRO did not shift with the addition of ChCl to the CPRO solution. This result further confirms the absence of interaction between CPRO and ChCl. However, the ChCl film exhibits exceptional electrocatalytic activity by providing high specific surface area and excellent electron transfer ability to the modified electrode for the oxidation of CPRO [36]. Fig. 4A shows that pure ChCl is UV inactive due to the lack of conjugation in the molecule.

3.3. Electrochemical behaviors of CPRO at bare CPE and ChCl/CPE

The voltammetric behaviors of CPRO at the bare CPE and ChCl/GCE were investigated using CV and SWV at a scan rate of 100 mVs^{-1} in the potential range of 0.7 to 1.2 V. Both bare CPE and ChCl/CPEs showed no CV and SWV signals in the blank solution. This may be due to poor

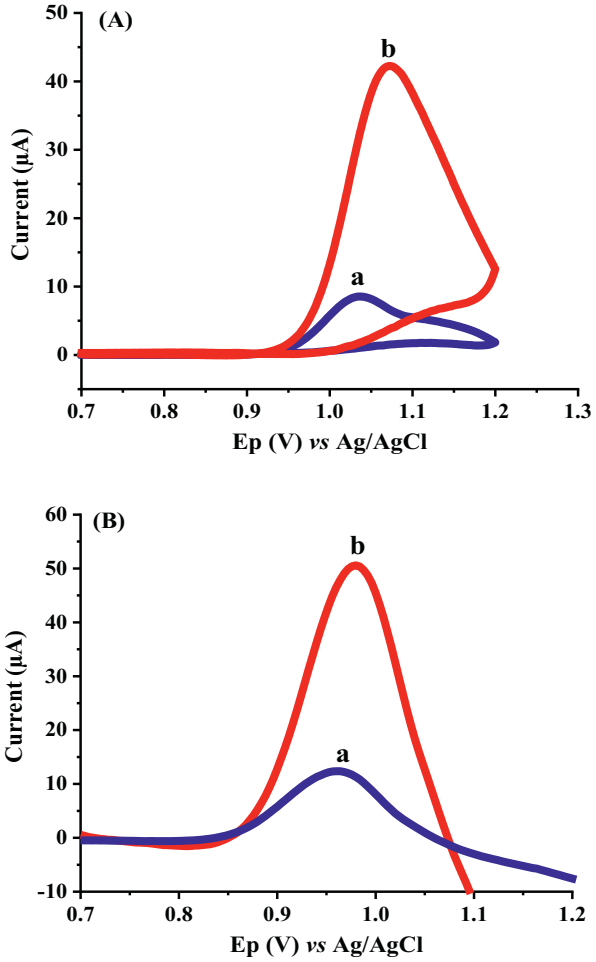

Fig. 5. (A) CVs of bare CPE (a) and ChCl/CPE (b) in 0.1 M CBS (pH 5.0) containing 50 μM CPRO at a scan rate of 100 mVs^{-1} and (B) SWVs of bare CPE (a) and ChCl/CPE (b) in 0.1 M CBS (pH 5.0) containing 50 μM CPRO at a scan rate of 100 mVs^{-1}.

electron transfer kinetics at the bare CPE and the absence of the target analyte in the blank solution. The CVs of a bare CPE (a) and ChCl/CPE (b) in 0.1 M CBS (pH 5.0) containing 50 μM CPRO are shown in Fig. 5A. The oxidation of CPRO is irreversible, with oxidation peak potentials of 1.037 V at the bare CPE and 1.073 V at the ChCl/CPE with no reduction peaks in the reverse scan. The oxidation signal of CPRO at the bare CPE is weak and appears at a lower potential. In contrast, the oxidation of CPRO at the ChCl/CPE produced a well-defined peak at 1.073 V with a shift in potential by about 0.036 V to a more positive value under the same conditions. A 5-fold increase in the peak current for the oxidation of CPRO at the modified electrode confirms the increase in active surface area and strong electrocatalytic activity of the ChCl film. The electrochemical response of CPRO was also studied by SWV using both electrodes, and similar results were obtained in terms of peak current enhancement and potential shifts (Fig. 5B).

3.4. Optimization of experimental conditions

3.4.1. Effect of supporting electrolytes

The effects of different supporting electrolyte solutions, such as acetate buffer (AB), Britton-Robinson buffer (BRB), citrate phosphate buffer (CPB), citrate buffer solution (CBS), and phosphate buffer solution (PBS), on the oxidation peak current response of CPRO were examined by SWV. As shown in Fig. S3, the peak current response obtained in CBS was significantly higher than that of the other supporting

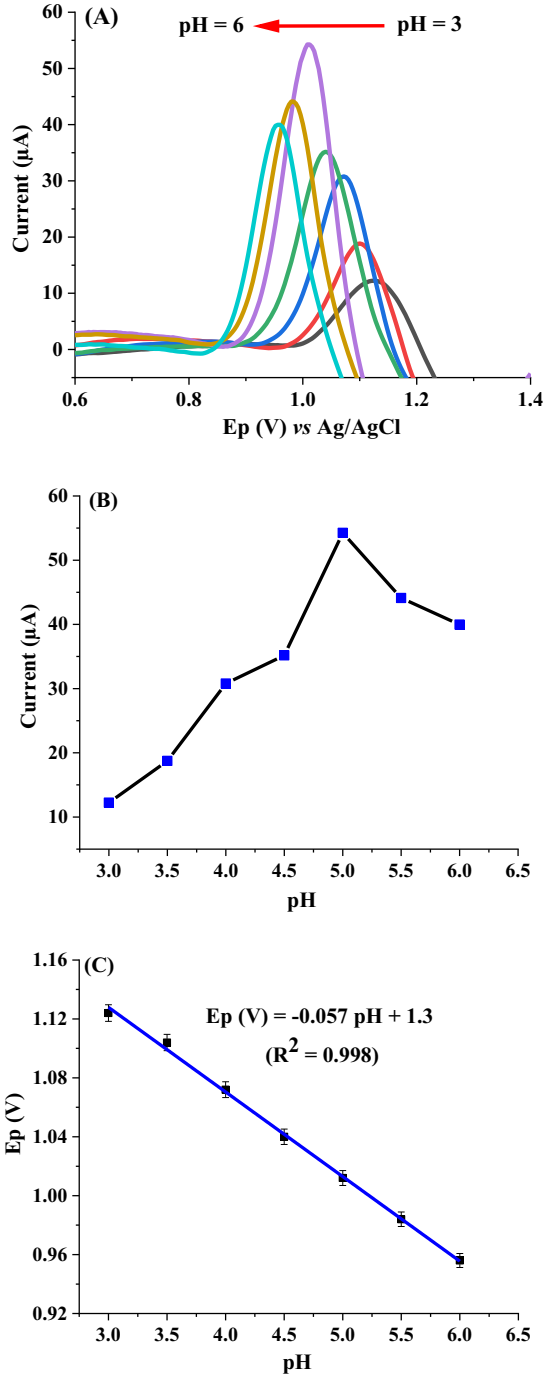

Fig. 6. (A) CVs of 50 μM CPRO at different pH values (3.0, 3.5, 4.0, 4.5, 5.0, 5.5, and 6.0) in 0.1 M CBS at a scan rate of 100 mVs^{-1}, (B) plot of Ip (μA) versus pH and (C) plot of Ep (V) versus pH.

electrolyte solutions. Therefore, 0.1 M CBS was chosen as a suitable supporting electrolyte for the electrochemical determination of CPRO at the ChCl/CPE.

3.4.2. *Effect of pH*

The electrochemical response of 50 μM CPRO in 0.1 M CBS was studied using SWV in the pH range 3.0–6.0 at a scan rate of 100 mVs^{-1}. The peak potential and current responses of CPRO varied dramatically as the pH of CBS increased from 3.0 to 6.0, as depicted in Fig. 6A, proving that the oxidation of CPRO depends on the pH of the supporting electrolyte solution. The oxidation peak current increased with

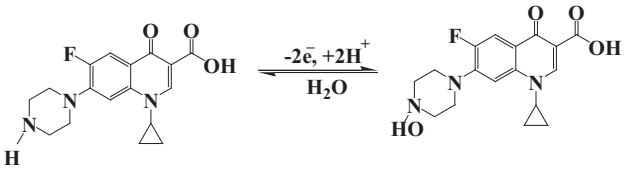

Scheme 1. Proposed reaction mechanism for the oxidation of CPRO.

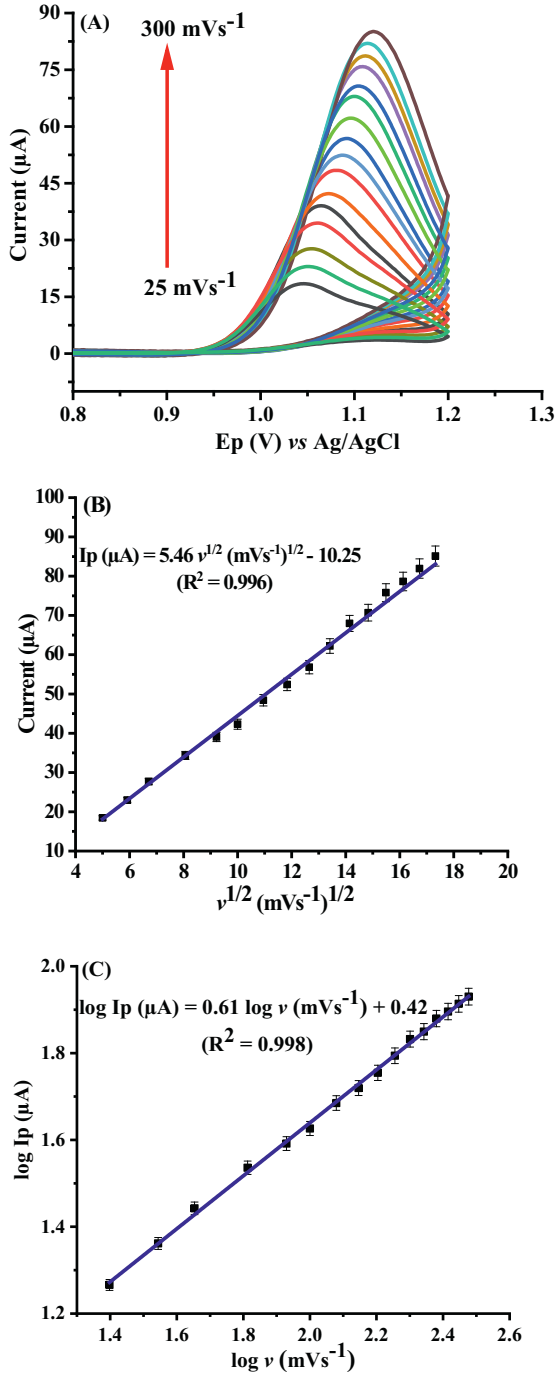

Fig. 7. (A) CVs of 50 μM CPRO in 0.1 M CBS at different scan rates (B) Ip (μA) versus $v^{1/2}$ $(mVs^{-1})^{1/2}$ and (C) plot of log Ip (μA) versus log v (mVs^{-1}) for 50 μM CPRO in 0.1 M CBS.

increasing pH up to 5.0 and then decreased with further increase (Fig. 6B). Therefore, pH 5.0 was chosen as the optimal value for subsequent experiments. Additionally, the influence of pH on the peak potential of CPRO was investigated. With increasing pH, it was found that the peak potential shifted to a more negative value, suggesting the involvement of protons in the electrode process. According to the Nernst equation [37], the relationship between Ep and pH is described as follows:

$$\text{Ep (V)} = 0.059(\text{m/n})\ \text{pH} + \text{b} \quad (3)$$

where Ep is the peak potential, n and m are the numbers of electrons and protons participating in the electrode reaction, and b is the intercept. From the plot of Ep (V) versus pH (Fig. 6C), the linear relationship was expressed by: Ep (V) = −0.057 pH + 1.3 ($R^2 = 0.998$). A typical shift of 57 mV per pH unit is nearly equal to the theoretical Nernst value of 59 mV per pH, proving that the number of electrons and protons involved in the electro-oxidation reaction of CPRO are equal [38]. The proposed reaction mechanism for the oxidation of CPRO is given in Scheme 1 [39].

3.4.3. Effect of scan rate

The effect of scan rate on the peak current and peak potential of CPRO in 0.1 M CBS (pH 5.0) was investigated using CV at scan rates ranging from 25 to 300 mVs^{-1}. As shown in Fig. 7A, there is a progressive increase in peak current with increasing scan rates from 25 to 300 mVs^{-1} along with a shift in peak potential to a more positive value, confirming that the oxidation of CPRO at the surface of ChCl/CPE is irreversible. The graph of Ip (μA) versus square root of scan rate (Fig. 7B) is linear, with the regression equation Ip (μA) = $5.46v^{1/2}$ $(mVs^{-1})^{1/2}$–10.25 ($R^2 = 0.996$). In addition, the log Ip versus log *v* plot yields the regression equation log Ip (μA) = 0.61 log *v* (mVs^{-1}) + 0.42, $R^2 = 0.998$ (Fig. 7C) with a slope of 0.61, which is close to the theoretical value of 0.5. The above results together with FT-IR and UV–Vis experiments (in Section 3.2), thus confirm that the voltammetric oxidation of CPRO at the surface of ChCl/CPE is primarily an irreversible diffusion controlled electrode process [38].

The number of electrons involved in the oxidation of irreversible electrode reactions was determined using the Laviron theory [40]. Ep (V) is given by the equation:

$$E_p = E^0 + \frac{2.303RT}{\alpha nF} log \frac{RTk^0}{\alpha nF} + \frac{2.303RT}{\alpha nF} log v \quad (4)$$

where E^0, α, n, k^0, *v*, F, R, and T denote the formal potential, electron transfer coefficient, number of electrons, heterogeneous rate constant, scan rate, Faraday constant (96,485C/mol), universal gas constant (8.314 J/K mol), and temperature (298 K). According to Eq. (4), the plot of Ep versus log *v* shows very good linearity. The slope (0.07) corresponds to 2.303RT/αnF, yielding αn = 0.845. For an irreversible electrode process, it is assumed that α is equal to 0.5 [37]. Using Eq. (4), the number of electrons transferred (n) was calculated to be 1.7, which is close to 2, indicating that the electrochemical oxidation of CPRO at the surface of ChCl/CPE involves a transfer of two protons and two electrons, which is consistent with previously reported literature values [41].

3.4.4. Optimization of SWV parameters for the determination of CPRO

Square wave parameters were optimized to obtain maximum peak current response for the oxidation of CPRO at the surface of ChCl/CPE. The relationship between SWV parameters and the peak current was examined by keeping two of the parameters constant and measuring the other in the frequency range (20–70 Hz), step potential (2–16 mV), and amplitude (20–90 mV). The optimal values for determining CPRO were selected by taking into account the lowest background current, the highest peak current signal, and sharp SWV peaks. These values are 40 Hz frequency, 10 mV step potential, and 40 mV amplitude (Fig. S4).

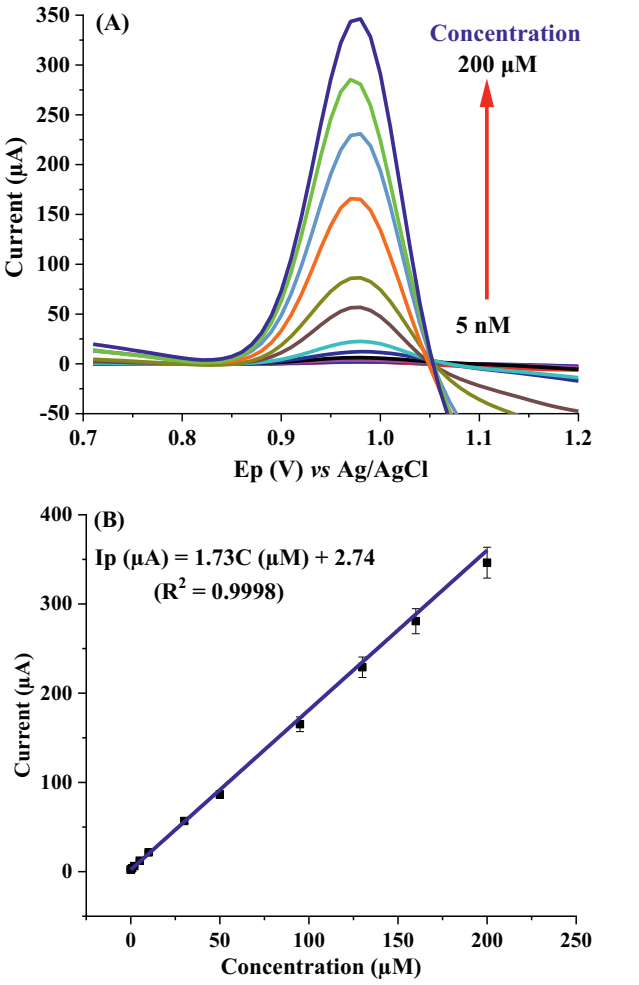

Fig. 8. (A) SWVs of 0.005, 0.06, 0.1, 0.8, 2.0, 5.0, 10.0, 30.0, 50.0, 95.0, 130.0, 160.0 and 200.0 μM CPRO at the ChCl/CPE in 0.1 M CBS and (B) plot of Ip (μA) versus concentration of CPRO.

3.5. Analytical determination of CPRO

Under the optimal experimental conditions, square wave responses were recorded for different CPRO concentrations in 0.1 M CBS. As depicted in Fig. 8A, when the concentration of CPRO increases, the peak current for the oxidation of CPRO also increases. The oxidation peak current is linearly correlated with concentration of CPRO from 0.005 μM to 200 μM, with a regression equation of Ip (μA) = 1.73C (μM) + 2.74 ($R^2 = 0.9998$) (Fig. 8B). Theoretically calculated detection, LOD, (3σ/m), and quantification limits, LOQ, (10σ/m), (S/N = 3), (where m and σ denote the slope of the calibration curve and standard deviation of the lowest values of the linear range), were found to be 0.36 nM and 1.2 nM, respectively. However, the developed sensor practically detects 2 nM CPRO (not inside the linear range) (Fig. S5). In addition, the performance of ChCl/CPE was compared to recently published literature values in terms of linear range and the limit of detection. As shown in Table 1, the ChCl/CPE demonstrates superior performance by offering the lowest detection limit and a broader linear range than recently reported sensors for the electrochemical determination of CPRO. Due to its low coat, simplicity, and fast response, ChCl/CPE is an excellent candidate for the electrochemical determination of CPRO in real samples.

Table 1
Comparison of ChCl/CPE with recently reported techniques for determining CPRO.

Sensors	Method	Real samples	Linear range (μM)	LOD (μM)	References
Co-MOFs/PLA [a]	DPV	Drug	0.5–150	0.017	[42]
GO/SPCE [b]	DPV	Milk	1–8	0.3	[43]
TiO_2/PVA/GCE [c]	DPV	Rain water	10–120	0.04	[44]
f-MWCNTs/PANI/GCE [d]	LSV	Pharmaceuticals	0.1–1, 1–20	0.08	[45]
f-MWCNT-coated GCE [e]	SWV	Hospital effluent, wastewater, natural water	5–100	0.16	[46]
$BaCuSi_4O_{10}$/GCE [f]	DPV	Pharmaceuticals	0.05–150	0.0009	[47]
Pt-RGO/GCE [g]	DPV	Tap water, river water	10–25	1.53	[48]
CRGO/GCE [h]	SWV	Pharmaceuticals, milk	6–60	0.5	[24]
Ch-AuMIP/GCE [i]	DPV	Tap water, milk, mineral water, pharmaceuticals	1–100	0.21	[49]
$BiPO_4$/GO-MMIPs/PGE [j]	SWSV	Blood serum, milk	39–740	0.4	[25]
Fe-g-C_3N_4/PGE [k]	DPV	Blood serum	0.001–1	0.0054	[50]
ChCl/CPE	SWV	CIP eye drops, eggs, river water	0.005–200	0.00036	This work

Abbreviations: [a]Co-MOFs/PLA: Co-metal organic frameworks/poly lactic acid, [b]GO/SPCE: Graphene oxide - screen printed electrode, [c]TiO_2/PVA: Titanium dioxide polyvinyl alcohol, [d]f-MWCNTs/PANI: Functionalized multiwall carbon nanotube-polyaniline, [e]f-MWCNT: Functionalized multiwall carbon nanotube, [f]$BaCuSi_4O_{10}$: Phyllosilicate effenbergerite, [g]Pt-RGO: Platinum nanoparticles - reduced graphene oxide, [h]CRGO: Chemically reduced graphene oxide, [i]Ch-AuMIP: Chitosan gold nanoparticles decorated molecularly imprinted polymer, [j]$BiPO_4$/GO-MMIPs/PGE: Bismuth phosphate, graphene oxide, magnetic molecularly imprinted polymer modified pencil graphite electrode, [k]Fe-g-C_3N_4/PGE: Iron decorated graphitic carbon nitride modified pencil graphite electrode.

3.6. Reproducibility, repeatability and stability of ChCl/CPE

The performance of the proposed sensor was assessed based on its repeatability, reproducibility and stability. The reproducibility of the sensor was evaluated by SWV responses for the oxidation of 20 μM CPRO in 0.1 M CBS (pH 5.0) using seven different ChCl/CPEs prepared in identical procedures (Fig. S6A). A RSD of 1.8% was obtained for the oxidation peak current responses, showing an excellent reproducibility of the proposed sensor for the determination of CPRO.

Intraday and interday repeatability studies were performed to evaluate the precision of the developed method. In the intraday repeatability study, 10 consecutive SWV measurements were performed on the same day using 20 μM CPRO in 0.1 M CBS. The RSD value obtained for the anodic peak current responses was 1.52% (Fig. S6B). In the interday repeatability study, the oxidation peak current response of the electrode was examined on three different days ($n = 3$), and the RSD value was calculated to be 1.26%. Therefore, the intraday and interday results showed that the proposed ChCl/CPE sensor has exceptional repeatability (Fig. S6C).

The stability of the ChCl/CPE was studied by measuring its response for the oxidation of 20 μM CPRO. The electrode was kept at 4 °C for a month and its response was checked every week. The initial oxidation current response was reduced by 2% after the first week, by 3.8% after the second week, by 4.8% after the third week, by 6.1% after one month, and the peak potential remained unchanged (Fig. S7). The RSD calculated for the current responses was 1.7%, indicating that the ChCl/CPE had very good long-term stability. Thus, it can be concluded that ChCl/CPE exhibits exceptional reproducibility and repeatability, as well as remarkable long-term stability for the electrochemical determination of CPRO.

Table 3
Summary of the comparison results between the labeled CPRO content and the value detected by the sensor.

Sample	Labeled content (% *w/v*)	Detected (% *w/v*)	% detected	RSD
Eye drops	0.3	0.298	99.3	1.7

3.7. Interference studies

The selectivity of ChCl/CPE for the detection of CPRO was investigated in the presences of a variety potentially interfering organic, inorganic, and antibiotic species. 50-fold concentrations of biologically interfering organic compounds such as uric acid, ascorbic acid, fructose, lactose, glucose, sucrose, folic acid, and urea were added to 5 μM CPRO in 0.1 M CBS, and the results show that these potential interferents did not significantly affect the oxidation signal of CPRO (Fig. S8 (A)). In addition, 100-fold excess concentrations of inorganic ions including Ca^{2+}, Cu^{2+}, Fe^{3+}, Mg^{2+}, K^+, CO_3^{2-}, NO_3^-, Cl^-, SO_4^{2-}, and HCO_3^- were introduced into the same CPRO solution, and no significant interference was observed for these common inorganic ions (Fig. S8 (B)). Furthermore, the interfering effects of common antibiotics, such as amoxicillin, chloramphenicol, doxycycline, and norfloxacin, was evaluated using a 20-fold excess concentration of each. It was observed that the presence of the antibiotics did not significantly affect the electrochemical responses of the sensor. As shown in Table 2, the relative percentage errors in the peak current response are <5%, indicating that the oxidation current of CPRO is unaffected even in the presences of excess concentrations of possibly interfering species. The voltammetric curves for the data given in Table 2 are shown in Fig. S8 (C). Therefore, the above observations are strong evidence for the excellent performance of ChCl/CPE for the selective determination of CPRO.

Table 2
The influence of commonly interfering inorganic, organic, and antibiotic species on the determination of 5 μM CPRO in 0.1 M CBS at the ChCl/CPE.

Interferents	Concentration (μM)	Relative percentage error (%)	Interferents	Concentration (μM)	Relative percentage error (%)
Cu^{2+}	500	−1.15	Uric acid	250	−1.37
K^+	500	−0.99	Lactose	250	−2.38
Fe^{3+}	500	−1.32	Glucose	250	−2.44
Ca^{2+}	500	−0.9	Sucrose	250	−1.84
Mg^{2+}	500	−0.89	Urea	250	−2.34
CO_3^{2-}	500	−1.15	Ascorbic acid	250	−2.79
NO_3^-	500	−0.99	Folic acid	250	−3.75
Cl^-	500	−1.32	Amoxicillin	100	−3.98
HCO_3^-	500	−0.9	Chloramphenicol	100	−3.23
SO_4^{2-}	500	−0.89	Doxycycline	100	−3.57
Fructose	250	−2.3	Norfloxacin	100	−3.91

Table 4
Summary of the recovery results for the determination of CPRO in eye drops, river water and egg samples using ChCl/CPE (n = 3).

Samples	Spiked (μM)	Found (μM)	Recovery (%)	RSD (%)
Eye drops	0	4.95	–	1.72
	5	9.85	98	0.51
	10	15.15	102	0.3
	20	24.42	97.4	0.27
River water	0	0.12	–	3.27
	5	4.98	97.2	3.48
	10	10.2	100.8	3.85
	20	19.68	97.8	3.01
Egg	0	–	–	–
	5	4.92	98.4	2.78
	10	9.76	97.6	3.71
	20	19.4	97	2.51

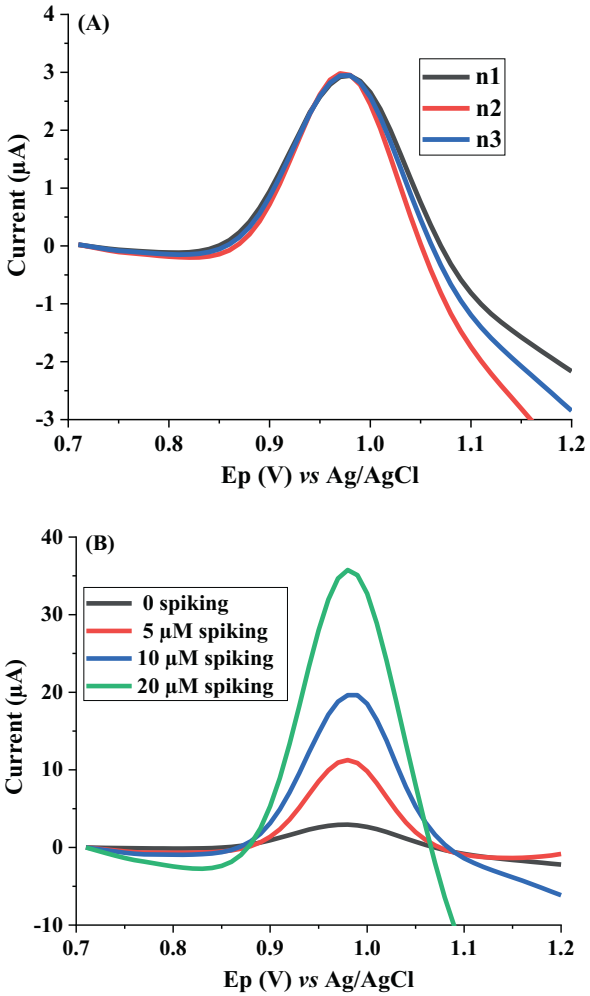

Fig. 9. (A) SWVs of unspiked water sample in 0.1 M CBS at ChCl/CPE and (B) SWVs of water samples in 0.1 M CBS (pH 5.0) spiked with 0, 5.0, 10.0, and 20 μM standard solutions of CPRO.

3.8. Analytical application

The determination of ciprofloxacin in eye drops, river water, and egg samples illustrated the practical application of the proposed sensor. For CPRO eye drops, experimentally obtained results and values labeled by the manufacturer are compared in Table 3. The results obtained with the ChCl/CPE are remarkably close to the labeled amount (RSD = 1.7%) provided by the manufacturer. Therefore, ChCl/CPE can be successfully applied for the electrochemical determination of CPRO in pharmaceutical eye drops. The standard addition method was used to quantify CPRO in river water samples, and the results are shown in Table 4. As illustrated in Fig. 9A, an oxidation peak was observed for CPRO in the unspiked river water sample, and the peak current increased with successive additions of standard solutions, indicating that the river water contains CPRO (Fig. 9B). However, no voltammetric response was observed for CPRO in unspiked egg samples, suggesting that CPRO is not present in egg samples or its concentration is below the detection limit.

Additionally, the reliability of the developed method was examined by spiking CPRO into eye drops, river water, and egg samples with an appropriate amount of standard solution and calculating the percentage recoveries. As presented in Table 4, very good recoveries ranging from 97% to 102% were obtained. Therefore, ChCl/CPE has excellent potential for the determination of CPRO in real samples with high selectivity, accuracy, and precision.

4. Conclusions

In this study, an ultrasensitive and inexpensive voltammetric sensor, ChCl/CPE, was developed for the accurate and precise determination of ciprofloxacin Compared to recently reported modified electrodes, the proposed sensor showed superior performance with a lower detection limit and a broader linear range, indicating high sensitivity of the method. The sensor demonstrated high selectivity for detecting CPRO in the presence of commonly interfering organic, inorganic, and antibiotic species, as well as excellent reproducibility, repeatability, and long-term stability. The proposed sensor showed good recovery results (97% to 102%) for the electrochemical detection of CPRO in real samples, including eye drops, river water, and egg samples without the need for complicated and time-consuming pretreatment procedures.

Data availability statement

All the data are included in the manuscript. There are no additional data with the authors.

CRediT authorship contribution statement

Wondimeneh Dubale Adane: Conceptualization, Methodology, Software, Resources, Formal analysis, Investigation, Writing – original draft. **Bhagwan Singh Chandravanshi:** Conceptualization, Writing – review & editing, Supervision. **Merid Tessema:** Writing – review & editing, Supervision.

Declaration of Competing Interest

The authors declare that they have no known competing financial interests or personal relationships that could have appeared to influence the work reported in this paper.

Data availability

No data was used for the research described in the article.

Acknowledgements

The authors gratefully acknowledge the Ethiopian Pharmaceutical Manufacturing S.C. for the provision of antibiotic standards and the Department of Chemistry, Addis Ababa University, Addis Ababa, Ethiopia for providing laboratory facilities.

Appendix A. Supplementary data

Supplementary data to this article can be found online at https://doi.org/10.1016/j.sbsr.2022.100547.

References

[1] K.K. Brandt, A. Amézquita, T. Backhaus, A. Boxall, A. Coors, T. Heberer, J. R. Lawrence, J. Lazorchak, J. Schönfeld, J.R. Snape, Y.G. Zhu, E. Topp, Ecotoxicological assessment of antibiotics: a call for improved consideration of microorganisms, Environ. Int. 85 (2015) 189–205, https://doi.org/10.1016/j.envint.2015.09.013.

[2] D.C. Rocha, C. da Silva Rocha, D.S. Tavares, S.L. de Morais Calado, M.P. Gomes, Veterinary antibiotics and plant physiology: an overview, Sci. Total Environ. 767 (2021), 144902, https://doi.org/10.1016/j.scitotenv.2020.144902.

[3] B. Ji, J. Zhang, C. Zhang, N. Li, T. Zhao, F. Chen, L. Hu, S. Zhang, Z. Wang, Vertically aligned ZnO/ZnS nano rod chip with improved photocatalytic activity for antibiotics degradation, ACS Appl. Nano Mater. 1 (2018) 793–799, https://doi.org/10.1021/acsanm. 7b00242.

[4] S. Bombaywala, A. Mandpe, S. Paliya, S. Kumar, Antibiotic resistance in the environment: a critical insight on its occurrence, fate, and eco-toxicity, Environ. Sci. Pollut. Res. 28 (2021) 24889–24916, https://doi.org/10.1007/s11356-021-13143-x.

[5] S. Bano, A.S. Ganie, R.I.A. Khan, S. Sultana, M.Z. Khan, S. Sabir, Designing and application of PPy/Bi_2MoO_6/chitosan nanocomposites for electrochemical detection of ciprofloxacin and benzene and evaluation of hydrogen evolution reaction, Surf. Interface 29 (2022), 101786, https://doi.org/10.1016/j.surfin.2022.101786.

[6] S.V. Kergaravat, N. Romero, L. Regaldo, G.R. Castro, S.R. Hernández, A. María Gagneten, Simultaneous electrochemical detection of ciprofloxacin and Ag(I) in a silver nanoparticle dissolution: application to ecotoxicological acute studies, Microchem. J. 162 (2021), 105832, https://doi.org/10.1016/j.microc.2020.105832.

[7] K. Cinková, D. Andrejčáková, L. Švorc, Electrochemical method for point-of-care determination of ciprofloxacin using boron-doped diamond electrode, Acta Chim. Slov. 9 (2016) 146–151, https://doi.org/10.1515/acs-2016-0025.

[8] N. Gissawong, S. Srijaranai, S. Boonchiangma, P. Uppachai, K. Seehamart, S. Jantrasee, E. Moore, S. Mukdasai, An electrochemical sensor for voltammetric detection of ciprofloxacin using a glassy carbon electrode modified with activated carbon, gold nanoparticles and supramolecular solvent, Mikrochim. Acta 188 (2021) 208, https://doi.org/10.1007/s00604-021-04869-z.

[9] P. Gayen, B.P. Chaplin, Selective electrochemical detection of ciprofloxacin with a porous nafion/multiwalled carbon nanotube composite film electrode, ACS Appl. Mater. Interfaces 8 (2016) 1615–1626, https://doi.org/10.1021/acsami.5b07337.

[10] P.S. Ganesh, B.E. Kumara Swamy, O.E. Feyami, E.E. Ebenso, Interference free detection of dihydroxybenzene isomers at pyrogallol film coated electrode: a voltammetric method, J. Electroanal. Chem. 813 (2018) 193–199, https://doi.org/10.1016/j.jelechem.2018.02.018.

[11] L. Wei, Y. Chen, D. Shao, J. Li, Simultaneous determination of nine quinolones in pure milk using PFSPE-HPLC-MS/MS with PS-PAN nanofibers as a sorbent, Foods 11 (2022) 1843, https://doi.org/10.3390/foods11131843.

[12] M.K. Matta, A. Chockalingam, A. Gandhi, S. Stewart, L. Xu, K. Shea, V. Patel, R. Rouse, LC-MS/MS based quantitation of ciprofloxacin and its application to antimicrobial resistance study in Balb/c mouse plasma, urine, bladder and kidneys, Anal. Methods 10 (2018) 1237–1246, https://doi.org/10.1039/C7AY02923C.

[13] R. Bosma, J. Devasagayam, A. Singh, C.M. Collier, Microchip capillary electrophoresis dairy device using fluorescence spectroscopy for detection of ciprofloxacin in milk samples, Sci. Rep. 10 (2020) 13548, https://doi.org/10.1038/s41598-020-70566-1.

[14] S. Palamy, W. Ruengsitagoon, Reverse flow injection spectrophotometric determination of ciprofloxacin in pharmaceuticals using iron from soil as a green reagent, Spectrochim. Acta A Mol. Biomol. Spectrosc. 190 (2018) 129–134, https://doi.org/10.1016/j.saa.2017.09.032.

[15] Y.M. Liu, L. Mei, H.Y. Yue, Y.M. Shi, L.J. Liu, Highly sensitive chemiluminescence detection of norfloxacin and ciprofloxacin in CE and its applications, Chromatographia 72 (2010) 337–341, https://doi.org/10.1365/s10337-010-1648-0.

[16] K.R. Reddy, P.K. Brahman, L. Suresh, Fabrication of high performance disposable screen printed electrochemical sensor for ciprofloxacin sensing in biological samples, Measurement 127 (2018) 175–186, https://doi.org/10.1016/j.measurement.2018.05.078.

[17] S. Tajik, H. Beitollahi, R. Hosseinzadeh, A. Aghaei Afshar, R.S. Varma, H.W. Jang, M. Shokouhimehr, Electrochemical detection of hydrazine by carbon paste electrode modified with ferrocene derivatives, ionic liquid, and CoS_2-carbon nanotube nanocomposite, ACS Omega 6 (2021) 4641–4648, https://doi.org/10.1021/acsomega.0c05306.

[18] S. Tajik, M.A. Taher, H. Beitollahi, Mangiferin DNA biosensor using double-stranded DNA modified pencil graphite electrode based on guanine and adenine signals, J. Electroanal. Chem. 720–721 (2014) 134–138, https://doi.org/10.1016/j.jelechem.2014.03.039.

[19] M. Mazloum-Ardakani, H. Beitollahi, Z. Taleat, H. Naeimi, N. Taghavinia, Selective voltammetric determination of d-penicillamine in the presence of tryptophan at a modified carbon paste electrode incorporating TiO_2 nanoparticles and quinizarine, J. Electroanal. Chem. 644 (2010) 1–6, https://doi.org/10.1016/j.jelechem.2010.02.034.

[20] M. Mazloum-Ardakani, Z. Taleat, A. Khoshroo, H. Beitollahi, H. Dehghani, Electrocatalytic oxidation and voltammetric determination of levodopa in the presence of carbidopa at the surface of a nanostructure based electrochemical sensor, Biosens. Bioelectron. 35 (2012) 75–81, https://doi.org/10.1016/j.bios.2012.02.014.

[21] A.S. Rajpurohit, N.S. Punde, C.R. Rawool, A.K. Srivastava, Application of carbon paste electrode modified with carbon nano fibers/polyaniline/platinum nanoparticles as an electrochemical sensor for the determination of Bezafibrate, Electroanalysis 30 (2018) 571–582, https://doi.org/10.1002/elan.201700781.

[22] P.S. Ganesh, B.E.K. Swamy, Voltammetric resolution of catechol and hydroquinone at eosin Y film modified carbon paste electrode, J. Mol. Liq. 220 (2016) 208–215, https://doi.org/10.1016/j.molliq.2016.04.078.

[23] M.P. Kingsley, P.K. Kalambate, A.K. Srivastava, Simultaneous determination of ciprofloxacin and paracetamol by adsorptive stripping voltammetry using copper zinc ferrite nanoparticles modified carbon paste electrode, RSC Adv. 6 (2016) 15101–15111, https://doi.org/10.1039/C5RA19861E.

[24] L. Faria, J. Pereira, G. Azevedo, M. Matos, R. Munoz, R. Matos, Square-wave voltammetry determination of ciprofloxacin in pharmaceutical formulations and milk using a reduced graphene oxide sensor, J. Braz. Chem. Soc. 30 (2019) 1947–1954, https://doi.org/10.21577/0103-5053.20190108.

[25] S. Kumar, P. Karfa, K.C. Majhi, R. Madhuri, Photocatalytic, fluorescent $BiPO_4$/graphene oxide based magnetic molecularly imprinted polymer for detection, removal and degradation of ciprofloxacin, Mater. Sci. Eng. C 111 (2020), 110777, https://doi.org/10.1016/j.msec.2020.110777.

[26] X. Hu, K.Y. Goud, V.S. Kumar, G. Catanante, Z. Li, Z. Zhu, J.L. Marty, Disposable electrochemical aptasensor based on carbon nanotubes-V_2O_5-chitosan nanocomposite for detection of ciprofloxacin, Sensors Actuators B Chem. 268 (2018) 278–286, https://doi.org/10.1016/j.snb.2018.03.155.

[27] S. Bahrani, Z. Razmi, M. Ghaedi, A. Asfaram, H. Javadian, Ultrasound-accelerated synthesis of gold nanoparticles modified choline chloride functionalized graphene oxide as a novel sensitive bioelectrochemical sensor: optimized meloxicam detection using CCD-RSM design and application for human plasma sample, Ultrason. Sonochem. 42 (2018) 776–786, https://doi.org/10.1016/j.ultsonch.2017.12.042.

[28] S.A. Shahamirifard, M. Ghaedi, Z. Razmi, S. Hajati, A simple ultrasensitive electrochemical sensor for simultaneous determination of gallic acid and uric acid in human urine and fruit juices based on zirconia-choline chloride-gold nanoparticles-modified carbon paste electrode, Biosens. Bioelectron. 114 (2018) 30–36, https://doi.org/10.1016/j.bios. 2018.05.009.

[29] Z. Parsaee, N. Karachi, S.M. Abrishamifar, M.R.R. Kahkha, R. Razavi, Silver-choline chloride modified graphene oxide: novel nano-bio-electrochemical sensor for celecoxib detection and CCD-RSM model, Ultrason. Sonochem. 45 (2018) 106–115, https://doi.org/10.1016/j.ultsonch.2018.03.009.

[30] K. Chullasat, P. Nurerk, P. Kanatharana, F. Davis, O.A. Bunkoed, Facile optosensing protocol based on molecularly imprinted polymer coated on CdTe quantum dots for highly sensitive and selective amoxicillin detection, Sensors Actuators B Chem. 254 (2018) 255–263, https://doi.org/10.1016/j.snb.2017.07.062.

[31] A. Martin Santos, A. Wong, A. Araújo Almeida, O. Fatibello-Filho, Simultaneous determination of paracetamol and ciprofloxacin in biological fluid samples using a glassy carbon electrode modified with graphene oxide and nickel oxide nanoparticles, Talanta 174 (2017) 610–618, https://doi.org/10.1016/j.talanta.2017.06.040.

[32] V.B. Patil, S.J. Malode, S.N. Mangasuli, S.M. Tuwar, K. Mondal, N.P. Shetti, An electrochemical electrode to detect theophylline based on copper oxide nanoparticles composited with graphene oxide, Micromachines 13 (2022) 1166, https://doi.org/10.3390/mi13081166.

[33] E.P. Randviir, A cross examination of electron transfer rate constants for carbon screen-printed electrodes using electrochemical impedance spectroscopy and cyclic voltammetry, Electrochim. Acta 286 (2018) 179–186, https://doi.org/10.1016/j.electacta.2018.08.021.

[34] J. Bhatt, D. Mondal, K. Prasad, Experimental evidence for the participation of deep eutectic solvents in silver chloride crystal formation at low temperature, J. Cryst. Growth 442 (2016) 95–97, https://doi.org/10.1016/j.jcrysgro.2016.03.007.

[35] S. Mostafa, M. El-Sadek, E.A. Alla, Spectrophotometric determination of ciprofloxacin, enrofloxacin and pefloxacin through charge transfer complex formation, J. Pharm. Biomed. Anal. 27 (2002) 133–142, https://doi.org/10.1016/S0731-7085(01)00524-6.

[36] P. Wang, Z. Mai, Z. Dai, Y. Li, X. Zou, Construction of Au nanoparticles on choline chloride modified glassy carbon electrode for sensitive detection of nitrite, Biosens. Bioelectron. 24 (2009) 3242–3247, https://doi.org/10.1016/j.bios.2009.04.006.

[37] A.J. Bard, L.R. Faulkner, Electrochemical Methods: Fundamentals and Applications, second ed., Wiley, New York, 2001.

[38] G.F. Alves, T.P. Lisboa, L.V. Faria, D.M. Farias, M.A.C. Matos, R.C. Matos, Disposable pencil graphite electrode for ciprofloxacin determination in pharmaceutical formulations by square wave voltammetry, Electroanalysis 33 (2021) 543–549, https://doi.org/10.1002/elan. 202060432.

[39] H. Bagheri, H. Khoshsafar, S. Amidi, Y.H. Ardakani, Fabrication of an electrochemical sensor based on magnetic multi-walled carbon nanotubes for the determination of ciprofloxacin, Anal. Methods 8 (2016) 3383–3390, https://doi.org/10.1039/C5AY03410H.

[40] H.M. Elqudaby, H.A.M. Hendawy, E.R. Souaya, G.G. Mohamed, G.M.G. Eldin, Utility of activated glassy carbon and pencil graphite electrodes for voltammetric determination of nalbuphine hydrochloride in pharmaceutical and biological fluids, Int. J. Electrochem. 2016 (2016) 1–9, https://doi.org/10.1155/2016/8621234.

[41] R. Chauhan, A.A.S. Gill, Z. Nate, R. Karpoormath, Highly selective electrochemical detection of ciprofloxacin using reduced graphene oxide/poly(phenol red) modified glassy carbon electrode, J. Electroanal. Chem. 871 (2020), 114254, https://doi.org/10.1016/j. jelechem. 2020.114254.

[42] M. Yahyapour, M. Ranjbar, A. Mohadesi, Determination of ciprofloxacin drug with molecularly imprinted polymer/Co-metal organic framework nanofiber on

modified glassy carbon electrode, J. Mater. Sci. Mater. Electron. 32 (2021) 3180–3190, https://doi.org/10.1007/s10854-020-05066-z.
[43] M. Pan, P. Guo, H. Liu, J. Lu, Q. Xie, Graphene oxide modified screen-printed electrode for highly sensitive and selective electrochemical detection of ciprofloxacin residues in milk, J. Anal. Sci. Technol. 12 (2021) 55, https://doi.org/10.1186/s40543-021-00309-y.
[44] J. Zhao, P. Huang, W. Jin, Electrochemical sensor based on TiO_2/polyvinyl alcohol nanocomposite for detection of ciprofloxacin in rainwater, Int. J. Electrochem. Sci. 16 (2021) 1–10, https://doi.org/10.20964/2021.10.01.
[45] P. Jain, R.V. Motghare, Electro-oxidation and determination of ciprofloxacin at *f*-MWCNT/poly-aniline glassy carbon electrode, J. Electrochem. Soc. 169 (2022), 056515, https://doi.org/10.1149/1945-7111/ac6bbf.
[46] A. Chaabani, T. Ben Jabrallah, N. Belhadj Tahar, Electrochemical oxidation of ciprofloxacin on COOH-functionalized multi-walled carbon nanotube-coated vitreous carbon electrode, Electrocatalysis 13 (2022) 402–413, https://doi.org/10.1007/s12678-022-00725-7.
[47] G. Muungani, V. Moodley, W.E. van Zyl, Solid-state synthesis of the phyllosilicate effenbergerite ($BaCuSi_4O_{10}$) for electrochemical sensing of ciprofloxacin antibiotic in pharmaceutical drug formulation, J. Appl. Electrochem. 52 (2022) 285–297, https://doi.org/10.1007/s10800-021-01633-2.
[48] T.S.H. Pham, S. Hasegawa, P. Mahon, K. Guérin, M. Dubois, A. Yu, Graphene nanocomposites based electrochemical sensing platform for simultaneous detection of multi drugs, Electroanalysis 34 (2022) 435–444, https://doi.org/10.1002/elan.202100485.
[49] S.G. Surya, S. Khatoon, A. Ait Lahcen, A.T.H. Nguyen, B.B. Dzantiev, N. Tarannum, K.N. Salama, A chitosan gold nanoparticles molecularly imprinted polymer based ciprofloxacin sensor, RSC Adv. 10 (2020) 12823–12832, doi.org/10.1039/D0RA01838D.
[50] H.S. Vedhavathi, B.P. Sanjay, M. Basavaraju, B.S. Madhukar, N. Kumara Swamy, Development of ciprofloxacin sensor using iron-doped graphitic carbon nitride as transducer matrix: analysis of ciprofloxacin in blood samples: original scientific paper, J. Electrochem. Sci. Eng. 12 (2022) 59–70, https://doi.org/10.5599/jese.1112.

Supplementary material

A simple, ultrasensitive and cost-effective electrochemical sensor for the determination of ciprofloxacin in various types of samples

Wondimeneh Dubale Adane[a], Bhagwan Singh Chandravanshi*[a], and Merid Tessema [a]

[a] Department of Chemistry, Addis Ababa University, P. O. Box 1176, Addis Ababa, Ethiopia

* Corresponding author: E-mail addresses: bscv2006@yahoo.coM

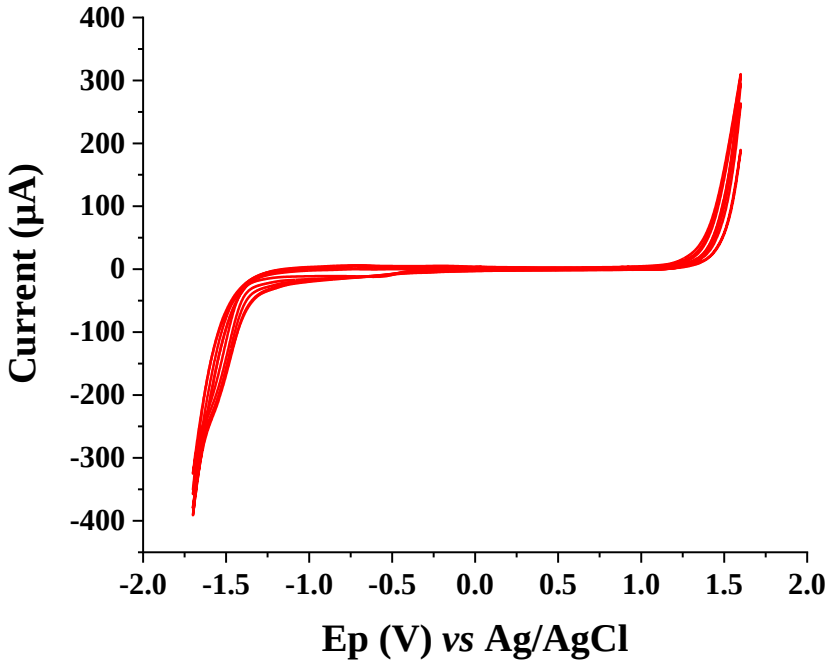

Fig. S1. CV of 0.002 M ChCl solution containing 0.01 M KCl in 0.1 M PBS (pH 7.0) at CPE for 14 cycles and scan rate of 25 mVs^{-1} in the potential ranges of -1.7 to 1.6 V.

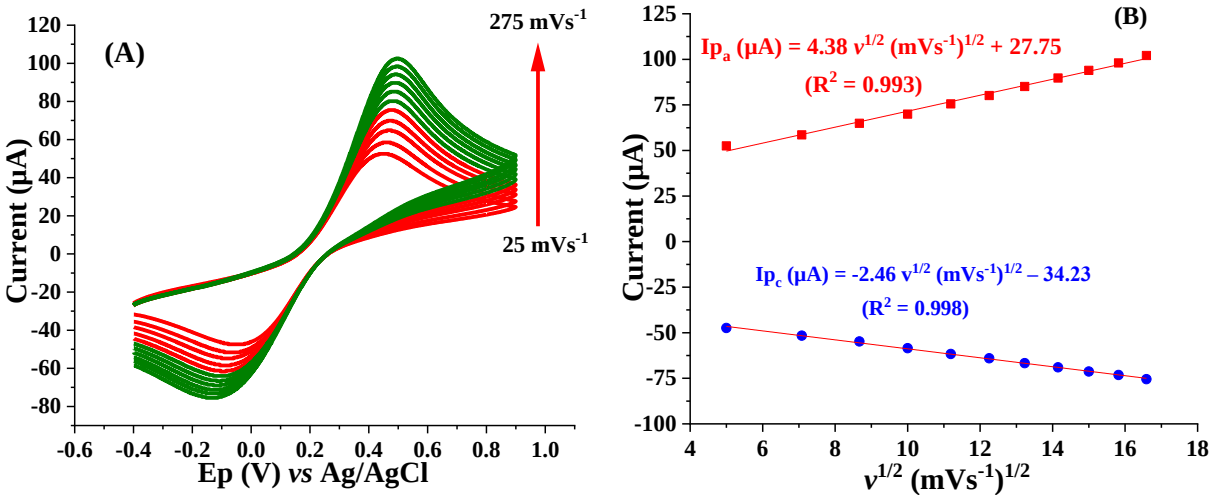

Fig. S2. CVs of 5 mM $K_3[Fe(CN)_6]$ at different scan rates using bare CPE (A) and plot of peak current versus square root of scan rate (B).

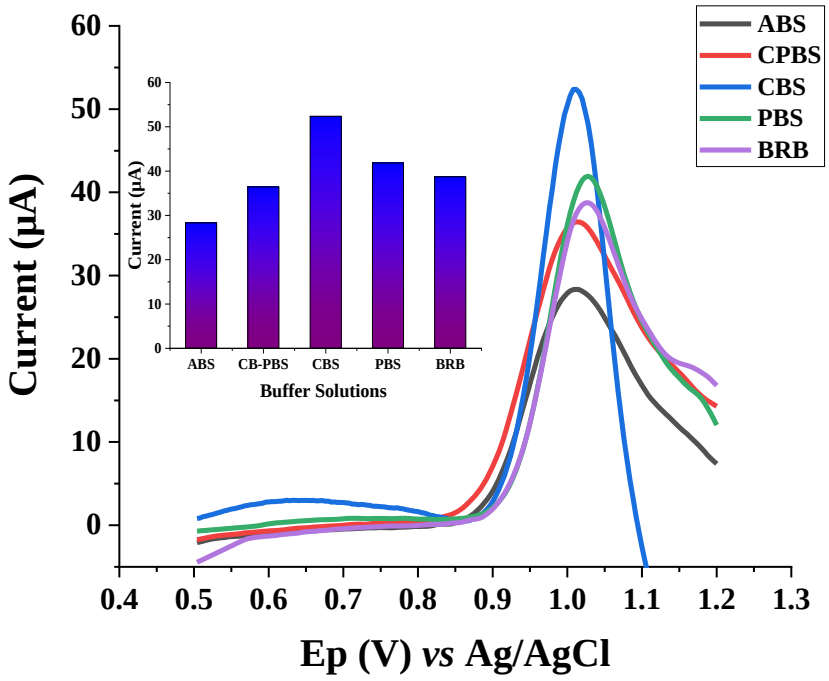

Fig. S3. SWVs of 50 µM CPRO in different supporting electrolytes

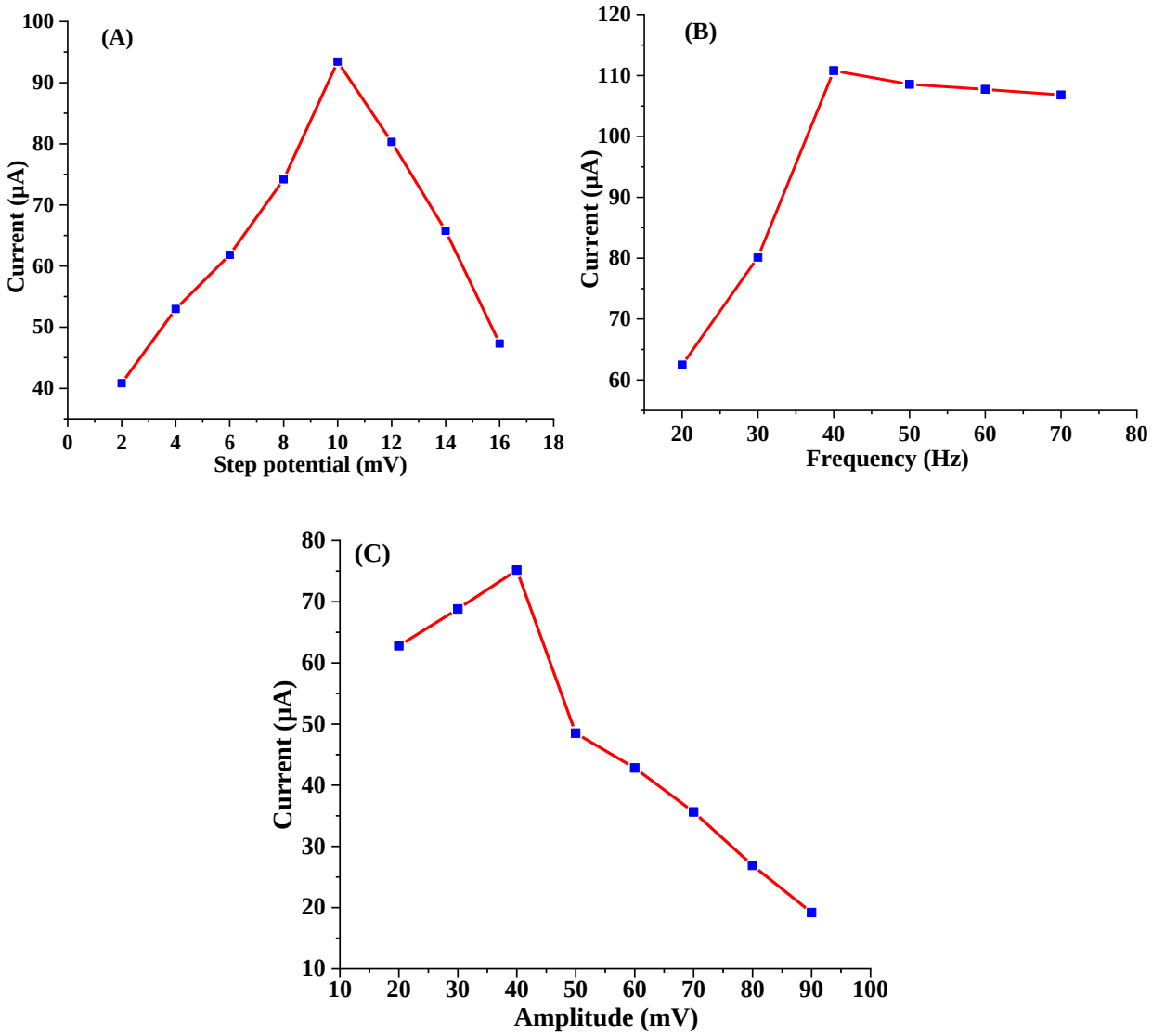

Fig. S4. The effect of SWV parameters: step potential (A); frequency (B); and amplitude (C) on the oxidation peak current of CIP.

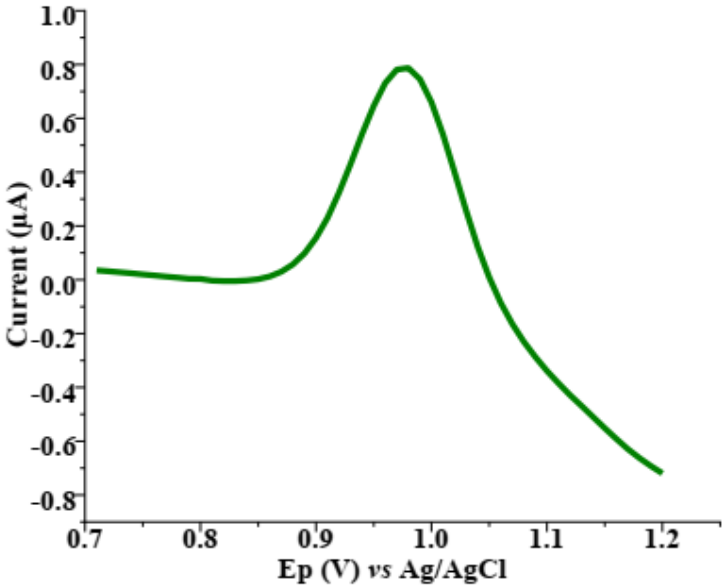

Fig. S5. SWV of practically detected 0.002 µM CPRO.

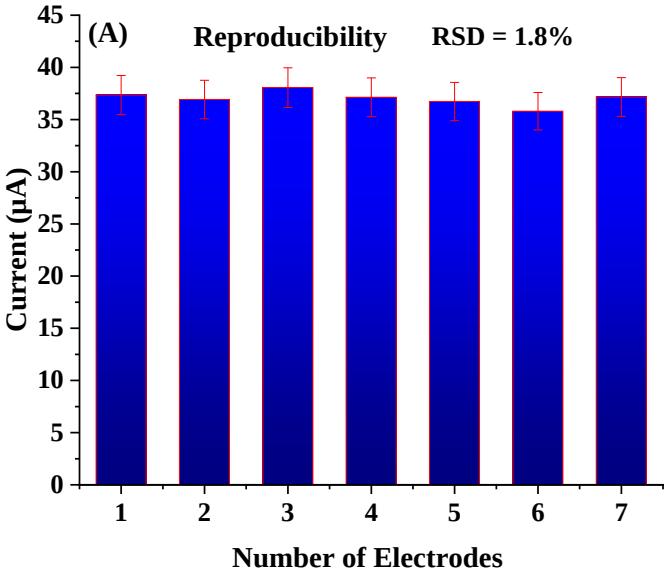

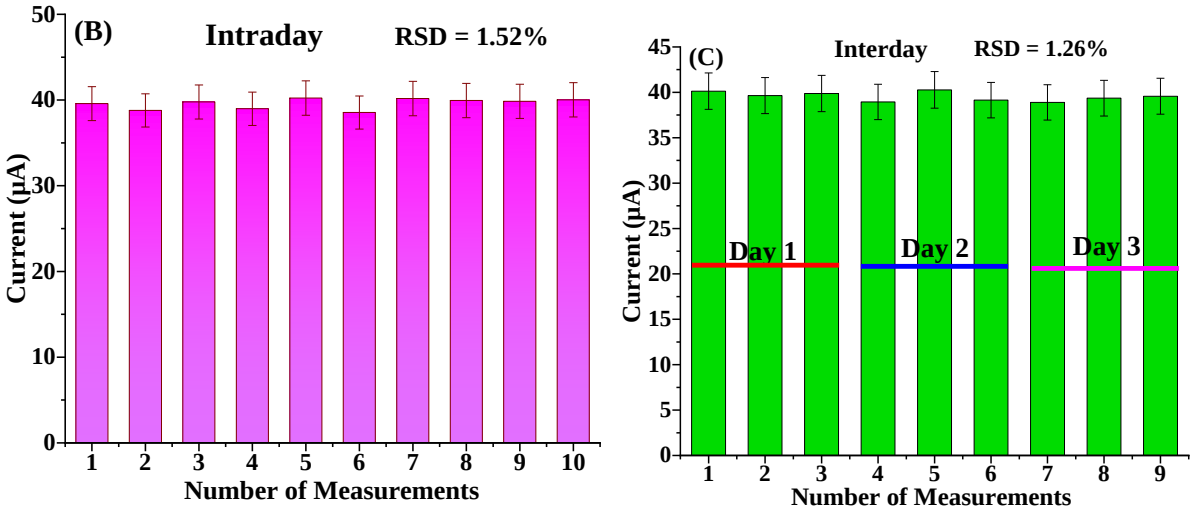

Fig. S6. Reproducibility analysis results of seven ChCl/CPEs, (A) Intraday repeatability analysis results of ChCl/CPE by ten measurements (B) and Interday repeatability analysis results of ChCl/CPE for three days (three measurements each day) (C).

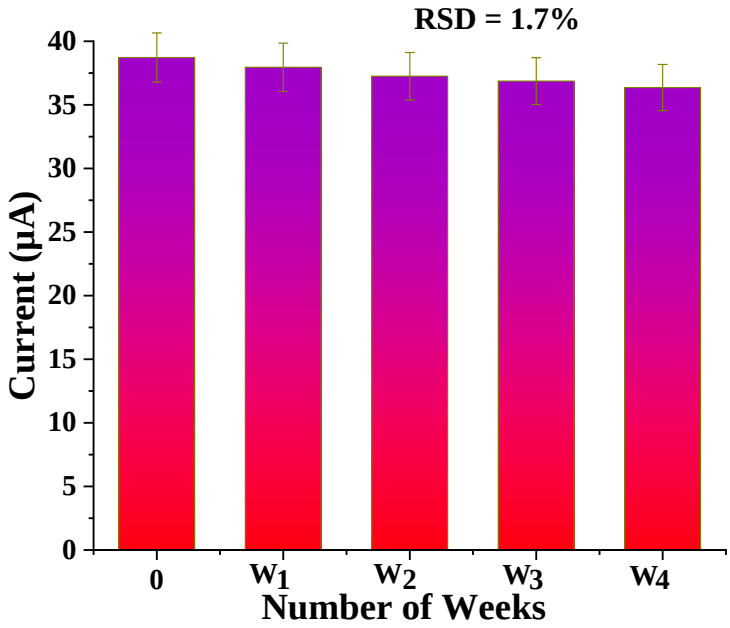

Fig. S7. Stability analysis results of ChCl/CPE.

Chapter Four: Paper II

Highly sensitive and selective electrochemical sensor for the simultaneous determination of tinidazole and chloramphenicol in food samples (egg, honey and milk)

Wondimeneh Dubale Adane, Bhagwan Singh Chandravanshi, Merid Tessema

Sensors & Actuators: B. Chemical 390 (2023) 134023

https://doi.org/10.1016/j.snb.2023.134023

Sensors & Actuators: B. Chemical 390 (2023) 134023

Contents lists available at ScienceDirect

Sensors and Actuators: B. Chemical

journal homepage: www.elsevier.com/locate/snb

Highly sensitive and selective electrochemical sensor for the simultaneous determination of tinidazole and chloramphenicol in food samples (egg, honey and milk)

Wondimeneh Dubale Adane, Bhagwan Singh Chandravanshi *, Merid Tessema

Department of Chemistry, Addis Ababa University, P. O. Box 1176, Addis Ababa, Ethiopia

ARTICLE INFO

Keywords:
Tinidazole
Chloramphenicol
Simultaneous determination
Choline chloride
Glassy carbon electrode
Electrochemical sensor

ABSTRACT

In this study, an environmentally friendly, highly selective, and sensitive electrochemical sensor was developed for the simultaneous determination of tinidazole (TIN) and chloramphenicol (CAP) using a choline chloride-modified glassy carbon electrode (ChCl/GCE). Electrochemical impedance spectroscopy (EIS), cyclic voltammetry (CV), scanning electron microscopy (SEM), and Fourier transform infrared (FT-IR) spectrometry techniques were utilized for electrochemical and morphological characterization. The proposed sensor showed an excellent performance with a wide linear range of 0.010–170 μM and 0.005–300 μM for TIN and CAP, respectively. The limit of detection (LOD) and quantification (LOQ) were 0.90 nM and 3.0 nM for TIN and 0.27 nM and 0.89 nM for CAP, respectively. ChCl/GCE demonstrated remarkable selectivity over potentially interfering species, including antibiotics, organic and inorganic substances, as well as exceptional repeatability, reproducibility, and long-term stability. The sensor was successfully applied to simultaneously determine TIN and CAP in food samples (eggs, honey, and milk) with acceptable recovery values of 93.0–104 % and relative standard deviations (RSD) below 5 %. Therefore, the developed electrochemical sensor is an excellent alternative for simultaneously determining TIN and CAP in food samples.

1. Introduction

Antibiotics have saved millions of lives and brought most infectious diseases that have plagued humanity for centuries under control [1]. Antibiotics are drugs commonly used to treat infectious diseases in humans and animals caused by particular microorganisms, including fungi, protozoa, microalgae, viruses, and bacteria [2]. They are utilized as growth promoters in animal husbandry (livestock and poultry) by altering the gut microbiota at a sub-therapeutic dose. Antibiotics suppress bacterial cell wall synthesis, restrict bacterial DNA synthesis, inhibit protein synthesis, block nascent RNA elongation, restrict the transcription cycle, and eliminate microbial communities [3]. They are used in humans to treat various bacterial infections, including gastrointestinal, urinary, genital, skin, and abdominal infections [4]. Due to the widespread and increasing usage of antibiotics, foods, drinks, and environmental resources have been contaminated with the parent chemicals and their metabolites. Antibiotic residues can be present in the food chain and accumulate in food, primarily through their use by food-producing animals when added to dairy products as chemical preservatives [5].

Humans are mainly affected by poor cell membrane permeability, myalgia, hepatotoxicity, nephrotoxicity, skin rash, tendon rupture, hyperactivity, gastrointestinal and cardiovascular diseases, and cancer due to antibiotic residues in foods of animal origin and water sources [6]. Widespread use, low production costs, misuse, and abuse of antibiotics in the pharmaceutical and animal husbandry industries result in their extensive presence in humans, animals, the environment, and food. As a result, some microorganisms have developed antibiotic resistance [1]. Antibiotic resistance is an adaptive genetic phenomenon possessed or acquired by bacteria, in which they can develop and persist even in the presence of therapeutic levels of antibiotics [7]. Antibiotic resistance has led to the failure of antibiotic treatments, higher mortality rates, and rising healthcare expenses, significantly endangering the public health of the entire world [8].

Tinidazole (TIN) (1-(2-ethyl sulfonyl ethyl)-2-methyl-5-nitroimidazole) is a widely used antibiotic belonging to the nitroimidazole derivatives, with anti-amoebiasis and anti-giardiasis properties [9]. It is an antiprotozoal agent used to treat infections caused by

* Corresponding author.
E-mail address: bscv2006@yahoo.com (B.S. Chandravanshi).

https://doi.org/10.1016/j.snb.2023.134023
Received 11 February 2023; Received in revised form 23 May 2023; Accepted 23 May 2023

Giardia lamblia, *Entamoeba histolytica*, and *Trichomonas vaginalis* [10]. TIN is currently used to treat periodontitis in adults and is more effective against periodontal anaerobic bacteria and in combination with aminopenicillin used to treat *Helicobacter pylori*, *Clostridium difficile*, and *Bacteroidetes* in children. Dizziness, physical fatigue, headache, upset stomach, and diarrhea are the common side effects of TIN [11,12]. Continuous consumption of TIN-containing foods can affect the human DNA system. Cytotoxic effluents from animal husbandry can also contaminate food and water sources and cause many adverse effects on humans, including carcinogenicity, and mutagenicity [13].

Chloramphenicol (CAP) was the first mass-produced antibiotic, also known as 2,2-dichloro-N-[2-hydroxy-1-(hydroxymethyl)-2-(4-nitrophenyl)ethyl] acetamide. It is a broad-spectrum antibiotic and is commonly used to treat infections in humans and animals. CAP is effective against Gram-positive and Gram-negative bacteria and is also used to treat typhoid fever and pediatric meningitis [14]. In addition, due to its low cost and high potency, CAP is widely used in animal feed production and domestic poultry as a therapeutic and prophylactic agent against bacteria, for superficial eye infections, aquaculture, and beekeeping. However, the abuse of CAP has resulted in the introduction of residues from animal products to the human body through the food chain and causes many chronic diseases such as cardiovascular collapse, leukemia, and aplastic anemia [14,15].

Various analytical techniques, including high-performance liquid chromatography (HPLC) [16], liquid chromatography-mass spectroscopy (LC-MS) [17], gas chromatography-mass spectroscopy (GC-MS) [18], capillary electrophoresis (CE) [19], and chemiluminescence [20], were previously reported for the determination of TIN and CAP. Although these techniques are accurate and precise, they have limitations, such as complicated operations, long analysis time, high instrument costs, and the need for skilled operators [21]. In contrast, electroanalytical methods are inexpensive, easy to use, highly sensitive and selective, amenable to miniaturization and portability, have short analysis times, and require minimal sample consumption [22].

Electrochemical sensors are devices widely used in public health, clinical diagnostics, food safety, and environmental analysis to detect a variety of target analytes, including antibiotics, proteins, metabolites, neurotransmitters, electrolytes, and heavy metals [23]. The working principle is that the electrical signal generated by the reaction of the target analyte is converted into an identifiable signal proportional to the concentration of the target substance [24]. Electrochemical sensing is the most effective method for antibiotic determination due to its high sensitivity, ability to work with small mass and volume samples with high reliability, and selectivity [25]. In addition, electrochemical sensors have several advantages, including simple measurement procedures, fast response time, low power consumption, a linear output, remarkable repeatability and accuracy, convenience and cost-effectiveness, and excellent sensitivity and selectivity [26,27]. Accordingly, in this study, the electrochemical method became the first choice for simultaneously determining TIN and CAP in food samples. Among the electrochemical methods, square-wave voltammetry in particular was employed to determine the analytes, as it offers advantages such as short analysis time, minimal sample consumption, background discrimination, and excellent sensitivity compared to other electrochemical analysis techniques [28].

Choline chloride (ChCl) is a non-toxic quaternary ammonium salt with $N^+(CH_3)_3$ and OH functional groups. The cationic polar group $N^+(CH_3)_3$ enhances electrostatic attraction, resulting in a uniformly positively charged surface to facilitate electron transfer between the analytes and the electrode. The OH group facilitates the immobilization of ChCl to the GCE surface by covalent linkage [21]. Hung et al. [29] reported the development of a Pd/Ag hollow structure-modified electrode by the galvanic replacement reaction in deep eutectic ChCl-based solvents to determine hydrazine in ponds and tap water. Parsaee et al. [30] reported the development of Ag-ChCl-GO composite-modified CPE for the detection of celecoxib in a human plasma sample. However, no previous literature report was found on the simultaneous electrochemical determination of TIN and CAP using ChCl-modified GCE.

This study reports a simple, low-cost, eco-friendly, ultrasensitive, super selective, and highly stable electrochemical sensor for the simultaneous determination of TIN and CAP in food samples (eggs, honey, and milk) using ChCl/GCE.

2. Experimental

2.1. Chemical and reagents

In this experiment, analytical-grade chemicals and reagents were used. Choline chloride (≥99 %) in KCl (98 %) (Wagtech International Ltd., UK) was purchased from Sigma-Aldrich, USA. Potassium hexacyanoferrate(III) (99 %) was purchased from (BDH Chemicals Ltd., England). All other chemicals and antibiotic standards were purchased from Sigma-Aldrich, USA.

2.2. Apparatus and instruments

The surface morphology of unmodified and modified electrodes was characterized using a scanning electron microscope (CX-200plus-Coxem, Korea). Electrochemical measurements were performed in 20 mL cells using a CHI 760D electrochemical analyzer (CH Instruments, USA). A Fourier transform infrared spectrometer was used to record infrared spectra (FT-IR, PerkinElmer, Spectrum 100, USA).

2.3. Sample preparation

The preparation of real samples was discussed in the Supplementary material.

2.4. Preparation of ChCl/GCE

Before modification, GCE was polished with 0.3 and 0.05 μm alumina slurry on a polishing pad and cleaned with distilled water. Then, the electrode was sonicated for 5 min in a 1:1 (v/v) mixture of ethanol and distilled water. For the electrochemical deposition of ChCl at the GCE (Fig. S1), CV was performed for fourteen cycles in 0.1 M phosphate buffer solution (PBS) (pH 7.0) containing 0.002 M ChCl in 0.01 M KCl in the potential range from −1.7 to 1.6 V at a scan rate of 25 mVs^{-1}. Then, the modified electrode (ChCl/GCE) was washed with distilled water to remove any physically adsorbed and unreacted species.

3. Results and discussion

3.1. Electrochemical characterization

EIS was used to examine the interfacial characteristics of the unmodified and modified electrodes in the frequency range from 0.1 Hz to 100 kHz. The Nyquist plots of bare GCE (a) and ChCl/GCE (b) in 5 mM $[Fe(CN)_6]^{3-/4-}$ containing 0.1 M KCl are shown in Fig. 1A. Charge transfer resistance (R_{ct}) is the resistance associated with the charge transfer mechanisms in electrode reactions. It controls the electron transfer kinetics of a substance at the electrode interface. The diameter of the semicircle in the Nyquist plot determines the charge transfer resistance at the electrode surface, and larger semicircles are obtained when there is slow electron transfer kinetics. R_{ct} is bound to the dielectric and insulating properties of the electrode/electrolyte interface; therefore, it is affected by changes in the electrode surface. R_{ct} values are 2.58×10^3 Ω for bare GCE and 44.4 Ω for ChCl/GCE. ChCl/GCE has lower resistance (lower impedance) than the bare GCE because the electrodeposition of ChCl on the surface of GCE results in reduced interfacial charge transfer resistance and increased electron exchange due to high conductivity and more electroactive sites provided by the

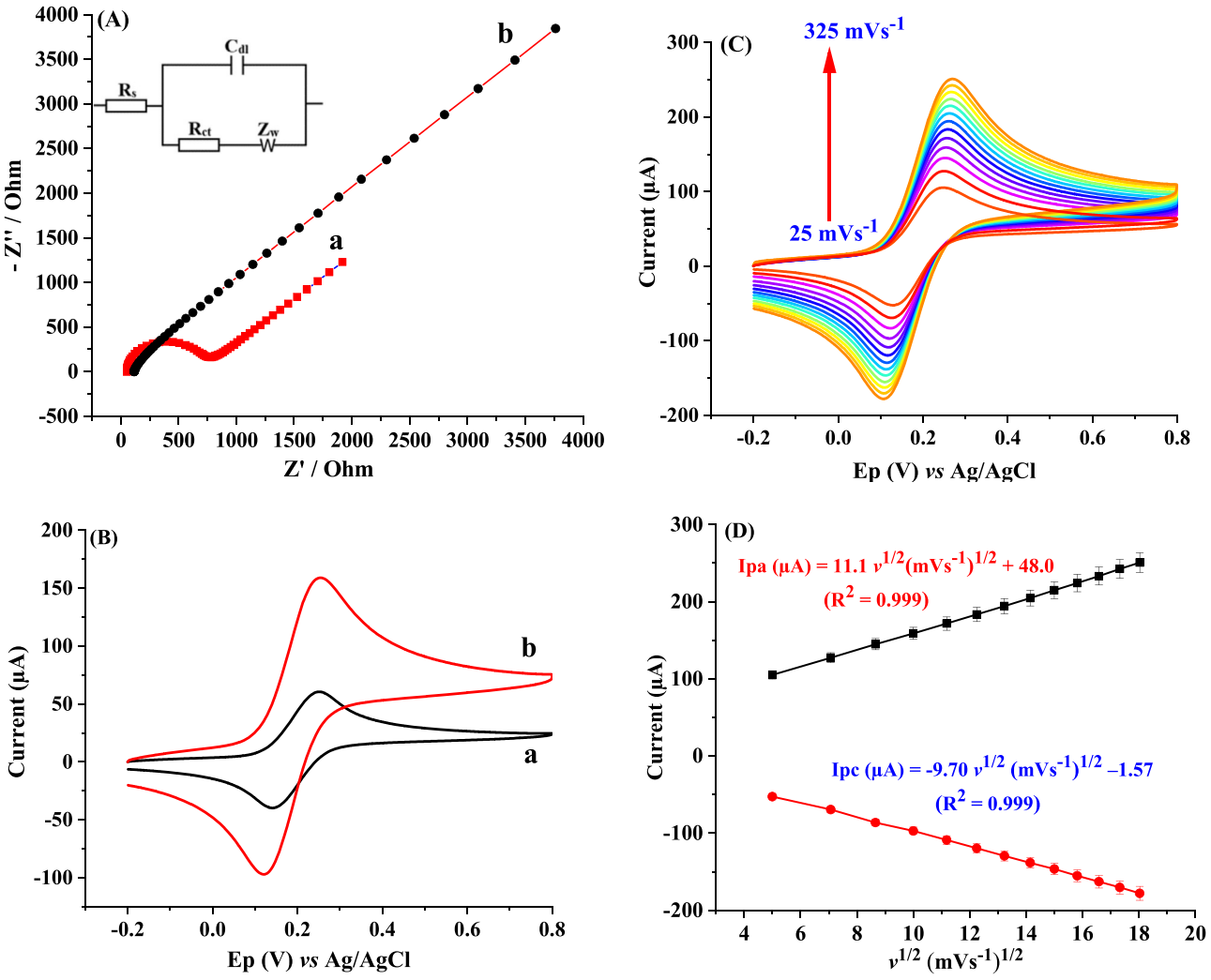

Fig. 1. (A) Nyquist plots of bare GCE (a) and ChCl/GCE (b) in 0.1 M KCl containing 5.0 mM $[Fe(CN)_6]^{3-/4-}$. (B) CV curves for the bare GCE (a) and ChCl/GCE (b) in 0.1 M KCl containing 5.0 mM $[Fe(CN)_6]^{3-/4-}$ at a scan rate of 100 mVs^{-1}. (C) CVs of 5 mM $[Fe(CN)_6]^{3-/4-}$ at different scan rates using ChCl/GCE and (D) plot of Ip (µA) vs. $v^{1/2}$ $(mVs^{-1})^{1/2}$ (n = 3, error bar = standard deviation (SD)).

ChCl to allow more $[Fe(CN)_6]^{3-/4-}$ to reach the electrode surface easily.

As shown in Fig. 1B, the anodic and cathodic peak currents of ChCl/GCE were higher than those of bare GCE. In addition, the peak current responses of the ChCl/GCE and bare GCE at different scan rates (25–325 mVs^{-1}) are shown in Fig. 1C and S2A. The linear relationship observed between the redox peak currents and the square root of scan rate (Fig. 1D and S2B) indicates that the mass transport is a diffusion-controlled process. Furthermore, CV scans were performed at a scan rate of 100 mVs^{-1} for a 5 mM $[Fe(CN)_6]^{3-/4-}$ redox probe in 0.1 M KCl to investigate the surface areas of bare GCE and ChCl/GCE. The electroactive surface areas of the bare GCE and the ChCl/GCE were determined by the Randles-Sevcik Eq. (1) [31].

$$Ip = 2{\cdot}69 \times 10^5 n^{3/2} A D^{1/2} C v^{1/2} \quad (1)$$

where I_p = peak current (A), D = diffusion coefficient (cm^2 s^{-1}), n = number of electrons (n = 1), v = scan rate (Vs^{-1}), C = concentration of $[Fe(CN)_6]^{3-/4-}$ (mol cm^{-3}), and A = electrode surface area (cm^2). As shown in Fig. 1D, the regression equation of the ChCl/GCE is Ipa (µA) = 11.1 $v^{1/2}$ $(mVs^{-1})^{1/2}$ + 48.0 (R^2 = 0.999), and that of the bare GCE is Ipa (µA) = 4.21 $v^{1/2}$ $(mVs^{-1})^{1/2}$ + 18.8 (R^2 = 0.999) (Fig. S2B). The slope of the graph Ipa (µA) vs. $v^{1/2}$ $(mVs^{-1})^{1/2}$ is used to calculate the electroactive surface areas. The calculated surface area for the modified electrode is 0.134 cm^2 and 0.027 cm^2 for the unmodified electrode. This finding demonstrates that the modified electrode has an electroactive surface area that is five times higher than that of the bare electrode. The heterogeneous rate constant (k°) was calculated using the following equation [32].

$$k^0 = \frac{RT}{R_{ct} A C F^2} \quad (2)$$

where k° = heterogeneous rate constant (cm s^{-1}), C = concentration of $[Fe(CN)_6]^{3-/4-}$ solution (mol cm^{-3}), R_{ct} = charge transfer resistance (Ω), A = surface area of electrode (cm^2), R = universal gas constant (8.314 J K^{-1} mol^{-1}), T = temperature (298 K), and F = Faraday constant (96485 C mol^{-1}). The calculated k° value for the unmodified electrode is 7.66×10^{-4} and 8.95×10^{-3} cm s^{-1} for the modified electrode. A higher k° value for ChCl/GCE indicates faster electron transfer and a higher electroactive surface area when compared to the bare GCE.

3.2. Morphological characterization

As shown in Fig. 2, there is a significant difference in the morphology of the two electrodes. The bare GCE surface has a smooth and homogenous appearance, as shown in Fig. 2A. In contrast, after modification (Fig. 2B), the number and size of pores at the surface of ChCl/GCE increased, resulting in irregular shapes with heterogeneous

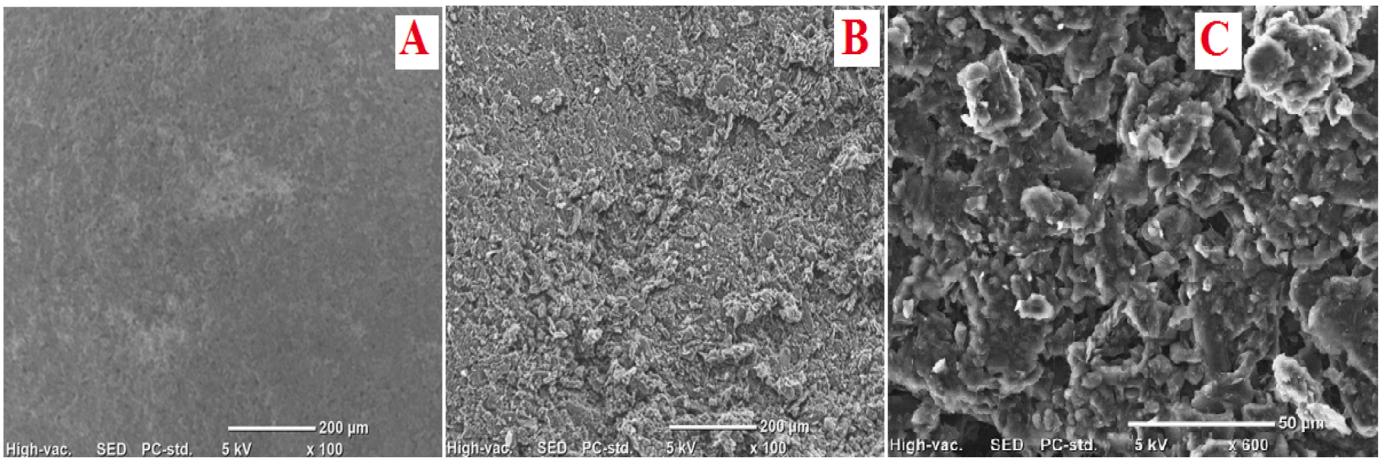

Fig. 2. SEM images of (A) bare GCE, (B) ChCl/GCE and (C) ChCl/GCE (deep resolution).

distributions. The SEM images of ChCl/GCE (Fig. 2C) (deep resolution) also show a non-uniform distribution of the ChCl with granular and coarse structures that increase the number of electroactive sites and the surface area of the modified electrode.

3.3. Electrochemical behaviors of TIN and CAP

The electrochemical behavior of 5 µM TIN and CAP was simultaneously investigated at bare GCE and ChCl/GCE in 0.1 M H_2SO_4 using cyclic voltammetry (CV) and square wave voltammetry (SWV) at a scan rate of 100 mVs^{-1} in the potential range of −0.7 to 0.0 V. No CV or SWV signals were observed for the target analytes in the blank solutions for either the bare GCE or ChCl/GCE. The electrochemical reduction of TIN and CAP is an irreversible reaction at the bare GCE and ChCl/GCE surfaces, with no oxidation peaks in the reverse scan (Fig. 3A). In addition, the reduction peak currents of the analytes at the bare GCE are weak, suggesting a slow rate of electron transfer kinetics. However, after modification, a significant increase in the current response was observed, and the peak potential shifted to a more negative potential compared to the bare GCE. The results show that the ChCl film has an excellent catalytic effect on the electrochemical reduction of TIN and CAP. The voltammetric responses of TIN and CAP were studied by SWV. Fig. 3B shows that the reduction peak current of the analytes at the ChCl/GCE was higher than the bare GCE. In addition, the peak-to-peak separation (ΔEp) of TIN and CAP was calculated to be 168 mV, indicating that the two analytes do not interfere with each other, and it is high enough for the simultaneous determination of TIN and CAP.

3.4. Optimization of experimental conditions

3.4.1. Effect of pH

SWV was used to investigate the effect of the supporting electrolyte solution pH on the electrochemical response of 5 µM TIN and CAP at a scan rate of 25 mVs^{-1} in the pH range of 0.5–2.5 (Fig. 4A). As shown in 4B (a) and 4C (a), the cathodic current responses for both analytes increased sharply from pH 0.5–1.0, and further increases in pH reduced the current responses of both TIN and CAP. Therefore, for subsequent experiments, pH 1.0 was selected as the optimal value. The poor response at lower pH can be attributed to the consumption (participation) of protons in the electrode processes. While the cathodic current responses decreased with increasing pH, this suggests that proton shortage may occur, or the analytes may become deprotonated at higher pH and switch from cations to anions, resulting in electrostatic attraction between the individual analyte and the modified electrode, reducing the current response. As shown in Fig. 4A, the cathodic potentials of TIN and CAP shifted to more negative values as the pH of the

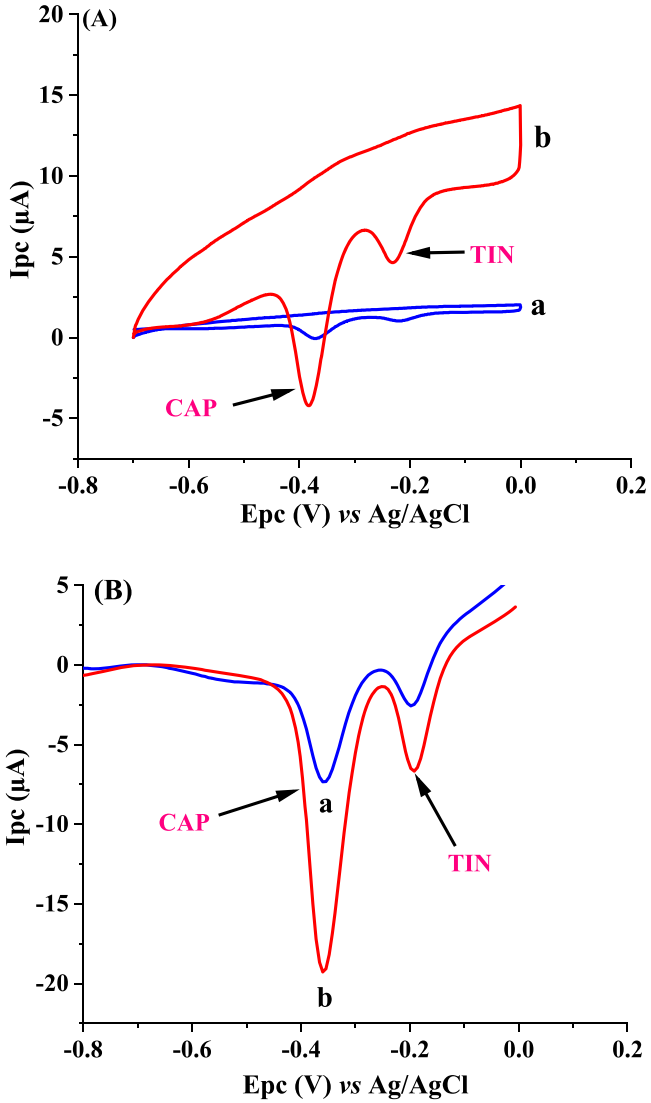

Fig. 3. (A) CVs and (B) SWVs of bare GCE (a) and ChCl/GCE (b) in 5 µM TIN and CAP at a scan rate of 100 mVs^{-1}.

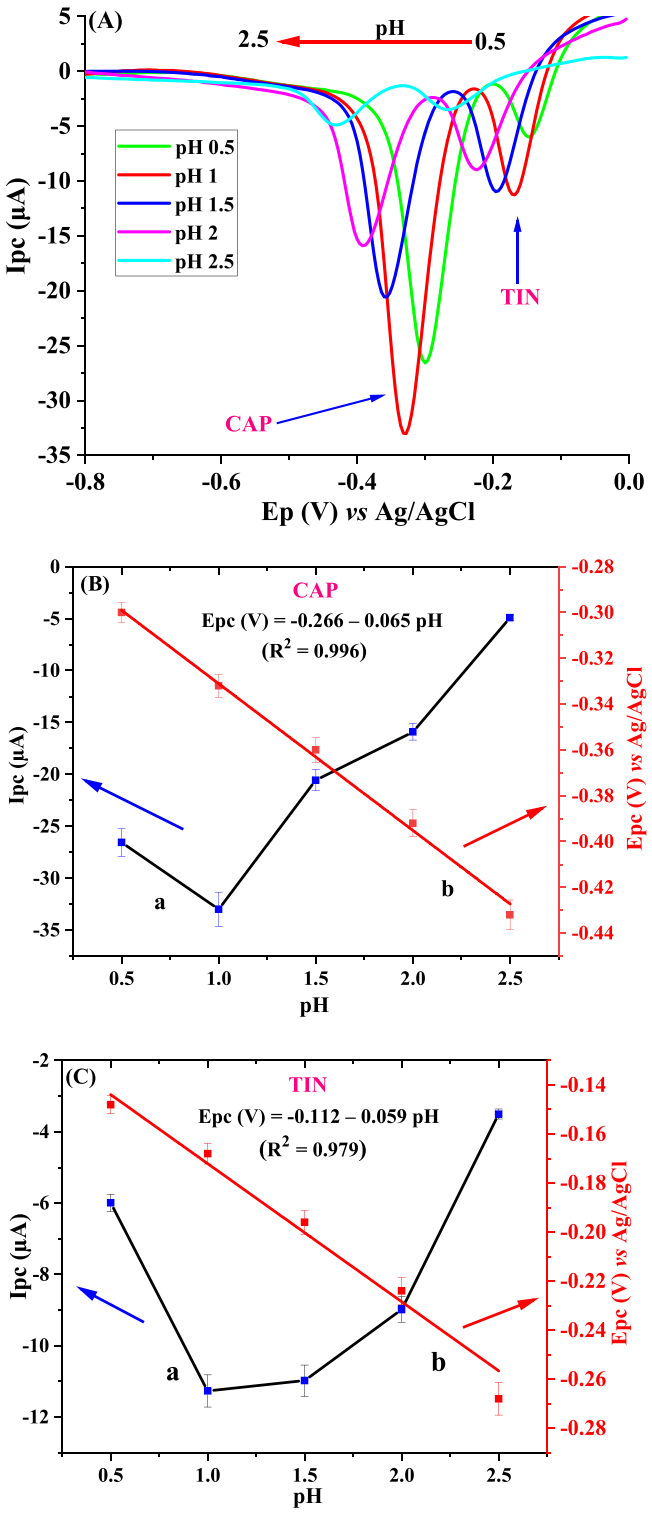

Fig. 4. (A) SWVs of 5 μM TIN and CAP at different pH values of 0.1 M H_2SO_4 at a scan rate of 100 mVs^{-1}, (B) and (C) plot of Ipc (μA) vs. pH (a) and Epc (V) vs. pH (b) for CAP and TIN, respectively (n = 3, error bar = SD).

supporting electrolyte increased. This indicates that protons are involved in the reduction of both analytes. The peak potentials exhibit linear relationships with pH (Epc (V) = −0.266 to 0.065 pH (R^2 = 0.996) for CAP (Fig. 4B (b)) and Epc (V) = −0.112 to 0.059 pH (R^2 = 0.979) for TIN (Fig. 4C (b))). The slope values of 65 mV/pH unit for CAP and 59 mV/pH unit for TIN are close to the Nernstian theoretical value of 59 mV/pH unit, indicating that the voltammetric reduction of both analytes involves a transfer of an equal number of protons and electrons, which is consistent with previous studies [12].

3.4.2. Effect of scan rate

In a 0.1 M H_2SO_4 solution containing 5 μM of TIN and CAP, CV was used to investigate the effect of scan rate in the range of 25–225 mVs^{-1}. As shown in Fig. 5 A, the peak current of CAP gradually increased as the scan rate increased from 25–225 mVs^{-1}. Furthermore, the peak potential shifts to more positive values, indicating the irreversibility of the electrochemical reduction of CAP. The peak current is linearly correlated with the square root of the scan rate given by the regression equation Ipc (μA) = $-2.26\,\nu^{1/2}$ $(mVs^{-1})^{1/2} - 2.68$, $R^2 = 0.995$ (Fig. 5B). In addition, the plot of log Ipc (μA) vs. log ν (mVs^{-1}) yields the linear regression equation log Ipc (μA) = 0.44 log ν (mVs^{-1}) + 0.53, R^2 = 0.992 (Fig. 5C) with a slope of 0.44, which is approximately close to the theoretical value of 0.5. The above results show that the electrochemical reduction of CAP is a diffusion-controlled electrode process [33]. Similarly, as shown in Fig. 6 A, the peak current of TIN gradually increased in the scan rate range from 25 m to 225 mVs^{-1}, with the peak potential shifting to a more positive value, confirming the reduction of TIN is an irreversible process. The peak current is linearly correlated with the square root of the scan rate given by Ipc (μA) = - 0.975 $\nu^{1/2}$ $(mVs^{-1})^{1/2} - 2.8$, $R^2 = 0.999$ (Fig. 6B). In addition, the plot of log Ipc (μA) vs. log ν (mVs^{-1}) gives a linear regression equation: log Ipc (μA) = 0.48 log ν (mVs^{-1}) + 0.05, $R^2 = 0.999$ (Fig. 6C) with a slope of 0.48, which is close to the theoretical value of 0.5. The above findings demonstrate that the reduction of TIN is a diffusion-controlled process [34]. Eq. (3) is applied to determine the number of electrons involved in an irreversible electrode reaction [21].

$$E_p = E^0 + \frac{2.303RT}{\alpha nF}\log\frac{RTk^0}{\alpha nF} + \frac{2.303RT}{\alpha nF}\log\nu \quad (3)$$

where E^0 = formal potential, ν = scan rate (Vs^{-1}), T = temperature (298 K), F = Faraday constant (96485 C mol^{-1}), k^0 = heterogeneous rate constant, R = universal gas constant (8.314 J $(K\ mol)^{-1}$), and n = number of electrons. As shown in Fig. S3A and B, the Ep vs. log ν graph shows good linearity for both TIN and CAP. The slope of the plot is 2.303RT/αnF, giving αn = 1.87 for TIN and 1.78 for CAP. For an irreversible electrode process, α is equal to 0.5. Using Eq. (3), the estimated number of electrons is 3.75 for TIN and 3.56 for CAP, which is nearly equal to four, indicating that the reduction of TIN and CAP involves the transfer of four protons ($4H^+$) and four electrons ($4e^-$), which is consistent with previous studies [12,35]. The proposed reaction mechanisms for the electrochemical reduction of TIN and CAP are given in Scheme 1 (the detailed reduction reaction mechanism for each analyte is given in Scheme S1) [12,35].

3.5. Simultaneous determination of TIN and CAP

In 0.1 M H_2SO_4, SWV was used to simultaneously determine TIN and CAP in the potential range of −0.9 to 0.0 V. It is noted that the cathodic peak current increases proportionally as the concentration of each analyte increases (Fig. 7A). A linear relationship was found between cathodic peak current and concentration in the range of 0.005–300 μM for CAP and 0.01–170 μM for TIN. The linear regression equations are Ipc (μA) = −1.86 C (μM) – 18.6 (R^2 = 0.999) for CAP (Fig. 7B (a)), and Ipc (μA) = −0.98 C (μM) – 2.57 (R^2 = 0.996) for TIN (Fig. 7B (b)). The limit of detection (LOD) is the lowest concentration of analyte in a sample that can be detected but not quantified (the lowest concentration of analyte that can be statistically distinguished from a blank signal). The limit of quantification (LOQ) is the lowest concentration of an analyte in a sample that can be quantified with acceptable accuracy and precision. The LOD (3σ/m, n = 3) and LOQ (10σ/m, n = 3) for CAP were found to be 0.27 nM and 0.89 nM, and for TIN are 0.9 nM and 3.0 nM, respectively (where m = slope of the calibration curve and σ = standard

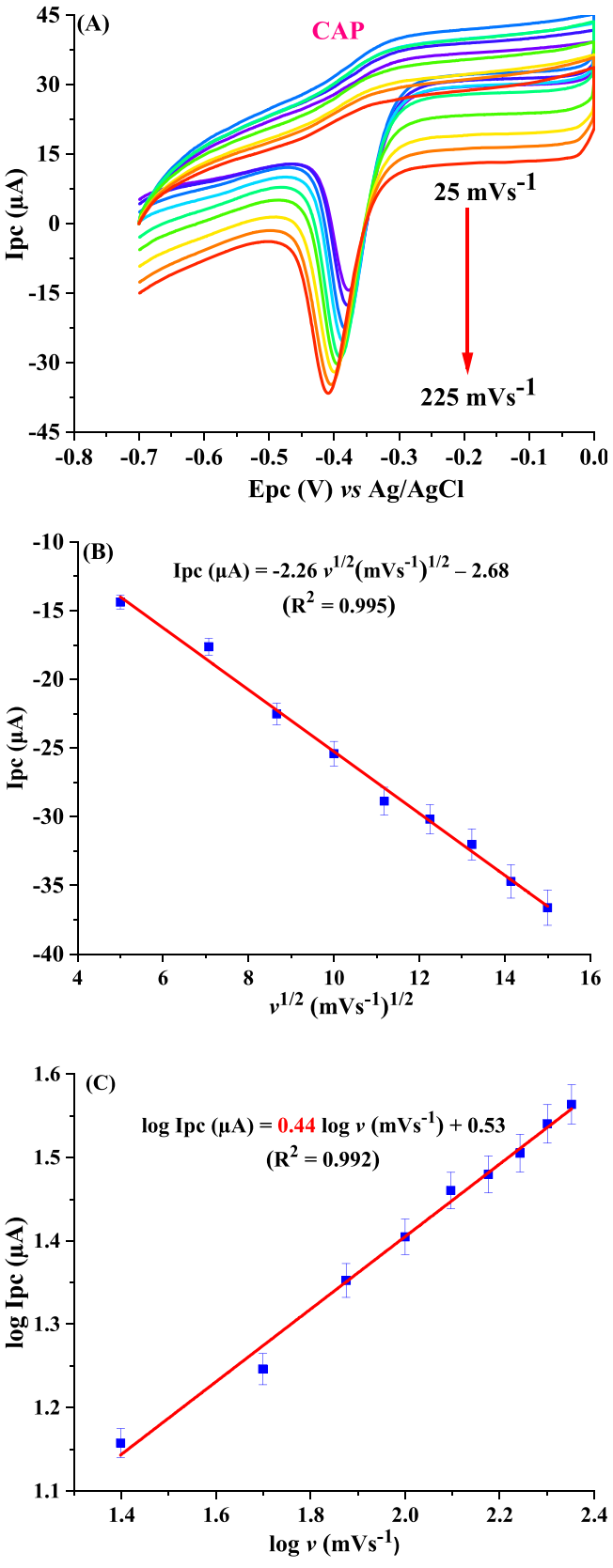

Fig. 5. (A) CVs of 5 µM CAP at different scan rates, (B) plot of Ipc (µA) vs. $v^{1/2}$ $(mVs^{-1})^{1/2}$, and (C) plot of log Ipc (µA) vs. log v (mVs^{-1}) (n = 3, error bar = SD).

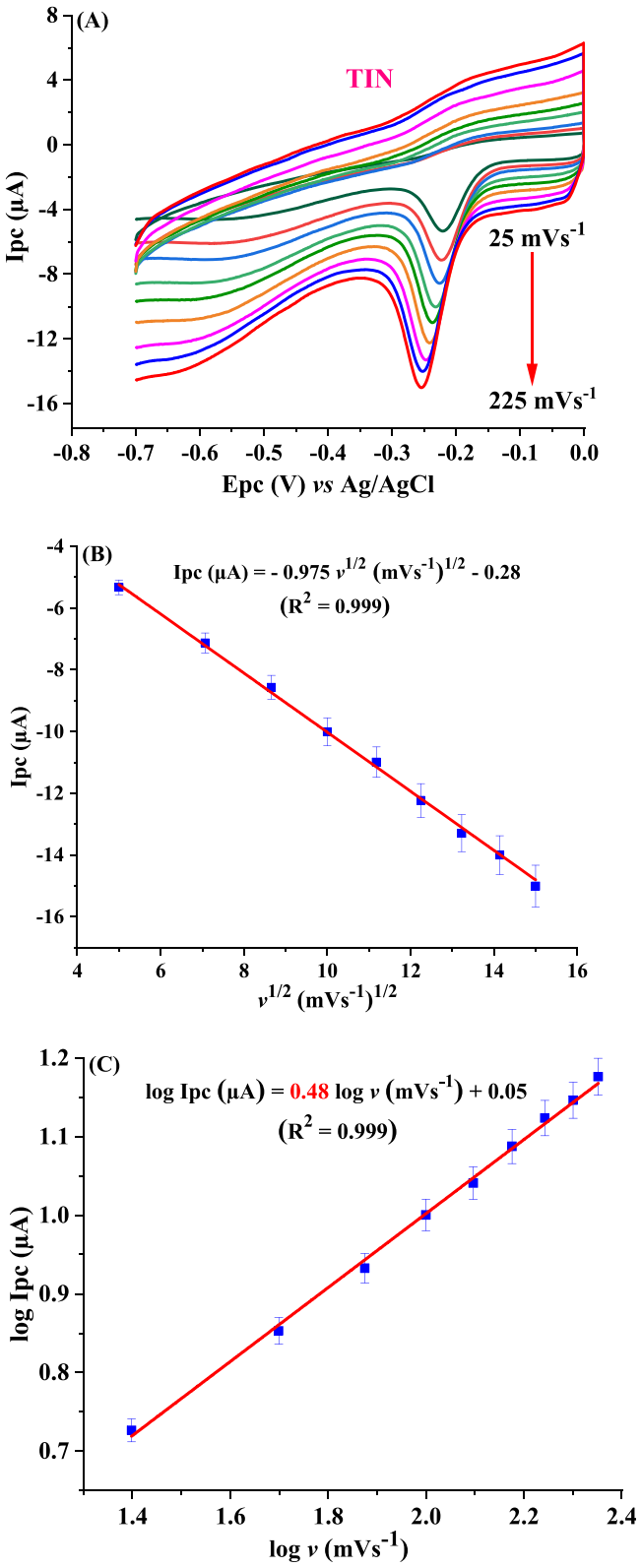

Fig. 6. (A) CVs of 5 µM TIN at different scan rates, (B) plot of Ipc (µA) vs. $v^{1/2}$ $(mVs^{-1})^{1/2}$, and (C) plot of log Ipc (µA) vs. log v (mVs^{-1}) (n = 3, error bar = SD).

deviation of the lowest value of the linear range). The performance of ChCl/GCE was compared with recently reported sensors for the electrochemical determination of TIN and CAP in terms of linear range and detection limit. As shown in Table 1, the proposed sensor performs best

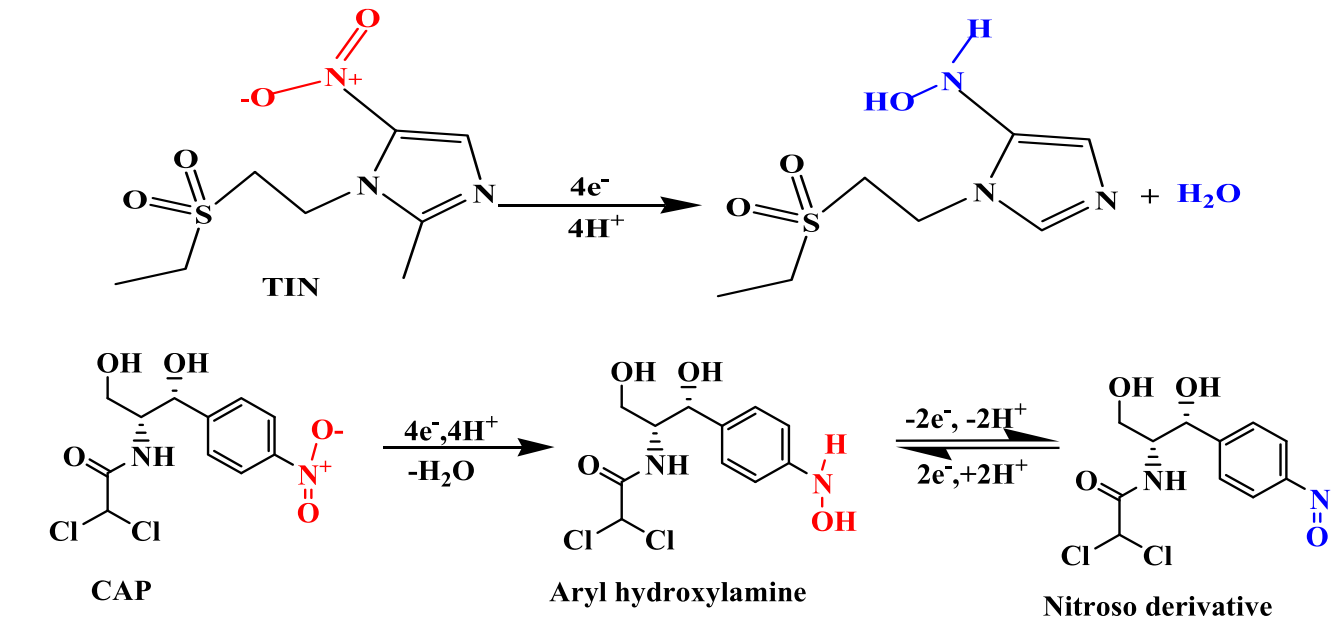

Scheme 1. Proposed reaction mechanisms for the electrochemical reduction of TIN and CAP.

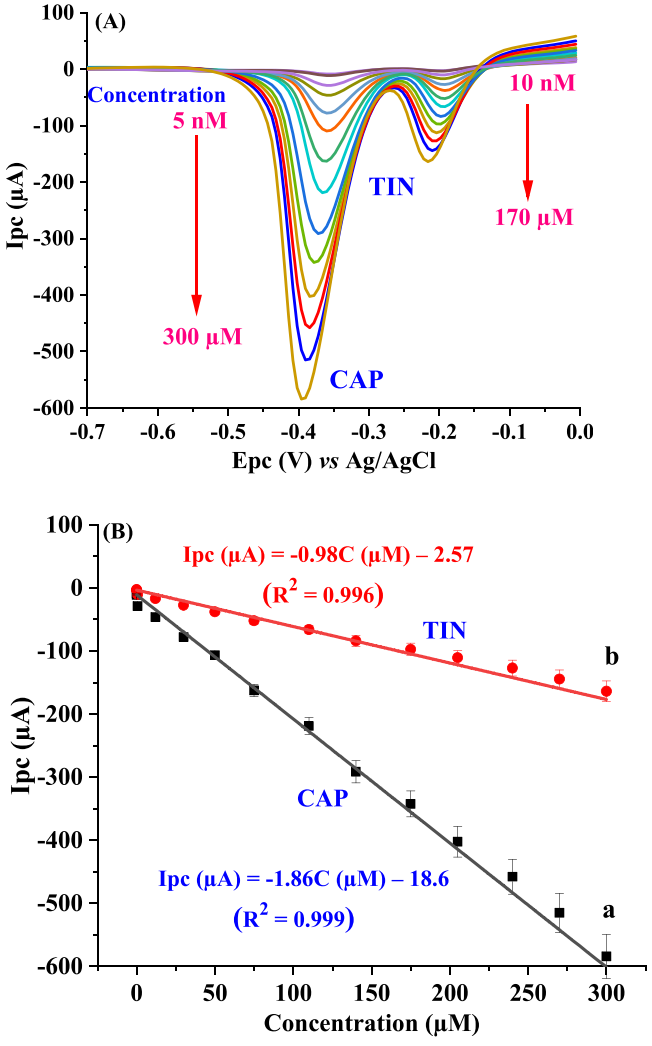

Fig. 7. (A) SWVs of different concentrations of CAP and TIN, and (B) plot of Ipc (µA) vs. concentration of CAP (a) and TIN (b) (n = 3, error bar = SD).

Table 1
Comparison of the performance of ChCl/GCE with recently reported sensors.

Sensors	Analytes	Real samples	Linear range (µM)	LOD (µM)	References
[a]Fe-MOF/Pt NPs/GCE	TIN	Tablets, biological samples	0.02–525	0.43	[36]
[b]Ag/ZrO_2/GCE	TIN	Blood serum	0.2–415	0.073	[12]
[c]CPE	TIN	Tablet	5–200	0.51	[10]
[d]Ni-MOF/PEDOT	TIN	Blood serum, urine	0.7–101 101–255	0.09	[34]
ChCl/GCE	TIN	Egg, honey, milk	0.01–170	0.0009	This work
[e]SWCNHs-COOH/GCE	CAP	Lake water	0.1–100	0.1	[15]
[f]ZnO-NPs/SWCNTS	CAP	Eye drops	10–140	0.03	[35]
[g]Ag/CMC/TiO_2/LIG	CAP	Tap, lake water	0.01–100	0.01	[37]
[h]rGO/PdNPs/GCE	CAP	Tap water, honey	0.05–1	0.05	[38]
ChCl/GCE	CAP	Egg, honey, milk	0.005–300	0.00027	This work

Abbreviations: [a] **Fe-MOF/Pt NPs:** iron-metal organic framework/platinum nanoparticles, [b] **Ag/ZrO_2:** silver/zirconium oxide, [c] **CPE**: carbon paste electrode, [d] **Ni-MOF/PEDOT**: nickel-metal organic framework/poly(3,4-ethylenedioxythiophene), [e] **SWCNHs-COOH**: carboxylic-group-functionalized single-walled carbon nanohorns, [f] **ZnO-NPs/SWCNTs**: zinc oxide nanoparticles/single-wall carbon nanotubes, [g] **Ag/CMC/TiO_2/LIG**: silver/sodium carboxymethyl cellulose/titanium oxide/laser-induced graphene, [h] **rGO/PdNPs**: palladium nanoparticles decorated graphene oxide.

with lower detection limits and broader linear ranges compared to others, due to the high electroactive surface areas, excellent electrocatalytic activity, and improved electrical conductivity of the ChCl film.

3.6. *Repeatability, reproducibility and stability*

Ten consecutive SWV measurements were performed to examine the repeatability of the proposed sensor (Fig. 8A). The RSD values were 2.28

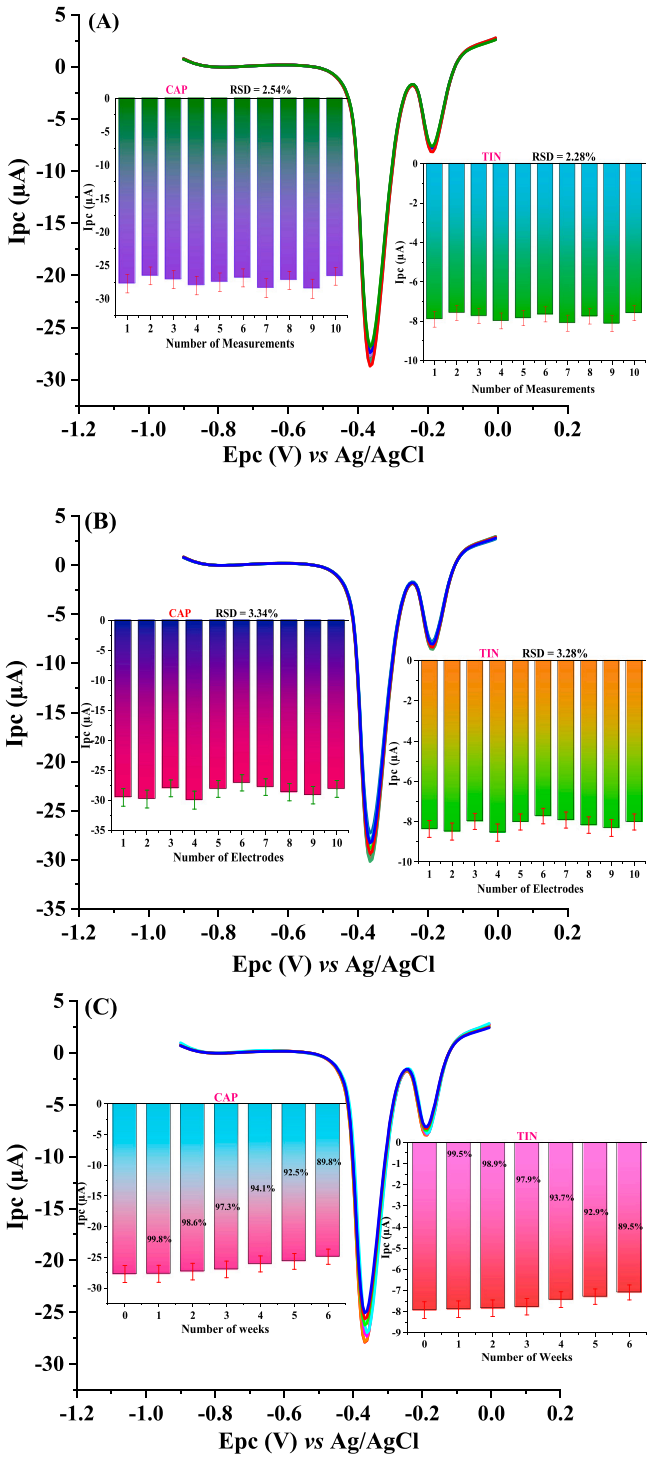

Fig. 8. (A) Repeatability and (B) reproducibility study results of ten consecutive SWV measurements, and (C) Stability study results of ChCl/GCE, Inset: bar graphs (n = 3, error bar = SD).

% for TIN and 2.54 % for CAP, indicating excellent repeatability of the sensor. The reproducibility of ChCl/GCE was evaluated by SWV analysis of ten identically prepared electrodes (Fig. 8B). The RSD values were calculated to be 3.28 % for TIN and 3.34 % for CAP, showing ChCl/GCE has very good reproducibility. The stability of the sensor was also tested by measuring current responses each week for six weeks (Fig. 8C). For 5 mM CAP, the RSD was 2.55 %, indicating that the peak current response was precise and the decline in the response over four weeks was insignificant. Generally, the sensor maintained its sensitivity for four weeks without significantly losing its current response. For 5 mM TIN, the RSD was 0.8 %, and the decline in the peak current response over three weeks was negligible. Therefore, the lifetime of the sensor to determine the TIN with high sensitivity was at least three weeks. There was a decline in the current response for CAP after four weeks and after three weeks for TIN. By the end of the sixth week, the peak currents for CAP and TIN had been reduced by 10.8 % and 10.5 %, respectively (Fig. 8C). This confirms the long-term stability of the sensor for the simultaneous determination of TIN and CAP.

3.7. Interference study

The effects of different potentially interfering species on the current responses of 5 µM TIN and CAP were assessed by SWV. Amoxicillin, doxycycline, norfloxacin, cloxacillin, and ampicillin, each at 100-fold excess concentrations, were tested for their interfering effects. The antibiotics have no significant effect on the electrochemical response of the sensor. Additionally, 200-fold excess concentrations of organic substances (uric acid, lactose, glucose, folic acid, sucrose, ascorbic acid, and fructose) were examined, and the interferents did not significantly affect the current responses of TIN and CAP. Finally, 500-fold excess concentrations of Cu^{2+}, K^{+}, Fe^{3+}, Ca^{2+}, Mg^{2+}, CO_3^{2-}, NO_3^{-}, Cl^{-}, HCO_3^{-} and SO_4^{2-} were tested, and no significant interference effects were observed. As shown in Fig. 9 and Table S1, the relative percentage errors for the current responses were less than 5 %, indicating the electrochemical responses were unaffected in the presence of excess concentrations of potentially interfering species.

3.8. Analytical application

SWV was performed to determine the concentrations of TIN and CAP in unspiked egg, honey, and milk samples, and neither TIN nor CAP showed any voltammetric responses. The result suggests that there are no TIN or CAP residues in the samples or that their concentrations are below the detection limit. Fig. 10 shows the current responses of egg samples spiked with standard solutions of TIN and CAP. As shown in Table 2, for the egg samples, very good recovery was obtained from 97.5 % to 103 % for TIN and 93–101 % for CAP. Figs. S4A and S4B show the peak current responses of honey and milk samples spiked with TIN and CAP. The honey samples yielded satisfactory recoveries of 94.7–99.5 % for TIN and 98.4–104 % for CAP. Similarly, milk samples yielded

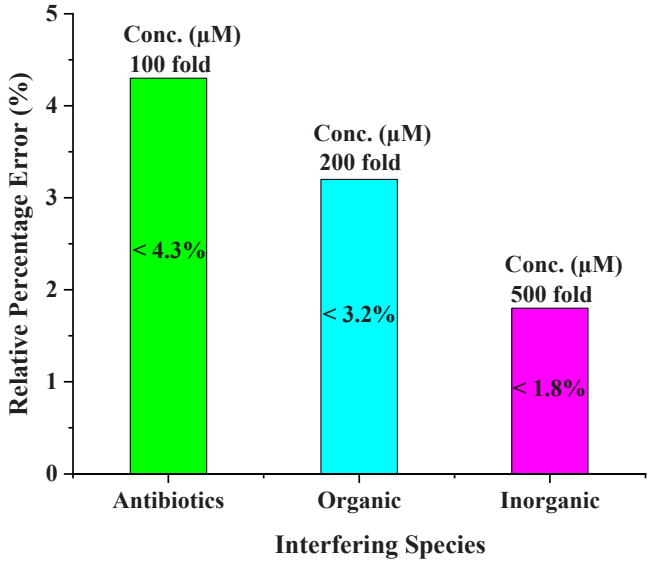

Fig. 9. Histogram showing the effect of potentially interfering species on the current responses of TIN and CAP.

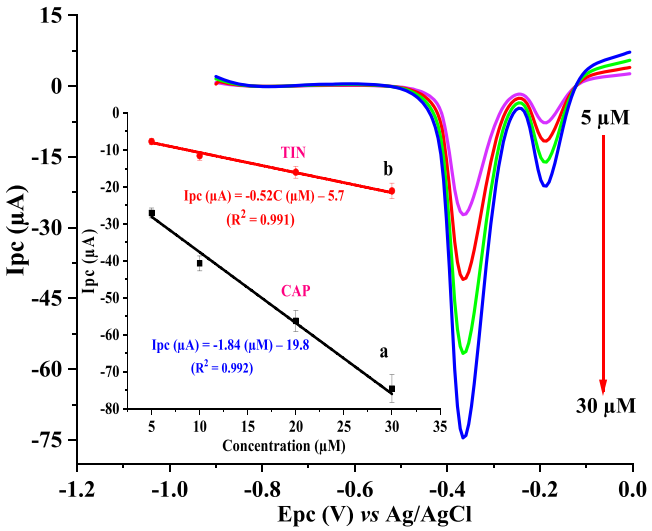

Fig. 10. SWVs of egg samples spiked with 5.0, 10.0, 20.0, and 30.0 μM standard solutions of TIN and CAP (Inset: n = 3, error bar = SD).

Table 2
Simultaneous determination of TIN and CAP in food samples.

Samples	Spiked (μM)	Found (μM)		Recovery (%)		RSD (%)	
		TIN	CAP	TIN	CAP	TIN	CAP
Egg	0	-	-	-	-	-	-
	5	5.14	4.65	103	93	3.01	3.14
	10	10.2	9.93	102	99.3	1.31	1.47
	20	19.7	20.2	98.6	101	2.98	3.16
	30	29.3	29.7	97.5	99.1	3.42	3.25
Honey	0	-	-	-	-	-	-
	5	4.87	5.27	97.4	104	4.9	4.44
	10	9.68	9.84	96.8	98.4	3.44	3.53
	20	18.9	20.0	94.7	100	3.91	3.61
	30	29.9	29.6	99.5	98.5	3.92	3.19
Milk	0	-	-	-	-	-	-
	5	5.13	4.95	103	99	1.92	2.13
	10	9.82	9.78	98.2	97.8	1.14	2.4
	20	19.6	20.1	97.8	101	1.46	2.87
	30	28.9	30.3	96.5	101	1.21	2.48

satisfactory recoveries of 96.5–103 % for TIN and 97.8–101 % for CAP. In general, average recoveries ranged from 93 % to 104 % with RSD less than 5 %, confirming the reliability of the proposed method for the simultaneous determination of TIN and CAP in food samples.

4. Conclusion

In this study, a highly sensitive, selective, and stable electrochemical sensor, ChCl/GCE, was developed for simultaneously determining TIN and CAP in food samples (eggs, honey, and milk). The outstanding performance of the sensor is due to the significantly increased electroactive surface area, electrocatalysis, and conductivity resulting from the extraordinary properties of the modifier. The proposed sensor demonstrates excellent repeatability, reproducibility, long-term stability, and high selectivity. The ChCl/GCE showed acceptable recoveries of 93–104 % with RSD of less than 5 % for the electrochemical determination of TIN and CAP in food samples. Therefore, the proposed electrochemical sensor has a high potential for real-time monitoring of TIN and CAP in food samples.

CRediT authorship contribution statement

Wondimeneh Dubale Adane: Conceptualization, Methodology, Software, Resources, Formal analysis, Investigation, Writing-original draft. **Bhagwan Singh Chandravanshi**: Conceptualization, Writing-review & editing, Supervision. **Merid Tessema:** Conceptualization, Writing-review & editing, Supervision.

Declaration of Competing Interest

The authors declare that they have no known competing financial interests or personal relationships that could have appeared to influence the work reported in this paper.

Data Availability

No data was used for the research described in the article.

Acknowledgements

The authors gratefully acknowledge the Department of Chemistry, Addis Ababa University, Addis Ababa, Ethiopia for providing laboratory facilities.

Appendix A. Supporting information

Supplementary data associated with this article can be found in the online version at doi:10.1016/j.snb.2023.134023.

References

[1] A. Pollap, J. Kochana, Electrochemical immunosensors for antibiotic detection, Biosensors 9 (2019) 61.
[2] K. Balamurugan, R. Rajakumaran, S.M. Chen, R. Karthik, J.J. Shim, P.M. Shafi, Massive engineering of spinel cobalt tin oxide/tin oxide-based electrocatalyst for the selective voltammetric determination of antibiotic drug furaltadone in water samples, J. Alloy. Compd. 882 (2021), 160750.
[3] L. Lan, Y. Yao, J. Ping, Y. Ying, Recent advances in nanomaterial-based biosensors for antibiotics detection, Biosens. Bioelectron. 91 (2017) 504–514.
[4] R. Lopez, S. Khan, A. Wong, M. Sotomayor, P.T. del, G. Picasso, Development of a new electrochemical sensor based on Mag-MIP selective toward amoxicillin in different samples, Front. Chem. 9 (2021), 615602.
[5] S. Zeb, A. Wong, S. Khan, S. Hussain, M.D.P.T. Sotomayor, Using magnetic nanoparticles/MIP-based electrochemical sensor for quantification of tetracycline in milk samples, J. Electroanal. Chem. 900 (2021), 115713.
[6] S.G. Surya, S. Khatoon, A. Ait Lahcen, A.T.H. Nguyen, B.B. Dzantiev, N. Tarannum, K.N.A. Salama, Chitosan gold nanoparticles molecularly imprinted polymer based ciprofloxacin sensor, RSC Adv. 10 (2020) 12823–12832.
[7] I.T. Carvalho, L. Santos, Antibiotics in the aquatic environments: a review of the European scenario, Environ. Int. 94 (2016) 736–757, https://doi.org/10.1016/j.envint.2016.06.025.
[8] G. Kapoor, S. Saigal, A. Elongavan, Action and resistance mechanisms of antibiotics: a guide for clinicians, J. Anaesthesiol. Clin. Pharm. 33 (2017) 300.
[9] S. Shahrokhian, S. Rastgar, Electrochemical deposition of gold nanoparticles on carbon nanotube coated glassy carbon electrode for the improved sensing of tinidazole, Electrochim. Acta 78 (2012) 422–429.
[10] A. Taye, M. Amare, Voltammetric determination of tinidazole in pharmaceutical tablets using carbon paste electrode, Bull. Chem. Soc. Ethiop. 30 (2016) 1.
[11] T. Sirisha, B. Gurupadayya, S. Sridhar, Simultaneous determination of ciprofloxacin and tinidazole in tablet dosage form by reverse phase high performance liquid chromatography, Trop. J. Pharm. Res. 13 (2014) 981.
[12] R. Pandiyan, Synthesis of Ag/ZrO_2 nanoparticles: a sensitive electrochemical sensor for determination of antibiotic drug tinidazole, Int. J. Electrochem. Sci. (2022). Article ID: 220414.
[13] K. Alagumalai, R. Shanmugam, S.M. Chen, S. Musuvadhi Babulal, A. Periyalagan, Novel electrochemical method for detection of cytotoxic tinidazole in aqueous media, Process Saf. Environ. Prot. 148 (2021) 992–1005.
[14] M. Yadav, V. Ganesan, R. Gupta, D.K. Yadav, P.K. Sonkar, Cobalt oxide nanocrystals anchored on graphene sheets for electrochemical determination of chloramphenicol, Microchem. J. 146 (2019) 881–887.
[15] S. Han, X. Zhang, H. Sun, J. Wei, H. Wang, S. Wang, J. Jin, Z. Zhang, Electrochemical behavior and voltammetric determination of chloramphenicol and doxycycline using a glassy carbon electrode modified with single-walled carbon nanohorns, Electroanalysis 34 (2022) 735–742.
[16] Y. Wang, P. Zhang, N. Jiang, X. Gong, L. Meng, D. Wang, N. Ou, H. Zhang, Simultaneous quantification of metronidazole, tinidazole, ornidazole and morinidazole in human saliva, J. Chromatogr. B 899 (2012) 27–30.
[17] H. Ye, S. Li, Y. Xi, Y. Shi, X. Shang, D. Huang, Highly sensitive determination of antibiotic residues in aquatic products by high-performance liquid chromatography–tandem mass spectrometry, Antibiotics 11 (2022) 1427.
[18] A. Azzouz, E. Ballesteros, Multi residue method for the determination of pharmacologically active substances in egg and honey using a continuous solid-

phase extraction system and gas chromatography–mass spectrometry, Food Chem. 178 (2015) 63–69.
[19] T.T.V. Tong, T.T. Cao, N.H. Tran, T.K.V. Le, D.C. Le, Green, cost-effective simultaneous assay of chloramphenicol, methylparaben, and propylparaben in eye-drops by capillary zone electrophoresis, J. Anal. Methods Chem. 2021 (2021) 1–11.
[20] B.J. Jia, X. He, P.L. Cui, J.X. Liu, J.P. Wang, Detection of chloramphenicol in meat with a chemiluminescence resonance energy transfer platform based on molecularly imprinted graphene, Anal. Chim. Acta 1063 (2019) 136–143.
[21] W.D. Adane, B.S. Chandravanshi, M. Tessema, A simple, ultrasensitive and cost-effective electrochemical sensor for the determination of ciprofloxacin in various types of samples, Sens. Bio-Sens. Res. 39 (2023), 100547.
[22] P.S. Ganesh, B.E. Kumara Swamy, O.E. Feyami, E.E. Ebenso, Interference free detection of dihydroxybenzene isomers at pyrogallol film coated electrode: a voltammetric method, J. Electroanal. Chem. 813 (2018) 193–199.
[23] Q. He, B. Wang, J. Liang, J. Liu, B. Liang, G. Li, Y. Long, G. Zhang, H. Liu, Research on the construction of portable electrochemical sensors for environmental compounds quality monitoring, Mater. Today Adv. 17 (2023), 100340.
[24] Q. Wang, Q. Xue, T. Chen, J. Li, Y. Liu, X. Shan, F. Liu, J. Jia, Recent advances in electrochemical sensors for antibiotics and their applications, Chin. Chem. Lett. 32 (2021) 609–619.
[25] Z. Yu, P. Cui, Y. Xiang, B. Li, X. Han, W. Shi, H. Yan, G. Zhang, Developing a fast electrochemical aptasensor method for the quantitative detection of penicillin G residue in milk with high sensitivity and good anti-fouling ability, Microchem. J. 157 (2020), 105077.
[26] R. Umapathi, S.M. Ghoreishian, S. Sonwal, G.M. Rani, Y.S. Huh, Portable electrochemical sensing methodologies for on-site detection of pesticide residues in fruits and vegetables, Coord. Chem. Rev. 453 (2022), 214305.
[27] O.A. Fouad, M.M.S. Wahsh, G.G. Mohamed, M.M.I. El Desssouky, M.R. Mostafa, Fabrication and characterization of mullite nano-ceramic materials for use in carbon paste ion selective electrode to estimate carcinogenic Cd(II) ion in real and human samples, Microchem. J. 190 (2023), 108623.
[28] T. Williams, R. Shum, D. Rappleye, Review-concentration measurements in molten chloride salts using electrochemical methods, J. Electrochem. Soc. 168 (2021), 123510.
[29] T.C. Hung, Y.R. Liu, P.C. Chou, C.W. Lin, Y.T. Hsieh, Electrochemical sensing of hydrazine using hollow Pd/Ag dendrites prepared by galvanic replacement from choline chloride-based deep eutectic solvents, J. Electroanal. Chem. 922 (2022), 116791.
[30] Z. Parsaee, N. Karachi, S.M. Abrishamifar, M.R.R. Kahkha, R. Razavi, Silver-choline chloride modified graphene oxide: novel nano-bio electrochemical sensor for celecoxib detection and CCD-RSM model, Ultrason. Sonochem. 45 (2018) 106–115.
[31] V.B. Patil, S.J. Malode, S.N. Mangasuli, S.M. Tuwar, K. Mondal, N.P. Shetti, An electrochemical electrode to detect theophylline based on copper oxide nanoparticles composited with graphene oxide, Micromachines 13 (2022) 1166.
[32] E.P. Randviir, A cross examination of electron transfer rate constants for carbon screen-printed electrodes using electrochemical impedance spectroscopy and cyclic voltammetry, Electrochim. Acta 286 (2018) 179–186.
[33] U. Rajaji, S. Manavalan, S.M. Chen, M. Govindasamy, T.W. Chen, T. Maiyalagan, Microwave-assisted synthesis of europium(III) oxide decorated reduced graphene oxide nanocomposite for detection of chloramphenicol in food samples, Compos. B: Eng. 161 (2019) 29–36.
[34] H. Wang, X. Feng, X. Bo, M. Zhou, L. Guo, Nickel-based metal-organic framework/crosslinked tubular poly(3,4-ethylenedioxythiophene) composite as an electro-catalyst for the detection of gallic acid and tinidazole, ChemElectroChem 7 (2020) 4031–4037.
[35] W. Wang, Electrochemical determination of chloramphenicol based on ZnO-NPs/SWCNTS composite modified glassy carbon electrode, Int. J. Electrochem. Sci. (2021), 210216.
[36] E. Saeb, K. Asadpour-Zeynali, Enhanced electrocatalytic reduction activity of Fe-MOF/Pt nanoparticles as a sensitive sensor for ultra-trace determination of tinidazole, Microchem. J. 172 (2022), 106976.
[37] C. Chang, Q. Wang, Q. Xue, F. Liu, L. Hou, S. Pu, Highly efficient detection of chloramphenicol in water using Ag and TiO_2 nanoparticles modified laser-induced graphene electrode, Microchem. J. 173 (2022), 107037.
[38] W. Yi, Z. Li, C. Dong, H.W. Li, J. Li, Electrochemical detection of chloramphenicol using palladium nanoparticles decorated reduced graphene oxide, Microchem. J. 148 (2019) 774–783.

Wondimeneh Dubale Adane is currently a Ph.D. student in analytical chemistry and works in the research group of Prof. B. S. Chandravanshi at Addis Ababa University, Addis Ababa, Ethiopia. He received his B.Ed. in Chemistry in 2005 from Debub University, Ethiopia, and his M.Sc. in Analytical Chemistry from Dilla University in 2012. His research focuses on the development of electrochemical sensors and biosensors for analytical applications in clinical, environmental, and forensic analysis. He is very familiar with the operation of various analytical instruments.

Bhagwan Singh Chandravanshi is a Professor of Analytical Chemistry in the Department of Chemistry of the College of Natural Sciences of Addis Ababa University, Addis Ababa, Ethiopia. His research area covers determination of nutrients and non-essential elements in food, environmental samples, medicinal plant samples, plant food samples, determination of psychoactive compounds in plants and drugs, development of voltammetric methods for determination of heavy metals and drugs, determination of pharmaceuticals in water and food samples using different analytical techniques such as carbon paste electrodes, ion selective electrodes potentiometry, solvent extraction and spectrophotometry, UV-Visible spectrophotometry, near and mid IR spectrometry, HPLC, GC-MS, ICP-MS, ICP-OES. He has supervised - 120 M.Sc. students and 15 PhD students. He has published 222 articles in different chemistry and related journals of international reputability.

Merid Tessema got his BSc and MSc degrees from Addis Ababa University (AAU), Ethiopia. He obtained his PhD degree in Analytical Chemistry from Addis Ababa University in 1997 in a Sandwich Program between Lund University, Sweden and Addis Ababa University. He is currently working as an Associate Professor and a Senior Research Supervisor in the area of Sensors and Biosensors. He has produced more than 50 publications having supervised several MSc and PhD students.

Supplementary Material

Highly sensitive and selective electrochemical sensor for the simultaneous determination of tinidazole and chloramphenicol in food samples (egg, honey and milk)

Wondimeneh Dubale Adane [a], Bhagwan Singh Chandravanshi [a]*, Merid Tessema [a]

[a] Department of Chemistry, Addis Ababa University, P. O. Box 1176, Addis Ababa, Ethiopia

* Corresponding author. E-mail addresses: bscv2006@yahoo.com

Preparation of ChCl/GCE

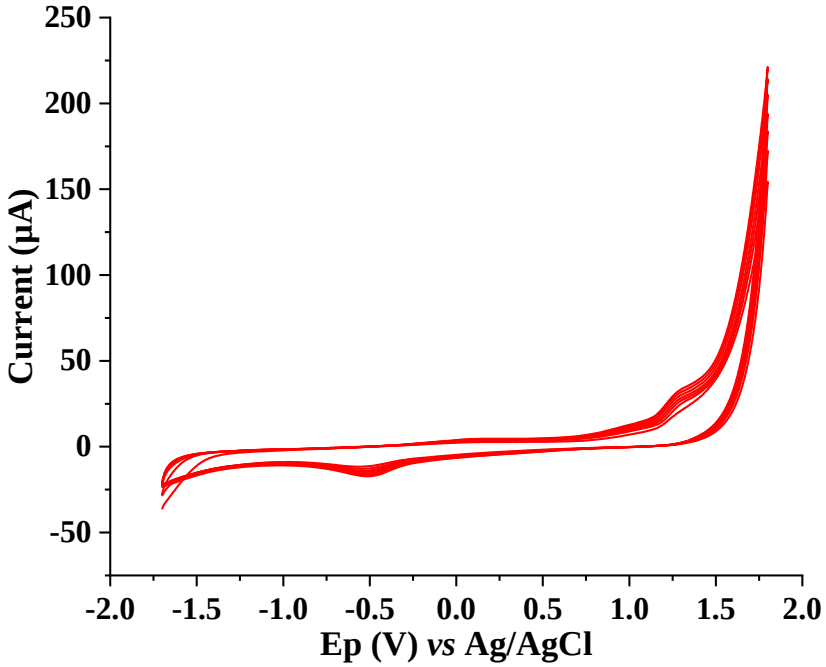

Fig. S1. CVs of 0.002 M ChCl solution containing 0.01 M KCl in 0.1 M PBS (pH 7.0) at GCE for fourteen cycles at a scan rate of 25 mVs^{-1} in the potential ranges of -1.7 to 1.6 V.

Electrochemical characterization

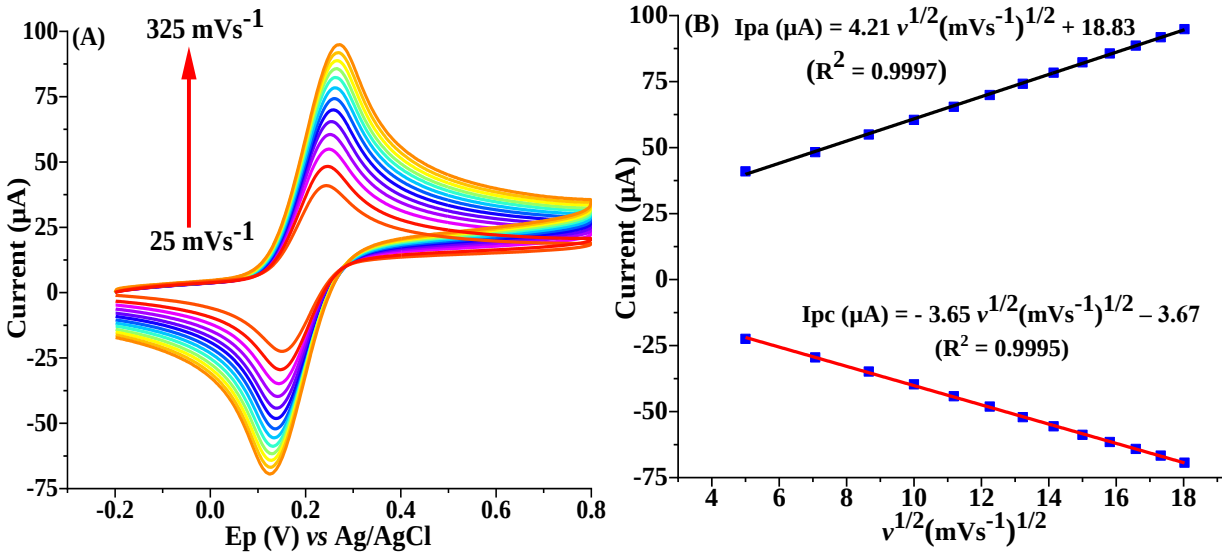

Fig. S2. (A) CVs of 5 mM $[Fe(CN)_6]^{3-/4-}$ at different scan rates using bare GCE and (B) plot of peak current vs. square root of scan rate.

Effect of scan rate

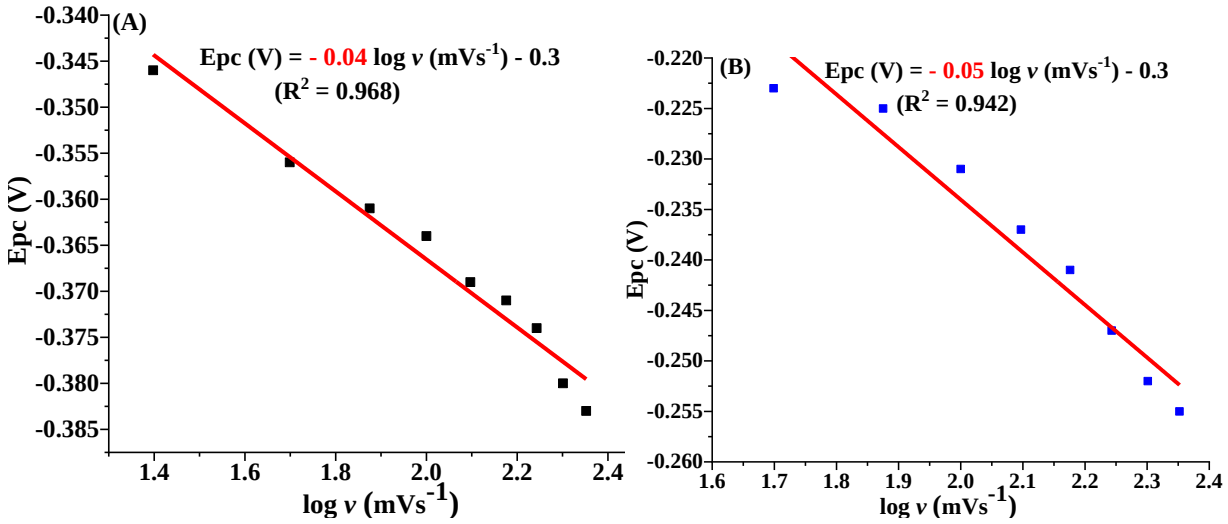

Fig. S3. (A) Plot of Epc (V) vs. log v (mVs^{-1}) for 5 µM CAP in 0.1 M H_2SO_4 and (B) Plot of Epc (V) vs. log v (mVs^{-1}) for 5 µM TIN in 0.1 M H_2SO_4.

Analytical application

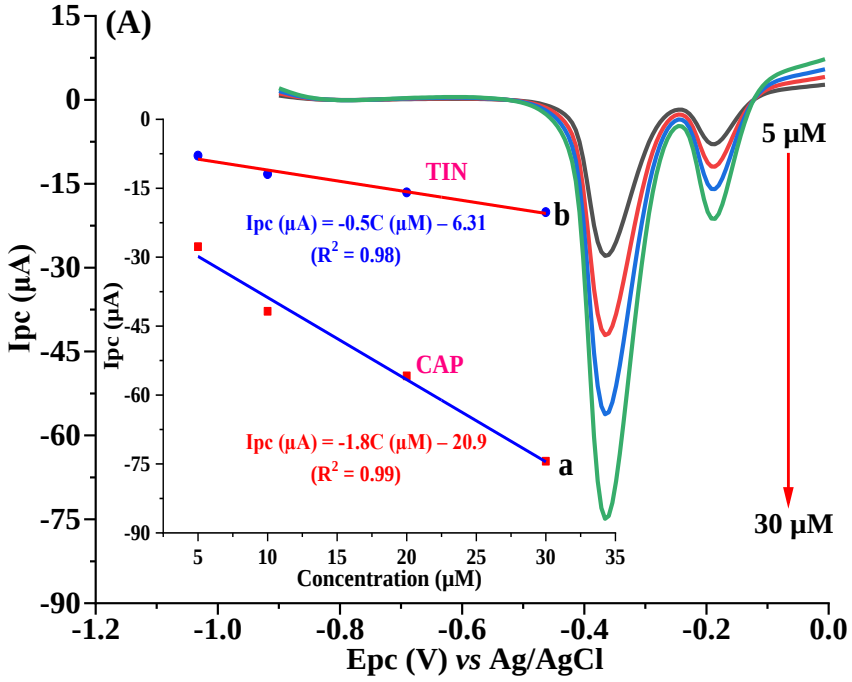

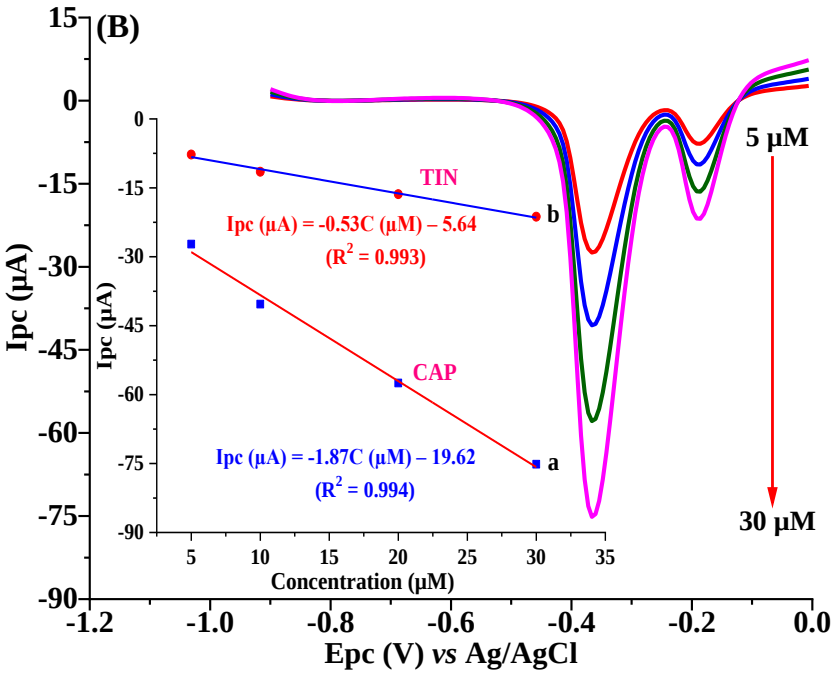

Fig. S4. (A) SWV of honey samples spiked with 5.0, 10.0, 20.0, and 30.0 µM standard solutions of TIN and CAP, and (B) SWV of milk samples spiked with 5.0, 10.0, 20.0, and 30.0 µM standard solutions of TIN and CAP.

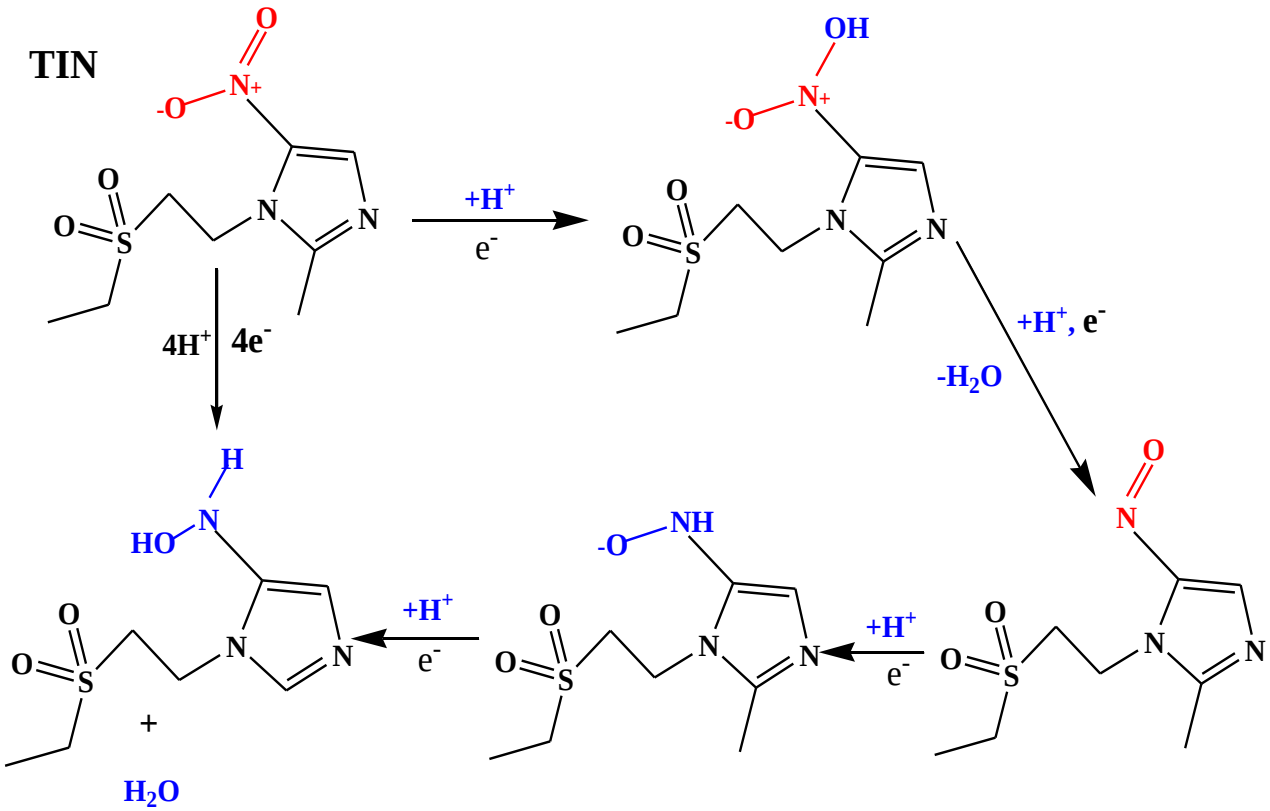

29

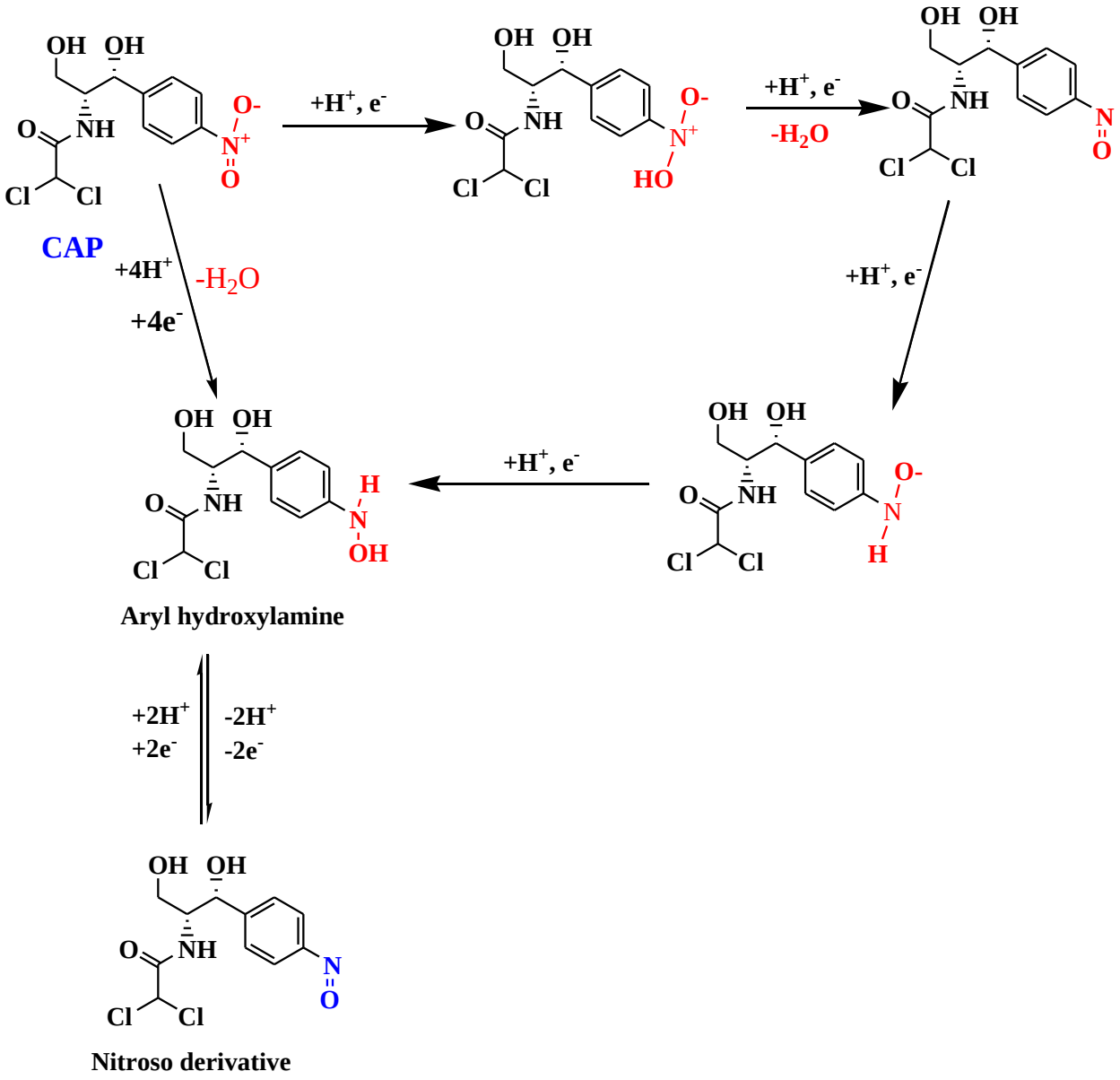

Scheme S1. Detailed reaction mechanisms for the electrochemical reduction of TIN and CAP

1. Preparation of solutions

By dissolving an adequate quantity of the analyte in 50 mL of 5% ethanol and distilled water (1:1, v/v), a 0.01 M stock solution of TIN was prepared. In addition, a 0.01 M CAP stock solution was prepared by adding a sufficient amount of the analyte to 50 mL of distilled water. The working solutions of TIN and CAP were prepared by diluting the stock solutions with 0.1 M

H_2SO_4. 75 mg potassium chloride and 28 mg choline chloride were added to 0.1 M phosphate buffer solution (PBS) (pH 7.0) to prepare a 0.002 M choline chloride solution.

2. Sample preparation

2.1. Milk sample

Milk samples were collected from Sebeta town in Oromia Regional State, Ethiopia. The samples were prepared by the following methods: 20 mL of acetonitrile and 5.0 mL of the milk sample were first mixed. The mixture was shaken for 10 min after 15 min of sonication and then centrifuged at 10,000 rpm for 10 min. The supernatant was then filtered through a 150 mm filter membrane. The filtrate was then transferred to a 25 mL volumetric flask, diluted with 0.1 M PBS (pH 7.0) to the appropriate concentration, and spiked with standard solutions of TIN and CAP.

2.2. Honey sample

Honey was purchased from a local supermarket in Addis Ababa, Ethiopia. The samples were prepared as follows: 1 g of honey was dissolved in 1 mL of 0.1 M HCl by magnetic stirring. A dilution ratio of 1:10 (v/v) in PBS (pH 7.4) was used to reduce the matrix effects, and the solution was filtered through a 150 mm filter membrane before analysis. The sample was then spiked with known concentrations of TIN and CAP standards.

2.3. Egg sample

ELFORA Agro-Industries Plc, a poultry farm in Bishoftu, Oromia Regional State, Ethiopia, provided egg samples. The sample was prepared as follows: the entire egg was first pureed with frequent stirring, and a 5.0 g egg sample was placed in a 15 ml centrifuge tube with 10 ml acetonitrile. After sonicating for 15 minutes, the solution was centrifuged at 2240 relative centrifugal force (RCF) for 10 min and the supernatant was filtered and poured into new centrifuge tubes. The mixture was then added and vortexed with 1.0 mL of 4.0 M ammonium acetate buffer (pH 6.75). 20 mL of dichloromethane was also added to the solution before centrifugation for 10 min at 2240 RCF. Before analysis, extracts were filtered through a 150 mm filter membrane and re-dissolved in a 2.0 ml pH 7.0 phosphate buffer.

3. Analytical procedure

After the preparation of the modified electrode (ChCl/GCE), its characteristics were investigated by SWV and CV. After this step, the electrochemical characterizations of the bare and modified electrodes were performed by CV and EIS. Based on the results, the electrochemical behavior of TIN and CAP was analyzed with CV, followed by the optimization of the experimental conditions, such as the effect of the supporting electrolyte (types and pH) and the SWV parameters (amplitude, frequency, and increment). Next, the calibration curve was constructed using successive additions of TIN and CAP standard solutions. Schematic of the experimental setup for the overall electrochemical determination process was given in Fig. S5. All measurements were performed in triplicate, and the TIN and CAP concentrations were determined simultaneously under the optimized experimental conditions. The limit of detection (LOD) was calculated as three times the standard deviation for the blank divided by the slope of the analytical curve. Likewise, the limit of quantification (LOQ) was calculated as ten times the standard deviation for the blank divided by the slope of the analytical curve. The repeatability, reproducibility, and stability of the proposed method were verified using repeatability studies followed by interference studies for various potentially interfering species on the current responses of 5 mM TIN and CAP by SWV. Finally, the accuracy and precision of the developed method were tested by spiking standard solutions of TIN and CAP into the eggs, honey, and milk samples and calculating the percentage recovery.

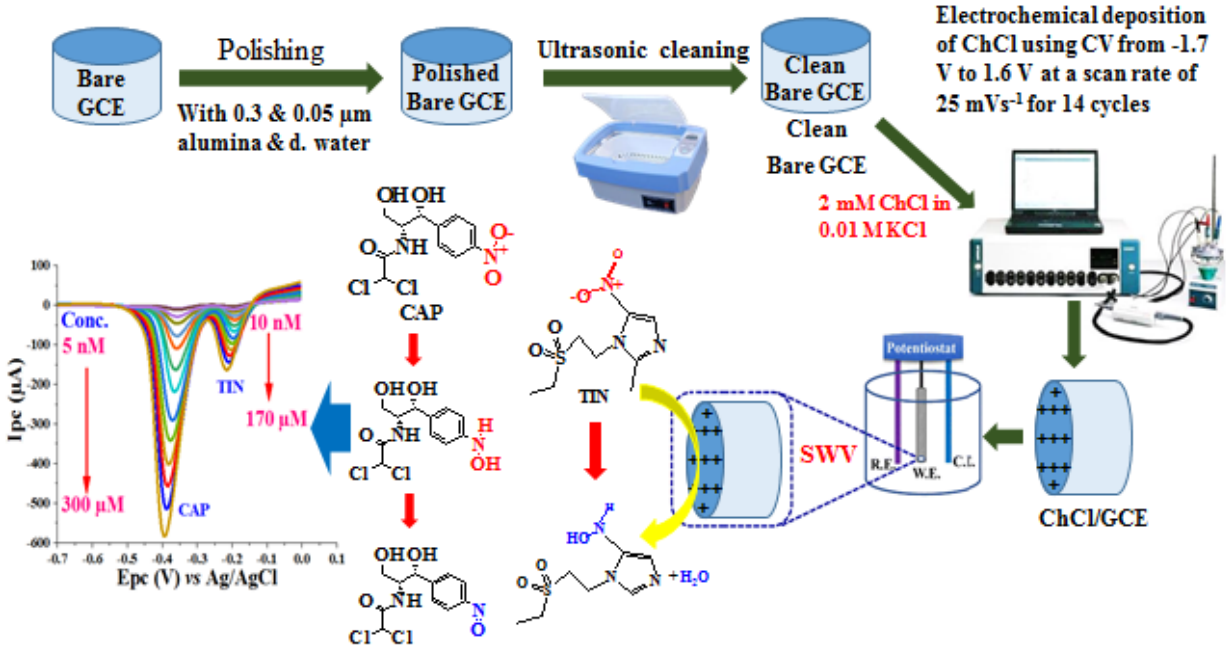

Fig. S5. Schematic representation of the experimental setup for the electrochemical determination process

4. Morphological characterization

The FT-IR spectra of pure choline chloride, the modified electrode, and the modified electrode in 5 µM TIN and CAP solution are shown in Fig. S6. As shown in Fig. S6A, the appearance of very strong broadband at the frequency of 3262 cm^{-1} corresponds to the OH stretching vibration of the ChCl modifier. The bands assigned to the C-H stretch of choline chlorides $-CH_3$ and $-CH_2$, as well as the C-C-O groups, range from 3000 to 2800 cm^{-1} and 1090 cm^{-1}. Between 900 and 1000 cm^{-1}, a distinct group of quaternary ammonium compounds is present, with the peak at 950 cm^{-1} attributed to the C-N of choline chloride. The ChCl/GCE spectra exhibit a little reduction in band strength and width along with a slight shift in the OH stretch to 3415 cm^{-1}, (Fig. S6B) due to less hydrogen bonding. The frequencies at 480, 618, 1618, and 2924 cm^{-1} decreased but remained unchanged compared to pure choline chloride. It indicates the presence of choline chloride on the modified electrode surface. $(CH_3)_3N^+$ in pure choline chloride is responsible for the distinctive absorption observed at 1464 cm^{-1}. Therefore, the above results indicate the deposition of choline chloride on the modified electrode surface.

Fig. S6C shows the spectra of ChCl/GCE in 5 µM TIN and CAP solution. There is no difference between the spectra of ChCl/GCE alone and ChCl/GCE in 5 µM TIN and CAP solution (Figs. S6B and S6C). The results show that there is no interaction between the target analytes and the electrode, whereas the modifier (ChCl) increases the number of electroactive sites and the surface area of the electrode and catalyzes the electrochemical reduction of TIN and CAP.

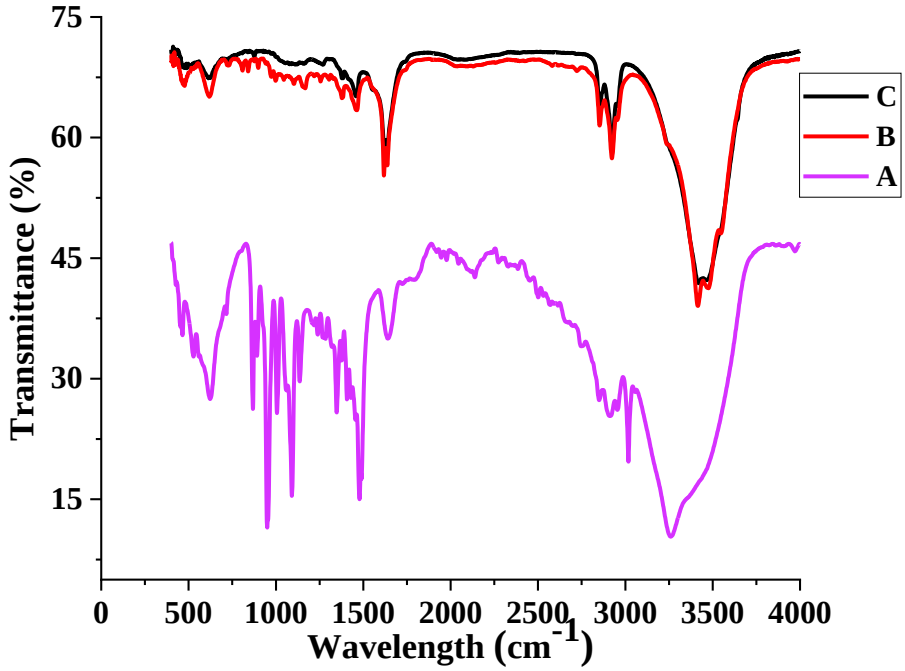

Fig. S6. FT-IR spectra of (A) pure ChCl, (B) ChCl/GCE and (C) ChCl/GCE in 5 µM TIN and CAP solution.

5. Effect of supporting electrolytes

The type of supporting electrolyte solution used in the voltammetric measurement has a significant influence on the peak current response and the shape of the voltammogram. Therefore, the selection of a suitable supporting electrolyte is of utmost importance before voltammetric determinations of target analytes. Based on the peak current intensity and the shape of the voltammogram, SWV was used to examine the effects of various supporting electrolyte solutions, including Britton-Robinson buffer (BRB), phosphate buffer solution (PBS), sulfuric acid, citrate buffer (CB), perchloric acid, and acetate buffer (AB). The peak current responses for both analytes obtained from H_2SO_4 were noticeably higher than the others (Fig. S7). Therefore,

for the simultaneous determination of TIN and CAP, H_2SO_4 was chosen as an appropriate supporting electrolyte.

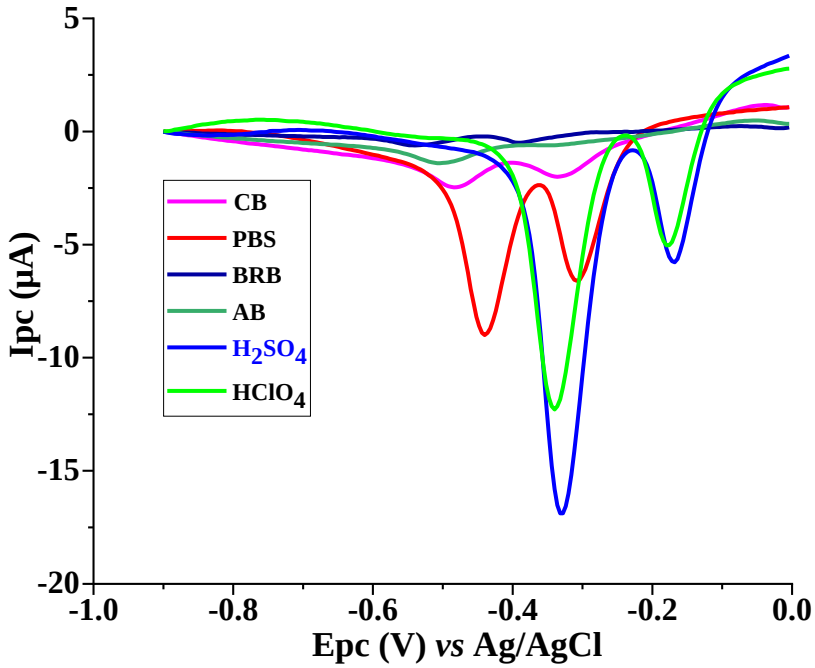

Fig. S7. SWVs of 5 µM TIN and CAP in different supporting electrolyte solutions.

6. Optimization of SWV parameters

The peak current response and shapes of a voltammogram are affected by SWV parameters such as pulse amplitude, step potential, and frequency. Therefore, in this study, the SWV parameters were optimized to obtain the maximum peak current response for the reduction of 5 µM TIN and CAP at the surface of ChCl/GCE. First, the effect of amplitude was investigated in the range of 10−80 mV by keeping the step potential and the frequency constant. The reduction currents of TIN and CAP increased up to 50 mV and then decreased (Fig. S8A). Therefore, an amplitude of 50 mV was chosen as the optimal value for the simultaneous determination of TIN and CAP in subsequent experiments. Likewise, we investigated the effect of step potentials in the range of 2−12 mV by keeping the amplitude and the frequency constant. The reduction peak currents of TIN and CAP increased up to 8 mV, and a further increase in the step potential decreased the peak currents of both analytes (Fig. S8B). Finally, the effect of frequency on the sensitivity of 5 µM TIN and CAP in 0.1 M H_2SO_4 was investigated in the range

of 30−120 Hz by keeping the amplitude and step potential constant. The maximum peak current response was obtained at 80 Hz for both analytes (Fig. S8C). Therefore, the frequency of 80 Hz was chosen as the optimal value for the simultaneous determination of TIN and CAP in subsequent experiments.

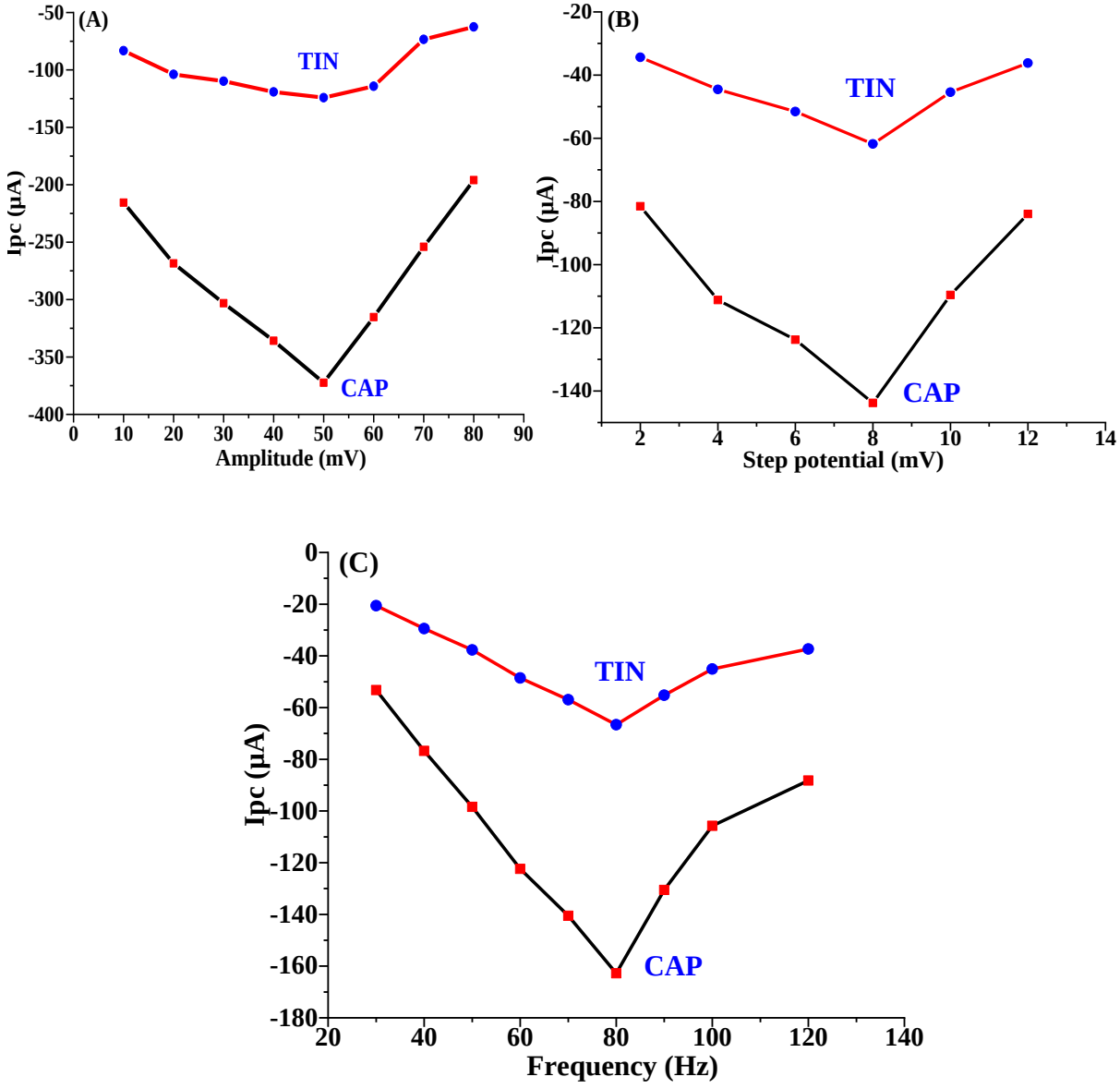

Fig. S8. The effect of SWV parameters: (A) amplitude; (B) step potential; and (C) frequency on the reduction peak current of 5 μM TIN and CAP in 0.1 M H_2SO_4.

7. Selective determination of TIN and CAP

SWV responses were recorded for different concentrations of TIN and CAP in 0.1 M H_2SO_4 under the optimal experimental conditions for selective determinations. As shown in Fig. S9A and C, for both analytes, when the concentration of each analyte increases, the corresponding reduction peak current also increases. For CAP, the reduction peak current was linearly correlated with a concentration between 4 nM and 320 µM with the regression equation of Ipc (µA) = -1.86C (µM) - 22.55 (R^2 = 0.999) (Fig. S9A and B). The LOD (3σ/m, S/N=3, n=3) is 0.15 nM, and the LOQ (10σ/m, S/N=3, n=3) is 0.49 nM (where m = slope of the calibration curve and σ = standard deviation of the lowest value of the linear range). Similarly, the linear range for TIN is 9 nM to 200 µM (Ipc (µA) = -1.12C (µM) + 0.13, R^2 = 0.998) (Fig. S9C and S9D). The LOD and LOQ are 0.49 nM and 1.63 nM, respectively.

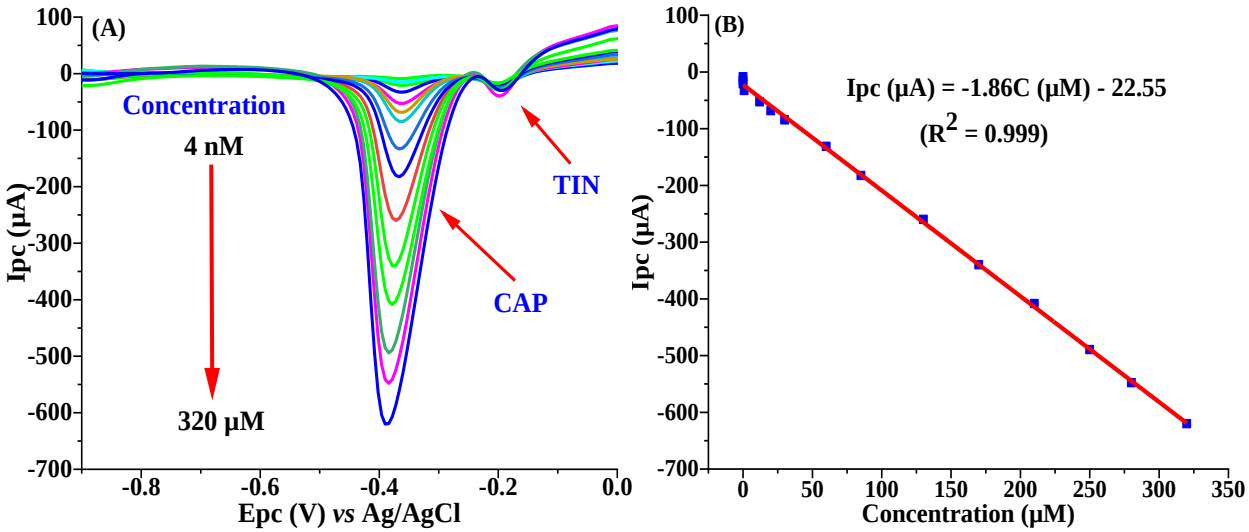

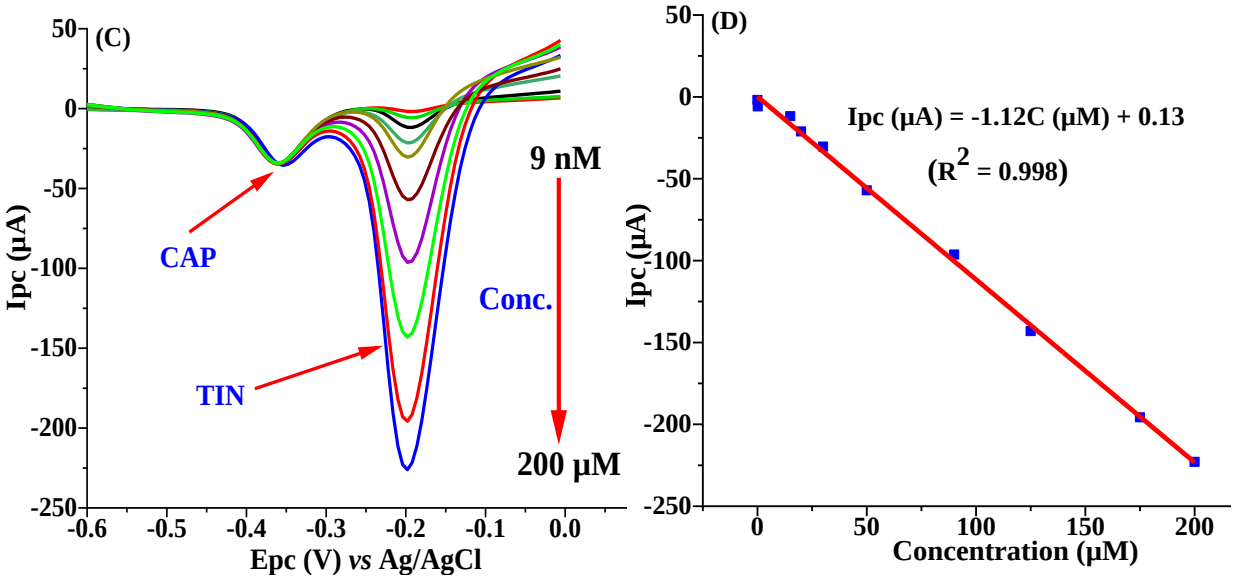

Fig. S9. (A) SWVs of 0.004, 0.007, 0.01, 0.8, 12, 20, 30, 60, 85, 130, 170, 210, 250, 280 and 320 µM CAP in 0.1 M H_2SO_4 at the ChCl/GCE, (B) plot of Ipc (µA) vs. concentration of CAP, (C) SWVs of 0.009, 0.1, 15, 20, 30, 50, 90, 125, 175 and 200 µM TIN in 0.1 M H_2SO_4 at the ChCl/GCE, and (D) plot of Ipc (µA) vs. concentration of TIN.

Table S1

The influence of coexisting substances on the determination of TIN and CAP.

Interferents	Conc. (µM)	Relative Percentage Error (%)
Antibiotics	100 fold	< 4.3%
Organic	200 fold	< 3.2%
Inorganic	750 fold	< 1.8%

Chapter Five: Paper III

A novel electrochemical sensor for the detection of metronidazole residues in food samples

Wondimeneh Dubale Adane, Bhagwan Singh Chandravanshi, Merid Tessema

Chemosphere 359 (2024) 142279

https://doi.org/10.1016/j.chemosphere.2024.142279

Chemosphere 359 (2024) 142279

Contents lists available at ScienceDirect

Chemosphere

journal homepage: www.elsevier.com/locate/chemosphere

A novel electrochemical sensor for the detection of metronidazole residues in food samples

Wondimeneh Dubale Adane, Bhagwan Singh Chandravanshi *, Merid Tessema **

Department of Chemistry, Addis Ababa University, P. O. Box 1176, Addis Ababa, Ethiopia

HIGHLIGHTS

- Novel electrochemical sensor was developed by integrating multiple nanocomposites.
- The senor was applied for the detection of metronidazole residues in food samples.
- The sensor showed wide linear range and picomolar LOD for detecting metronidazole.
- Current response was not affected by the presence of commonly coexisting species.

GRAPHICAL ABSTRACT

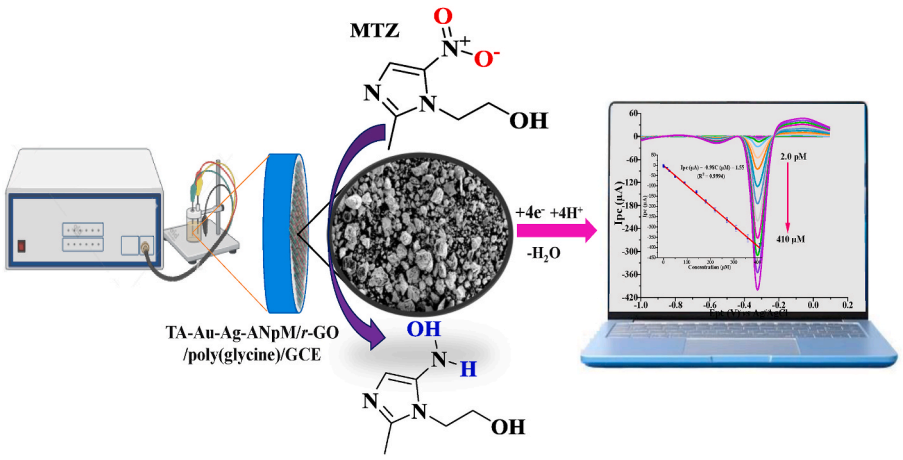

ARTICLE INFO

Handling Editor: Grzegorz Lisak

Keywords:
Antibiotic residues
Metronidazole
Thermally annealed gold–silver alloy nanoporous matrices
Reduced graphene oxide
Electrochemical sensor

ABSTRACT

The widespread use and misuse of antibiotics in pharmaceuticals and animal farming has resulted in their accumulation in food sources and the environment, posing significant threats to human health, the environment, and the global economy. In this study, we have developed a hypersensitive, and ultra-selective electrochemical sensor, the first of its kind, by integrating a thermally annealed gold-silver alloy nanoporous matrix (TA-Au-Ag-ANpM) with reduced graphene oxide (*r*-GO) and poly(glycine) at the surface of a glassy carbon electrode (GCE). This sensor aims to detect life-threatening metronidazole (MTZ) residues in food samples. TA-Au-Ag-ANpM/*r*-GO/poly(glycine)/GCE was thoroughly characterized using a range of analytical techniques, including UV–Vis, FT-IR, XRD, SEM, and EDX. Furthermore, its electrochemical properties were investigated by cyclic voltammetry (CV), square wave voltammetry (SWV), and electrochemical impedance spectroscopy (EIS). The sensor exhibited outstanding performance, with a broad linear range of 2.0 pM–410 μM. The limits of detection (LOD) and quantification (LOQ) were determined to be 0.0312 pM and 0.104 pM, respectively. The TA-Au-Ag-ANpM/*r*-GO/poly(glycine)/GCE exhibited exceptional reproducibility, repeatability, stability, and resistance to interferences. Moreover, the sensor demonstrated outstanding performance in detecting MTZ residues in milk powder, pork,

* Corresponding author.
** Corresponding author.
E-mail addresses: bscv2006@yahoo.com (B.S. Chandravanshi), tessemamerid@yahoo.com (M. Tessema).

https://doi.org/10.1016/j.chemosphere.2024.142279
Received 27 January 2024; Received in revised form 2 May 2024; Accepted 6 May 2024
Available online 7 May 2024

and chicken meat samples, achieving very good recoveries (96.9%–101.4%) with a relative standard deviation (RSD) below 5%. This performance highlights the potential for practical applications in food safety and quality monitoring. Therefore, the developed sensor contributes to the advancement of electrochemical sensing technology and its application in ensuring food safety and integrity by combating antibiotic residues.

1. Introduction

Antibiotics, well-known for their efficacy against pathogenic microbes, are extensively used to treat a variety of infectious diseases in both animals and humans. Apart from their therapeutic uses, antibiotics are also utilized as performance enhancers and growth promoters in animal farming. They play key roles in regulating reproductive cycles, improving breeding performance, and serving as prophylactic agents (Majdinasab et al., 2020; Wang et al., 2022). In humans, antibiotics predominantly target infections of the genital, abdominal, urinary tract, skin, and gastrointestinal systems. They exhibit effectiveness against conditions such as leprosy, tuberculosis, strep throat, bronchitis, pneumonia, arthritis, sinusitis, and typhoid fever. Their mechanisms of action primarily involve inhibiting bacterial cell wall and protein synthesis, interfering with bacterial DNA synthesis, impeding nascent RNA elongation, and eradicating microbial populations (Adane et al., 2023a). The extensive use of antimicrobials has led to the release of their residues into the environment through the direct disposal of unused or expired medications from medical facilities and pharmaceutical industries. Furthermore, due to incomplete absorption and metabolism in humans and animals, a significant portion of ingested antibiotics is excreted relatively quickly, entering the environment as metabolites or precursors (Vatovec et al., 2021). This environmental contamination extends to consumables such as fish, meat, eggs, honey, milk, and poultry, raising concerns about potential health hazards for humans. The accumulation of antibiotic residues in food products poses significant health risks, including hepatotoxicity, nephropathy, allergies, oncogenicity, myelotoxicity, reproductive anomalies, mutagenicity, immunopathological effects, and anaphylactic shock (Kogularasu et al., 2023; Majdinasab et al., 2020).

Antibiotic resistance, a critical public health concern, arises from bacteria evolving to withstand antibiotics, primarily due to their widespread and inappropriate usage in human and animal medicine. The environment, including soil, water, and waste disposal sites, serves as a significant breeding ground for antibiotic-resistant bacteria and genes (Larsson and Flach, 2022). Excessive antibiotic use in agriculture, pharmaceutical manufacturing, and healthcare exacerbates the problem (Kumar and Pal, 2018). The presence of antibiotic residues in the environment further amplifies resistance, posing a substantial risk to human health. These residues exert selective pressure on bacteria, promoting the survival and proliferation of antibiotic-resistant strains. Persistent exposure to residual antibiotics in food, water, and soil perpetuates a continuous stimulus for the evolution of resistance genes in bacterial populations (Manyi-Loh et al., 2018). Antibiotic resistance poses a significant public health challenge and has serious consequences. It escalates the complexity of treating infections, resulting in higher healthcare costs, elevated mortality rates, and prolonged illness duration. Additionally, antibiotic resistance diminishes the efficacy of vital medical procedures, including organ transplantation, chemotherapy, and surgery (Dadgostar, 2019). Hence, the development of innovative analytical approaches is imperative to tackle the escalating antibiotic residue crisis.

Metronidazole (MTZ), a nitroimidazole antibiotic, was initially introduced in 1959 for treating *T. vaginalis* infections but has since expanded its therapeutic reach to encompass a wide array of diseases caused by Bacteroides, Fusobacteria, and Clostridia species. Its applications now include treating conditions such as rosacea, endocarditis, septicemia, Helicobacter pylori-related ailments, Giardia lamblia infections, Crohn's disease, and various dental, gynecological, bone, joint, and respiratory infections (Yu et al., 2023). In livestock farming, MTZ serves as both a nutritional and medicinal supplement to enhance the growth and well-being of animals while combating parasitic infections (Lan et al., 2023). Recent studies have highlighted significant side effects associated with prolonged exposure to MTZ. These include migraines, anorexia, blurred vision, hormonal imbalance, convulsions, potential damage to human DNA, and mutagenic and carcinogenic toxicities such as optic nerve damage, epileptic seizures, and malignant tumors (Huang et al., 2023; Qi et al., 2023). The improper use and overuse of MTZ in livestock can result in the presence of its residues in animal tissues, endangering consumers along the food chain. The misuse and uncontrolled release of antibiotics into the environment contribute to the development of drug-resistant genes, poising a significant global health hazard (Lan et al., 2023). Therefore, the development of an innovative electroanalytical sensor to quantify life-threatening MTZ residues in food samples is crucial for ensuring both human well-being and food safety.

Several monometallic nanoparticles have been utilized as electrode modifiers in electroanalytical and catalytic applications. However, bimetallic alloy nanoparticles have gained considerable interest due to their enhanced electrical conductivity and electrocatalytic capabilities. The nanoparticles have been extensively explored for both electrocatalytic and electroanalytical purposes. Their catalytic performance and electroactive surface area benefit from synergistic effects arising from factors such as elemental composition, shape, and structure of the constituent metals (Sangkaew et al., 2022). The diverse morphologies of bimetallic alloy nanoparticles have captivated researchers, offering promising avenues for innovation in various fields. For instance, Yu et al. (2017) demonstrated the fabrication of hollow Au–Ag nanorices, unlocking potential applications in surface plasmon-related technologies such as surface-enhanced Raman spectroscopy (SERS), plasmon-driven chemical reactions (PDSC), multipolar antennas, and metamaterials. Li et al. (2018) achieved remarkable advancements in hydrogen peroxide detection using highly sensitive microelectrodes featuring Pt–Pd nanocorals fabricated via one-step electrochemical deposition. Swathy et al. (2023) developed a turn-off fluorescence sensor for rapid histamine detection in biological samples using tryptophan-capped Au/Ag bimetallic nanoclusters. Mao et al. (2022) fabricated Pt–Fe alloy nanoparticles on 3D N-doped carbon nano-flowers, paving the way for efficient electrochemical biosensors in the early diagnosis and treatment of squamous cell carcinoma (SCCA). These innovative studies underscore the versatility and potential of bimetallic alloy nanoparticles in advancing electroanalytical and catalytic technologies for various applications.

Carbonaceous electrodes are widely used in the development of electrochemical sensors because of their wide potential range, cost-effectiveness, low electrical impedance, and the ability to be chemically modified (Adane et al., 2023b). Graphene, known for its exceptional physicochemical characteristics such as mechanical strength, significant surface area, high conductivity, elasticity, tunable optical properties, biocompatibility, and durability, stands out among carbon-based materials. Reduced graphene oxide (*r*-GO) is particularly favored for electrode modification due to its impressive thermal stability, large surface area, and excellent electrical conductivity (Chai et al., 2023). Furthermore, *r*-GO demonstrates robust electrocatalytic capabilities, a heightened electroactive surface area, minimal surface fouling, and cost-effectiveness, making it a preferred choice for sensor fabrication. Consequently, electrochemical sensors incorporating *r*-GO exhibit outstanding performance due to their wide electrochemical

potential range. Integration of bimetallic nanocomposites with carbon-based substrates as supporting materials offers synergistic enhancements to sensor electrochemical behavior, leading to improved signal response, sensitivity, and precision (Duan et al., 2020). In this study, *r*-GO was combined with TA-Au-Ag-ANpM nanocomposites to develop an innovative electrochemical sensor, broadening its analytical applications. The incorporation of *r*-GO enhances conductivity, reduces internal resistance, and promotes charge transfer, ultimately elevating sensor performance (Mummoorthi et al., 2023).

Conductive polymers have emerged as compelling candidates for fabricating voltammetric sensing platforms, offering improved reproducibility, sensitivity, and stability. The electropolymerization of various monomers allows the formation of conductive polymers with unique physicochemical properties (Wang et al., 2023). Poly(amino acids), particularly poly(glycine), have gained a significant attention for their distinctive electrochemical sensing capabilities of various analytes, due to their outstanding electrocatalytic performance, compatibility, and electrical conductance (Sedhu et al., 2023). Electropolymerization of glycine offers several advantages, such as affordability, increased electroactive surface area, selectivity, remarkable sensitivity, and stability. Poly(glycine) has been extensively explored in electrochemical detection applications. For instance, Matijašević et al. (2023) developed a simple voltammetric sensor using a poly(glycine)-modified GCE to detect ibuprofen in pharmaceutical formulations. Sedhu et al. (2023) fabricated a voltammetric sensing platform by modifying a platinum electrode (PGE) with poly(glycine) to quantify riboflavin in pharmaceuticals and food products. İslamoğlu et al. (2023) introduced a poly (glycine)-coated GCE to detect paracetamol in antipyretic baby syrup. Bhimaraya et al. (2023) introduced a rapid analytical tool that utilizes a poly(glycine)-layered carbon paste electrode (CPE) for detecting levofloxacin in medical samples.

Several analytical techniques, such as spectrophotometry (Rasheed, 2023), LC-ESI MS/MS (Islam et al., 2023), chromatographic methods (Elmansi et al., 2023), fluorescence (Qi et al., 2023), chemiluminescence (Shishavan and Amjadi, 2021), and UPLC-MS/MS (Stancil et al., 2018), have been employed for determining MTZ in various matrices. Despite their sensitivity and selectivity, these methods are encumbered by complex operational procedures, time-consuming sample preparation, extended analysis times, high equipment costs, and the necessity for skilled operators (Adane et al., 2023b; Maheshwaran et al., 2023). In contrast, voltammetric techniques offer cost-effectiveness, rapidity, user-friendliness, high specificity, sensitivity, portability, and the potential for miniaturization (Adane et al., 2023a). As a result, electrochemical methods were chosen to determine MTZ residues in food samples in this study. Among these, square wave voltammetry (SWV) was selected for its numerous advantages, including ultra-fast analysis, minimal sample usage, background differentiation, and heightened specificity (Williams et al., 2021).

Accurate and efficient electrochemical sensors are essential for detecting antibiotic residues in various matrices due to the significant threat they pose to human health. Various electrochemical sensors have been documented for the detection of MTZ in different matrices, such as GR/Fe_3O_4NPs/GCE (Zokhtareh et al., 2023), CNF–NiCo-LDH-GCE (Vilian et al., 2020), *f*-Co/*r*-GO/GCE (Huang et al., 2023), and $CeVO_4$/GCE (Radha and Wang, 2023). Despite their innovative features, they often exhibit some limitations such as higher detection limits and narrow linear ranges. Herein, we introduce a groundbreaking electrochemical sensor that demonstrates exceptional performance and represents a significant advancement in this field. The sensor was developed by integrating TA-Au-Ag-ANpM with *r*-GO and poly(glycine) nanocomposites to detect MTZ residues in pork meat, chicken meat, and milk powder samples. TA-Au-Ag-ANpM/*r*-GO/poly(glycine)/GCE was thoroughly characterized using analytical methods such as UV–Vis, FT-IR, XRD, SEM, and EDX, as well as electrochemical techniques including EIS, CV, and SWV. The sensor demonstrated remarkable capability in detecting MTZ across a wide concentration range, down to the picomolar level. The combination of the distinct characteristics of the individual nanocomposite modifiers within the sensor resulted in a synergistic effect, enhancing sensitivity, selectivity, and stability. This was demonstrated by the improved and well-defined current responses to the ultra-trace analyte concentrations. Furthermore, the sensor exhibited outstanding reproducibility, repeatability, and selectivity. Finally, it was effectively used to quantify MTZ residues in food samples, showing good recoveries and relative standard deviation (RSD) values below 5%.

2. Experimental

The chemicals, reagents, apparatus, and instruments used in this research, as well as the rationale behind material choice and the detailed sample preparation procedures, are described in the Supplementary Material.

2.1. Preparation of r-GO

$NaBH_4$, a potent hydride donor, readily reduces the oxygen functional groups in GO. The $NaBH_4$-mediated reduction process induces conjugation within the graphene lattice, leading to the formation of *r*-GO (Khan and Shaida, 2023). The reduction of GO suspension with $NaBH_4$ was performed as follows: first, 1 g of GO was solubilized in 100 mL of deionized water. Subsequently, 0.5 g of $NaBH_4$ was added to the solution and stirred at room temperature for 30 min. After the stirring step, the solution was filtered to remove any remaining unreduced GO residues. Finally, the resulting *r*-GO was subjected to multiple rinses with distilled water and dried under vacuum. This method facilitates the conversion of GO into *r*-GO and potentially enhances its electrical and mechanical properties for electrochemical applications.

2.2. Synthesis of TA-Au-Ag-ANpM

The TA-Ag-NpM was synthesized as follows. Initially, 0.1 M solutions of $AgNO_3$ and CTAB were mixed in a 1:1 vol ratio, serving as the precursor solution for stabilizing the nanoporous matrices. Subsequently, for the controlled development of nanoporous structures in the following reduction steps, the pH was regulated within the range of 10–11 by adding 0.1 M NaOH. The reduction of silver ions to form Ag nanoporous structures was initiated by gradually adding $NaBH_4$ (0.1 M, 10 mL). Heating the mixture for 7 h at 120 °C in an oil bath promoted the interaction of $AgNO_3$ and facilitated the formation of a stable Ag nanoporous matrix. The solution was cooled, centrifuged, and thoroughly washed with ethanol to obtain the desired nanoporous Ag matrix. A crucial step in the synthesis involved controlled thermal treatment in an oven for 2 h at 175 °C. The annealing process plays a pivotal role in consolidating the nanoporous Ag structure, leading to enhanced stability and improved properties. The synthesized TA-Ag-NpM was stored as a colloidal suspension by dispersing it in distilled water.

The TA-Au-Ag-ANpM was synthesized using the galvanic replacement reaction method (Yu et al., 2017). During this process, TA-Ag-NpM was collected by centrifugation from a colloidal suspension, and then re-dispersed in distilled water. The obtained dispersion was mixed with 6 mL 0.15 M PVP in a 100 mL flask and placed in an oil bath at 90 °C with continuous stirring. Subsequently, 4 mL of 0.001 M $HAuCl_4$ was gradually introduced at a rate of 3 mL/h. Lastly, the resulting TA-Au-Ag-ANpM was subjected to centrifugation, washing, and re-dispersion in 96% C_2H_5OH for subsequent experiments.

2.3. Preparation of TA-Au-Ag-ANpM/r-GO/GCE

Before modification, the GCE was polished using 0.3 and 0.05 μm alumina slurries, rinsed with distilled water, sonicated in ethanol/water (1:1), and activated voltammetrically in 0.1 M H_2SO_4 through ten-cycle

potential scans ranging from −0.4 to 1.2 V (100 mVs^{-1}, scan rate). To fabricate the TA-Au-Ag-ANpM/*r*-GO nanocomposite, 4 mL of the TA-Au-Ag-ANpM dispersion was mixed with 2 mL of *r*-GO dispersion and stirred vigorously at ambient temperature for 30 min. This ensured a complete integration of TA-Au-Ag-ANpM into the *r*-GO surface. Then after, the mixture was heated at 30 °C for 25 min in a water bath. The resulting TA-Au-Ag-ANpM/*r*-GO composite was subjected to ultrasonication, centrifugation, and repeated washing. The dried nanocomposite was then dispersed in deionized water through ultrasonication for 15 min, resulting in a 10 mL dispersion for subsequent use.

To prepare the TA-Au-Ag-ANpM/*r*-GO/GCE, 10 μL of the TA-Au-Ag-ANpM/*r*-GO dispersion was drop-casted onto the activated GCE and dried at room temperature. Similar procedures were applied to fabricate the other modified electrodes.

2.4. Preparation of TA-Au-Ag-ANpM/r-GO/poly(glycine)/GCE

To fabricate the intended electrode, cyclic voltammetry was conducted for 14 cycles in pH 4.0 ABS (0.1 M) containing 0.04 M glycine in the potential range of −1.7 V–1.6 V at a scan rate of 25 mVs^{-1} for the electro-polymerization of glycine at the surface of TA-Au-Ag-ANpM/*r*-GO/GCE (Fig. S1A). Subsequently, the fabricated sensor (TA-Au-Ag-ANpM/*r*-GO/poly(glycine)/GCE) was prepared for further applications by rinsing it with distilled water.

3. Results and discussion

3.1. Analytical characterization

The UV–Vis spectrum of TA-Ag-NpM exhibited a sharp absorption peak at λ_{max} = 401 nm, which is indicative of the localized surface plasmon resonance characteristics of the Ag particles (Fig. 1A(a)). The sharpness of the peak indicates that the nanoparticles are well-dispersed and uniformly sized. The average size of TA-Ag-NpM particles was calculated to be approximately 38 nm. TA-Au-Ag-ANpM displayed a distinct broad peak at λ_{max} = 416 nm, suggesting that the incorporation of Au into the alloy decreased the size to 25 nm and shifted the absorption peak to a longer wavelength (Fig. 1A(b)). The observed variations in the two spectra arise from changes in the composition and dimensions of the annealed nanoporous matrices, which affect their

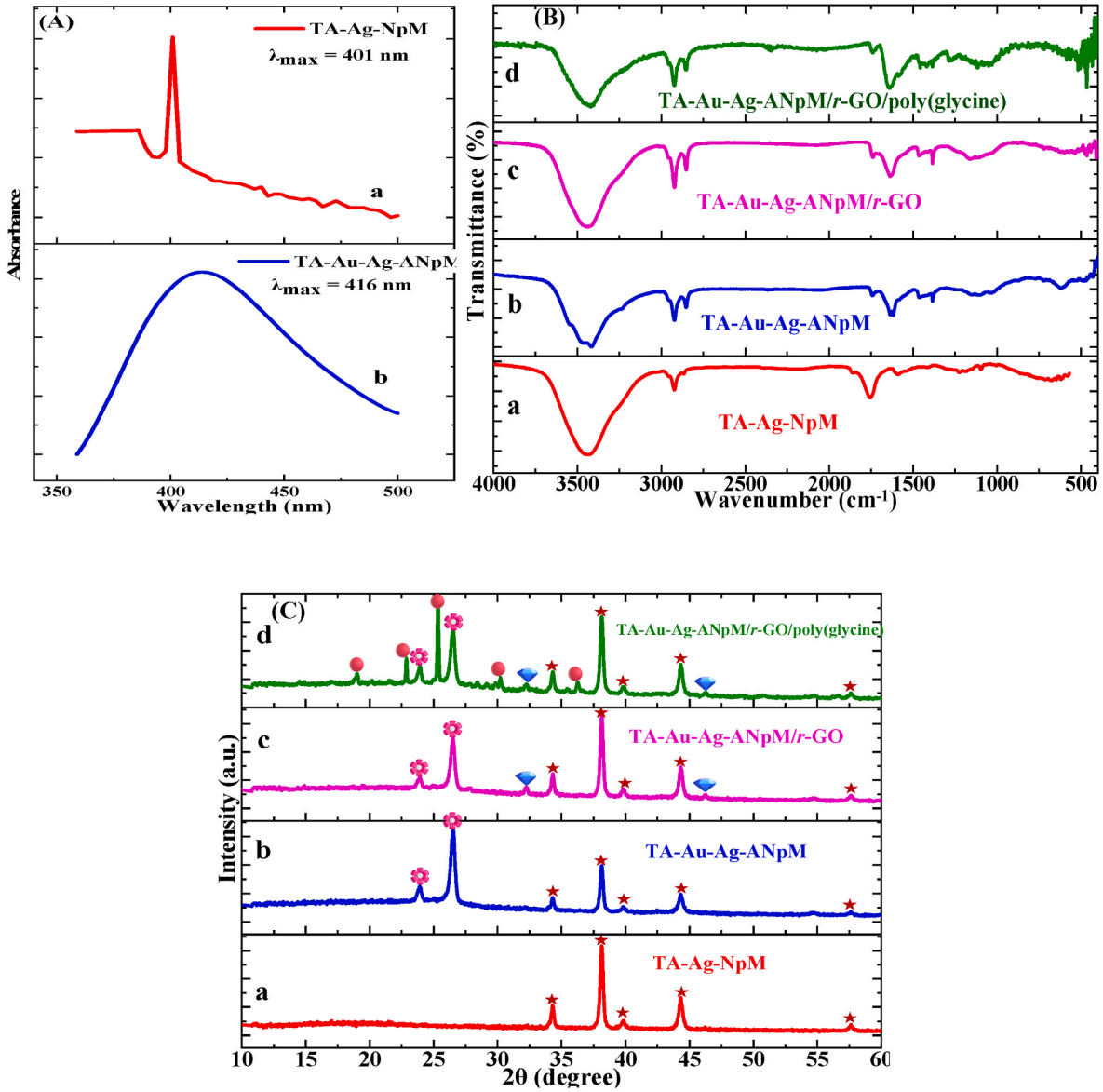

Fig. 1. (A) UV–Vis spectra of TA-Ag-NpM (a), TA-Au-Ag-ANpM (b), (B) FT-IR spectra and (C) XRD patterns of TA-Ag-NpM (a), TA-Au-Ag-ANpM (b), TA-Au-Ag-ANpM/*r*-GO (c), and TA-Au-Ag-ANpM/*r*-GO/poly(glycine) (d).

optical characteristics. As surface area directly influences catalytic activity, the alloyed nanoporous matrix with the smallest particle size and largest surface area exhibited superior catalytic performance in preparing the intended sensor.

The FT-IR spectrum of TA-Ag-NpM (Fig. 1B(a)) showed a reduced intensity of the Ag–O stretching vibration at 572 cm^{-1}, suggesting partial breaking of the Ag–O bonds during annealing. Likewise, the reduced stretching vibrations of C–O and C=O suggest the reorganization of oxygen-related functional groups on the nanoporous surface. The peak at 1754 cm^{-1} indicates the introduction of COOH groups onto the TA-Ag-NpM surface. FT-IR analysis of TA-Au-Ag-ANpM (Fig. 1B(b)) reveals a characteristic peaks associated with the Au and Ag nanoporous matrices. Confirmatory stretching signals included Au–O at 540 cm^{-1} and Au–Ag at 860 cm^{-1}, confirming alloying of Au and Ag. Silver-related stretching vibrations, such as Ag–O at 568 cm^{-1}, C–O at 1078 cm^{-1}, and C–H at 2856 and 2929 cm^{-1}, suggest the presence of silver atoms that stabilize alkyl chains. The peaks at 1629 cm^{-1} and 3459 cm^{-1} indicate the presence of C=O and O–H groups on the nanoporous structure. The FT-IR analysis of TA-Au-Ag-ANpM/*r*-GO (Fig. 1B(c)) demonstrates the integration of *r*-GO into nanoporous matrices. The characteristic peaks of *r*-GO, C=C (1612 cm^{-1}), and the aromatic ring stretching vibration at 1553 cm^{-1} confirm their incorporation into the electrode. The FTIR spectra of TA-Au-Ag-ANpM/*r*-GO and TA-Au-Ag-ANpM/*r*-GO/poly (glycine) (Fig. 1B(d)) are similar, with a few distinct peaks setting them apart. The presence of amide I (1736 cm^{-1}), amide II (1578 cm^{-1}), C–N (1289 cm^{-1}), and N–O (1120 cm^{-1}) vibrations in the spectra of TA-Au-Ag-ANpM/*r*-GO/poly(glycine) unequivocally differentiates it from TA-Au-Ag-ANpM/*r*-GO. These peaks strongly confirm the successful incorporation of poly(glycine) into the nanoporous matrix.

X-ray diffraction (XRD) analysis was conducted to investigate the dimensions and crystal structure of the nanoporous matrices. Consistent results obtained from UV–Vis and XRD measurements of the nanoporous matrix size validated the structural features determined using these techniques. The consistency of the results enhances the reliability and validity of the findings, enabling a comprehensive understanding of the material. The XRD diffraction peaks of TA-Ag-NpM at $2\theta = 34.3°$, 38.1°, 39.9°, 44.2°, and 57.68° (Fig. 1C(a)) were indexed to the (100), (111), (200), (220), and (311) planes, respectively, and are characteristic of face-centered cubic (FCC) structured Ag metal crystals (JCPDS PDF card number 04–0783), consistent with previous reports (Al-Ansari et al., 2019). The distinctive XRD peak observed at 26.54° (Fig. 1C(b)) corresponds to the (111) crystal plane in TA-Au-Ag-ANpM, suggesting the formation of a potential intermetallic alloy. The amorphous structure of the nanoporous matrix was further confirmed by the characteristic peak at 23.92°, which was assigned to the (100) plane (Zhao et al., 2023). The XRD peaks with diminished intensity at 32.2° and 46.46° (Fig. 1C(c)) correspond to the (002) and (111) planes of *r*-GO, respectively (Kumar et al., 2019), confirming the successful incorporation of *r*-GO into TA-Au-Ag-ANpM. The diffractogram of the TA-Au-Ag-ANpM/*r*-GO/poly (glycine) (Fig. 1C(d)) exhibited characteristic peaks of its constituent components, TA-Au-Ag-ANpM, *r*-GO, and poly(glycine), confirming the successful preparation of the sensor.

The SEM image of *r*-GO (Fig. 2a) provides valuable insight into its morphology. The multifunctional material exhibits a rough, irregular, and heterogeneous structure, as well as porosity, all of which contribute to its distinctive characteristics. As shown in the EDX spectra (Fig. S2 (d)), *r*-GO is mainly composed of C (77.6%) and O (22.4%), indicating its high degree of purity. The SEM analysis of TA-Ag-NpM revealed a porous crystalline structure with agglomerated silver matrices that were baked and had irregular shapes (Fig. 2b). These matrices are non-uniformly distributed and possess rough surfaces, which enhance the conductivity and overall performance of TA-Ag-NpM. The average size of TA-Ag-NpM was found to be 36–41 nm, which is consistent with UV–Vis and XRD measurements. The SEM analysis of TA-Au-Ag-ANpM (Fig. 2c) reveals a more or less uniform size distribution ranging from 21 to 26 nm. TA-Au-Ag-ANpM, similar to TA-Ag-NpM, has a porous structure with rough and irregular crystalline surfaces. The EDX spectra of TA-Ag-NpM (Fig. S2(e)) show the presence of C (43.18%), O (4.8%),

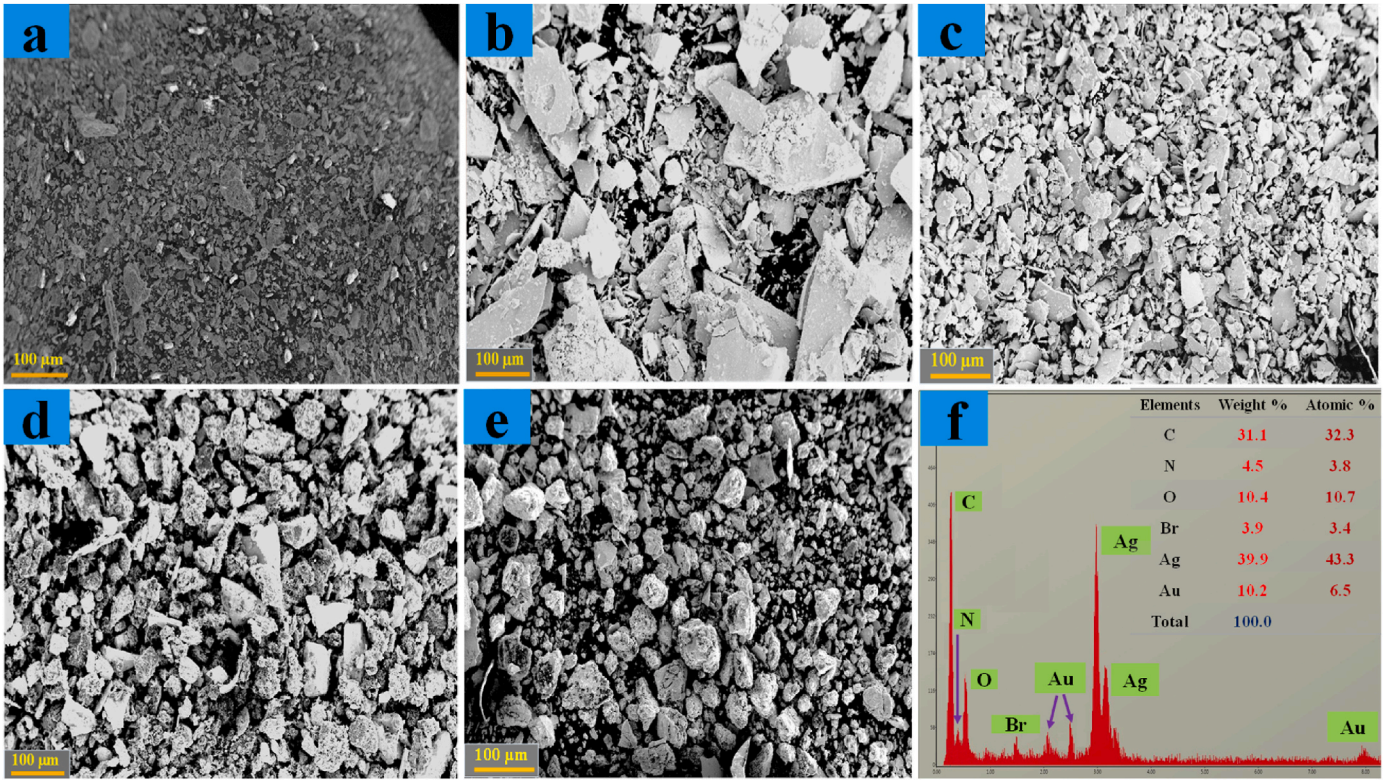

Fig. 2. SEM images of *r*-GO (a), TA-Ag-NpM (b), TA-Au-Ag-ANpM (c), TA-Au-Ag-ANpM/*r*-GO (d), and TA-Au-Ag-ANpM/*r*-GO/poly(glycine) (e), and EDX spectra of TA-Au-Ag-ANpM/*r*-GO/poly(glycine) (f).

Br (4.05%), and Ag (47.97%); those of TA-Au-Ag-ANpM (Fig. S2(f)) contain C (38.70%), O (4.30%), Br (3.63%), Ag (42.99%), and Au (10.38%), indicating that gold has been successfully incorporated into TA-Ag-NpM. TA-Au-Ag-ANpM particles were evenly dispersed within the *r*-GO, resulting in crystalline nanoporous matrices with irregular shapes, uniform sizes, and noticeable cavities (Fig. 2d). This observation clearly indicates that TA-Au-Ag-ANpM particles have been successfully incorporated into the *r*-GO structure. The elemental mapping of TA-Au-Ag-ANpM/*r*-GO (Fig. S2(i)) showed the presence of C (30.8%), O (7.7%), Br (3.6%), Ag (45.2%), and Au (12.7%). The SEM image in Fig. 2e depicts a well-executed coating of the TA-Au-Ag-ANpM/*r*-GO surface with a poly(glycine) film, resulting in a crystalline amorphous nanoporous matrix with a uniform arrangement. The corresponding EDX spectra in Fig. 2f show the presence of C (31.1%), N (4.5%), O (10.4%), Br (3.9%), Ag (39.9%), and Au (10.2%), confirming the successful preparation of the designed sensor.

3.2. Electrochemical characterization

EIS was conducted using a 5.0 mM $[Fe(CN)_6]^{3-/4-}$ redox probe in a 0.1 M KCl solution across frequencies ranging from 0.1 Hz to 100 kHz (inset Fig. 3A). Employing a Randles equivalent circuit model for data fitting, the Nyquist plot provides values for the charge transfer resistance (R_{ct}) and diffusion coefficient of reactants and products. These values are deduced from the semicircle diameter and the slope of the straight-line. A lower R_{ct} value indicates higher efficiency in the electrochemical reaction, as it signifies reduced impedance to electron transfer between the bulk solution and the reaction interface. The unmodified GCE exhibited a larger R_{ct} (4152 Ω) (Fig. 3A), due to its poor electrical conductivity. In contrast, the *r*-GO/poly(glycine)/GCE exhibited a significantly lower R_{ct} value (2746.5 Ω) compared to that of the unmodified GCE, owing to the admirable conductivity of the *r*-GO/poly(glycine) composite. At the TA-Au-Ag-ANpM/GCE surface, the value of R_{ct} was further reduced to 1624 Ω, highlighting the exceptional electrical conductivity and catalytic properties of TA-Au-Ag-ANpM. This demonstrates the outstanding ability to facilitate electron movement between the electrode and electrolyte. The semicircle diameter of TA-Au-Ag-ANpM/*r*-GO/GCE (R_{ct} = 596 Ω) was significantly decreased, compared to TA-Au-Ag-ANpM/poly(glycine)/GCE (R_{ct} = 1114.3 Ω). The semicircle diameter reached its minimum value at the surface of TA-Au-Ag-ANpM/*r*-GO/poly(glycine)/GCE (R_{ct} = 172.4 Ω), suggesting that the TA-Au-Ag-ANpM/*r*-GO/poly(glycine) nanocomposite significantly enhanced the electrical conductivity of the developed sensor.

To delve deeper into interfacial and electrical properties, CV was conducted on both the modified and unmodified electrodes at different stages in a 5.0 mM $[Fe(CN)_6]^{3-/4-}$ solution with 0.1 M KCl at a scan rate of 50 mVs^{-1}. The prominent redox peaks observed, spanning from −0.2 to +0.8 V across all electrodes, validate the reversible nature of the redox reaction of the probe. However, the bare GCE (Fig. 3B(a)) exhibited the lowest current and the highest ΔEp (186 mV), a consequence of its limited electrical conductivity. Modification of the bare electrode with *r*-GO/poly(glycine) nanocomposites increased the electrical conductivity of *r*-GO/poly(glycine)/GCE and decreased the ΔEp value to 135 mV (Fig. 3B(b)). Modification of the bare electrode with TA-Au-Ag-ANpM increased the redox current response of TA-Au-Ag-ANpM/GCE by further lowering the ΔEp value to 98 mV (Fig. 3B(c)), which suggests that TA-Au-Ag-ANpM has very good electrical conductivity and electron transfer ability. In the case of TA-Au-Ag-ANpM/poly(glycine)/GCE and TA-Au-Ag-ANpM/*r*-GO/GCE, the voltammogram exhibits a more symmetrical shape, accompanied by an increase in peak current response and a reduction in ΔEp values. This is attributed to the superior conductivity of the modified nanocomposites, resulting in a potential shift towards more negative values (Fig. 3B(d and f)). At the TA-Au-Ag-ANpM/*r*-GO/poly(glycine)/GCE (Fig. 3B(f)), the peak current response reached its maximum value with ΔEp decreasing to 55 mV, indicating that the modifiers synergistically improved the overall performance of the sensor; these results are consistent with the EIS findings.

Electroactive surface area measurement is a critical phenomenon in voltammetric reactions as it directly affects the catalytic efficiency and sensitivity of the sensor. CV was employed to determine the electroactive surface areas of the electrodes at various modification stages. The surface areas of the electrodes were determined by applying Equation (1) from Randles-Sevcik. (Adane et al., 2023a).

$$I_p = 2.69x10^5 n^{3/2} A D^{1/2} C v^{1/2} \quad (1)$$

where I_p = peak current, C = concentration of $[Fe(CN)_6]^{3-/4-}$ (mol cm^{-3}), v = scan rate (Vs^{-1}), D = diffusion coefficient (cm^2 s^{-1}), n = number of electrons (n = 1), and A = electrode surface area (cm^2). The electroactive areas of bare GCE, *r*-GO/poly(glycine)/GCE, TA-Au-Ag-ANpM/GCE, TA-Au-Ag-ANpM/poly(glycine)/GCE, TA-Au-Ag-ANpM/*r*-GO/GCE, and TA-Au-Ag-ANpM/*r*-GO/poly(glycine)/GCE were determined to be 0.038, 0.061, 0.089, 0.106, 0.127, and 0.154 cm^2, respectively. The electroactive area of TA-Au-Ag-ANpM/*r*-GO/poly(glycine)/GCE exceeded that of the bare GCE by four times and also the other electrodes. Furthermore, the electroactive surface area of the developed sensor exceeds that of several previously reported electrochemical sensors, including ZnCo/C800-Nafion/GCE (0.082 cm^2) (Baikeli et al., 2020), Fe_3O_4/N/C@MWCNTs-2-600/GCE (0.134 cm^2) (Yuan et al.,

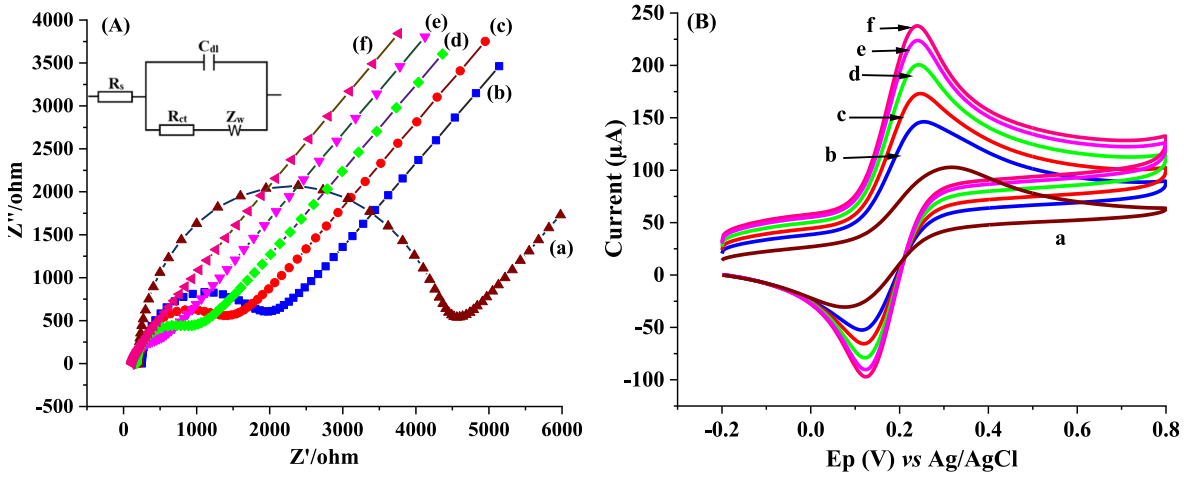

Fig. 3. Nyquist plots (A) and CVs (B) of bare GCE (a), *r*-GO/poly(glycine)/GCE (b), TA-Au-Ag-ANpM/GCE (c), TA-Au-Ag-ANpM/poly(glycine)/GCE (d), TA-Au-Ag-ANpM/*r*-GO/GCE (e), and TA-Au-Ag-ANpM/*r*-GO/poly(glycine)/GCE (f).

2019), ZnV MS/GCE (0.067 cm^2) (Kesavan and Chen, 2021), and Fe/NC-Nafion/GCE (0.091 cm^2) (Doulache et al., 2020). Overall, the results suggest a synergistic effect among TA-Au-Ag-ANpM, *r*-GO, and poly(glycine) nanocomposites, which enlarged the electroactive area and facilitated the electron transfer kinetics of the sensor.

3.3. Electrochemical behavior of MTZ

CV and SWV experiments were conducted to investigate the voltammetric properties of both modified and unmodified electrodes in a solution containing 15 μM MTZ in 0.1 M H_2SO_4 (pH 2) with a scan rate of 100 mVs^{-1}. Notably, the blank solution exhibited no distinct CV or SWV peaks, implying the absence of the analytes or their presence below detectable thresholds. However, modifying of the electrodes significantly enhanced the electrochemical signal of the analytes and shifted their peak potentials towards more negative values. The bare GCE shows a weak cathodic current response (Figs. S3A and B) during the reduction of MTZ, suggesting sluggish electron transfer kinetics and low electrical conductivity. Modifying the bare electrode with *r*-GO and poly(glycine) increases the surface area and conductivity, resulting in a substantial enhancement in current at the *r*-GO/poly(glycine)/GCE electrode. Furthermore, the TA-Au-Ag-ANpM/GCE demonstrates a higher response due to the unique porous structure of the annealed alloy matrices and its crystalline composition. The framework provides a high surface area-to-volume ratio and eliminates grain boundaries, thereby improving electrode conductivity (Sharma et al., 2017). The voltammetric reduction of the analyte resulted in a higher cathodic current response at the TA-Au-Ag-ANpM/*r*-GO/GCE compared to the TA-Au-Ag-ANpM/poly (glycine)/GCE. The results suggest that *r*-GO has superior electron transfer capabilities and higher conductivity than the poly(glycine). Moreover, the highest current response was achieved with the TA-Au-Ag-ANpM/*r*-GO/poly(glycine)/GCE configuration. This suggests that the synergistic effect of the nanocomposites enhances the sensitivity of the sensor to detect ultra-trace concentrations of the analyte, boosts the electroactive surface area, and facilitates efficient electron transfer.

3.4. Optimization of experimental conditions

The supplementary material provides a brief summary of the optimization process for the proposed sensor, detailing the number of electropolymerization cycles, the effect of supporting electrolyte solutions, the mixing ratio of nanocomposites, and the volume of drop-casting species.

3.4.1. Effect of pH

The pH of the supporting electrolyte is critical in electrochemical analysis as it influences various factors such as current response, electrode potentials, analyte mobility, electrode stability, and the shape of the voltammogram. Optimizing the pH of the supporting electrolyte solution is imperative to achieve precise and consistent electrochemical outcomes. As depicted in Fig. 4A, the effect of H_2SO_4 pH on the electrochemical response of 15 μM MTZ was investigated across a pH spectrum from 1.0 to 3.5 using SWV. The cathodic current of the analyte showed an increasing trend with the rising pH of H_2SO_4 up to 2.0, followed by a sharp decrease (Fig. 4B(a)). At lower pH values (pH 1.0 to 2.0), the acidic environment promotes the protonation of MTZ molecules, leading to the formation of protonated species. The protonation facilitates the reduction of MTZ, leading to an increase in the cathodic current. Beyond pH 2.0, however, the pronounced decrease in reduction current may be attributed to the deprotonation of the molecules. At higher pH values, the solution becomes more alkaline, leading to the deprotonation of the MTZ molecules and the generation of negatively charged species. These deprotonated species show weakened electrochemical activity and a lower tendency for reduction at the electrode surface. Consequently, the cathodic current experiences a sharp decline when the pH value exceeds 2.0. Therefore, a pH of 2.0 was selected as the optimal condition for the subsequent experiments. The peak potential of MTZ shifts towards less positive values with increasing pH, indicating the active involvement of protons in the electro-reduction of MTZ. A strong relationship between pH and the reduction potential of MTZ was observed, as described by the equation E_{pc} (V) = −0.22 – 0.05 pH (R^2 = 0.996) (Fig. 4B(b)). The slope value of 0.05 V/pH was close to the Nernstian theoretical value (0.059 V/pH), suggesting that the electrochemical reduction of MTZ involves the transfer of an equal number of electrons and protons, which is in good agreement with previous studies (Nikodimos and Amare, 2016).

3.4.2. Effect of scan rate

Electrochemical investigation was conducted using CV to investigate the effect of varying scan rates from 25 to 350 mVs^{-1} on the Ipc (μA) and Epc (V) of 15 μM MTZ. The absence of an anodic peak in the reverse scan and the shift of Epc (V) towards less positive values as the scan rate increased (Fig. S4A), suggest that the electro-reduction of the analyte at the TA-Au-Ag-ANpM/*r*-GO/poly(glycine)/GCE surface is an irreversible process. A linear correlation was observed between Ipc (μA) and the square root of the scan rate ($v^{1/2}$), expressed as Ipc (μA) = $-1.17v^{1/2}$ $(mVs^{-1})^{1/2}$ + 3.76 (R^2 = 0.990) (Fig. S4B). This result strongly indicates that the electrode process governing the reduction of the MTZ is predominantly diffusion-controlled. Furthermore, a linear relationship was established between log Ipc (μA) and log *v* (mVs^{-1}), given by the equation log Ipc (μA) = −0.51 log *v* (mVs^{-1}) + 0.53 (R^2 = 0.998) with a slope of 0.51 (Fig. S4C). The close proximity between the slope and the

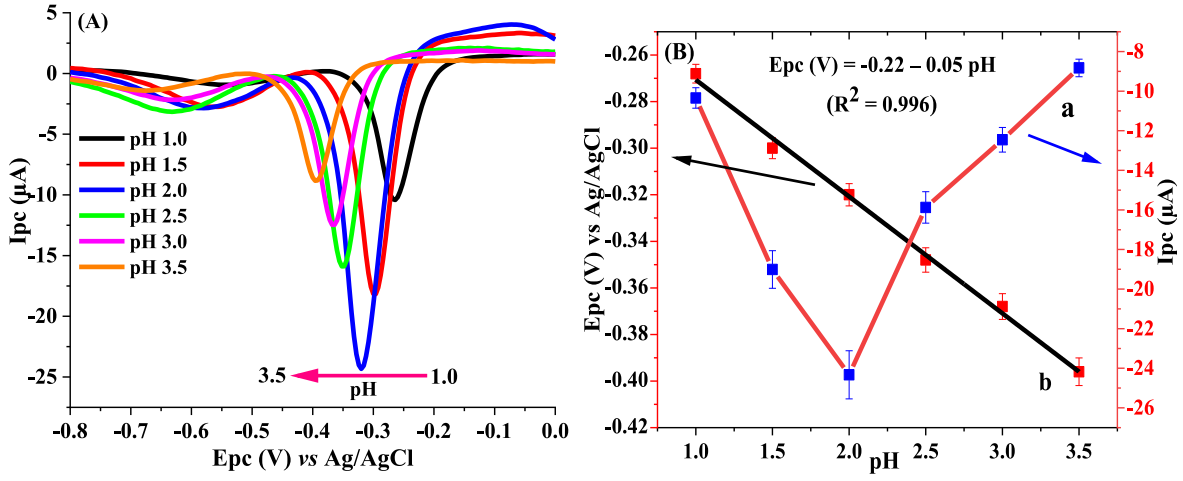

Fig. 4. (A) SWVs of 15 μM MTZ at different pH of 0.1 M H_2SO_4, (B) Ipc *vs.* pH (a) and Epc *vs.* pH (b).

theoretical value (0.5) further confirms the diffusion-controlled nature of the analyte electro-reduction at the TA-Au-Ag-ANpM/*r*-GO/poly (glycine)/GCE surface.

Laviron's theory provides a method to calculate the number of electrons involved in an irreversible reduction process using Equation (2) (Adane et al., 2023a).

$$E_p = E^0 + \frac{2.303RT}{\alpha nF}\log\frac{RTk^0}{\alpha nF} + \frac{2.303RT}{\alpha nF}\log \nu \quad (2)$$

where, E^0 = formal potential, ν = scan rate, T = temperature, F = Faraday constant, k^0 = heterogeneous rate constant, R = universal gas constant, and n = number of electrons. A strong correlation between Epc (V) and log ν (mVs^{-1}) was observed for the analyte. The slope of the plot, representing 2.303RT/αnF, was used to calculate αn, which yielded a value of 1.945. Typically, the transfer coefficient (α) for irreversible electrode reactions is assumed to be 0.5 (Adane et al., 2023b). Therefore, the number of electrons (n) involved in the electro-reduction of MTZ was determined to be 3.89 (≈4) (Scheme 1). This finding agrees with a previous investigation (Mao et al., 2017) that shows the voltammetric reduction of MTZ involves the transfer of four electrons and four protons.

3.5. Electrochemical determination of MTZ

This study aimed to introduce a novel ultra-sensitive electrochemical sensor for detecting MTZ residues in food samples. SWV was conducted under optimized experimental conditions within the potential range of −1.2 to 0.1 V in H_2SO_4 solution (0.1 M, pH 2.0). The cathodic current exhibited a linear increase with the analyte concentration (Fig. 5), indicating a strong correlation between Ipc (μA) and MTZ concentration in the range of 2.0 pM–410 μM. This relationship is described by the equation: Ipc (μA) = −0.98C (μM) – 1.55 (R^2 = 0.9994) (inset Fig. 5). The limits of detection (LOD) and quantification (LOQ) were determined to be 0.0312 pM and 0.104 pM, respectively. The remarkably low LOD and LOQ values of the sensor emphasize its exceptional ability to detect even trace amounts of MTZ residues in food samples. The exceptional performances observed in the sensor were mainly due to its nanocomposite compositions. TA-Au-Ag-ANpM nanoparticles offer a large electroactive area and catalytic activity, enhancing sensitivity and electron transfer kinetics. The *r*-GO enhances conductivity, stability, and surface area, facilitating effective charge transfer and analyte adsorption. Furthermore, poly(glycine) immobilizes the target analyte, enhancing selectivity and potentially reducing nonspecific adsorption and interference. Therefore, the extremely high sensitivity of the TA-Au-Ag-ANpM/*r*-GO/poly(glycine)/GCE positions it at the forefront of electroanalytical chemistry, making it a pioneering analytical device.

The comparison presented in Table 1 highlights the exceptional performance of the developed sensor, showing a significantly lower detection limit and a wider linear range compared to all the methods reported. This is attributed to its high electroactive surface area, excellent electrocatalytic activity, and improved electrical conductivity compared to previously reported values. These achievements are superior when compared with previously reported values, indicating a significant advancement in electrochemical sensor technology. Such advancements not only mark a major milestone in the field but also signify a substantial contribution to the broader scientific community. Overall, this comparative analysis highlights the transformative impact of our study and its potential to drive further innovations in electrochemical sensing.

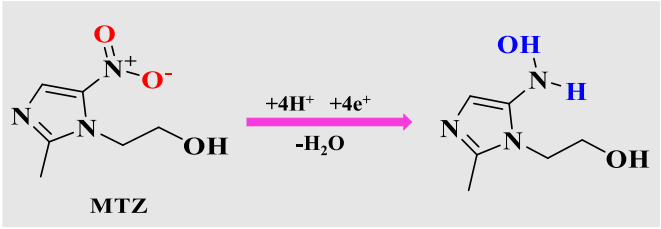

Scheme 1. Schematic illustration of the electro-reduction reaction of MTZ.

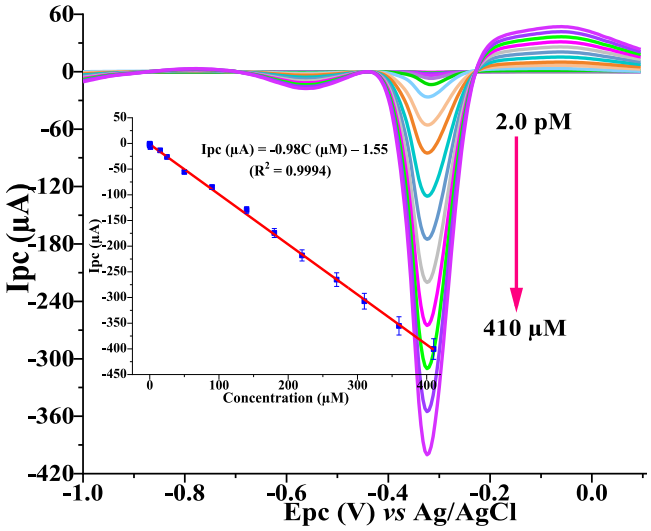

Fig. 5. SWVs of different concentrations of MTZ (Inset: Ipc *vs.* conc.).

Table 1
Comparison of the developed sensor to sensors in recent literature.

Sensors	Samples	Linear range (μM)	LOD (nM)	Ref.
f-Co/*r*-GO/GCE	Serum	25 pM–0.5	0.015	Huang et al. (2023)
GR/Fe_3O_4NPs/GCE	Aqueous samples	0.05–5 5–120	0.23	(Zokhtareh et al., 2023)
$CuCo_2O_4$/N-CNTs/MIP-GCE	Tablets, human serum and urine	0.005–0.1 0.1–100	0.48	(Wang et al., 2019)
GCE/Gr/Bi	Tap Water	0.005–260	0.9	Yu et al. (2023)
LFO/*r*GO/GCE	Human urine and milk	0.2–1221	48	(Pandiyan et al., 2023)
CNF–NiCo-LDH-GCE	Pharmaceuticals and urine	0.003–0.057	0.13	(Vilian et al., 2020)
Ag_2TiO_3/GCE	Urine and tablet	0.1–104.3	11	Vinothkumar et al. (2021)
$CeVO_4$/GCE	Environmental samples	0.02–75	4.5	(Radha and Wang, 2023)
TA-Au-Ag-ANpM/*r*-GO/poly (glycine)/GCE	Food samples	2.0 pM–410	0.0312 pM	This work

[a]pM = Picomolar.

3.6. Reproducibility, repeatability and stability

Reliable and consistent scientific results depend on crucial factors such as reproducibility, repeatability, and stability. To assess reproducibility, ten batches of TA-Au-Ag-ANpM/*r*-GO/poly(glycine)/GCE were fabricated using the same experimental procedure. SWV measurements, performed with a 15 μM MTZ solution containing 0.1 M H_2SO_4 under the optimized conditions, revealed remarkable reproducibility with RSD of 3.2% (Fig. S5A). Regarding repeatability, nine consecutive SWV measurements were conducted for 15 μM MTZ, resulting in a very low RSD of 2.43% (Fig. S5B), thereby demonstrating

the outstanding repeatability of the sensor. The stability of the sensor was thoroughly investigated over a span of two months by monitoring its current response to the analyte on a weekly basis (Fig. S5C). Despite weekly use and storage at 4 °C, the response of the sensor decreased by only 4.4% by the end of the eighth week, highlighting the long-term stability of TA-Au-Ag-ANpM/r-GO/poly(glycine)/GCE. In general, the developed sensor demonstrated exceptional reproducibility, repeatability, and long-term stability.

3.7. Selectivity

The anti-interference capability of TA-Au-Ag-ANpM/*r*-GO/poly (glycine)/GCE was assessed by detecting 15 μM MTZ in the presence of excess concentrations of commonly co-existing interferents. The cathodic currents for 15 μM MTZ remained unaffected in the presence of a 200-foldexcess concentration of antibiotics (cephalexin, erythromycin, azithromycin, tinidazole, ampicillin, amoxicillin, cloxacillin, chloramphenicol, and ciprofloxacin), a 600-fold excess of organic molecules (dopamine, glucose, ascorbic acid, fructose, folic acid, urea, sucrose, uric acid, and lactose), and an 850-fold excess of inorganic substances (Cu^{2+}, Fe^{3+}, HCO_3^-, NO_3^-, Ca^{2+}, Mg^{2+}, SO_4^{2-}, and CO_3^{2-}). Table S1 illustrates that the relative percentage error of the current response remained below 5% for all tested interferents. It confirms the remarkable selectivity of TA-Au-Ag-ANpM/*r*-GO/poly(glycine)/GCE in detecting MTZ in the presence of excess concentrations of co-existing interferents.

3.8. Analysis of real samples

The practical utility of TA-Au-Ag-ANpM/*r*-GO/poly(glycine)/GCE for real sample application was assessed through a spiking experiment to determine the residues of MTZ in milk powder, pork, and chicken meat samples. The percentage recoveries were determined by adding known concentrations of MTZ standards (0, 5, 15, 25, and 30 μM) to the food samples (Table S2). Before spiking the MTZ standards into the food samples, the initial current response of the food samples was recorded. Voltammetric currents were not observed in unspiked food samples, indicating that MTZ residues were either absent or below the detection limit. Afterwards, the percentage recoveries of the analyte in spiked food samples were determined. The recovery values of the three food samples were consistently high (96.9–101.4%), demonstrating the reliability of the method. The RSD values were found to be very low and comparable (1.55–2.89%), indicating the precision of the method. In addition, the validity of the developed method was investigated by analyzing MTZ tablets obtained from a local pharmacy, which were used as reference material. As shown in Table S3, the detected amounts by the developed sensor were largely comparable to the values labeled by the manufacturer. The results provide additional conformation for the accuracy and precision of the developed method. Furthermore, to assess the significance of the difference between the experimental results and the labeled amount, a statistical analysis (*t*-test) was conducted at a 95% confidence level. As shown in Table S4, the *t*-test statistical analysis result revealed no significant difference between the experimental results and the amount specified by the manufacturer, further confirming the effectiveness of the developed method. In general, the better recoveries, lower RSD values, and results of statistical analysis indicate that TA-Au-Ag-ANpM/r-GO/poly(glycine)/GCE is a highly effective and reliable device for detecting MTZ residues in practical applications.

4. Conclusion

In this study, a pioneering hypersensitive electrochemical sensor was developed for detecting hazardous residues of MTZ in food samples. The morphological, interfacial, and elemental composition of the proposed sensor were examined using an array of analytical and electrochemical techniques. The TA-Au-Ag-ANpM/*r*-GO/poly(glycine)/GCE sensor outperformed recently reported sensors in terms of lowest LOD and a wider linear range due to its outstanding characteristics: increased electroactive surface area, elevated electrocatalytic activity, and improved electrical conductivity. The sensor's response remained unaffected in the presence of numerous coexisting interferents, including organic, inorganic, and antibiotic species, demonstrating remarkably high selectivity and specificity. Furthermore, the sensor exhibited long-lasting stability, exceptional reproducibility, and repeatability. Therefore, TA-Au-Ag-ANpM/*r*-GO/poly(glycine)/GCE is an ideal candidate for real-time monitoring of hazardous residues of MTZ in food samples. In our upcoming research endeavors, we plan to delve into the detection of various antibiotics and environmental toxins, including hazardous heavy metals and micro-plastics. This expansion aims to enhance the utility and versatility of our sensor. Through these efforts, we aspire to make meaningful contributions to ongoing initiatives in food safety and environmental monitoring.

CRediT authorship contribution statement

Wondimeneh Dubale Adane: Writing – original draft, Validation, Software, Resources, Methodology, Investigation, Formal analysis, Data curation, Conceptualization. **Bhagwan Singh Chandravanshi:** Writing – review & editing, Supervision, Conceptualization. **Merid Tessema:** Writing – original draft, Supervision, Conceptualization.

Declaration of competing interest

The authors declare that they have no known competing financial interests or personal relationships that could have appeared to influence the work reported in this paper.

Data availability

No data was used for the research described in the article.

Acknowledgements

The authors gratefully acknowledge the Department of Chemistry, Addis Ababa University, Addis Ababa, Ethiopia for providing laboratory facilities.

Appendix A. Supplementary data

Supplementary data to this article can be found online at https://doi.org/10.1016/j.chemosphere.2024.142279.

References

Adane, W.D., Chandravanshi, B.S., Tessema, M., 2023a. Highly sensitive and selective electrochemical sensor for the simultaneous determination of tinidazole and chloramphenicol in food samples (egg, honey and milk). Sensor. Actuator. B Chem. 390, 134023 https://doi.org/10.1016/j.snb.2023.134023.

Adane, W.D., Chandravanshi, B.S., Tessema, M., 2023b. A simple, ultrasensitive and cost-effective electrochemical sensor for the determination of ciprofloxacin in various types of samples. Sens. Bio-Sens. Res. 39, 100547 https://doi.org/10.1016/j.sbsr.2022.100547.

Al-Ansari, M., Alkubaisi, N., Gopinath, K., Karthika, V., Arumugam, A., Govindarajan, M., 2019. Facile and cost-effective Ag nanoparticles fabricated by lilium lancifolium leaf extract: antibacterial and antibiofilm potential. J. Cluster Sci. 30 (4), 1081–1089. https://doi.org/10.1007/s10876-019-01569-w.

Baikeli, Y., Mamat, X., Wumaer, M., Muhetaer, M., Aisa, H.A., Hu, G., 2020. Electrochemical determination of metronidazole using a glassy carbon electrode modified with nanoporous bimetallic carbon derived from a ZnCo-based metal-organic framework. J. Electrochem. Soc. 167 (11), 116513 https://doi.org/10.1149/1945-7111/ab9d94.

Bhimaraya, K., Manjunatha, J.G., Moulya, K.P., Tighezza, A.M., Albaqami, M.D., Sillanpää, M., 2023. Detection of levofloxacin using a simple and green electrochemically polymerized glycine layered carbon paste electrode. Chemosensors 11 (3), 191. https://doi.org/10.3390/chemosensors11030191.

Chai, X., Li, Y., Ma, C., Guo, M., Fan, Z., Zhao, J., Cheng, B., 2023. A voltammetric sensor based on a reduced graphene oxide/β-cyclodextrin/silver nanoparticle/

polyoxometalate nanocomposite for detecting uric acid and tyrosine. Anal. Methods 15 (20), 2528–2535. https://doi.org/10.1039/D3AY00207A.
Dadgostar, P., 2019. Antimicrobial resistance: implications and costs. Infect. Drug Resist. 12, 3903–3910. https://doi.org/10.2147/IDR.S234610.
Doulache, M., Bakirhan, N.K., Saidat, B., Ozkan, S.A., 2020. Highly sensitive and selective electrochemical sensor based on polyglycine modified glassy carbon electrode for simultaneous determination of amlodipine and ramipril from biological samples. J. Electrochem. Soc. 167 (2), 027511 https://doi.org/10.1149/1945-7111/ab68cd.
Duan, D., Ding, Y., Li, L., Ma, G., 2020. Rapid quantitative detection of melatonin by electrochemical sensor based on carbon nanofibers embedded with FeCo alloy nanoparticles. J. Electroanal. Chem. 873, 114422 https://doi.org/10.1016/j.jelechem.2020.114422.
Elmansi, H., El-Awady, M.I., Barghash, S., El-Razeq, S.A., Belal, F., 2023. Green versatile micellar electrokinetic chromatographic method for determination of six antimicrobial and anti-inflammatory drugs in combined dosage forms. Acta Chromatogr. 35 (3), 233–246. https://doi.org/10.1556/1326.2022.01057.
Huang, J., Qiu, Z., Lin, J., Lin, J., Zhu, F., Lai, G., Li, Y., 2023. Ultrasensitive determination of metronidazole using flower-like cobalt anchored on reduced graphene oxide nanocomposite electrochemical sensor. Microchem. J. 188, 108444 https://doi.org/10.1016/j.microc.2023.108444.
Islam, S.F., Kabir, MdH., Yasmin, S., Alam, M.J., Ahmed, S., Rahman, M.S., 2023. A modified QuEChERS method development to analyze tylosin and metronidazole antibiotics residue in shrimp (penaeus monodon) using LC-ESI MS/MS. Front. Sustain. Food Syst. 7, 1013319 https://doi.org/10.3389/fsufs.2023.1013319.
İslamoğlu, N., Mülazımoğlu, A.D., Mulazimoglu, I.E., 2023. Sensitive and selective determination of paracetamol in antipyretic children's syrup with polyglycine modified glassy carbon electrode. Anal. Methods 15, 4149–4158. https://doi.org/10.1039/D3AY00789H.
Kesavan, G., Chen, S.M., 2021. Sonochemical-assisted synthesis of zinc vanadate microstructure for electrochemical determination of metronidazole. J. Mater. Sci. Mater. Electron. 32 (7), 9377–9391. https://doi.org/10.1007/s10854-021-05601-6.
Khan, M.U., Shaida, M.A., 2023. Reduction mechanism of graphene oxide including various parameters affecting the C/O ratio. Mater. Today Commun. 36, 106577 https://doi.org/10.1016/j.mtcomm.2023.106577.
Kogularasu, S., Lee, Y.Y., Chang-Chien, G.P., Govindasamy, M., Sheu, J.K., 2023. Review-nanofibers: empowering electrochemical sensors for reliable detection of food and environmental toxins. J. Electrochem. Soc. 170 (7), 077514 https://doi.org/10.1149/1945-7111/ace8c2.
Kumar, A., Pal, D., 2018. Antibiotic resistance and wastewater: correlation, impact and critical human health challenges. J. Environ. Chem. Eng. 6, 52–58. https://doi.org/10.1016/j.jece.2017.11.059.
Kumar, A., Sadanandhan, A.M., Jain, S.L., 2019. Silver doped reduced graphene oxide as a promising plasmonic photocatalyst for oxidative coupling of benzylamines under visible light irradiation. New J. Chem. 43 (23), 9116–9122. https://doi.org/10.1039/C9NJ00852G.
Lan, Y., Bao, W., Liang, C., Li, G., Zhou, L., Yang, J., Wei, L., Su, Q., 2023. Synthesis of copper–nitrogen codoped carbon quantum dots using frangipani as a carbon source and application of metronidazole determination. Chem. Pap. 77 (2), 1005–1015. https://doi.org/10.1007/s11696-022-02487-4.
Larsson, D.G.J., Flach, C.F., 2022. Antibiotic resistance in the environment. Nat. Rev. Microbiol. 20, 257–269. https://doi.org/10.1038/s41579-021-00649-x.
Li, H., Zhao, H., He, H., Shi, L., Cai, X., Lan, M., 2018. Pt-Pd bimetallic nanocoral modified carbon fiber microelectrode as a sensitive hydrogen peroxide sensor for cellular detection. Sensor. Actuator. B Chem. 260, 174–182. https://doi.org/10.1016/j.snb.2017.12.179.
Maheshwaran, S., Kogularasu, S., Chen, S.M., Chen, W.H., Lee, Y.Y., Chang-Chien, G.P., 2023. Ultra-trace detection of sulfathiazole, an anti-infective agent and environmental contaminant, using electrochemical sensing with holmium vanadate-graphene oxide nanocomposites. J. Taiwan Inst. Chem. Eng. 153, 105233 https://doi.org/10.1016/j.jtice.2023.105233.
Majdinasab, M., Mishra, R.K., Tang, X., Marty, J.L., 2020. Detection of antibiotics in food: new achievements in the development of biosensors. TrAC, Trends Anal. Chem. 127, 115883 https://doi.org/10.1016/j.trac.2020.115883.
Manyi-Loh, C., Mamphweli, S., Meyer, E., Okoh, A., 2018. Antibiotic use in agriculture and its consequential resistance in environmental sources: potential public health implications. Molecules 23, 795. https://doi.org/10.3390/molecules23040795.
Mao, A., Li, H., Yu, L., Hu, X., 2017. Electrochemical sensor based on multi-walled carbon nanotubes and chitosan-nickel complex for sensitive determination of metronidazole. J. Electroanal. Chem. 799, 257–262. https://doi.org/10.1016/j.jelechem.2017.05.049.
Mao, Y.W., Zhang, J.K., Chen, D.N., Wang, A.J., Feng, J.J., 2022. Bimetallic PtFe alloyed nanoparticles decorated on 3D hollow N-doped carbon nanoflowers as efficient electrochemical biosensing interfaces for ultrasensitive detection of SCCA. Sensor. Actuator. B Chem. 370, 132416 https://doi.org/10.1016/j.snb.2022.132416.
Matijašević, I., Kulizić, M., Bacetić, L., Gavrilović, D., Baošić, R., Lolić, A., 2023. Polyglycine modified glassy carbon electrode for ibuprofen determination. ChemistrySelect 8 (24), e202300827. https://doi.org/10.1002/slct.202300827.
Mummoorthi, G., Arjunan, S., Selvaraj, M., Rokhum, S.L., Mani, N., Periyasamy, S., Rajendran, R., 2023. High-performance solid-state asymmetric supercapacitor based on α-Fe_2O_3/r-GO/GCN composite electrode material for energy storage application. Surface. Interfac. 41, 103166 https://doi.org/10.1016/j.surfin.2023.103166.
Nikodimos, Y., Amare, M., 2016. Electrochemical determination of metronidazole in tablet samples using carbon paste electrode. J. Anal. Chem. 2016, 1–7. https://doi.org/10.1155/2016/3612943.
Pandiyan, R., Vinothkumar, V., Chen, S.M., Sangili, A., Kim, T.H., 2023. Integrated $LaFeO_3$/rGO nanocomposite for the sensitive electrochemical detection of antibiotic drug metronidazole in urine and milk samples. Appl. Surf. Sci. 635, 157672 https://doi.org/10.1016/j.apsusc.2023.157672.
Qi, H., Qiu, L., Zhang, X., Yi, T., Jing, J., Sami, R., Alanazi, S.F., Alqahtani, Z., Aljabri, M. D., Rahman, M.M., 2023. Novel N-doped carbon dots derived from citric acid and urea: fluorescent sensing for determination of metronidazole and cytotoxicity studies. RSC Adv. 13 (4), 2663–2671. https://doi.org/10.1039/D2RA07150A.
Radha, A., Wang, S.F., 2023. Insight into lanthanides $REVO_4$ (RE= Ce, Pr, Nd): a comparative study on re-site variants in electrochemical detection of metronidazole in environmental samples. Environ. Sci.: Nano 10, 3122–3135. https://doi.org/10.1039/D3EN00384A.
Rasheed, Q.N., 2023. Direct and indirect spectrophotometric methods for determination of metronidazole in pharmaceutical formulations. Egypt. J. Chem. 66 (2), 73–78. https://doi.org/10.21608/ejchem.2022.128576.5693.
Sangkaew, P., Ngamaroonchote, A., Sanguansap, Y., Karn-orachai, K., 2022. Emerging electrochemical sensor based on bimetallic AuPt NPs for on-site detection of hydrogen peroxide adulteration in raw cow milk. Electrocatalysis 13 (6), 794–806. https://doi.org/10.1007/s12678-022-00763-1.
Sedhu, N., Kumar, J.J., Sivaguru, P., Raj, V., 2023. Electrochemical detection of riboflavin in pharmaceutical and food samples using in situ electropolymerized glycine coated pencil graphite electrode. J. Electroanal. Chem. 928, 117037 https://doi.org/10.1016/j.jelechem.2022.117037.
Sharma, S., Prakash, V., Mehta, S.K., 2017. Graphene/silver nanocomposites-potential electron mediators for proliferation in electrochemical sensing and SERS activity. TrAC, Trends Anal. Chem. 86, 155–171. https://doi.org/10.1016/j.trac.2016.10.004.
Shishavan, Y.H., Amjadi, M., 2021. A new enhanced chemiluminescence reaction based on polymer dots for the determination of metronidazole. Spectrochim. Acta Mol. Biomol. Spectrosc. 260, 119992 https://doi.org/10.1016/j.saa.2021.119992.
Stancil, S.L., Van Haandel, L., Abdel-Rahman, S., Pearce, R.E., 2018. Development of a UPLC-MS/MS method for quantitation of metronidazole and 2-hydroxy metronidazole in human plasma and its application to a pharmacokinetic study. J. Chromatogr. B 1092, 272–278. https://doi.org/10.1016/j.jchromb.2018.06.024.
Swathy, S., Pallam, G.S., Kumar, K.G., 2023. Tryptophan capped gold–silver bimetallic nanoclusters-based turn-off fluorescence sensor for the determination of histamine. Talanta 256, 124321. https://doi.org/10.1016/j.talanta.2023.124321.
Vatovec, C., Kolodinsky, J., Callas, P., Hart, C., Gallagher, K., 2021. Pharmaceutical pollution sources and solutions: survey of human and veterinary medication purchasing, use, and disposal. J. Environ. Manag. 285, 112106 https://doi.org/10.1016/j.jenvman.2021.112106.
Vilian, A.T.E., Ranjith, K.S., Lee, S.J., Umapathi, R., Hwang, S.K., Oh, C.W., Huh, Y.S., Han, Y.K., 2020. Hierarchical dense Ni-Co layered double hydroxide supported carbon nanofibers for the electrochemical determination of metronidazole in biological samples. Electrochim. Acta 354, 136723. https://doi.org/10.1016/j.electacta.2020.136723.
Vinothkumar, V., Abinaya, M., Chen, S.M., Sethupathi, V., Muthuraj, V., 2021. Ultrasound assisted synthesis of silver titanate for the differential pulse voltammetric determination of antibiotic drug metronidazole. Phys. E: Low-Dimens, Syst. Nanostructures. 134, 114865 https://doi.org/10.1016/j.physe.2021.114865.
Wang, T., Zhang, L., Zhang, C., Deng, D., Wang, D., Luo, L., 2023. Simultaneous determination of xanthine and hypoxanthine using polyglycine/rGO-modified glassy carbon electrode. Molecules 28 (3), 1458. https://doi.org/10.3390/molecules28031458.
Wang, X., Xie, Y., Lin, L., 2022. Recent development of microfluidic biosensors for the analysis of antibiotic residues. TrAC, Trends Anal. Chem. 157, 116797 https://doi.org/10.1016/j.trac.2022.116797.
Wang, Y., Yao, L., Liu, X., Cheng, J., Liu, W., Liu, T., Sun, M., Zhao, L., Ding, F., Lu, Z., Zou, P., Wang, X., Zhao, Q., Rao, H., 2019. $CuCo_2O_4$/N-doped CNTs loaded with molecularly imprinted polymer for electrochemical sensor: preparation, characterization and detection of metronidazole. Biosens. Bioelectron. 142, 111483 https://doi.org/10.1016/j.bios.2019.111483.
Williams, T., Shum, R., Rappleye, D., 2021. Review-concentration measurements in molten chloride salts using electrochemical methods. J. Electrochem. Soc. 168 (12), 123510 https://doi.org/10.1149/1945-7111/ac436a.
Yu, K., Sun, X., Pan, L., Liu, T., Liu, A., Chen, G., Huang, Y., 2017. Hollow Au–Ag alloy nanorices and their optical properties. Nanomaterials 7 (9), 255. https://doi.org/10.3390/nano7090255.
Yu, T., Glennon, L., Fenelon, O., Breslin, C.B., 2023. Electrodeposition of bismuth at a graphene modified carbon electrode and its application as an easily regenerated sensor for the electrochemical determination of the antimicrobial drug metronidazole. Talanta 251, 123758. https://doi.org/10.1016/j.talanta.2022.123758.
Yuan, S., Bo, X., Guo, L., 2019. In-situ insertion of multi-walled carbon nanotubes in the Fe_3O_4/N/C composite derived from iron-based metal-organic frameworks as a catalyst for effective sensing acetaminophen and metronidazole. Talanta 193, 100–109. https://doi.org/10.1016/j.talanta.2018.09.065.
Zhao, H., Guo, M., Li, F., Zhou, Y., Zhu, G., Liu, Y., Ran, Q., Nie, F., Dubovyk, V., 2023. Fabrication of gallic acid electrochemical sensor based on interconnected super-P carbon black@mesoporous silica nanocomposite modified glassy carbon electrode. JMR&T 24, 2100–2112. https://doi.org/10.1016/j.jmrt.2023.03.129.
Zokhtareh, R., Rahimnejad, M., Najafpour-Darzi, G., Karimi-Maleh, H., 2023. A novel sensing platform for electrochemical detection of metronidazole antibiotic based on green-synthesized magnetic Fe_3O_4 nanoparticles. Environ. Res. 216, 114643 https://doi.org/10.1016/j.envres.2022.114643.

Supplementary Material

A novel electrochemical sensor for the detection of metronidazole residues in food samples

Wondimeneh Dubale Adane[a], Bhagwan Singh Chandravanshi*[a], Merid Tessema**[a]

[a] Department of Chemistry, Addis Ababa University, P. O. Box 1176, Addis Ababa, Ethiopia

*Corresponding author. E-mail address: bscv2006@yahoo.com

**Corresponding author. E-mail address: tessemamerid@yahoo.com

Experimental

Chemical and reagents

All chemicals and reagents used in this experiment were of analytical grade and used without further purification. Graphite oxide (GO) was obtained from Nanjing Xianfeng Nano Co. (Nanjing, China). Tetrachloroauric acid ($HAuCl_4$), silver nitrate ($AgNO_3$), sodium borohydride ($NaBH_4$), and sodium citrate ($Na_3C_6H_5O_7$) were purchased from Shanghai Sinopharm Chemical Reagent Co., Ltd. (China). Nitric acid (HNO_3), and sulfuric acid (H_2SO_4) were bought from Merck Chemicals, Germany. Glycine was obtained from Labtech Chemicals, India. Potassium hexacyanoferrate (III) (99%) was purchased from BDH Chemicals Ltd., England. Polyethylene glycol 600 (PEG 600, MW ≈ 570–630) was obtained from Chengdu Kelong Chemical Reagent Factory (Chengdu, China). Polyvinyl pyrrolidone (PVP, K15, MW ≈ 40,000) was obtained from Research Lab Fine Chem Industries (Mumbai, India). All other chemicals and antibiotic standards were purchased from Sigma-Aldrich, USA. Glassware was washed with aqua regia ($HCl:HNO_3$ in a 3:1 ratio by volume) and rinsed with deionized water before the experiments. All aqueous solutions were prepared with Milli-Q water (18.2MΩ cm), which was obtained from a Millipore water purification system. Metronidazole capsules (Metroleb-250) (Lenen Laboratories PVT. LTD., India) were purchased from a local pharmacy in Addis Ababa, Ethiopia.

85.58 mg of metronidazole standard was dissolved in 50 mL of distilled water to produce a 0.01 M stock solution. The stock solution was then diluted with 0.1 M H_2SO_4 (pH 2) to prepare working solutions for the analyte.

Apparatus and instruments

Electrochemical measurements were performed in 20 mL cells using a CHI 760D electrochemical analyzer (CH Instruments, USA). A conventional three-electrode system was used throughout the experiment, consisting of a working electrode (either the bare or modified GCE), a platinum wire counter electrode, and silver-silver chloride (Ag/AgCl (3M KCl)) reference electrode. The structural morphology was characterized using a scanning electron microscope (SEM, CX-200plus, Coxem, Korea), and the elemental analysis was performed using energy-dispersive X-ray spectroscopy (EDS). The X-ray diffraction (XRD) pattern of the nanocomposites was recorded using a BRUKER ECOD 8 advance diffractometer with Cu Kα radiation (wavelength $\lambda = 0.15406$ nm) at room temperature. Fourier transform infrared (FT-IR) spectra were recorded using a PerkinElmer Spectrum 100 FT-IR spectrometer (PerkinElmer, USA). UV-Vis spectra were recorded using a Lambda 950 UV-Vis spectrometer (PerkinElmer, USA). pH was measured using a Senses Ion + MM150 pH meter (China). Solid chemicals were weighed using an electronic digital balance (Model: Scientech ZSA 120, USA). A centrifuge (model 8001, China) and an ultrasonic cleaner (model YJ5120-B, China) were used during nanocomposite preparation. In addition, a magnetic stirrer and a vacuum pump were used throughout the experiments.

Sample preparation

Preparation of milk powder sample

Milk powder samples were purchased from a local supermarket in Addis Ababa, Ethiopia. Real samples for analysis were prepared as follows. First, milk powder (5.0 mg) was accurately weighed and mixed with 20 mL acetonitrile solution. After 15 min of sonication and 10 min of shaking, the mixture was centrifuged at 10,000 rpm for 10 min, and the supernatant was filtered through a 150 mm filter membrane. A portion of the filtrate solution was then transferred to a volumetric flask and diluted with 0.1 M PBS (pH 7) to a total volume of 25 mL. Finally, the diluted sample solutions were spiked with 0, 5, 15, 25, and 30 µM MTZ standard solutions in triplicates. After an incubation time of 45 min, the samples were analyzed without further treatment.

Preparation of pork and chicken meat samples

Pork and chicken meat samples were purchased from a local supermarket in Addis Ababa, Ethiopia. Each sample was thoroughly homogenized before extraction. To extract the target analyte, 5 g of the homogenized meat sample was mixed with 20 mL of a 0.1 M PBS (pH 5) solution. The meat sample and PBS solution were thoroughly mixed using a vortex mixer for 35 min to ensure complete dispersion of the sample in the solvent. Subsequently, the mixture was subjected to ultrasonic treatment for 45 min. This step aimed at facilitating the efficient extraction of the desired components from the meat matrix, thereby enhancing the quality and accuracy of the analysis. Then, the mixture was centrifuged at 4,000 rpm for 15 min. This centrifugation step was performed precisely to separate the constituents, and as a result, a clear solution containing the extracted analyte was collected. Afterwards, a portion of the filtrate solution was transferred to a volumetric flask and diluted with 0.1 M PBS (pH 5) to a total volume of 25 mL. Finally, the diluted solutions were spiked with 0, 5, 15, 25, and 30 µM MTZ standard solutions in triplicates. Following a one hour incubation period, the samples were analyzed without any additional treatment.

The rationale behind material choice

The choice of materials for fabricating the envisioned sensor was guided by careful consideration of the following pivotal factors:

1. The rationale behind choosing gold (Au) and silver (Ag) as electrode modifiers lies in their respective unique properties and surface chemistry, including excellent conductivity, chemical stability, surface reactivity, biocompatibility, and catalytic activity.
    a. Both gold (Au) and silver (Ag) demonstrate notable **chemical stability**, with Au known for its exceptional resilience in aqueous environments, ensuring sustained electrode integrity and performance under harsh conditions, while Ag exhibits excellent stability in various electrochemical settings, particularly in aqueous solutions, guaranteeing the enduring performance and reliability of silver-modified electrodes.
    b. Gold and silver are both **biocompatible materials**, with gold being well suited for use in electrochemical systems because of its compatibility and effectiveness in biomedical and

biosensing applications. On the other hand, silver is widely acknowledged as biocompatible and non-toxic material, making it an ideal choice for different electrochemical applications.

c. Both Au and Ag exhibit outstanding electrical **conductivity**, facilitating efficient electron transfer at the electrode interface, thereby enhancing the sensitivity and response of electrochemical sensors and detection systems.

d. Both Au and Ag nanoparticles, along with silver-modified electrodes, have a remarkable **catalytic activity** in specific electrochemical reactions, thereby enhancing the sensitivity, selectivity, and overall performance of electrochemical sensors and catalysts.

2. The rationale behind choosing gold-silver alloyed nanoporous matrices as electrode modifiers stems from their unique combination of properties, which leverage the advantages of both metals while offering additional benefits.

a. **Synergistic properties**: Au and Ag alloys can combine the desirable characteristics of both metals, such as high conductivity, chemical stability, and catalytic activity, resulting in enhanced overall performance compared with individual metals.

b. **Tunable properties**: The composition of gold-silver alloys can be precisely controlled to tailor the material properties, such as conductivity, catalytic activity, and surface morphology, to meet specific application requirements.

c. **Nanoporous structure**: The nanoporous structure of the alloyed matrices provides a high surface-area-to-volume ratio, which promotes increased analyte accessibility and facilitates rapid mass transport of the target analyte to the electrode surface, improving sensitivity and response times in electrochemical sensing and detection.

d. **Enhanced catalytic activity**: The presence of gold and silver nanoparticles within the nanoporous matrix can synergistically enhance the catalytic activity towards various electrochemical reactions, further improving the performance and selectivity of electrochemical sensors and catalysts.

e. **Chemical stability:** alloyed nanoporous matrices exhibit excellent chemical stability, ensuring long-term electrode integrity and performance under a range of electrochemical conditions.

Generally, the chemistry behind using gold-silver alloyed nanoporous matrices as electrode modifiers involves interactions between the alloyed metal surface, electrolyte, and analyte species.

The composition and morphology of the alloyed matrices influence the surface reactivity, electron transfer kinetics, and catalytic behavior, ultimately determining the electrochemical performance of the modified electrode. Furthermore, the nanoporous structure provides ample active sites for analyte adsorption and reaction while facilitating the efficient mass transport of ions and molecules to the electrode surface. Surface modification or functionalization can further enhance the electrochemical properties of a material, allowing for tailored surface chemistry and improved performance in specific applications.

3. The rationale behind choosing thermally annealed gold-silver nanoporous matrices as electrode modifiers lies in their unique combination of properties and the chemistry behind their formation, which offers significant advantages for electrochemical applications.

a. **Synergistic properties:** gold and silver alloys possess complementary characteristics such as high electrical conductivity, chemical stability, and catalytic activity. Annealing nanoporous matrices at elevated temperatures allows for the formation of a well-defined alloy structure, optimizing the synergistic effects between gold and silver to enhance the electrochemical performance.

b. **Controlled morphology:** the annealing process enables precise control over the morphology and composition of the nanoporous matrices, allowing for the creation of tailored structures with optimized surface area, pore size distribution, and surface roughness. This controlled morphology enhances the accessibility of active sites for analyte interactions and promotes efficient mass transport of ions and molecules to the electrode surface.

c. **Improved stability:** thermally annealed gold-silver nanoporous matrices exhibit enhanced chemical and thermal stability compared to their non-annealed counterparts. The annealing process helps stabilize the alloy structure and minimize surface defects, ensuring long-term electrode integrity and performance under a range of electrochemical conditions.

d. **Enhanced catalytic activity:** the annealing-induced structural changes in nanoporous matrices can lead to the formation of active catalytic sites on the alloy surface, enhancing the catalytic activity towards specific electrochemical reactions. This enhanced catalytic activity contributes to improved sensitivity, selectivity, and response time in electrochemical sensing and catalysis applications.

e. **Surface modification:** the annealed nanoporous matrices can be further functionalized or modified with specific molecules, nanoparticles, or surface coatings to tailor their electrochemical properties for specific applications. Surface modification strategies can enhance the surface reactivity, promote selective analyte binding, or introduce additional functionalities to the electrode surface.

4. The rationale behind integrating reduced graphene oxide (r-GO) and poly(glycine) with thermally annealed gold-silver nanoporous matrices as electrode modifiers is to leverage the unique properties of each component to create a multifunctional composite with enhanced electrochemical performance.

a. **Synergistic properties**: reduced graphene oxide (*r*-GO) possesses high electrical conductivity, a large surface area, and excellent mechanical strength, making it an ideal candidate for improving electron transfer kinetics and enhancing the overall conductivity of the electrode. On the other hand, poly(glycine) offers biocompatibility, hydrophilicity, and potential for functionalization, enabling tailored surface chemistry and specific interactions with the analytes.

b. **Enhanced stability**: integrating *r*-GO and poly(glycine) with thermally annealed gold-silver nanoporous matrices enhanced the stability and mechanical robustness of the electrode, ensuring long-term performance and resistance to degradation under harsh electrochemical conditions.

c. **Surface functionalization**: the presence of poly(glycine) allows for the surface functionalization of the electrode with biomolecules, enzymes, or other functional groups, enabling selective analyte detection and tailored sensing applications. Additionally, the integration of *r*-GO provided a conductive scaffold for efficient electron transport, enhancing the sensitivity and response of the electrode.

d. **Catalytic activity**: the synergistic combination of thermally annealed gold-silver nanoporous matrices, *r*-GO, and poly(glycine) may lead to the formation of active catalytic sites on the electrode surface, promoting specific electrochemical reactions and improving the overall catalytic activity of the composite material.

e. **Electrochemical performance**: the integration of *r*-GO and poly(glycine) with thermally annealed gold-silver nanoporous matrices resulted in a composite material with enhanced electrochemical performance, including improved sensitivity, selectivity, and stability.

This multifunctional composite holds promise for various electrochemical applications such as sensing, detection, and energy storage.

Generally, the chemistry behind this integration involves the interaction between the functional groups present in *r*-GO, poly(glycine), and the surface of thermally annealed gold-silver nanoporous matrices. Covalent and non-covalent interactions between these components facilitate the formation of a stable composite structure with synergistic properties, enabling enhanced electrochemical performance and tailored functionality for specific applications.

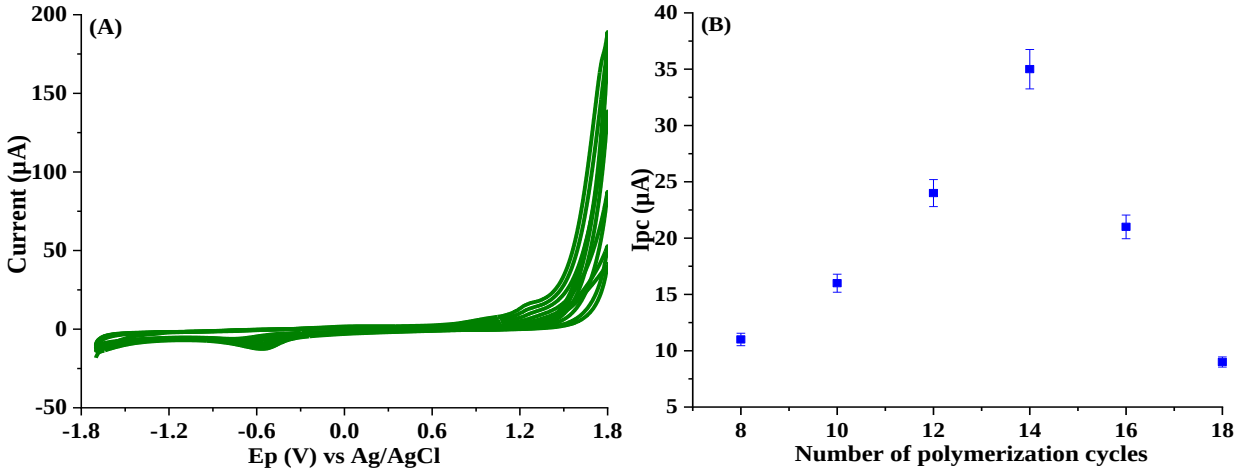

Fig. S1. (A) CV for the electropolymerization of 0.04 M glycine with 0.1 M ABS (pH 4.0) at the surface of TA-Au-Ag-ANpM/*r*-GO/GCE for 14 cycles in a potential ranges of -1.7 to 1.6 V at a scan rate of 25 mVs^{-1}, and (B) Ipc *vs.* the number of polymerization cycles for 15 µM MTZ.

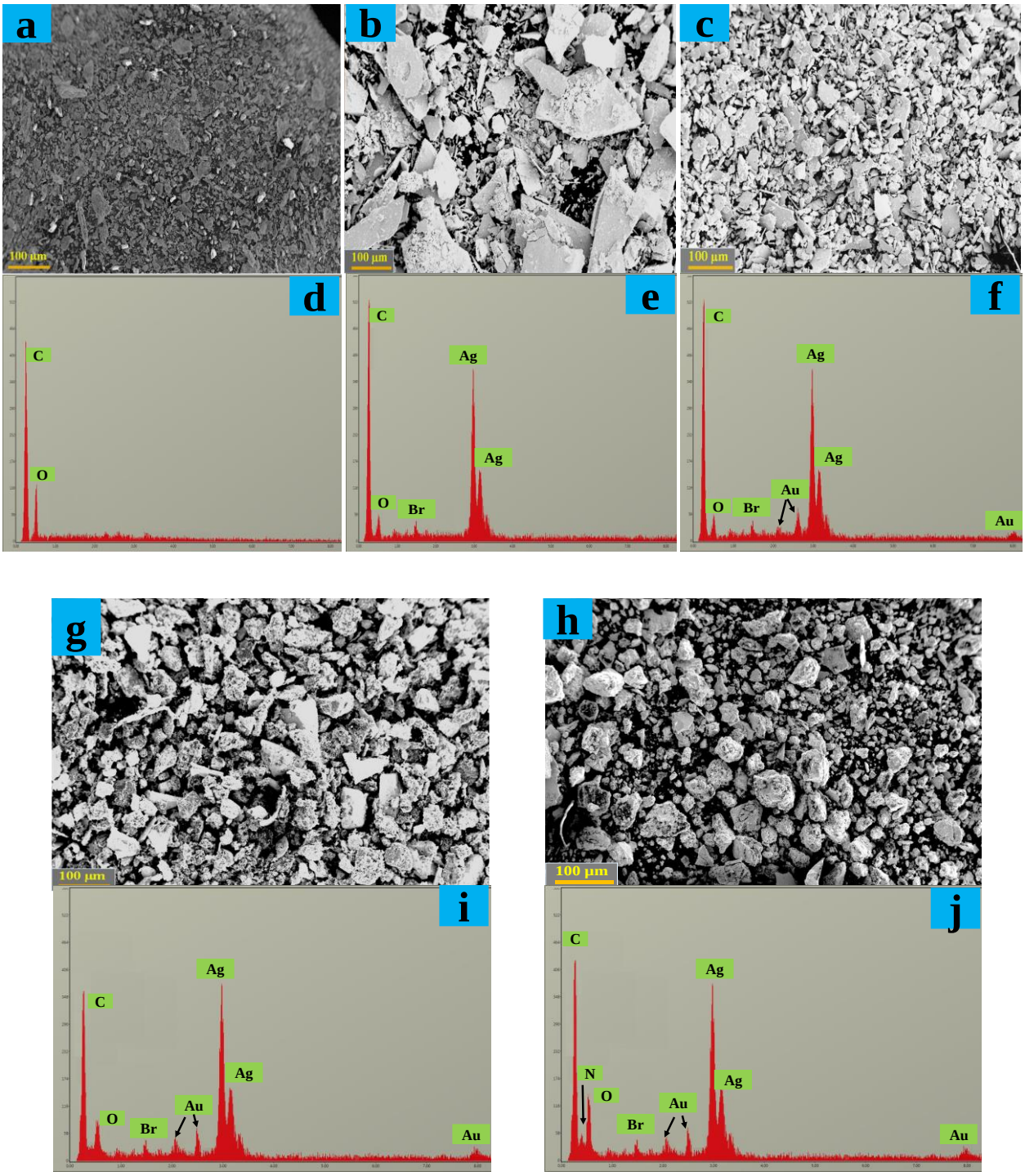

Fig. S2. SEM and EDX spectra of *r*-GO (a and d), TA-Ag-NpM (b and e), TA-Au-Ag-ANpM (c and f), TA-Au-Ag-ANpM/*r*-GO (g and i), and TA-Au-Ag-ANpM/*r*-GO/poly(glycine) (h and j).

Electrochemical behavior of MTZ

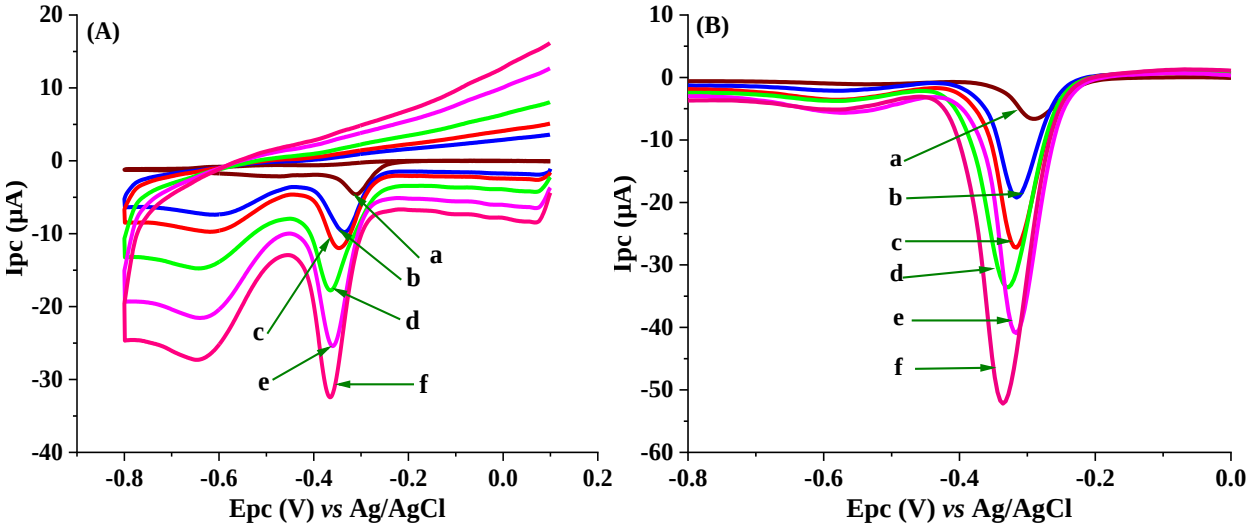

Fig. S3. CVs (A) and SWVs (B) of 15 μM MTZ in 0.1 M H_2SO_4 (pH 2) at the bare GCE (a), *r*-GO/poly(glycine)/GCE (b), TA-Au-Ag-ANpM/GCE (c), TA-Au-Ag-ANpM/poly(glycine)/GCE (d), TA-Au-Ag-ANpM/*r*-GO/GCE (e), and TA-Au-Ag-ANpM/*r*-GO/poly(glycine)/GCE (f).

Effect of electrolyte solutions

The selection of an appropriate electrolyte solution significantly influences the shapes of voltammograms and the resulting current intensity in voltammetric experiments. Therefore, it is vital to select the appropriate supporting electrolyte before conducting any electrochemical analysis. To assess the influence of different supporting electrolytes, SWV was used. Several supporting electrolytes, each with its unique effect on the electrochemical response of the analyte, were investigated. The supporting electrolytes included acetate buffer, BRB, PBS, H_2SO_4, CBS, $HClO_4$, and CB-PBS. Among the examined electrolytes, H_2SO_4 provided the maximum current response (Fig. SM1). The response of H_2SO_4 was well-defined and large enough, confirming its superiority as the optimal medium. Therefore, H_2SO_4 was selected as the suitable electrolyte solution for determining MTZ.

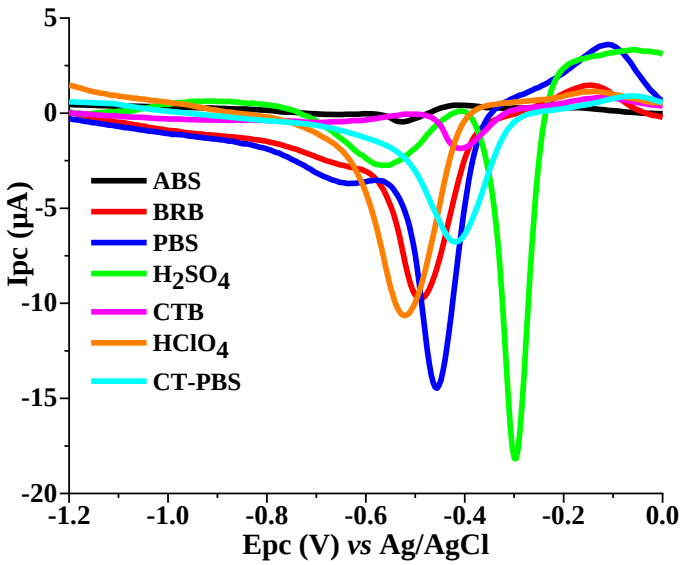

Fig. SM1. SWVs of 15 μM MTZ in different supporting electrolyte solutions.

Optimization of experimental conditions

Optimization of the number of electropolymerization cycles

The performance of the modified electrode is affected by the number of polymerization cycles. The more cycles, the thicker the film and the more porous the structure. The structural change affects the sensitivity of the sensor by enhancing the active surface area available for interaction with the analyte. However, if the film becomes too thick, it can act as an insulator and hinder the flow of electrons, reducing sensitivity. The optimal number of polymerization cycles for poly(glycine) was determined by performing a series of CV experiments in 0.1 M ABS (pH 4.0) with 0.04 M glycine at the surface of TA-Au-Ag-ANpM/*r*-GO/GCE (potential range: -1.7 V to 1.6 V, and scan rate: 25 mVs^{-1}). As shown in Fig. S1B, the peak current response increased with the number of cycles up to 14, after which it started to drop. The drop is due to the formation of a thicker and more insulating poly(glycine) film at the surface of TA-Au-Ag-ANpM/*r*-GO/GCE. Therefore, 14 polymerization cycles were selected as the optimal value for next experiments.

Optimization of the ratio of TA-Au-Ag-ANpM and *r*-GO

Optimizing the ratio of different nanocomposites at the surface of modified electrodes is essential for achieving the best balance of electrical conductivity, electroactive surface area, catalytic activity, stability, and cost-efficiency. The mixing ratio of the two nanocomposites, TA-Au-Ag-ANpM and *r*-GO, was optimized to achieve the highest performance for the proposed sensor. A thorough evaluation was conducted to determine the optimal ratio that maximizes the performance of the sensor. Different mixing ratios of TA-Au-Ag-ANpM and *r*-GO were tested while keeping other experimental parameters constant. The highest peak current response for 15 µM MTZ at the surface of TA-Au-Ag-ANpM/r-GO/poly(glycine)/GCE was observed when the mixing ratio of TA-Au-Ag-ANpM and *r*-GO was equal to 2:1 (Fig. SM2A). The ratio revealed greater performance over all other combinations experimented. Therefore, the 2:1 ratio of TA-Au-Ag-ANpM and *r*-GO was chosen as the optimal amount for fabricating the proposed sensor. This ensures that the modified electrode maintains an ideal balance between the nanocomposites, resulting in an electrode that offers exceptional performance for electrochemical sensing applications in determining MTZ in food samples.

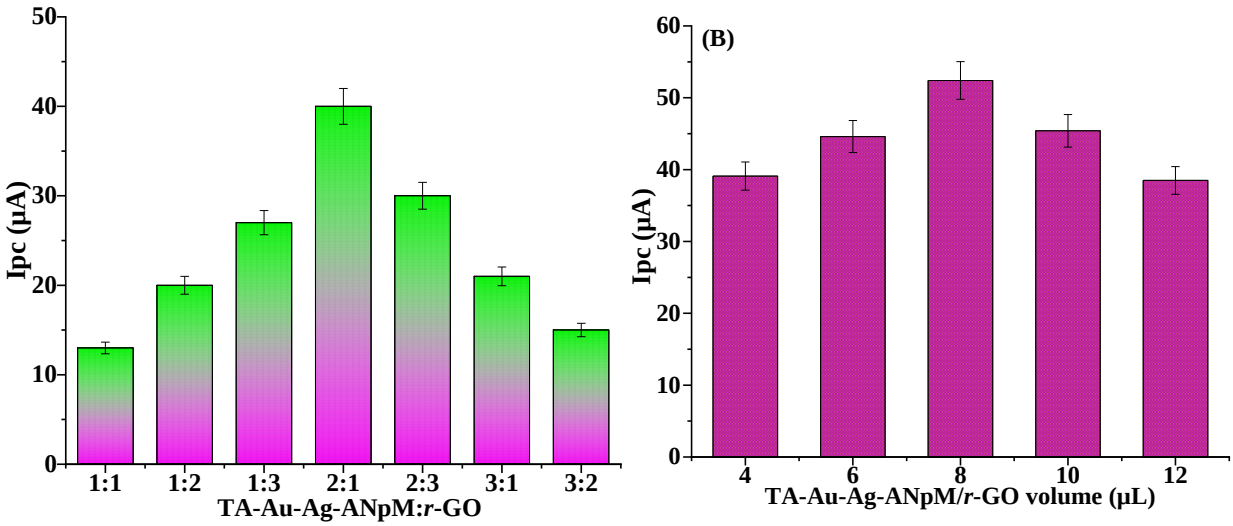

Fig. SM2. Plot for the optimization of the mixing ratio of TA-Au-Ag-ANpM and *r*-GO (A) and the volume of drop-casting TA-Au-Ag-ANpM/*r*-GO dispersion (B) to prepare TA-Au-Ag-ANpM/*r*-GO/poly(glycine)/GCE for the determination of 15 µM MTZ.

Optimization of the volume of drop-casting TA-Au-Ag-ANpM/*r*-GO dispersion

Optimizing the drop-casting volume of TA-Au-Ag-ANpM/*r*-GO dispersion over the modified electrode surface is critical to ensure the efficiency of the modifications. The chosen amount affects the thickness and uniformity of the resulting layer, which has a significant effect on the overall performance of the electrode. To optimize the drop-casting volume, we conducted a systematic study of different amounts of TA-Au-Ag-ANpM/*r*-GO and examined how each affected the performance of the electrode in the determination of 15 µM MTZ. As shown in Fig. SM2B, the optimal drop-casting volume of TA-Au-Ag-ANpM/*r*-GO dispersion was 8 µL. This volume not only produced the highest cathodic current response, but it also maintained excellent electrochemical performance. We decided to use 8 µL of TA-Au-Ag-ANpM/*r*-GO dispersion as the optimal volume for preparing TA-Au-Ag-ANpM/*r*-GO/poly(glycine)/GCE in all subsequent experiments. The choice strikes an ideal balance, ensuring that the coating of the modified electrode has the right thickness for superior performance for detecting MTZ in food samples.

Effect of scan rate

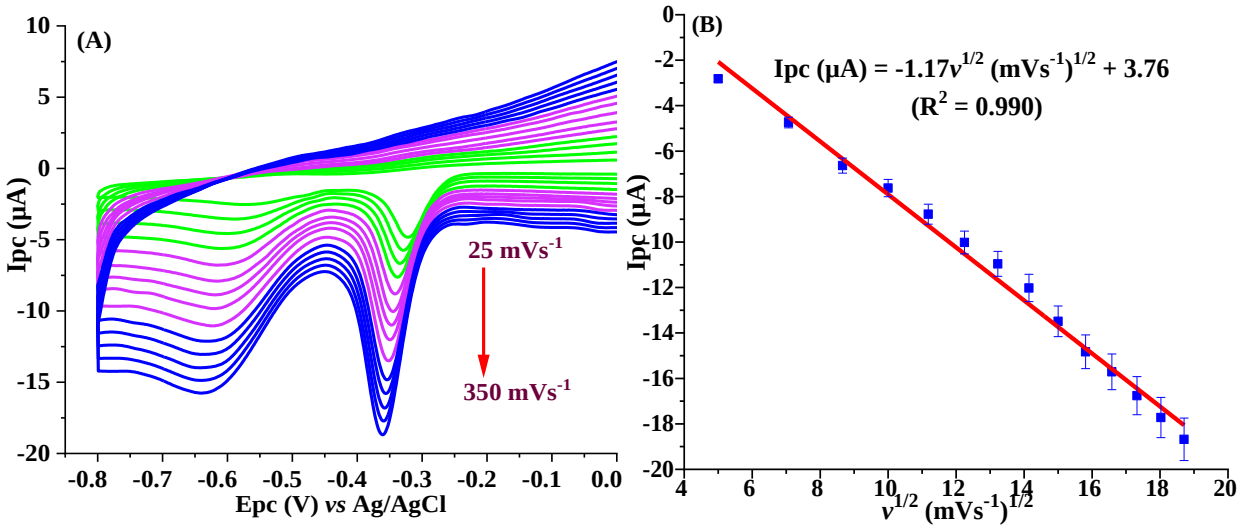

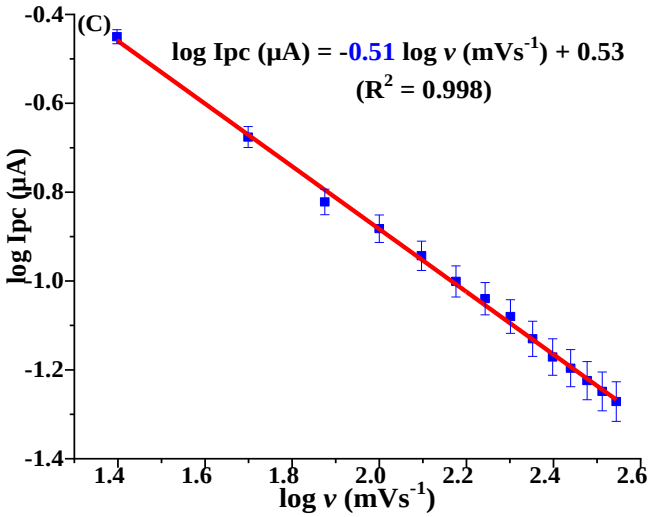

Fig. S4. CVs of 15 µM MTZ (A) at different scan rates, Ipc *vs.* $v^{1/2}$ (B), and log Ipc *vs.* log *v* (C).

Optimization of SWV parameters

Accurate and reliable electrochemical results depend on the efficient optimization of SWV parameters. In SWV analysis, the three instrumental variables (frequency, amplitude, and step potential) plays a crucial role. This study investigates the effect of these parameters on the cathodic current response of 15 µM MTZ in 0.1 M H_2SO_4 (pH 2). Initially, we examined the effect of frequency within the range of 40 to 120 Hz while keeping the amplitude and step potential constant. The current response showed an ascending trend with increasing frequency, peaking at 80 Hz (Fig. SM3A). Consequently, 80 Hz was selected as the optimal frequency for subsequent experiments. Next, the amplitude was optimized within the range of 40–110 mV while keeping the frequency and step potential constant. Notably, the cathodic current for the analyte increased until it reached its maximum at an amplitude of 80 mV, followed by a decline (Fig. SM3B). Therefore, 80 mV was identified as the optimal amplitude for the next measurements. Finally, the influence of step potential was examined in the range of 2–14 mV while keeping other SWV variables constant. The current response increased with the step potential until it peaked at 8 mV, after which it declined (Fig. SM3C). Consequently, 8 mV was designated as the optimal step potential for subsequent experiments.

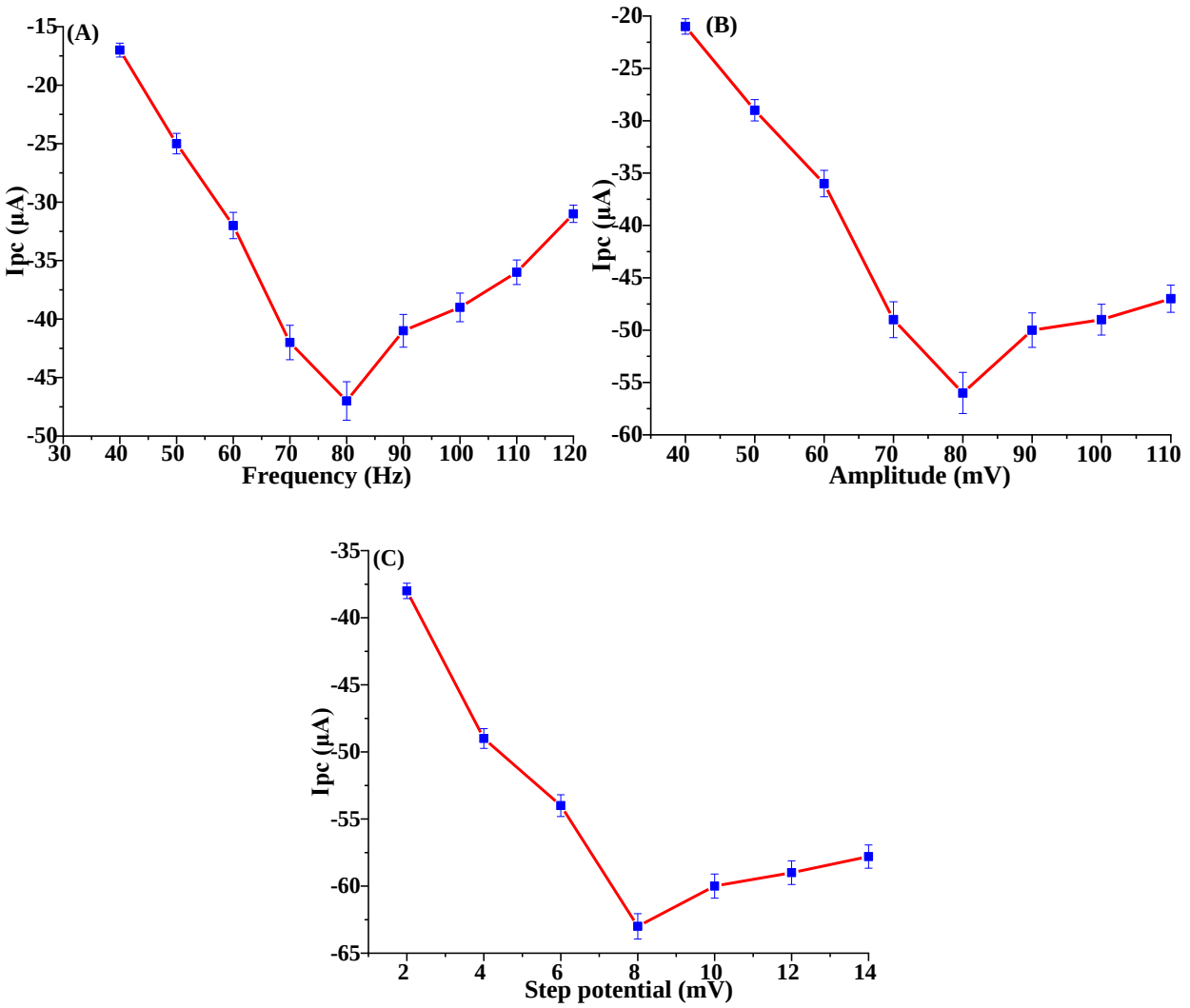

Fig. SM3. The influence of SWV parameters: frequency (A); amplitude (B); and step potential (C) on the cathodic current response of 15 µM MTZ.

Reproducibility, repeatability and stability

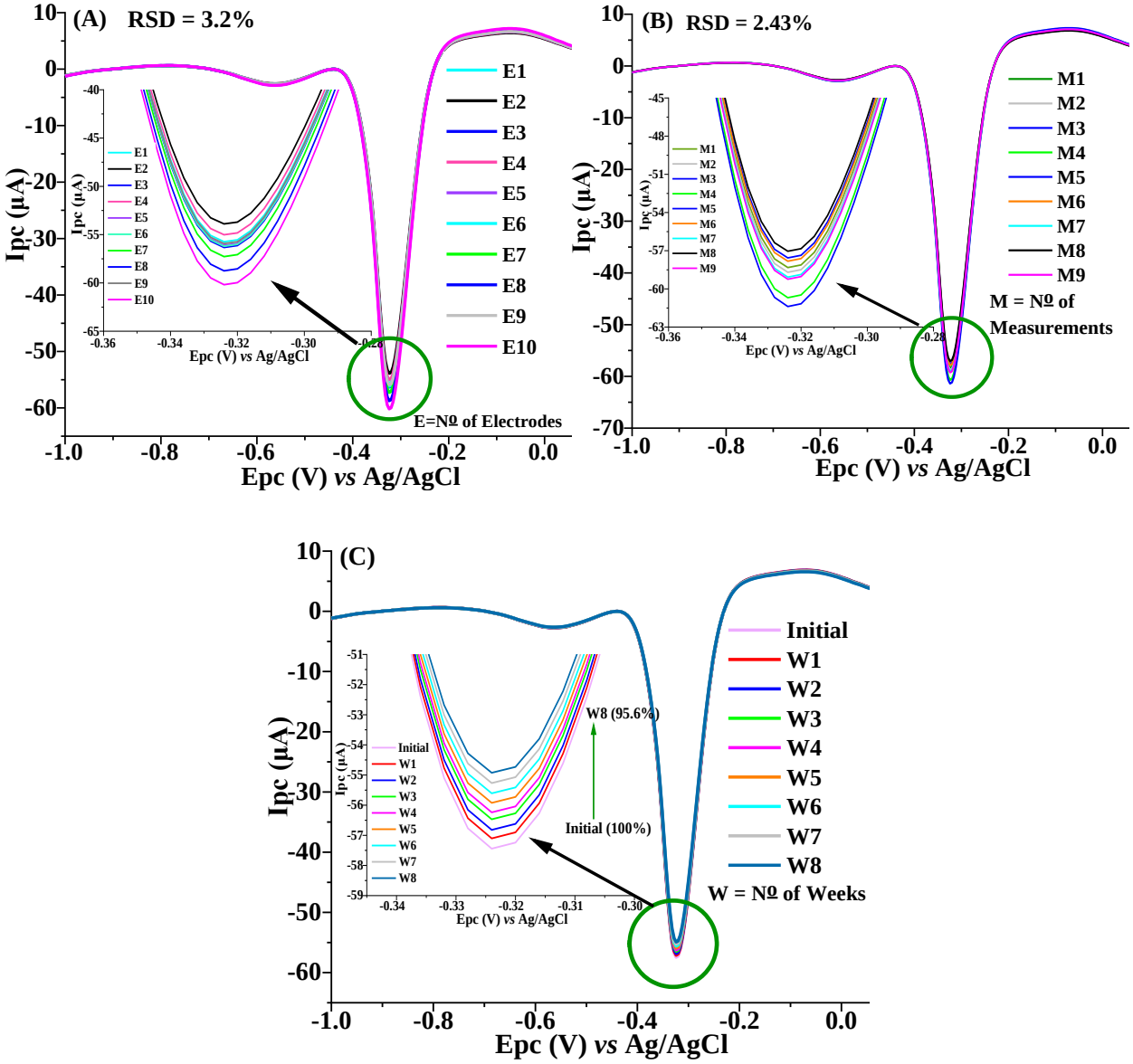

Fig. S5. (A) Reproducibility of ten electrodes, (B) repeatability of nine consecutive SWV measurements, and (C) eight weeks stability of TA-Au-Ag-ANpM/*r*-GO/poly(glycine)/GCE.

Selectivity

Table S1: The effect of coexisting substances on the electrochemical response of the sensor

Interferents	Conc. (µM)	Relative Percentage Error (%)	Interferents	Conc. (µM)	Relative Percentage Error (%)
Cephalexin	200	3.31	Folic Acid	600	2.98
Erythromycin	200	4.03	Urea	600	2.18
Azithromycin	200	3.98	Sucrose	600	2.39
Tinidazole	200	3.57	Uric Acid	600	2.77
Ampicillin	200	4.12	Lactose	600	2.21
Amoxicillin	200	4.27	Cu^{2+}	850	1.57
Cloxacillin	200	3.25	Fe^{3+}	850	1.63
Chloramphenicol	200	3.38	HCO_3^-	850	1.82
Ciprofloxacin	200	3.61	NO_3^-	850	1.08
Dopamine	600	2.36	Ca^{2+}	850	1.24
Glucose	600	2.51	Mg^{2+}	850	1.51
Ascorbic Acid	600	2.64	SO_4^{2-}	850	0.98
Fructose	600	2.49	CO_3^{2-}	850	0.76

Analysis of real samples

Table S2: Result of triplicate spiking experiments.

Samples	Spiked (µM)	Found* (µM)	Recovery (%)	RSD (%)
Milk powder	0	-	-	-
	5	4.89 ± 0.24	97.8	1.74
	10	10.14 ± 0.96	101.4	2.65
	25	24.71 ± 1.38	98.8	1.94
	30	30.33 ± 1.85	101.1	1.55
Pork meat	0	-	-	-
	5	5.04 ± 0.33	100.8	3.01
	10	9.93 ± 0.65	99.3	2.37
	25	25.32 ± 1.11	101.3	2.89
	30	29.55 ± 1.76	98.5	2.49
Chicken meat	0	-	-	-
	5	4.93 ± 0.27	98.6	1.61
	10	9.71 ± 0.84	97.1	2.42
	25	24.22 ± 1.63	96.9	1.89
	30	30.06 ± 1.42	100.2	2.21

*Mean values of triplicate measurements

Table S3. The amount of MTZ detected in tablet samples using the developed sensor.

Tablet	Sample (µM)	Found* (µM)	Detected (mg/tablet)	Labelled amount (mg/tablet)	Recovery (%)	RSD (%)
Metroleb-250 (India)	5	4.92 ± 0.42	246.00	250	98.4	1.85
	15	14.75 ± 1.13	245.83	250	98.3	1.94
	30	29.71 ± 1.77	244.87	250	97.9	2.11
	45	44.58 ± 2.02	247.67	250	99.1	1.73

*Mean values of triplicate measurements

Table S4. Comparison of an experimentally detected amount with labelled value at a 95% confidence level (t-test).

Detected (mg/tablet)	Labelled amount (mg/tablet)	$t_{calculated}$	$t_{critical}$ (n = 3, p = 0.05)	Remarks
246.00	250	1.52	4.3	No significant difference
245.83	250	1.51	4.3	No significant difference
244.67	250	1.73	4.3	No significant difference
247.67	250	0.95	4.3	No significant difference

Chapter Six: Paper IV

A cutting-edge electrochemical sensing platform for the simultaneous determination of the residues of antimicrobial drugs, rifampicin and norfloxacin, in water samples

Wondimeneh Dubale Adane, Bhagwan Singh Chandravanshi, Negash Getachew, Merid Tessema

Analytica Chimica Acta 1312 (2024) 342746

https://doi.org/10.1016/j.aca.2024.342746

Analytica Chimica Acta 1312 (2024) 342746

Contents lists available at ScienceDirect

Analytica Chimica Acta

journal homepage: www.elsevier.com/locate/aca

A cutting-edge electrochemical sensing platform for the simultaneous determination of the residues of antimicrobial drugs, rifampicin and norfloxacin, in water samples

Wondimeneh Dubale Adane, Bhagwan Singh Chandravanshi *, Negash Getachew, Merid Tessema **

Department of Chemistry, Addis Ababa University, P. O. Box 1176, Addis Ababa, Ethiopia

HIGHLIGHTS

- Cutting-edge sensor for simultaneously detecting antibiotic residues in water bodies.
- The sensor excels with the lowest LOD, wide linear range, and exceptional features.
- Current response was unaffected in the presence of several coexisting interferents.
- Ideal candidate for real-time monitoring of RAMP and NFX residues in water samples.

GRAPHICAL ABSTRACT

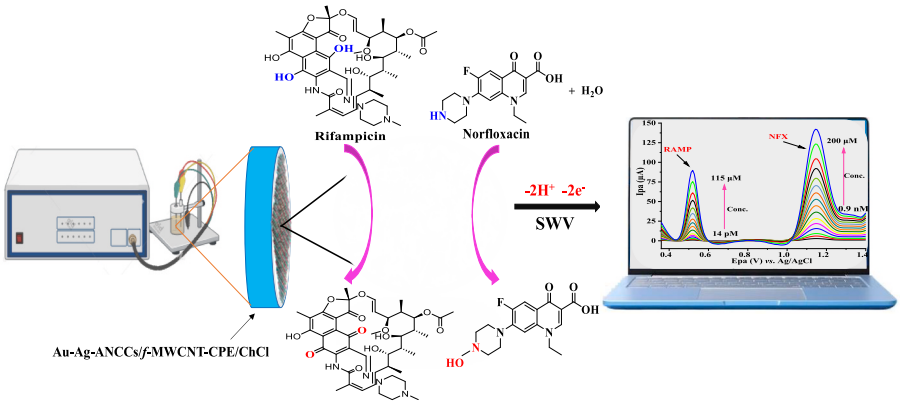

ARTICLE INFO

Handling Editor: Nicola Cioffi

Keywords:
Gold-silver alloy nanocorals clusters
Choline chloride
Electrochemical sensor
Antibiotic residues
Rifampicin
Norfloxacin

ABSTRACT

Background: The widespread use and abuse of antibiotics has resulted in the pollution of water sources with antibiotic residues, posing a threat to human health, the environment, and the economy. Therefore, a highly sensitive and selective method is required for their detection in water samples. Herein, advanced ultrasensitive electrochemical sensor platform was developed by integrating gold-silver alloy nanocoral clusters (Au–Ag-ANCCs) with functionalized multi-walled carbon nanotube-carbon paste electrode (*f*-MWCNT-CPE) and choline chloride (ChCl) nanocomposites for simultaneously determining the residues of antimicrobial drugs, rifampicin (RAMP) and norfloxacin (NFX), in water samples.

Results: The developed sensor (Au–Ag-ANCCs/*f*-MWCNTs-CPE/ChCl) was extensively characterized using several analytical (UV–Vis, FT-IR, XRD, SEM, and EDX) and electrochemical (EIS, CV, and SWV) techniques. It exhibited outstanding performance in a wide linear range, from 14 pM to 115 µM for RAMP, and from 0.9 nM to 200 µM for NFX, with a limit of detection (LOD, 3σ/m, S/N = 3, n = 5) and a limit of quantification (LOQ, 10σ/m, S/N =

* Corresponding author.
** Corresponding author.
E-mail addresses: bscv2006@yahoo.com (B.S. Chandravanshi), tessemamerid@yahoo.com (M. Tessema).

https://doi.org/10.1016/j.aca.2024.342746
Received 23 March 2024; Received in revised form 14 May 2024; Accepted 18 May 2024
Available online 20 May 2024

3, n = 5) values of 2.7 pM and 8.85 pM for RAMP, and 0.14 nM and 0.47 nM for NFX, respectively. The sensor also exhibited exceptional reproducibility, stability, and resistance to interference.
Significance: The developed sensor was effectively utilized to determine RAMP and NFX residues in hospital wastewater, river, and tap water samples, yielding recoveries within the range of 96.8–103 % and relative standard deviations below 5 %. Generally, the proposed sensor demonstrated remarkable performance in detecting the target analytes, making it an ideal tool and the first of its kind for addressing global antibiotic residue pollutants in water sources.

1. Introduction

Since their discovery, antibiotics have served as crucial medications to treat a wide range of infectious diseases, such as those affecting the gastrointestinal tract, urinary tract, genitourinary tract, skin, and abdomen. They are also prescribed for conditions like pneumonia, typhoid, bronchitis, sinusitis, arthritis, tuberculosis, strep throat, and leprosy [1]. In addition, antibiotics are frequently used in animal husbandry as feed additives to enhance performance and promote growth. Antibiotics target the primary function of microbes, such as inhibiting cell wall and protein synthesis, restricting bacterial DNA synthesis, and impeding the elongation of newly formed RNA. This action prevents the growth and reproduction of microorganisms [2]. Excessive use and abuse of antibiotics have resulted in life-threatening reactions in the host body, such as allergies, liver toxicity, blood disorders, kidney toxicity, nerve toxicity, hearing loss, and skin sensitivity [3]. Most antibiotics are excreted as parent drugs or metabolites through feces or urine, entering the environment and contributing to soil and water pollution due to their complex molecular composition. Waste from pharmaceutical factories, hospitals, and animal husbandry exacerbates pollution. The presence of antibiotic residues in water sources and the environment significantly contributes to the development of resistance in certain microorganisms [4,5]. Moreover, the presence of excess antibiotic residues in water sources poses serious health threats, including childhood obesity, digestive and reproductive system disorders, bone marrow toxicity, mutagenicity, anaphylactic shock, and cancer [6]. Therefore, the development of effective and sensitive analytical devices for quantifying life-threatening antibiotic residues in water sources is crucial for protecting human health and the environment.

Rifampicin (RAMP), (3-[(4-methyl-1-piperazinyl)imino] methyl), is widely prescribed for the treatment of severe bacterial infections, including tuberculosis, meningitis, leprosy, and HIV-associated infections [7]. Recent research has also revealed that RAMP has a strong binding affinity for the COVID-19 protease. Thus, it is currently prescribed for the prevention of coronavirus [8]. Despite its significance, prolonged use and overdose of RAMP may result in adverse toxic effects, including loss of appetite, vomiting, hepatotoxicity, nausea, gastrointestinal upset, allergic rashes, and renal failure [9,10]. RAMP residues contaminate water sources, primarily from human urine or fecal extracts as well as from waste generated by pharmaceuticals and animal husbandry. Owing to its high solubility and environmental stability, RAMP is not completely removed by wastewater treatment systems [11]. Consequently, the residues in the aquatic environment can result in the development of antibiotic-resistant bacteria (ARB) and the potential transmission of ARBs to humans and terrestrial animal pathogens [12]. Therefore, to prevent toxicity and maximize the effectiveness of RAMP therapy, its residues should be strictly monitored in the environment and various water sources.

Norfloxacin (NFX), (1-ethyl-6-fluoro-1,4-dihydro-4-oxo-7-(piperazine-1-yl)-1H-quinolone -3-carboxylic acid), is extensively used for treating a wide range of infectious diseases, such as gonococcal urethritis, respiratory, ophthalmic, urinary, skin, and gastrointestinal infections [13,14]. Its mechanism of action involves the inhibition of DNA gyrase A, an essential enzyme responsible for bacterial DNA replication, making NFX effective against a broad spectrum of monoderm and diderm bacteria [15]. Despite its efficiency, NFX has several side effects, including vomiting, depression, nausea, giddiness, anorexia, drowsiness, headache, and a bitter taste in the mouth [13]. Furthermore, owing to its frequent misuse in animal husbandry and medical practices, poor absorption, and inefficient metabolic breakdown, NFX residues accumulate in water bodies, posing potential ecological risks, including disruption of aquatic ecosystems, the development of antibiotic-resistant bacteria, alteration in microbial communities, bioaccumulation of residues in food chains, and contamination of drinking water. The presence of NFX residues in drinking water and food sources has toxic effects on animals, plants, and microorganisms, posing a public health hazard [16]. Hence, it is imperative to design an electrochemical tool that is selective and practical for addressing the challenges of NFX residue in water bodies.

Bimetallic alloy nanoparticles have been extensively studied for electrochemical sensing applications because of their exceptional sensitivity, outstanding detection capabilities, and robust stability [17]. Their morphology, size, and composition further enhance their catalytic performance and synergistic properties, broadening their potential applications in cancer treatment, nanomedicine, catalysis, and DNA delivery [18]. In particular, gold–silver alloy nanoparticles have gained significant attention due to their exceptional electrocatalytic activity, electrical conductivity, and optical features [19]. Similarly, multiwalled carbon nanotubes (MWCNTs) possess exceptional physicochemical characteristics, rendering them ideal electrode modifiers for electrochemical sensors [20]. However, their poor solubility and dispersion in solvents necessitate functionalization before use to optimize their surface properties and ensure uniform dispersion [21]. This involves the addition of functional groups, such as carboxyl, amine, and hydroxyl groups, using various methods including electrochemical, chemical, mechanical, and plasma processing [22]. Additionally, choline chloride (ChCl), a nontoxic ammonium salt, possesses bifunctional groups that enable its attachment to electrode surfaces, establishing a positively charged interface that enhances the transfer of electrons. This makes ChCl an attractive material for electrode surface modification [23]. Herein, a novel electrochemical sensor, the first of its kind, was developed by considering the benefits of the above three modifiers. It is capable of accurately detecting life-threatening residues of RAMP and NFX in water samples.

Several analytical methods have been reported for quantifying RAMP and NFX across various matrices, including capillary electrophoresis [24], spectrophotometry [25], chemiluminescence [26], and HPLC [27]. While these methods boast sensitivity and selectivity, they have several limitations, including intricate operational procedures, protracted sample preparation, extended analysis time, the need for skilled personnel, and high equipment costs. Whereas, voltammetric approaches are economical, expeditious, user-centric, highly specific, portable, and can be miniaturized [23]. Hence, electrochemical approaches are the preferred method for simultaneously detecting RAMP and NFX residues. Among these electrochemical techniques, SWV stands out for its numerous advantages, including rapid analysis, minimal sample consumption, background discrimination, and increased sensitivity [28], which makes it suitable for the simultaneous determination of targeted analytes.

The global concern regarding water contamination by antibiotic residues has reached unprecedented levels. These persistent pollutants

pose significant threats to ecosystems, human health, and aquatic life, while also jeopardizing water supplies. Urgent actions are imperative to mitigate the adverse effects of antibiotic residue pollution and safeguard the integrity of ecosystems and the health of future generations. To address this pressing issue, this study aimed to develop a novel electrochemical sensing platform comprising Au–Ag-ANCCs decorated with *f*-MWCNT-CPE and ChCl composites for simultaneously detecting RAMP and NFX residues in water samples. The precursors for preparing the intended sensor were selected by considering several important factors. Au–Ag-ANCCs offer superior electrical conductivity and facilitate electron transfer during the electrochemical reactions. Additionally, their bimetallic nature enhances catalytic activity, sensitivity, and selectivity. The high surface area of the nanocoral clusters improves the sensing capability of the sensor. The *f*-MWCNTs boost the stability and dispersion, facilitate rapid electron transfer, and amplify the sensitivity. Finally, ChCl modification imparts ionic liquid properties, enhancing analyte recognition, stability, and reproducibility for reliable analytical results. Before electrochemical analysis, Au–Ag-ANCCs/*f*-MWCNT-CPE/ChCl was subjected to extensive surface characterization. The sensor demonstrated exceptional performance in detecting RAMP and NFX residues, with wide linear ranges and picomolar detection limits. The remarkable selectivity, sensitivity, and real-time applicability of the device were demonstrated by the intense current responses to ultra-low concentrations of the analytes in hospital wastewater, river water, and tap water samples.

2. Experimental

2.1. Chemical and reagents

Pristine multi-walled carbon nanotubes (MWCNTs) with 99 % purity were obtained from Sigma-Aldrich (USA). Tetrachloroauric acid ($HAuCl_4$), silver nitrate ($AgNO_3$), sodium borohydride ($NaBH_4$), and sodium citrate ($Na_3C_6H_5O_7$) were purchased from Shanghai Sinopharm Chemical Reagent Co. Ltd., China. Nitric acid (HNO_3), sulfuric acid (H_2SO_4), and sodium citrate were purchased from Merck Chemicals, Germany. Choline chloride (99 %) in potassium chloride (KCl, 98 %) (Wagtech International Ltd., UK) was obtained from Sigma-Aldrich (USA). Graphite powder (BDH Laboratory Supplies, Poole, England) and paraffin oil (Uvasol Merck, Germany) were used for the preparation of the carbon paste electrode. Potassium hexacyanoferrate(III) (99 %) was purchased from BDH Chemicals Ltd. (England). All other chemicals and antibiotic standards were purchased from Sigma-Aldrich (USA). All chemicals and reagents used in this experiment were of analytical grade and used without further purification. All aqueous solutions were prepared using Milli-Q water (18.2 MΩ cm) obtained from a Millipore water purification system. Glassware was washed with aqua regia (HCl:HNO_3 in a 3:1 ratio by volume) and rinsed with deionized water before the experiments. 411.47 mg of RAMP was dissolved in 50 mL of distilled water to make a 0.01 M RAMP stock solution. Similarly, a 0.01 M stock solution of NFX was prepared by dissolving 159.67 mg of the analyte in

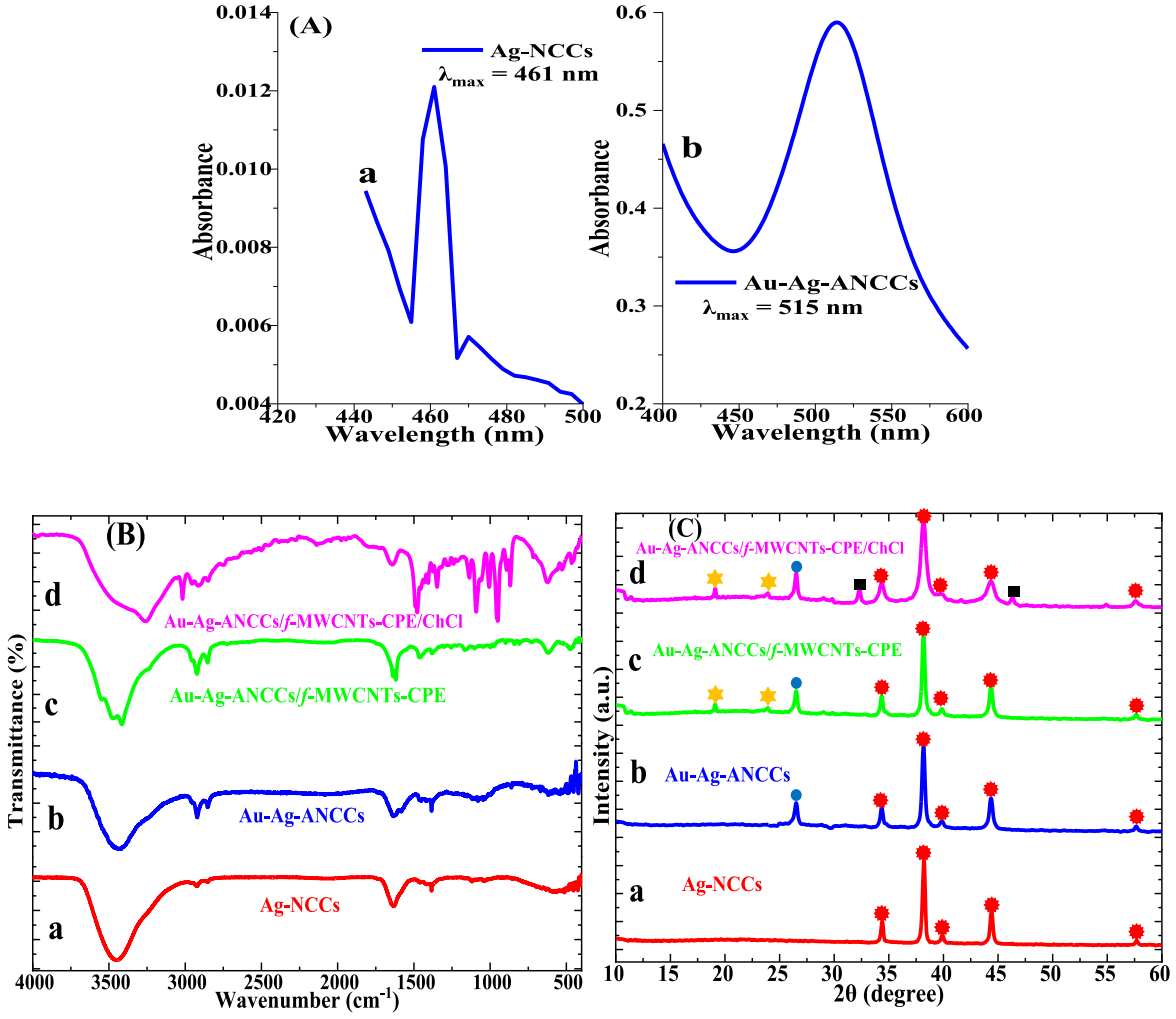

Fig. 1. (A) UV–Vis spectra of Ag–NCCs (a), Au–Ag-ANCCs (b), (B) FT-IR spectra and (C) XRD patterns of Ag–NCCs (a), Au–Ag-ANCCs (b), Au–Ag-ANCCs/*f*-MWCNTs-CPE (c), and Au–Ag-ANCCs/*f*-MWCNTs-CPE/ChCl (d).

50 mL of glacial acetic acid. The stock solutions are diluted with 0.1 M PBS (pH 5) to prepare working solutions for each analyte.

2.2. Apparatus and instruments

Electrochemical measurements were conducted in 20 mL cells using a CHI 760D electrochemical analyzer (CH Instruments, USA). A conventional three-electrode system was used throughout the experiment, consisting of a working electrode (either bare CPE or modified CPE), a platinum wire counter electrode, and a silver-silver chloride (Ag/AgCl (3 M KCl)) reference electrode. The structural morphology was characterized using a scanning electron microscope (SEM, CX-200plus, Coxem, Korea), and the elemental analysis was performed using energy-dispersive X-ray spectroscopy (EDS). The X-ray diffraction (XRD) pattern of the nanocomposites was recorded using a BRUKER ECOD 8 advance diffractometer with Cu Kα radiation (wavelength $\lambda = 0.15406$ nm) at room temperature. Fourier transform infrared (FT-IR) spectra were recorded using a PerkinElmer Spectrum 100 FT-IR spectrometer (PerkinElmer, USA). UV–Vis spectra were recorded using a Lambda 950 UV–Vis spectrometer (PerkinElmer, USA). The pH was measured using a Senses Ion + MM150 pH meter (China). Solid chemicals were weighed using an electronic digital balance (Model: Scientech ZSA 120, USA). A centrifuge (Model 8001, China) and an ultrasonic cleaner (Model YJ5120-B, China) were used during the preparation of the

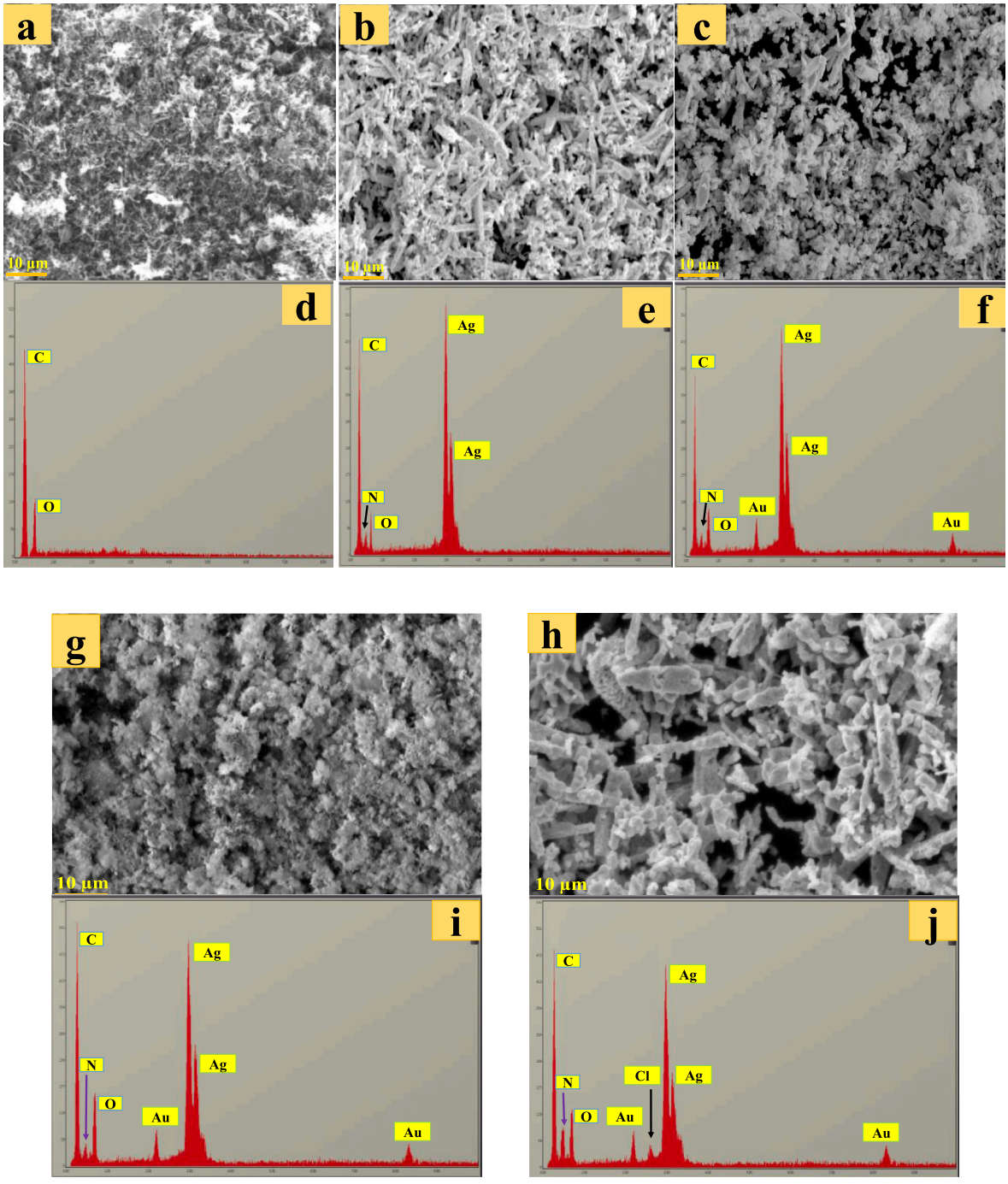

Fig. 2. SEM images and EDX spectrums of *f*-MWCNTs-CPE (a and d), Ag–NCCs (b and e), Au–Ag-ANCCs (c and f), Au–Ag-ANCCs/*f*-MWCNTs-CPE (g and i), Au–Ag-ANCCs/*f*-MWCNTs-CPE/ChCl (h and j).

nanocomposite. In addition, a magnetic stirrer and a vacuum pump were used throughout the experiment.

2.3. Preparation of water samples

Water samples, each 500 mL, were collected from three distinct sites in Addis Ababa, Ethiopia: St. Paulos Hospital, Akaki River, and Arat Killo Campus of Addis Ababa University. The samples were stored at 4 °C to maintain their original condition until analysis. Before analysis, each sample was filtered three times using 150 mm filter paper to remove impurities. Then, the filtered samples were diluted with a phosphate buffer solution at a 1:5 ratio to facilitate accurate analysis. For analysis, the samples were spiked with different concentrations of standard solutions of the analytes to demonstrate the overall robustness of the analytical process. No additional pretreatment steps were taken before the comprehensive analysis, ensuring that the analytical results would accurately reflect the exact composition of the collected water samples.

2.4. Preparation of f-MWCNTs and CPE

The chemical oxidation process for synthesizing *f*-MWCNTs was conducted as described by Ref. [29], with slight modifications. In this procedure, 3 g of pristine MWCNTs was refluxed for 24 h in a 150 mL solution containing a 1:3 mixture of HNO_3 and H_2SO_4. The reflux process was enhanced by magnetic stirring to facilitate the introduction of functional groups onto the surface of the nanotubes. Subsequently, the mixture was cooled overnight, centrifuged, washed, and filtered until the pH of the solution reached 7.0. The acid-functionalized MWCNTs (*f*-MWCNTs) was then dried in an oven at 80 °C for 24 h.

CPE was prepared by thoroughly mixing 70 mg of graphite powder with 30 μL of paraffin oil for 25 min using an agate mortar and pestle. The homogenized paste was then packed into a 1.0 mL syringe equipped with a copper wire for electrical contact. Subsequently, the surface of the electrode was meticulously polished on white paper to a mirror-like finish. When a fresh electrode was required, the previous electrode was carefully removed from the upper tip surface, replaced with a new paste, and subjected to further polishing.

2.5. Synthesis of Au–Ag-ANCCs

The synthesis of Ag–NCCs was conducted as follows: initially, 2 mL of 0.1 M $AgNO_3$ and 10 mL of 0.1 M PVP were added into a 100 mL flask containing 15 mL of 0.1 M PEG 600 solution under vigorous stirring for 20 min. Then, 4 mL of 1 % $Na_3C_6H_5O_7$ was added to initiate the reduction of Ag ions. The addition of a stabilizing agent prevents agglomeration and regulates the size and morphology of the clusters. Subsequently, the mixture was heated in an oil bath at 130 °C for 10 h. During this process, $AgNO_3$ and PVP reacted to form Ag nanocoral clusters stabilized by PEG 600 molecules. Controlled temperature and stirring conditions facilitated the gradual formation of Ag nanocoral clusters, exhibiting distinctive branch-like structures. The yellowish solution was allowed to cool, undergo centrifugation, and washed several times.

The synthesis of Au–Ag-ANCCs begins with a precise alloying process, converting the prepared Ag-NCC into its gold-based counterpart. Initially, 5 mL of 0.01 M $HAuCl_4$ solution was mixed with the Ag-NCC suspension in a vessel under vigorous stirring for 15 min to ensure the uniform distribution of gold ions. This step facilitates the incorporation of gold into the silver nanostructures, forming the basis for alloyed nanocoral clusters. Subsequently, the reaction mixture was heated in an oil bath at 90 °C for 3 h with continuous stirring. Following this, 3 mL of 0.1 M $NaBH_4$ was gradually added to activate the reduction process, leading to the formation of Au–Ag alloy nanocoral clusters. The pH of the reaction mixture was maintained at 10 throughout the process by periodically adding 0.1 M NaOH, which facilitated gold ion reduction and stabilized the resulting alloy nanostructures. Additionally, 4 mL of a 1 % PVP solution was added as a stabilizing agent to maintain the colloidal stability and create a protective layer. This layer helps to prevent aggregation by promoting electrostatic repulsion and inhibiting the formation of larger agglomerates. Finally, the synthesized Au–Ag-ANCCs were centrifuged, washed, and dried under vacuum. To the best of our knowledge, when gold and silver combine to form an alloy, there is typically no change in the oxidation state of each element. Both gold and silver generally maintain their stable oxidation states (i.e. zero oxidation state) in most chemical environments.

2.6. Preparation of Au–Ag-ANCCs/f-MWCNTs-CPE

To prepare the nanocomposite, 5 mg of *f*-MWCNTs was first dispersed in 2.5 mL N,N-dimethylformamide and sonicated for 45 min. Then, the *f*-MWCNTs dispersion was mixed with the Au–Ag-ANCCs dispersion (ratio 1:1) and ultrasonicated for 50 min. Finally, 8 μL of Au–Ag-ANCCs/*f*-MWCNTs dispersion was drop-casted onto a CPE, dried at 40 °C for 15 min, and termed as Au–Ag-ANCCs/*f*-MWCNTs-CPE.

2.7. Fabrication of Au–Ag-ANCCs/f-MWCNTs-CPE/ChCl

To fabricate the desired electrode, electrodeposition of 0.002 M ChCl

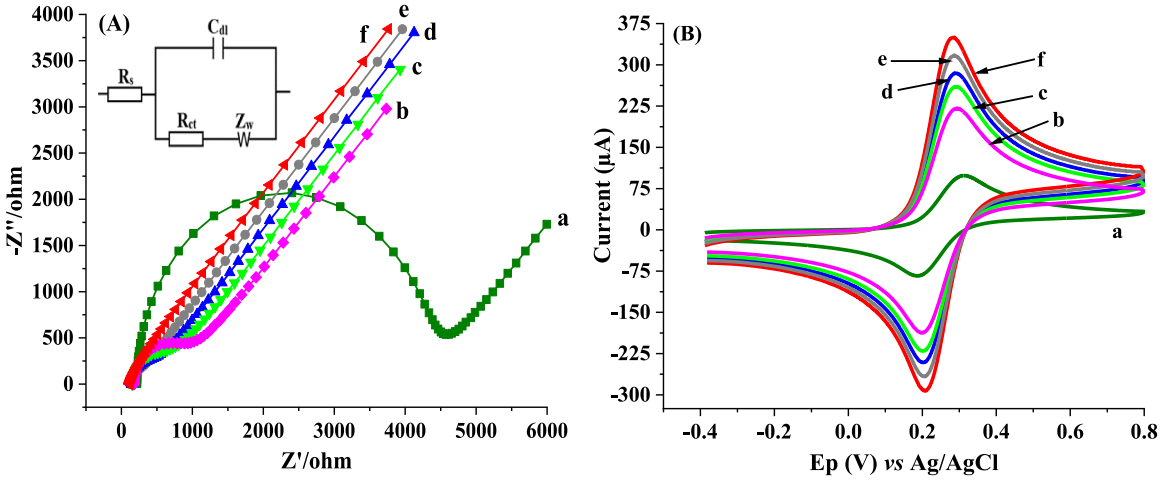

Fig. 3. (A) Nyquist plots and (B) CVs of bare CPE (a), *f*-MWCNTs-CPE/ChCl (b), Au–Ag-ANCCs/CPE (c), Au–Ag-ANCCs/ChCl/CPE (d), Au–Ag-ANCCs/*f*-MWCNTs-CPE (e), and Au–Ag-ANCCs/*f*-MWCNTs-CPE/ChCl (f) in 5.0 mM $[Fe(CN)_6]^{3-/4-}$ containing 0.1 M KCl at a scan rate of 50 mVs^{-1}.

containing 0.01 M KCl was performed at the surface of Au–Ag-ANCCs/*f*-MWCNTs-CPE using CV for 16 consecutive potential sweeps between −1.7 V and +1.6 V in 0.1 M PBS (pH 7.0) at a scan rate of 25 mVs^{-1} (Fig. S1A). Subsequently, the fabricated sensor (Au–Ag-ANCCs/*f*-MWCNTs-CPE/ChCl) was rinsed with deionized water and prepared for subsequent utilization.

3. Results and discussion

3.1. Analytical characterizations

The UV–Vis spectrum of Ag–NCCs revealed a distinct absorption peak at λ_{max} = 461 nm, indicating the localized surface plasmon resonance properties of the Ag particles (Fig. 1A(a)). The sharpness of the peaks implies mono-dispersity and uniformity in particle size, with an average calculated size of around 33 nm. As shown in Fig. 1A(b), Au–Ag-ANCCs displayed a distinct broad peak at λ_{max} = 515 nm, suggesting that the incorporation of Au into the alloy reduced the size (22 nm) and shifted the absorption peak to a longer wavelength. The observed variations in the two spectra arise from changes in the composition and sizes of the nanocoral clusters, which influence their optical characteristics. As surface area directly influences catalytic activity, the alloyed nanocoral clusters with the smallest particle size and largest surface area exhibited superior catalytic performance in preparing the intended sensor.

The FT-IR spectra of the Ag–NCCs (Fig. 1B(a)) exhibited characteristic peaks corresponding to Ag–O (568 cm^{-1}), C–H bending (1037 and 1120 cm^{-1}), C–O (1385 cm^{-1}), C═O (1629 cm^{-1}), C–H (2856 and 2929 cm^{-1}), and O–H (3459 cm^{-1}) stretching vibrations. The FT-IR spectra of the Au–Ag-ANCCs (Fig. 1B(b)) displayed peaks attributed to Ag–O (540 cm^{-1}), Au–O (620 cm^{-1}), Au–Ag (860 cm^{-1}) (confirming the alloying of Au and Ag), C–O (1078 cm^{-1}), C–H (2856 and 2929 cm^{-1}), and O–H (3438 and 1640 cm^{-1}) stretching vibrations. The FT-IR spectrum of Au–Ag-ANCCs/*f*-MWCNT-CPE (Fig. 1B(c)) exhibited a peak at 1567 cm^{-1}, associated with to the C═C stretching vibration of *f*-MWCNTs, and a peak at 1150 cm^{-1}, linked to the C–*O*–C stretching vibration of the CPE. The FT-IR spectra of Au–Ag-ANCCs/*f*-MWCNT-CPE/ChCl (Fig. 1B(d)) displayed peaks at 867 cm^{-1} (C–Cl stretching), 952 cm^{-1} (quaternary ammonium group stretching), and 1481 cm^{-1} ($((CH_3)_3N^+$ group stretching), confirming the incorporation of ChCl into the bimetallic alloy nano cluster.

XRD was used to assess the crystal structure and size of the nanocoral clusters. Consistent results obtained from the UV–Vis and XRD measurements of the nanocoral clusters size validated the structural features determined using these techniques. The consistency of the results enhances the reliability and validity of the findings, enabling a comprehensive understanding of the material. The XRD peaks of Ag–NCCs (Fig. 1C(a)) at 2θ = 34.42°, 38.24°, 40.08°, 44.46°, and 57.72° were indexed to the (100), (111), (200), (220), and (311) planes, respectively. These peaks are characteristic of face-centered-cubic (FCC) structured Ag metal crystals, consistent with previous reports [30]. The 2θ values for the Au–Ag-ANCCs and Ag–NCCs are almost identical because Au and Ag have similar lattice constants. However, XRD analysis of Au–Ag-ANCCs (Fig. 1C(b)) revealed an additional characteristic peak at 26.48°, which was attributed to the (111) crystal plane, suggesting the formation of a potential intermetallic alloy substance [31]. The peaks at 27.86°, 32.36°, and 46.36° (Fig. 1C(c)) correspond to the (002), (004), and (100) planes of typical graphite, respectively [32], confirming the successful incorporation of *f*-MWCNT into Au–Ag-ANCCs. The XRD spectra of the Au–Ag-ANCCs/*f*-MWCNTs-CPE/ChCl (Fig. 1C(d)) exhibited characteristic peaks of its constituent components, Au–Ag-ANCCs, *f*-MWCNTs-CPE, and ChCl, confirming the successful fabrication of the sensor.

The morphology of Au–Ag-ANCCs/*f*-MWCNTs-CPE/ChCl and its constituents were examined using SEM. The SEM image of *f*-MWCNT-CPE displayed a uniform distribution of carbon nanotubes within the CPE, along with well-dispersed pores and cavities, irregularly shaped agglomerates, and a uniform surface roughness (Fig. 2a). The EDX spectra revealed that the *f*-MWCNT-CPE was predominantly composed of C (78.9 %) and O (21.1 %) (Fig. 2d), indicating high purity. Subsequent SEM analysis of the Ag–NCCs revealed a striking morphology characterized by irregularly shaped, three-dimensional nanocoral clusters with interconnected branches resembling coral reefs (Fig. 2b). These clusters exhibited non-uniform distributions, rough surfaces, and porous networks, contributing to enhanced catalytic activity, and electrical conductivity. Further SEM examination of Au–Ag-ANCCs (Fig. 2c) revealed highly irregular, non-uniform nanocoral clusters with a rough porous network, contributing to exceptional catalytic, electrical, and sensing applicability. The EDX spectra of Ag–NCCs (Fig. 2e) showed the presence of C (32.0 %), N (3.3 %), O (7.1 %), and Ag (57.6 %). The Au–Ag-ANCCs (Fig. 2f) contained C (26.5 %), N (3.1 %), O (7.3 %), Ag (52.6 %), and Au (10.5 %), confirming the successful incorporation of Au into the Ag–NCCs. This incorporation enhances their electroactive surface area, electrical conductivity, and catalytic properties. Fig. 2g illustrates the uniform dispersion of Au–Ag-ANCCs particles in the *f*-MWCNTs-CPE composite. These particles retained their non-uniform distribution, rough surfaces, and porous networks with irregular shapes and prominent cavities, indicating their successful incorporation into *f*-MWCNT-CPE. The elemental mapping of Au–Ag-ANCCs/*f*-

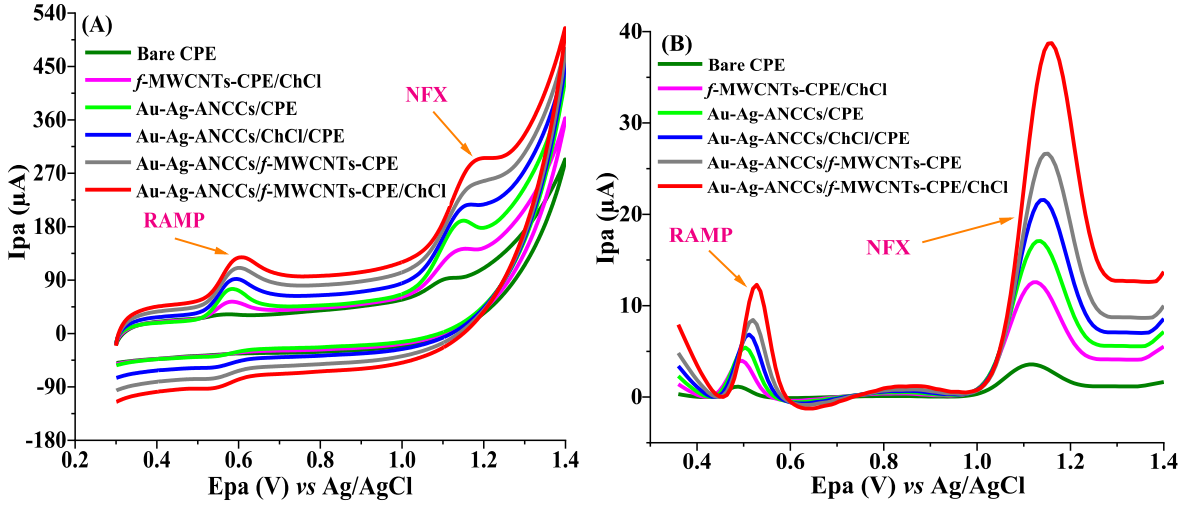

Fig. 4. (A) CVs and (B) SWVs of 15 µM RAMP and NFX in 0.1 M PBS (pH 5) on different electrodes at a scan rate of 100 mVs^{-1}.

MWCNT-CPE (Fig. 2i) confirmed the presence of C (31.9 %), N (2.9 %), O (9.9 %), Ag (47.4 %), and Au (7.9 %). Furthermore, the effective electrodeposition of the ChCl film at the surface of Au–Ag-ANCCs/*f*-MWCNTs-CPE is shown in Fig. 2h, forming three-dimensional nanocoral clusters with rough and asymmetrical surfaces. This coating significantly contributes to the enhancement of electrical conductivity, catalytic capability, and electroactive surface area of Au–Ag-ANCCs/*f*-MWCNT-CPE/ChCl. The corresponding EDX spectra (Fig. 2j) confirmed the presence of C (30.1 %), N (2.9 %), O (7.7 %), Cl (3.1 %), Ag (45.0 %), and Au (11.2 %), thus validating the successful preparation of the intended sensor.

3.2. Electrochemical characterizations

Electrochemical impedance spectroscopy (EIS) analysis was conducted on various electrodes in a frequency range from 0.1 Hz to 100 kHz with 5.0 mM $[Fe(CN)_6]^{3-/4-}$ containing 0.1 M KCl (Fig. 3A). The experimental data were fitted using a Randles equivalent circuit model, and the resulting values were presented in the form of a Nyquist plot (inset Fig. 3A). The semicircular segment of the EIS curve corresponds to the rate-limiting step in the electrochemical reaction. The diameter of this semicircle represents the charge transfer resistance (R_{ct}). The linear segment corresponds to the diffusion process, which becomes the rate-limiting step during the transportation of reactants and products to and from the electrode surface [33]. The type of modifier used influences the diameter of the semicircle. The R_{ct} values of the bare CPE, *f*-MWCNTs-CPE/ChCl, Au–Ag-ANCCs/CPE, Au–Ag-ANCCs/ChCl/CPE, Au–Ag-ANCCs/*f*-MWCNTs-CPE, and Au–Ag-ANCCs/*f*-MWCNTs-CPE/ChCl were calculated to be 4684, 2359, 1787, 1145, 613, and 216 Ω, respectively. The R_{ct} value is the lowest for Au–Ag-ANCCs/*f*-MWCNTs-CPE/ChCl, indicating that the modifier (Au–Ag-ANCCs/*f*-MWCNTs/ChCl) has the best electron transfer capability and electrical conductivity.

Cyclic voltammetry (CV) was conducted to examine the electrical and interfacial properties of different electrodes at various stages in 5.0 mM $[Fe(CN)_6]^{3-/4-}$ containing 0.1 M KCl at a scan rate of 50 mVs^{-1} (Fig. 3B). Due to the poor electrical conductivity, weak redox peaks with a peak-to-peak separation (ΔEp) of 126 mV were observed at the bare CPE (Fig. 3B(a)). After modifying the bare electrode with *f*-MWCNTs and ChCl nanocomposites, the peak current response of *f*-MWCNTs-CPE/ChCl increased and ΔEp decreased to 103 mV (Fig. 3B(b)). Au–Ag-ANCCs further decreased ΔEp to 89 mV (Fig. 3B(c)), suggesting that the modifier enhanced the electron transfer capacity and electrical conductivity of Au–Ag-ANCCs/CPE. For Au–Ag-ANCCs/ChCl/CPE and Au–Ag-ANCCs/*f*-MWCNTs-CPE (Fig. 3B(d and e)), the peak current responses increased significantly, and ΔEp decreased to 81 mV and 67 mV, respectively, due to the synergistic effects of the composite modifiers. The peak current response reached its maximum value at the surface of Au–Ag-ANCCs/*f*-MWCNTs-CPE/ChCl (Fig. 3B(f)), with a decrease in ΔEp to 51 mV. The combined effects of the nanocomposite modifiers significantly improved the overall performance of the suggested sensor, as evidenced by the agreement between the CV and EIS findings.

Electroactive surface area measurement is a critical phenomenon in voltammetric reactions as it directly affects the catalytic efficiency and sensitivity of electrodes. As a result, CV was employed to measure the electroactive surface area of electrodes at different modification stages using the Randles–Ševčík equation (1) [28].

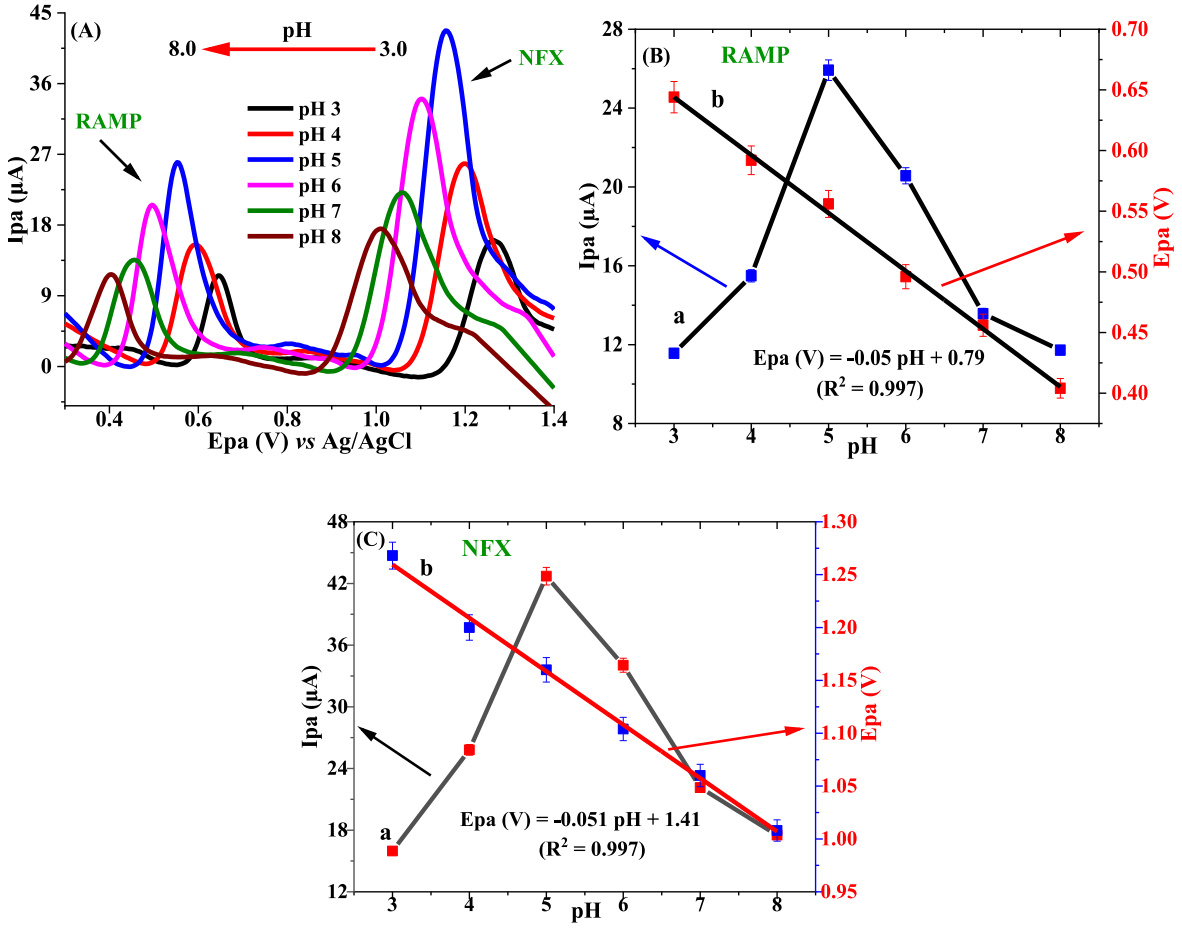

Fig. 5. (A) SWVs of 15 μM RAMP and NFX at different pH values of PBS, (B) and (C) Ipa (μA) *vs.* pH (a) and Epa (V) *vs.* pH (b) for RAMP and NFX, respectively.

$$I_p = 2.69x10^5 n^{3/2} AD^{1/2} Cv^{1/2} \quad (1)$$

where I_p = peak current, D = diffusion coefficient, n = number of electrons, v = scan rate, C = concentration of $[Fe(CN)_6]^{3-/4-}$, and A = electrode surface area. Electroactive areas were determined for bare CPE, *f*-MWCNTs-CPE/ChCl, Au–Ag-ANCCs/CPE, Au–Ag-ANCCs/ChCl/CPE, Au–Ag-ANCCs/*f*-MWCNTs-CPE, and Au–Ag-ANCCs/*f*-MWCNTs-CPE/ChCl, resulting in values of 0.036, 0.078, 0.097, 0.119, 0.152, and 0.185 cm^2, respectively. The surface area of Au–Ag-ANCCs/*f*-MWCNTs-CPE/ChCl is five times higher than that of the unmodified carbon paste electrode. This increase is attributed to the synergistic effect of Au–Ag-ANCCs, *f*-MWCNTs, and ChCl, which improve electron transfer kinetics and enhance the surface area.

3.3. Electrochemical behaviors of RAMP and NFX at different electrodes

The voltammetric characteristics of 15 μM RAMP and NFX were simultaneously examined using square wave voltammetry (SWV) and CV at a scan rate of 100 mVs^{-1} within a potential range of 0.3–1.4 V at various electrodes (bare CPE and other modified electrodes) (Fig. 4A). No voltammetric currents were recorded from the blank solution across the different electrodes, indicating either the absence of analytes or their presence below the detection limit. The absence of reduction peaks during the reverse CV scan suggests the irreversibility of the electro-oxidation of RAMP and NFX. Notably, the electrode modifications significantly enhanced the electrochemical responses of the analytes and shifted the peak potentials to more positive values. The weak peak currents observed for the bare CPE indicate sluggish electron transfer kinetics and its poor electrical conductivity. The *f*-MWCNT-CPE/ChCl exhibited a notable increase in the peak current, which is attributed to the high surface area and conductivity of the *f*-MWCNTs. ChCl, known for its substantial adsorption capacity and effective film-forming properties, plays a crucial role in the accumulation of target analytes [23]. The higher anodic currents observed at Au–Ag-ANCCs/CPE are attributed to the combined effects of alloying and restructuring in Au–Ag-ANCCs. The alloying of Au and Ag enhances the electrical properties, while the nanocoral cluster structure increases conductivity by providing a large surface area for electron movement and reducing the distance that electrons travel [34]. The successive modification of Au–Ag-ANCCs/CPE with ChCl and *f*-MWCNTs resulted in a gradual enhancement in the peak current. Therefore, Au–Ag-ANCCs/*f*-MWCNTs-CPE/ChCl exhibited the highest peak current response due to the synergistic effects of all modifying nanocomposites.

As shown in Fig. 4B, SWV was utilized to further examine the voltammetric behavior of RAMP and NFX. The bare electrode had low anodic peak currents due to its low catalytic activity and negligible adsorption capacity. In contrast, Au–Ag-ANCCs/*f*-MWCNTs-CPE/ChCl exhibited the highest anodic peak current response because of its synergistically enhanced conductivity, large surface area, and strong electron transfer kinetics. This agreed well with the CV results. The ΔEp between RAMP and NFX was 632 mV, which is more than enough for the simultaneous determination of the analytes. Therefore, Au–Ag-ANCCs/*f*-MWCNTs-CPE/ChCl was successfully applied to simultaneously determine RAMP and NFX residues in water samples.

3.4. Optimization of experimental conditions

The Supplementary Material provides comprehensive information on optimizing the mixing ratio of nanocomposites, and the volume of drop-cast dispersions.

3.4.1. Effect of electrolyte solutions

The selection of an appropriate electrolyte solution significantly influences the voltammogram shapes and the resulting current intensity in voltammetric experiments. Therefore, it is vital to select a suitable supporting electrolyte before conducting electrochemical analysis. To assess the influence of different supporting electrolytes, SWV was employed. Various electrolyte solutions were tested, including phosphate buffer solution (PBS), citrate-phosphate buffer solution (CT-PBS), citrate buffer (CTB), Britton-Robinson buffer (BRB), acetate buffer solution (ABS), and H_2SO_4. Among the electrolytes examined, PBS showed the highest peak current response (Fig. S2). The current response of PBS was well-defined and sufficiently large for both analytes, confirming its superiority as an optimal medium. Therefore, PBS was selected as a suitable electrolyte solution to simultaneously determine the residues of RAMP and NFX.

3.4.2. Effect of pH

The influence of pH variation on the voltammetric responses of 15 μM RAMP and NFX was examined using SWV at a scan rate of 25 mVs^{-1}.

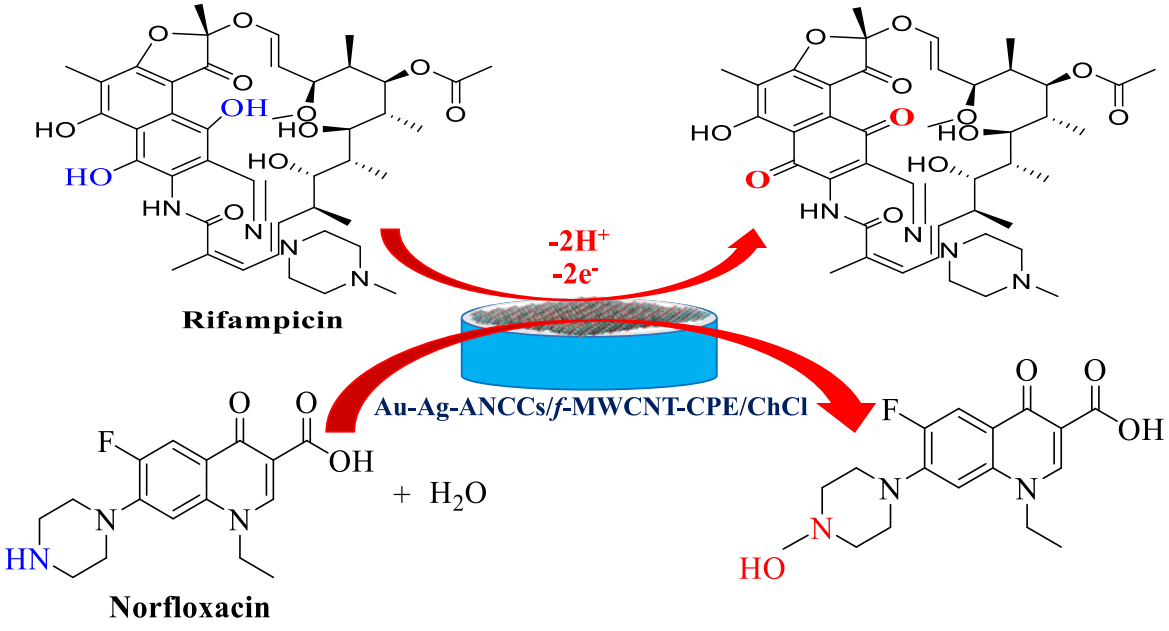

Scheme 1. Schematic illustration of the electro-oxidation of RAMP and NFX.

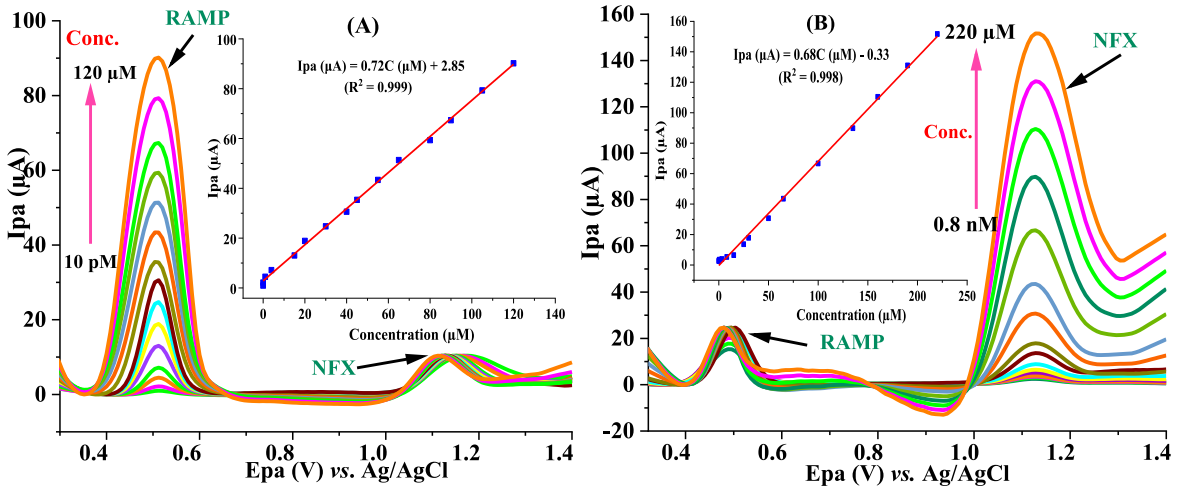

Fig. 6. SWVs for different concentrations RAMP (A) and NFX (B) (Inset: Ipa *vs.* conc.).

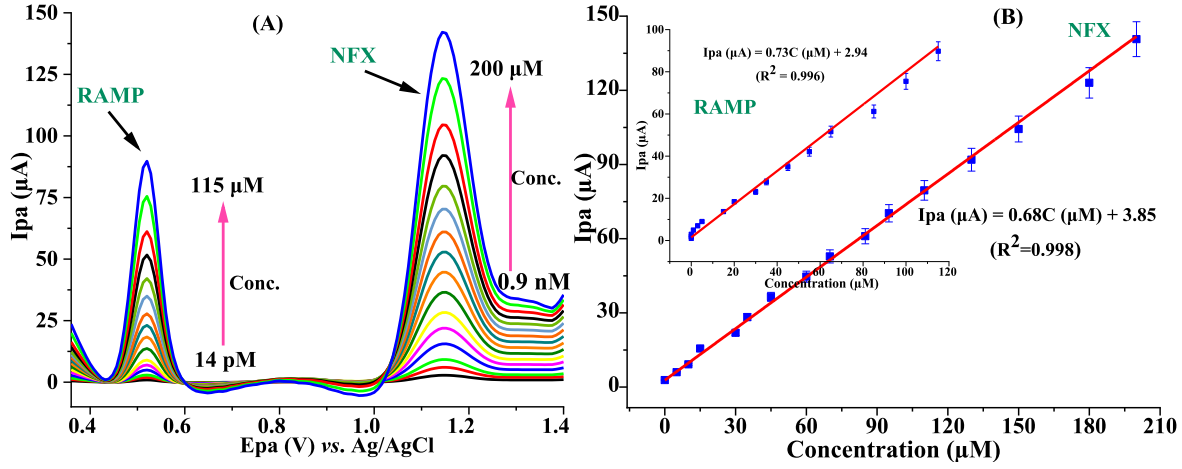

Fig. 7. (A) SWVs of different concentration of RAMP and NFX and (B) Ipa (µA) *vs.* conc. of NFX (Inset: Ipa *vs.* conc. of RAMP).

The Ipa (µA) of both RAMP and NFX gradually increases with an increase in pH, ranging from 3.0 to 5.0 (Fig. 5B(a) and C(a)). However, a subsequent increase in pH resulted in a decrease in current responses. The increase in anodic current up to pH 5.0 and the subsequent decline at higher pH values are due to a complex interplay of factors, including the availability of protons, changes in electrolyte composition, alterations in electrode potential, and other side reactions. Consequently, the optimal pH for further use was determined to be 5.0. Furthermore, the anodic potential of both RAMP and NFX shifted to less positive values with an increase in pH (Fig. 5A). The shift in potential indicates the active involvement of protons (H^+) in the analytes electro-oxidation. To quantify this relationship, a linear correlation was established between pH and oxidation potential, given by the equations Epa (V) = −0.05 pH + 0.79 (R^2 = 0.996) (Fig. 5B(b)) for RAMP and Epa (V) = −0.051 pH + 1.41 (R^2 = 0.997) (Fig. 5C(b)) for NFX. Notably, the slope values of 50 and 51 mV/pH for RAMP and NFX, respectively, closely equals the Nernstian theoretical value (59 mV/pH). It suggests that the electro-oxidation of RAMP and NFX involves the transfer of an equal number of electrons and protons, which aligns with the findings of previous reports [7,13].

3.4.3. *Effect of scan rate*

Electrochemical examination was performed using CV to investigate how varying the scan rate from 25 to 300 mVs^{-1} affects Ipa (µA) and Epa (V) of 15 µM RAMP and NFX. As depicted in Figs. S3A and B, the current intensity of both RAMP and NFX steadily increases with an increase in the scan rate, accompanied by a shift in potential towards less negative values. These findings imply that the electro-oxidation of both analytes at the surface of Au–Ag-ANCCs/*f*-MWCNTs-CPE/ChCl follows an irreversible electrode process. Regression equations were formulated to establish a correlation between the current response and the square root of the scan rate. The equations are Ipa (µA) = $21.22\nu^{1/2}$ $(mVs^{-1})^{1/2}$–46.09 (R^2 = 0.992) (Fig. S3C(a)) and Ipa (µA) = $7.96\ \nu^{1/2}$ $(mVs^{-1})^{1/2}$ + 5.92, (R^2 = 0.993) (Fig. S3C(b)) for RAMP and NFX, respectively. Furthermore, log Ipa *vs.* log *ν* plots were constructed to analyze the behavior of the analytes towards the electrode. The log Ipa (µA) *vs.* log *ν* (mVs^{-1}) for RAMP and NFX resulted in linear regression equations with slopes of 0.48 and 0.59, respectively (Fig. S3D(a and b)). The proximity of the slope values to the theoretical value of 0.5 suggests that the reaction of RAMP and NFX at the Au–Ag-ANCCs/*f*-MWCNTs-CPE/ChCl surface is predominantly controlled by diffusion processes [35,36]. To quantify the number of electrons involved in the electrode reaction, Equation (2) was employed [23].

$$E_p = E^0 + \frac{2.303RT}{\alpha nF}\log\frac{RTk^0}{\alpha nF} + \frac{2.303RT}{\alpha nF}\log \nu \quad (2)$$

where, E^0 = formal potential, *ν* = scan rate, T = temperature, F = Faraday constant, k^0 = heterogeneous rate constant, R = universal gas constant, and n = number of electrons. A strong linear correlation was

Table 1
Comparison of the developed device in the context of existing sensors.

Electrodes	Analytes	Samples	Linear range (μM)	LOD (μM)	Ref.
GCE/NiHCF	RAMP	Urine	19.6–170	0.65	[38]
PMel-Au_{nano}/GCE	RAMP	Biological samples	0.08–15	0.03	[7]
TFA@Nb_2CT_x	RAMP	Pharmaceutical and blood serum	100 pM–1.0	4.8 pM	[9]
C-dots/$CuFe_2O_4$/CPE	RAMP	Biological fluids and pharmaceuticals	0.07–8	0.022	[39]
MWCNT/MnO_2/AuNPs/GCE	RAMP	Blood serum and Tablets	0.75–200	0.25	[40]
Au–Ag-ANCCs/*f*-MWCNTs-CPE/ChCl	RAMP	Water samples	14 pM–115	2.7 pM	This work
MWCNT-CPE/pRGO-ANSA/Au	NFX	Pharmaceutical and rat plasma	0.03–1.0 1.0–50	0.016	[15]
MIP/MWCNT/GCE	NFX	Urine	0.1–8	0.046	[41]
APT-BDD	NFX	Urine	0.157–12.5	0.04	[42]
CuO/MWCNTs/GCE	NFX	Tablets	1.0–47.7	0.321	[14]
Au–Ag-ANCCs/*f*-MWCNTs-CPE/ChCl	NFX	Water samples	0.0009–200	0.00014	This work

observed between Epa (V) and log ν (mVs^{-1}) for RAMP and NFX. The slope of each plot corresponding to 2.303RT/αnF was used to calculate αn. The values of αn were 0.865 for RAMP and 0.804 for NFX. The transfer coefficient (α) is typically assumed to be 0.5 for irreversible electrode reactions [37]. The number of electrons (n) involved in the electro-oxidation of RAMP and NFX are 1.73 and 1.61, respectively, which is closely to two. It is in close agreement with previous reports [7,15], which showed that the voltammetric oxidation of RAMP and NFX involves the transfer of two protons and two electrons. The schematic illustration for the electro-oxidation of RAMP and NFX is given in Scheme 1.

3.4.4. Optimization of SWV parameters

SWV responses are largely dependent on three instrumental parameters: the amplitude, frequency, and step potential. Herein, the effect of these experimental parameters on the current responses of 15 μM RAMP and NFX was examined. First, the effect of amplitude was examined within the range of 10–70 mV while keeping the step potential and frequency constant. The anodic current gradually increased up to 50 mV for both analytes and then declined (Fig. S4A). Therefore, 50 mV was set as the optimal amplitude for next the measurements. Next, while keeping the amplitude and step potential constant, the frequency was varied from 20 to 90 Hz. As shown in Fig. S4B, both analytes exhibited the maximum current response at 70 Hz. Therefore, 70 Hz was selected as the optimal frequency to determine the analytes. Finally, the influence of the step potential was examined within the range of 2–14 mV while maintaining constant amplitude and frequency. The current responses of both RAMP and NFX increased up to 10 mV, but further increases in the step potential resulted in a decrease in peak current (Fig. S4C). Consequently, a step potential of 10 mV was selected as the optimal value for subsequent experiments.

3.5. Determination of RAMP and NFX

3.5.1. Individual determination of RAMP and NFX

The SWV responses were carefully monitored in 0.1 M PBS under optimized experimental conditions, using various concentrations of RAMP and NFX. The anodic current response of RAMP and NFX exhibited a significant increase with increasing concentration (Fig. 6A and B). While examining RAMP individually, the oxidation current and concentration showed a strong correlation in the linear range of 10 pM–120 μM, given by the equation Ipa (μA) = 0.72C (μM) + 2.85, (R^2 = 0.999) (Fig. 6A and the inset graph). The LOD (3σ/m, S/N = 3, n = 5) and LOQ (10σ/m, S/N = 3, n = 5) were calculated to be 2.33 pM and 7.78 pM, respectively. Similarly, NFX exhibits a linear response from 0.8 nM to 220 μM, expressed by the equation Ipa (μA) = 0.68C (μM) - 0.33 (R2 = 0.998) (Fig. 6B and inset graph). Notably, LOD and LOQ are found to be 0.16 nM and 0.53 nM, respectively. The exceptionally low LOQ and LOD values highlight the remarkable sensing capability of the developed sensor, positioning it as an ideal tool for the accurate and precise detection of RAMP and NFX residues in water samples.

3.5.2. Simultaneous determination of RAMP and NFX

This research aimed to develop an ultra-sensitive voltammetric sensor for simultaneously detecting RAMP and NFX residues in water samples using Au–Ag-ANCCs/*f*-MWCNTs-CPE/ChCl. Subsequently, SWV was conducted under the optimized experimental conditions within a potential range of 0.2–1.4 V. Fig. 7A illustrates a linear increase in oxidation current corresponding to the concentrations of the analytes. A strong correlation was observed between concentration and the anodic current, ranging from 14 pM to 115 μM for RAMP and 0.9 nM to 200 μM for NFX, given by the equations: Ipa (μA) = 0.73C (μM) + 2.94 (R^2 = 0.996) for RAMP (Fig. 7B inset plot) and Ipa (μA) = 0.68C (μM) +

Table 2
Summary of spiking experiment results.

Samples	Spiked (μM)	Found (μM)		Recovery (%)		RSD (%)	
		RAMP	NFX	RAMP	NFX	RAMP	NFX
Tap water	0	–	–	–	–	–	–
	5	4.93	4.86	98.6	97.2	2.46	2.33
	15	15.24	14.87	101.6	99.1	2.59	2.51
	25	24.69	24.26	98.8	97	3.23	1.62
	35	35.17	35.82	100.5	102.3	1.74	1.89
River water	0	0.11	0.24	–	–	3.49	3.27
	5	5.12	5.08	98.2	98.8	2.49	2.65
	15	14.74	15.39	96.9	101.7	1.53	1.52
	25	25.26	24.56	100.2	97.7	2.84	2.6
	35	36.22	34.83	102.9	99.1	2.59	2.38
Hospital wastewater	0	0.17	0.29	–	–	3.56	4.16
	5	5.42	5.25	103	101.2	2.56	2.43
	15	15.02	14.71	98.3	96.8	1.78	1.94
	25	25.71	25.91	101.8	102.9	2.52	2.69
	35	34.43	34.98	97.6	99.4	2.72	2.59

3.85 ($R^2 = 0.998$) for NFX (Fig. 7B). The LOD and LOQ for RAMP were calculated as 2.7 pM and 8.85 pM, respectively, and for NFX, determined as 0.14 nM and 0.47 nM, respectively. The remarkably low LOD and LOQ values obtained while simultaneously determining RAMP and NFX affirm the exceptional capability of the sensor in detecting ultra-trace concentrations of these potentially hazardous residues in environmental samples. Moreover, the sensor's heightened sensitivity elevates it to the forefront of electroanalytical chemistry, demonstrating its status as a cutting-edge analytical tool. This combination of sensitivity and analytical performance distinguishes the Au–Ag-ANCCs/*f*-MWCNTs-CPE/ChCl as a pioneering platform in the field.

The efficiency of the developed sensor was assessed in comparison to sensors recently documented in the literature. The comparison relies on the basic parameters, particularly LOD and linear range. The proposed sensor outperformed existing sensors with significantly lower LOD and a broad linear range, as shown in Table 1. The remarkable performance can be ascribed to the outstanding characteristics of the sensor, including a higher electroactive surface area, high electrocatalytic activity, and enhanced electrical conductivity, due to the synergistic effects of the introduced modifiers, Au–Ag-ANCCs, *f*-MWCNTs-CPE, and ChCl. Therefore, Au–Ag-ANCCs/*f*-MWCNTs-CPE/ChCl emerged as a new standard for simultaneously determining RAMP and NFX residues in water samples.

3.6. Repeatability, reproducibility and stability

SWV is a versatile electrochemical method for assessing the performance of modified electrodes. It is an ideal technique for evaluating the reproducibility, repeatability, and stability of modified electrodes. Here, SWV was used to evaluate these aspects for Au–Ag-ANCCs/*f*-MWCNTs-CPE/ChCl while quantifying RAMP and NFX simultaneously. First, the repeatability was assessed by performing nine consecutive measurements of 15 μM RAMP and NFX (Fig. S5A). The RSD values for the anodic current responses were 4.32 % for RAMP and 4.28 % for NFX, indicating acceptable repeatability for simultaneously determining the analytes. Next, nine replicate square wave measurements were performed using a single electrode to evaluate the reproducibility of Au–Ag-ANCCs/*f*-MWCNTs-CPE/ChCl. The RSD values were 1.75 % for RAMP and 1.49 % for NFX (Fig. S5B), indicating that the sensor exhibits exceptional reproducibility in quantifying the analytes. Finally, the current responses of the sensor were monitored weekly for seven weeks to assess its storage stability. It was stored at 4 °C after each weekly use. Remarkably, the sensor demonstrated long-term stability, with anodic current responses decreasing by 10.09 % for RAMP and 9.8 % for NFX over the entire storage period (Fig. S5C).

3.7. Selectivity

The selectivity of Au–Ag-ANCCs/*f*-MWCNTs-CPE/ChCl was evaluated by measuring the current response to 15 μM of RAMP and NFX in the presence of potentially interfering substances. The tolerance limit, which is the highest concentration of interferents that results in a relative percentage error of less than 5 % for analyte determination, was determined. As illustrated in Table S1, the detection of 15 μM RAMP and NFX was not significantly affected by the presence of potentially interfering substances, even at higher concentrations. Commonly co-existing antibiotics (cephalexin, chloramphenicol, tinidazole, azithromycin, ampicillin, cloxacillin, and amoxicillin) at 150-fold excess amounts, organic compounds (sucrose, folic acid, fructose, glucose, uric acid, dopamine, urea, vitamin C, and lactose) at 250-fold excess concentrations, and inorganic species (HCO_3^-, NO_3^-, SO_4^{2-}, CO_3^{2-}, Cl^-, Ca^{2+}, K^+, Mg^{2+}, Cu^{2+}, and Fe^{3+}) at 750-fold excess concentrations did not considerably affect the detection of RAMP and NFX. The relative percentage error values were below five percent for all interferents, confirming the high selectivity of the developed sensor.

3.8. Real sample analysis

The performance of the fabricated sensor for simultaneously determining RAMP and NFX residues in water samples was assessed using SWV. Various concentrations (0, 5, 15, 25, and 35 μM) of RAMP and NFX were spiked into the water samples and analyzed without any pretreatment. The practical applicability of Au–Ag-ANCCs/*f*-MWCNTs-CPE/ChCl was examined using the standard addition method (Table 2). No voltammetric signals were detected for either RAMP or NFX in unspiked tap water samples, indicating either the absence of the analytes or concentrations below detectable limits. Whereas, the current responses increased linearly with the successive addition of standard solutions. The recoveries of RAMP and NFX ranged from 96.9 % to 103 % and 96.8 %–102.9 %, respectively, demonstrating the accuracy and precision of the developed method. In contrast, unspiked river and hospital wastewater samples exhibited strong peak current responses, suggesting the presence of polluting residues of RAMP and NFX. The recoveries for river water (96.9 %–102.9 % for RAMP and 97.7 %–101.7 % for NFX) and hospital wastewater (97.6 %–103 % for RAMP and 96.8 %–102.9 % for NFX) were impressive and reassuring, confirming the reliability and efficiency of the sensor. The overall average recoveries ranged from 96.8 % to 103 %, with RSD below 5 %. This consistent and robust performance highlights the practical utility of Au–Ag-ANCCs/*f*-MWCNTs-CPE/ChCl for simultaneously detecting RAMP and NFX residues in water samples.

4. Conclusions

Herein, a novel ultrasensitive electrochemical sensing platform was developed for simultaneously detecting RAMP and NFX residues in water samples. Thorough comprehensive analyses of surface morphology and elemental composition were performed using various analytical and electrochemical techniques, Au–Ag-ANCCs/*f*-MWCNTs-CPE/ChCl exhibited superior performance, surpassing recently reported sensors by its lowest LOD and broader linear range. This superiority is attributed to its exceptional features, including a larger electroactive surface area, high electrocatalytic activity, and enhanced electrical conductivity. The sensor showed excellent selectivity; even in the presence of several coexisting interferents, including organic, inorganic, and antibiotic species, its current response was not significantly affected. Furthermore, it exhibited long-lasting stability, outstanding reproducibility, and repeatability. Finally, the sensor was successfully applied for simultaneously detecting RAMP and NFX residues in hospital wastewater, river water, and tap water samples. The analysis result showed the presence of RAMP and NFX residues in Akaki River and hospital wastewater samples, suggesting a potential threats to human health and ecosystems. To mitigate these risks, different measures such as proper medication disposal, enhanced wastewater treatment, stringent regulations, prudent antibiotic use, and public awareness are imperative. Collaboration among scientists, policymakers, and stakeholders is vital to addressing this issue through research, advocacy, technological advancements, and community engagement. In general, Au–Ag-ANCCs/*f*-MWCNTs-CPE/ChCl emerges as an ideal candidate for real-time monitoring of life-threatening residues of RAMP and NFX in water sources, offering promising solutions to safeguard water quality and human health.

CRediT authorship contribution statement

Wondimeneh Dubale Adane: Writing – original draft, Validation, Resources, Methodology, Investigation, Formal analysis, Data curation, Conceptualization. **Bhagwan Singh Chandravanshi:** Writing – review & editing, Supervision, Conceptualization. **Negash Getachew:** Writing – original draft, Supervision, Conceptualization. **Merid Tessema:** Supervision, Conceptualization.

Declaration of competing interest

The authors declare that they have no known competing financial interests or personal relationships that could have appeared to influence the work reported in this paper.

Data availability

No data was used for the research described in the article.

Acknowledgements

The authors express their gratitude to the Department of Chemistry at Addis Ababa University, Addis Ababa, Ethiopia, for generously offering the laboratory resources.

Appendix A. Supplementary data

Supplementary data to this article can be found online at https://doi.org/10.1016/j.aca.2024.342746.

References

[1] R. Lopez, S. Khan, A. Wong, M. Sotomayor, P.T. del, G. Picasso, Development of a new electrochemical sensor based on mag-MIP selective toward amoxicillin in different samples, Front. Chem. 9 (2021) 615602, https://doi.org/10.3389/fchem.2021.615602.
[2] R. Ding, Y. Chen, Q. Wang, Z. Wu, X. Zhang, B. Li, L. Lin, Recent advances in quantum dots-based biosensors for antibiotics detection, J. Pharm. Anal. 12 (3) (2022) 355–364, https://doi.org/10.1016/j.jpha.2021.08.002.
[3] C. Yılmaz, G. Ozcengiz, Antibiotics: pharmacokinetics, toxicity, resistance and multidrug efflux pumps, Biochem. Pharmacol. 133 (2017) 43–62, https://doi.org/10.1016/j.bcp.2016.10.005.
[4] K. Balamurugan, R. Rajakumaran, S.M. Chen, R. Karthik, J.J. Shim, P.M. Shafi, Massive engineering of spinel cobalt tin oxide/tin oxide-based electrocatalyst for the selective voltammetric determination of antibiotic drug furaltadone in water samples, J. Alloys Compd. 882 (2021) 160750, https://doi.org/10.1016/j.jallcom.2021.160750.
[5] L. Fu, S. Mao, F. Chen, S. Zhao, W. Su, G. Lai, A. Yu, C.T. Lin, Graphene-based electrochemical sensors for antibiotic detection in water, food and soil: a scientometric analysis in citespace (2011–2021), Chemosphere 297 (2022) 134127, https://doi.org/10.1016/j.chemosphere.2022.134127.
[6] J. Chen, G.G. Ying, W.J. Deng, Antibiotic residues in food: extraction, analysis, and human health concerns, J. Agric. Food Chem. 67 (27) (2019) 7569–7586, https://doi.org/10.1021/acs.jafc.9b01334.
[7] S. Amidi, Y.H. Ardakani, M. Amiri-Aref, E. Ranjbari, Z. Sepehri, H. Bagheri, Sensitive electrochemical determination of rifampicin using gold nanoparticles/poly-melamine nanocomposite, RSC Adv. 7 (64) (2017) 40111–40118, https://doi.org/10.1039/C7RA04865C.
[8] H. Soni, DrV.K. Gautam, S. Sharma, J.K. Malik, Rifampicin as potent inhibitor of COVID - 19 main protease: in-silico docking approach, SJMPS 6 (9) (2020) 588–593, https://doi.org/10.36348/sjmps.2020.v06i09.001.
[9] M. Ankitha, N. Shabana, P.V. Vaishag, P.A. Rasheed, A novel flexible electrode with highly stable trifluoroacetic acid modified Nb_2CT MXene for the sensitive detection of rifampicin, J. Electroanal. Chem. 928 (2023) 117088, https://doi.org/10.1016/j.jelechem.2022.117088.
[10] F. Zivari-Moshfegh, F. Javanmardi, D. Nematollahi, A comprehensive electrochemical study on anti-tuberculosis drug rifampicin. Investigating reactions of rifampicin-quinone with other anti-tuberculosis drugs, isoniazid, pyrazinamide and ethambutol, Electrochim. Acta 457 (2023) 142487, https://doi.org/10.1016/j.electacta.2023.142487.
[11] W. Cai, X. Weng, Z. Chen, Highly efficient removal of antibiotic rifampicin from aqueous solution using green synthesis of recyclable nano-Fe_3O_4, Environ. Pollut. 247 (2019) 839–846, https://doi.org/10.1016/j.envpol.2019.01.108.
[12] M. Shafaati, M. Miralinaghi, R.H.S.M. Shirazi, E. Moniri, The use of chitosan/Fe_3O_4 grafted graphene oxide for effective adsorption of rifampicin from water samples, Res. Chem. Intermed. 46 (12) (2020) 5231–5254, https://doi.org/10.1007/s11164-020-04259-9.
[13] M. Devaraj, R.K. Deivasigamani, S. Jeyadevan, Enhancement of the electrochemical behavior of CuO nanoleaves on MWCNTs/GC composite film modified electrode for determination of norfloxacin, Colloids Surf., B 102 (2013) 554–561, https://doi.org/10.1016/j.colsurfb.2012.08.051.
[14] O.T. Vu, Q.H. Nguyen, T. Nguy Phan, T.T. Luong, K. Eersels, P. Wagner, L.T. N. Truong, Highly sensitive molecularly imprinted polymer-based electrochemical sensors enhanced by gold nanoparticles for norfloxacin detection in aquaculture water, ACS Omega 8 (3) (2023) 2887–2896, https://doi.org/10.1021/acsomega.2c04414.
[15] Z. Liu, M. Jin, J. Cao, J. Wang, X. Wang, G. Zhou, A. Van Den Berg, L. Shui, High-sensitive electrochemical sensor for determination of norfloxacin and its metabolism using MWCNT-CPE/pRGO-ANSA/Au, Sens. Actuators B Chem. 257 (2018) 1065–1075, https://doi.org/10.1016/j.snb.2017.11.052.
[16] B. Prutthiwanasan, C. Phechkrajang, L. Suntornsuk, Fluorescent labelling of ciprofloxacin and norfloxacin and its application for residues analysis in surface water, Talanta 159 (2016) 74–79, https://doi.org/10.1016/j.talanta.2016.05.080.
[17] P. Veerakumar, C. Koventhan, S.M. Chen, Copper-palladium alloy nanoparticles immobilized over porous carbon for voltammetric determination of dimetridazole, J. Alloys Compd. 931 (2023) 167474, https://doi.org/10.1016/j.jallcom.2022.167474.
[18] G. Das, S. Seo, I.J. Yang, L.T.H. Nguyen, H.S. Shin, J.K. Patra, Sericin mediated gold/silver bimetallic nanoparticles and exploration of its multi-therapeutic efficiency and photocatalytic degradation potential, Environ. Res. 229 (2023) 115935, https://doi.org/10.1016/j.envres.2023.115935.
[19] L. Feng, G. Gao, P. Huang, K. Wang, X. Wang, T. Luo, C. Zhang, Optical properties and catalytic activity of bimetallic gold-silver nanoparticles, Nano Biomed. Eng. 2 (4) (2010) 258–267, https://doi.org/10.5101/nbe.v2i4.p258-267.
[20] J. Huang, Y. Xiang, J. Li, Q. Kong, H. Zhai, R. Xu, F. Yang, X. Sun, Y. Guo, A novel electrochemiluminescence aptasensor based on copper-gold bimetallic nanoparticles and its applications, Biosens. Bioelectron. 194 (2021) 113601, https://doi.org/10.1016/j.bios.2021.113601.
[21] B. Arumugram, S. Palanisamy, S.K. Ramaraj, M. Chiesa, Single-crystalline MoO_3/functionalized multiwalled carbon nanotube nanocomposites for sensing phenothiazine in biological samples, Surf. Interfaces. 38 (2023) 102829, https://doi.org/10.1016/j.surfin.2023.102829.
[22] O.F. Farag, E. Abdel-Fattah, Synthesis and characterization PVA/plasma-functionalized MWCNTs nanocomposites films, J. Polym. Res. 30 (5) (2023) 183, https://doi.org/10.1007/s10965-023-03550-8.
[23] W.D. Adane, B.S. Chandravanshi, M. Tessema, A Simple, ultrasensitive and cost-effective electrochemical sensor for the determination of ciprofloxacin in various types of samples, Sens. Bio-Sens. Res. 39 (2023) 100547, https://doi.org/10.1016/j.sbsr.2022.100547.
[24] X. Wu, X. Che, Z. Qiu, J. Chao, Z. Kong, H. Li, Simultaneous determination of three antituberculosis drugs in the serum of patients with spinal tuberculosis by capillary electrophoresis, Anal. Methods 13 (37) (2021) 4307–4313, https://doi.org/10.1039/D1AY00711D.
[25] S.A. Al-Tamrah, M.A. Abdalla, A.A. Al-Otibi, Spectrophotometric determination of norfloxacin using bromophenol blue, Arab. J. Chem. 12 (8) (2019) 3993–3997, https://doi.org/10.1016/j.arabjc.2015.02.005.
[26] R. Shokri, M. Amjadi, Boron and nitrogen Co-doped carbon dots as a chemiluminescence probe for sensitive assay of rifampicin, J. Photochem. Photobiol., A 425 (2022) 113694, https://doi.org/10.1016/j.jphotochem.2021.113694.
[27] M. Gamal, H.M. Ali, S.M. Fraihat, T.A. Seaf Elnasr, Simultaneous determination of piroxicam and norfloxacin in biological fluids by high-performance liquid chromatography with fluorescence detection at zero-order emission mode, Lumin. 34 (6) (2019) 644–650, https://doi.org/10.1002/bio.3648.
[28] W.D. Adane, B.S. Chandravanshi, M. Tessema, Highly sensitive and selective electrochemical sensor for the simultaneous determination of tinidazole and chloramphenicol in food samples (egg, honey and milk), Sens. Actuators B Chem. 390 (2023) 134023, https://doi.org/10.1016/j.snb.2023.134023.
[29] M. Konni, A.S. Dadhich, S. Babu Mukkamala, Impact of surface modifications on hydrogen uptake by Fe@f-MWCNTs and Cu@f-MWCNTs at non-cryogenic temperatures, Int. J. Hydrogen Energy 42 (2) (2017) 953–959, https://doi.org/10.1016/j.ijhydene.2016.09.085.
[30] M. Khatami, S. Pourseyedi, M. Khatami, H. Hamidi, M. Zaeifi, L. Soltani, Synthesis of silver nanoparticles using seed exudates of sinapis arvensis as a novel bioresource, and evaluation of their antifungal activity, Bioresour. Bioprocess. 2 (1) (2015) 19, https://doi.org/10.1186/s40643-015-0043-y.
[31] S.S. Godipurge, S. Yallappa, N.J. Biradar, J.S. Biradar, B.L. Dhananjaya, G. Hegde, K. Jagadish, G. Hegde, A facile and green strategy for the synthesis of Au, Ag and Au–Ag alloy nanoparticles using aerial parts of R. hypocrateriformis extract and their biological evaluation, Enzyme Microb. Technol. 95 (2016) 174–184, https://doi.org/10.1016/j.enzmictec.2016.08.006.
[32] Z. Zhu, H.N. Luk, Y.S. Liu, R.J. Wu, M.H. Chung, X.J. Chang, Preparation of bimetallic Au-Pd/MWCNTs electrode for detection of dopamine, Minerals 12 (9) (2022) 1145, https://doi.org/10.3390/min12091145.
[33] Y. Jiang, Y. Li, Y. Li, S. Li, A sensitive enzyme-free hydrogen peroxide sensor based on a chitosan–graphene quantum dot/silver nanocube nanocomposite modified electrode, Anal. Methods 8 (11) (2016) 2448–2455, https://doi.org/10.1039/C5AY02976G.
[34] Y. Tong, X. Yan, J. Liang, S.X. Dou, Metal-based electrocatalysts for methanol electro-oxidation: progress, opportunities, and challenges, Small 17 (9) (2021) 1904126, https://doi.org/10.1002/smll.201904126.
[35] X. Cui, D. Cao, R. Djellabi, M. Qiao, Y. Wang, S. Zhao, R. Mao, Y. Gong, X. Zhao, B. Yang, Enhancement of Ni/NiO/graphitized carbon and β-cyclodextrin/reduced graphene oxide for the electrochemical detection of norfloxacin in water sample, J. Electroanal. Chem. 851 (2019) 113407, https://doi.org/10.1016/j.jelechem.2019.113407.
[36] D. Kul, Electrochemical determination of rifampicin based on its oxidation using multi-walled carbon nanotube-modified glassy carbon electrodes, Turk J. Pharm. Sci. 17 (4) (2020) 398–407, https://doi.org/10.4274/tjps.galenos.2019.33600.
[37] Z. Liu, Y. Zhou, Y. Wang, Q. Cheng, K. Wu, Enhanced oxidation and detection of toxic ractopamine using carbon nanotube film-modified electrode, Electrochim. Acta 74 (2012) 139–144, https://doi.org/10.1016/j.electacta.2012.04.041.
[38] P.R. Oliveira, A.F. Schibelbain, E.G.C. Neiva, A.J.G. Zarbin, L.H. Marcolino, M. F. Bergamini, Nickel Hexacyanoferrate supported at nickel nanoparticles for

voltammetric determination of rifampicin, Sens. Actuators B Chem. 260 (2018) 816–823, https://doi.org/10.1016/j.snb.2017.12.198.

[39] S. Shiri, N. Pajouheshpoor, H. Khoshsafar, S. Amidi, H. Bagheri, An electrochemical sensor for the simultaneous determination of rifampicin and isoniazid using a C-dots@$CuFe_2O_4$ nanocomposite modified carbon paste electrode, New J. Chem. 41 (24) (2017) 15564–15573, https://doi.org/10.1039/C7NJ03029K.

[40] E. Khezerloo, F. Hekmat, S. Shahrokhian, A.I. Zad, Sensitive voltammetric determination of rifaximin by electrode modified by nanocomposite of MWCNT/MnO_2/AuNPs, Diam. Relat. Mater. 139 (2023) 110280, https://doi.org/10.1016/j.diamond.2023.110280.

[41] H. Da Silva, J. Pacheco, J. Silva, S. Viswanathan, C. Delerue-Matos, Molecularly imprinted sensor for voltammetric detection of norfloxacin, Sens. Actuators B Chem. 219 (2015) 301–307, https://doi.org/10.1016/j.snb.2015.04.125.

[42] F. Karahan, Z. Başı, E. Keskin, P.T. Pınar, Y. Yardım, Z. Şentürk, Electrochemical determination of fluoroquinolone antibiotic norfloxacin in the presence of anionic surfactant using the anodically pretreated boron-doped diamond electrode, ChemistrySelect 5 (42) (2020) 12862–12868, https://doi.org/10.1002/slct.202002921.

Supplementary Material

A cutting-edge electrochemical sensing platform for the simultaneous determination of the residues of antimicrobial drugs, rifampicin and norfloxacin, in water samples

Wondimeneh Dubale Adane[a], Bhagwan Singh Chandravanshi*[a], Negash Getachew[a], Merid Tessema** [a]

[a] Department of Chemistry, Addis Ababa University, P. O. Box 1176, Addis Ababa, Ethiopia
* Corresponding author. E-mail address: bscv2006@yahoo.com
** Corresponding author. E-mail address: tessemamerid@yahoo.com

Rifampicin and norfloxacin selection and their relationship

The selection of rifampicin and norfloxacin for the present study stems from their essential role in clinical settings, where they are commonly prescribed for bacterial infections across a range of illnesses. Given their widespread use, these antibiotics are commonly found in environmental matrices such as water, soil, and food products, highlighting the importance of monitoring them to ensure public health and safety.

Regarding the relationship between rifampicin and norfloxacin, it is important to note that they belong to different classes of antibiotics and are used to treat different types of bacterial infections. Rifampicin is a broad-spectrum antibiotic commonly used to treat tuberculosis and other bacterial infections, while norfloxacin belongs to the fluoroquinolone class of antibiotics and is primarily used to treat urinary tract infections and certain gastrointestinal infections. Despite their differences, both rifampicin and norfloxacin are frequently found together in environmental samples because of their widespread use. Therefore, studying the occurrence and behavior of these antibiotics collectively provides valuable insights into their environmental fate, potential interactions, and overall effect on public and environmental health.

The development of innovative electrochemical sensors for detecting rifampicin and norfloxacin in water samples is crucial for ensuring human and environmental safety. Given that antibiotic residues in water sources pose risks such as antibiotic resistance and adverse effects on

aquatic ecosystems. Therefore, sensitive and selective electrochemical sensors play a vital role in monitoring and mitigating antibiotic contamination, safeguarding human and environmental health.

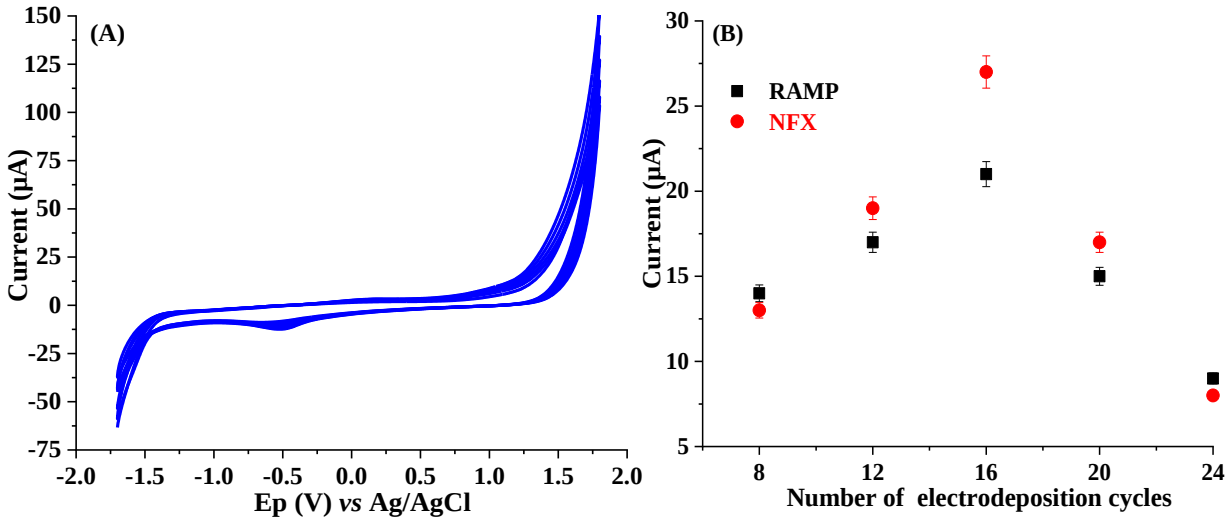

Fig. S1. (A) CV for the electrochemical deposition of 0.002 M ChCl with 0.01 KCl in 0.1 M PBS (pH 7.0) at the surface of Au-Ag-ANCCs/*f*-MWCNTs-CPE for 16 cycles at scan rate of 25 mVs^{-1} in the potential range of -1.7 V to 1.6 V, and (B) plot for the optimization of the number of electrodeposition cycles *vs.* peak current of 15 µM RAMP and NFX.

Material characterization and electrochemical properties

Material characterization techniques, such as UV-Vis, FT-IR, XRD, EDX, and SEM play a crucial role in understanding the composition, structural and surface properties of the modified electrodes. By examining the structure and surface morphology, one can gain insights into the nature of the modifications and the resulting changes in electrochemical behavior.

1. Surface characterization helps in elucidating the nature of the modifications applied to the electrodes. For instance, SEM analysis can reveal changes in surface morphology, such as roughness or the presence of deposited layers. This information aids in understanding the structural changes induced by modifications and provides insights into the surface chemistry, composition, and functional groups introduced. These modifications can

significantly affect the electrochemical properties of the electrode by altering the surface energy, charge-transfer kinetics, and adsorption/desorption behavior of the analytes.

2. Modification of the electrodes often leads to changes in their functionality and electroactive surface area. For example, functionalization with specific molecules or nanoparticles can enhance electrocatalytic activity or increase the available surface area for electron transfer reactions. Material characterization techniques can quantify these changes by measuring parameters such as the surface roughness, surface area, and elemental composition. The observed increase in the electroactive surface area directly influences the sensitivity, selectivity, and detection limits of the sensor, in general, the electrochemical properties.

Therefore, the correlation between material characterization and electrochemical properties lies in understanding how structural modifications affect surface properties relevant to electrochemical processes. Characterization techniques provide valuable insights into the structural, morphological, and compositional properties of the electrodes, which directly influence their electrochemical behavior. By understanding how modifications impact the surface morphology, surface chemistry, composition, and electroactive surface area, electrode design can be optimized for enhanced electrochemical performance. This correlation underlines the importance of employing comprehensive characterization approaches to tailor the electrode properties and improve the sensor sensitivity, selectivity, and overall performance in electrochemical applications.

Effect of electrolyte solutions

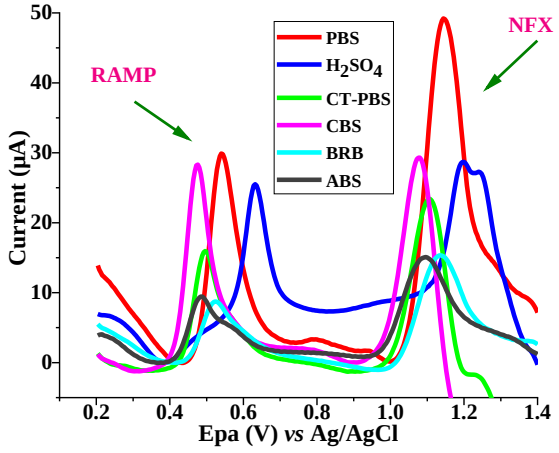

Fig. S2. SWVs of 25 µM RAMP and NFX in different supporting electrolyte solutions.

Optimization of the number of electrodeposition cycles

The number of polymerization cycles has a significant effect on the performance of the modified electrode. Increasing the number of cycle results in a thicker and more porous film, which enhances sensor sensitivity. However, an excessively high number of cycles can reduce film conductivity, diminishing the sensitivity of the sensor. We optimized the number of polymerization cycles by conducting polymerizations in a 0.1 M PBS (pH 7.0) containing 0.002 M ChCl and 0.01 M KCl in the potential range of -1.7 V to 1.6 V at a scan rate of 25 mVs^{-1} on Au-Ag-ANCCs/*f*-MWCNTs-CPE surface. As shown in Fig. S1B, the peak current response increased with the number of ChCl electrodeposition cycles at the Au-Ag-ANCCs/*f*-MWCNTs-CPE surface up to 16 cycles, after which it decreases. This decrease is due to the excessive accumulation of the ChCl film, which becomes thicker and more insulating. The thick layer hinders efficient electron transfer between the Au-Ag-ANCCs/*f*-MWCNTs-CPE/ChCl and the analytes, reducing electrode conductivity and sensitivity to analytes. Therefore, 16 electrodeposition cycles were chosen as the optimal value for subsequent experiments.

Optimization of the ratio of Au-Ag-ANCCs and *f*-MWCNTs

In the field of electrochemical sensors, optimizing the mixing ratio of nanocomposites is of great importance. This process allows researchers to improve the performance of a sensor to meet the specific requirements for different applications. In this study, we investigated the mixing ratio of Au-Ag-ANCCs and *f*-MWCNTs to achieve the highest peak current response in simultaneously detecting 15 µM RAMP and NFX in environmental samples. As shown in Fig. SA, the optimal mixing ratio of Au-Ag-ANCCs and *f*-MWCNTs, which produced the highest anodic peak current response was 1:1. The result indicates a remarkable synergy between the two nanocomposites. Au-Ag-ANCCs have the inherent properties of high electrical conductivity and electroactive surface area, which contribute significantly to the electrochemical response of the sensor. On the other hand, *f*-MWCNTs have unique properties such as robust mechanical strength and exceptional flexibility. When these two nanocomposites are mixed in a 1:1 ratio, their complementary properties helps to develop a sensor with remarkable sensitivity to the target analytes. This synergy, resulting from the interaction of Au-Ag-ANCCs and *f*-MWCNTs, is reflected in the ability of the sensor in the detection of RAMP and NFX. This makes it novel and an excellent

candidate for electrochemical applications that require high precision and accuracy. Therefore, we determined that the 1:1 ratio of Au-Ag-ANCCs and *f*-MWCNTs is the optimal configuration for fabricating Au-Ag-ANCCs/*f*-MWCNTs-CPE/ChCl.

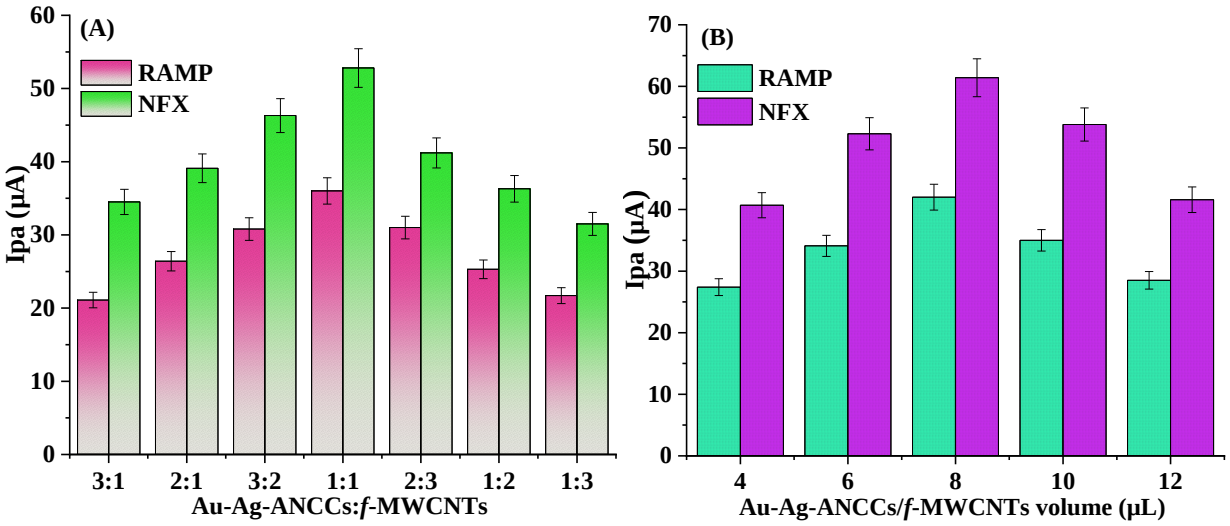

Fig. SM1. Optimization diagram for the mixing ratio of Au-Ag-ANCCs and *f*-MWCNTs (A) and drop-casted volume of Au-Ag-ANCCs/*f*-MWCNTs dispersion (B) to prepare the sensor.

Optimization of the drop-casted volume of nanocomposites

The volume of the drop-casted dispersion is vital because it can affect the thickness of the coating and the performance of a sensor. The optimal volume of the drop-casted dispersion depends on the specific sensor design and properties of the nanocomposite solution. A very small volume will result in a thin layer that may not be sufficient to cover the entire surface of the sensor. It can result in a poor signal transduction and reduced sensitivity. However, excess volume of the dispersion can result in a thick layer that can block the pores of the sensor and hinder the electrochemical reaction. Herein, the drop-casting volume of Au-Ag-ANCCs/*f*-MWCNTs dispersion was optimized to achieve the highest peak current response in simultaneously determining 15 µM RAMP and NFX in water samples at the surface of Au-Ag-ANCCs/*f*-MWCNTs-CPE/ChCl. As shown in Fig. SB, the optimal drop casting volume of the Au-Ag-ANCCs/*f*-MWCNTs dispersion, which produced the highest anodic peak current response was 8

µL. Therefore, 8 µL of Au-Ag-ANCCs/*f*-MWCNTs dispersion was selected as the optimum value for preparing the proposed sensor in subsequent experiments.

Effect of scan rate

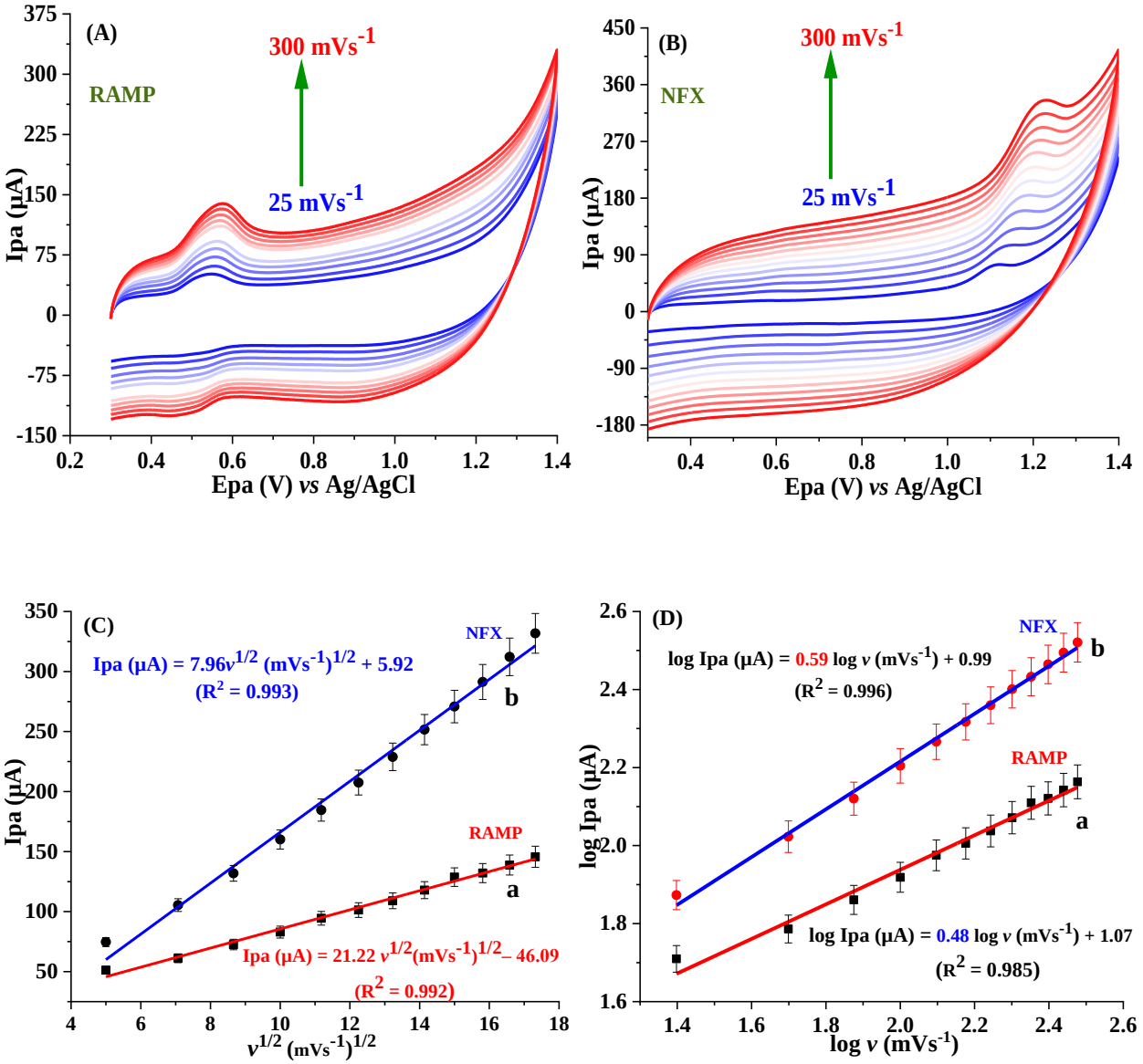

Fig. S3. CVs of 15 µM RAMP (A) and NFX (B) at different scan rates, plots of Ipa *vs.* $v^{1/2}$ (C), and log Ipa *vs*. log *v* (D).

Optimization of SWV parameters

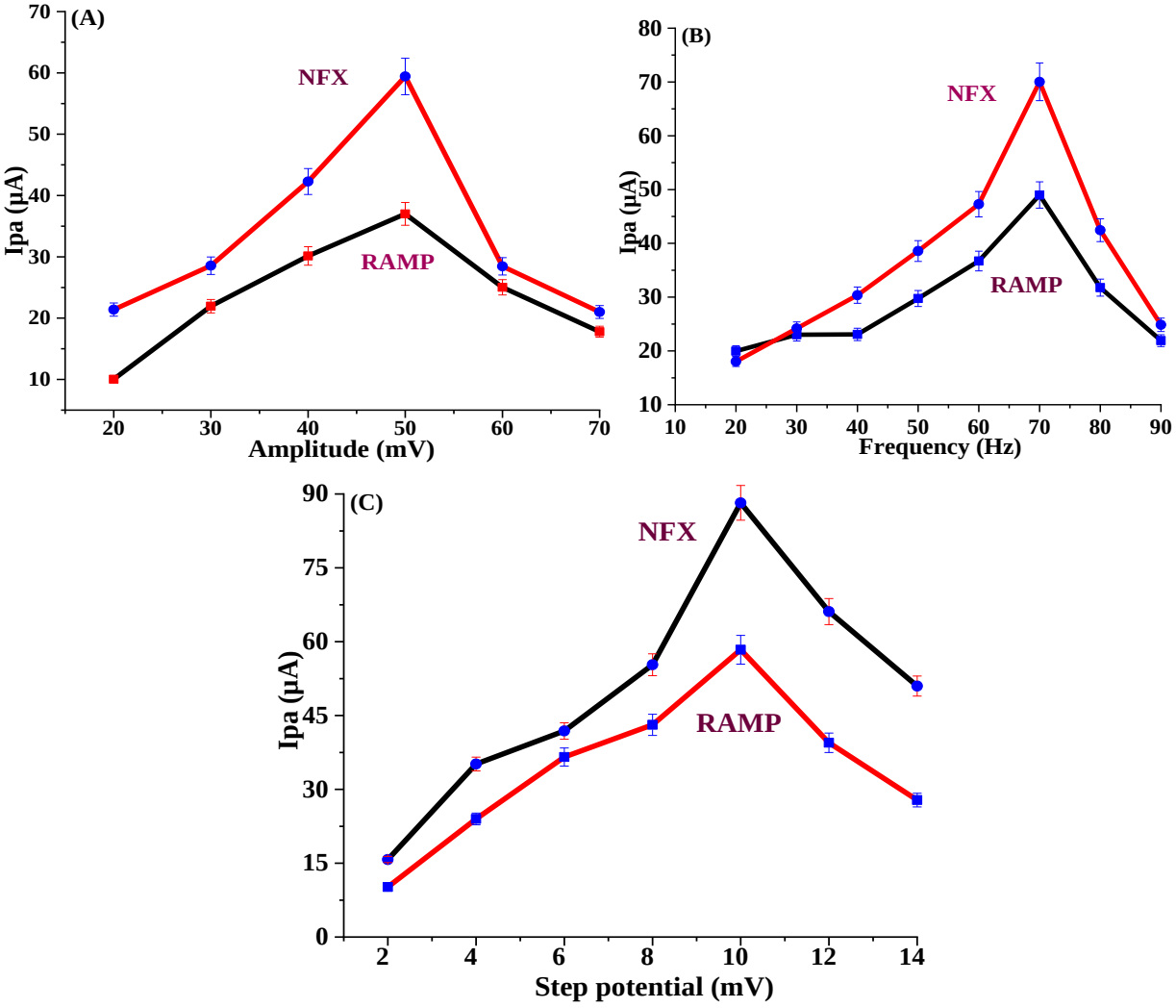

Fig. S4. The effects of SWV parameters: (A) amplitude; (B) frequency; and (C) step potential on the anodic current responses of 15 µM RAMP and NFX.

Repeatability, reproducibility and stability

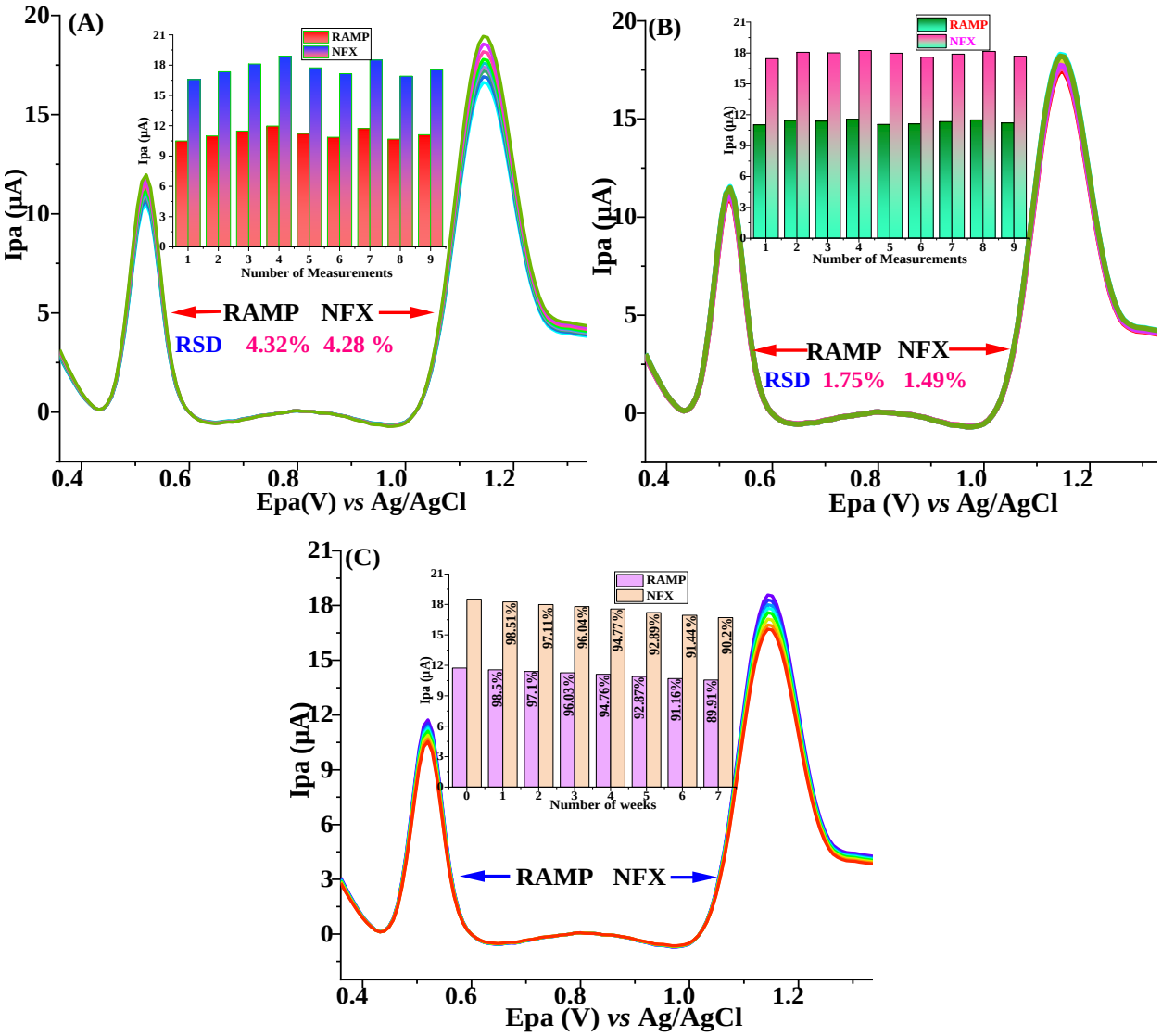

Fig. S5. Repeatability (A) and reproducibility (B) of nine consecutive SWV measurements, and stability (C) of Au-Ag-ANCCs/*f*-MWCNTs-CPE/ChCl (Inset: bar graphs).

Selectivity

Table S1: The effect of co-existing species on the current response of the sensor in detecting RAMP and NFX.

Interferents	Conc. (µM)	Relative Percentage Error (%) RAMP	NFX	Interferents	Conc. (µM)	Relative Percentage Error (%) RAMP	NFX
Cephalexin	150	-4.7	-4.69	Sucrose	250	-2.15	-2.15
Chloramphenicol	150	-3.14	-3.05	Vitamin C	250	-2.21	-2.22
Tinidazole	150	-3.27	-3.26	Lactose	250	-2.15	-2.17
Azithromycin	150	-3.99	-3.98	HCO_3^-	750	-0.76	-0.78
Ampicillin	150	-4.39	-4.38	NO_3^-	750	-1.01	-1.02
Cloxacillin	150	-4.34	-4.25	SO_4^{2-}	750	-0.96	-0.97
Amoxicillin	150	-4.02	-4.01	CO_3^{2-}	750	-1.1	-1.12
Fructose	250	-2.03	-2.11	Cl^-	750	-1.2	-1.21
Uric Acid	250	-2.09	-2.09	Ca^{2+}	750	-0.76	-0.78
Dopamine	250	-1.88	-1.89	K^+	750	-1.01	-1.02
Glucose	250	-1.6	-1.68	Mg^{2+}	750	-0.96	-0.97
Folic acid	250	-2.3	-2.31	Cu^{2+}	750	-1.1	-1.12
Urea	250	-1.83	-1.85	Fe^{3+}	750	-1.2	-1.21

Chapter Seven: Paper V

Hypersensitive electrochemical sensor based on thermally annealed gold–silver alloy nanoporous matrices for the simultaneous determination of sulfathiazole and sulfamethoxazole residues in food samples

Wondimeneh Dubale Adane, Bhagwan Singh Chandravanshi, Merid Tessema

Food Chemistry 457 (2024) 140071

https://doi.org/10.1016/j.foodchem.2024.140071

Food Chemistry 457 (2024) 140071

Contents lists available at ScienceDirect

Food Chemistry

journal homepage: www.elsevier.com/locate/foodchem

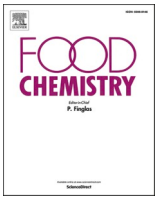

Hypersensitive electrochemical sensor based on thermally annealed gold–silver alloy nanoporous matrices for the simultaneous determination of sulfathiazole and sulfamethoxazole residues in food samples

Wondimeneh Dubale Adane, Bhagwan Singh Chandravanshi *, Merid Tessema *

Department of Chemistry, Addis Ababa University, P. O. Box, 1176, Addis Ababa, Ethiopia

ARTICLE INFO

Keywords:
Antibiotic residues
Sulfathiazole
Sulfamethoxazole
Gold–silver alloy nanoporous matrices
Electrochemical sensor
Food samples

ABSTRACT

In this study, we have developed a novel, hypersensitive, and ultraselective electrochemical sensor containing thermally annealed gold–silver alloy nanoporous matrices (TA-Au-Ag-ANpM) integrated with *f*-MWCNTs-CPE and poly(L-serine) nanocomposites for the simultaneous detection of sulfathiazole (SFT) and sulfamethoxazole (SFM) residues in honey, beef, and egg samples. TA-Au-Ag-ANpM/*f*-MWCNTs-CPE/poly(L-serine) was characterized using an extensive array of analytical (UV–Vis, FT-IR, XRD, SEM, and EDX), and electrochemical (EIS, CV and SWV) techniques. It exhibited outstanding performance over a wide linear range, from 4.0 pM to 490 μM for SFT and 4.0 pM to 520 μM for SFM, with picomolar detection and quantification limits (0.53 pM and 1.75 pM for SFT, 0.41 pM and 1.35 pM for SFM, respectively). The sensor demonstrated exceptional repeatability, reproducibility, and anti-interference capability, with percentage recovery of 95.6–102.4% in food samples and RSD below 5%. Therefore, the developed sensor is an ideal tool to address the current antibiotic residue crisis in food sources.

1. Introduction

Antibiotics are substances that can kill microorganisms or inhibit their proliferation. They are produced naturally by living organisms or artificially in controlled laboratory environments (Bacanli & Başaran, 2019). Antibiotics represent a revolutionary breakthrough for the treatment of infectious diseases. They are widely available, highly effective, and have proven success in fighting bacterial infections. Antibiotics are among the most commonly prescribed therapeutic agents in the world. They are also used in animal husbandry to improve feeding performance, productivity, and growth (Ghasemabadi & Sadeghi, 2023). However, due to their ability to accumulate in the food chain, even traces of antibiotics have detrimental effects on human well-being, leading to harmful consequences, such as organ toxicity and hearing impairment (Tadic et al., 2021). In addition, the widespread use and misuse of antibiotics reduce the effectiveness of their therapy by promoting the spread of resistance genes. Consequently, animals and humans encounter a severe threat from the emergence of antibiotic-resistant bacteria (ARB), which are expected to spread to other groups of microorganisms (Tran et al., 2022). Therefore, the control of antibiotics is of utmost importance for human health and safety.

The misuse of antibiotics causes significant environmental pollution and the accumulation of residual traces in edible products, such as dairy products, eggs, honey, and milk (Wei et al., 2023). These residual compounds can cause a spectrum of adverse effects including immunopathological effects, carcinogenicity, genetic alterations, allergic reactions, fertility problems, and bone marrow and liver toxicity in humans (Bacanli & Başaran, 2019). Furthermore, the misuse of antibiotics has led to the emergence of ARB, even without direct exposure to antibiotics (Zainab et al., 2020). ARBs pose a global challenge that threatens human and animal welfare, economic stability, food security, and ecological balance. The annual number of ARB-related deaths has exceeds 700,000, and projections indicate further escalation if not intervened quickly (Hanna et al., 2023). The presence of antibiotic residues in the environment plays an important role in the emergence and spread of ARBs. There are different sources of antibiotic residues in the environment, including the pharmaceutical and chemical sectors, agricultural and food-related activities, healthcare facilities, and municipal wastewater (Van Boeckel et al., 2014). Antibiotic residues in the environment are emerging contaminants that pose latent health risks. The most pressing hazard posed by antibiotic residues to the environment and human well-being is their potential to accelerate the

* Corresponding authors.
E-mail addresses: bscv2006@yahoo.com (B.S. Chandravanshi), tessemamerid@yahoo.com (M. Tessema).

https://doi.org/10.1016/j.foodchem.2024.140071
Received 22 February 2024; Received in revised form 26 May 2024; Accepted 9 June 2024
Available online 13 June 2024

spread of ARB (Gokulan et al., 2017). Given the growing global concern over antibiotic residues and their far-reaching consequences, the development of a revolutionary analytical approach becomes an urgent necessity to closely monitor and effectively address this pressing issue.

Sulfathiazole (SFT) (4-amino-N-(1,3-thiazol-2-yl)benzenesulfonamide) is a synthetic antibiotic with low-cost and potent therapeutic properties. It is commonly used to treat bacterial infections in both humans and animals. Its primary action is to induce bacteriostasis by impeding the formation of dihydrofolic acid (Khan et al., 2006). The extensive use of SFT in animal husbandry is the main reason for its accumulation in various animal organs, leading to profound effects on the hematopoietic system of humans and animals (Sun et al., 2020). SFT is widely used in beekeeping to control *Bacillus larvae*. However, when mixed with sucrose powder for administration to bees, the honey is unintentionally contaminated with SFT residues. Moreover, SFT residues can contaminate animal products intended for human consumption, such as meat, milk, and eggs, posing a potential risk (Sadeghi & Oliaei, 2021). The extensive use of SFTs in healthcare and animal husbandry has led to increased residues that are released into the environment *via* human and animal excreta, either in their original form or as metabolites (Wang et al., 2023). These residues are often found in water bodies and food sources due to their increased mobility and resistance to conventional wastewater treatment methods. SFT residues not only pose potential risks to human health and ecological stability, but can also induce genetic mutations in bacteria, thereby contributing to the development of ARBs. Several countries have introduced strict regulations for the use of pharmaceuticals, including SFTs, to protect food safety by preserving the quality of animal products (Sun et al., 2020). Therefore, the development of selective and sensitive electrochemical sensors to detect SFT residues in various matrices is crucial and an active area of research.

Sulfamethoxazole (SFM) is a versatile bacteriostatic sulfonamide antibiotic with a broad spectrum of activity that exhibits inhibitory activity against a variety of bacterial strains, including both gram-positive and gram-negative. SFM is commonly prescribed for the treatment of chronic bronchitis and various infections affecting the intestine, respiratory tract, and urinary tract in humans. SFM has also been used as a growth promoter in animal husbandry (Chokkareddy et al., 2022; Pan et al., 2023). At its core, it interferes with bacterial enzymes critical for folic acid synthesis, an important component of bacterial proliferation (De Oliveira et al., 2023). Folic acid is derived from dihydropteroic acid, and SFM interferes with dihydropteroate synthase, thereby stopping the production of dihydropteroic acid (Kumar et al., 2022a). The main adverse effects of SFM include queasiness, gastrointestinal problems, allergic reactions, dermatitis, vomiting, and loss of appetite. In addition, prolonged exposure to SFM results in various blood-related abnormalities, including a decreased platelet count, absence of granulocytes, abnormal red blood cell formation, increased eosinophil levels, and sulfhemoglobinemia (Yeh et al., 2022). SFM is the most important drug used to treat tract infections, despite the fact that treatment failure has been linked to growing bacterial resistance to this drug. In developing countries, SFM is often used as first-line treatment, making bacterial resistance a challenge, especially in the treatment of patients with severe respiratory infections. The use of SFM to prevent *Pneumocystis carinii* infections has led to a rapid increase in multidrug resistance of bacterial pathogens in HIV/AIDS patients (Eliopoulos & Huovinen, 2001). In addition, SFM is non-biodegradable; therefore, its residues and metabolites pose a significant threat to both food safety and the ecosystem. SFM residues that accumulate in the environment result in bacterial resistance, which ultimately leads to severe toxicity (Kumar et al., 2022b). Therefore, the development of electroanalytical sensors capable of accurately and sensitively detecting SFM residues in food samples is of paramount importance to ensure consumer well-being and safety.

Nanoparticles made of bimetallic alloys have been thoroughly investigated in the field of electrochemical sensing and have shown remarkable features, such as increased sensitivity, high detection capability, and robust stability. These nanoparticles have attracted considerable attention due to their superior properties compared with their monometallic counterparts (Veerakumar et al., 2023). Their morphology, size, and composition enhance their catalytic performance and synergistic properties, which expand their potential applications in cancer treatment, nanomedicine, catalysis, DNA delivery, and biosensing (Das et al., 2023). Therefore, various studies have been conducted on alloy nanoparticles with different morphologies to investigate their potential applications in diverse fields. Yu et al. (2017) fabricated hollow Au—Ag nanorices, opening up promising possibilities for surface plasmon applications, such as SERS, PDSC, multipolar antennas, and metamaterials. Li et al. (2018) pushed the limits of H_2O_2 detection with a highly sensitive microelectrode using Pt—Pd nanocorals prepared by one-step electrochemical deposition. Swathy et al. (2023) developed a turn-off fluorescence sensor for rapid detection of histamine in biologicals using tryptophan-capped Au/Ag bimetallic nanoclusters. Mao et al. (2022) fabricated nanoparticles of Pt—Fe alloy on 3D N-doped carbon nano-flowers, paving the way for efficient electrochemical biosensors for early diagnosis and therapy of SCCA.

Multi-walled carbon nanotubes (MWCNTs) are multipurpose materials with exceptional physicochemical properties, including outstanding electrical conductivity, high surface area, broad potential window, excellent electrocatalytic activity, robust surface antifouling properties, and remarkable chemical stability. These properties make MWCNTs a ubiquitous choice for electrode modifiers in electrochemical sensors (Geng et al., 2024; Huang et al., 2021). However, due to the lack of functional groups and limited number of active sites, MWCNTs are poorly soluble and dispersible in organic and aqueous solvents. Accordingly, the functionalization of MWCNTs prior to their use maximizes their surface properties and ensures homogeneous dispersion (Arumugam et al., 2023). During functionalization, various groups, including –COOH, –NH_2, and –OH, are incorporated into the surface of the nanotube. MWCNTs can be functionalized using various techniques including mechanical, chemical, electrochemical, and plasma methods (Farag & Fattah, 2023).

Electropolymerization of L-serine results in a conductive film containing electroactive –NH_2 and –C=O moieties. These moieties enable interactions with the target analyte *via* hydrogen bonding or electrostatic forces, thereby increasing the sensitivity of the electrode (Rabie et al., 2023). Poly(L-serine)-modified electrodes exhibit a high surface area, exceptional flexibility, enhanced catalytic performance, and improved chemical stability due to the robust attachment of the anionic functional group of the polymer onto the electrode surface (Narayana et al., 2015). Due to their strong interactions with the electrode surface, they are promising materials for electrochemical sensing applications. Modification of an electrode with poly(L-serine) can reduce overpotential, improve electron transfer dynamics, and enrich analytes during voltammetric reactions (Hung et al., 2022). Poly(L-serine) has proven to be effective for the detection of a variety of analytes. Hung et al. (2022) prepared a GCE modified with poly(L-serine)/r-GO/nafion for the electrochemical identification of naproxen in aqueous solution. Naderi and Jalali (2020) described the use of poly(L-serine)/AuNPs/MWCNTs/GCE for the electrochemical detection of progesterone in human blood serum. Harshitha et al. (2021) employed an electropolymerization technique to develop a poly(L-serine) modified CPE for the electrochemical determination of catechol in coffee powder. Prinith et al. (2021) developed and used a composite paste electrode containing poly(L-serine), graphite, and carbon nanotubes to electrochemically quantify riboflavin in pharmaceutical, beverage, and dairy samples.

Several analytical methods have been reported for the quantification of SFT and SFM in a range of matrices, including HPLC-MS/MS (Fornazari et al., 2021), chemiluminescence (Huamin et al., 2013), capillary electrophoresis (Jamal et al., 2019), HPLC (Amini & Ahmadiani, 2007), and immunoassay (Nesterenko et al., 2023). Although these methods are sensitive and selective, they have some limitations, including complex operational procedures, time-consuming sample preparation, longer

analysis times, high equipment prices, and the need for skilled operators (Adane et al., 2023a). However, voltammetric methods are cost-effective, fast, user-friendly, highly selective, sensitive, portable, and can be miniaturized. They also offer rapid analysis and require minimal sample volume (Adane et al., 2023b). Therefore, electrochemical techniques were the preferred choice for the simultaneous determination of SFT and SFM in this study. Among the various electrochemical techniques, SWV was chosen because of its several merits, including ultra-fast analysis, negligible sample usage, background differentiation, and enhanced selectivity (Williams et al., 2021).

In this study, we have developed a hypersensitive electrochemical sensor, the first of its kind, by integrating TA-Au-Ag-ANpM with *f*-MWCNT-CPE and poly(L-serine) nanocomposites for the simultaneous detection of SFT and SFM residues in honey, beef, and egg samples. The TA-Au-Ag-ANpM component enhances catalytic activity and stability due to its nanoporous structure, whereas *f*-MWCNTs improve the conductivity and surface area of the sensor. Additionally, poly(L-serine) ensures biocompatibility and promotes effective analyte interactions. Thus, the integrated nanocomposites synergistically contribute to the superior performance of the sensor, offering exceptional sensitivity and extraordinary selectivity. Before the electrochemical analysis, TA-Au-Ag-ANpM/*f*-MWCNTs-CPE/poly(L-serine) was exhaustively examined using several analytical methods, including UV–Vis, FT-IR, XRD, SEM, and EDX. Under the optimized experimental conditions, the developed sensor exhibited remarkable performance, achieving picomolar detection limits and a wide linear range for the detection of target analytes. The sensor outperformed recently reported sensors in terms of the lowest LOD and a wider linear range, which is attributed to its outstanding properties, including a larger electroactive surface area, exceptional electrocatalytic activity, and remarkable electrical conductivity. Furthermore, the hypersensitivity and ultra-selectivity of the sensor were proved by enhanced and well-defined current responses to ultra-trace concentrations of the analytes. The current response of TA-Au-Ag-ANpM/*f*-MWCNT-CPE/poly(L-serine) to the target analytes remained unaffected in the presence of excess concentrations of potentially interfering co-existing species. Consequently, the developed sensor was successfully applied for the simultaneous detection of SFT and SFM residues in different food samples.

2. Experimental

2.1. Chemical and reagents

All chemicals and reagents used in this study were of analytical grade. Pristine multi-walled carbon nanotubes (MWCNTs) with 99% purity was purchased from Sigma-Aldrich, USA. Nitric acid (HNO_3), and sulfuric acid (H_2SO_4) were bought from Merck Chemicals, Germany. Tetrachloroauric acid ($HAuCl_4$), silver nitrate ($AgNO_3$), sodium borohydride ($NaBH_4$), and sodium citrate ($Na_3C_6H_5O_7$) were purchased from Shanghai Sinopharm Chemical Reagent Co. Ltd., China. Graphite powder (BDH Laboratory Supplies Poole, England), and paraffin oil (Uvasol Merck, Germany) were used for the preparation of carbon paste electrode. L-serine ($C_3H_7NO_3$) was obtained from Aladdin (Shanghai, China). Potassium hexacyanoferrate(III) (99%) was purchased from BDH Chemicals Ltd., England. Polyethylene glycol 600 (PEG 600, MW ≈ 570–630) was obtained from Chengdu Kelong Chemical Reagent Factory (Chengdu, China). Polyvinyl pyrrolidone (PVP, K15, MW ≈ 40,000) was obtained from Research Lab Fine Chem Industries (Mumbai, India). All other chemicals and antibiotic standards were purchased from Sigma-Aldrich, USA. Glassware was washed with aqua regia (HCl:HNO_3 in a 3:1 ratio by volume) and rinsed with deionized water before the experiments. All aqueous solutions were prepared with Milli-Q water (18.2 MΩ cm), which was obtained from a Millipore water purification system.

A stock solution of 0.01 M SFT was prepared by dissolving 127.66 mg of the SFT standard in 50 mL of DMSO. Similarly, a 0.01 M SFM stock solution was prepared by dissolving 126.64 mg of the SFM standard in 50 mL of DMSO. The stock solutions were diluted with 0.1 M PBS (pH 6) to prepare working solutions for each target analyte.

2.2. Apparatus and instruments

Electrochemical measurements were performed in 20 mL cells using a CHI 760D electrochemical analyzer (CH Instruments, USA). A conventional three-electrode system was used throughout the experiment, consisting of a working electrode (either bare CPE or modified CPE), a platinum wire counter electrode, and silver-silver chloride (Ag/AgCl (3 M KCl)) reference electrode. The structural morphology was characterized using a scanning electron microscope (SEM, CX-200plus, Coxem, Korea), and the elemental analysis was performed using energy-dispersive X-ray spectroscopy (EDX). The X-ray diffraction (XRD) pattern of the nanocomposites was recorded using a BRUKER ECOD 8 advance diffractometer with Cu Kα radiation (wavelength $\lambda = 0.15406$ nm) at room temperature. Fourier transform infrared (FT-IR) spectra were recorded using a PerkinElmer Spectrum 100 FT-IR spectrometer (PerkinElmer, USA). UV–Vis spectra were recorded using a Lambda 950 UV–Vis spectrometer (PerkinElmer, USA). pH was measured using a Senses Ion + MM150 pH meter (China). Solid chemicals were weighed using an electronic digital balance (Model: Scientech ZSA 120, USA). A centrifuge (model 8001, China) and an ultrasonic cleaner (model YJ5120-B, China) were used during nanocomposite preparation. In addition, a magnetic stirrer and a vacuum pump were used throughout the experiment.

2.3. Sample preparation

2.3.1. Honey samples

Honey was purchased from a local supermarket in Addis Ababa, Ethiopia. The samples were prepared as follows: 1.0 g of honey was dissolved in 1.0 mL of 0.1 M HCl with magnetic stirring. A dilution ratio of 1:10 (*v*/v) in PBS (pH 7.4) was used to reduce the matrix effect, and then filtered through a 150 mm filter membrane before analysis. Afterwards, the samples were spiked with known concentrations of SFT and SFM standards.

2.3.2. Beef samples

Beef samples were purchased from local butcheries in Addis Ababa, Ethiopia. First, the samples were homogenized before extraction. To extract the target analyte, 8 g of the homogenized beef sample was mixed with 20 mL of a 0.1 M PBS solution. The meat sample and PBS solution were thoroughly mixed using a vortex mixer to ensure complete dispersion of the sample in the solvent. Subsequently, the mixture was subjected to ultrasonic treatment for 45 min. This facilitates the efficient extraction of the target analyte from the beef matrix, thereby enhancing the quality and accuracy of our analysis. Then, the mixture was centrifuged at 4000 rpm for 15 min. Centrifugation was performed to separate the constituents, and as a result, a clear solution containing the extracted analyte was collected. Finally, the samples were spiked with appropriate concentrations of SFT and SFM standard solutions.

2.3.3. Egg samples

Egg samples were collected from the Elfora Agro-Industries plc poultry farm in Bishoftu, Ethiopia, and stored at 4 °C until analysis. The samples were prepared as described below: first, the whole egg was homogenized with constant stirring. Then, 10 mL of acetonitrile was added to 5.0 g of egg in a 15 mL centrifuge tube. The mixture was sonicated for 15 min, centrifuged at 2240 relative centrifugal force (RCF) for 10 min, and then the supernatant was transferred to another 15 mL polypropylene centrifuge tube. 1.0 mL of 4.0 M ammonium acetate buffer (pH 6.75) was then added to the mixture and vortexed. Additionally, 20 mL of dichloromethane was added to the mixture and centrifuged at 2240 RCF for 10 min. The supernatant was then collected

and evaporated at 40 °C. Finally, the extract was re-dissolved in 2.0 mL of PBS (pH 7.0) and filtered through a 150 mm filter membrane before analysis.

2.4. Preparation of *f*-MWCNTs and CPE

The *f*-MWCNTs was synthesized using a chemical oxidation process (Konni et al., 2017). In this method, 3 g of pristine MWCNTs was refluxed for 24 h in a 150 mL solution consisting of a 1:3 mixture of HNO_3 and H_2SO_4. The reflux procedure was augmented by magnetic stirring, facilitating the introduction of functional groups onto the surface of carbon nanotubes. Subsequently, the mixture was allowed to cool overnight. The resulting mixture was subjected to centrifugation, followed by successive washings with distilled water and several filtrations until the solution reached pH 7.0. The resulting acid-functionalized MWCNTs (*f*-MWCNTs) was subjected to drying in an oven at 80 °C for 24 h.

A carbon paste electrode was crafted by thoroughly grinding 70 mg of graphite powder with 30 μL of paraffin oil for 25 min using a mortar and pestle. This homogenous mixture was then carefully packed into a 1 mL syringe fitted with a copper wire for electrical contact. The electrode surface was meticulously smoothed on white paper until a mirror-like finish was achieved. When a fresh electrode was required, the previous paste was carefully removed from the upper tip surface, replaced with a new paste, and subjected to further polishing.

2.5. Synthesis of TA-Au-Ag-ANpM

The synthesis of TA-Ag-NpM was conducted as follows: initially, 0.1 M $AgNO_3$ and 0.1 M CTAB solutions were mixed in a 1:1 volume ratio, serving as the precursor solution for stabilizing the nanoporous matrices. Subsequently, for the controlled development of nanoporous structures in subsequent reduction steps, the pH was regulated within the range of 10 to 11 through the addition of 0.1 M NaOH. The reduction of silver ions to form Ag nanoporous structures was initiated with a gradual addition of 10 mL of 0.1 M $NaBH_4$. Heating the mixture at 120 °C for 7 h in an oil bath promoted the interaction of $AgNO_3$ and the formation of a stable Ag nanoporous matrix. The solution was cooled to room temperature, centrifuged to remove excess reactants, and thoroughly washed with ethanol to obtain the desired nanoporous Ag matrix. A crucial step in the synthesis involved controlled thermal treatment in an oven at 175 °C for 2 h. This annealing process plays a pivotal role in consolidating the nanoporous Ag structure, leading to enhanced stability and improved properties. The synthesized TA-Ag-NpM was stored as a colloidal suspension by dispersing in distilled water.

TA-Au-Ag-ANpM was synthesized using the galvanic replacement reaction method (Yu et al., 2017). In this process, TA-Ag-NpM was collected by centrifugation from a colloidal suspension, followed by re-dispersion in distilled water. The resulting dispersion was mixed with a solution of PVP (0.15 M, 6 mL) in a 100 mL flask. The assembled flask was placed in an oil bath operating at 90 °C under continuous stirring, and 4 mL of $HAuCl_4$ solution (0.001 M) was added at a rate of 3 mL/h. Ultimately, the synthesized TA-Au-Ag-ANpMs were centrifuged, washed, and re-dispersed in 97% ethanol for subsequent experiments.

2.6. Preparation of TA-Au-Ag-ANpM/*f*-MWCNTs-CPE

To prepare the nanocomposite, 4 mg *f*-MWCNTs was first dissolved in 3 mL DMSO and homogenized with an ultrasonic device for 45 min. Then, the *f*-MWCNTs solution was mixed with the TA-Au-Ag-ANpM suspension (ratio 1:1) and sonicated for 45 min. Finally, 7 μL of TA-Au-Ag-ANpM/*f*-MWCNTs dispersion was drop-casted onto CPE, dry at 40 °C for 15 min, and termed as TA-Au-Ag-ANpM/*f*-MWCNTs-CPE.

2.7. Fabrication of TA-Au-Ag-ANpM/*f*-MWCNTs-CPE/poly(L-serine)

To fabricate the desired electrode, electropolymerization of L-serine was performed at the surface of TA-Au-Ag-ANpM/*f*-MWCNTs-CPE by CV for 12 consecutive potential sweeps between −1.7 V and +1.6 V in 0.1 M BRB (pH 5.0) containing 0.04 M L-serine at a scan rate of 25 mVs^{-1} (Fig. S1 A). Subsequently, the fabricated sensor (TA-Au-Ag-ANpM/*f*-MWCNTs-CPE/poly(L-serine)) was rinsed with distilled water and made ready for subsequent utilization.

3. Results and discussion

3.1. Analytical characterizations

The analytical investigation of TA-Au-Ag-ANpM/*f*-MWCNT-CPE/poly(L-serine) provides a comprehensive understanding of the composition and structural features of the sensor. The complexity of the developed sensor was investigated using various analytical techniques such as UV–Vis, FT-IR, XRD, SEM, and EDX.

The UV–Vis spectrum of TA-Ag-NpM shows a sharp absorption peak at $\lambda_{max} = 401$ nm, indicating the localized surface plasmon resonance properties of the Ag particles (Fig. 1A(a)). The sharpness of the peak indicates that the particles are monodisperse and uniform in size. The average size of TA-Ag-NpM particles was calculated to be approximately 38 nm. As shown in Fig. 1A(b), TA-Au-Ag-ANpM exhibited a pronounced broad peak at $\lambda_{max} = 416$ nm, indicating that the incorporation of Au into the alloy reduced the size (25 nm) and shifted the absorption peak to a longer wavelength. The observed variations in the two spectra were due to changes in the composition and dimensions of the thermally annealed nanoporous matrices, which affected their optical properties. Since the surface area has a direct influence on the catalytic activity, the alloyed nanoporous matrix with the smallest particle size and largest surface area showed superior catalytic performance during the preparation of the intended sensor.

The FT-IR spectrum of TA-Ag-NpM (Fig. 1B(a)) showed a reduced intensity of the Ag—O stretching vibration at 572 cm^{-1}, indicating the partial breaking of Ag—O bonds during thermal annealing. Likewise, the diminished stretching vibrations of C—O and C═O suggest the restructuring of oxygen-related functional groups on the nanoporous surface. The peak at 1754 cm^{-1} indicates the introduction of COOH groups onto the TA-Ag-NpM surface. The FT-IR spectrum of TA-Au-Ag-ANpM (Fig. 1B(b)) displays characteristic peaks associated with the Au and Ag nanoporous matrices. Confirmatory stretching signals included Au—O at 540 cm^{-1} and Au—Ag at 860 cm^{-1} (confirming the alloying of Au and Ag). Silver-related stretching vibrations, such as Ag—O at 568 cm^{-1}, C—O at 1078 cm^{-1}, and C—H at 2856 and 2929 cm^{-1}, suggest the presence of silver atoms and stabilizing of alkyl chains. The peaks at 1629 cm^{-1} and 3459 cm^{-1} indicate the presence of C═O and O—H on the nanoporous structure. The FT-IRs of TA-Au-Ag-ANpM/*f*-MWCNT-CPE (Fig. 1B(c)) and TA-Au-Ag-ANpM/*f*-MWCNT-CPE/poly(L-serine) (Fig. 1B(d)) exhibited high degree of similarity, sharing the characteristic peaks associated with TA-Au-Ag-ANpM and *f*-MWCNT-CPE. However, the electropolymerization of poly(L-serine) onto TA-Au-Ag-ANpM/*f*-MWCNT-CPE introduced distinct peaks that unequivocally differentiated the two materials. These peaks included amide I (1460 cm^{-1}) and amide II (1385 cm^{-1}) stretching vibrations, indicative of C═O groups and N—H bending vibrations in poly(L-serine). Additionally, the presence of the C—N stretching vibration at 1258 cm^{-1} and the N—H bending vibration at 1168 cm^{-1} further confirmed the integration of poly(L-serine) into TA-Au-Ag-ANpM/*f*-MWCNT-CPE.

XRD was used to evaluate the crystal structure and size of the nanoporous matrix. Consistent results obtained from UV–Vis and XRD measurements of the nanoporous matrix validated the structural features determined using these techniques. The consistency of the results enhances the reliability and validity of the findings, enabling a

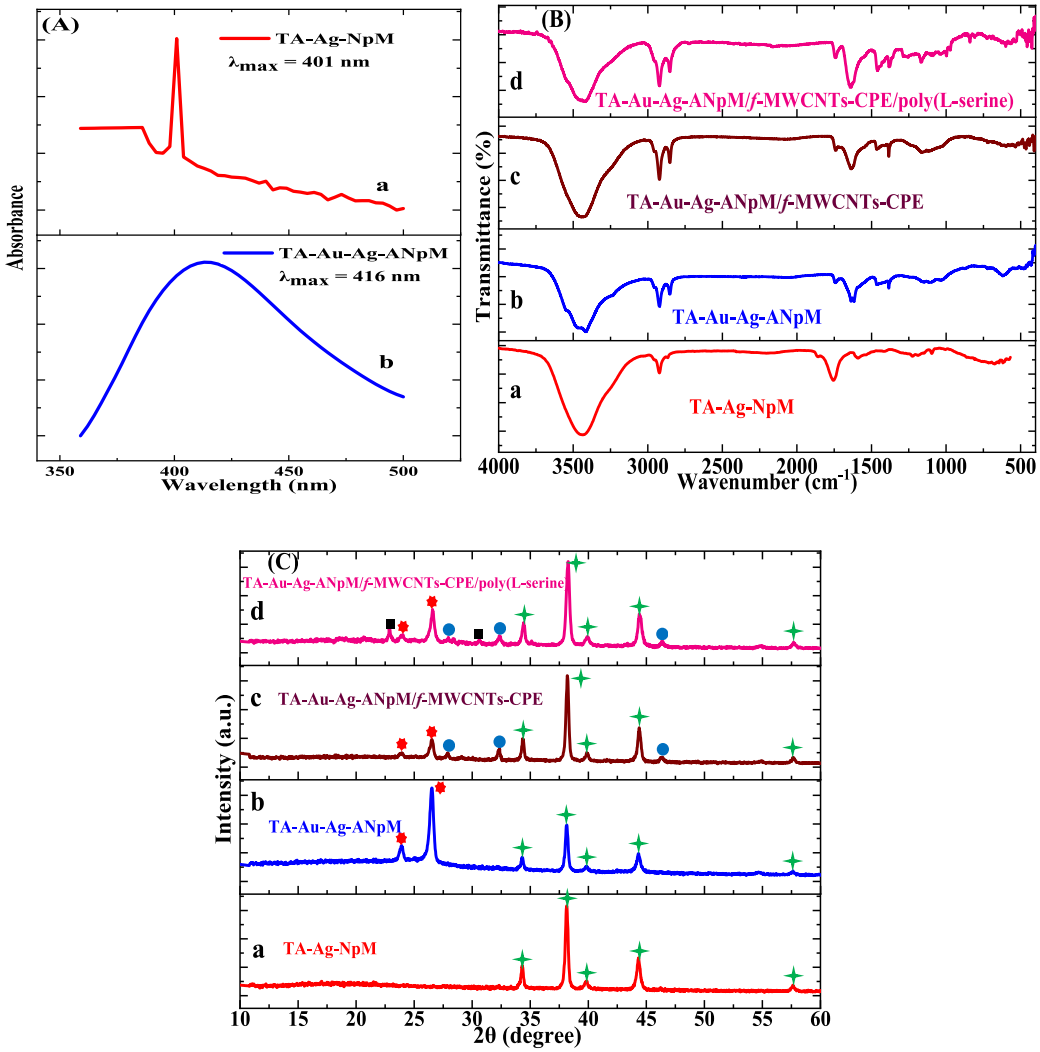

Fig. 1. (A) UV–Vis spectra of TA-Ag-NpM (a), TA-Au-Ag-ANpM (b), (B) FT-IR spectra, and (C) XRD patterns of TA-Ag-NpM (a), TA-Au-Ag-ANpM (b), TA-Au-Ag-ANpM/*f*-MWCNTs-CPE (c), and TA-Au-Ag-ANpM/*f*-MWCNTs-CPE/poly(L-serine) (d).

comprehensive understanding of the material. As shown in Fig. 1C(a), the XRD diffraction peaks of TA-Ag-NpM at 2θ = 34.3°, 38.1°, 39.9°, 44.2°, and 57.68° were indexed to the (100), (111), (200), (220), and (311) planes, respectively, and are characteristic of face-centered-cubic (FCC) structured Ag metal crystals (JCPDS PDF card number 04–0783), which is consistent with previous reports (Al-Ansari et al., 2019). XRD analysis of TA-Au-Ag-ANpM (Fig. 1C(b)) revealed a characteristic peak at 26.54°, attributed to the (111) crystal plane, indicating the formation of a potential intermetallic alloy compound. The amorphous structure of the nanoporous matrix was further confirmed by the characteristic peak at 23.92°, which was assigned to the (100) plane (Zhao et al., 2023). The XRD peaks at 27.86°, 32.36°, and 46.36° (Fig. 1C(c)) correspond to the (002), (004), and (100) planes of typical graphite, respectively (Zhu et al., 2022), confirming the successful incorporation of *f*-MWCNT into TA-Au-Ag-ANpM. The XRD spectra of the TA-Au-Ag-ANpM/*f*-MWCNTs-CPE/poly(L-serine) (Fig. 1C(d)) exhibited characteristic peaks of its constituent components, TA-Au-Ag-ANpM, *f*-MWCNTs-CPE, and poly(L-serine), confirming the successful fabrication of the sensor.

The surface morphology of TA-Au-Ag-ANpM/*f*-MWCNTs-CPE/poly (L-serine) and its constituents were examined by SEM. The *f*-MWCNT-CPE exhibited a uniform distribution of carbon nanotube within the CPE (Fig. 2(a)). In addition to adequately dispersed pores and cavities, *f*-MWCNT-CPE exhibited irregularly shaped agglomerates and uniform surface roughness. As shown in the EDX spectrum of *f*-MWCNT-CPE ((Fig. S2(d)), it was primarily composed of C (78.9%) and O (21.1%), indicating a high degree of purity. SEM examination of TA-Ag-NpM revealed a porous crystalline structure with baked agglomerated silver matrices of irregular shapes (Fig. 2(b)). These matrices were non-uniformly distributed and possessed rough surfaces, which enhanced the conductivity and overall performance of TA-Ag-NpM. The average sizes of TA-Ag-NpM were found to be 36–41 nm, consistent with the UV–Vis and XRD results. SEM analysis of TA-Au-Ag-ANpM (Fig. 2(c)) reveals a more or less uniform size distribution, with an average size of 21–26 nm. TA-Au-Ag-ANpM, similar to TA-Ag-NpM, had a porous structure with rough and irregular crystalline facets. The EDX spectrum of TA-Ag-NpM (Fig. S2(e)) showed the presence of C (43.18%), O (4.8%), Br (4.05%), and Ag (47.97%); those of TA-Au-Ag-ANpM (Fig. S2 (f)) contained C (38.7%), O (4.3%), Br (3.63%), Ag (42.99%), and Au (10.38%), indicating the successful integration of Au into TA-Ag-NpM. The integration of gold into TA-Ag-NpM not only boosted the electro-active area, but also facilitated electron transport, resulting in superior catalytic performance. The TA-Au-Ag-ANpM particles were evenly dispersed in the *f*-MWCNT-CPE (Fig. 2(d)), resulting in irregular and porous cavities, suggesting that TA-Au-Ag-ANpM nanoparticles were effectively integrated into the *f*-MWCNT-CPE. The elemental mapping of TA-Au-Ag-ANpM/*f*-MWCNT-CPE (Fig. S2(i)) showed the presence of C (41.2%), O (20.5%), Br (4.5%), Ag (26%), and Au (7.8%). The SEM image of TA-Au-Ag-ANpM/*f*-MWCNTs-CPE/poly(L-serine) (Fig. 2(e))

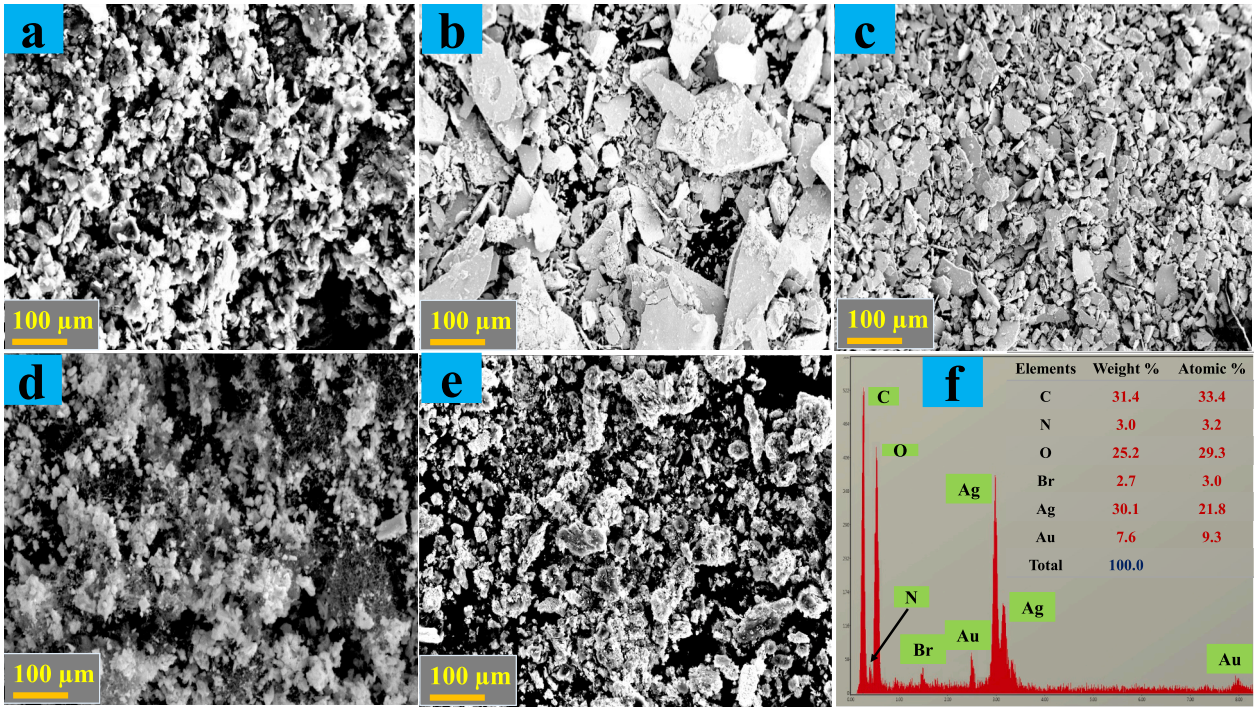

Fig. 2. SEM images of *f*-MWCNTs-CPE (a), TA-Ag-NpM (b), TA-Au-Ag-ANpM (c), TA-Au-Ag-ANpM/*f*-MWCNTs-CPE (d), and TA-Au-Ag-ANpM/*f*-MWCNTs-CPE/poly (L-serine) (e), and EDX spectra of TA-Au-Ag-ANpM/*f*-MWCNTs-CPE/poly(L-serine) (f).

shows an amorphous and nanoporous matrix with an irregular arrangement, significantly increasing the electroactive surface area. The EDX spectra of TA-Au-Ag-ANpM/*f*-MWCNT-CPE/poly(L-serine) (Fig. 2 (f)) shows the presence of C (31.4%), N (3.0%), O (25.2%), Br (2.7%), Ag (30.1%), and Au (7.6%), confirming the successful preparation of the intended sensor.

3.2. Electrochemical characterization

EIS analysis was conducted using a 5 mM $[Fe(CN)_6]^{3-/4-}$ redox probe containing 0.1 M KCl in the frequency range of 0.1 Hz to 100 kHz (inset Fig. 3A). By fitting the data to a Randles equivalent circuit model, the Nyquist plot provides values for the charge transfer resistance (R_{ct}) and diffusion coefficient of reactants and products, obtained from the semicircle diameter and straight-line slope, respectively. As shown in Fig. 3A, the bare CPE electrode exhibited the highest R_{ct} value (4753 Ω) due to its low conductivity. After modifying the CPE with *f*-MWCNTs and poly(L-serine) nanocomposites, the R_{ct} reduced significantly (2674 Ω). At the surface of TA-Au-Ag-ANpM/CPE, the R_{ct} further decreased to 1921 Ω. This demonstrates the excellent electrical conductivity of TA-Au-Ag-ANpM and its ability to facilitate the flow of electrons between the electrode and electrolyte solution. The given EIS curves also showed that the R_{ct} of TA-Au-Ag-ANpM/*f*-MWCNTs-CPE is much lower (718 Ω) compared to TA-Au-Ag-ANpM/poly(L-serine)/CPE (1223 Ω). The decreased R_{ct} value of TA-Au-Ag-ANpM/*f*-MWCNTs-CPE can be attributed to the high electrical conductivity of the *f*-MWCNTs. Finally, the TA-Au-Ag-ANpM/*f*-MWCNTs-CPE/poly(L-serine) showed a significant decrease in the R_{ct} (194 Ω) value, indicating its larger electroactive surface area and excellent electrical conductivity due to the synergistic effect of the nanocomposites.

CV was conducted to examine the electrical and surface properties of individual electrodes at different stages within 0.5 mM $[Fe(CN)_6]^{3-/4-}$

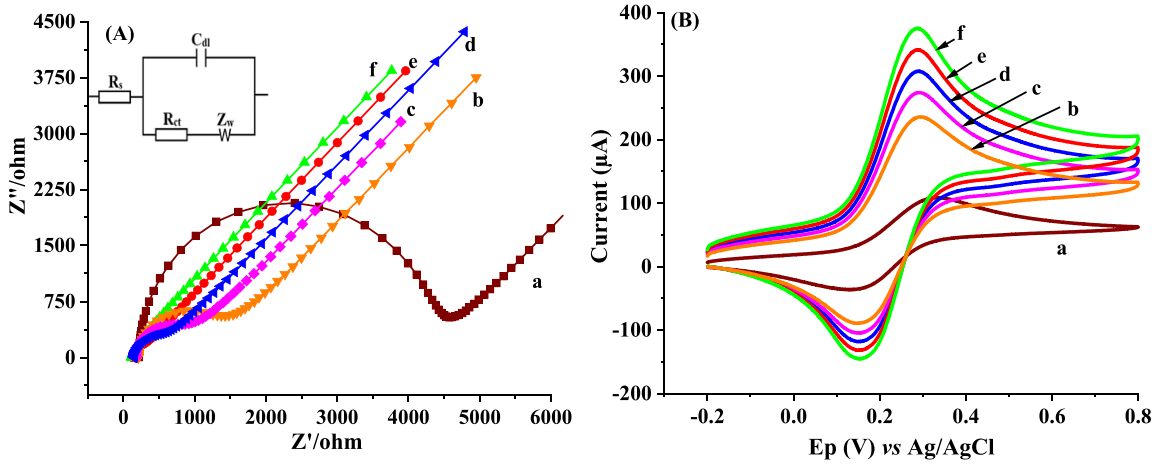

Fig. 3. Nyquist plots (A) and CVs (B) of bare CPE (a), *f*-MWCNTs-CPE/poly(L-serine) (b), TA-Au-Ag-ANpM/CPE (c), TA-Au-Ag-ANpM/poly(L-serine)/CPE (d), TA-Au-Ag-ANpM/*f*-MWCNTs-CPE (e), and TA-Au-Ag-ANpM/*f*-MWCNTs-CPE/poly(L-serine) (f).

containing 0.1 M KCl at a scan rate of 50 mVs^{-1}. As shown in Fig. 3B, both modified and bare electrodes exhibited a pair of redox peaks, indicating a quasi-reversible electron transfer mechanism. Due to the poor electrical conductivity, weak redox peaks with a peak-to-peak separation (ΔEp) of 194 mV were observed at the bare CPE (Fig. 3B (a)). A pair of distinct redox peaks with increased peak current responses and a reduced ΔEp (141 mV) were observed at the surface of the *f*-MWCNTs-CPE/poly(L-serine) compared to the bare electrode (Fig. 3B (b)) due to the enhanced electrical conductivity of the modifiers. When TA-Au-Ag-ANpM/CPE was used, a sharp and well-defined redox peak with a remarkable increase in the peak current was observed (Fig. 3B (c)). The observed decrease in ΔEp (0.101 mV), accompanied by significantly elevated peak currents for TA-Au-Ag-ANpM/CPE, is the best evidence for its exceptional electrical conductivity and electron transfer ability. Furthermore, the CV of TA-Au-Ag-ANpM/*f*-MWCNTs-CPE showed a higher redox peak current response and lower ΔEp than that of TA-Au-Ag-ANpM/poly(L-serine)/CPE (Fig. 3B(d and e)), indicating improved transfer of electrons and increased electroactive area due to *f*-MWCNTs. However, the maximum current response was achieved at the TA-Au-Ag-ANpM/*f*-MWCNTs-CPE/poly(L-serine) electrode (Fig. 3B(f)), by decreasing ΔEp to 52 mV. The synergistic effects of the nanocomposite modifiers enhanced the overall performance of the proposed sensor, as supported by the agreement between the CV and EIS results.

Electroactive surface area measurement is a critical phenomenon in voltammetric reactions as it directly affects the catalytic efficiency and sensitivity of the electrodes. As a result, CV was utilized to measure the electroactive surfaces of the electrodes at different modification stages. The electroactive surface areas were calculated using the Randles-Sevcik eq. (1) (Adane et al., 2024).

$$I_p = 2.69x10^5 n^{3/2} A D^{1/2} C v^{1/2} \quad (1)$$

where I_p = peak current (A), A = electrode surface area (cm^2), n = number of electrons ($n = 1$), D = diffusion coefficient ($cm^2\ s^{-1}$), v = scan rate (Vs^{-1}), and C = concentration of $[Fe(CN)_6]^{3-/4-}$ (mol cm^{-3}). The electroactive surface areas of bare CPE, *f*-MWCNTs-CPE/poly(L-serine), TA-Au-Ag-ANpM/CPE, TA-Au-Ag-ANpM/poly(L-serine)/CPE, TA-Au-Ag-ANpM/*f*-MWCNTs-CPE, and TA-Au-Ag-ANpM/*f*-MWCNTs-CPE/poly (L-serine) were calculated as 0.041, 0.074, 0.111, 0.127, 0.146, and 0.179 cm^2, respectively. TA-Au-Ag-ANpM/*f*-MWCNTs-CPE/poly(L-serine) has more than a fourfold higher electroactive surface area than the bare CPE due to the synergistic enhancement achieved by the integration of TA-Au-Ag-ANpM, *f*-MWCNTs, and poly(L-serine) nanocomposites.

3.3. Electrochemical behavior of SFT and SFM at different electrodes

The voltammetric characteristics of electrodes at different stages of modification were studied using CV and SWV in 15 μM SFT and SFM solutions in 0.1 M PBS (100 mVs^{-1} scan rate). No discernible CV or SWV peaks were observed in the blank solution, suggesting that the analytes may be either absent or exist below the detection limits. The modifications made to the electrodes significantly enhanced the electrochemical response of the analytes and shifted their peak potentials towards more positive values. As depicted in Fig. 4A and B, the bare CPE displayed weak and less pronounced anodic peak currents for SFT and SFM oxidation, suggesting weak conductivity and sluggish electron transfer. Modification of the bare electrode with *f*-MWCNTs-CPE/poly(L-serine) enhanced the conductivity and electroactive area, resulting in an elevated peak response compared to that of the unmodified electrode, owing to the synergistic influence of *f*-MWCNTs and poly(L-serine). TA-Au-Ag-ANpM/CPE showed a more pronounced peak current response than the bare and *f*-MWCNTs-CPE/poly(L-serine) electrodes. The enhanced conductivity of the electrode was due to the porous structure and single-crystal nature of the thermally annealed alloy matrix. The porosity maximizes the active site exposure, whereas the single-crystal composition minimizes the interfacial resistance owing to the absence of grain boundaries (Sharma et al., 2017). The electrochemical oxidation of SFT and SFM resulted in higher current responses with TA-Au-Ag-ANpM/*f*-MWCNTs-CPE compared to TA-Au-Ag-ANpM/poly(L-serine)/CPE. This suggests that the *f*-MWCNTs have superior electron transfer ability, enhanced conductivity, and a more active surface than poly(L-serine). However, the maximum peak current response was observed for TA-Au-Ag-ANpM/*f*-MWCNTs-CPE/poly(L-serine). This indicates that the nanocomposites synergistically boosted the electron flow, electroactive area, and trace analyte detection. In general, the SWV results agreed well with the CV findings. The SWV plot showed that the ΔEp between SFT and SFM was 648 mV, which was large enough for the simultaneous determination of the analytes.

3.4. Optimization of experimental conditions

3.4.1. Effect of electrolyte solution

Herein, we have investigated the effects of different supporting electrolytes using SWV. The electrolytes tested were phosphate, acetate, citrate, H_2SO_4, BRB, and citrate-phosphate buffer solutions. The experimental findings showed that phosphate buffer solution (PBS) had the

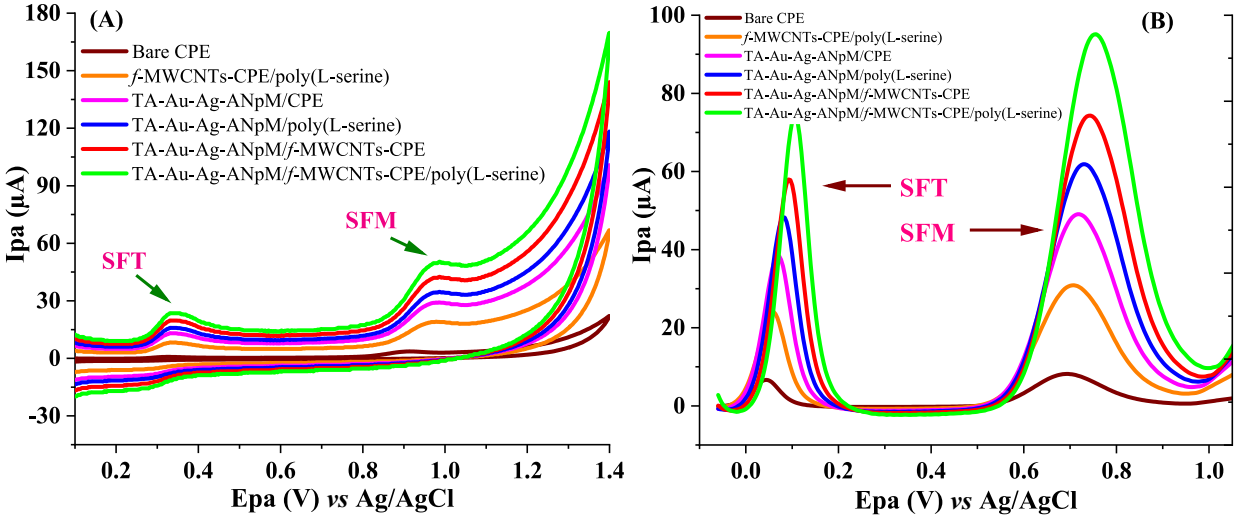

Fig. 4. Electrochemical responses of various electrodes to 15 μM SFT and SFM in 0.1 M PBS (pH 6) at 100 mVs^{-1} using CV (A) and SWV (B).

highest current response among all the electrolytes (Fig. S3). PBS was superior to the other supporting electrolytes due to its remarkable performance and pronounced influence on the shape of a voltammogram and current response. Therefore, PBS was the best choice for simultaneously determining SFT and SFM.

3.4.2. Optimization of the number of electropolymerization cycles

To find the optimal number of polymerization cycles for L-serine, a series of repetitive cycles were performed in a solution containing 0.04 M L-serine and 0.1 M BRB (pH 5.0). The cycles were performed within a specified potential range (−1.7 V to 1.6 V) at a scan rate of 25 mVs^{-1} at the TA-Au-Ag-ANpM/*f*-MWCNTs-CPE surface. The results show that the peak current response increased as the number of L-serine electropolymerization cycles at the surface of TA-Au-Ag-ANpM/*f*-MWCNTs-CPE increased (Fig. S1B). However, the response reached its maximum at 12 cycles and started to decline afterward. The decline is due to an excessive electropolymerization process, resulting in the formation of a thicker and more insulating L-serine layer at the surface of TA-Au-Ag-ANpM/*f*-MWCNTs-CPE. As the L-serine film becomes thicker, it impedes the transfer of electrons between the TA-Au-Ag-ANpM/*f*-MWCNTs-CPE/poly(L-serine) and the analytes detected. Consequently, electrode conductivity and sensitivity decreased. Therefore, 12 polymerization cycles were determined to be the optimal value for subsequent experiments.

3.4.3. Optimization of the ratio of TA-Au-Ag-ANpM and f-MWCNTs

To accomplish the optimization, the mixing ratio of two vital nanocomposites, namely TA-Au-Ag-ANpM, and *f*-MWCNTs, was closely examined and adjusted to reach the sensor's peak performance level. A methodical assessment was carried out to get the precise ratio that would yield the highest performance for the sensor. Various combinations of TA-Au-Ag-ANpM and *f*-MWCNTs were examined while all other experimental parameters remained constant. Notably, the investigation revealed that the highest peak current response, particularly in the detection of 15 μM SFT and SFM at the surface of TA-Au-Ag-ANpM/*f*-MWCNTs-CPE/poly(L-serine), was observed when the mixing ratio of TA-Au-Ag-ANpM to *f*-MWCNTs was at 1:1 (Fig. S5 A). Consequently, the 1:1 ratio of TA-Au-Ag-ANpM and *f*-MWCNTs was chosen as the optimal ratio for fabricating the proposed sensor. The choice ensures that the modified electrode maintains a perfect balance between the two composites, thereby resulting in an electrode that excels in performance for electrochemical sensing applications, particularly for determining SFT and SFM residues in food samples.

3.4.4. Optimization of drop-casted volume

A small volume results in a thin layer that may not cover the entire sensor surface, which can result in poor signal transmission and reduced sensitivity. A large volume can result in a thick layer that can block the pores of the sensor and disrupt the electrochemical reaction. In this study, the drop-cast volume of TA-Au-Ag-ANpM/*f*-MWCNTs dispersion was optimized to achieve the highest peak current response from the TA-Au-Ag-ANpM/*f*-MWCNTs-CPE/poly(L-serine) sensor while detecting 15 μM SFT and SFM. As shown in Fig. S5B, the optimal amount is 7 μL as it produces the highest anodic current responses.

3.4.5. Effect of pH

Electrochemical measurements are very sensitive to the pH of the electrolyte. It affects the electrode stability, current response, analyte mobility, and stability. Therefore, the selection of an appropriate pH is essential for accurate and reliable measurements. SWV was employed to evaluate how the electrochemical responses of 15 μM SFT and SFM varied with the PBS pH, ranging from 4.0 to 8.0 using TA-Au-Ag-ANpM/*f*-MWCNTs-CPE/poly(L-serine). Fig. 5A shows that the anodic current responses of the SFT and SFM increased as the pH increased from 4 to 6 and then decreased at higher pH values. Therefore, 0.1 M PBS pH 6.0 was chosen as the optimal pH for subsequent experiments, as it gave a well-defined voltammogram with higher sensitivity (Figs. 5B(a) and 5C (a)). Moreover, as the pH of the PBS solution increased, the anodic potentials of both SFT and SFM steadily shifted towards lower positive

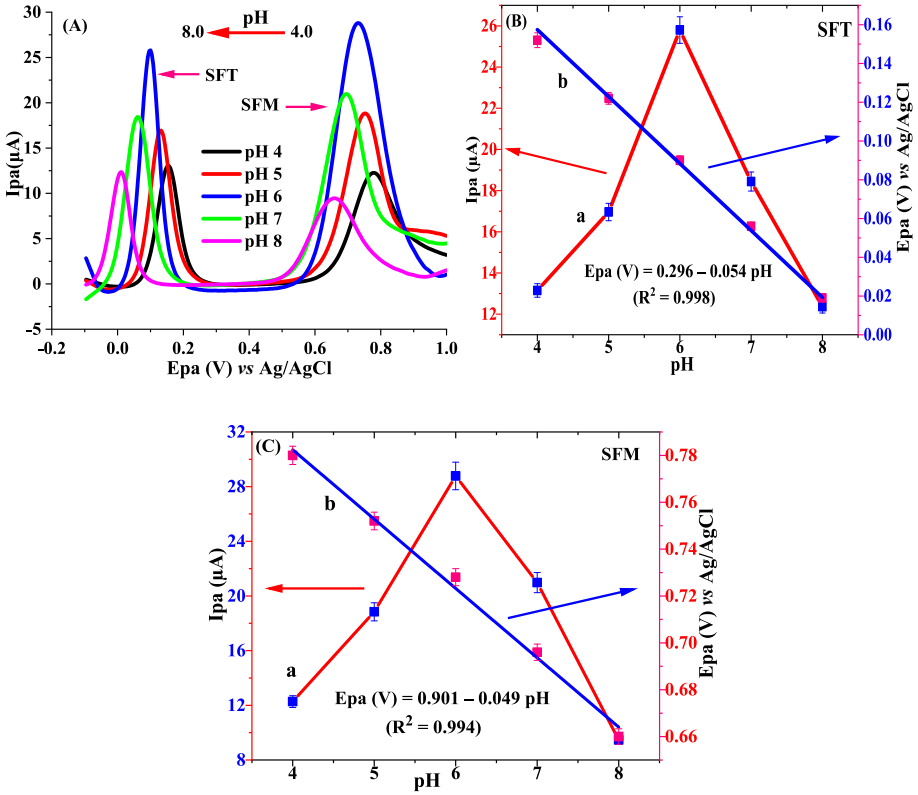

Fig. 5. (A) SWV of 15 μM SFT and SFM at different pH of PBS, (B) and (C) pH *vs.* Ipa (μA) (a) and pH *vs.* Epa (V) (b) of SFT and SFM, respectively.

values. This trend indicates the crucial role of protons in the electro-oxidation reaction. The regression equations are Epa (V) = 0.296–0.054 pH (R^2 = 0.998) (Fig. 5B(b)) and Epa (V) = 0.901–0.049 pH (R^2 = 0.994) (Fig. 5C(b)) for SFT and SFM, respectively. The slope values of 0.054 and 0.049 V/pH for SFT and SFM, respectively, were close to the theoretical Nernstian value of 0.059 V/pH. This suggests that an equal number of electrons and protons are involved in the electro-oxidation of the analytes, which is in accordance with earlier reports (Balasubramanian et al., 2018; Ghasemabadi & Sadeghi, 2023).

3.4.6. Effect of scan rate

Electrochemical responses of 15 μM SFT and SFM at the surface of TA-Au-Ag-ANpM/*f*-MWCNTs-CPE/poly(L-serine) were studied in 0.1 M PBS (pH 6) using SWV within a scan rate ranges of 25–325 mVs^{-1}. Fig. S4A shows that increasing the scan rate resulted in a higher Ipa (μA) response and a shift to a more positive oxidation potential. Furthermore, the absence of cathodic peaks in the back-scan confirms the fully irreversible nature of the electrochemical reactions at the sensor surface. The Ipa (μA) of the SFT and SFM increased linearly with the square root of the scan rate. The correlation equations are found to be Ipa (μA) = 0.49 $\nu^{1/2}$ $(mVs^{-1})^{1/2}$–0.17 (R^2 = 0.997) for SFT and Ipa (μA) = 0.77 $\nu^{1/2}$ $(mVs^{-1})^{1/2}$ + 2.81 (R^2 = 0.994) for SFM, as illustrated in Fig. S4B(a and b), respectively. This observation suggests that the electrochemical oxidations of SFT and SFM are primarily controlled by diffusion processes, which agrees well with previous research findings (Balasubramanian et al., 2018; Maheshwaran et al., 2022). Furthermore, the plots of log Ipa (μA) *vs.* log ν (mVs^{-1}) are linearly correlated and given by log Ipa (μA) = 0.55 ν (mVs^{-1}) – 0.47 (R^2 = 0.991) for SFT and log Ipa (μA) = 0.47 ν (mVs^{-1}) + 0.28 (R^2 = 0.994) for SFM, as depicted in Figs. S4C(a and b)). Notably, the slopes of the lines are 0.54 and 0.47, closely approximating the theoretical value of 0.5. This correspondence highlights the dominant effect of diffusion-controlled mechanisms on TA-Au-Ag-ANpM/*f*-MWCNTs-CPE/poly(L-serine). Laviron's theory of irreversible electrode processes, as described in Eq. (2) (Adane et al., 2024) was used to determine the number of electrons (n) involved in the electrode reaction, establishing a relationship between Ep (V) and log ν (mVs^{-1}).

$$E_p = E^0 + \frac{2.303RT}{\alpha nF} log \frac{RTk^0}{\alpha nF} + \frac{2.303RT}{\alpha nF} log\nu \quad (2)$$

where, E^0 = formal potential, ν = scan rate, T = temperature, F = Faraday constant, k^0 = heterogeneous rate constant, R = universal gas constant, and n = number of electrons. A strong correlation was found between the plots of Epa *vs.* log ν (mVs^{-1}), for both SFT and SFM. The slope of each plot, corresponding to 2.303RT/αnF, was used to calculate αn. The values of αn were 0.984 and 0.899 for SFT and SFM, respectively. The transfer coefficient (α) is typically assumed to be 0.5 for irreversible electrode reactions (Adane et al., 2023a). The numbers of electrons (n) involved in the electrochemical oxidation of SFT and SFM were 1.968 and 1.798, respectively, which were close to two. It is in line with earlier research that reported the transfer of two protons and two electrons during the electrochemical oxidation of SFT and SFM (Balasubramanian et al., 2018; Maheshwaran et al., 2022). Schematic illustrations of the possible electrochemical reactions of the SFT and SFM at the surface of the sensor are provided in Scheme S1.

3.4.7. Optimization of SWV parameters

SWV responses are largely dependent on three instrumental parameters: amplitude, frequency, and step potential. Herein, the effect of these experimental parameters on the current responses of 15 μM SFT and SFM were examined in 0.1 M PBS (pH 6). First, the effect of amplitude was investigated in the range of 40–120 mV at a constant frequency and step potential. The anodic current increased to 90 mV for both analytes and then decreased (Fig. S6 A). Therefore, 90 mV was set as the optimal amplitude for next measurements. Subsequently, the influence of frequency was investigated in the range of 20–80 Hz while keeping amplitude and step potential constant. The current response showed a direct correlation with frequency, peaking at 50 Hz (Fig. S6B). As a result, 50 Hz was selected as the optimal frequency for subsequent experimental procedures. Finally, the influence of the step potential was investigated in the range of 2–16 mV while keeping the other parameters constant. As shown in Fig. S6C, the anodic currents for both analytes increased with increasing step potential, reaching a maximum at 10 mV before decreasing. Consequently, 10 mV was chosen as the optimal value for subsequent experiments.

3.5. Simultaneous determination of SFT and SFM

The relationship between analyte concentration and peak current response is essential for quantifying analytes in real samples and determining their LOD and LOQ. To evaluate the electroanalytical performance of TA-Au-Ag-ANpM/*f*-MWCNTs-CPE/poly(L-serine), SWV was used to determine varying concentrations of SFT and SFM under the optimized experimental conditions. Fig. 6A demonstrates a direct relationship between the anodic current and the concentrations of SFT and SFM. The oxidation current gradually increases with consistent increases in analytes concentration. The anodic current was linearly correlated with concentrations between 4 pM and 490 μM for SFT, and 4 pM to 520 μM for SFM. The corresponding linear regression equations were Ipa (μA) = 0.78C (μM) + 7.04 (R^2 = 0.9992) for SFT (Fig. 6B(a)) and Ipa (μA) = 1.01C (μM) + 8.88 (R^2 = 0.9991) for SFM (Fig. 6B(b)). The LOD (3σ/m, S/N = 3, *n* = 7) and LOQ (10σ/m, S/N = 3, n = 7) values for SFT were determined to be 0.53 pM and 1.75 pM, while for SFM, they were found to be 0.41 pM and 1.35 pM, respectively.

Furthermore, the performance of the developed sensor was extensively compared with those of recently reported sensors in terms of the linear range and detection limit. As shown in Table 1, TA-Au-Ag-ANpM/*f*-MWCNTs-CPE/poly(L-serine) exhibited superior performance with extremely low detection limits and wide linear ranges, outperforming all recently reported sensors. It is because of the improved electroactive surface area, excellent electrocatalytic activity, and enhanced electrical conductivity of the constituents of the sensor. This significant advance in electrochemical sensor technology represents a breakthrough and remarkable contribution to the scientific community, making the sensor an excellent candidate for the simultaneous determination of SFT and SFM residues in food samples.

3.6. Reproducibility, repeatability and stability

SWV is a powerful electrochemical technique that can provide accurate and quantitative information on the performance of modified electrodes. Its versatility makes it ideal for evaluating the reproducibility, repeatability, and stability of modified electrodes. Herein, SWV was used to assess the reproducibility, repeatability, and stability of TA-Au-Ag-ANpM/*f*-MWCNTs-CPE/poly(L-serine) while simultaneously quantifying 15 μM SFT and SFM in 0.1 M PBS. First, ten different electrodes were prepared under identical conditions to evaluate the reproducibility of the fabricated sensor. The RSD values were 2.96% for SFT and 2.77% for SFM (Fig. S7A). These results demonstrate the exceptional reproducibility of the sensor, confirming its capability to detect SFT and SFM residues in honey, beef, and egg samples. Next, nine replicate square wave measurements were performed using a single electrode to evaluate the repeatability of TA-Au-Ag-ANpM/*f*-MWCNTs-CPE/poly(L-serine). The RSD values were 2.2% for SFT and 2.36% for SFM (Fig. S7B), suggesting that the sensor has a very good repeatability to quantify the analytes. Finally, the current responses of the sensor were monitored weekly for two and a half months to measure its stability. It was stored at 4 °C after each weekly use. Remarkably, the sensor demonstrated long-term stability, with anodic current responses decreasing by only 5.27% for SFT and 5.11% for SFM over the entire storage period (Fig. S7C).

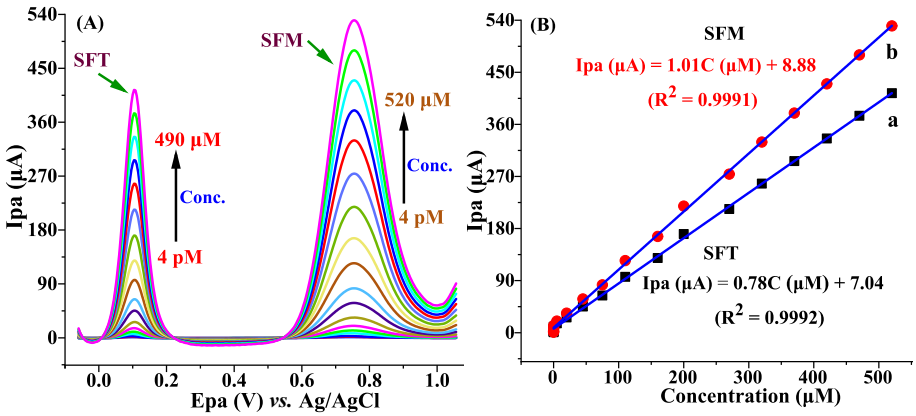

Fig. 6. SWV corresponding to various concentrations of the analytes (A) and Ipa (µA) *vs.* conc. (B).

Table 1
Evaluating the performance of developed sensor in comparison to recent technology.

Electrodes	Targets	Matrices	Linear range (µM)	LOD (µM)	Ref.
MIP/CuS/Au-COF/GCE	SFT	Chicken and pork liver	10 pM–100	4.3 pM	(Sun et al., 2020)
TASV/GCE	SFT	River water and urine	0.01–364	0.0058	(Maheshwaran et al., 2022)
N, B, F-CDs	SFT	River water, soil, milk, and egg samples	31.3–39.2 39.2–176	0.216	(Chen et al., 2021)
Mn_3O_4/g-C_3N_4/CPE	SFT	Water and milk samples	0.75–100	0.11	(Ghasemabadi & Sadeghi, 2023)
Poly(*IL*)CuNCs	SFT	Milk and honey	99.8–509	27.4	(Sadeghi & Oliaei, 2021)
TA-Au-Ag-ANpM/*f*-MWCNTs-CPE/poly(L-serine)	SFT	Honey, beef, and egg samples	4 pM – 490	0.53 pM	This work
Ce(III)-doped CuO/SPE	SFM	Biological and drug samples	0.03–360	0.01	(Akbari et al., 2022)
IL-f-ZnONPs/MWCNTs-GCE	SFM	Pharmaceuticals	0.025–2.53	0.025	(Chokkareddy et al., 2022)
TFAB-COF/PANI/GCE	SFM	Environmental water	1–450	0.107	(Pan et al., 2023)
3Ds-CME/AgNPs	SFM	Different samples	10–50	0.96	(De Oliveira et al., 2023)
GR-ZnO/GCE	SFM	Lake water, tap water, urine and serum	1–220	0.4	(Yue et al., 2020)
TA-Au-Ag-ANpM/*f*-MWCNTs-CPE/poly(L-serine)	SFM	Honey, beef, and egg samples	4 pM–520	0.41 pM	This work

3.7. Selectivity

Determining the selectivity of TA-Au-Ag-ANpM/*f*-MWCNTs-CPE/poly(L-serine) is essential for its practical applicability. SWV was employed to assess its selectivity for detecting 15 µM SFT and SFM in the presence of potentially interfering substances. SFT and SFM measurements were considered to be unaffected by interfering species if resulted in a relative error of less than 5%. As shown in Table S1, the detection of 25 µM SFT and SFM was not affected by up to 800-fold excess of commonly co-exiting species in food samples (lactose, ascorbic acid, urea, dopamine, uric acid, folic acid, glucose, sucrose, and fructose), 250 times for antibiotics (ciprofloxacin, azithromycin, metronidazole, tinidazole, cloxacillin, ampicillin, amoxicillin, chloramphenicol, erythromycin, and cephalexin), and 1000 times higher for inorganic species (Ca^{2+}, HCO_3^-, K^+, NO_3^-, Mg^{2+}, CO_3^{2-}, SO_4^{2-}, Cu^{2+}, Cl^-, and Fe^{3+}). In general, the fabricated sensor is a promising tool for ensuring food safety and public health. Its exceptional selectivity makes it a valuable device for regulatory agencies, pharmaceuticals, food producers, and consumers.

3.8. Analytical applications

The practicability of TA-Au-Ag-ANpM/*f*-MWCNT-CPE/poly(L-serine) for application in real samples was evaluated by spiking experiments using SWV. The standard addition method was used to determine the percentage recoveries. Known concentrations of the SFT and SFM standards (0, 5, 10, 25, and 50 µM) were added to the food samples (Table 2). Before the standards were added to the honey, beef, and egg samples, their initial current responses were recorded. No current responses were observed in the unspiked samples, indicating the absence of SFT and SFM residues or their concentrations were below the detection limit. Then, the percentage recoveries were determined in spiked food samples, which ranged from 96.7 to 102.4% for SFT and 95.6 to 102.3% for SFM. The RSD values were also low, ranged from 1.56 to 2.84% for SFT and 1.58 to 2.98% for SFM. In addition, the validity of the developed method was verified by performing analyses for SFT and SFM drugs from a local pharmacy, which were used as reference materials. As shown in Tables S2 and S3, the amounts of SFT and SFM detected with the developed sensor were comparable to those values labeled by the manufacturers of the analytes. The results further

Table 2
Summary of triplicate spiking experiment results.

Samples	Spiked (µM)	Found (µM)		Recovery (%)		RSD (%)	
		SFT	SFM	SFT	SFM	SFT	SFM
Honey	0	–	–	–	–	–	–
	5	5.12	5.08	102.4	101.6	2.21	1.98
	10	9.68	10.12	96.8	101.2	1.76	1.79
	25	25.37	24.76	101.5	99.04	2.53	2.49
	50	48.78	47.82	97.6	95.6	2.07	2.11
Beef	0	–	–	–	–	–	–
	5	4.87	5.09	97.4	101.8	1.89	2.03
	10	10.26	10.23	101.6	102.3	1.56	1.78
	25	25.12	24.89	100.5	99.6	2.54	2.26
	50	51.18	48.98	102.4	98	2.84	2.98
Egg	0	–	–	–	–	–	–
	5	5.07	5.06	101.4	101.2	1.56	1.58
	10	10.03	10.08	100.3	100.8	1.82	1.76
	25	24.18	24.69	96.7	98.8	1.94	1.94
	50	48.87	51.11	97.7	102.2	1.75	1.67

conform the accuracy and precision of the developed method. In general, the exceptional recoveries, lower RSD values, and results from method validation analysis show that TA-Au-Ag-ANpM/*f*-MWCNT-CPE/poly(L-serine) is a highly effective and reliable innovation for the simultaneous detection of SFT and SFM residues in practical applications.

4. Conclusion

In this study, a novel electrochemical sensor comprising a thermally annealed gold–silver alloy nanoporous matrix decorated with *f*-MWCNTs-CPE and poly(L-serine) composites was developed for the simultaneous determination of SFT and SFM residues in honey, beef, and egg samples. The morphological and elemental composition of the developed sensor were examined using various analytical techniques. TA-Au-Ag-ANpM/*f*-MWCNTs-CPE/poly(L-serine) was found to be superior to recently reported sensors with the lowest LOD and a broader linear range owing to its exceptional features: higher electroactive surface area, high electrocatalytic activity, and enhanced electrical conductivity. The sensor responses withstanding the influence of potentially interfering substances, including organic, inorganic, and antibiotic species, demonstrate its remarkably high selectivity. In addition, the sensor exhibited exceptional repeatability, reproducibility, and long-term stability. Therefore, TA-Au-Ag-ANpM/*f*-MWCNTs-CPE/poly(L-serine) is the best tool for real-time monitoring of life-threatening residues of SFT and SFM in food samples.

Statement on Data Availability

All the data supporting the results of this study are reported in the article.

CRediT authorship contribution statement

Wondimeneh Dubale Adane: Writing – original draft, Software, Resources, Investigation, Formal analysis, Conceptualization. **Bhagwan Singh Chandravanshi:** Writing – review & editing, Supervision, Conceptualization. **Merid Tessema:** Writing – review & editing, Supervision, Conceptualization.

Declaration of competing interest

We want to affirm that there are no recognized conflicts of interest associated with this publication, and this study has not received dedicated funding from any public, commercial, or non-profit sector funding entity.

The authors declare that they have no known competing financial interests or personal relationships that could have appeared to influence the work reported in this paper.

Data availability

No data was used for the research described in the article.

Acknowledgements

The authors express their gratitude to the Department of Chemistry at Addis Ababa University, Addis Ababa, Ethiopia, for generously offering the laboratory resources.

Appendix A. Supplementary data

Supplementary data to this article can be found online at https://doi.org/10.1016/j.foodchem.2024.140071.

References

Adane, W. D., Chandravanshi, B. S., & Tessema, M. (2023a). A simple, ultrasensitive and cost-effective electrochemical sensor for the determination of ciprofloxacin in various types of samples. *Sensing and Bio-Sensing Research, 39*, Article 100547. https://doi.org/10.1016/j.sbsr.2022.100547

Adane, W. D., Chandravanshi, B. S., & Tessema, M. (2023b). Highly sensitive and selective electrochemical sensor for the simultaneous determination of tinidazole and chloramphenicol in food samples (egg, honey and milk). *Sensors and Actuators B: Chemical, 390*, Article 134023. https://doi.org/10.1016/j.snb.2023.134023

Adane, W. D., Chandravanshi, B. S., & Tessema, M. (2024). A novel electrochemical sensor for the detection of metronidazole residues in food samples. *Chemosphere, 359*, Article 142279. https://doi.org/10.1016/j.chemosphere.2024.142279

Akbari, J. H., Rajabizadeh, A., Dehghannoudeh, G., & Moghaddam, H. M. (2022). Electrochemical determination of sulfamethoxazole in biological and drug samples using Ce (III)-doped CuO modified electrode. *Measurement, 203*, Article 111936. https://doi.org/10.1016/j.measurement.2022.111936

Al-Ansari, M., Alkubaisi, N., Gopinath, K., Karthika, V., Arumugam, A., & Govindarajan, M. (2019). Facile and cost-effective ag nanoparticles fabricated by lilium lancifolium leaf extract: Antibacterial and antibiofilm potential. *Journal of Cluster Science, 30*(4), 1081–1089. https://doi.org/10.1007/s10876-019-01569-w

Amini, H., & Ahmadiani, A. (2007). Rapid and simultaneous determination of sulfamethoxazole and trimethoprim in human plasma by high-performance liquid chromatography. *Journal of Pharmaceutical and Biomedical Analysis, 43*(3), 1146–1150. https://doi.org/10.1016/j.jpba.2006.09.004

Arumugam, B., Palanisamy, S., Ramaraj, S. K., & Chiesa, M. (2023). Single-crystalline MoO_3/functionalized multiwalled carbon nanotube nanocomposites for sensing phenothiazine in biological samples. *Surfaces and Interfaces, 38*, Article 102829. https://doi.org/10.1016/j.surfin.2023.102829

Bacanli, M., & Başaran, N. (2019). Importance of antibiotic residues in animal food. *Food and Chemical Toxicology, 125*, 462–466. https://doi.org/10.1016/j.fct.2019.01.033

Balasubramanian, P., Settu, R., Chen, S. M., & Chen, T. W. (2018). Voltammetric sensing of sulfamethoxazole using a glassy carbon electrode modified with a graphitic carbon nitride and zinc oxide nanocomposite. *Microchimica Acta, 185*(8), 396. https://doi.org/10.1007/s00604-018-2934-z

Chen, L., Liu, Y., Cheng, G., Fan, Z., Yuan, J., He, S., & Zhu, G. (2021). A novel fluorescent probe based on N, B, F co-doped carbon dots for highly selective and sensitive determination of sulfathiazole. *Science of the Total Environment, 759*, Article 143432. https://doi.org/10.1016/j.scitotenv.2020.143432

Chokkareddy, R., Kanchi, S., & Redhi, G. G. (2022). A novel IL-f-ZnONPs@MWCNTs nanocomposite fabricated glassy carbon electrode for the determination of sulfamethoxazole. *Journal of Molecular Liquids, 359*, 11923. https://doi.org/10.1016/j.molliq.2022.119232

Das, G., Seo, S., Yang, I. J., Nguyen, L. T. H., Shin, H. S., & Patra, J. K. (2023). Sericin mediated gold/silver bimetallic nanoparticles and exploration of its multi-therapeutic efficiency and photocatalytic degradation potential. *Environmental Research, 229*, Article 115935. https://doi.org/10.1016/j.envres.2023.115935

De Oliveira, W. B. V., Lisboa, T. P., Da Silva, G. C., Oliveira, R. S., De Souza, C. C., Matos, M. A. C., … Matos, R. C. (2023). Chemometric tools applied to silver nanoparticles electrodeposition in 3D-printed disposable device for the determination of sulfamethoxazole in different samples by voltammetry. *Microchemical Journal, 193*, Article 109091. https://doi.org/10.1016/j.microc.2023.109091

Eliopoulos, G. M., & Huovinen, P. (2001). Resistance to trimethoprim-sulfamethoxazole. *Clinical Infectious Diseases, 32*(11), 1608–1614. https://doi.org/10.1086/320532

Farag, O. F., & Fattah, E. A. (2023). Synthesis and characterization PVA/plasma-functionalized MWCNTs nanocomposites films. *Journal of Polymer Research, 30*(5), 183. https://doi.org/10.1007/s10965-023-03550-8

Fornazari, A. L. D. T., Labriola, V. F., Da Silva, B. F., Castro, L. F., Perussi, J. R., Vieira, E. M., & Azevedo, E. B. (2021). Coupling zero-valent iron and Fenton processes for degrading sulfamethazine, sulfathiazole, and norfloxacin. *Journal of Environmental Chemical Engineering, 9*(4), Article 105761. https://doi.org/10.1016/j.jece.2021.105761

Geng, L., Sun, J., Liu, M., Huang, J., Dong, J., Guo, Z., Guo, Y., & Xia Sun, X. (2024). Molecularly imprinted polymers-aptamer electrochemical sensor based on dual recognition strategy for high sensitivity detection of chloramphenicol. *Food Chemistry, 437*, Article 137933. https://doi.org/10.1016/j.foodchem.2023.137933

Ghasemabadi, J. J., & Sadeghi, S. (2023). Facile fabrication of an electrochemical sensor for the determination of two sulfonamide antibiotics in milk, honey and water samples using the effective modification of carbon paste electrode with graphitic carbon nitride and manganese oxide nanostructures. *Journal of Food Composition and Analysis, 120*, Article 105294. https://doi.org/10.1016/j.jfca.2023.105294

Gokulan, K., Cerniglia, C. E., Thomas, C., Pineiro, S. A., & Khare, S. (2017). Effects of residual levels of tetracycline on the barrier functions of human intestinal epithelial cells. *Food and Chemical Toxicology, 109*, 253–263. https://doi.org/10.1016/j.fct.2017.09.004

Hanna, N., Tamhankar, A. J., & Lundborg, C. S. (2023). The development of an integrated environment–human risk approach for the prioritization of antibiotics for policy decisions. *Science of Total Environment, 880*, Article 163301. https://doi.org/10.1016/j.scitotenv.2023.163301

Harshitha, B. T., Manjunatha, J. G., Pushpanjali, P. A., Karthik, C. S., Sandeep, S., Mallu, P., … Anwer, K. M. (2021). Efficient electrochemical determination of catechol with hydroquinone at poly (L-serine) layered carbon paste electrode. *ChemistrySelect, 6*(26), 6764–6772. https://doi.org/10.1002/slct.202101809

Huamin, Q., Lulu, F., Li, X., Li, L., Min, S., & Chuannan, L. (2013). Determination sulfamethoxazole based chemiluminescence and chitosan/graphene oxide-

molecularly imprinted polymers. *Carbohydrate Polymers, 92*(1), 394–399. https://doi.org/10.1016/j.carbpol.2012.09.092

Huang, J., Xiang, Y., Li, J., Kong, Q., Zhai, H., Xu, R., Yang, F., Sun, X., & Guo, Y. (2021). A novel electrochemiluminescence aptasensor based on copper-gold bimetallic nanoparticles and its applications. *Biosensors and Bioelectronics, 194*, Article 113601. https://doi.org/10.1016/j.bios.2021.113601

Hung, C. M., Huang, C. P., Chen, C. W., & Dong, C. D. (2022). A poly-(L-serine)/reduced graphene oxide–nafion supported on glassy carbon (PLS/rGO−Nafion/GCE) electrode for the detection of naproxen in aqueous solutions. *Environmental Science and Pollution Research, 29*(9), 12450–12461. https://doi.org/10.1007/s11356-021-15511-z

Jamal, S., Baderia, V. K., Agrawal, Y. K., & Sanghi, S. K. (2019). Fluorescence detection and identification of eight sulphonamides using capillary electrophoresis on released excipients in lake water. *Arabian Journal of Chemistry, 12*(7), 1338–1344. https://doi.org/10.1016/j.arabjc.2014.10.039

Khan, F., Roychowdhury, S., Nemes, R., Vyas, P., Woster, P., & Svensson, C. (2006). Effect of pro-inflammatory cytokines on the toxicity of the arylhydroxylamine metabolites of sulphamethoxazole and dapsone in normal human keratinocytes. *Toxicology, 218*(2–3), 90–99. https://doi.org/10.1016/j.tox.2005.10.002

Konni, M., Dadhich, A. S., & Babu, M. S. (2017). Impact of surface modifications on hydrogen uptake by Fe@f-MWCNTs and cu@f-MWCNTs at non-cryogenic temperatures. *International Journal of Hydrogen Energy, 42*(2), 953–959. https://doi.org/10.1016/j.ijhydene.2016.09.085

Kumar, P. S., Sreeja, B. S., Kumar, K. K., & Padmalaya, G. (2022a). Static and dynamic analysis of sulfamethoxazole using GO/ZnO modified glassy carbon electrode by differential pulse voltammetry and amperometry techniques. *Chemosphere, 302*, Article 134926. https://doi.org/10.1016/j.chemosphere.2022.134926

Kumar, P. S., Sreeja, B. S., Kumar, K. K., & Padmalaya, G. (2022b). Investigation of nafion coated GO-ZnO nanocomposite behavior for sulfamethoxazole detection using cyclic voltammetry. *Food and Chemical Toxicology, 167*, Article 113311. https://doi.org/10.1016/j.fct.2022.113311

Li, H., Zhao, H., He, H., Shi, L., Cai, X., & Lan, M. (2018). Pt-Pd bimetallic nanocoral modified carbon fiber microelectrode as a sensitive hydrogen peroxide sensor for cellular detection. *Sensors and Actuators B: Chemical, 260*, 174–182. https://doi.org/10.1016/j.snb.2017.12.179

Maheshwaran, S., Balaji, R., Chen, S. M., Liao, Y. C., Chandrasekar, N., Ethiraj, S., & Samuel, M. S. (2022). Fabrication of 2D–0D Ti_3AlC_2@$SmVO_4$ heterojunction nanocomposites for ultrasensitive electrochemical detection of sulfathiazole in environmental samples. *Journal of Environmental Chemical Engineering, 10*(6), Article 108956. https://doi.org/10.1016/j.jece.2022.108956

Mao, Y. W., Zhang, J. X., Chen, D. N., Wang, A. J., & Feng, J. J. (2022). Bimetallic PtFe alloyed nanoparticles decorated on 3D hollow N-doped carbon nanoflowers as efficient electrochemical biosensing interfaces for ultrasensitive detection of SCCA. *Sensors and Actuators B: Chemical, 370*, Article 132416. https://doi.org/10.1016/j.snb.2022.132416

Naderi, P., & Jalali, F. (2020). Poly-L-serine/AuNPs/MWCNTs as a platform for sensitive voltammetric determination of progesterone. *Journal of the Electrochemical Society, 167*(2), Article 027524. https://doi.org/10.1149/1945-7111/ab6a7f

Narayana, P. V., Madhusudana, T. R., Gopal, P., Mohan, M. R., & Ramakrishna, G. N. (2015). Electrocatalytic boost up of epinephrine and its simultaneous resolution in the presence of serotonin and folic acid at poly(serine)/multi-walled carbon nanotubes composite modified electrode: A voltammetric study. *Materials Science and Engineering: C, 56*, 57–65. https://doi.org/10.1016/j.msec.2015.06.011

Nesterenko, I. S., Hendrickson, O. D., Smirnova, N. I., Eremin, S. A., & Sotnikov, D. V. (2023). Development of a polarization fluorescent immunoassay for sulfathiazole and its application for honey testing. *Applied Biochemistry and Microbiology, 59*(1), 93–98. https://doi.org/10.1134/S0003683823010052

Pan, Z., Wei, Y., Guo, H., Liu, B., Sun, L., Lu, Z., Wei, X., Zhang, H., Chen, Y., & Yang, W. (2023). Sensitive detection of sulfamethoxazole by an electrochemical sensing platform with a covalent organic framework in situ grown on polyaniline. *Microporous and Mesoporous Materials, 348*, Article 112409. https://doi.org/10.1016/j.micromeso.2022.112409

Prinith, N. S., Manjunatha, J. G., Tigari, G., & ALOthman, Z. A., Alanazi, A. M., & Pandith, A.. (2021). Mechanistic insights into the voltammetric determination of riboflavin at poly (serine) modified graphite and carbon nanotube composite paste electrode. *ChemistrySelect, 6*(40), 10746–10757. https://doi.org/10.1002/slct.202103184

Rabie, E. M., Shamroukh, A. A., Assaf, F. H., & Khodari, M. (2023). A novel sensor based on calcium oxide fabricated from eggshell waste conjugated with L-serine polymer film modified carbon paste electrode for sensitive detection of moxifloxacin in human serum and pharmaceutical constituents. *Sensors and Actuators A: Physical, 356*, Article 114351. https://doi.org/10.1016/j.sna.2023.114351

Sadeghi, S., & Oliaei, S. (2021). Microextraction of sulfathiazole from milk and honey samples using a polymeric ionic liquid membrane followed by fluorometric determination. *Journal of Food Composition and Analysis, 97*, Article 103774. https://doi.org/10.1016/j.jfca.2020.103774

Sharma, S., Prakash, V., & Mehta, S. K. (2017). Graphene/silver nanocomposites-potential electron mediators for proliferation in electrochemical sensing and SERS activity. *TrAC Trends in Analytical Chemistry, 86*, 155–171. https://doi.org/10.1016/j.trac.2016.10.004

Sun, Y., Gao, H., Xu, L., Waterhouse, G. I. N., Zhang, H., Qiao, X., & Xu, Z. (2020). Ultrasensitive determination of sulfathiazole using a molecularly imprinted electrochemical sensor with CuS microflowers as an electron transfer probe and au@COF for signal amplification. *Food Chemistry, 332*, Article 127376. https://doi.org/10.1016/j.foodchem.2020.127376

Swathy, S., Pallam, G. S., & Girish Kumar, K. (2023). Tryptophan capped gold–silver bimetallic nanoclusters-based turn-off fluorescence sensor for the determination of histamine. *Talanta, 256*, Article 124321. https://doi.org/10.1016/j.talanta.2023.124321

Tadic, D., Bleda Hernandez, M. J., Cerqueira, F., Matamoros, V., Pina, B., & Bayona, J. M. (2021). Occurrence and human health risk assessment of antibiotics and their metabolites in vegetables grown in field-scale agricultural systems. *Journal of Hazardous Materials, 401*, Article 123424. https://doi.org/10.1016/j.jhazmat.2020.123424

Tran, T. T. T., Do, M. N., Dang, T. N. H., Tran, Q. H., Le, V. T., Dao, A. Q., & Vasseghian, Y. A. (2022). State-of-the-art review on graphene-based nanomaterials to determine antibiotics by electrochemical techniques. *Environmental Research, 208*, Article 112744. https://doi.org/10.1016/j.envres.2022.112744

Van Boeckel, T. P., Gandra, S., Ashok, A., Caudron, Q., Grenfell, B. T., Levin, S. A., & Laxminarayan, R. (2014). Global antibiotic consumption 2000 to 2010: An analysis of national pharmaceutical sales data. *The Lancet Infectious Diseases, 14*(8), 742–750. https://doi.org/10.1016/S1473-3099(14)70780-7

Veerakumar, P., Koventhan, C., & Chen, S. M. (2023). Copper-palladium alloy nanoparticles immobilized over porous carbon for voltammetric determination of dimetridazole. *Journal of Alloys and Compounds, 631*, Article 167474. https://doi.org/10.1016/j.jallcom.2022.167474

Wang, X., He, Z., Xie, Y., Zhang, Y., & Wang, Y. (2023). An FeP/carbon composite derived from a Phytic acid-Fe^{3+} complex for sulfathiazole degradation through peroxymonosulfate activation. *Chemosphere, 313*, Article 137562. https://doi.org/10.1016/j.chemosphere.2022.137562

Wei, X., Liu, C., Qin, H., Ye, Z., Liu, X., Zong, B., Li, Z., & Mao, S. (2023). Fast, specific, and ultrasensitive antibiotic residue detection by monolayer WS2-based field-effect transistor sensor. *Journal of Hazardous Materials, 443*, Article 130299. https://doi.org/10.1016/j.jhazmat.2022.130299

Williams, T., Shum, R., & Rappleye, D. (2021). Review-concentration measurements in molten chloride salts using electrochemical methods. *Journal of the Electrochemical Society, 168*(12), Article 123510. https://doi.org/10.1149/1945-7111/ac436a

Yeh, S. H., Huang, M. S., & Huang, C. H. (2022). Electrochemical sensors for sulfamethoxazole detection based on graphene oxide/graphene layered composite on indium tin oxide substrate. *Journal of Taiwan Institute of Chemical Engineers, 131*, Article 104155. https://doi.org/10.1016/j.jtice.2021.11.022

Yu, K., Sun, X., Pan, L., Liu, T., Liu, A., Chen, G., & Huang, Y. (2017). Hollow au–ag alloy nanorices and their optical properties. *Nanomaterials, 7*(9), 255. https://doi.org/10.3390/nano7090255

Yue, X., Li, Z., & Zhao, S. (2020). A new electrochemical sensor for simultaneous detection of sulfamethoxazole and trimethoprim antibiotics based on graphene and ZnO nanorods modified glassy carbon electrode. *Microchemical Journal, 159*, Article 105440. https://doi.org/10.1016/j.microc.2020.105440

Zainab, S. M., Junaid, M., Xu, N., & Malik, R. N. (2020). Antibiotics and antibiotic resistant genes (ARGs) in groundwater: A global review on dissemination, sources, interactions, environmental and human health risks. *Water Research, 187*, Article 116455. https://doi.org/10.1016/j.watres.2020.116455

Zhao, H., Guo, M., Li, F., Zhou, Y., Zhu, G., Liu, Y., Ran, Q., Nie, F., & Dubovyk, V. (2023). Fabrication of gallic acid electrochemical sensor based on interconnected super-P carbon black@mesoporous silica nanocomposite modified glassy carbon electrode. *Journal of Material Research and Technology, 24*, 2100–2112. https://doi.org/10.1016/j.jmrt.2023.03.129

Zhu, Z., Luk, H. N., Liu, Y. S., Wu, R. J., Chung, M. H., & Chang, X. J. (2022). Preparation of bimetallic au-Pd/MWCNTs electrode for detection of dopamine. *Minerals, 12*(9), 1145. https://doi.org/10.3390/min12091145

Supplementary Material

Hypersensitive electrochemical sensor based on thermally annealed gold–silver alloy nanoporous matrices for the simultaneous determination of sulfathiazole and sulfamethoxazole residues in food samples

Wondimeneh Dubale Adane[a], Bhagwan Singh Chandravanshi*[a], Merid Tessema** [a]

[a] Department of Chemistry, Addis Ababa University, P. O. Box 1176, Addis Ababa, Ethiopia

* Corresponding author. E-mail address: bscv2006@yahoo.com

** Corresponding author. E-mail address: tessemamerid@yahoo.com

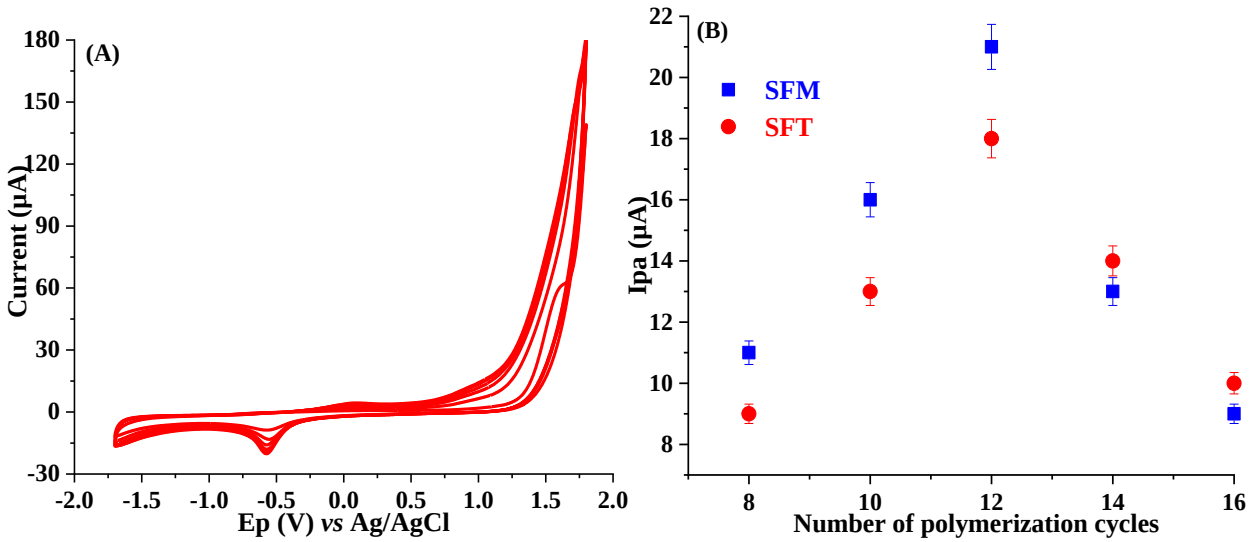

Fig. S1. CV for the electropolymerization of 0.04 M L-serine with 0.1 M BRB (pH 5.0) at the surface of TA-Au-Ag-ANpM/*f*-MWCNTs-CPE for 12 consecutive potential sweeps between -1.7 to 1.6 V, and (B) plot for the optimization of the number of electropolymerization cycles *vs*. Ipa (µA) of 15 µM SFT and SFM.

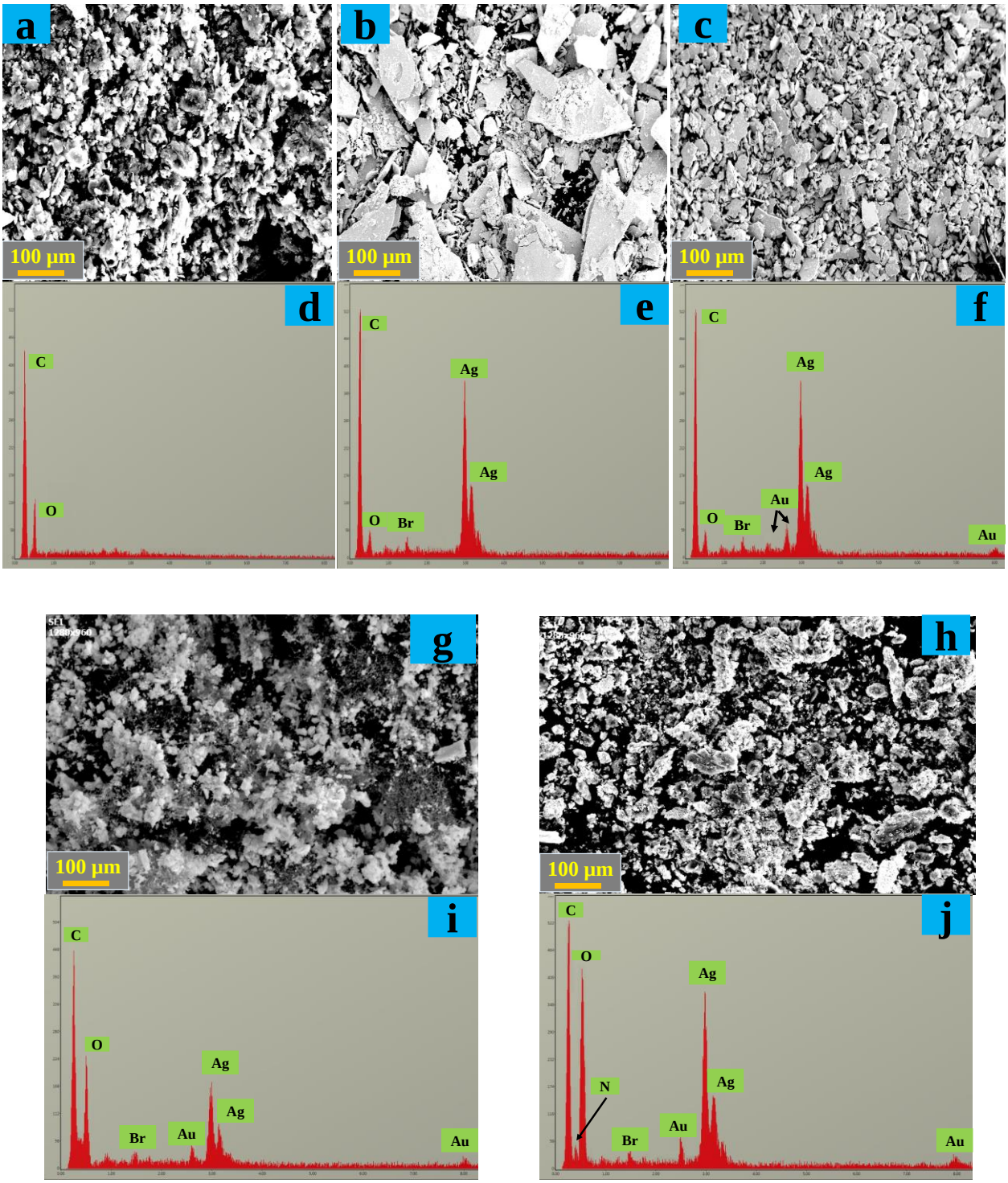

Fig. S2. SEM and EDX spectra of *f*-MWCNTs-CPE (a and d), TA-Ag-NpM (b and e), TA-Au-Ag-ANpM (c and f), TA-Au-Ag-ANpM/*f*-MWCNTs-CPE (g and i), and TA-Au-Ag-ANpM/*f*-MWCNTs-CPE/poly(L-serine) (h and j), respectively.

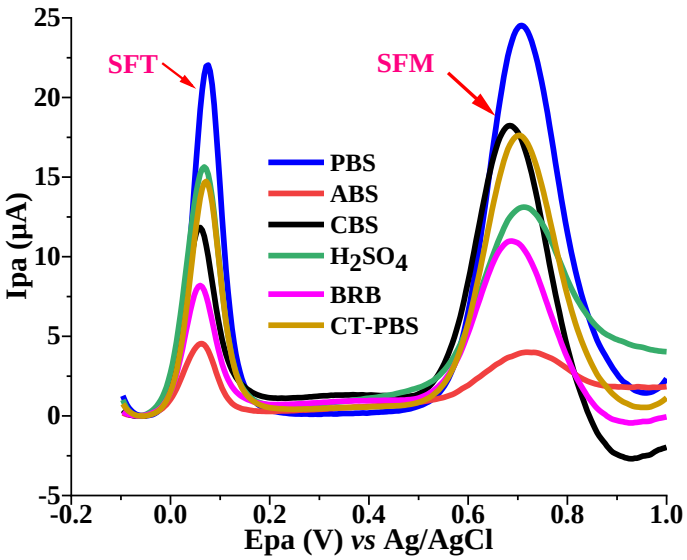

Fig. S3. SWVs of 15 µM SFT and SFM in different supporting electrolyte solutions.

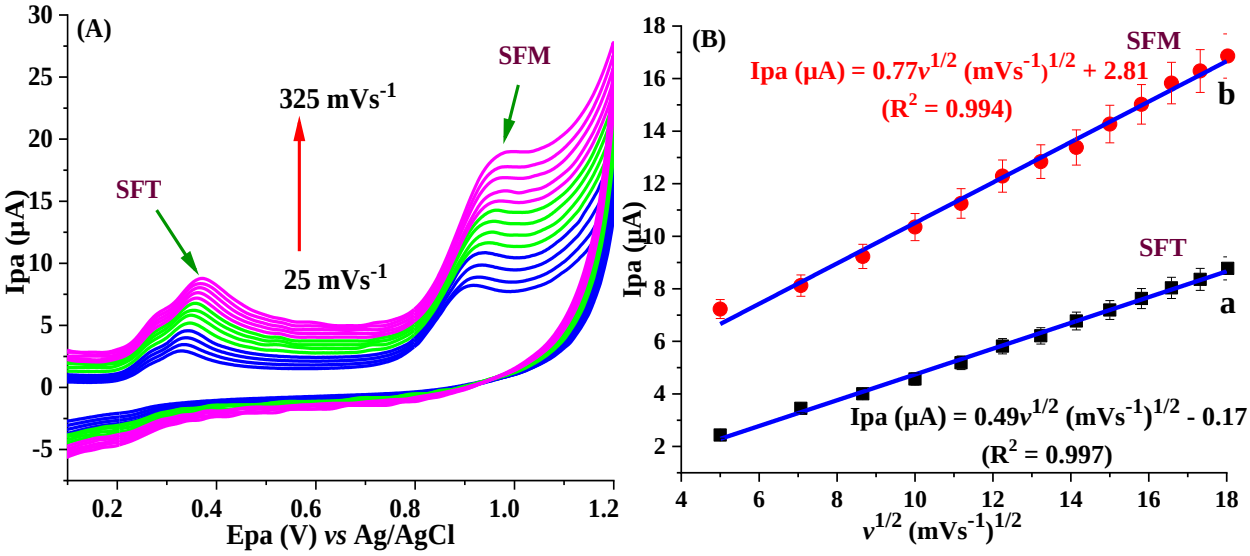

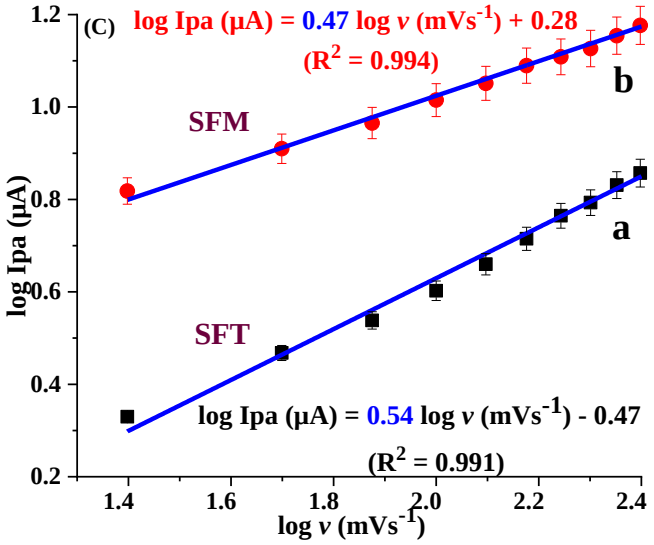

Fig. S4. CVs of 15 μM SFT and SFM (A) at different scan rates, plots of $v^{1/2}$ $(mVs^{-1})^{1/2}$ *vs*. Ipa (μA) (B), and log *v* (mVs^{-1}) *vs*. log Ipa (μA) (C).

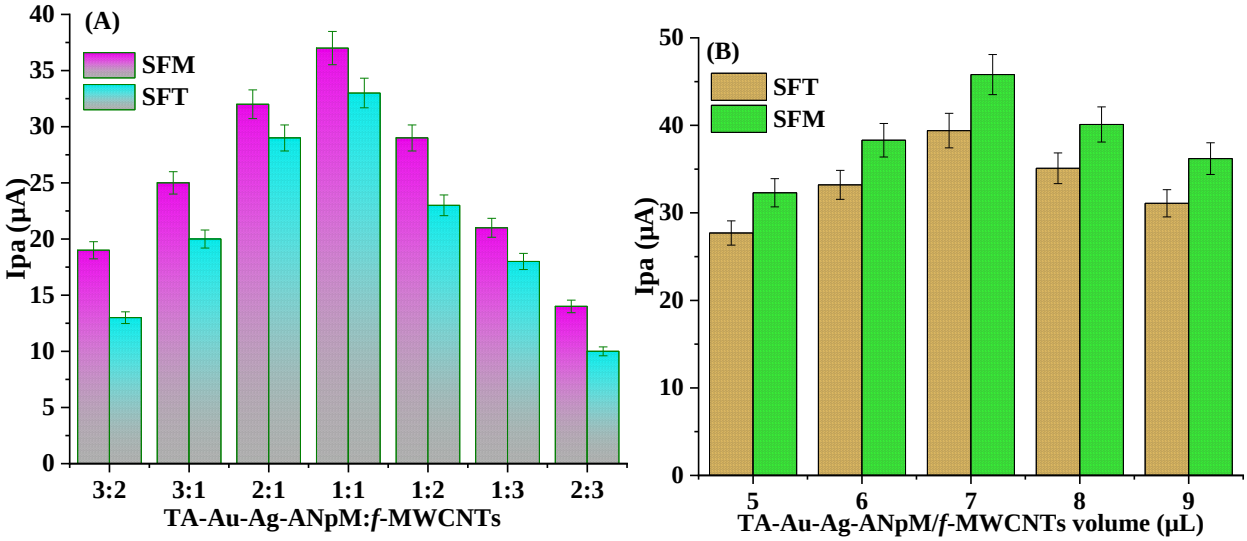

Fig. S5. Optimization diagram for the ratio of TA-Au-Ag-ANpM and *f*-MWCNTs (A) and the volume of TA-Au-Ag-ANpM/*f*-MWCNTs dispersion (B) in the preparation of TA-Au-Ag-ANpM/*f*-MWCNTs-CPE/poly(L-serine) for the detection of 15 μM SFT and SFM

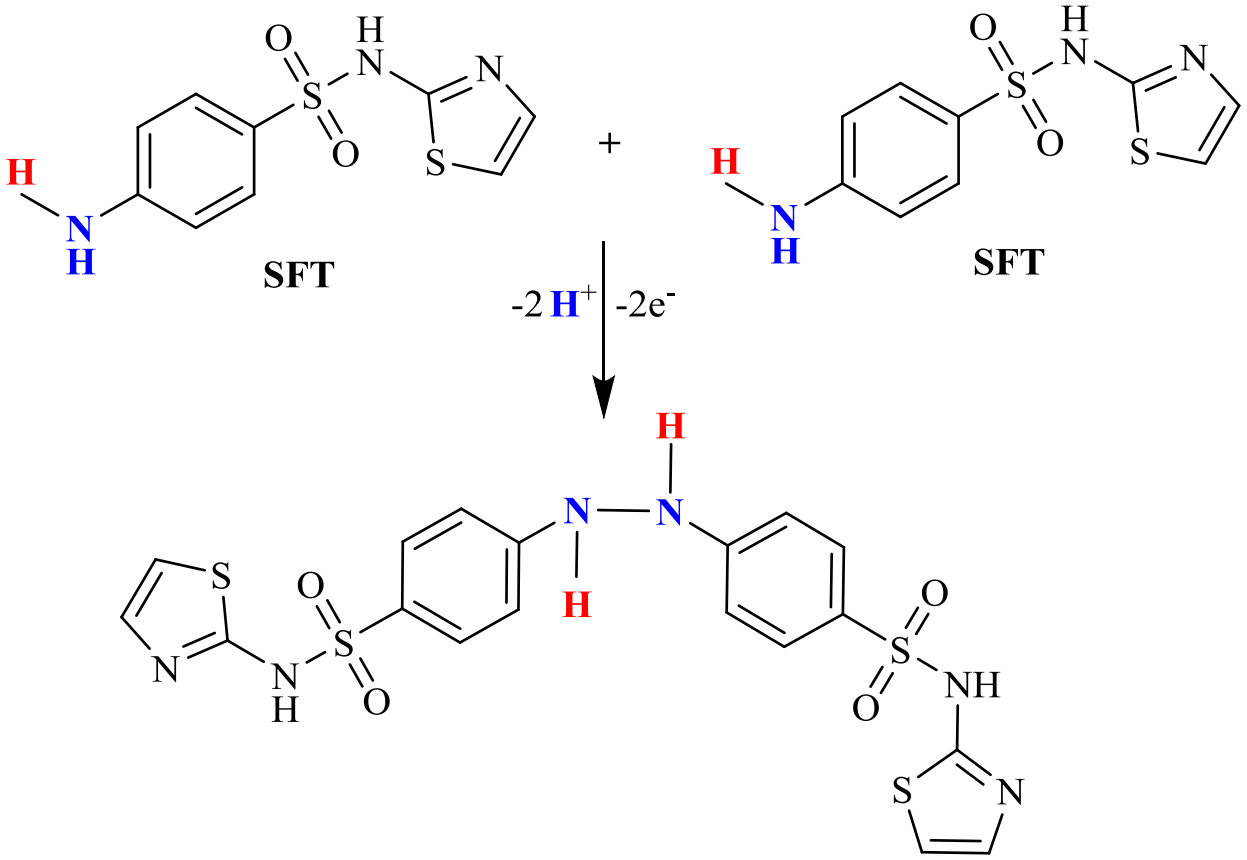
SFT
SFT
-2 H+
-2e-

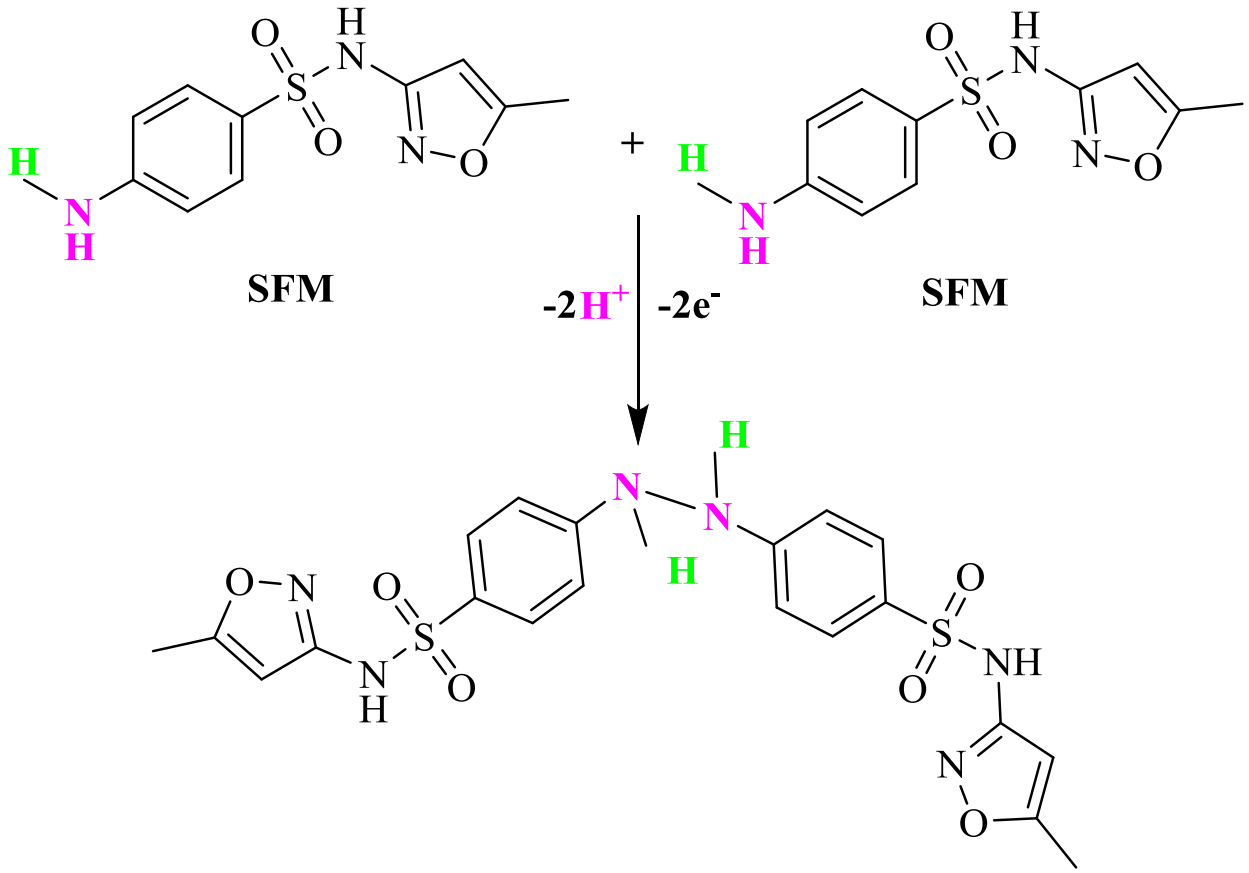

Scheme. S1. Schematic illustrations for the possible electrochemical reactions of SFT and SFM at the surface of the sensor.

Optimization of SWV parameters

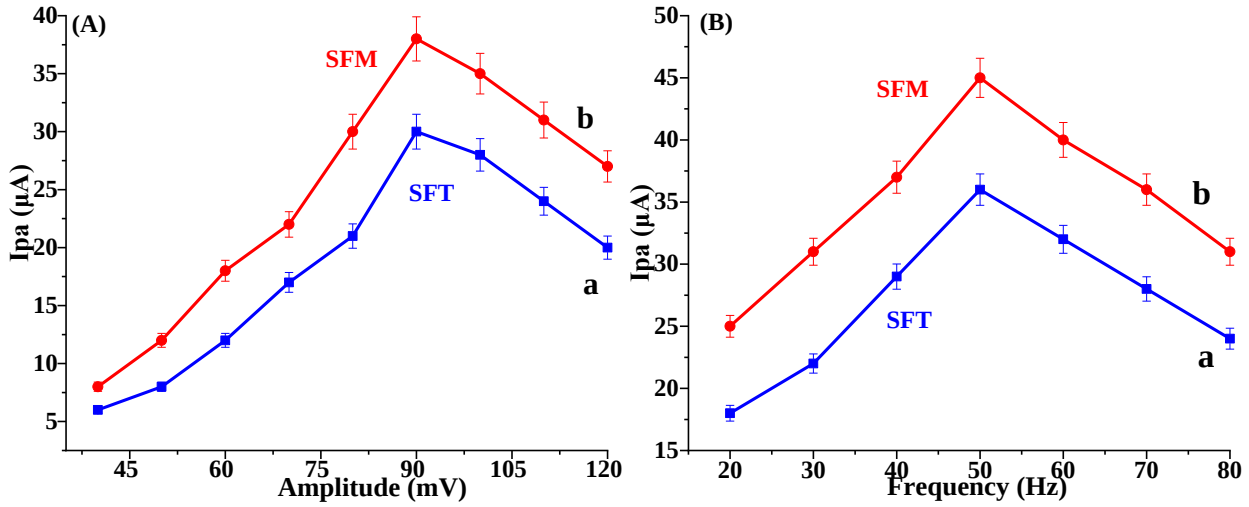

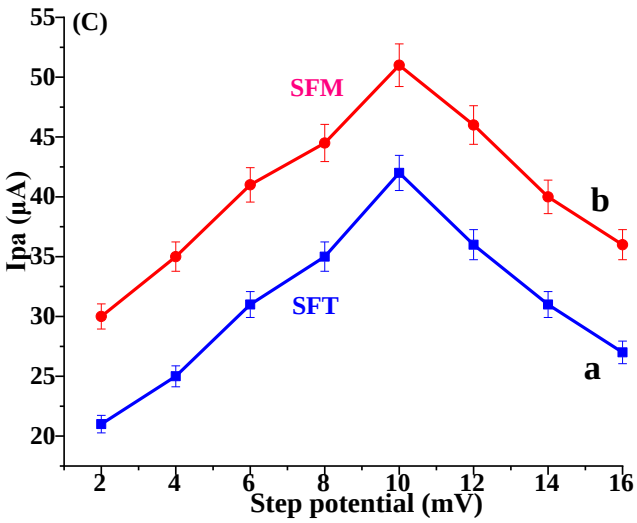

Fig. S6. The effect of SWV parameters: amplitude (A); frequency (B); and step potential (C) on the anodic current responses of 15 μM SFT and SFM.

Reproducibility, repeatability and stability

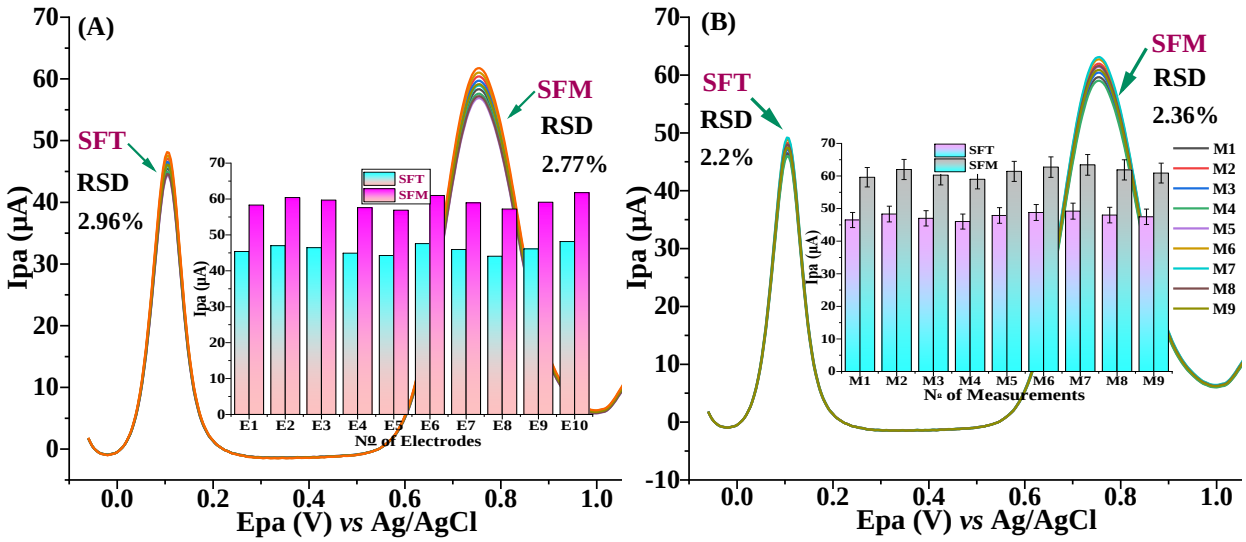

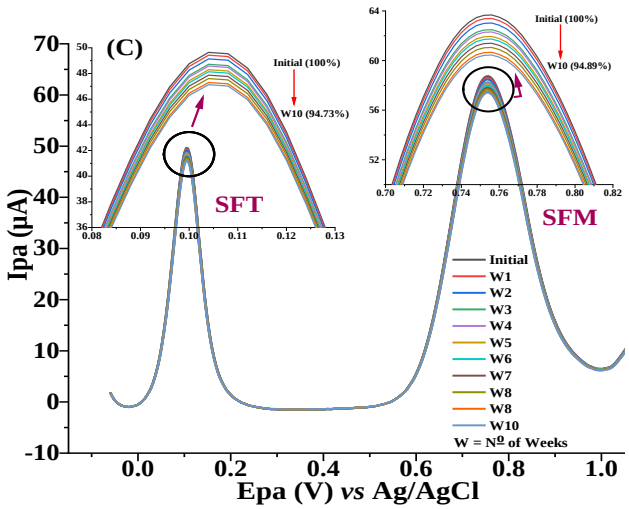

Fig. S7. (A) Reproducibility of ten electrodes, (B) repeatability of nine consecutive SWV measurements, and (C) ten week stability of TA-Au-Ag-ANpM/*f*-MWCNTs-CPE/poly(L-serine) (Inset: bar graphs).

Selectivity

Table S1: The effect of co-existing species on the current response of the sensor

Interferents	Conc. (µM)	Relative Percentage Error (%)		Interferents	Conc. (µM)	Relative Percentage Error (%)	
		SFT	SFM			SFT	SFM
Lactose	800	2.21	2.19	Amoxicillin	250	4.52	4.47
Ascorbic Acid	800	2.54	2.52	Chloramphenicol	250	4.37	4.31
Urea	800	2.67	2.69	Ampicillin	250	4.53	4.58
Dopamine	800	2.57	2.57	Cephalexin	250	4.12	4.19
Uric Acid	800	2.06	2.09	Ca^{2+}	1000	0.97	0.97
Folic Acid	800	2.87	2.88	HCO_3^-	1000	1.02	1.06
Glucose	800	2.11	2.14	K^+	1000	1.54	1.51
Sucrose	800	2.49	2.51	NO_3^-	1000	1.78	1.71
Fructose	800	2.28	2.32	Mg^{2+}	1000	1.35	1.29
Ciprofloxacin	250	4.27	4.27	CO_3^{2-}	1000	1.18	1.06
Azithromycin	250	4.13	4.16	SO_4^{2-}	1000	1.72	1.64
Metronidazole	250	4.28	4.33	Cu^{2+}	1000	1.66	1.62
Tinidazole	250	4.51	4.49	Cl^-	1000	1.27	1.24
Cloxacillin	250	4.33	4.33	Fe^{3+}	1000	1.05	1.05

Table S2. The amount of SFT detected in the pharmaceutical sample using the developed sensor.

SFT	Sample (µM)	Found* (µM)	Detected (mg/tablet)	Labelled amount (mg/tablet)	Recovery (%)	RSD (%)
Eli Lilly and Company Indianapolis, USA	5	4.94	247.0	250	98.8	2.43
	10	9.83	245.8	250	98.3	1.85
	25	24.77	247.7	250	99.1	1.76
	50	48.91	244.6	250	97.8	2.24

*Mean values of triplicate measurements

Table S3. The amount of SFM detected in the pharmaceutical sample using the developed sensor.

SFM	Sample (µM)	Found* (µM)	Detected (mg/mL)	Labelled amount (mg/mL)	Recovery (%)	RSD (%)
TEVA Pharmaceutical Ind. Ltd., Israel	5	4.86	77.8	80	97.2	2.31
	10	9.88	79.1	80	98.8	1.86
	25	24.67	78.9	80	98.7	1.97
	50	49.56	79.3	80	99.1	2.42

*Mean values of triplicate measurements

Chapter Eight: Paper VI

A novel hypersensitive electrochemical sensor (Au-Ag-ANCCs/*r*-GO/poly(L-histidine)/GCE) for the simultaneous determination of vancomycin and ceftriaxone residues in chicken meat, fish, and milk samples

Wondimeneh Dubale Adane, Bhagwan Singh Chandravanshi, Yonas Chebude, Merid Tessema

Chemical Engineering Journal

(Revised Manuscript under Review)

A novel hypersensitive electrochemical sensor (Au-Ag-ANCCs/*r*-GO/poly(L-histidine)/GCE) for the simultaneous determination of vancomycin and ceftriaxone residues in chicken meat, fish, and milk samples

Wondimeneh Dubale Adane[a], Bhagwan Singh Chandravanshi*[a], Yonas Chebude[a], Merid Tessema**[a]

[a]Department of Chemistry, Addis Ababa University, P. O. Box 1176, Addis Ababa, Ethiopia

*Corresponding author. E-mail address: bscv2006@yahoo.com

**Corresponding author. E-mail address: tessemamerid@yahoo.com

ABSTRACT

The extensive use of antibiotics in humans and animals has resulted in the presence of their residues in food and the environment, posing a substantial threat to human health, the environment, and the global economy. Herein, we developed a pioneering, hypersensitive, and ultraselective electrochemical sensor using gold-silver alloy nanocoral clusters (Au-Ag-ANCCs) decorated with reduced graphene oxide (*r*-GO) and poly(L-histidine) composites for the simultaneous determination of vancomycin (VAN) and ceftriaxone (CFT) residues in food samples. The developed sensor (Au-Ag-ANCCs/*r*-GO/poly(L-histidine)/GCE) was characterized using a wide variety of analytical techniques, including UV-Vis, FT-IR, XRD, SEM, and EDX. The electrochemical behavior of the sensor was examined by electrochemical impedance spectroscopy (EIS), cyclic voltammetry (CV), and square wave voltammetry (SWV). The sensor demonstrated extraordinary performance within a broader linear range from 1.0 pM to 120 μM for VAN and from 1.0 pM to 290 μM for CFT. The limit of detection (LOD, 3σ/m, S/N = 3 and n = 10) and limit of quantification (LOQ, 10σ/m, S/N = 3 and n = 10) are 0.11 pM and 0.36 pM for VAN, and 0.017 pM and 0.057 pM for CFT, respectively. Au-Ag-ANCCs/*r*-GO/poly(L-histidine)/GCE exhibited exceptional reproducibility, stability, and anti-interference capability. Moreover, the sensor was successfully applied to detect VAN and CFT residues in food samples (chicken meat, fish, and milk) and provided remarkable recoveries (96.2–102.1%) and relative standard deviations below 5%. Therefore, the fabricated sensor exhibited outstanding performance in detecting the target analytes, making it an ideal tool for addressing the prevailing global antibiotic residue crisis in food samples.

Keywords: Antibiotic residues; Vancomycin; Ceftriaxone; Gold-silver alloy nanocoral clusters; Electrochemical sensor; Food samples

1. Introduction

Antibiotics are highly effective agents that have both bacteriostatic and bactericidal properties against harmful microorganisms. They are therefore widely used in the treatment of various infectious diseases in humans and animals. In addition, antibiotics are frequently used in animal husbandry to promote growth and to improve feeding performance. Antibiotics are also administered to animals to control their reproductive cycle, breeding performance, and prophylaxis [1]. In humans, antibiotics are mainly used to treat infections of genitals, abdomen, urinary tract, skin, and gastrointestinal tract. They are also used to treat leprosy, tuberculosis, streptococci, bronchitis, pneumonia, arthritis, sinusitis, and typhoid fever. Their main mechanisms of action include preventing the synthesis of bacterial cell walls and proteins, limiting the synthesis of bacterial DNA, impeding the elongation of nascent RNA, and killing microbial communities [2]. Antibiotic residues, which are persistent organic pollutants, are released into the environment from hospitals and pharmaceutical industries, as well as through the direct disposal of unused or expired drugs. In addition, most antibiotics are poorly absorbed and not fully metabolized by humans and animals. Therefore, a high percentage of the ingested dose of most antibiotics is excreted through urine and feces within a few hours of administration, either as precursors or metabolites, and is released into the environment [3]. The administration of antibiotics in livestock farming can also result in the accumulation of their residues in animal derived food. As a result, humans are susceptible to the fatal toxic effects of antibiotic residues, including liver toxicity, kidney damage, allergic reactions, carcinogenic effects, mutagenicity, reproductive disorders, immunopathological consequences, and others [1].

The excessive use of antibiotics, cheap production, and misuse have together contributed to the development of antibiotic resistance in certain microorganisms. At therapeutic doses of antibiotics, bacteria can evolve and survive due to an adaptive genetic process known as antimicrobial resistance (AMR). In recent years, AMR has emerged as a significant threat to public health worldwide, leading to failure of antibiotic therapy and an increase in mortality rates and healthcare costs [2]. In recent years, several alarming reports have been published describing this

burning problem. In 2020, the World Health Organization (WHO) classified AMR as one of the top ten global threats to public health. It is currently estimated that around 700,000 deaths per year are attributable to AMR. Without the implementation of preventive measures, this number could rise to 10 million deaths by 2050. If this were to happen, the associated global costs would amount to 100 trillion US dollars by 2050 [4]. Without effective antimicrobial agents, the success of modern medicine, which depends on the availability of effective antimicrobial therapies, including cancer chemotherapy, organ transplantation, and other major surgeries, would be severely jeopardized [5]. Therefore, researchers are actively developing effective, sensitive, and selective methods to quantify life-threatening antibiotic residues in various matrices to protect human health and ensure safety.

Vancomycin (VAN), a glycopeptide antibiotic, is widely used in the treatment of severe gram-positive bacterial infections. These include infections caused by methicillin-resistant *Staphylococcus aureus (MRSA)*, methicillin-resistant *Staphylococcus epidermidis (MRSE)*, pseudomembranous colitis associated with *Clostridium difficile*, and an alternative for people with β-lactam allergies. It is also used to prevent endocarditis and to manage infections associated with prosthesis implantation [6,7]. The antibiotic acts via three primary mechanisms: it inhibits peptidoglycan synthesis, alters the permeability of the cell membrane, and interferes with RNA synthesis in the cytoplasm [7]. Treatment with VAN is considered as the last alternative and is only recommended if other antimicrobial agents are ineffective due to the patient's response. Due to its narrow therapeutic window, the low dose of VAN results in inadequate bacterial killing and the development of AMRs, while overdose is mainly associated with severe toxic side effects, such as nephrotoxicity, red man syndrome, thrombocytopenia, ototoxicity, and mortality [8]. The widespread use and misuse of antibiotics in animal husbandry contributes significantly to the emergence of AMR bacteria in the environment. *Salmonella, E. coli,* and *S. aureus* are the most prominent bacteria responsible for food safety. *S. aureus* has been detected in a variety of locations, including on the skin and in the noses of humans, poultry, milk, and livestock. According to recent studies, *S. aureus* is a vancomycin-resistant pathogen that increases the burden of antimicrobial resistance [9]. Therefore, to minimize toxicity and optimize therapy of VAN, its residues should be strictly monitored in environmental and food samples.

Ceftriaxone (CFT), a versatile cephalosporin, is an effective antibiotic for treating numerous infections caused by both gram-negative and gram-positive bacteria, making it valuable for human, animal, and aquatic healthcare. CFT is mainly prescribed for the treatment of numerous diseases, including Salmonella spp., gonorrhea, pneumonia, meningitis, and urinary tract infections [10]. Prolonged use of CFT may result in the formation of asymptomatic kidney stones, while increased doses can frequently induce transient deposits in the gallbladder and bile ducts. The temporary formation of CFT in the gallbladder can lead to abdominal pain, bloating, and an unsettled stomach. Infant red syndrome, also known as severe erythroderma, often occurs in infants treated with CFT. In addition, excessive use of CFT prolongs bleeding time and leads to hemolysis, diarrhea, and skin rash [11]. Large amounts of CFT residues are discharged into rivers, lakes, and the environment from pharmaceuticals, hospitals, humans, and animal husbandry. Due to their misuse and resistance to biodegradation, CFT residues remain in the environment and pose potentially hazardous risks to humans [12]. Therefore, it is essential to develop an electrochemical sensor that is sensitive, selective, and reliable to detect CFT residues in food and environmental samples.

Nanoparticles made of bimetallic alloy have been thoroughly investigated in the field of electrochemical sensing and have shown remarkable properties, such as increased sensitivity, high detection capability, and robust stability [13]. Their morphology, size, and composition endow them with enhanced catalytic performance and synergistic properties, expanding their potential applications in cancer treatment, nanomedicine, catalysis, DNA transfer, and biosensing [14]. Gold-silver alloy nanoparticles have generated excitement in the scientific community due to their exceptional catalytic abilities, electrical conductivity, and optical properties [15]. Zhao et al. reported a novel and simple voltammetric sensing platform for the detection of dissolved H_2S using GCE modified with Au-Ag core-shell nanoparticles [16]. Kong et al. proposed a voltammetric sensor for the detection of the anthracycline anticancer drug daunorubicin in human serum samples by modifying GCE with nitrogen-doped *r*-GO loaded with Au-Ag nanoparticles [17]. Zhao et al. reported a voltammetric sensor assembly using SPCE modified with Au-Ag NPs for the simultaneous detection of chromium ions (Cr^{3+} and Cr^{6+}) [18]. Bao et al. designed a sensing platform by constructing a core-shell of Au-Ag NPs on carboxylated graphene, which enabled the simultaneous detection of I^- and NO_2^- in water samples [19]. In another application, Yu et al.

highlighted the excellent antioxidant properties of hollow Au-Ag alloy nanorice, showing its broad potential in the domains associated with surface plasmons [20]. To the best of our knowledge, the development of an electrochemical sensor by integrating Au-Ag-ANCCs with *r*-GO and poly(L-histidine) composites has not yet been reported. It is crucial to fill this gap and develop a novel electrochemical sensor utilizing the advantages of Au-Ag-ANCCs as a modifier.

The distinctive properties of carbon-based materials, including their broad potential window, low electrical resistance, affordability, and ease of chemical modification, make them an ideal choice to advance the field of electroanalytical sensors [21]. Graphene exhibits exceptional physical and chemical properties, including excellent conductivity, large surface area, biocompatibility, and durability [22]. Reduced graphene oxide (*r*-GO) is widely used to modify various electrodes due to its exceptional conductivity, higher electroactive area, exceptional electrical conductivity, outstanding thermal stability, and mechanical properties [23]. In addition, *r*-GO exhibits strong electrocatalytic ability, large electroactive area, minimal surface fouling, and favorable price. As a result, electrochemical sensors containing *r*-GO show excellent performance due to the wide range of electrochemical potential [22]. The combination of bimetallic nanocomposites as catalysts with carbon-based substrates as supporting materials would synergistically improve the performance of an electrode, resulting in improved signal response, sensitivity, and accuracy [24]. Herein, we integrated *r*-GO into Au-Ag-ANCCs nanocomposites to develop an electrochemical sensor with extended analytical applications. The integration of *r*-GO improved the electrical conductivity, minimized the internal resistance, and increased the charge transfer during electrochemical reactions, which ultimately improved the performance of the sensor [25].

Electrodes modified with amino acid-based polymers have gained a significant attention in electrochemical sensing applications due to their stability, non-toxicity, compatibility, cost-effectiveness, and tunable physicochemical properties [26]. In this study, poly(L-histidine), an excellent polyelectrolyte, was inventively integrated with *r*-GO and Au-Ag-ANCCs to modify GCE and develop a novel electrochemical sensor. R-GO interacts non-covalently with the lipophilic π-π conjugated imidazole groups in the side chain of poly(L-histidine). Furthermore, the free amino groups of poly(L-histidine) interact covalently with the COOH group of *r*-GO by forming amide bonds [27]. The transfer of electrons relies heavily on π-π interactions; therefore,

their incorporation into Au-Ag-ANCCs significantly enhances electrocatalytic activities [28]. In general, the poly(L-histidine) layer boosts the electron transfer ability of the electrode and improves the catalytic activity of the nanocomposites. The enhancement arises from the various functional groups formed after modification, including imidazole rings, COOH, and NH_2 groups [26].

Several analytical methods have been reported for the quantification of VAN and CFT in various matrices, including capillary zone electrophoresis [29], UHPLC–MS/MS [30], spectrophotometry [31], chemiluminescence [32], and LC–MS/MS [33]. Although these techniques are sensitive and selective, they have some limitations, such as complex operational procedures, time-consuming sample preparation, longer analysis times, high equipment prices, and the need for skillful operators [21]. On the other hand, voltammetric methods are inexpensive, user-friendly, highly specific, sensitive, portable, and can be miniaturized. They also offer rapid analysis and require minimal reagent volume [2]. Therefore, electrochemical techniques were the preferred choice for the simultaneous detection of VAN and CFT residues in this study. Among the various electrochemical techniques, SWV was selected due to its numerous advantages, including ultra-fast analysis, minimal sample consumption, background discrimination, and high sensitivity [34].

Electrochemical sensors with high sensitivity, selectivity, and efficacy are crucial for the detection of life-threatening antibiotic residues in various matrices, as these residues pose a significant risk to human health. Herein, we have developed a pioneering electrochemical sensing platform by integrating Au-Ag-ANCCs with *r*-GO and poly(L-histidine) composites for the simultaneous detection of VAN and CFT residues in food samples. Au-Ag-ANCCs/*r*-GO/poly(L-histidine)/GCE was extensively characterized by various analytical methods such as UV-Vis, FT-IR, XRD, SEM, and EDX. The sensor showed a wide linear range and ultra-small detection limit for both analytes. The combination of the different properties of the individual modifiers in the sensor resulted in a synergistic effect, which enhanced sensitivity, selectivity, and stability. This was reflected by the improved and well-defined current responses to ultra-trace analyte concentrations. In addition, the sensor exhibited excellent reproducibility, repeatability, and remarkable selectivity. Finally, the sensor was effectively utilized for the simultaneous detection

of VAN and CFT residues in real samples, showing high recoveries and RSD values below 5%. These results underline the exceptional performance of the developed sensor.

2. Experimental

The chemicals and reagents, apparatus, and instruments used in this study as well as the sample preparation procedures are detailed in the Supplementary Material.

2.1. Preparation of *r*-GO

$NaBH_4$, a potent hydride donor, readily reduced the oxygen functional groups in GO. The $NaBH_4$-mediated reduction process produces conjugation within the graphene lattice and results in the formation of *r*-GO [35]. The reduction of GO suspension with $NaBH_4$ was performed as follows: first, 1.0 g GO was dissolved in 100 mL deionized water. Then, 0.5 g of $NaBH_4$ was added to the solution and stirred for 30 min at ambient temperature. After the stirring, the solution was filtered to remove residuals of unreduced GO. Finally, the resulting *r*-GO was subjected to multiple rinsing with distilled water and dried in vacuum. This method facilitates the conversion of GO into *r*-GO and potentially improves its electrical and mechanical properties for electrochemical applications.

2.2. Synthesis of Au-Ag-ANCCs

A complex preparation procedure was employed for the synthesis of Ag-NCCs, requiring a careful control of reaction parameters and a precise chemical reduction process to reveal its exceptional characteristics. Initially, 2 mL of 0.1 M $AgNO_3$ and 10 mL of 0.1 M PVP were added into a 100 mL flask containing 15 mL of 0.1 M PEG 600 solution under vigorous stirring for 20 min. Then, 4 mL of 1% $Na_3C_6H_5O_7$ was added to initiate the reduction of Ag ions. The addition of stabilizing agent prevents agglomeration and regulates the size and morphology of the clusters. Subsequently, the mixture was heated in an oil bath at 130 °C for 10 h, during which $AgNO_3$ and PVP reacted to form Ag nanocoral clusters stabilized by PEG 600 molecules. Controlled temperature and stirring conditions facilitated the gradual formation of Ag nanocoral clusters, exhibiting distinctive branch-like structures. The yellowish solution was allowed to cooling, centrifugation, and washing several times.

The synthesis of Au-Ag-ANCCs employs a precise and controlled alloying process, transforming the prepared Ag-NCCs into their gold-based counterparts. Initially, 5 mL 0.01 M $HAuCl_4$ solution was mixed with the Ag-NCCs suspension in a separate vessel under vigorous stirring for 15 min to ensure the uniform distribution of gold ions. This step facilitates the incorporation of gold into the silver nanostructures, forming the basis for alloyed nanocoral clusters. Subsequently, the reaction mixture was heated in an oil bath at 90 °C for three hours with continuous stirring. Alongside, 3 mL 0.1 M $NaBH_4$ was gradually added to activate the reduction process, leading to the formation of Au-Ag alloy nanocoral clusters. The pH of the reaction mixture was maintained at 10 throughout the process by the periodic additions of 0.1 M NaOH, promoting gold ion reduction and stabilizing the resulting alloy nanostructures. Additionally, 4 mL of 1% PVP solution was introduced as a stabilizing agent to preserve the colloidal stability and form a protective layer, preventing aggregation through electrostatic repulsion and inhibiting the formation of larger agglomerates. Finally, the synthesized Au-Ag-ANCCs was centrifuged, washed, and dried in vacuum.

2.3. Preparation of Au-Ag-ANCCs/*r*-GO/GCE

Before modification, the GCE undergo polishing with 0.3 and 0.05 µm alumina slurries, rinsing with distilled water, sonication in ethanol/water (1:1), and electrochemical activation in 0.1 M H_2SO_4 through ten cycle potential scans from -0.4 to 1.2 V (100 mVs^{-1}, scan rate). To fabricate the Au-Ag-ANCCs/*r*-GO nanocomposite, 6 mL of Au-Ag-ANCCs dispersion was mixed with 4 mL of *r*-GO dispersion and stirred vigorously for 30 min at ambient temperature. This ensured a comprehensive integration of Au-Ag-ANCCs into the *r*-GO surface. Then, the mixture was heated in a water bath at 30 °C for 25 min. The resulting composite was subjected to ultrasonication, centrifugation, and repeated washing. The dried nanocomposite was then dispersed in deionized water through 20 min ultrasonication, resulting in a 15 mL dispersion for subsequent use.

To prepare the Au-Ag-ANCCs/*r*-GO/GCE, 8 µL of the Au-Ag-ANCCs/*r*-GO dispersion was drop-casted at the activated GCE and subjected to drying at room temperature. A similar procedure was applied to fabricate other modified electrodes.

2.4. Preparation of Au-Ag-ANCCs/*r*-GO/poly(L-histidine)/GCE

To fabricate the proposed electrode, cyclic voltammetry was performed for 14 cycles in 0.1 M PBS (pH 7.0) containing 0.06 M L-histidine in the potential range of -1.7 V to 1.6 V at a scan rate of 25 mVs^{-1} for electropolymerization of L-histidine at the surface of Au-Ag-ANCCs/*r*-GO/GCE (Fig. S1A). Afterwards, the fabricated sensor (Au-Ag-ANCCs/*r*-GO/poly(L-histidine)/GCE) was rinsed with distilled water and readied for subsequent application. The general preparation procedures for the developed sensor are illustrated in Scheme 1.

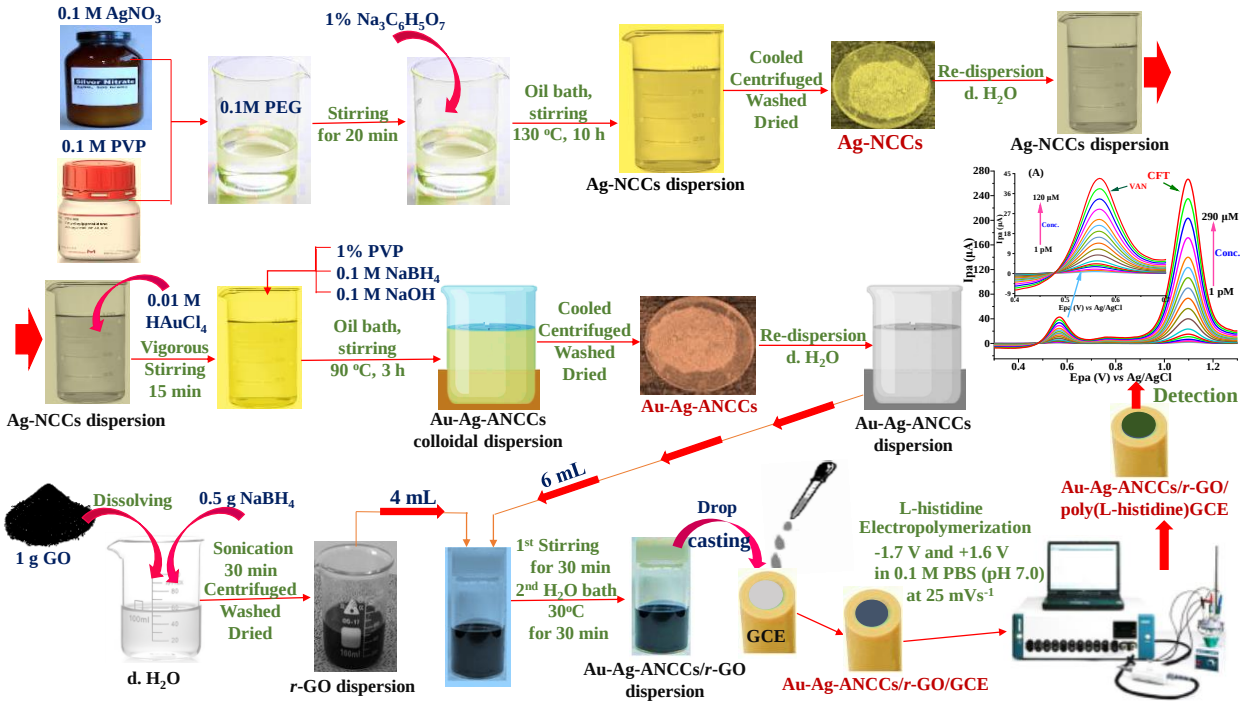

Scheme 1. Schematic illustration of the preparation procedures for the proposed sensor.

3. Results and discussion

3.1. Analytical characterizations

The in-depth investigation of Au-Ag-ANCCs/*r*-GO/poly(L-histidine)/GCE reveals a comprehensive understanding of the sensor's composition and interfacial makeup. The complexities of the developed sensor were examined using various analytical methodologies including UV-Vis, FT-IR, XRD, SEM, and EDX.

The UV-Vis spectrum of Ag-NCCs revealed a distinct absorption peak at λmax = 461 nm, signifying the localized surface plasmon resonance properties of the Ag particles (Fig. 1A(a)). The peak's sharpness implies mono-dispersity and uniformity in particle size, with an average calculated size of around 33 nm. As shown in Fig. 1A(b), Au-Ag-ANCCs displayed a distinct broad peak at λ_{max} = 515 nm, suggesting that the incorporation of Au into the alloy decreased the size (22 nm) and shifted the absorption peak to a longer wavelength. The observed variations in the two spectra arise from changes in the composition and sizes of the nanocoral clusters, which influence their optical characteristics. As surface area directly influences catalytic activity, the alloyed nanocoral clusters with the smallest particle size and largest surface area exhibited superior catalytic performance in preparing the intended sensor.

As shown in Figs. 1B(a-d), FT-IR was employed for the characterization of Ag-NCCs, Au-Ag-ANCCs, Au-Ag-ANCCs/*r*-GO, and Au-Ag-ANCCs/*r*-GO/poly(L-histidine) composites. FT-IR of Ag-NCCs exhibited characteristic peaks corresponding to Ag-O stretching (568 cm^{-1}), C-H bending (1037 and 1120 cm^{-1}), Ag-O stretching (1385 cm^{-1}), C=O stretching (1629 cm^{-1}), C-H stretching (2856 and 2929 cm^{-1}), and O-H stretching (3459 cm^{-1}). FT-IR of Au-Ag-ANCCs displayed peaks attributed to Ag-O stretching (540 cm^{-1}), Au-O stretching (620 cm^{-1}), Au-Ag stretching (860 cm^{-1}) confirming the alloying of Au and Ag, C-O stretching (1078 cm^{-1}), C-H stretching (2856 and 2929 cm^{-1}), and O-H stretching (3438 and 1640 cm^{-1}). The incorporation of *r*-GO into the Au-Ag-ANCCs was confirmed by the presence of C=C stretching (1612 cm^{-1}) and aromatic ring stretching (1553 cm^{-1}) vibrations. The successful integration of poly(L-histidine) into the Au-Ag-ANCCs/*r*-GO composite was confirmed by the amide I (1625 cm^{-1}) and II (1578 cm^{-1}) stretching vibrations.

XRD was used to evaluate the crystal structure and size of the nanocoral clusters. Consistent results obtained from the UV-Vis and XRD measurements of the nanocoral cluster size confirmed the structural features determined using these techniques. Consistency of the results enhances the reliability and validity of the findings, enabling a comprehensive understanding of the material. As shown in Fig. 1C(a), the XRD diffraction peaks of Ag-NCCs at 2θ = 34.42°, 38.24°, 40.08°, 44.46°, and 57.72° were indexed to the (100), (111), (200), (220), and (311) planes, respectively, and were characteristic of face-centered-cubic (FCC) structured Ag metal crystals (JCPDS card number 04-0783), consistent with previous reports [36]. The 2θ values for the Au-Ag-ANCCs and

Ag-NCCs are almost identical, as Au and Ag have similar lattice constants (JCPDS: 4-0783 and 4-0784). However, XRD analysis of Au-Ag-ANCCs (Fig. 1C(b)) revealed an additional characteristic peak at 26.52°, which was attributed to the (111) crystal plane, suggesting the formation of a potential intermetallic alloy compound [37]. The XRD peaks at 32.42° and 46.34° (Fig. 1C(c)) correspond to the (002) and (111) planes of *r*-GO, respectively [38], with diminished intensity, confirming the successful incorporation of *r*-GO into Au-Ag-ANCCs. The spectra of the Au-Ag-ANCCs/*r*-GO/poly(L-histidine)/GCE (Fig. 1C(d)) exhibited characteristic XRD peaks of its constituent components, Au-Ag-ANCCs, *r*-GO, and poly(L-histidine), confirming the successful preparation of the sensor.

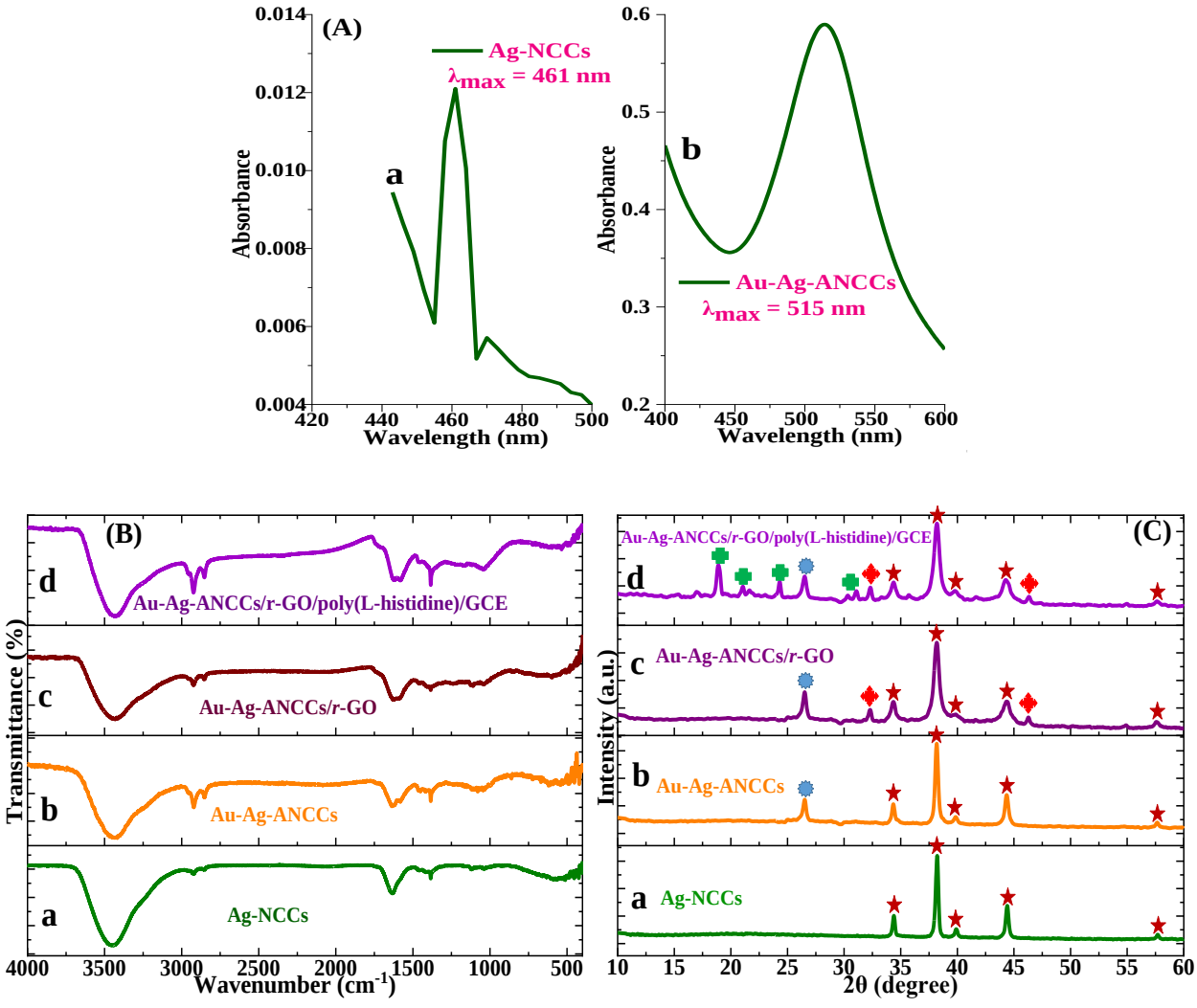

Fig. 1. (A) UV-Vis spectra of Ag-NCCs (a), Au-Ag-ANCCs (b), (B) FT-IR spectra and (C) XRD patterns of Ag-NCCs (a), Au-Ag-ANCCs (b), Au-Ag-ANCCs/*r*-GO (c), and Au-Ag-ANCCs/*r*-GO/poly(L-histidine)/GCE (d).

The SEM image of *r*-GO presented in Fig. 2(a) provides valuable insight into its morphology. This multifunctional material exhibits a rough, irregular, and heterogeneous structure, as well as porosity, all of which contribute to its distinctive characteristics. As shown in the EDX spectra (Fig. S2(d)), *r*-GO is mainly composed of C (77.6%) and O (22.4 %), indicating its high degree of purity. The SEM analysis of Ag-NCCs revealed a beautiful morphology characterized by irregularly shaped, and three-dimensional nanocoral clusters with interconnected branches resembling coral reefs (Fig. 2(b)). These nanocoral clusters exhibit non-uniform distribution, rough surfaces, and porous networks. The average size of the Ag-NCCs was determined to be 31–35 nm, which is consistent with the UV-Vis and XRD findings. SEM examination of Au-Ag-ANCCs in Fig. 2(c) revealed highly irregular, non-uniform nanocoral clusters comprising a rough porous network (average size of 20–24 nm). The EDX spectra of Ag-NCCs (Fig. S2(e)) showed the presence of C (32.0%), N (3.3%), O (7.1%), and Ag (57.6%), as well as Au-Ag-ANCCs (Fig. S2(f)) contained C (26.5%), N (3.1%), O (7.3%), Ag (52.6%), and Au (10.5%), indicating that Au was successfully incorporated into the Ag-NCCs. The incorporation of Au into Ag-NCCs enhanced the conductivity, active area, and catalytic properties of Au-Ag-ANCCs. Fig. 2(d) shows the uniform distribution of Au-Ag-ANCCs particles into the *r*-GO matrix. The Au-Ag-ANCC particles maintained their crystalline nano-porosity and interconnectivity with irregular shapes and noticeable cavities. This indicates that Au-Ag-ANCC particles were successfully incorporated into *r*-GO, resulting in a delicate balance between their irregular shape and the interconnected network of *r*-GO. Elemental mapping of Au-Ag-ANCCs/*r*-GO (Fig. S2(i)) confirmed the presence of C (35.3%), O (7.4%), Ag (46.9%), and Au (10.4%). As shown in Fig. 2(e), the coating of the Au-Ag-ANCCs/*r*-GO surface with a poly(L-histidine) film, forms an amorphous coral nanoporous cluster with a rough and irregular surface. This coating significantly enhanced the electrical conductivity, electroactive surface area, and catalytic capability of Au-Ag-ANCCs/*r*-GO/poly(L-histidine)/GCE. The corresponding EDX spectra in Fig. 2(f) confirm the presence of C (31.4%), N (4.7%), O (7.4%), Ag (46.0%), and Au (10.5%), thus validating the successful fabrication of the proposed sensor.

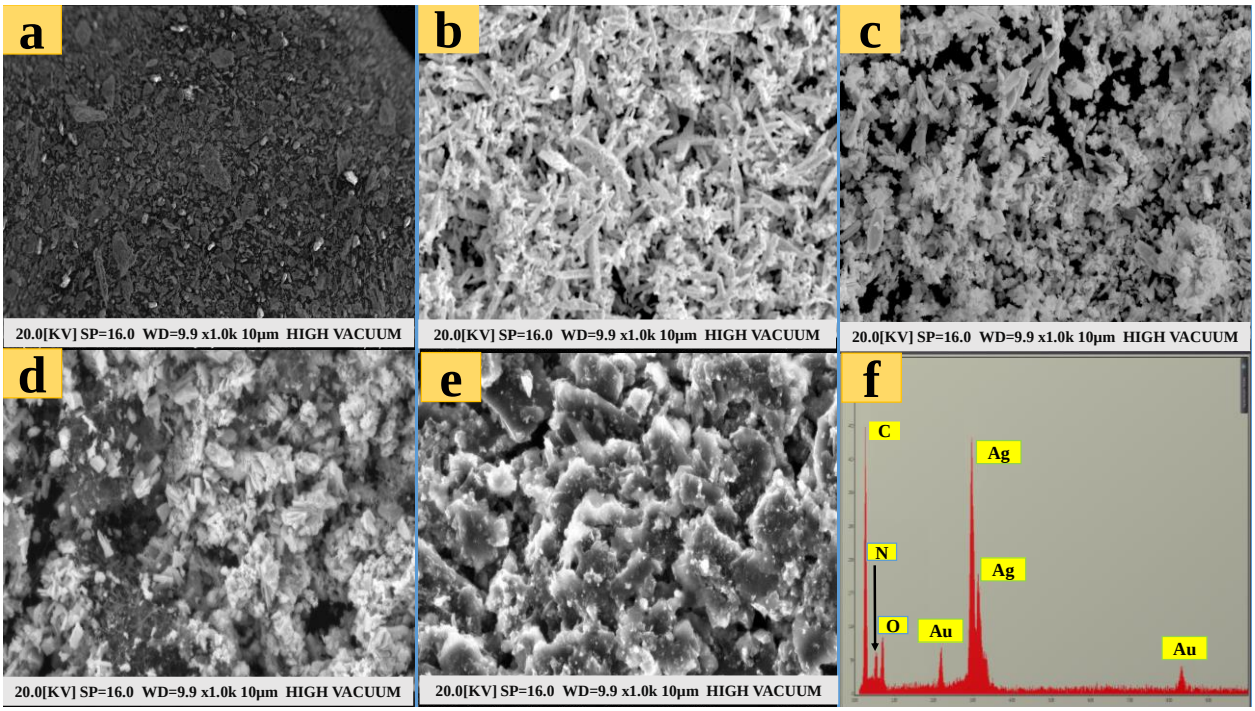

Fig. 2. SEM images of *r*-GO (a), Ag-NCCs (b), Au-Ag-ANCCs (c), Au-Ag-ANCCs/*r*-GO (d), and Au-Ag-ANCCs/*r*-GO/poly(L-histidine)/GCE (e), and EDX spectra of Au-Ag-ANCCs/*r*-GO/poly(L-histidine)/GCE (f).

3.2. Electrochemical characterization

EIS served as a powerful tool for examining the transfer of electrons and interfacial characteristics across diverse electrodes in electrochemical reactions. Its significance in electroanalytical research lies in its capacity to provide crucial insights into reaction dynamics. In this study, EIS was employed to probe the interface properties of both unmodified and modified electrodes across a frequency range from 0.1 Hz to 100 kHz with 5 mM $[Fe(CN)_6]^{3-/4-}$ solution in 0.1 M KCl. Applying a Randles equivalent circuit model for data fitting (inset Fig. 3A), the corresponding values are presented in the Nyquist plot, where the semicircular diameter represents the charge transfer resistance (R_{ct}). As shown in Fig. 3A, a larger diameter semicircle with an R_{ct} value of 4121 Ω is obtained at the bare GCE. The diameter of the *r*-GO/poly(L-histidine)/GCE semicircle is reduced to 2574 Ω due to the combined conductivity of *r*-GO and poly(L-histidine) composites. At the surface of Au-Ag-ANCCs/GCE, the R_{ct} has further decreased to 1795 Ω due to the excellent electrical conductivity of Au-Ag-ANCCs. At the surface of Au-Ag-

ANCCs/poly(L-histidine)/GCE, the R_{ct} (559 Ω) decreased more than that of Au-Ag-ANCCs/*r*-GO/GCE (R_{ct} = 871 Ω) because of the high electrical conductivity of the poly(L-histidine) film. Furthermore, the semicircular diameter of Au-Ag-ANCCs/*r*-GO/poly(L-histidine)/GCE is the smallest of all (164 Ω), suggesting that the synergistic effect of all modifiers significantly enhanced the sensor's performance.

To examine the electrochemical properties of the electrodes at different stages of modifications, CV was performed in a redox probe solution of 5 mM $[Fe(CN)_6]^{3-/4-}$ in 0.1 M KCl (scan rate: 50 mVs^{-1}). The unmodified GCE exhibited the lowest current response compared to the others, attributed to its sluggish electrical conductivity (Fig. 3B(a)). The peak current response of the *r*-GO/poly(L-histidine)/GCE surpassed that of the bare GCE, due to the enhanced electrical conductivity of the *r*-GO/poly(L-histidine) composite (Fig. 3B(b)). In Fig. 3B(c), the modification of the GCE with Au-Ag-ANCCs resulted in an enhanced redox current response, indicating the outstanding electron transfer capability and conductivity of Au-Ag-ANCCs. Compared to the other three electrodes (bare GCE, *r*-GO/poly(L-histidine)/GCE, and Au-Ag-ANCCs/GCE), the redox peak current responses of Au-Ag-ANCCs/*r*-GO/GCE and Au-Ag-ANCCs/poly(L-histidine)/GCE are significantly improved (Fig. 3B(d and e)). This is attributed to high electrocatalytic activity and electrical conductivity of *r*-GO and poly(L-histidine). The peak current response reached its maximum value at the surface of Au-Ag-ANCCs/*r*-GO/poly(L-histidine)/GCE (Fig. 3B(f)), with peak-to-peak separation (ΔEp) reaching the lowest value. The results indicate that the synergistic effects of the modifiers significantly enhanced the catalytic activity, electron transfer capability, electroactive surface area, and electrical conductivity of the sensor.

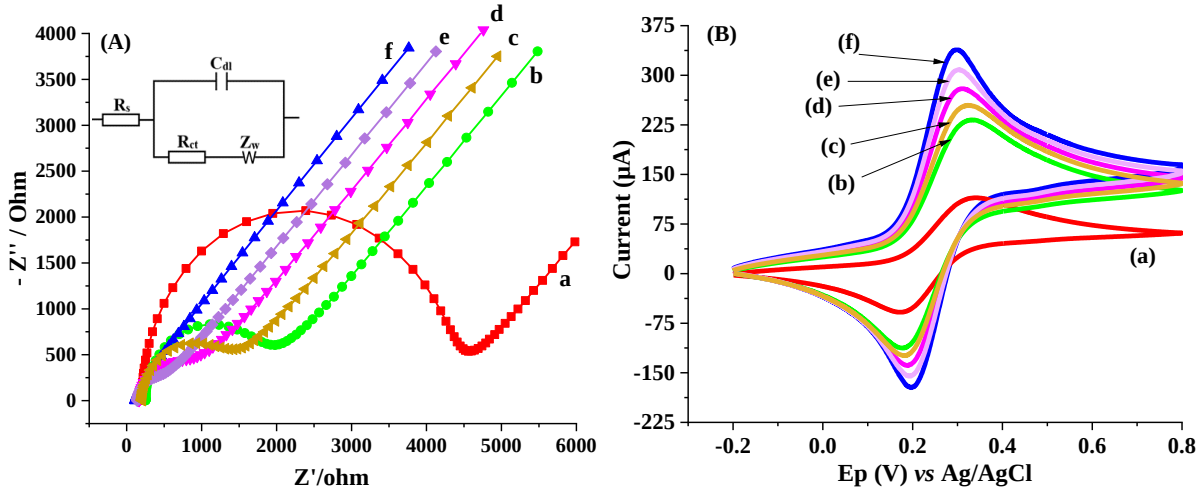

Fig. 3. Nyquist plots (A) and CVs (B) of bare GCE (a), *r*-GO/poly(L-histidine)/GCE (b), Au-Ag-ANCCs/GCE (c), Au-Ag-ANCCs/*r*-GO/GCE (d), Au-Ag-ANCCs/poly(L-histidine)/GCE (e), and Au-Ag-ANCCs/*r*-GO/poly(L-histidine)/GCE (f).

Electroactive surface area measurement is critical phenomena in voltammetric reactions as it directly affects catalytic efficiency and sensitivity of electrodes. Herein, CV was employed to estimate the electroactive surface area of electrodes at different modification stages using Randles-Sevcik equation (1) [2].

$$I_p = 2.69 \times 10^5 n^{3/2} A D^{1/2} C v^{1/2} \quad (1)$$

where I_p = peak current (A), D = diffusion coefficient ($cm^2\ s^{-1}$), n = number of electrons (n = 1), *v* = scan rate (Vs^{-1}), C = concentration of $[Fe(CN)_6]^{3-/4-}$ ($mol\ cm^{-3}$), and A = electrode surface area (cm^2). The electroactive surface areas of bare GCE, *r*-GO/poly(L-histidine)/GCE, Au-Ag-ANCCs/GCE, Au-Ag-ANCCs/*r*-GO/GCE, Au-Ag-ANCCs/poly(L-histidine)/GCE, and Au-Ag-ANCCs/*r*-GO/poly(L-histidine)/GCE were calculated to be 0.037, 0.082, 0.105, 0.133, 0.164, and 0.197 cm^2, respectively. Au-Ag-ANCCs/*r*-GO/poly(L-histidine)/GCE has an electroactive surface area four times larger than the bare GCE and also the other modified electrodes. This is because the *r*-GO and poly(L-histidine) synergistically increases the electroactive surface area and improve the electron transfer kinetics of the sensor.

3.3. Electrochemical behavior of VAN and CFT at different electrodes

The voltammetric characteristics of electrodes at different stages of modification were investigated using SWV and CV in 25 µM VAN and CFT containing 0.1 M PBS (pH 7) (scan rate: 100 mVs^{-1}). Despite the electrode variations, no voltammetric currents were recorded from the blank solution. This indicates that the analytes are either potentially absent from the blank solution or existing below the detection limits. The absence of reduction peaks during the reverse CV scan indicates that the electrochemical oxidations of VAN and CFT are irreversible. Interestingly, the electrode modifications significantly improved the electrochemical responses of the analytes and shifted their peak potentials to more positive values. The bare GCE (Fig. 4A) exhibited weak and non-distinct anodic peak currents for VAN and CFT, indicating sluggish electron transfer. In

contrast, *r*-GO/poly(L-histidine)/GCE showed significantly higher current responses. The enhancement can be attributed to the combined effect of poly(L-histidine) and *r*-GO, which forming a conductive network with electroactive sites at the electrode surface. The combined effects of increased surface area, improved adsorption, and reduced resistance, all contribute to the observed enhancements in conductivity and electron transfer kinetics of *r*-GO/poly(L-histidine)/GCE [39]. The higher anodic peak currents observed at the Au-Ag-ANCCs/GCE are due to the combined effects of alloying and nanostructuring in the Au-Ag-ANCCs. The alloying of Au and Ag improves electrical properties, while the nanocoral cluster structure further increases conductivity by providing a large surface area [40]. The oxidation currents of VAN and CFT are higher at Au-Ag-ANCCs/poly(L-histidine)/GCE than at Au-Ag-ANCCs/*r*-GO/GCE. The result indicates that poly(L-histidine) has superior electron transfer ability, enhanced conductivity, and robust electrocatalytic activity compared to *r*-GO. The maximum peak current response is observed for Au-Ag-ANCCs/*r*-GO/poly(L-histidine)/GCE, suggesting that the synergistic effect of the nanocomposites promotes performance of the sensor.

SWV was performed for 25 µM VAN and CFT in 0.1 M PBS (pH 7) at the bare GCE and various modified electrodes (Fig. 4B). The bare GCE showed poor responses for VAN and CFT electro-oxidation, due to its limited electrical conductivity and catalytic ability. In contrast, *r*-GO/poly(L-histidine)/GCE showed a significantly improved SWV response due to the combined properties of *r*-GO and poly(L-histidine). The Au-Ag-ANCCs/GCE showed higher anodic current response compared to the bare and *r*-GO/poly(L-histidine)/GCE due to the robust electrical conductivity and fast electron transfer kinetics of the Au-Ag-ANCCs. Further modification of Au-Ag-ANCCs/GCE with *r*-GO and poly(L-histidine) resulted in a higher current response for the oxidation of VAN and CFT at the Au-Ag-ANCCs/poly(L-histidine)/GCE compared to Au-Ag-ANCCs/*r*-GO/GCE. This improved current response indicates faster electron transfer between the electrode and the analytes. Consistent with the CV results, the most pronounced SWV responses for the electrochemical oxidation of VAN and CFT were observed at the surface of Au-Ag-ANCCs/*r*-GO/poly(L-histidine)/GCE, demonstrating the synergistic effects of all the nanocomposites.

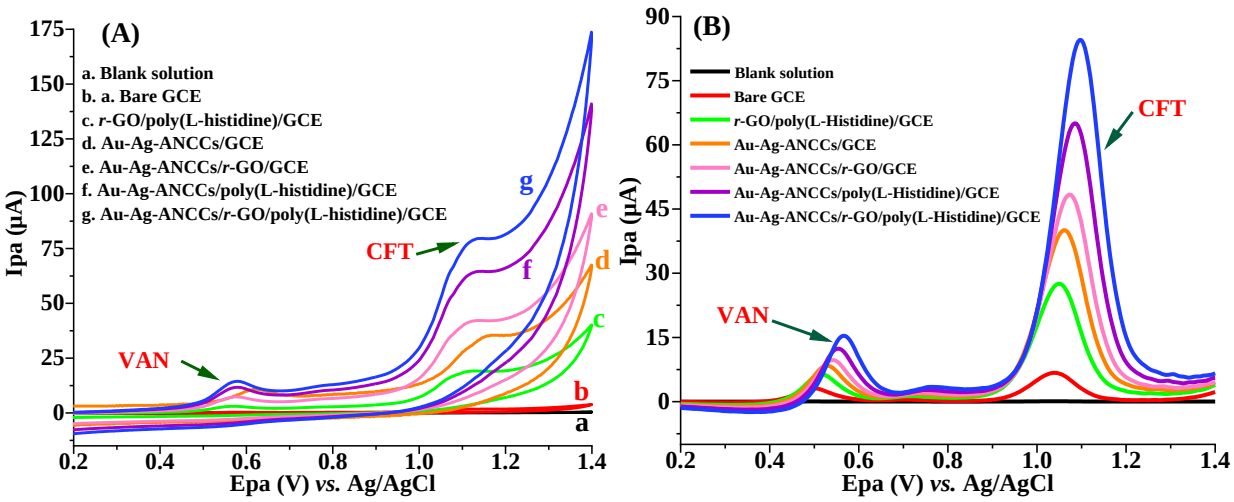

Fig. 4. (A) CVs and (B) SWVs of 25 µM VAN and CFT at different modified electrodes.

3.4. Optimization of experimental conditions

The Supplementary Material offers a concise summary of the optimization procedures, including the count of electropolymerization cycles, nanocomposites mixing ratio, and the volume of drop-casting species.

3.4.1. Effect of electrolyte solution

The electrolyte solution used in voltammetric techniques has a significant effect on the shape of the resulting voltammogram, peak-to-peak separation (ΔEp) and the current response. Therefore, it is necessary to select the appropriate supporting electrolyte before conducting any electrochemical analysis. Herein, SWV was used to examine how different supporting electrolytes affect the electrochemical results. The tested electrolytes include phosphate buffer, sulfuric acid, citrate-phosphate buffer, Britton-Robinson buffer, acetate buffer, ammonium-acetate buffer, and citrate buffer. The phosphate buffer solution (PBS) produced significantly higher current responses than the others (Fig. S3). Based on its demonstrated superiority, PBS was chosen as the suitable electrolyte solution for simultaneously determining VAN and CFT.

3.4.2. Effect of pH

The pH of the supporting electrolyte solution is one of the crucial parameters that can influence the responses of electrochemical reactions. It can affect the activity of electrodes, the stability of analytes, the interaction between the electrode and analyte, and the electro-oxidation/reduction of analytes. The effect of varying the pH of PBS on the anodic current responses of 25 µM VAN and CFT was investigated in the range of 4.0 to 8.0 at the surfaces of Au-Ag-ANCCs/*r*-GO/poly(L-histidine)/GCE (Fig. 5A). The anodic current response for 25 µM VAN and CFT gradually increased with the pH of PBS from 4.0 to 7.0 and reached its maximum at pH 7.0 (Figs. 5B(a) and 5C(a)). However, a further increase in pH resulted in a decrease in current responses. Therefore, pH 7.0 of PBS was selected as the optimal pH for subsequent experiments. As illustrated in Fig. 5A, the anodic peak potentials of VAN and CFT show a similar trend and shift to less positive values as the pH of the PBS increases, indicating that protons (H^+) are intensively involved in the electrode reactions. The relationship between peak potential and pH of PBS was given by the linear regression equations Epa (V) = 1.05 – 0.056pH (R^2 = 0.994) (Fig. 5B(b)) and Epa (V) = 1.19 – 0.053pH (R^2 = 0.996) (Fig. 5C(b)) for VAN and CFT, respectively. The slope values of 0.056 and 0.053 V/pH (volte per pH units) for VAN and CFT, respectively, are close to the theoretical Nernstian value of 0.059 V/pH. This suggest that an equal number of electrons and protons were involved in the electro-oxidation of the analytes, in accordance with earlier reports [41,42].

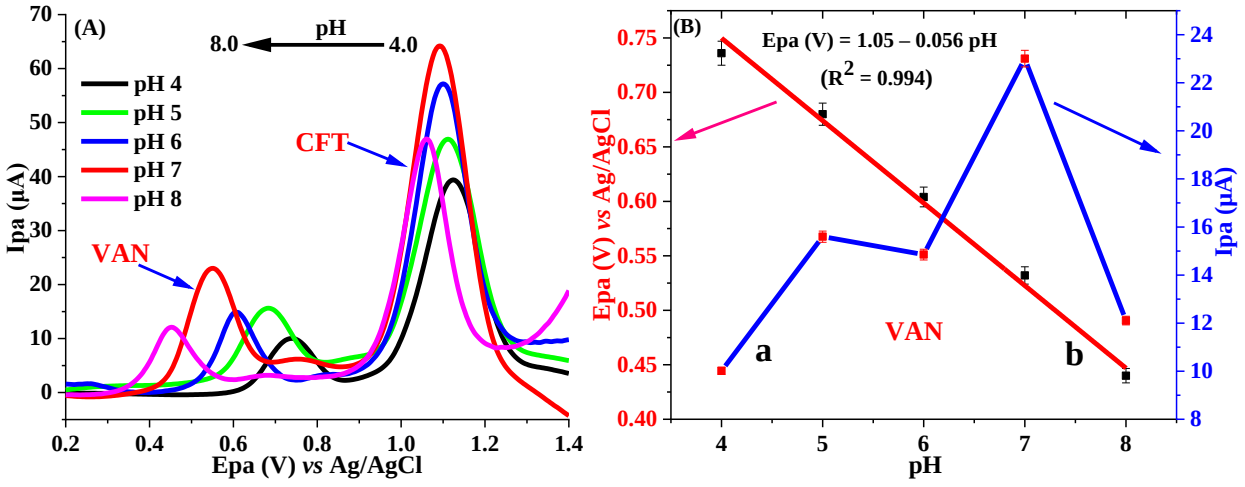

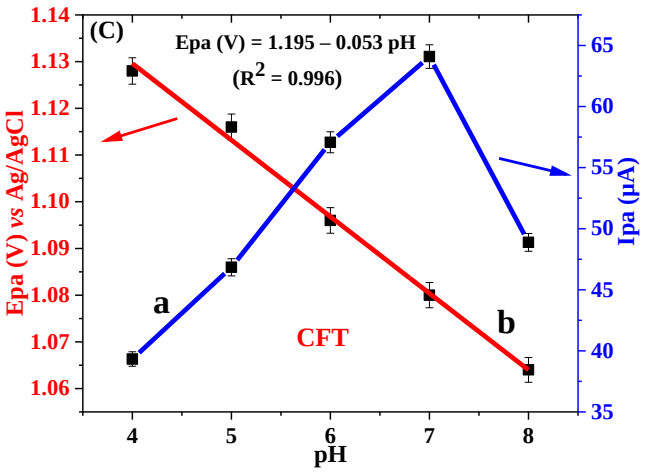

Fig. 5. (A) SWV of 25 µM VAN and CFT at different pH of PBS, (B) and (C) Ipa (µA) *vs.* pH (a) and Epa (V) *vs.* pH (b) for VAN and CFT, respectively.

3.4.3. Effect of scan rate

Electrochemical responses of 25 µM VAN and CFT at the surface of Au-Ag-ANCCs/*r*-GO/poly(L-histidine)/GCE were studied in 0.1 M PBS (pH 7) using SWV within a scan rate ranges from 25–300 mVs^{-1}. As depicted in Figs. 6A and B, the absence of reduction peaks in the reverse scan and the shift of oxidation potential towards more positive values as the scan rate increases indicate that the voltammetric reactions of VAN and CFT at the Au-Ag-ANCCs/*r*-GO/poly(L-histidine)/GCE surface are entirely irreversible electrode processes. On the other hand, the anodic current response (Ipa) of the analytes showed a linear increase with the square root of the scan rate ($v^{1/2}$). This observation indicates that the electrode processes are predominantly diffusion-controlled. The correlation equations are given as Ipa (µA) = 0.73 $v^{1/2}$ $(mVs^{-1})^{1/2}$ + 4.98 (R^2 = 0.994) and Ipa (µA) = 1.82 $v^{1/2}$ $(mVs^{-1})^{1/2}$ + 5.01 (R^2 = 0.995) for VAN and CFT, respectively (Fig. 6C(a and b)). Additionally, log Ipa (µA) *vs.* log *v* (mVs^{-1}) are linearly correlated, as given by log Ipa (µA) = 0.56 *v* (mVs^{-1}) – 0.45 (R^2 = 0.992) and log Ipa (µA) = 0.48 *v* (mVs^{-1}) + 0.1 (R^2 = 0.990) for VAN and CFT with slopes of 0.56 and 0.46, respectively (Figs. 6D(a and b)). The slopes are almost close to the theoretical value of 0.5, further demonstrating that diffusion-controlled mechanisms dominate the electrochemical reactions of VAN and CFT at the surface of Au-Ag-ANCCs/*r*-GO/poly(L-histidine)/GCE. Equation (2) was utilized to determine the number of electrons involved in an irreversible electrochemical reaction [2].

$$E_p = E^0 + \frac{2.303RT}{\alpha nF}\log\frac{RTk^0}{\alpha nF} + \frac{2.303RT}{\alpha nF}\log v \quad (2)$$

where, E^0 = formal potential, v = scan rate, T = temperature, F = Faraday constant, k^0 = heterogeneous rate constant, R = universal gas constant, and n = number of electrons. A strong correlation was observed between the anodic peak potential (Epa) and the logarithm of the scan rate (log v (mVs^{-1})) for both VAN and CFT. The slope of each plot corresponding to 2.303RT/αnF was used to calculate αn. The values of αn were 0.48 for VAN and 0.53 for CFT. The transfer coefficient (α) is typically used to be 0.5 for irreversible electrode reactions [43], and the number of electrons (n) involved in the electrochemical oxidation of VAN and CFT are 0.96 and 1.06, respectively, which closely equals one. It is in close agreement with previous studies [41,42], which showed that the voltammetric oxidation of VAN and CFT involves the transfer of one proton and one electron. A schematic illustration for the proposed electro-oxidation reactions of VAN and CFT at the surface of the developed sensor is shown in Scheme S1.

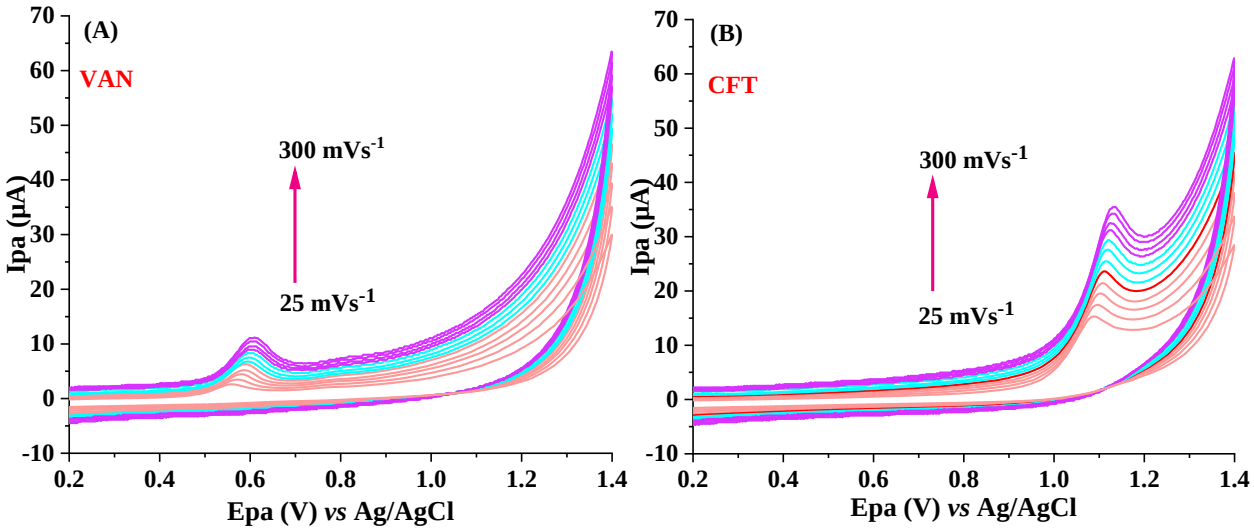

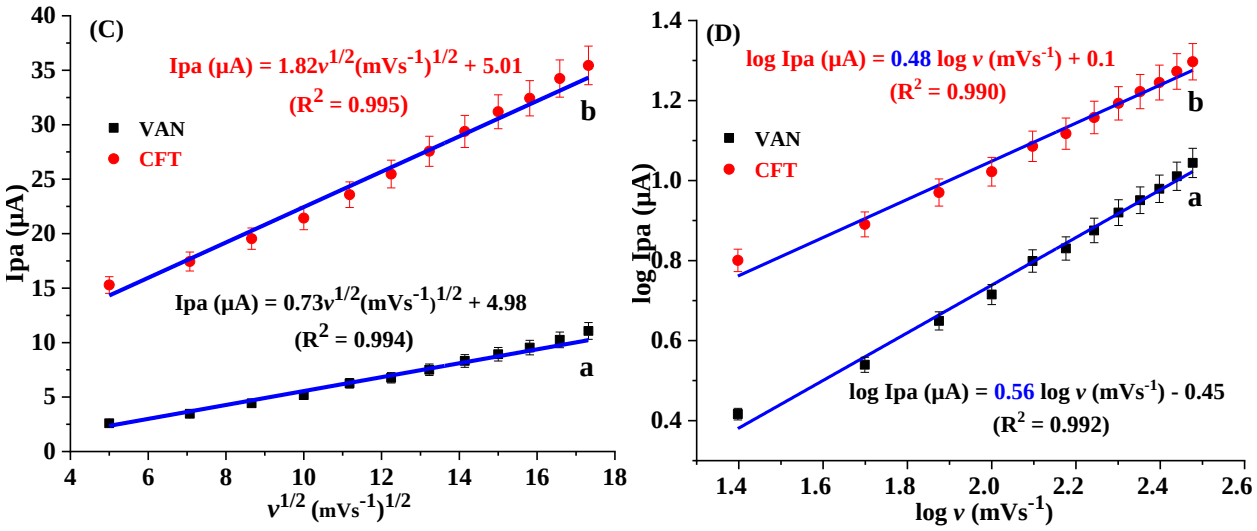

Fig. 6. CVs of 25 μM VAN (A) and CFT (B) at different scan rates, plots of $v^{1/2}$ (mVs^{-1})$^{1/2}$ *vs.* Ipa (μA) (C), and log v (mVs^{-1}) *vs.* log Ipa (μA) (D).

3.4.4. Optimization of SWV parameters

SWV is a widely used technique for measuring the concentration of various analytes in different matrices. Optimizing SWV parameters is crucial for achieving accurate and reliable electrochemical measurements. The intensity of current responses generated by SWV depends largely on instrumental parameters such as amplitude, frequency, and step potential. Herein, we investigated the effects of these parameters on the anodic current responses of 25 μM VAN and CFT in a 0.1 M PBS at pH 7. First, the influence of amplitude was examined within the range of 30-110 mV while keeping the step potential and frequency constant. Maximum peak current response for both analytes was observed at an amplitude of 70 mV. Therefore, 70 mV was selected as the optimal amplitude as it provided a balance between sensitivity and signal-to-noise ratio. Next, amplitude and step potential were maintained constant while varying the frequency from 20 to 100 Hz. Both analytes exhibited their maximum current response at 80 Hz. Therefore, 80 Hz was selected as the optimal frequency for determining the analytes. Finally, an investigation of step potentials within the 2 to 16 mV range was conducted, maintaining constant amplitude and frequency. Accordingly, a step potential of 10 mV was identified as the optimal value for subsequent experiments, ensuring a highest sensitivity for the simultaneous determination of VAN and CFT.

3.5. Electrochemical determination of VAN and CFT

3.5.1. Individual determination of VAN and CFT

SWV was used to evaluate the analytical performance of Au-Ag-ANCCs/*r*-GO/poly(L-histidine)/GCE for precise quantification of VAN and CFT under the optimized experimental conditions. While separately studying the analytes, the oxidation currents of both VAN and CFT increased gradually with increasing concentration (Fig. 7A and B). Notably, linear anodic current responses were observed within the concentration ranges of 0.6 pM to 125 µM for VAN and 0.85 pM to 300 µM for CFT. The regression equations, which indicate a strong correlation between the anodic currents and concentration, are Ipa (µA) = 0.33C (µM) + 2.68 (R^2 = 0.991) for VAN and Ipa (µA) = 0.88C (µM) + 12.75 (R^2 = 0.996) for CFT (inset plots). LOD and LOQ (S/N = 3, n = 10) values are found to be 0.03 pM and 0.1 pM for VAN, and 0.01 pM and 0.04 pM for CFT, respectively. These ultra-low LOD and LOQ values demonstrate the hypersensitivity of the developed sensor for the precise and accurate determination of VAN and CFT individually.

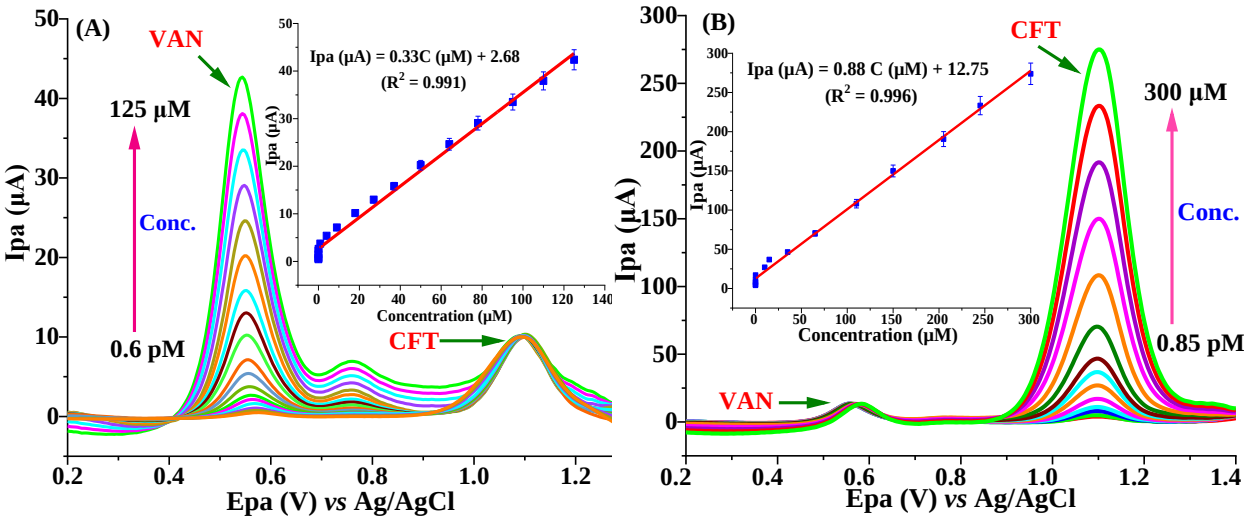

Fig. 7. SWVs for different concentrations VAN (A) and CFT (B) (Inset: Ipa (µA) *vs.* Conc.)

3.5.2. Simultaneous determination of VAN and CFT

The main goal of this study is to fabricate an electrochemical sensing platform that exhibit exceptional sensitivity for simultaneously quantifying VAN and CFT residues in food samples.

The sensor utilized, Au-Ag-ANCCs/*r*-GO/poly(L-histidine)/GCE, was a novel approach to detect the analytes. The anodic current responses showed a gradual increase with the continuous addition of VAN and CFT (Fig. 8A), demonstrating a direct proportionality between the oxidation currents and analyte concentrations. A linear correlation between the anodic currents and concentration was observed in the ranges of 1.0 pM to 120 µM for VAN and 1.0 pM to 290 µM for CFT. The corresponding linear regression equations were Ipa (µA) = 0.14C (µM) + 2.93 (R^2 = 0.996) for VAN and Ipa (µA) = 0.87C (µM) + 7.07 (R^2 = 0.998) for CFT (Fig. 8B). The LOD and LOQ for VAN were found to be 0.11 pM and 0.36 pM, respectively. Correspondingly, for CFT, the LOD and LOQ values were determined to be 0.017 pM and 0.057 pM, respectively. These low LOD and LOQ values show the remarkable sensing capability of the Au-Ag-ANCCs/*r*-GO/poly(L-histidine)/GCE for the simultaneous detection of trace residues of VAN and CFT in food samples.

The performance of the developed sensor was compared to that of recently reported sensors for the electrochemical detection of VAN and CFT, based on the key parameters of LOD and linear range. The developed sensor outperformed existing sensors with a significantly lower LOD and a wider linear range, as shown in Table 1. The enhanced performance can be attributed to the unique features of the sensor, such as a higher electroactive surface area, superior electrocatalytic activity, and improved electrical conductivity. These features are all due to the synergistic effects of the incorporated modifiers, Au-Ag-ANCCs, *r*-GO, and poly(L-histidine). Consequently, Au-Ag-ANCCs/*r*-GO/poly(L-histidine)/GCE can be a promising alternative for simultaneously detecting VAN and CFT residues in food samples.

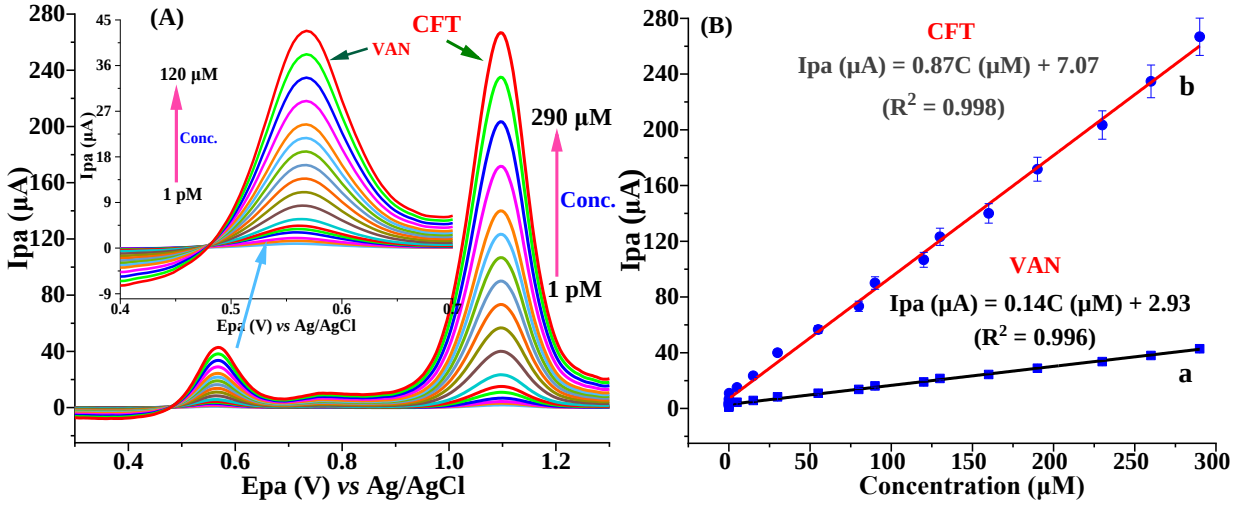

Fig. 8. (A) SWVs of different concentration of VAN and CFT and (B) plots of Ipa (μA) *vs.* conc. of VAN (a) and CFT (b).

Table 1: Evaluating the performance of the developed method in comparison with the existing sensors.

Electrodes	Targets	Matrices	Linear range (μM)	LOD (μM)	Ref.
BCTMOF-PAA/GCE	VAN	Urine and serum	0.001–0.5	0.001	[8]
Graphene/GCE	VAN	Human plasma	0.7–50	0.2	[44]
Graphene-AuNS/SPE	VAN	Human serum	1–100	0.29	[45]
NanoMIPs/LPG	VAN	Porcine plasma	0.01–700	0.01	[46]
NanoMIPs	VAN	Blood plasma	1 pM–0.07	0.25 pM	[47]
Au-Ag-ANCCs/*r*-GO/poly(L-histidine)/GCE	VAN	Chicken meat, fish, and milk	1 pM–120	0.11 pM	This work
PtNPs/MWCNT/GCE	CFT	Pharmaceutical and clinical preparations	0.01–10	0.009	[41]
CAC-PU/Pt electrode	CFT	Synthetic urine	100–1500	52	[48]
SiO_2/ZrO_2/Cdot-N/SPE	CFT	Synthetic urine, urine, and tap water	0.0078–40.02	0.0002	[49]
$NiFe_2O_4$-NPs/GCE	CFT	Pharmaceuticals and biological fluids	0.01–3.2	0.0016	[11]
PNCs/*r*-GO/PGE	CFT	Pharmaceutical and blood serum	10 pM–0.03	1.8 pM	[50]
Au-Ag-ANCCs/*r*-GO/poly(L-histidine)/GCE	CFT	Chicken meat, fish, and milk	1 pM–290	0.017 pM	This work

3.6. Reproducibility, repeatability, and stability

It is critical to examine the reproducibility, repeatability, and stability of the fabricated sensor to ensure the reliability and accuracy of electrochemical measurements for analyzing real samples. In this study, SWV was used to evaluate the reproducibility, repeatability, and storage stability of Au-Ag-ANCCs/*r*-GO/poly(L-histidine)/GCE while simultaneously determining 15 μM VAN and CFT in 0.1 M PBS. Initially, ten electrodes were fabricated under identical experimental conditions to evaluate the reproducibility of the sensor. The analysis yielded RSD values of 4.23% for VAN

and 4.02% for CFT (Fig. 9A). These results demonstrate the acceptable reproducibility of the developed sensor, confirming its reliability for detecting VAN and CFT residues in food samples. Next, ten successive square wave measurements were performed using a single electrode to assess the repeatability of Au-Ag-ANCCs/*r*-GO/poly(L-histidine)/GCE. The RSD values were 1.72% for VAN and 1.17% for CFT (Fig. 9B), suggesting that the sensor has a remarkable repeatability to quantify the analytes. Finally, the current responses of the sensor were regularly monitored over eight weeks to evaluate its stability, where it was stored at 4°C after each weekly use. Impressively, the sensor maintained long-term stability, with anodic current responses decreasing by only 5.55% for VAN and 4.58% for CFT throughout the storage period (Fig. 9C). Generally, the sensor's outstanding reproducibility, repeatability, and long-term make it an ideal tool for detecting the anti-microbial drugs residue.

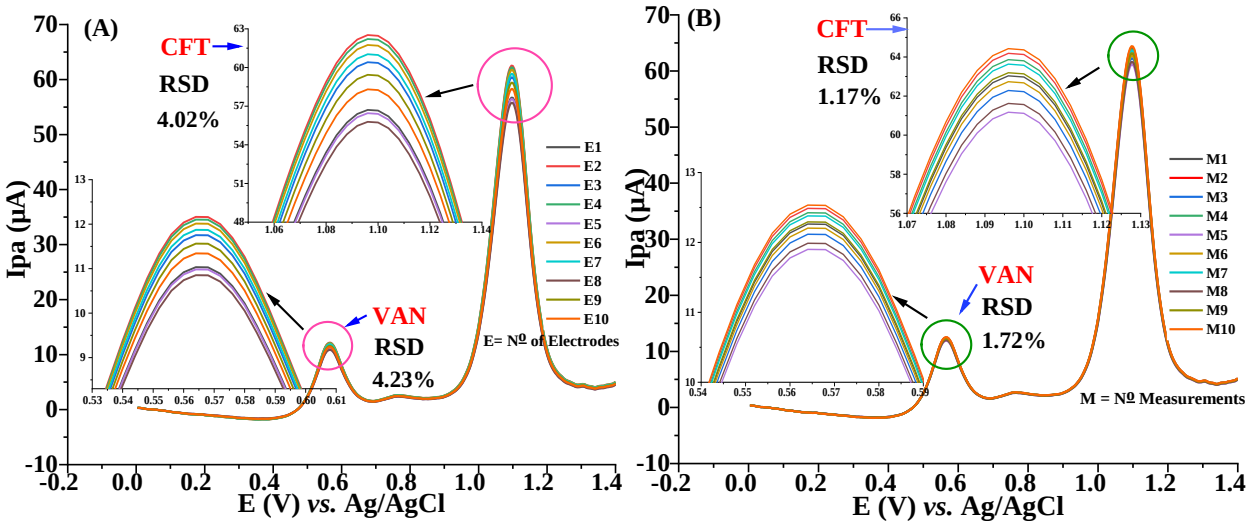

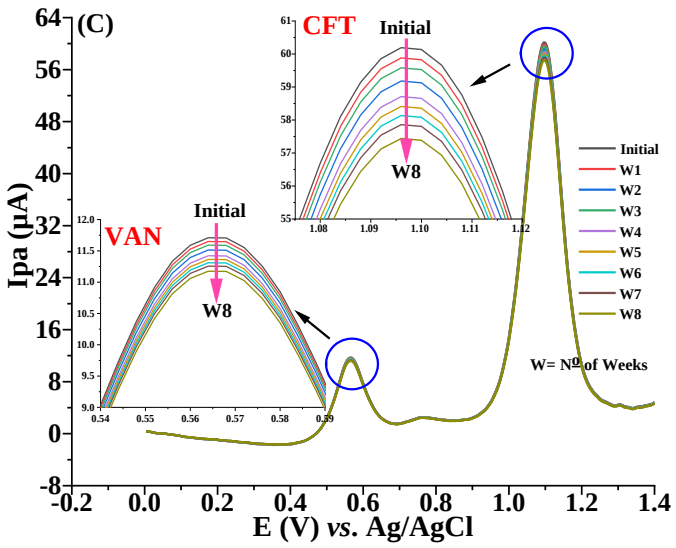

Fig. 9. Reproducibility (A), repeatability (B), and stability (C) of the developed sensor.

3.7. Selectivity

The selectivity of Au-Ag-ANCCs/*r*-GO/poly(L-histidine)/GCE was assessed by measuring its current response to 25 µM VAN and CFT in the presence of potential interfering substances. The tolerance limit was defined as the highest concentration of interferents that resulted in a relative percentage error of less than 5% while determining the analytes. As shown in Fig. S5 and Table S1, the detection of 25 µM VAN and CFT was not affected by the presence of interfering substances at concentrations 900 times greater for inorganic species (Ca^{2+}, K^{+}, Mg^{2+}, Cu^{2+}, Fe^{3+}, HCO_3^{-}, NO_3, SO_4^{2-}, CO_3^{2-}, and Cl^{-}), 750 times greater for organic compounds (fructose, folic acid, urea, sucrose, uric acid, dopamine, glucose, ascorbic acid, and lactose), and 200 times for antibiotics (azithromycin, chloramphenicol, tinidazole, ampicillin, cloxacillin, erythromycin, amoxicillin ciprofloxacin and cephalexin). Generally, the relative percentage errors values were below five percent for all interferents, confirming the selectivity and applicability of Au-Ag-ANCCs/*r*-GO/poly(L-histidine)/GCE for the simultaneous determination of target analytes.

3.8. Analytical application

SWV evaluated the efficiency of Au-Ag-ANCCs/*r*-GO/poly(L-histidine)/GCE for concurrent quantification of VAN and CFT in chicken meat, fish, and milk. The samples were spiked with varying concentrations of VAN and CFT (5, 10, 20, and 40 µM) to determine their

percentage recoveries (Table 2). Before spiking a standard solution of VAN and CFT to the food samples, their initial voltammetric responses were measured. From the unspiked food samples, no noticeable electrochemical signals were observed, indicating that the food samples contain no residues of VAN and CFT or their concentrations being within the non-detectable range. Next, percentage recoveries of the analytes in spiked chicken meat, fish, and milk samples were determined. The recovery rates were high and consistent in all the three matrices, ranging from 97.7% to 101.5% for VAN and 98.2% to 101.9% for CFT. The RSD values were also low and comparable for both food samples, ranging from 1.84% to 2.75% for VAN and 1.89% to 2.82% for CFT. The high recovery ranges and low RSD values obtained in the analysis of the food samples demonstrate that Au-Ag-ANCCs/*r*-GO/poly(L-histidine)/GCE is a highly effective and reliable tool for detecting VAN and CFT residues in real-world applications.

Table 2: Summary of spiking experiment results (n = 3).

Samples	Spiked (µM)	Found (µM)		Recovery (%)		RSD (%)	
		VAN	CFT	VAN	CFT	VAN	CFT
Chicken meat	0	-	-	-	-	-	-
	5	5.02	4.91	100.4	98.2	2.22	2.29
	10	9.97	10.15	97.7	101.5	1.98	1.92
	20	20.25	20.08	101.3	100.4	1.84	1.89
	40	39.56	39.47	98.9	98.7	2.06	1.98
Fish	0	-	-	-	-	-	-
	5	4.84	4.86	96.8	97.2	1.74	1.81
	10	9.79	9.62	97.9	96.2	1.96	2.05
	20	20.41	20.34	102.1	101.7	1.85	1.78
	40	40.22	40.04	100.6	100.1	2.21	2.18
Milk	0	-	-	-	-	-	-
	5	5.07	4.82	101.4	96.4	2.36	2.31
	10	10.1	10.19	101	101.9	2.75	2.82
	20	20.12	19.76	100.6	98.8	2.43	2.39
	40	39.72	40.44	99.3	101.1	2.12	2.07

5. Conclusion

In this study, a novel electrochemical sensor was developed for the simultaneous detection of VAN and CFT residues in food samples (chicken meat, fish, and milk). The interfacial, morphological, and elemental compositions of the developed sensor were examined using several analytical and electrochemical techniques. Au-Ag-ANCCs/*r*-GO/poly(L-histidine)/GCE surpassed recently reported sensors with the lowest LOD and a broader linear range because of its exceptional features: higher electroactive surface area, high electrocatalytic activity, and enhanced electrical conductivity. The current response of the sensor remained unaffected in the presence of excess concentration of potentially coexisting interferents, including organic, inorganic, and antibiotic species, demonstrating its outstanding selectivity. In addition, the sensor exhibited exceptional repeatability, reproducibility, and long-term stability. Therefore, Au-Ag-ANCCs/*r*-GO/poly(L-histidine)/GCE is an ideal candidate for real-time monitoring of life-threatening residues of VAN and CFT in food samples.

Statement on Data Availability

All the data supporting the results of this study are reported in the article.

CRediT authorship contribution statement

Wondimeneh Dubale Adane: Conceptualization, Methodology, Software, Resources, Formal analysis, Investigation, Writing-original draft. **Bhagwan Singh Chandravanshi**: Conceptualization, Writing-review & editing, Supervision. **Yonas Chebude:** Writing-review & editing, Instrumental analysis, Formal analysis. **Merid Tessema:** Conceptualization, Writing-review & editing, Supervision.

Declaration of competing interest

We wish to confirm that there are no known conflicts of interest related to this publication and that this research has not received specific funding from any public, commercial or non-profit sector funding body.

Acknowledgements

The authors express their gratitude to the Department of Chemistry at Addis Ababa University, Addis Ababa, Ethiopia, for generously offering the laboratory resources.

References

[1] M. Majdinasab, R.K. Mishra, X. Tang, J.L. Marty, Detection of antibiotics in food: new achievements in the development of biosensors, TrAC, Trends Anal. Chem. 127 (2020), 115883, https://doi.org/10.1016/j.trac.2020.115883.

[2] W.D. Adane, B.S. Chandravanshi, M. Tessema, Highly sensitive and selective electrochemical sensor for the simultaneous determination of tinidazole and chloramphenicol in food samples (egg, honey and milk), Sens. Actuators B Chem. 390 (2023), 134023, https://doi.org/10.1016/j.snb.2023.134023.

[3] C. Vatovec, J. Kolodinsky, P. Callas, C. Hart, K. Gallagher, pharmaceutical pollution sources and solutions: survey of human and veterinary medication purchasing, use, and disposal. J. Environ. Manage. 285 (2021), 112106, https://doi.org/10.1016/j.jenvman.2021.112106.

[4] K. Rudnicki, K. Sipa, M. Brycht, P. Borgul, S. Skrzypek, L. Poltorak, Electrochemical sensing of fluoroquinolone antibiotics, TrAC, Trends Anal. Chem. 128 (2020), 115907, https://doi.org/10.1016/j.trac.2020.115907.

[5] G. Igrejas, J.L. Capelo, C. Lodeiro, P. Poeta, Editorial: surveying antimicrobial resistance: The new complexity of the problem, Front. Microbiol. 11 (2020), 1144, https://doi.org/10.3389/fmicb.2020.01144.

[6] A. Cetinkaya, E. Yıldız, S.I. Kaya, M.E. Çorman, L. Uzun, S.A. Ozkan, A green synthesis route to develop molecularly imprinted electrochemical sensor for selective detection of vancomycin from aqueous and serum samples, Green Anal. Chem. 2 (2022), 100017, https://doi.org/10.1016/j.greeac.2022.100017.

[7] X. Cheng, J. Ma, J. Su, An overview of analytical methodologies for determination of vancomycin in human plasma, Molecules 27 (21) (2022) 7319, https://doi.org/10.3390/molecules27217319.

[8] A.A.S. Gill, S. Singh, N. Agrawal, Z. Nate, T.E. Chiwunze, N.B. Thapliyal, R. Chauhan, R. Karpoormath, A poly(acrylic acid)-modified copper-organic framework for electrochemical determination of vancomycin, Microchim. Acta 187 (1) (2020) 79, https://doi.org/10.1007/s00604-019-4015-3.

[9] A.I. Aqib, A.F. Alsayeqh, Vancomycin drug resistance, an emerging threat to animal and public health, Front. Vet. Sci. 9 (2022), 1010728, https://doi.org/10.3389/fvets.2022.1010728.

[10] C. Zhang, Y. Shi, Z. Wang, C. Liu, Y. Hou, J. Bi, L. Wu, Electrostatic interaction and surface S vacancies synergistically enhanced the photocatalytic degradation of ceftriaxone sodium, Chemosphere 311 (2023), 137053, https://doi.org/10.1016/j.chemosphere.2022.137053.

[11] K. Akhtar, J. Ahmed Baig, S. Ahmed Solangi, S. Hussain, H. Elhosiny Ali, S. Perveen, T. Gul Kazi, H. Imran Afridi, Biosynthesis and characterization of $NiFe_2O_4$-NPs for electrochemical detection of ceftriaxone from biological and pharmaceutical samples, Microchem. J. 191 (2023), 108808, https://doi.org/10.1016/j.microc.2023.108808.

[12] G.D. Noudeh, M. Asdaghi, N.D. Noudeh, M. Dolatabadi, S. Ahmadzadeh, Response surface modeling of ceftriaxone removal from hospital wastewater, Environ. Monit. Assess. 195 (1) (2023) 217, https://doi.org/10.1007/s10661-022-10808-z.

[13] P. Veerakumar, C. Koventhan, S.M. Chen, Copper-palladium alloy nanoparticles immobilized over porous carbon for voltammetric determination of dimetridazole, J. Alloys Compd. 931 (2023), 167474, https://doi.org/10.1016/j.jallcom.2022.167474.

[14] G. Das, S. Seo, I.J. Yang, L.T.H. Nguyen, H.S. Shin, J.K. Patra, Sericin mediated gold/silver bimetallic nanoparticles and exploration of its multi-therapeutic efficiency and photocatalytic degradation potential, Environ. Res. 229 (2023), 115935, https://doi.org/10.1016/j.envres.2023.115935.

[15] L. Sun, Y. Yin, P. Lv, W. Su, L. Zhang, Green controllable synthesis of Au–Ag Alloy nanoparticles using chinese wolfberry fruit extract and their tunable photocatalytic activity, RSC Adv. 8 (8) (2018) 3964–3973, https://doi.org/10.1039/C7RA13650A.

[16] Y. Zhao, Y. Yang, L. Cui, F. Zheng, Q. Song, Electroactive Au@Ag nanoparticles driven electrochemical sensor for endogenous H_2S detection, Biosens. Bioelectron. 117 (2018), 53–59, https://doi.org/10.1016/j.bios.2018.05.047.

[17] F.Y. Kong, L. Yao, R.F. Li, H.Y. Li, Z.X. Wang, W.X. Lv, W. Wang, Synthesis of nitrogen-doped reduced graphene oxide loading with Au-Ag bimetallic nanoparticles for electrochemical detection of daunorubicin, J. Alloys Compd. 797 (2019), 413–420, https://doi.org/10.1016/j.jallcom.2019.04.276.

[18] K. Zhao, L. Ge, T.I. Wong, X. Zhou, G. Lisak, Gold-silver nanoparticles modified electrochemical sensor array for simultaneous determination of chromium (III) and chromium (VI) in wastewater samples, Chemosphere 281 (2021), 130880, https://doi.org/10.1016/j.chemosphere.2021.130880.

[19] Z. Bao, H. Zhong, X. Li, A. Zhang, Y. Liu, P. Chen, Z. Cheng, H. Qian, Core-shell Au@Ag nanoparticles on carboxylated graphene for simultaneous electrochemical sensing of iodide and nitrite, Sens. Actuators B Chem. 345 (2021), 130319, https://doi.org/10.1016/j.snb.2021.130319.

[20] K. Yu, X. Sun, L. Pan, T. Liu, A. Liu, G. Chen, Y. Huang, Hollow Au–Ag alloy nanorices and their optical properties, Nanomaterials 7 (9) (2017) 255, https://doi.org/10.3390/nano7090255.

[21] W.D. Adane, B.S. Chandravanshi, M. Tessema, A simple, ultrasensitive and cost-effective electrochemical sensor for the determination of ciprofloxacin in various types of samples, Sens. Bio-Sens. Res. 39 (2023), 100547, https://doi.org/10.1016/j.sbsr.2022.100547.

[22] N.M. Yousif, R.M. Attia, M.R. Balboul, Adrenaline biosensors based on rGO/Ag nanocomposites functionalized textiles using advanced electron beam irradiation technique, J. Organomet. Chem. 972 (2022), 122392, https://doi.org/10.1016/j.jorganchem.2022.122392.

[23] X. Chai, Y. Li, C. Ma, M. Guo, Z. Fan, J. Zhao, B. Cheng, A Voltammetric sensor based on a reduced graphene oxide/*β*-cyclodextrin/silver nanoparticle/polyoxometalate nanocomposite for detecting uric acid and tyrosine, Anal. Methods 15 (20) (2023) 2528–2535, https://doi.org/10.1039/D3AY00207A.

[24] D. Duan, Y. Ding, L. Li, G. Ma, Rapid Quantitative detection of melatonin by electrochemical sensor based on carbon nanofibers embedded with FeCo alloy nanoparticles, J. Electroanal. Chem. 873 (2020) 114422, https://doi.org/10.1016/j.jelechem.2020.114422.

[25] G. Mummoorthi, S. Arjunan, M. Selvaraj, S.L. Rokhum, N. Mani, S. Periyasamy, R. Rajendran, High-performance solid-state asymmetric supercapacitor based on α-Fe_2O_3/r-GO/GCN composite electrode material for energy storage application, Surf. Interfaces. 41 (2023), 103166, https://doi.org/10.1016/j.surfin.2023.103166.

[26] K. Kaewjua, W. Siangproh, A novel tyramine sensing-based polymeric L-histidine film-coated screen-printed graphene electrode: capability for practical applications, Electrochim. Acta 419 (2022), 140388, https://doi.org/10.1016/j.electacta.2022.140388.

[27] J. Zhou, Y. Chen, L. Lan, C. Zhang, M. Pan, Y. Wang, B. Han, Z. Wang, J. Jiao, Q. Chen, A novel catalase mimicking nanocomposite of Mn(II)-poly-L-histidine-carboxylated multi walled carbon nanotubes and the application to hydrogen peroxide sensing, Anal. Biochem. 567 (2019), 51–62, https://doi.org/10.1016/j.ab.2018.12.007.

[28] Y. Chen, X.M. Liu, X. Wu, X.C. Liu, W.H. Dong, B.K. Han, X. Du, C. Zhang, Y.Y. Zhang, H.T. Wang, Q. Chen, An array of poly-L-histidine functionalized multi-walled carbon nanotubes on 4-aminothiophenol self-assembled monolayer and the application for sensitively glucose sensing. Electrochim. Acta 258 (2017), 988–997, https://doi.org/10.1016/j.electacta.2017.11.150.

[29] A. Solangi, S. Memon, A. Mallah, N. Memon, M.Y. Khuhawar, M.I. Bhanger, Determination of ceftriaxone, ceftizoxime, paracetamol, and diclofenac sodium by capillary zone electrophoresis in pharmaceutical formulations and in human blood serum, Turk. J. Chem. 34 (6) (2010) 921–934, https://doi.org/10.3906/kim-1005-628.

[30] J. Huo, Y. Guo, B. Zhang, Z. Zhao, G. Shi, S. Mei, A UHPLC–MS/MS method for the simultaneous determination of vancomycin, norvancomycin, meropenem, and moxalactam in human plasma and its clinical application, J. Mass Spectrom. 58 (6) (2023) e4925, https://doi.org/10.1002/jms.4925.

[31] H.S.A. Al-ward, M.Q. Al-Abachi, M.R. Ahmed, Spectrophotometric analysis of vancomycin hydrochloride in pure and pharmaceutical injections via batch and cloud point extraction techniques, Baghdad Sci. J. 20 (2) (2023) 0245, https://doi.org/10.21123/bsj.2022.6686.

[32] M. Iranifam, Z. Dadashi, Chemiluminescence determination of vancomycin by using NiS nanoparticles–luminol–O_2 system, Spectrochim. Acta A Mol. Biomol. Spectrosc. 267 (2022), 120489, https://doi.org/10.1016/j.saa.2021.120489.

[33] L.H. Hidalgo, M.V.G. Navarro, S.D. Penchala, L.E.L. Cortes, A. De Alarcón, R.L. Márquez, L.F.L. Cortes, A.G. Valencia, Ceftriaxone pharmacokinetics by a sensitive and simple LC–MS/MS method: development and application, J. Pharm. Biomed. Anal. 198 (2020), 113484, https://doi.org/10.1016/j.jpba.2020.113484.

[34] T. Williams, R. Shum, D. Rappleye, Review-concentration measurements in molten chloride salts using electrochemical methods, J. Electrochem. Soc. 168 (12) (2021) 123510, https://doi.org/10.1149/1945-7111/ac436a.

[35] M.U. Khan, M.A. Shaida, Reduction mechanism of graphene oxide including various parameters affecting the C/O ratio, Mater. Today Commun. 36 (2023), 106577, https://doi.org/10.1016/j.mtcomm.2023.106577.

[36] M. Khatami, S. Pourseyedi, M. Khatami, H. Hamidi, M. Zaeifi, L. Soltani, Synthesis of silver nanoparticles using seed exudates of sinapis arvensis as a novel bioresource, and evaluation of their antifungal activity, Bioresour. Bioprocess. 2 (1) (2015) 19, https://doi.org/10.1186/s40643-015-0043-y.

[37] S.S. Godipurge, S. Yallappa, N.J. Biradar, J.S. Biradar, B.L. Dhananjaya, G. Hegde, K. Jagadish, G. Hegde, A facile and green strategy for the synthesis of Au, Ag and Au–Ag Alloy nanoparticles using aerial parts of R. Hypocrateriformis extract and their biological evaluation, Enzyme Microb. Technol. 95 (2016), 174–184, https://doi.org/10.1016/j.enzmictec.2016.08.006.

[38] A. Kumar, A.M. Sadanandhan, S.L. Jain, Silver doped reduced graphene oxide as a promising plasmonic photocatalyst for oxidative coupling of benzylamines under visible light irradiation, New J. Chem. 43 (23) (2019) 9116–9122, https://doi.org/10.1039/C9NJ00852G.

[39] M.A. Khaleque, M.I. Hossain, M.R. Ali, M.S. Bacchu, M.A. Saad Aly, M.Z.H. Khan, Nanostructured wearable electrochemical and biosensor towards healthcare management: a review, RSC Adv. 13 (33) (2023) 22973–22997, https://doi.org/10.1039/D3RA03440B.

[40] Y. Tong, X. Yan, J. Liang, S.X. Dou, Metal-based electrocatalysis for methanol electro-oxidation: progress, opportunities, and challenges, Small 17 (9) (2021) 1904126, https://doi.org/10.1002/smll.201904126.

[41] S. Shahrokhian, N. Hosseini-Nassab, Z. Kamalzadeh, Fabrication of an electrochemical sensor based on the electrodeposition of Pt nanoparticles on multiwalled carbon nanotubes film for voltammetric determination of ceftriaxone in the presence of lidocaine, assisted by factorial-based response-surface methodology, J Solid State Electrochem 18 (1) (2014) 77–88, https://doi.org/10.1007/s10008-013-2243-8.

[42] B. Feier, A. Blidar, L. Vlase, C. Cristea, The complex fingerprint of vancomycin using electrochemical methods and mass spectrometry, Electrochem. Commun. 104 (2019), 106474, https://doi.org/10.1016/j.elecom.2019.05.023.

[43] Z. Liu, Y. Zhou, Y. Wang, Q. Cheng, K. Wu, Enhanced oxidation and detection of toxic ractopamine using carbon nanotube film-modified electrode, Electrochim. Acta 74 (2012), 139–144, https://doi.org/10.1016/j.electacta.2012.04.041.

[44] M. Hadi, T. Mollaei, Electroanalytical determination of vancomycin at a graphene-modified electrode: comparison of electrochemical property between graphene, carbon nanotube, and carbon black, Electroanalysis 31 (7) (2019) 1224–1228, https://doi.org/10.1002/elan.201800497.

[45] A. Blidar, B. Feier, A. Pusta, A.M. Drăgan, C. Cristea, Graphene–gold nanostructures hybrid composites screen-printed electrode for the sensitive electrochemical detection of vancomycin, Coatings 9 (10) (2019) 652, https://doi.org/10.3390/coatings9100652.

[46] S. Korposh, I. Chianella, A. Guerreiro, S. Caygill, S. Piletsky, S.W. James, R.P. Tatam, Selective vancomycin detection using optical fiber long period gratings functionalized with molecularly imprinted polymer nanoparticles, Analyst 139 (9) (2014) 2229–2236, https://doi.org/10.1039/C3AN02126B.

[47] I. Chianella, A. Guerreiro, E. Moczko, J.S. Caygill, E.V. Piletska, I.M.P. De Vargas Sansalvador, M.J. Whitcombe, S.A. Piletsky, Direct replacement of antibodies with molecularly imprinted polymer nanoparticles in ELISA-development of a novel assay for vancomycin, Anal. Chem. 85 (17) (2013) 8462–8468, https://doi.org/10.1021/ac402102j.

[48] C. Ben Ali Hassine, O. Güngör, M. Burç, I. Özcan, S. Köytepe, S. Titretir Duran, Electrochemical determination of ceftriaxone using polyurethane-modified electrode containing caffeic acid and chitosan, Polym. Plast. Technol. Mater. 61 (6) (2022) 609–623, https://doi.org/10.1080/25740881.2021.2005092.

[49] F.W.L. Silva, L.L. Name, D.Y. Tiba, B.F. Braz, R.E. Santelli, T.C. Canevari, F.H. Cincotto, High sensitivity, low-cost, and disposability: a novel screen-printed electrode developed for direct electrochemical detection of the antibiotic ceftriaxone, Talanta 266 (2024), 125075, https://doi.org/10.1016/j.talanta.2023.125075.

[50] M. Rouhani, A. Soleymanpour, Ultrasensitive electrochemical determination of trace ceftizoxime using a thin film of preyssler nanocapsules on pencil graphite electrode surface modified with reduced graphene oxide, Microchem. J. 165 (2021), 106160, https://doi.org/10.1016/j.microc.2021.106160.

Supplementary Material

A novel hypersensitive electrochemical sensor (Au-Ag-ANCCs/*r*-GO/poly(L-histidine)/GCE) for the simultaneous determination of vancomycin and ceftriaxone residues in chicken meat, fish, and milk samples

Wondimeneh Dubale Adane[a], Bhagwan Singh Chandravanshi*[a], Yonas Chebude[a], Merid Tessema**[a]

[a]Department of Chemistry, Addis Ababa University, P. O. Box 1176, Addis Ababa, Ethiopia

*Corresponding author. E-mail address: bscv2006@yahoo.com

**Corresponding author. E-mail address: tessemamerid@yahoo.com

2. Experimental

2.1. Chemical and reagents

Graphite oxide (GO) was obtained from Nanjing Xianfeng Nano Co. (Nanjing, China). L-Histidine ($C_6H_9N_3O_2$) was obtained from Sigma-Aldrich, USA. Silver nitrate ($AgNO_3$), tetrachloroauric acid ($HAuCl_4$), sodium borohydride ($NaBH_4$), and sodium citrate ($Na_3C_6H_5O_7$) were purchased from Shanghai Sinopharm Chemical Reagent Co., Ltd. (China). Nitric acid (HNO_3), and sulfuric acid (H_2SO_4) were bought from Merck Chemicals, Germany. Potassium hexacyanoferrate (III) (99%) was purchased from BDH Chemicals Ltd., England. Ethylene glycol ($C_2H_6O_2$) was obtained from TCI America. All other chemicals and antibiotic standards were purchased from Sigma-Aldrich, USA. Glassware was washed with aqua regia ($HCl:HNO_3$ in a 3:1 ratio by volume) and rinsed with deionized water before the experiments. All aqueous solutions were prepared with Milli-Q water (18.2MΩ cm), which was obtained from a Millipore water purification system. All chemicals and reagents used in this experiment were of analytical grade and used without further purification. A stock solution of 0.01 M VAN was prepared by dissolving 724.65 mg of VAN standard in 50 mL of distilled water. Similarly, a 0.01 M CFT stock solution was prepared by dissolving 227.29 mg of CFT standard in 50 mL of distilled water. The stock solutions were diluted with 0.1 M PBS (pH 7) to prepare working solutions for each target analyte.

2.2. Apparatus and instruments

Electrochemical measurements were performed in 20 mL cells using a CHI 760D electrochemical analyzer (CH Instruments, USA). A conventional three-electrode system was used throughout the experiments, consisting of a working electrode (either bare GCE or modified electrodes), a platinum wire counter electrode, and silver-silver chloride (Ag/AgCl (3M KCl)) reference electrode. The structural morphology was characterized using a scanning electron microscope (SEM, CX-200plus, Coxem, Korea), and the elemental analysis was performed using hyphenated energy-dispersive X-ray spectroscopy (EDX). The X-ray diffraction (XRD) pattern of the nanocomposites was recorded using a BRUKER ECOD 8 advance diffractometer with Cu Kα radiation (wavelength λ = 0.15406 nm) at room temperature. Fourier transform infrared (FT-IR) spectra were recorded using a PerkinElmer Spectrum 100 FT-IR spectrometer (PerkinElmer, USA). UV-Vis spectra were recorded using a Lambda 950 UV-Vis spectrometer (PerkinElmer, USA). The pH was measured using a Senses Ion + MM150 pH meter (China). Solid chemicals were weighed using an electronic digital balance (Model: Scientech ZSA 120, USA). A centrifuge (model 8001, China) and an ultrasonic cleaner (model YJ5120-B, China) were used during nanocomposite preparation. In addition, a magnetic stirrer and a vacuum pump were used throughout the experiment.

2.3. Preparation of real samples

2.3.1. Preparation of chicken meat sample

Chicken meat samples were obtained from a local supermarket in Addis Ababa, Ethiopia, and thoroughly homogenized before extraction. Subsequently, 5 g of the homogenized meat was vortexed with 20 ml of 0.1 M PBS and sonicated for 50 min. After centrifugation at 10,000 rpm for 10 min, a clear solution was obtained. Finally, different concentrations of known VAN and CFT standard solutions (5, 10, 20, and 40 µM) were spiked for analysis.

2.3.2. Preparation of fish sample

Fish samples collected from a local supermarket in Addis Ababa, Ethiopia were stored in a deep freezer until analysis. Approximately 2 g of homogenized fish sample was weighed into a 50 mL falcon tube, followed by the addition of 5 mL of water and 5 mL of acetonitrile. The mixture

was vortexed for 5 min to ensure thorough mixing. Subsequently, 5 g of $MgSO_4$ and 2 g of NaCl were added to the falcon tube and manually shaken for 2 min to promote solid-phase extraction. The resulting mixture was centrifuged at 4000 rpm for 15 min to separate the supernatant from the solid phase. The collected supernatant was carefully transferred to another falcon tube. After 5 min vortexing, the mixture was centrifuged again at 10,000 rpm for 10 min, resulting in a clear solution enriched with the analytes of interest. Finally, to quantify the concentrations of VAN and CFT in the samples, the samples were spiked with appropriate concentrations (5, 10, 20, and 40 µM) of VAN and CFT standard solutions.

2.3.3. Preparation of milk sample

Milk samples were obtained from Sululta town in the Oromia Regional State of Ethiopia and processed as follows: first, 5.0 mL of the milk sample was mixed with 20 mL of acetonitrile. After subjecting the mixture to 15 min of sonication and 10 min of shaking, it was centrifuged at 10,000 rpm for 10 min. Following centrifugation, the supernatant was filtered through a 150 mm filter membrane. The resulting filtrate was subsequently transferred to a 25 mL volumetric flask and diluted to the mark using PBS (pH 7). Finally, the samples were spiked with appropriate concentrations of VAN and CFT standards.

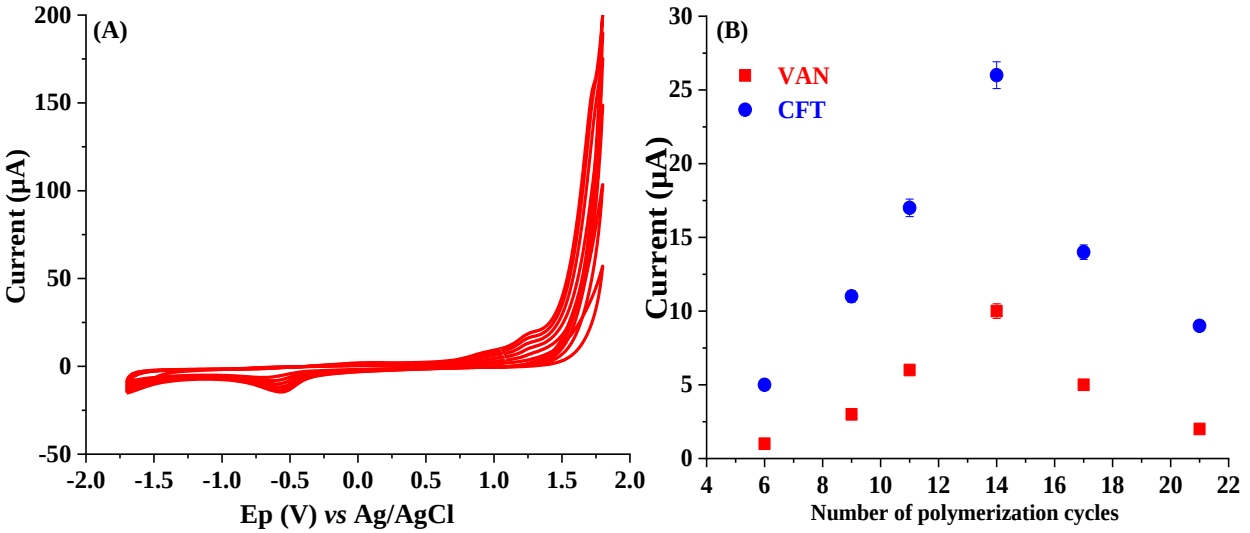

Fig. S1. (A) CV for the electrochemical polymerization of 0.06 M L-histidine in 0.1 M PBS (pH 7.0) at the surface of Au-Ag-ANCCs/*r*-GO/GCE for 14 cycles at scan rate of 25 mVs^{-1} in the

potential range of -1.7 to 1.6 V, and (B) plot for the optimization of the number of polymerization cycles *vs*. anodic peak current of 25 µM VAN and CFT.

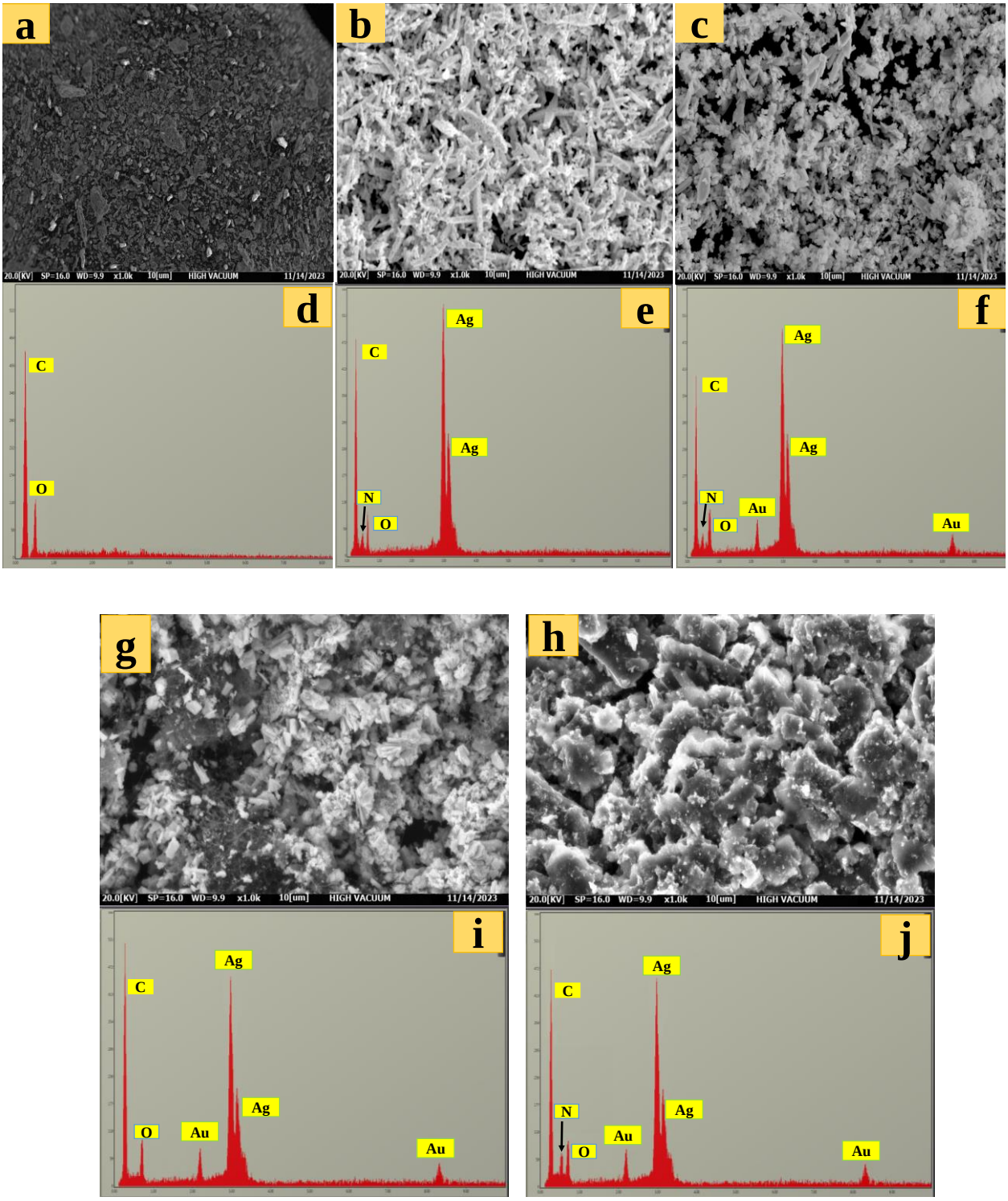

Fig. S2. SEM and EDX spectra of *r*-GO (a and d), Ag-NCCs (b and e), Au-Ag-ANCCs (c and f), Au-Ag-ANCCs/*r*-GO (g and i), and Au-Ag-ANCCs/*r*-GO/poly(L-histidine)/GCE (h and j), respectively.

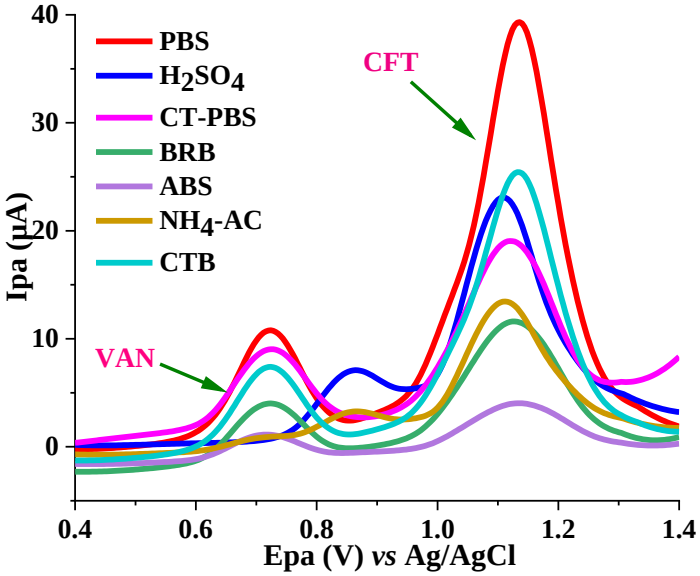

Fig. S3. SWVs of 25 µM VAN and CFT in different supporting electrolyte solutions.

3. Optimization of experimental conditions

3.1. Optimization of the number of electropolymerization cycles

The number of polymerization cycles has a significant influence on the performance of the modified electrode. With repeated cycles, the film thickness increases and becomes more porous, which can enhance sensor sensitivity by providing a higher electroactive surface area for analyte interaction. However, an excessively high cycle count can reduce film conductivity due to increased insulation, impeding electron transfer between the electrode and analytes, and reducing sensor sensitivity. Achieving an optimal number of polymerization cycles requires balancing film thickness and conductivity. To optimize the L-histidine polymerization cycles, a series of repetitive cycles were conducted in a 0.1 M PBS solution (pH 7.0) containing 0.06 M L-histidine within the potential range of -1.7 V to 1.6 V at a scan rate of 25 mVs^{-1} on the Au-Ag-ANCCs/*r*-GO/GCE surface. As shown in Fig. S1B, the peak current response increased with the number of L-histidine electropolymerization cycles, reaching its peak at 14 cycles before declining. This

decline is due to an excessive electropolymerization process, resulting in the formation of a thick insulating L-histidine layer on the Au-Ag-ANCCs/*r*-GO/GCE surface. As this layer thickens, it hampers efficient electron transfer between the Au-Ag-ANCCs/*r*-GO/poly(L-histidine)/GCE and the analytes, thus reducing electrode conductivity and sensitivity. Consequently, 14 polymerization cycles were selected as the optimal value for subsequent experiments.

3.2. Optimization of the ratio of Au-Ag-ANCCs and *r*-GO

The optimization of the mixing ratio of nanocomposites is a vital step in the development of electrochemical sensors. The desired performance for a specific application can be achieved by carefully selecting the ratio of the nanocomposites. Herein, the mixing ratio of Au-Ag-ANCCs and *r*-GO was optimized to achieve the highest peak current response for detecting 25 µM VAN and CFT. As shown in Fig. S4A, the optimal ratio of Au-Ag-ANCCs and *r*-GO that resulted in the highest anodic peak current response is 1:2. The boost in performance at the 1:2 mixing ratio may be due to the synergistic effect of the two nanocomposites. Au-Ag-ANCCs provides high electrical conductivity and electroactive surface area, while *r*-GO gives high mechanical strength and flexibility. The combination of these two properties makes the developed sensor highly sensitive to the target analytes. Therefore, the 1:2 ratio of Au-Ag-ANCCs and *r*-GO was selected as the optimum value for the preparation of the proposed sensor in subsequent experiments.

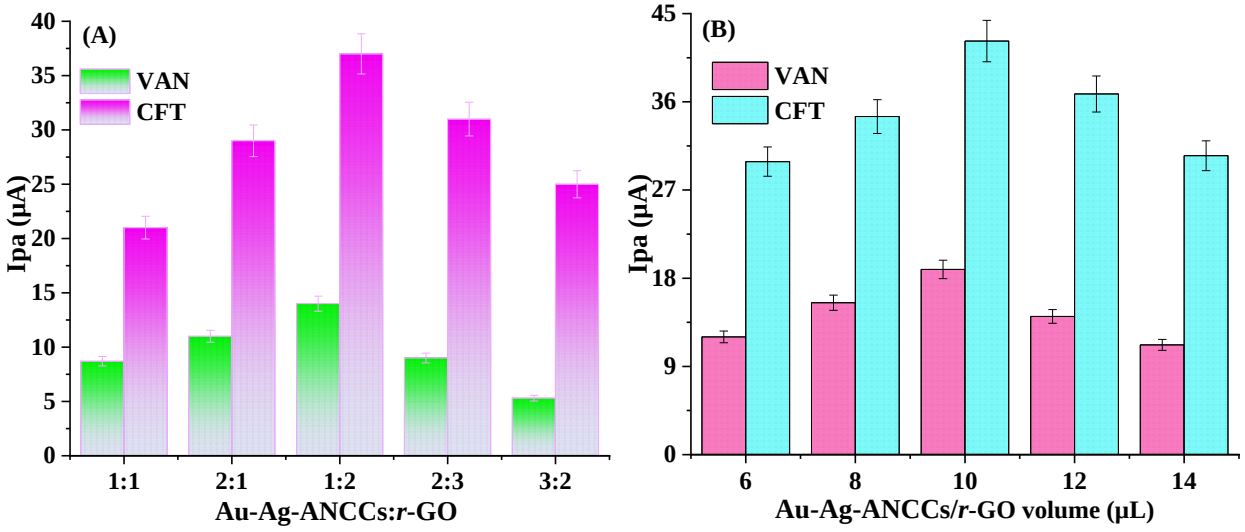

Fig. S4. Diagram for optimizing the ratio of Au-Ag-ANCCs and *r*-GO (A), and drop-casting volume of Au-Ag-ANCCs/*r*-GO dispersion (B) to prepare Au-Ag-ANCCs/*r*-GO/poly(L-histidine)/GCE.

3.3. Optimization of the drop-casted volume of Au-Ag-ANCCs/*r*-GO

Optimizing the drop casted volume of Au-Ag-ANCCs/*r*-GO dispersion at the surface of the modified electrode is crucial to ensuring effective modification. The selected volume influences the thickness and uniformity of the modified layer, which can affect the performance of the electrode. To optimize the drop-casted amount, we tested different volumes of Au-Ag-ANCCs/*r*-GO and evaluated the resulting electrode performance by simultaneously detecting 25 µM VAN and CFT in food samples. As shown in Fig. S4B, the optimal drop casted volume of the Au-Ag-ANCCs/*r*-GO dispersion, which produced the highest current response while maintaining excellent electrochemical performance compared to the others, was 10 µL. Therefore, 10 µL of Au-Ag-ANCCs/*r*-GO dispersion was selected as the optimum value for preparing Au-Ag-ANCCs/*r*-GO/poly(L-histidine)/GCE for subsequent experiments.

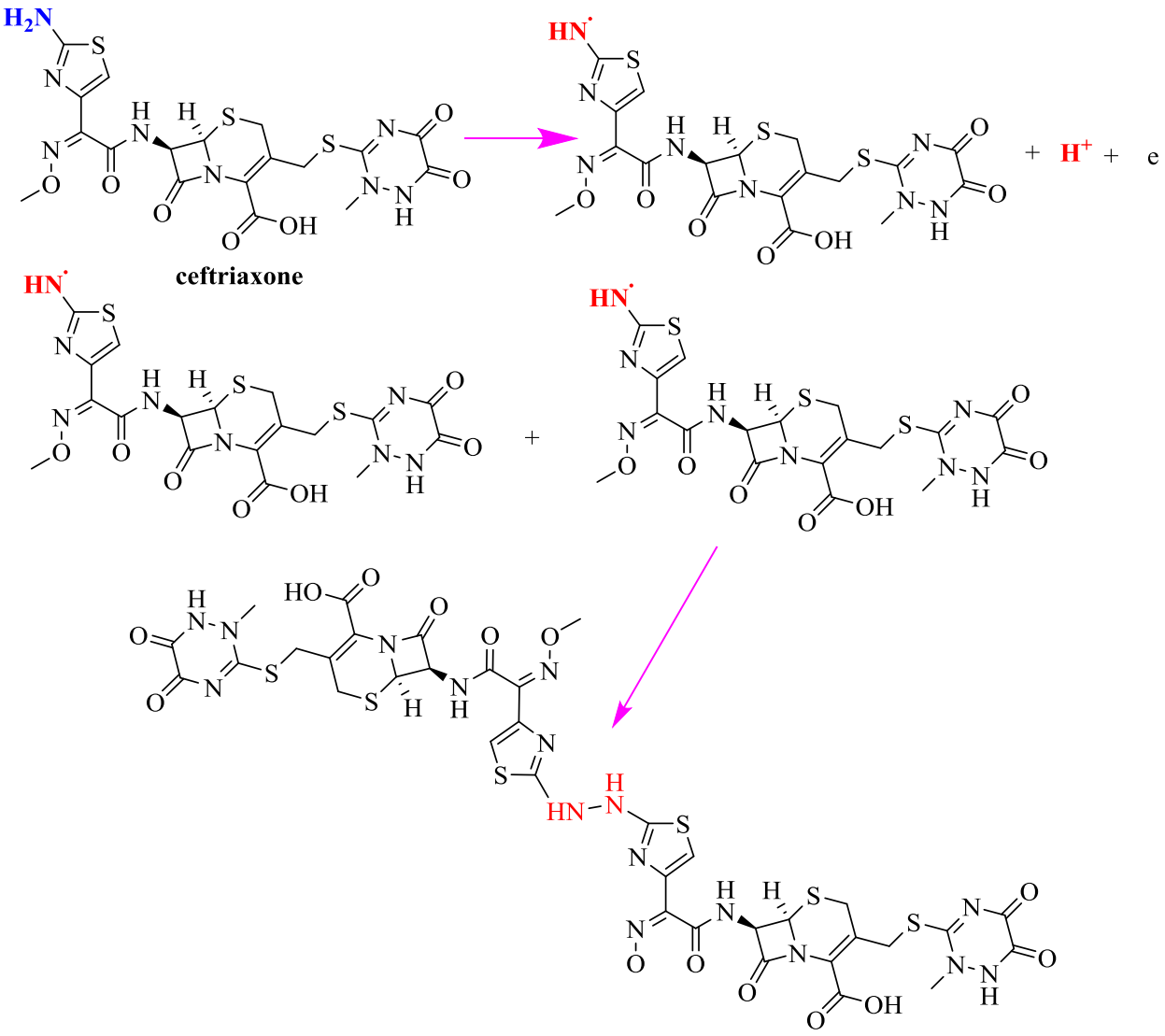
ceftriaxone

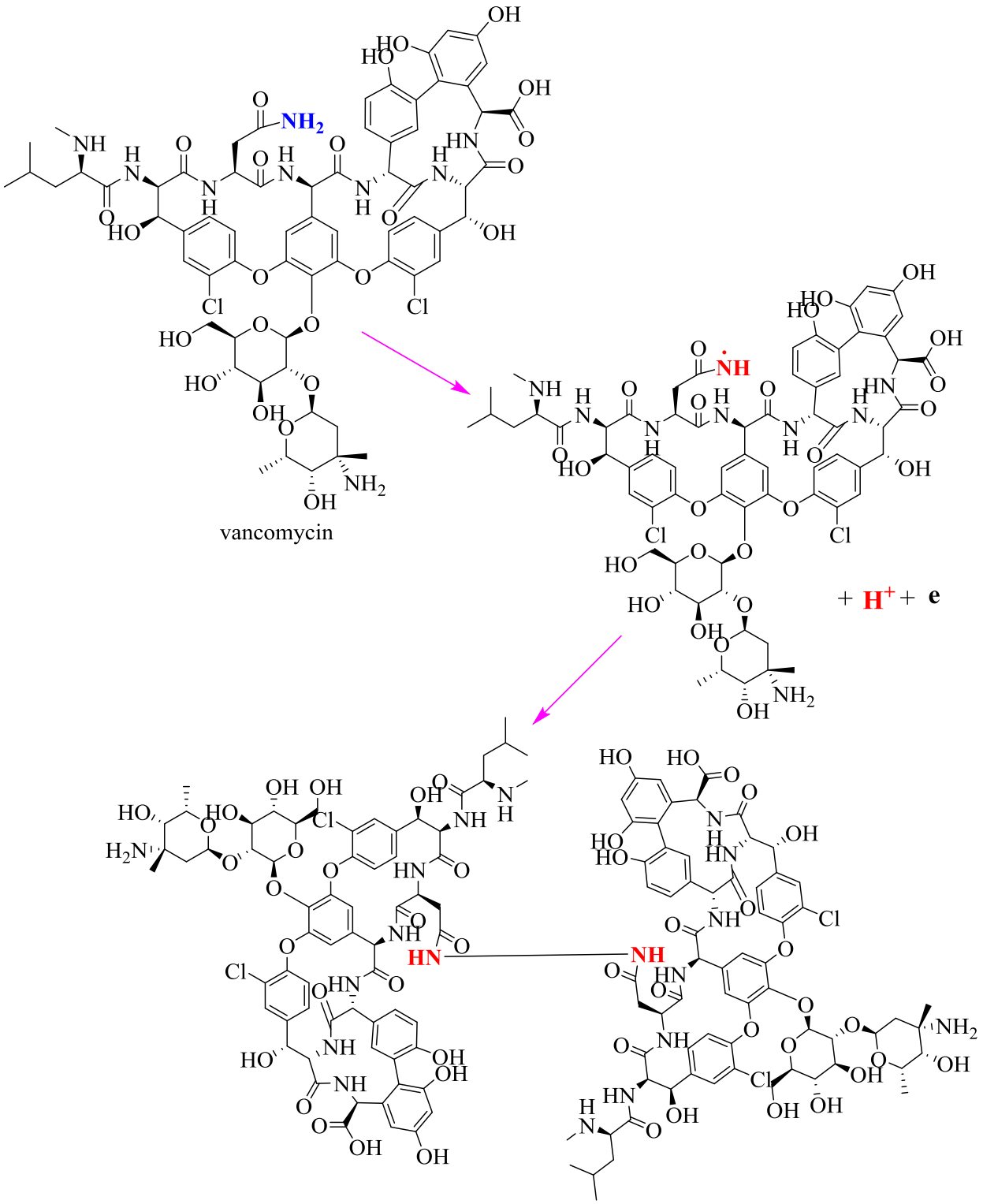

Scheme S1. The proposed electro-oxidation mechanism of CFT and VAN at the Au-Ag-ANCCs/*r*-GO/poly(L-histidine)/GCE.

4. Selectivity

Table S1: The effect of coexisting substances on the electrochemical response of the sensor to detect VAN and CFT.

Interferents	Conc. (µM)	Relative Percentage Error (%)		Interferents	Conc. (µM)	Relative Percentage Error (%)	
		VAN	CFT			VAN	CFT
Ca^{2+}	900	0.96	1.02	Uric Acid	750	2.25	2.25
K^{+}	900	1.97	1.91	Dopamine	750	2.47	2.81
Mg^{2+}	900	1.23	1.18	Glucose	750	2.22	2.17
Cu^{2+}	900	1.77	1.82	Ascorbic acid	750	2.21	2.19
Fe^{3+}	900	0.85	0.92	Lactose	200	2.35	2.35
HCO_3^-	900	0.96	0.96	Azithromycin	200	4.15	4.18
NO_3^-	900	1.45	1.45	Chloramphenicol	200	4.22	4.19
SO_4^{2-}	900	1.63	1.58	Tinidazole	200	4.37	4.37
CO_3^{2-}	900	1.11	1.15	Ampicillin	200	4.42	4.43
Cl^-	900	1.36	1.41	Cloxacillin	200	4.57	4.56
Fructose	750	2.33	2.38	Erythromycin	200	4.61	4.58
Folic acid	750	2.19	2.21	Amoxicillin	200	4.57	4.61
Urea	750	2.68	2.71	Ciprofloxacin	200	4.33	4.33
Sucrose	750	2.47	2.38	Cephalexin	200	4.54	4.58

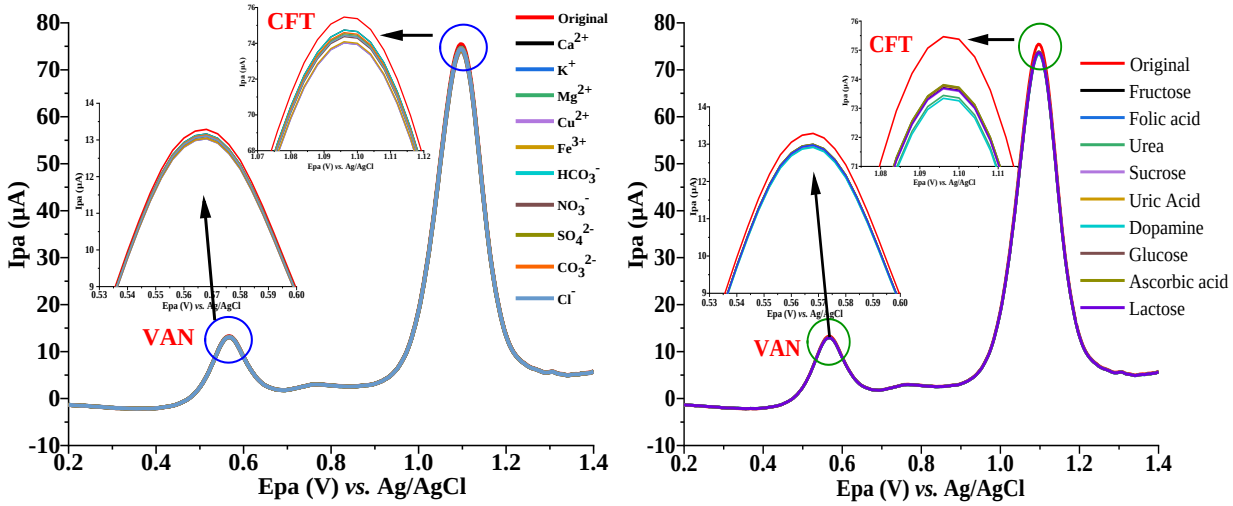

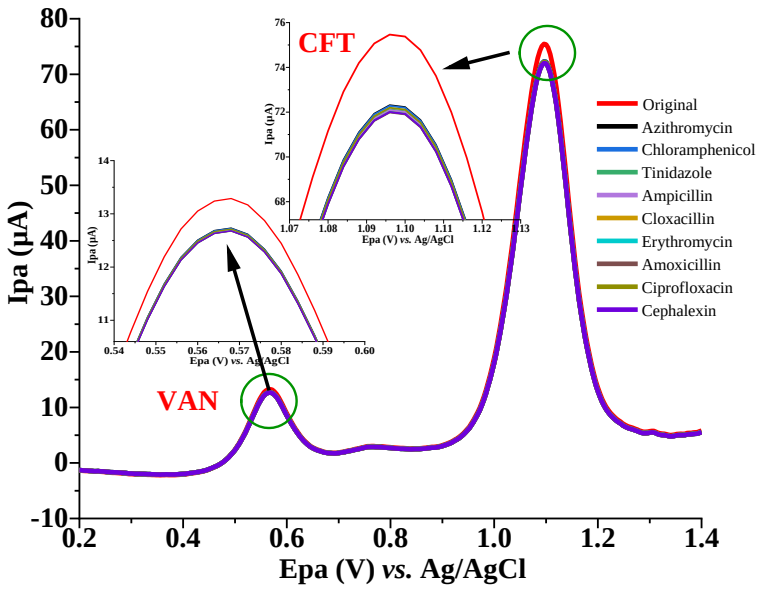

Fig. S5. Results of selectivity analysis conducted for the sensor.

Chapter Nine: Paper VII

Ultra-performance multi-elemental nanocomposites electrochemical sensor for the simultaneous determination of the residues of nitrofurantoin and furazolidone in poultry, fish, honey, dairy products and municipal wastewater

Wondimeneh Dubale Adane, Bhagwan Singh Chandravanshi, Merid Tessema

Sensing and Bio-Sensing Research

(Under Review)

Ultra-performance multi-elemental nanocomposites electrochemical sensor for the simultaneous determination of the residues of nitrofurantoin and furazolidone in poultry, fish, honey, dairy products and municipal wastewater

Wondimeneh Dubale Adane[a], Bhagwan Singh Chandravanshi*[a], Merid Tessema**[a]

[a]Department of Chemistry, Addis Ababa University, P. O. Box 1176, Addis Ababa, Ethiopia

*Corresponding author. E-mail address: bscv2006@yahoo.com

**Corresponding author. E-mail address: tessemamerid@yahoo.com

ABSTRACT

This study presents a novel ultra-performance multi-elemental nanocomposite electrochemical sensor for the simultaneous detection of nitrofurantoin (NFT) and furazolidone (FZD) residues in food and municipal wastewater. The sensor was developed by integrating gold-silver-alloy nanocoral clusters (Au-Ag-ANCCs) with a zinc oxide nanoparticle-carbon paste electrode (ZnO-NPs-CPE) and polyethylene oxide (PEO) nanocomposites. The surface morphology and elemental composition of Au-Ag-ANCCs/ZnO-NPs-CPE/PEO were characterized using various analytical (FT-IR, XRD, SEM, and EDX) and electrochemical (EIS, CV, and SWV) techniques. The electroactive surface area of the sensor was determined to be 0.214 cm^2, approximately five-fold higher than that of the bare CPE (0.045 cm^2). The sensor demonstrated exceptional performance over a wide linear range, from 1.0 pM to 250 µM for NFT and 0.9 nM to 360 µM for FZD. The detection and quantification limits were found to be 0.26 pM and 0.88 pM for NFT and 0.023 pM and 0.076 pM for FZD, respectively. Moreover, the sensor exhibited excellent repeatability, reproducibility, long-term stability, and anti-interference capabilities. While applied to detect AZM and ENF residues in poultry, fish, honey, dairy products and municipal wastewater, the sensor exhibited excellent recoveries of 96.3–102.8% and relative standard deviations between 1.87% and 1.53%. Generally, the developed sensor represents a significant advancement in addressing the global antibiotic residue pollution crisis.

Keywords: Electrochemical sensor; Antibiotic residues; Nitrofurantoin; Furazolidone, Multi-elemental nanocomposite

1. Introduction

Antibiotics, which are pivotal in modern medicine, have transformed healthcare by effectively combatting bacterial infections and saving countless lives. Prescribed for a spectrum of infectious diseases ranging from gastrointestinal to respiratory ailments, antibiotics also serve a critical role in promoting growth and improving feed efficiency in animal husbandry [1]. By targeting fundamental bacterial processes, such as cell wall synthesis, protein synthesis, DNA replication, RNA elongation, and transcription, antibiotics impede bacterial growth and reproduction [2]. However, their misuse and incomplete metabolism can lead to adverse effects including allergic reactions, liver and kidney damage, blood disorders, nerve issues, hearing loss, and skin sensitivity [3]. Furthermore, the extensive use of antibiotics in livestock farming contaminates animal-derived foods, contributing to environmental antibiotic resistance genes and posing health risks including obesity, digestive disorders, bone marrow issues, and cancer, even at low residual concentrations. The indiscriminate use of antibiotics has spurred antibiotic resistance, a significant global health concern, resulting in treatment failure, increased mortality, and increased healthcare costs [4]. Given these challenges, the development of sensitive and selective devices for detecting antibiotic residues is crucial to combat antibiotic pollution and protect public health.

Nitrofurantoin (NFT), ((E)-1-[(5-nitro 2-furyl)methylideneamino]imidazolidine-2,4-dione), is mainly used to combat Escherichia coli and Enterococcus, the primary pathogens responsible for urinary tract infections in humans. Additionally, due to its broad-spectrum antimicrobial activity, low cost, and high efficiency, NFT is extensively utilized as an additive of feed in animal husbandry to address bacterial and protozoal infections and to prevent coccidiosis in poultry and livestock [5]. However, the extensive use of NFT can result in adverse effects, such as loss of appetite, diarrhea, nausea, and vomiting, along with potential risks of hepatotoxicity, mutagenicity, carcinogenic activity, and teratogenesis [5,6]. In animal husbandry, NFT is commonly administered orally either through animal feed or drinking water, leading to the accumulation of its residues in animal products, including meat, milk, eggs, and other tissues [7]. Improper disposal of animal waste can result in environmental contamination, impacting groundwater and surface water. The accumulation of NFT residues in food sources poses a significant risk to public health,

potentially harming humans and contributing to the development of antibiotic-resistant bacteria [8].

Furazolidone (FZD), (3-(5-nitrofurfurylideneamino)-2-oxazolidinone), a nitrofuran derivative, has typically been used as a chemotherapeutic agent to combat bacterial and protozoal infections such as dysentery, gastritis, enteritis, and gastric ulcers [9]. However, its primary application has shifted to the prevention and treatment of microbial infectious diseases in animal husbandry and aquaculture caused by pathogens such as Salmonella, Shigella, Staphylococci, and Escherichia coli. The presence of FZD residues in the food chain poses substantial health risks due to their mutagenic, carcinogenic, and teratogenic properties [10], leading to a severe outcomes such as decreased white blood cells, skin inflammation, stomach cramps, and suppressed cell growth. Moreover, FZD can damage human DNA and hinder cell growth. Consequently, due to these detrimental effects, FZD has been banned in many countries, including China, the European Union, and the United States. Nonetheless, its illicit use in livestock, poultry, and aquaculture persists, resulting in residues in meat, eggs, honey, and milk, thereby posing a significant threat to human health through the food chain [9].

In recent years, nanocomposites have been extensively used for cancer treatment, water purification, environmental conservation, and food packaging. The integration of nanotechnology with voltammetric methods has led to the development of robust electrochemical devices for accurate analyte detection. This synergy provides advantages, such as prolonged stability, expanded electroactive area, heightened mass transfer, and enhanced catalytic performance [11]. Bimetallic alloy nanoparticles have emerged as promising candidates for electrochemical sensing, due to their exceptional sensitivity, superior detection capabilities, and robust stability [12]. Their morphology, size, and composition further enhance their catalytic performance and synergistic properties, extending their potential applications in domains such as cancer treatment, nanomedicine, catalysis, and DNA delivery [13]. In particular, gold–silver alloy nanoparticles have attracted significant interest owing to their outstanding electrocatalytic properties, electrical conductivity, and optical features [14]. Similarly, zinc oxide nanoparticles (ZnO-NPs) have gained a significant attention for electrochemical applications due to their remarkable electrocatalytic activity, high electron transfer kinetics, good electrical conductivity, remarkable chemical stability, broad electrochemical potential windows, and facile synthesis. Furthermore, the intrinsic

non-toxicity and biocompatibility of ZnO-NPs make them highly suitable for diverse device fabrication [15].

Polyethylene oxide (PEO) is well-known for its versatility as an electrode modifier in electrochemical applications, exerting a significant influence on and enhancing electrical conductivity. Its incorporation as an electrode modifier has resulted in remarkable improvements in conductivity, fostering an environment conducive to electron movement during electrochemical reactions [16]. Furthermore, PEO used as a dispersing agent, preventing undesirable particle agglomeration at the electrode surface and ensuring the formation of a uniform and conductive layer. It effectively reduces impedance, thereby enhances the charge transfer efficiency at the electrode-electrolyte interface [17]. The biocompatibility of PEO extends its utility, in biological or bio-electrochemical applications, facilitating interactions between analytes and electrodes while preserving electrical conductivity. Moreover, PEO serves as a protective layer, shielding the electrode surface from undesired reactions and corrosion, thereby contributing to the overall stability and longevity of the electrode in various environments [18].

A range of analytical techniques has been utilized for the quantification of NFT and FZD in diverse matrices, including chemiluminescence [19], LC-MS [20], ELISA [21], spectrophotometry [22], and UHPLC-DAD assay [23]. Although these methods offer sensitivity and selectivity, they have several limitations, such as intricate operational procedures, time-consuming sample preparation, prolonged analysis times, high equipment prices, and the necessity for experienced hands. Conversely, voltammetric approaches present notable advantages, including cost-effectiveness, rapid analysis, user-friendliness, high specificity, portability, potential for miniaturization, and minimal sample volume requirements [24]. Consequently, electrochemical techniques have become the preferred option for simultaneously detecting NFT and FZD residues. Among the electrochemical techniques, SWV was selected due to its numerous advantages, including ultra-fast analysis, minimal sample consumption, background differentiation, and high sensitivity [25].

This study presents a cutting-edge multi-elemental electrochemical sensing platform by integrating Au-Ag-ANCCs with ZnO-NP-CPE and PEO nanocomposites. This pioneering sensor was designed for the simultaneous detection of NFT and FZD residues in poultry, fish, honey,

dairy products, and municipal wastewater samples. Before electrochemical analysis, Au-Ag-ANCCs/ZnO-NPs-CPE/PEO was subjected to comprehensive surface characterization and elemental composition analysis. The sensor demonstrated exceptional performance in detecting NFT and FZD, with broad linear ranges and detection limits in the picomolar range. Its outstanding selectivity and sensitivity were confirmed through sharp current responses to ultra-low concentrations, underscoring its remarkable specificity, stability, and reliability.

2. Experimental

2.1. Chemical and reagents

Zinc nitrate hexahydrate ($Zn(NO_3)_2.6H_2O$), and sodium hydroxide (NaOH) were purchased from LOBA Chemie Pvt. Ltd (India) and Molychem (India), respectively. Tetrachloroauric acid ($HAuCl_4$), silver nitrate ($AgNO_3$), sodium borohydride ($NaBH_4$), and sodium citrate ($Na_3C_6H_5O_7$) were procured from Shanghai Sinopharm Chemical Reagent Co., Ltd. (China). Nitric acid (HNO_3), sulfuric acid (H_2SO_4), and sodium citrate were acquired from Merck Chemicals (Germany). Graphite powder (BDH Laboratory Supplies, Poole, England) and paraffin oil (Uvasol Merck, Germany) were used for the preparation of the carbon paste electrode. Potassium hexacyanoferrate (III) (99%) was obtained from BDH Chemicals Ltd. (England). Polyvinyl pyrrolidone (PVP, K15, MW ≈ 40,000) was provided by Research Lab. Fine Chem. Industries (Mumbai, India). All other chemicals and antibiotic standards were obtained from Sigma-Aldrich (USA). Chemicals and reagents utilized in this experiment were of analytical grade and used without further purification. Glassware was cleaned with aqua regia ($HCl:HNO_3$ in a 3:1 ratio by volume) and washed with deionized water before the experiments. Aqueous solutions were prepared using Milli-Q water (18.2MΩ cm) obtained from a Millipore water purification system. Dissolving 59.5 mg of NFT in 25 mL of dimethyl formamide (DMF) yielded its 0.01 M stock solution. For FZD a 0.01 M stock solution was prepared by dissolving 56.3 mg of the analyte in 25 mL of dimethyl sulfoxide (DMSO). These stock solutions were further diluted with 0.1 M PBS (pH 7) to prepare the working solutions for each analyte.

2.2. Apparatus and instruments

Electrochemical measurements were performed in 20 mL cells with a CHI 760D electrochemical analyzer (CH Instruments, USA). A conventional three-electrode system was employed, consisting of a working electrode (either bare CPE or modified CPE), a platinum wire counter electrode, and silver-silver chloride (Ag/AgCl (3M KCl)) reference electrode. The surface morphologies of modified electrodes were characterized using a scanning electron microscope (SEM, CX-200plus, Coxem, Korea), and elemental analysis was performed using energy-dispersive X-ray spectroscopy (EDS). X-ray diffraction (XRD) patterns of the nanocomposites were recorded using a BRUKER ECOD 8 advance diffractometer with Cu Kα radiation (wavelength λ = 0.15406 nm) at room temperature. Fourier transform infrared (FT-IR) spectra were obtained using a PerkinElmer Spectrum 100 FT-IR spectrometer (PerkinElmer, USA). The pH measurements were conducted with a Senses Ion+MM150 pH meter (China). Solid chemicals were weighed using an electronic digital balance (Model: Scientech ZSA 120, USA). A centrifuge (model 8001, China) and an ultrasonic cleaner (model YJ5120-B, China) were utilized during nanocomposite preparation. Additionally, a magnetic stirrer and a vacuum pump were employed throughout the experiment.

2.3. Preparation of ZnO-NPs and CPE

Zinc oxide nanoparticles were synthesized using a modified co-precipitation method based on Kotresh et al.'s report [26]. Initially, 2.5 g of NaOH was dissolved in 100 mL of deionized water and heated to 55°C with constant stirring. Simultaneously, 7.5 g of $Zn(NO_3)_2 \cdot 6H_2O$ was dissolved in 100 mL of deionized water. The pre-warmed NaOH solution was then gradually added to the $Zn(NO_3)_2 \cdot 6H_2O$ solution and continuously stirred for 2.5 hrs at 45°C. Subsequently, the solution was left to settle for 3 hrs. The mixture was filtered to isolate the solid ZnO-NPs from the liquid component. The nanoparticles were then thoroughly washed with deionized water to remove impurities. Finally, the washed ZnO-NPs were dried at 120°C for 6 hrs and calcined at 240°C for 3 hrs.

70 mg of powdered graphite was thoroughly mixed with 30 µL of paraffin oil for 25 mins using an agate mortar and pestle to prepare the CPE. The resulting homogenized paste was packed

into a 1.0 mL syringe fitted with a Cu wire for electrical contact. The electrode surface was then polished on white paper to achieve a mirror-like finish. When a fresh electrode was required, the previous electrode was carefully removed from the upper tip surface, replaced with a new paste, and subjected to further polishing.

2.4. Synthesis of Au-Ag-ANCCs

The synthesis of Ag-NCCs was performed as follows: initially, 0.1 M $AgNO_3$ (2 mL) and 0.1 M polyvinyl pyrrolidone (PVP, K15, MW ≈ 40,000) (10 mL) were added into a 100 mL flask containing 15 mL of 0.1 M polyethylene glycol (PEG 600) solution under vigorous stirring for 20 min. Then, 4 mL of 1% $Na_3C_6H_5O_7$ was added to initiate the reduction of Ag ions. The addition of stabilizing agent prevents agglomeration and regulates the size and morphology of the clusters. Subsequently, the mixture was heated in an oil bath at 130°C for 10 hrs, during which $AgNO_3$ and PVP reacted to form Ag nanocoral clusters stabilized by PEG 600 molecules. Controlled temperature and stirring conditions facilitated the gradual formation of Ag nanocoral clusters, exhibiting distinctive branch-like structures. The yellowish solution was allowed to cooling, centrifugation, and washing several times.

The synthesis of Au-Ag alloy nanocoral clusters (Au-Ag-ANCCs) involves a controlled alloying process, converting Ag-NCCs into their gold-based counterparts. Initially, 5 mL 0.01 M $HAuCl_4$ solution was vigorously stirred with the Ag-NCCs suspension for 15 min to ensure homogeneous distribution of gold ions, facilitating their incorporation into the silver nanostructures and forming the basis for alloyed nanocoral clusters. Then, the reaction mixture was heated in an oil bath at 90°C for 3 hrs with continuous stirring. Subsequently, 3 mL of 0.1 M $NaBH_4$ was gradually added to activate the reduction process, resulting in the formation of Au-Ag-ANCCs. The pH of the reaction mixture was maintained at 10 by periodic additions of 0.1 M NaOH, promoting gold ion reduction and stabilizing the resulting alloy nanostructures. Additionally, 4 mL of 1% PVP solution was introduced as a stabilizing agent to maintain colloidal stability and form a protective layer. Finally, the synthesized Au-Ag-ANCCs were centrifuged, washed, and vacuum dried.

2.5. Preparation of Au-Ag-ANCCs/ZnO-NPs-CPE

First, 10 mg of ZnO-NPs were dispersed in 8 mL of dimethyl sulfoxide (DMSO) and subjected to 45 min of homogenization using an ultrasonic device. Subsequently, the dispersion of ZnO-NPs was mixed with the Au-Ag-ANCCs dispersion at a ratio of 3:4 and subjected to ultrasonication for 45 min. Afterwards, 7 µL of the resulting Au-Ag-ANCCs/ZnO-NPs dispersion was drop-casted onto a CPE, dried at 20°C for 10 min, and referred to as Au-Ag-ANCCs/ZnO-NPs-CPE.

2.6. Fabrication of Au-Ag-ANCCs/ZnO-NPs-CPE/PEO

Electropolymerization of 0.01 M PEO containing 0.01 M KCl was performed at the surface of Au-Ag-ANCCs/ZnO-NPs-CPE using CV for ten consecutive potential scans between -1.7 V and +1.6 V in 0.1 M PBS (pH 7.0) at a scan rate of 25 mVs^{-1} (Fig. S1A). Subsequently, the developed sensor (Au-Ag-ANCCs/ZnO-NPs-CPE/PEO) was rinsed with ethanol and deionized water.

3. Results and discussion

3.1. Analytical characterizations

The XRD peaks of Ag-NCCs, observed at 2θ=34.42°, 38.24°, 40.08°, 44.46°, and 57.72° (Fig. 1A(a)), corresponding to the (100), (111), (200), (220), and (311) crystal planes, respectively, (with average size of 33 nm), indicating a face-centered cubic (FCC) structure of Ag metal crystals (JCPDS card number 04-0783), consistent with previous findings [27]. The XRD analysis of Au-Ag-ANCCs (Fig. 1A(b)) revealed almost identical 2θ values to Ag-NCCs, with an additional peak at 26.52° attributed to the (111) crystal plane, suggesting potential intermetallic alloy compound formation, average size of was determined to be 22 nm. Fig. 1A(c) illustrates the XRD pattern of ZnO-NPs-CPE, showing peaks at 2θ=23.86°, 26.94°, 32.08°, 34.64°, 36.62°, 47.7°, 54.56°, and 56.96°, corresponding to the crystal planes (100), (002), (101), (102), (110), (103), (112), and (201), respectively, revealing the hexagonal crystal structure of the material (JCPSD card no. 01-007-2551) [28]. Fig. 1A(d) shows the XRD spectrum of Au-Ag-ANCCs/ZnO-NPs-CPE, confirming the successful integration of the constituent materials in the nanocomposite electrode,

as demonstrated by the characteristic XRD peaks corresponding to each nanomaterial. The XRD spectra of Au-Ag-ANCCs/ZnO-NPs-CPE/PEO (Fig. 1A(e)) exhibited characteristic peaks of its constituent components, confirming the successful preparation of the sensor. While PEO typically lacks distinct diffraction peaks owing to its amorphous nature, peaks at 2θ=19.94° and 21.08° may correspond to crystalline forms of PEO within the sensor.

The SEM image of Ag-NCCs revealed a visually attractive morphology characterized by irregularly shaped, three-dimensional nanocoral clusters with interconnected branches resembling coral reefs (Fig. 1B(a)). These nanocoral clusters exhibited non-uniform distribution, rough surfaces, and porous networks. The average size range of 31–35 nm for the Ag-NCCs was confirmed and aligned with the results of the XRD analysis. The SEM analysis of Au-Ag-ANCCs (Fig. 1B(b)) demonstrated the presence of highly irregular, non-uniform nanocoral clusters comprising a rough porous network with an average size of 20–24 nm. The energy-dispersive X-ray (EDX) spectra of the Ag-NCCs (Fig. S2B(d)) indicates the presence of C(32.0%), N(3.3%), O(7.1%), and Ag(57.6%). Similarly, the EDX of Au-Ag-ANCCs (Fig. S2B(e)) contained C(26.5%), N(3.1%), O(7.3%), Ag(52.6%), and Au(10.5%), suggesting successful incorporation of Au into the Ag-NCCs. Thus, the incorporation of Au into Ag-NCCs is expected to enhance the conductivity, active area, and catalytic properties of the resulting Au-Ag-ANCCs. The SEM image of the ZnO-NPs-CPE (Fig. 1B(c)) provides valuable insight into its morphology, revealing a rough surface and irregular structure with a non-uniform distribution of ZnO NPs. The EDX spectra (Fig. S2B(f)) showed that ZnO-NPs-CPE was mainly composed of C(34.6%), O(15.6%), and Zn(49.8%), confirming the high degree of purity of the synthesized material. Fig. 1B(d) illustrates the uniform distribution of the Au-Ag-ANCC particles within the ZnO-NPs-CPE matrix, forming an integrated nanocomposite material (Au-Ag-ANCCs/ZnO-NPs-CPE). The resulting nanocomposite electrode exhibited a well-defined crystalline nanoporous structure with rough and irregular shapes as well as noticeable interconnected cavities. This confirms the successful incorporation of Au-Ag-ANCC particles into the ZnO-NPs-CPE matrices. The elemental mapping of the Au-Ag-ANCCs/ZnO-NPs-CPE (Fig. S2B(i)) confirmed the presence of C(13.1%), N(2.5%),O(7.1%), Zn(36.5%), Ag(31.4%), and Au(9.4%). The SEM image in Fig. 1B(e) shows the surface morphology of Au-Ag-ANCCs/ZnO-NPs-CPE/PEO, revealing that the PEO film effectively coated the surface, resulting in a rough, non-uniform, and irregular texture. The

corresponding EDX spectra (Fig. 1B(f)) showed the presence of C(21.3%), N(6.3%), O(14.7%), Zn(26.2%), Ag(24.9%), and Au(6.6%), confirming the successful fabrication of the proposed multi-elemental nanocomposite electrochemical sensor.

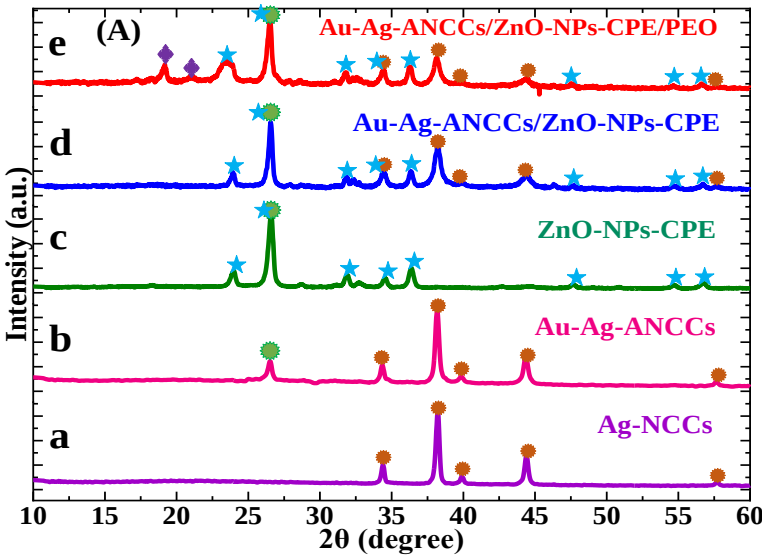

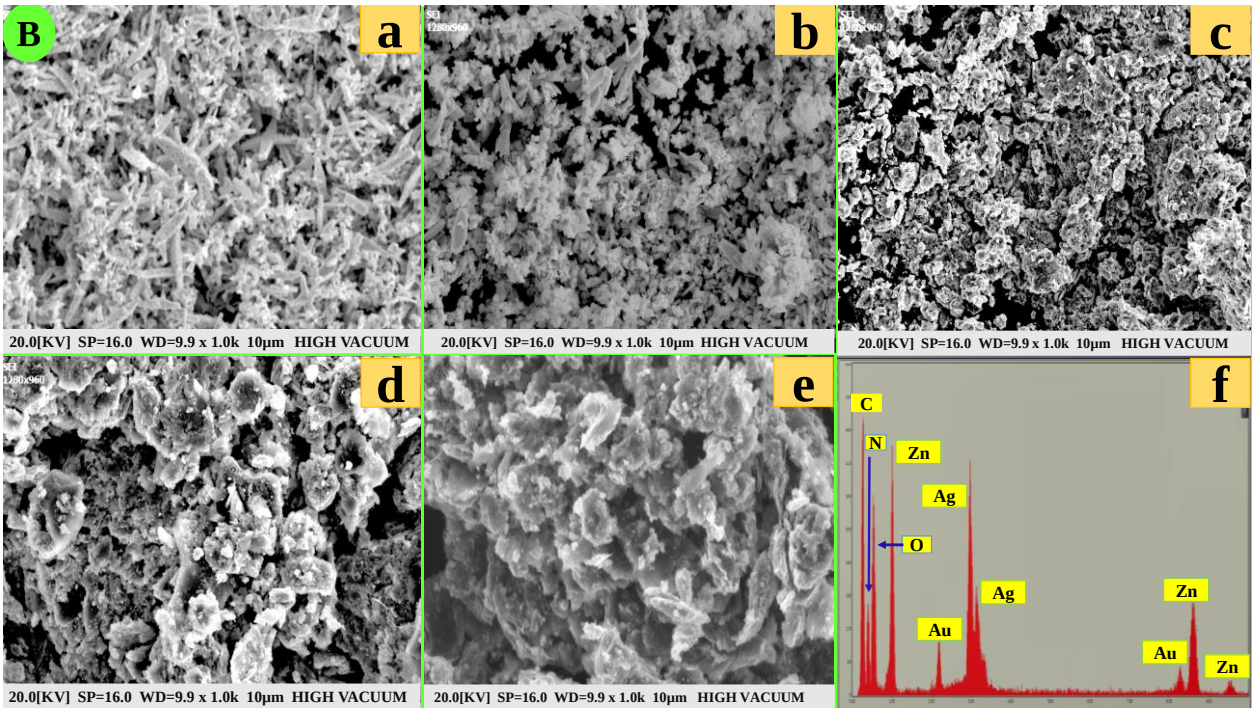

Fig. 1. (A) XRD patterns, (B) SEM images of Ag-NCCs (a), Au-Ag-ANCCs (b), ZnO-NPs-CPE (c), Au-Ag-ANCCs/ZnO-NPs-CPE (d), Au-Ag-ANCCs/ZnO-NPs-CPE/PEO (e), and (B) EDX spectra of Au-Ag-ANCCs/ZnO-NPs-CPE/PEO (f).

3.2. Electrochemical characterizations

The electrodes were subjected to extensive electrochemical impedance spectroscopy (EIS) analysis, spanning in a frequency range of 0.1 to 100, 000 Hz, utilizing a solution containing 5 mM $[Fe(CN)_6]^{3-/4-}$ in 0.1 M KCl (Fig. 2A). The obtained experimental data were fitted to the Randles equivalent circuit model and depicted in a Nyquist plot (inset, Fig. 2A). In the EIS curve, the semicircular segment denotes the rate-limiting step of the electrochemical reaction, and the diameter of the semicircle represents the charge transfer resistance (R_{ct}) [24]. The R_{ct} values for the bare CPE, ZnO-NPs-CPE/PEO, Au-Ag-ANCCs-CPE, Au-Ag-ANCCs-CPE/PEO, Au-Ag-ANCCs/ZnO-NPs-CPE, and Au-Ag-ANCCs/ZnO-NPs-CPE/PEO, were found to be 4826Ω, 2845Ω, 1978Ω, 1274Ω, 864Ω, and 141Ω, respectively. The lowest R_{ct} value was obtained from the Au-Ag-ANCCs/ZnO-NPs-CPE/PEO configuration, indicating a significant enhancement in the conductivity, electron transfer capability, and electroactive surface area.

The voltammetric characteristics of the electrodes were further assessed with CV with a redox probe of 5 mM $[Fe(CN)_6]^{3-/4-}$ containing 0.1 M KCl at a scan rate of 50 mVs^{-1} (Fig. 2B). The bare CPE exhibited weak redox current and the widest peak-to-peak separation (ΔEp = 196 mV), attributed to its limited electrical conductivity (Fig. 2B(a)). In contrast, the ZnO-NPs-CPE/PEO (Fig. 2B(b)) and Au-Ag-ANCCs-CPE (Fig. 2B(c)) showed distinct redox current responses and lower ΔEp values (151 mV and 124 mV, respectively). The current responses significantly increased for Au-Ag-ANCCs-CPE/PEO (Fig. 2B(d)) and Au-Ag-ANCCs/ZnO-NPs-CPE (Fig. 2B(e)), accompanied by reduced ΔEp values (105 mV and 86 mV, respectively). Expressively, the current response at the surface of the Au-Ag-ANCCs/ZnO-NPs-CPE/PEO (Fig. 2B(f)) reached its maximum value with a decrease in ΔEp to 62 mV, indicating the synergistic enhancement in the overall performance of the sensor by the nanocomposite modifiers, in line with the EIS findings.

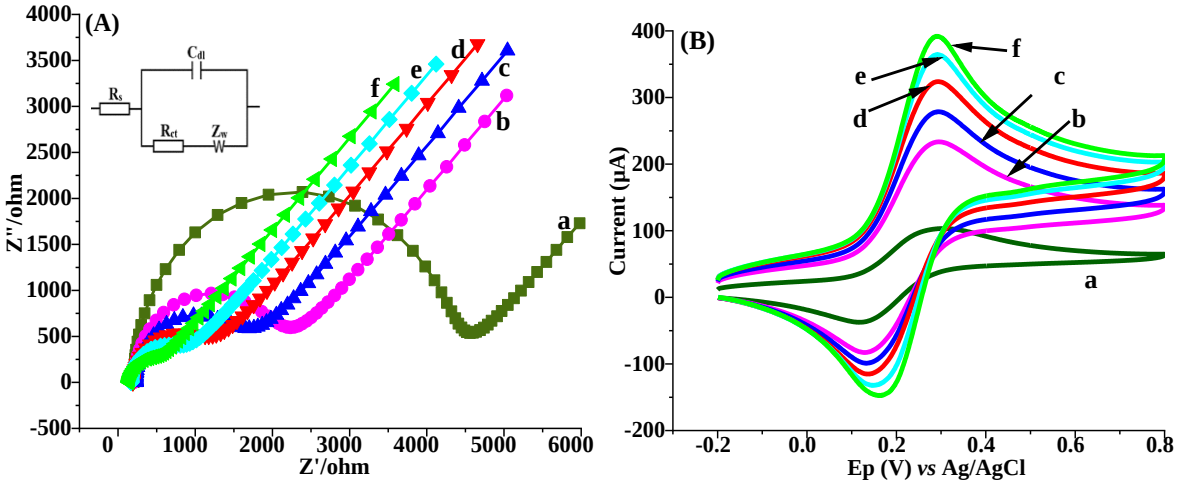

Fig. 2. (A) Nyquist plots and (B) CVs of bare CPE (a), ZnO-NPs-CPE/PEO (b), Au-Ag-ANCCs-CPE (c), Au-Ag-ANCCs-CPE/PEO (d), Au-Ag-ANCCs/ZnO-NPs-CPE (e), Au-Ag-ANCCs/ZnO-NPs-CPE/PEO (f).

Quantification of electroactive surface area is crucial for electrochemical reactions because of its direct influence on the catalytic efficiency and sensitivity of the electrodes. In this study, CV was used to evaluate the electroactive surfaces of electrodes at different modification stages. The determination was performed by applying the Randles-Sevcik equation (1) [25].

$$I_p = 2.69 \times 10^5 n^{3/2} A D^{1/2} C v^{1/2} \quad (1)$$

where n = number of electrons, I_p = peak current, C = concentration of $[Fe(CN)_6]^{3-/4-}$, v = scan rate, D = diffusion coefficient, and A = electrode surface area. The electroactive areas were determined to be 0.045 cm^2, 0.081 cm^2, 0.127 cm^2, 0.139 cm^2, 0.165 cm^2, and 0.214 cm^2 for the bare CPE, ZnO-NPs-CPE/PEO, Au-Ag-ANCCs-CPE, Au-Ag-ANCCs-CPE/PEO, Au-Ag-ANCCs/ZnO-NPs-CPE, and Au-Ag-ANCCs/ZnO-NPs-CPE/PEO, respectively. Notably, the Au-Ag-ANCCs/ZnO-NPs-CPE/PEO exhibited almost a fivefold increase in electroactive area compared to the bare CPE.

3.3. Electrochemical behaviors of NFT and FZD

The voltammetric behaviors of 25 µM NFT and FZD were examined via SWV and CV at 100 mVs^{-1} (scan rate) within a potential range of -0.9–0.2 V on both unmodified and modified

electrodes. Blank solutions showed no detectable CV currents, indicating the absence of analytes or their concentration below the detection limit. The nonexistence of oxidation peaks in the reverse CV scan (Fig. 3A) indicates the irreversibility of FZD electrode reaction, while NFT exhibited a reversible electrode reaction. Weak current responses were noted at bare CPE, indicating sluggish electron transfer kinetics and insufficient electrical conductivity. In contrast, ZnO-NPs-CPE/PEO and Au-Ag-ANCCs-CPE exhibited amplified currents, attributed to enhanced electrical conductivity facilitated by ZnO-NPs and the alloying of Au and Ag with the formation of nanocoral clusters, respectively. These enhancements contributed to increased electroactive area and reduced electron travel distance [29]. The improved CV responses at the surface of Au-Ag-ANCCs-CPE/PEO were attributed to the favorable contribution of the PEO film. Furthermore, the combined effects of electrical conductivity from both Au-Ag-ANCCs and ZnO-NPs nanocomposites resulted in an increased CV response at the Au-Ag-ANCCs/ZnO-NPs-CPE. The highest CV responses were observed at the Au-Ag-ANCCs/ZnO-NPs-CPE/PEO, underlining the synergistic effects of the constituent nanocomposites.

The voltammetric properties of 25 µM NFT and FZD were further investigated using SWV at different electrode configurations (Fig. 3B). The bare CPE exhibited the lowest reduction current due to its limited catalytic activity. In contrast, Au-Ag-ANCCs/ZnO-NPs-CPE/PEO demonstrated the highest reduction currents for both analytes, consistent with the CV results. Furthermore, the peak-to-peak separation (ΔEp=728 mV) between NFT and FZD provided sufficient differentiation for simultaneously determining the analytes.

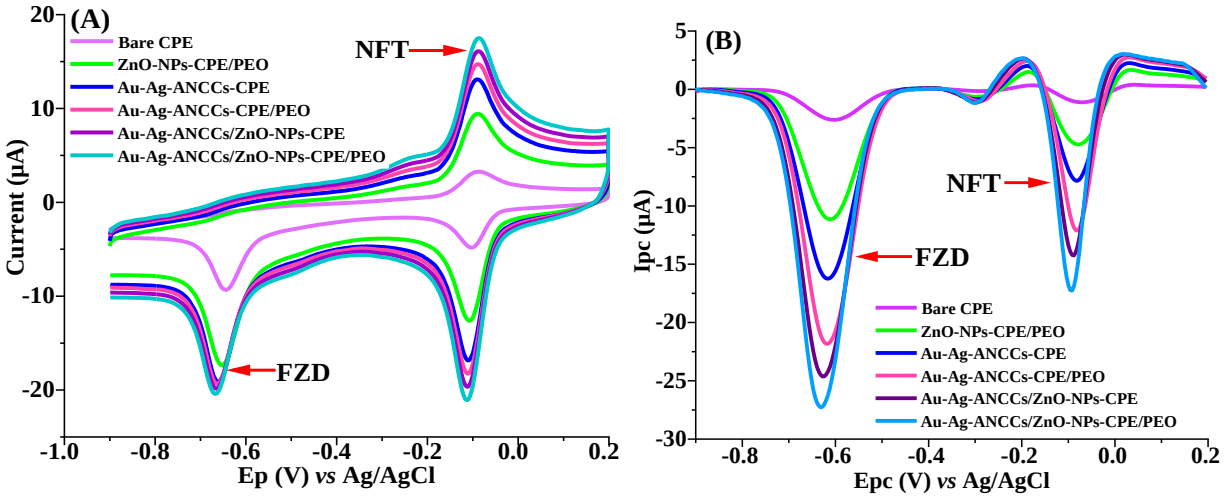

Fig. 3. (A) CVs and (B) SWVs of 25 µM NFT and FZD at different electrodes.

3.4. Optimization of experimental conditions

The Supplementary Material provides comprehensive details on procedures for sample preparation and optimization of electrolyte solutions, nanocomposite mixing ratio, drop-casting volume, and SWV parameters.

3.4.2. Effect of pH

The effect of pH variations on the current responses of 25 µM NFT and FZD were investigated using SWV at 25 mVs^{-1} (scan rate). The Ipc of both analytes increased gradually within the pH range of 5.0 to 7.0 (Figs. 4B(a) and C(a)). However, a subsequent increase in the pH resulted in a decline in the current responses. Consequently, the optimum pH for further analysis was determined to be 7.0. Furthermore, the Epc of both NFT and FZD shifted towards more positive values with pH (Fig. 4A), indicating the involvement of protons in the electro-reduction of the analytes. A linear correlation was observed between pH and Epc, given by the equations: Epc (V) = 0.055 – 0.346 (R^2 = 0.999) (Fig. 4B(b)) for NFT, and Epc(V) = 0.057–0.886 (R^2 = 0.998) (Fig. 4C(b)) for FZD. The slope values of 55 and 57 mV/pH for NFT and FZD, respectively, closely approximated the Nernstian theoretical value of 59 mV/pH, suggesting the electro-reduction of NFT and FZD involves the transfer of an equal number of electrons and protons, consistent with findings from previous reports [30,31].

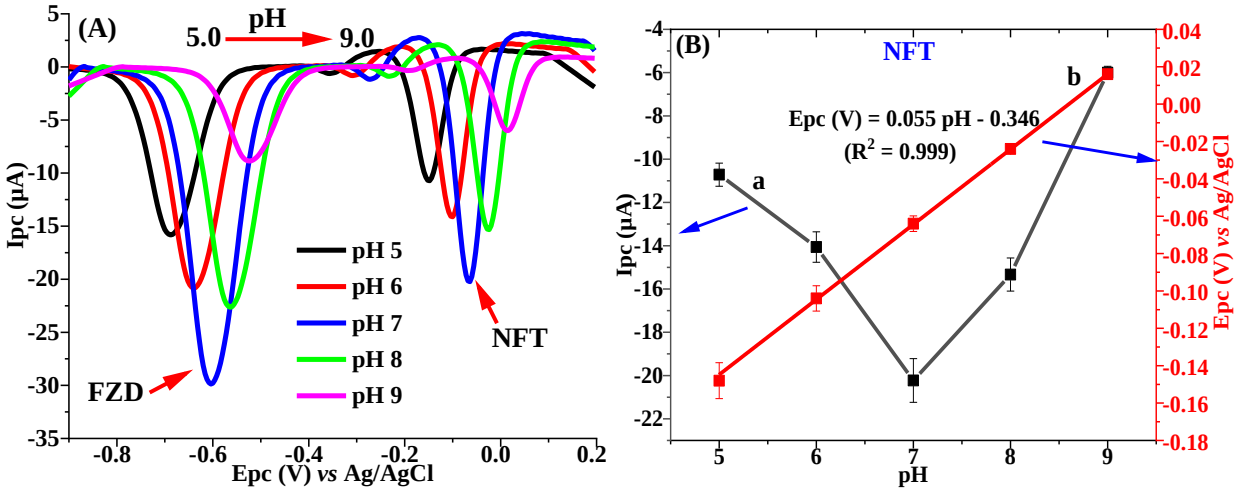

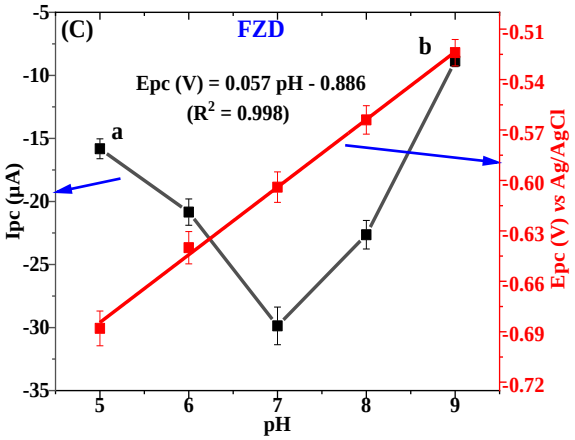

Fig. 4. (A) SWVs of 25 µM NFT and FZD at different pH values, (B) and (C) Ipc *vs.* pH (a) and Epc *vs.* pH (b) for NFT and FZD, respectively.

3.4.3. Effect of scan rate

CV was used to examine the effects of different scan rates (ranging from 25 to 325 mVs^{-1}) on the peak current and peak potential of 25 µM NFT and FZD (Fig. 5A). The current intensities for both analytes steadily increased with increasing scan rate. For FZD, the increase was accompanied by a potential shift towards more negative values, indicating an irreversible electro-reduction process, while NFT displayed a reversible electrode reaction. A linear connection was observed between the current response and the square root of the scan rate for both analytes (Fig. 5B(a and b)). The equations representing the correlation were: Ipc (µA) = -1.46 $v^{1/2}$ $(mVs^{-1})^{1/2}$ – 0.8 (R^2 = 0.996) for NFT and Ipc (µA) = -0.61$v^{1/2}$ $(mVs^{-1})^{1/2}$ –12.7 (R^2 = 0.995) for FZD. Moreover, the log Ipc *vs.* log *v* plots displayed linear regression equations with slopes of 0.55 and 0.47 for NFT and FZD, respectively (Fig. 5C(a and b)). The slope values, which are close to the theoretical value of 0.5, indicate that the reaction of NFT and FZD at the surface of Au-Ag-ANCCs/ZnO-NPs-CPE/PEO was predominantly governed by diffusion controlled processes [30,32]. Equation (2) [24] was used to calculate the number of electrons involved in the electrode reaction.

$$E_p = E^0 + \frac{2.303RT}{\alpha nF}\log\frac{RTk^0}{\alpha nF} + \frac{2.303RT}{\alpha nF}\log v \qquad (2)$$

where, E^0 = formal potential, *v* = scan rate, F = Faraday constant, T = temperature, n = number of electrons, k^0 = heterogeneous rate constant, and R = universal gas constant. A very good linear

correlation was observed between Epc and log *v* for both NFT and FZD. The slope of each plot, corresponding to 2.303RT/αnF, was used to calculate αn, resulting in 1.875 for the NFT and 1.962 for the FZD. For irreversible electrode reactions, the transfer coefficient (α) was assumed to be 0.5 [25]. The number of electrons (n) involved in the electro-reduction of NFT and FZD were determined to be 3.75 and 3.924, respectively, nearly equal to four. This finding is consistent with those of previous studies [30,32], demonstrating that the electro-reduction of NFT and FZD comprises a transfer of four protons and four electrons. Fig. 5D shows a schematic illustration of the reaction mechanism for the electrochemical reduction of the analytes.

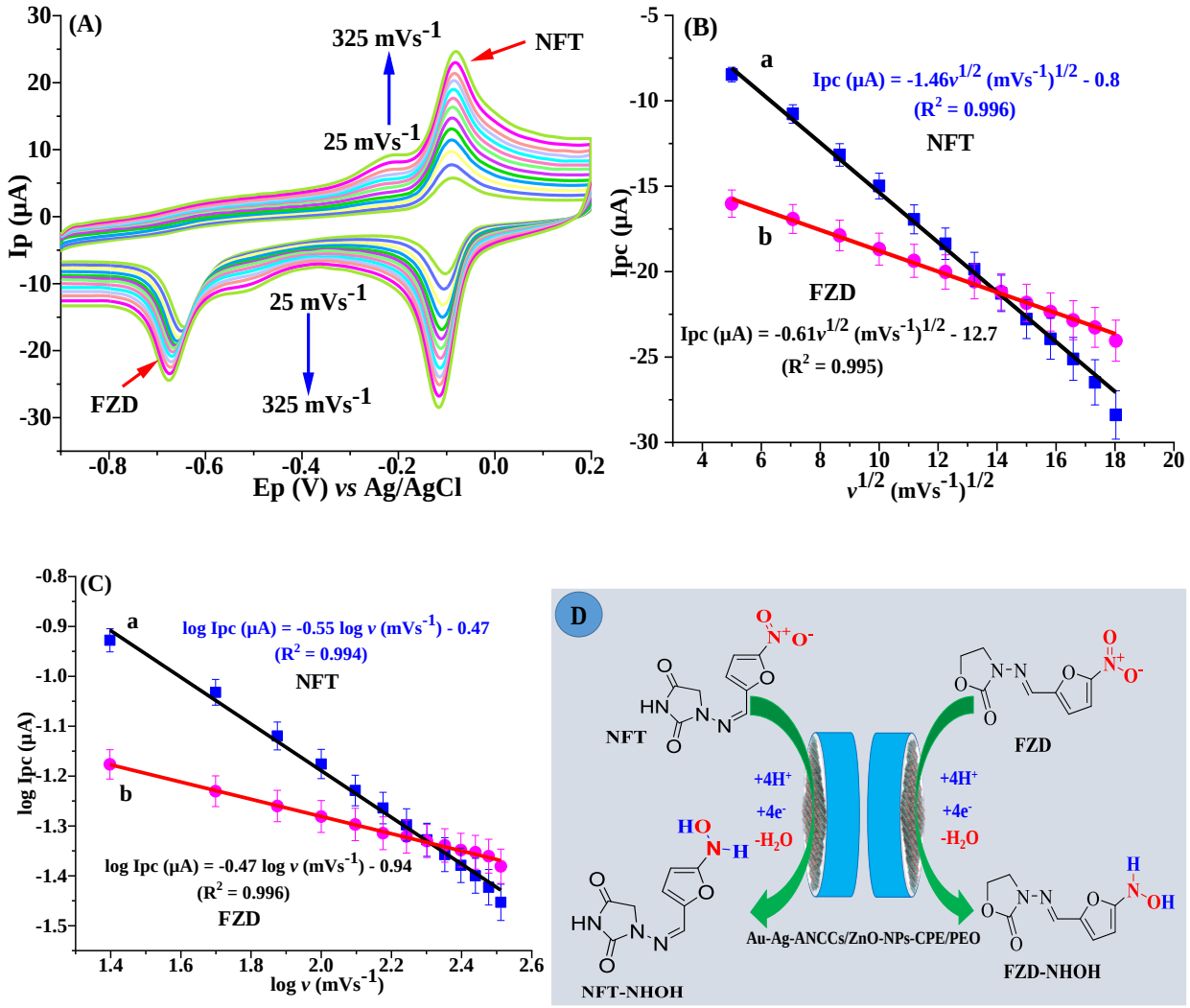

Fig. 5. CVs of 25 µM NFT and FZD (A) at different scan rates, Ipa *vs.* $v^{1/2}$ (B), log Ipa *vs.* log *v* (C), and schematic illustration for the electrode reaction of the analytes (D).

3.4.5. Simultaneous determination of NFT and FZD

This study aimed to develop an ultra-high-performance multi-elemental nanocomposite electrochemical sensor for simultaneously detecting NFT and FZD residues in various food and environmental samples using Au-Ag-ANCCs/ZnO-NPs-CPE/PEO. To attain the objective, SWV was performed under optimized experimental conditions within a potential range of -0.9 to 0.2 V. A strong linear relationship was observed between concentration and the Ipc of the analytes, ranging from 1.0 pM to 250 µM for NFT and 0.9 nM to 360 µM for FZD (Fig. 6A). The relationships are given as: Ipc (µA) = -0.997C (µM) – 1.68 (R^2 = 0.9994) for NFT (inset plot Fig. 6B) and Ipc (µA) = -0.989C (µM) – 8.13 (R^2 = 0.9995) for FZD (Fig. 6B). The limits of detection (LOD) and quantification (LOQ) were found to be 0.26 pM and 0.88 pM for NFT, and 0.023 pM and 0.076 pM for FZD, respectively. The remarkably low LOD and LOQ values obtained while simultaneously determining NFT and FZD confirms the exceptional capability of the sensor for detecting ultra-low concentrations of the analytes. Moreover, the exceptional sensitivity of Au-Ag-ANCCs/ZnO-NPs-CPE/PEO places its position in the frontline of electroanalytical chemistry.

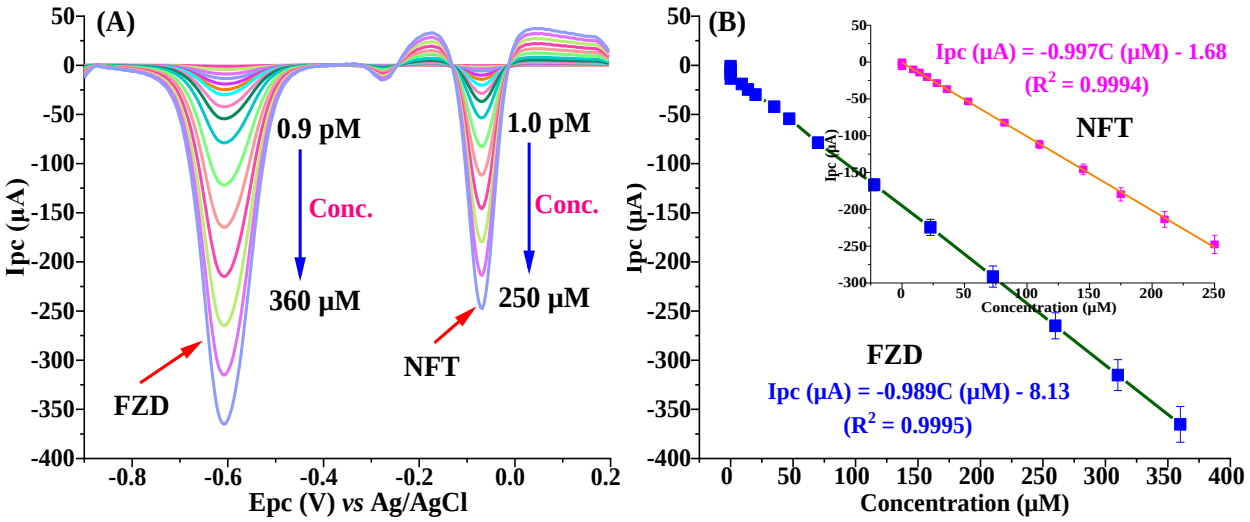

Fig. 6. SWVs of different concentration of NFT and FZD (A), and Ipc *vs.* conc. (B).

The developed sensor was assessed by comparing its performance with that of recently reported sensors based on LOD and linear range. The proposed sensor surpassed its existing counterparts by demonstrating a substantially lower LOD and wide linear range (Table 1). The

outstanding performance of the sensor is due to its larger electroactive surface area and enhanced electrocatalytic activity and electrical conductivity resulting from the synergistic effects of the incorporated modifiers.

Table 1: Comparison of the developed sensor with reported values.

Electrodes	Analytes	Samples	Linear range (μM)	LOD (μM)	Ref.
Ag-$Ni(OH)_2$/GCE	NFT	Tablets and blood serum	0.11–13 13–212	0.079	[33]
α-Fe_2O_3/h-BN NCs	NFT	Biological fluids	0.025–22.95	0.015	[34]
Pd–Ti_3C_2Tx–P	NFT	Hospital waste	0.001–0.14	0.01 nM	[35]
$BaSnO_3$/GCE	NFT	Plasma, urine, and milk	0.01–42.65 42.65–557.7	0.062	[5]
ZnO HPs/P-CN	NFT	Water and human urine	0.01–111	0.002	[36]
Au-Ag-ANCCs/ZnO-NPs-CPE/PEO	NFT	Foods and water	1.0 pM–250	0.26 pM	This work
Pd_1/N-C/GCE	FZD	Tap and lake water	0.01–50 50–300	3.3 nM	[9]
$Mn_3Co_3O_4$/MWCNT/SPCE	FZD	Serum and urine	0.05–650	0.55nM	[37]
$CoWO_4$/N-rGO/GCE	FZD	Urine and wastewater	0.09–799	0.022	[38]
c-MWCNT/PMo_{12}/MIP/GCE	FZD	Foods	0.006–0.6	3.38 nM	[39]
Au-Ag-ANCCs/ZnO-NPs-CPE/PEO	FZD	Foods and water	0.9 nM–360	0.023 pM	This work

3.6. Reproducibility, repeatability, stability and selectivity

Nine replicate SWV measurements were performed using a single sensor to assess the repeatability of Au-Ag-ANCCs/ZnO-NPs-CPE/PEO while simultaneously quantifying 15 μM NFT and FZD. NFT and FZD exhibited RSD values of 3.13% and 3.32%, respectively (Fig. S3A), indicating excellent repeatability. To evaluate reproducibility, ten electrodes were prepared under identical conditions. NFT and FZD exhibited RSD values of 2.99% and 2.96%, respectively (Fig. S3B), indicating exceptional reproducibility. Stability of Au-Ag-ANCCs/ZnO-NPs-CPE/PEO was examined by monitoring its current response weekly for two and a half months, with storage at 4°C after each weekly use. The sensor exhibited long-term stability, with a 6.46% decrease in the

current response for NFT and 6.35% decrease for FZD over the entire storage period (Fig. S3C). Finally, the selectivity was examined by subjecting the sensor to potentially co-existing interfering substances in the presence of 15 µM NFT and FZD. The sensor's current response for the target analytes remained unaffected in the presence of 250-fold excess concentrations of antibiotics (azithromycin, amoxicillin, tinidazole, ciprofloxacin, vancomycin, rifampicin, metronidazole, chloramphenicol, norfloxacin, erythromycin, and ceftriaxone), 750-times common interferents (folic acid, urea, sucrose, dopamine, glucose, fructose, uric acid, lactose, and ascorbic acid), and 1000-times higher concentrations of inorganic species (K^+, SO_4^{2-}, Cu^{2+}, Mg^{2+}, HCO^{3-}, Cl^-, Fe^{3+}, NO_3^-, Ca^{2+}, and CO_3^{2-}) (Table S1), demonstrating remarkable selectivity of the developed sensor.

3.7. Analytical application

The applicability of Au-Ag-ANCCs/ZnO-NPs-CPE/PEO for real-sample analysis was evaluated via spiking experiments. The standard addition method was employed to determine the percentage recovery. Known concentrations of NFT and FZD standards (0, 5, 10, 30, and 45 µM) were added to the chicken meat, fish, honey, milk, and wastewater samples (Table S2). Before spiking the standard solutions into the samples, their initial current responses were recorded. No current responses were observed in the unspiked samples, indicating the absence of NFT and FZD residues, or their concentrations below the detection limit. Subsequently, the percentage recoveries in the spiked samples ranged from 96.3% to 102.4% for NFT and 96.4% to 102.8% for FZD. Furthermore, the relative standard deviation (RSD) values were found to be very low, ranging from 1.87% to 2.53% for NFT and 1.91% to 2.49% for FZD. These exceptional recovery ranges and low RSD values highlight the efficiency and reliability of the developed sensor for simultaneously determining NFT and FZD residues in real-time applications.

5. Conclusions

This study presented a novel hypersensitive multi-elemental nanocomposite electrochemical sensing platform for simultaneously detecting NFT and FZD residues in food and wastewater samples. Several analytical and electrochemical techniques were utilized to characterize the surface morphology and elemental composition of the sensor. Au-Ag-ANCCs/ZnO-NPs-CPE/PEO showed superior performance compared to previously reported sensors, with a picomolar LOD and a wide linear range. This performance was attributed to the increased electroactive surface area, electrocatalytic activity, and electrical conductivity. The sensor revealed exceptional selectivity in the presences of several co-existing interferents. Furthermore, it exhibited excellent long-term stability, reproducibility, and repeatability, making it ideal-tool for the real-time monitoring of the target analytes in food and wastewater samples. The developed novel sensor holds great promise for sensitive and selective determination of NFT and FZD residues in various food and environmental samples.

Availability of data and materials

All the data are included in the manuscript. There are no additional data with the authors.

Author contribution

Wondimeneh Dubale Adane: Conceptualization, Methodology, Software, Resources, Data analysis, Investigation, Writing-original draft. **Bhagwan Singh Chandravanshi**: Conceptualization, Writing-review & editing, Supervision. **Merid Tessema:** Conceptualization, Writing-review & editing, Supervision.

Declaration of competing interest

The authors declare that they have no known competing financial interests or personal relationships that could have appeared to influence the work reported in this paper.

Acknowledgements

The authors express their gratitude to the Department of Chemistry at Addis Ababa University, Addis Ababa, Ethiopia, for generously offering the laboratory resources.

References

[1] D.F. Pancu, A. Scurtu, I.G. Macasoi, D. Marti, M. Mioc, C. Soica, D. Coricovac, D. Horhat, M. Poenaru, C. Dehelean, Antibiotics: conventional therapy and natural compounds with antibacterial activity-a pharmaco-toxicological screening, Antibiotics 10 (2021) 401. https://doi.org/10.3390/antibiotics10040401.

[2] R. Ding, Y. Chen, Q. Wang, Z. Wu, X. Zhang, B, Li, L. Lin, Recent advances in quantum dots-based biosensors for antibiotics detection, J. Pharm. Anal. 12 (2022) 355–364. https://doi.org/10.1016/j.jpha.2021.08.002.

[3] K. Rehman, S.H. Kamran, A.M.S. Hamid, Toxicity of antibiotics. In antibiotics and antimicrobial resistance genes in the environment, Elsevier (2020) 234–252. https://doi.org/10.1016/B978-0-12-818882-8.00016-4.

[4] J. Chen, G.G. Ying, W.J. Deng, Antibiotic residues in food: extraction, analysis, and human health concerns, J. Agric. Food Chem. 67 (2019) 7569–7586. https://doi.org/10.1021/acs.jafc.9b01334.

[5] M. Balamurugan, K. Alagumalai, T.W. Chen, S.M. Chen, X. Liu, M. Selvaganapathy, Simultaneous electrochemical determination of nitrofurantoin and nifedipine with assistance of needle-shaped perovskite structure: barium stannate fabricated glassy carbon electrode, Microchim. Acta 188 (2021) 19. https://doi.org/10.1007/s00604-020-04645-5.

[6] A. Kijima, Y. Ishii, S. Takasu, K. Matsushita, K. Kuroda, D. Hibi, Y. Suzuki, T. Nohmi, T. Umemura, Chemical structure-related mechanisms underlying in vivo genotoxicity induced by nitrofurantoin and its constituent moieties in gpt delta rats, Toxicology 331 (2015) 125–135. https://doi.org/10.1016/j.tox.2015.03.003.

[7] S. Kummari, K.V. Sunil, G.K. Vengatajalabathy, Facile electrochemically reduced graphene oxide-multi-walled carbon nanotube nanocomposite as sensitive probe for *in-vitro* determination of nitrofurantoin in biological fluids, Electroanalysis 32 (2020) 2452–2462. https://doi.org/10.1002/elan.202060157.

[8] K. Ugoeze, C. Alalor, C. Ibezim, B. Chinko, P. Owonaro, C. Anie, N. Okoronkwo, A. Mgbahurike, C. Ofomata, D. Alfred-Ugbenbo, G. Ndukwu, Environmental and human health impact of antibiotics waste mismanagement: a review, Adv. Environ. Eng. Res. 05 (2024) 1–21. https://doi.org/10.21926/aeer.2401005.

[9] C. Han, W. Yi, Z. Li, C. Dong, H. Zhao, M. Liu, Single-atom palladium anchored n-doped carbon enhanced electrochemical detection of furazolidone, Electrochim. Acta 447 (2023) 142083. https://doi.org/10.1016/j.electacta.2023.142083.

[10] T. Kokulnathan, G. Almutairi, S.M. Chen, T.W. Chen, F. Ahmed, N. Arshi, B. AlOtaibi, Construction of lanthanum vanadate/functionalized boron nitride nanocomposite: the electrochemical sensor for monitoring of furazolidone, ACS Sustainable Chem. Eng. 9 (2021) 2784–2794. https://doi.org/10.1021/acssuschemeng.0c08340.

[11] R. Rajeev, R. Datta, A. Varghese, Y.N. Sudhakar, L. George, Recent advances in bimetallic based nanostructures: synthesis and electrochemical sensing applications, Microchem. J. 163 (2021) 105910. https://doi.org/10.1016/j.microc.2020.105910.

[12] P. Veerakumar, C. Koventhan, S.M. Chen, Copper-palladium alloy nanoparticles immobilized over porous carbon for voltammetric determination of dimetridazole, J. Alloys Compd. 931 (2023) 167474. https://doi.org/10.1016/j.jallcom.2022.167474.

[13] G. Das, S. Seo, I.J. Yang, L.T.H. Nguyen, H.S. Shin, J.K. Patra, Sericin mediated gold/silver bimetallic nanoparticles and exploration of its multi-therapeutic efficiency and photocatalytic degradation potential, Environ. Res. 229 (2023) 115935. https://doi.org/10.1016/j.envres.2023.115935.

[14] L. Feng, G. Gao, P. Huang, K. Wang, X. Wang, T. Luo, C. Zhang, Optical properties and catalytic activity of bimetallic gold-silver nanoparticles, Nano Biomed. Eng. 2 (2010) 258–267. https://doi.org/10.5101/nbe.v2i4.p258-267.

[15] J. Jiang, R. Zhang, M.H. Lee, W. Wu, Flexible piezo-electrocatalytic uric acid sensor, Nano Energy 118 (2023) 108978. https://doi.org/10.1016/j.nanoen.2023.108978.

[16] F. Lin, X. Zhang, X. Liu, Y. Xu, Z. Sun, L. Zhang, Z. Huang, R. Mi, X. Min, Polyethylene glycol/modified carbon foam composites for efficient light-thermal conversion and storage, Polymer 228 (2021) 123894. https://doi.org/10.1016/j.polymer.2021.123894.

[17] A. Ehsani, M. Moftakhar, Enhanced electrochemical pseudocapacitance performance of poly tyramine composite on the surface of polyethylene glycol modified electrode, Plast. Rubber Compos. 415 (2023) 415–419. https://doi.org/10.1080/14658011.2023.2219085.

[18] J. Mo, D. Zhang, M. Sun, L. Liu, W. Hu, B. Jiang, L. Chu, M. Li, Polyethylene oxide as a multifunctional binder for high-performance ternary layered cathodes, Polymers 13 (2021) 3992. https://doi.org/10.3390/polym13223992.

[19] T.R. Mohammadi, S. Dadfarnia, A.M. Haji Shabani, Chemiluminescence determination of furazolidone in poultry tissues and water samples after selective solid phase microextraction using magnetic molecularly imprinted polymers, New J. Chem. 42 (2018) 10751–10760. https://doi.org/10.1039/C8NJ01670D.

[20] P.S. Chu, M.I. Lopez, Determination of nitrofuran residues in milk of dairy cows using liquid chromatography−tandem mass spectrometry, J. Agric. Food Chem. 55 (2007) 2129–2135. https://doi.org/10.1021/jf063391v.

[21] I. Diblikova, K.M. Cooper, D.G. Kennedy, M. Franek, Monoclonal antibody-based ELISA for the quantification of nitrofuran metabolite 3-amino-2-oxazolidinone in tissues using a simplified sample preparation, Anal. Chem. Acta 540 (2005) 285–292. https://doi.org/10.1016/j.aca.2005.03.039.

[22] M.C. Mahedero, T.G. Díaz, S.G. Pascual, Resolution of ternary mixtures of nitrofurantoin, furaltadone and furazolidone by partial least-square analysis to the spectrophotometric signals after photo-decomposition, J. Pharm. Biomed. Anal. 29 (2002) 477–485. https://doi.org/10.1016/S0731-7085(02)00092-4.

559 [23] R.A. Wijma, K.E.J. Hoogtanders, S. Croes, J.W. Mouton, R.J.M. Brüggemann,
560 Development and validation of a fast and sensitive UHPLC-DAD assay for the quantification
561 of nitrofurantoin in plasma and urine, J. Pharm. Biomed. Anal. 174 (2019) 161–167.
562 https://doi.org/10.1016/j.jpba.2019.05.054.

563 [24] W.D. Adane, B.S. Chandravanshi, M.A. Tessema, Simple, ultrasensitive and cost-effective
564 electrochemical sensor for the determination of ciprofloxacin in various types of samples,
565 Sens. Bio-Sens. Res. 39 (2023) 100547. https://doi.org/10.1016/j.sbsr.2022.100547.

566 [25] W.D. Adane, B.S. Chandravanshi, M.A. Tessema, Highly sensitive and selective
567 electrochemical sensor for the simultaneous determination of tinidazole and
568 chloramphenicol in food samples (egg, honey and milk), Sens. Actuators B: Chem. 390
569 (2023) 134023. https://doi.org/10.1016/j.snb.2023.134023.

570 [26] M.G. Kotresh, M.K. Patil, S.R. Inamdar, Reaction temperature based synthesis of ZnO
571 nanoparticles using co-precipitation method: detailed structural and optical characterization,
572 Optik 243 (2021) 167506. https://doi.org/10.1016/j.ijleo.2021.167506.

573 [27] M. Khatami, S. Pourseyedi, M. Khatami, H. Hamidi, M. Zaeifi, L. Soltani, Synthesis of silver
574 nanoparticles using seed exudates of sinapis arvensis as a novel bioresource, and evaluation
575 of their antifungal activity, Bioresour. Bioprocess 2 (2015) 19.
576 https://doi.org/10.1186/s40643-015-0043-y.

577 [28] M.M. Chikkanna, S.E. Neelagund, K.K. Rajashekarappa, Green Synthesis of zinc oxide
578 nanoparticles (ZnO NPs) and their biological activity, SN Appl. Sci. 1 (2019) 117.
579 https://doi.org/10.1007/s42452-018-0095-7.

580 [29] Y. Tong, X. Yan, J. Liang, S.X. Dou, Metal-based electrocatalysts for methanol electro-
581 oxidation: progress, opportunities, and challenges, Small 17 (2021) 1904126.
582 https://doi.org/10.1002/smll.201904126.

583

[30] J.N. Baby, B. Sriram, S.F. Wang, M. George, Effect of various deep eutectic solvents on the sustainable synthesis of $MgFe_2O_4$ nanoparticles for simultaneous electrochemical determination of nitrofurantoin and 4-nitrophenol, ACS Sustainable Chem. Eng. 8 (2020) 1479–1486. https://doi.org/10.1021/acssuschemeng.9b05755.

[31] S. Shahrokhian, L. Naderi, M. Ghalkhani, Modified glassy carbon electrodes based on carbon nanostructures for ultrasensitive electrochemical determination of furazolidone, Mater. Sci. Eng. C 61 (2016) 842–850. https://doi.org/10.1016/j.msec.2016.01.025.

[32] S.M. Babulal, T.W. Chen, S.M. Chen, W.A. Al-Onazi, A.M. Al-Mohaimeed, Manganese molybdenum oxide micro rods adorned porous carbon hybrid electrocatalyst for electrochemical determination of furazolidone in environmental fluids, Catalysts 11 (2021) 1397. https://doi.org/10.3390/catal11111397.

[33] M. Ezazi, K. Asadpour-Zeynali, E. Saeb, Synergistic incorporation of Ag into nickel hydroxide nanostructure to enhance the electroctrocatalytic determination of nitrofurantoin, Inorg. Chem. Commun. 160 (2024) 111913. https://doi.org/10.1016/j.inoche.2023.111913.

[34] G. Sridharan, C.J.T. Godwin, R. Atchudan, S. Arya, M. Govindasamy, S.M. Osman, A.K. Sundramoorth, Iron oxide decorated hexagonal boron nitride modified electrochemical sensor for the detection of nitrofurantoin in human urine samples, J. Taiwan Inst. Chem. Eng. (2024) 105320. https://doi.org/10.1016/j.jtice.2023.105320.

[35] S.H. Tumrani, R.R. Neiber, Z. Pitafi, I.A. Ahmed, R.A. Soomro, M.M. Ibrahim, S. Karakuş, Z.M. El-Bahy, Synergistic integration of few-layer thick MXenes and small Pd nanocubes for enhanced electrochemical nitrofurantoin detection: implications in pharmaceutical pollutant monitoring, J. Environ. Chem. Eng. 11 (2023) 111152. https://doi.org/10.1016/j.jece.2023.111152.

[36] F. Ahmed, T. Kokulnathan, A. Umar, S. Akbar, S. Kumar, N.M. Shaalan, N. Arshi, M.G. Alam, A. Aljaafari, A. Alshoaibi, Zinc oxide/phosphorus-doped carbon nitride composite as potential scaffold for electrochemical detection of nitrofurantoin, Biosensors 12 (2022) 856. https://doi.org/10.3390/bios12100856.

[37] P.S. Ballur, R. Sakthivel, L.Y. Lin, Y.F. Duann, J.H. He, T.Y. Liu, R.J. Chung, MOF derived 2D-flake-like structured $Mn_3Co_3O_4$ integrated acid functionalized MWCNT for electrochemical detection of antibiotic furazolidone in biological fluids, Appl. Surf. Sci. 611 (2023) 155784. https://doi.org/10.1016/j.apsusc.2022.155784.

[38] C. Bhuvaneswari, A. Elangovan, C. Sharmila, K. Sudha, G. Arivazhagan, Fabrication of cobalt tungstate/N-rGO nanocomposite: application towards the detection of antibiotic drug-furazolidone, Colloids Surf. A: Physicochem. Eng. 656 (2023) 130299. https://doi.org/10.1016/j.colsurfa.2022.130299.

[39] Y.L. Huang, B. Zhang, Y.L. Li, L. Wang, L. Dong, J. Li, Molecularly imprinted sensor based on carboxylated carbon nanotubes/keggin-type polyoxometalates nanocomposite for the detection of furazolidone, Tungsten (2023). https://doi.org/10.1007/s42864-023-00242-0.

Supplementary Material

Ultra-performance multi-elemental nanocomposites electrochemical sensor for the simultaneous determination of the residues of nitrofurantoin and furazolidone in poultry, fish, honey, dairy products and municipal wastewater

Wondimeneh Dubale Adane[a], Bhagwan Singh Chandravanshi*[a], Merid Tessema** [a]

[a] Department of Chemistry, Addis Ababa University, P. O. Box 1176, Addis Ababa, Ethiopia

* Corresponding author. E-mail address: bscv2006@yahoo.com

** Corresponding author. E-mail address: tessemamerid@yahoo.com

Sample preparation

Chickens meat

Chicken meat samples were purchased from a local supermarket in Addis Ababa, Ethiopia, and homogenized before extraction. To extract the target analyte, 5 g of the homogenized meat sample was mixed with 20 mL of a 0.1 M PBS solution. The meat sample and PBS solution were thoroughly mixed using a vortex mixer to ensure complete dispersion of the sample in the solvent. Subsequently, the mixture was subjected to ultrasonic treatment for 45 min. This step aimed at facilitating the efficient extraction of the desired components from the meat matrix, thereby enhancing the quality and accuracy of our analysis. Then, the mixture was centrifuged at 4,000 rpm for 15 min. This centrifugation step was performed precisely to separate the constituents, and as a result, a clear solution containing the extracted analyte was collected. Finally, the sample was spiked with appropriate concentrations of NFT and FZD standard solutions.

Fish

Fish samples collected from a local supermarket in Addis Ababa, Ethiopia and stored in a deep freezer until analysis. Approximately 2 g of homogenized fish sample was weighed into a 50 mL falcon tube, followed by the addition of 5 mL of water and 5 mL of acetonitrile. The mixture was vortexed for 5 min to ensure thorough mixing. Subsequently, 5 g of $MgSO_4$ and 2 g of NaCl were added to the falcon tube and manually shaken for 2 min to promote solid-phase extraction.

The resulting mixture was centrifuged at 4000 rpm for 15 min to separate the supernatant from the solid phase. The collected supernatant was carefully transferred to another falcon tube. After 5 min vortexing, the mixture was centrifuged again at 10,000 rpm for 10 min, resulting in a clear solution enriched with the analytes of interest. Finally, to quantify the concentrations of the analytes in the samples, the samples were spiked with different concentrations (0, 5, 10, 30, and 45 µM) of NFT and FZD standard solutions.

Honey

Honey was purchased from a local supermarket in Addis Ababa, Ethiopia. The samples were prepared as follows: 1 g of honey was dissolved in 1 mL of 0.1 M HCl with magnetic stirring. A dilution ratio of 1:10 (v/v) in PBS (pH 7.4) was used to reduce the matrix effect, and then filtered through a 150 mm filter membrane before analysis. Afterwards, the samples were spiked with known concentrations of NFT and FZD standards.

Milk

Milk samples were obtained from Sululta town in the Oromia Regional State of Ethiopia and processed as follows: first, 5.0 mL of the milk sample was mixed with 20 mL of acetonitrile. After subjecting the mixture to 15 min of sonication and 10 min of shaking, it was centrifuged at 10,000 rpm for 10 min. Following centrifugation, the supernatant was filtered through a 150 mm filter membrane. The resulting filtrate was subsequently transferred to a 25 mL volumetric flask and diluted to the mark using PBS (pH 7). Finally, the samples were spiked with different concentrations of NFT and FZD standards.

Municipal wastewater

Municipal wastewater sample (approximately 800 mL) was sourced from the Kality Wastewater Treatment Plant in Addis Ababa, Ethiopia. Careful collection procedures were followed to ensure sample integrity, with proper labeling and storage under controlled conditions. Subsequent steps involved mechanical cleaning and primary filtration to remove suspended solids, followed by overnight settling to separate liquid from solid components. Further filtration using a 150 mm filter paper was performed several times, and the sample was diluted with a phosphate

buffer solution before being spiked with standard solutions of the analytes. No additional pretreatment was conducted before analysis. The prepared sample was then stored at 4°C until analysis.

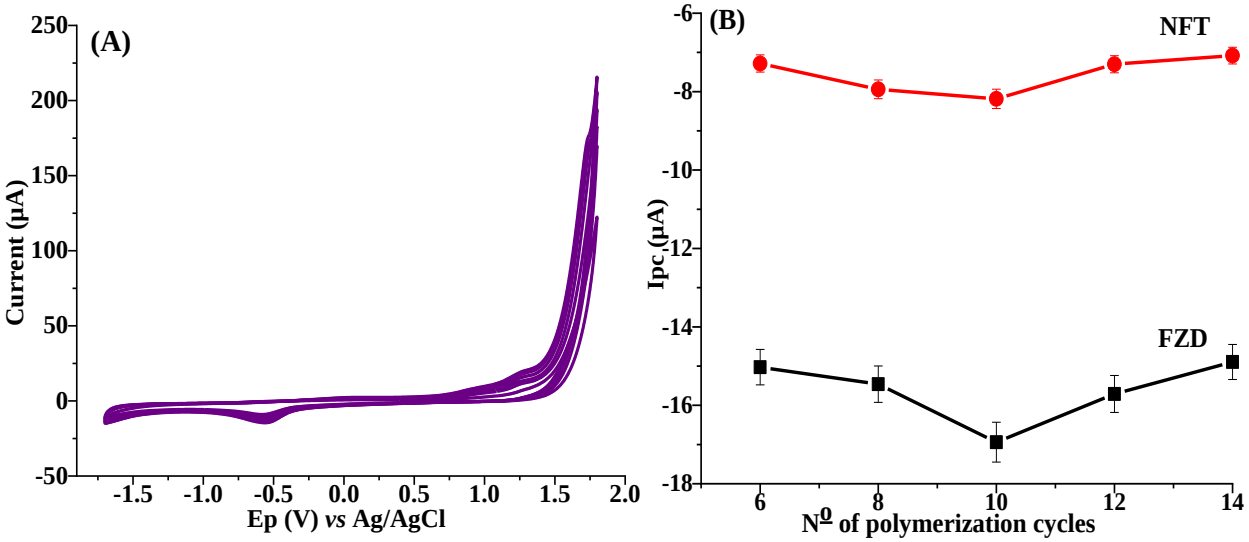

Fig. S1. (A) CV for the electropolymerization of 0.01 M PEO containing 0.01 M KCl in 0.1 M PBS (pH 7.0) at the surface of Au-Ag-ANCCs/ZnO-NPs-CPE for 10 cycles in a potential ranges of -1.7 to 1.6 V at a scan rate of 25 mVs^{-1}, and (B) Ipc *vs.* the number of polymerization cycles for 15 µM NFT and FZD.

Analytical characterizations

The FT-IR spectra of the Ag-NCCs (Fig. S2A(a)) revealed characteristic peaks showing the presence of Ag-O stretching vibrations at around 568cm^{-1}, along with peaks attributed to C-H bending vibrations of the alkyl chain in PVP at 1037cm^{-1} and 1120cm^{-1}. Additional peaks included Ag-O stretching at 1385cm^{-1} and C=O stretching at 1629cm^{-1}, as well as C-H and O-H stretching vibrations at 2856cm^{-1}, 2929cm^{-1}, and 3459cm^{-1}, respectively. In the spectra of Au-Ag-ANCCs (Fig. S2A(b)), the peaks at 3438cm^{-1} and 1640cm^{-1} correspond to O-H stretching and bending vibrations, while the broad peak at 1078cm^{-1} indicates C-O bond stretching vibrations. The peaks at 540cm^{-1} and 620cm^{-1} represent Ag-O and Au-O stretching vibrations, respectively, confirming the coordination of oxygen between Ag and Au. In ZnO-NPs-CPE (Fig. S2A(c)), peaks in the 400–500cm^{-1} and 500–900cm^{-1} regions signify Zn-O stretching and bending vibrations, respectively.

The sharp peaks at 1684cm^{-1} and 1639cm^{-1} indicate C-O and C-H stretching vibrations, whereas a strong peak at 3490cm^{-1} suggests O-H bond stretching vibrations. The FT-IR spectra of Au-Ag-ANCCs/ZnO-NPs-CPE (Fig. S2A(d)) exhibit distinct peaks corresponding to the metal-oxygen and metal-metal bonds of Au-Ag-ANCCs in the 500–900cm^{-1} range, along with peaks related to ZnO-NPs. The successful incorporation of PEO into the Au-Ag-ANCCs/ZnO-NPs-CPE nanocomposite structure was demonstrated by characteristic peaks at approximately 1003cm^{-1} and 1112cm^{-1} (Fig. S2A(e)), indicating C-O-C stretching vibrations specific to ether linkages, as well as peaks at 2922cm^{-1} and 1626cm^{-1} corresponding to C-H and C=C vibration, confirming the presence and integration of PEO within the nanocomposite structure.

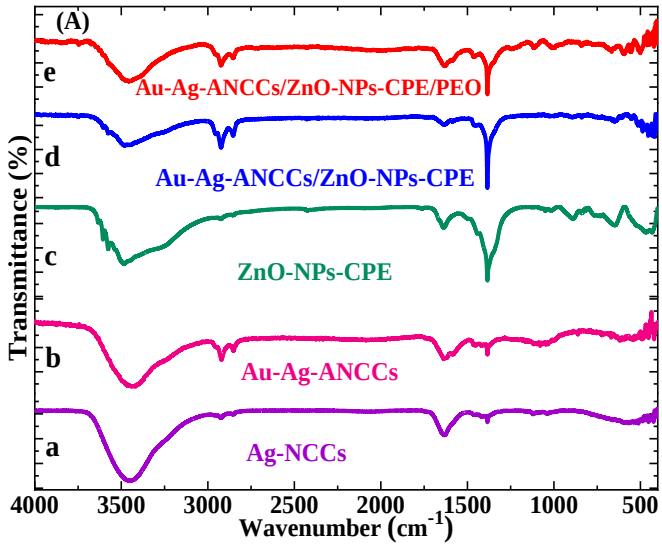

Fig. S2A. FT-IR spectra of Ag-NCCs (a), Au-Ag-ANCCs (b), ZnO-NPs-CPE (c), Au-Ag-ANCCs/ZnO-NPs-CPE (d), and Au-Ag-ANCCs/ZnO-NPs-CPE/PEO (e).

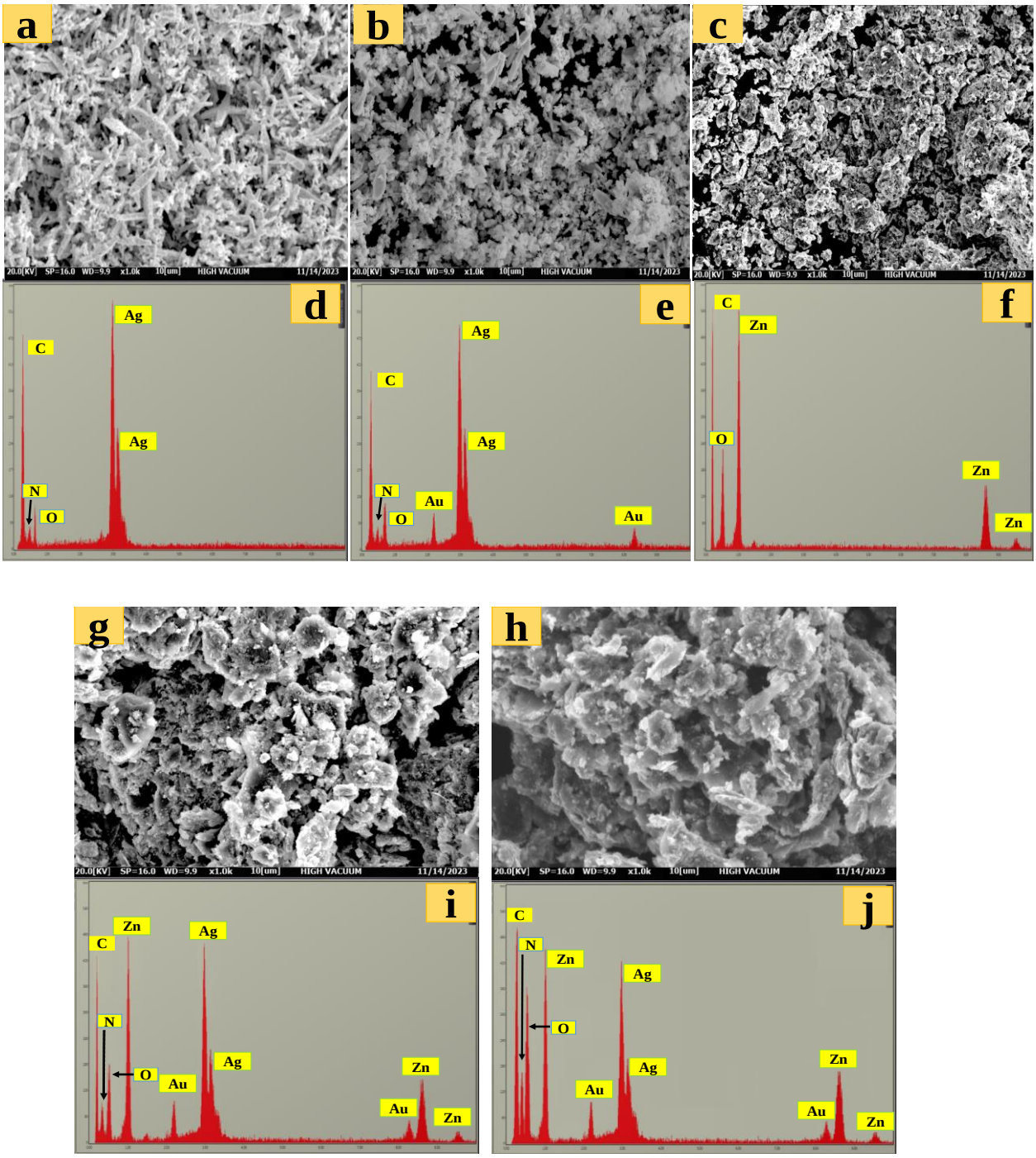

Fig. S2B. SEM images and EDX spectra of Ag-NCCs (a and d), Au-Ag-ANCCs (b and e), ZnO-NPs-CPE (c and f), Au-Ag-ANCCs/ZnO-NPs-CPE (g and i), Au-Ag-ANCCs/ZnO-NPs-CPE/PEO (h and j).

Effects of supporting electrolytes

The type of supporting electrolyte solution significantly influences the shape of the voltammogram and the current response in the electrochemical analysis, making it critical to select the appropriate supporting electrolyte before conducting any analysis. Various supporting electrolytes, including citrate buffer, citrate-phosphate buffer, acetate buffer, phosphate buffer, Britton-Robinson buffer, ammonium chloride, and sulfuric acid, were thoroughly evaluated using square wave voltammetry (SWV). Phosphate buffer solution (PBS) provided a clear and adequately sized current response for both analytes, establishing its superiority as the optimal medium (Fig. SA). Therefore, PBS was selected as the most suitable supporting electrolyte solution for simultaneously determining the NFT and FZD residues across diverse matrices throughout the experiment.

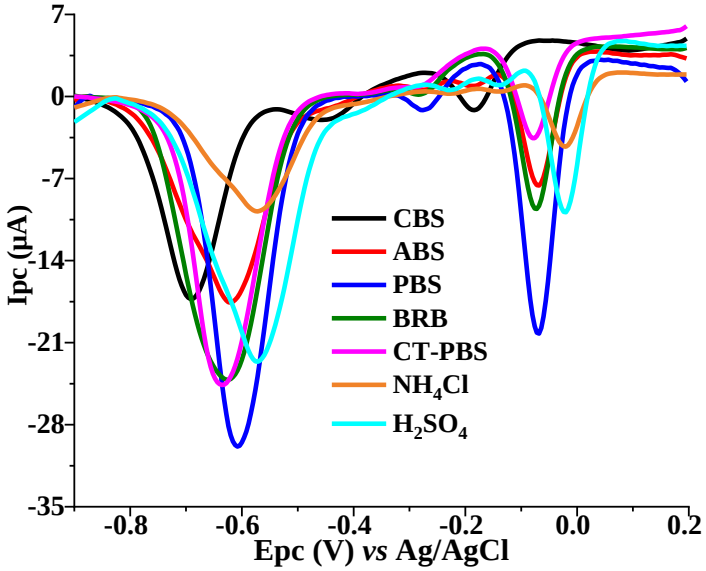

Fig. SA. SWVs of 25 µM NTF and FZD in different supporting electrolyte solutions.

Optimization of the nanocomposites mixture ratio and volume of drop-cast species

While optimizing the nanocomposites mixing ratio for the preparation of Au-Ag-ANCCs/ZnO-NPs-CPE/PEO, the optimum proportion of ZnO-NPs and Au-Ag-ANCCs was found to be 3:4, resulting in the highest current response for detecting 25 µM NFT and FZD, as shown in Fig. SB(a). This superior performance is attributed to synergistic effects, such as high electrical

conductivity, catalytic activity, and electroactive surface area of the two nanocomposites, which enhance the sensitivity of the sensor to the target analytes. Thus, a 3:4 ratio for ZnO-NPs and Au-Ag-ANCCs, respectively, was selected as the optimal value for preparing the sensor in subsequent experiments.

To ensure effective modification of the CPE surface, optimizing the drop-cast volume of the Au-Ag-ANCCs/ZnO-NPs dispersion mixture is essential. This volume directly impacts the thickness and uniformity of the modified layer, thereby influencing electrode performance. To identify the optimal drop-cast amount, various volumes of the dispersion mixture were tested, assessing the current response of the modified electrode for simultaneous detection of 25 µM NFT and FZD. As depicted in Fig. SB(b), the highest current response was obtained with a drop-cast volume of 7 µL. Accordingly, 7 µL of the Au-Ag-ANCCs/ZnO-NPs dispersion mixture was selected as the optimal volume for preparing the Au-Ag-ANCCs/ZnO-NPs-CPE for subsequent experiments.

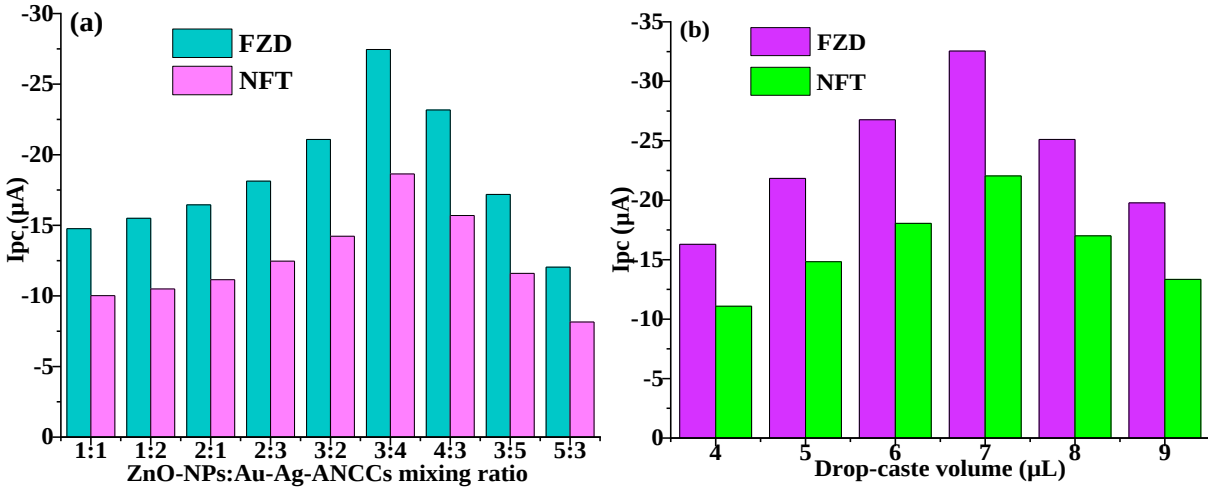

Fig SB. Diagram for the optimization of the nanocomposite dispersion mixing ratio and drop-cast volume.

Optimization of SWV parameters

The current responses of 25 µM NFT and FZD in 0.1 M PBS (pH 7) were examined in relation to the three key SWV instrumental parameters: amplitude, frequency, and step potential. First, the effect of amplitude was explored over a range of 40–110 mV at a constant frequency and

step potential, revealing an increase in cathodic current up to 80 mV for both analytes before a decline (Fig. SC(A)). Thus, 80 mV was identified as the optimal amplitude for subsequent measurements. Next, the influence of the frequency was studied within the range of 20–90 Hz while maintaining the amplitude and step potential constant, showing a direct correlation between the current response and frequency, with a peak observed at 60 Hz (Fig. SC(B)). Consequently, 60 Hz was selected as the optimal frequency for subsequent experimental procedures. Finally, the effect of step potential was examined across the range of 2–14 mV with the other parameters held constant, revealing an increase in the reduction currents for both analytes as the step potential increased, peaking at 8 mV before declining (Fig. SC(C)). Therefore, 8 mV was chosen as the optimal value for the subsequent experiments.

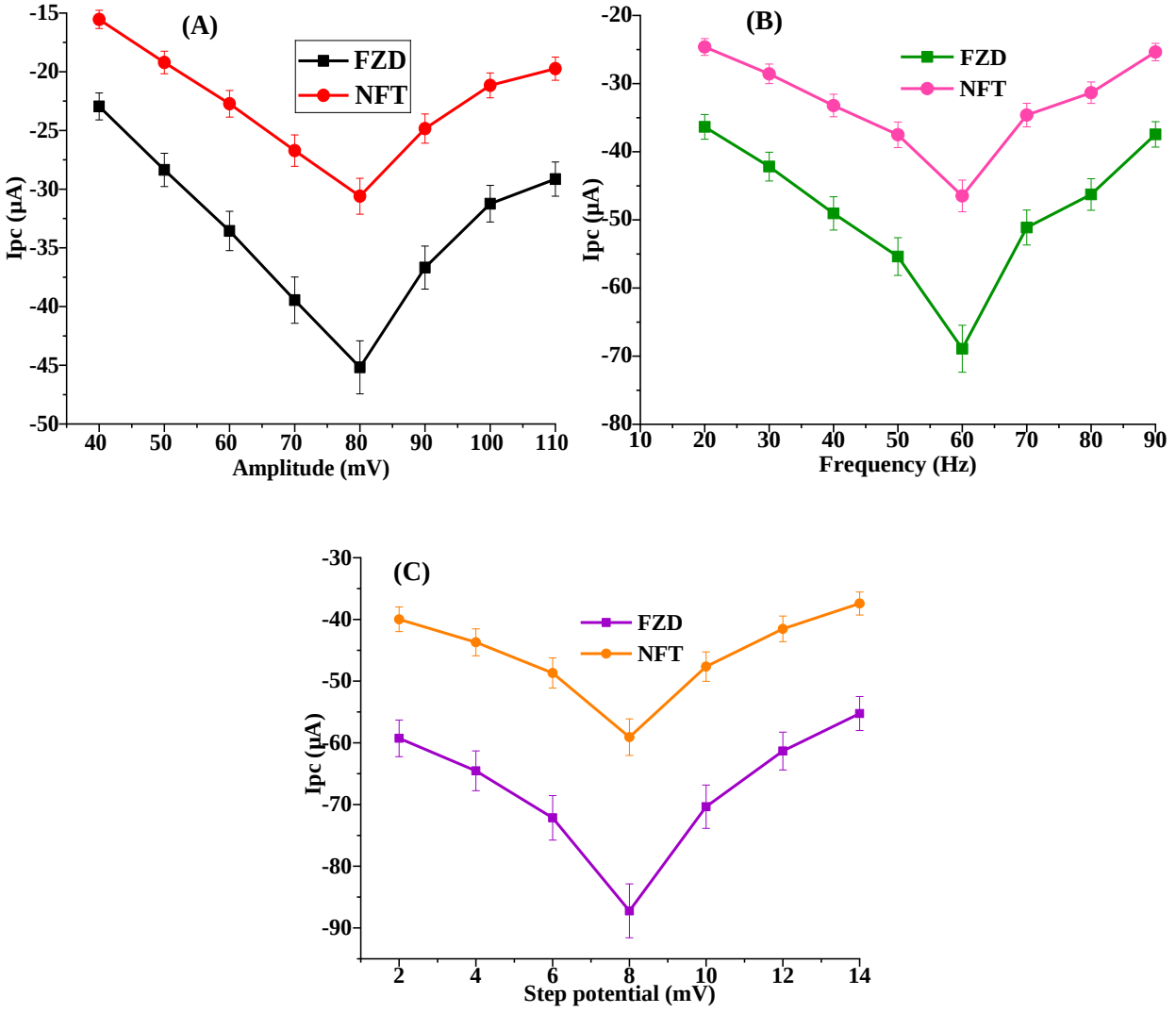

Fig. SC. The effect of SWV parameters: amplitude (A), frequency (B), and step potential (C) on the anodic current responses of 25 µM NFT and FZD.

Repeatability, reproducibility, stability and selectivity

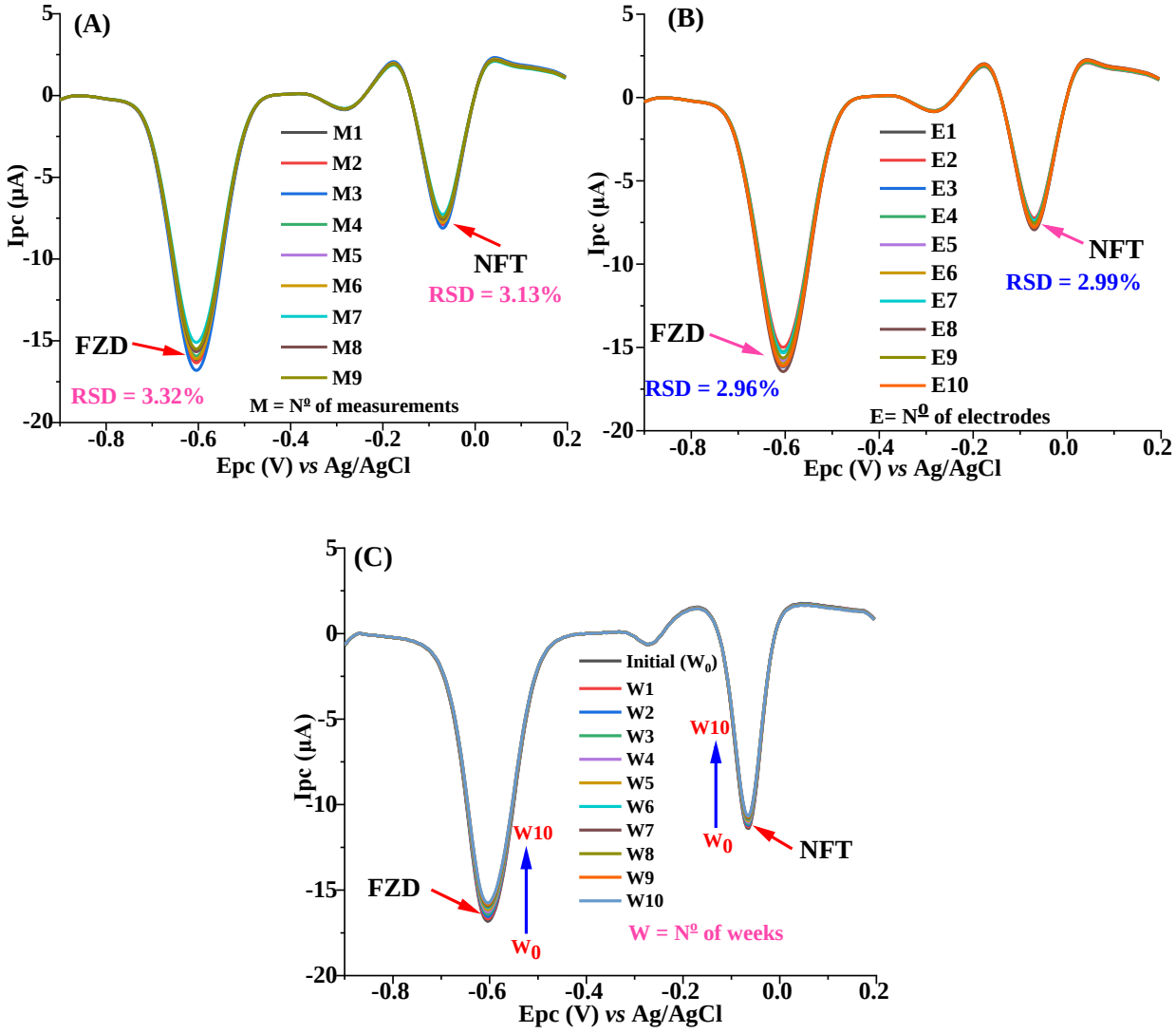

Fig. S3. Repeatability (A), reproducibility (B), and stability (C) of the developed sensor.

Table S1: The effect of co-existing interferents on the current response of the sensor.

Interferents	Conc. (µM)	Relative percentage error (%)		Interferents	Conc. (µM)	Relative percentage error (%)	
		NFT	FZD			NFT	FZD
Azithromycin	250	3.13	3.19	Fructose	750	2.26	2.21
Amoxicillin	250	3.45	3.43	Glucose	750	2.33	2.34
Tinidazole	250	3.26	3.29	Sucrose	750	2.31	2.28
Ciprofloxacin	250	3.65	3.61	Ascorbic Acid	750	2.22	2.22
Vancomycin	250	3.19	3.22	Lactose	750	2.24	2.29
Rifampicin	250	3.48	3.45	K^+	1000	0.96	0.96
Metronidazole	250	3.25	3.25	SO_4^{2-}	1000	0.91	0.97
Chloramphenicol	250	3.37	3.34	Cu^{2+}	1000	0.93	0.98
Norfloxacin	250	3.16	3.12	Mg^{2+}	1000	0.91	0.97
Erythromycin	250	3.29	3.32	HCO^{3-}	1000	0.93	0.97
Ceftriaxone	250	3.28	3.28	Cl^-	1000	0.96	0.96
Urea	750	2.26	2.28	Fe^{3+}	1000	0.96	0.96
Dopamine	750	2.21	2.24	NO_3^-	1000	0.93	0.98
Uric Acid	750	2.17	2.17	Ca^{2+}	1000	0.94	0.96
Folic Acid	750	2.33	2.28	CO_3^2	1000	0.94	0.96

Analytical application

Table S2: Summary of spiking experiment results.

Samples	Spiked (µM)	Found (µM)		Recovery (%)		RSD (%)	
		NFT	FZD	NFT	FZD	NFT	FZD
Chicken Meat	0	-	-	-	-	-	-
	5	5.11	5.04	102.2	100.8	2.09	2.01
	10	9.87	10.02	98.7	100.2	2.53	2.34
	30	30.55	29.67	101.1	98.9	2.17	2.17
	45	45.21	44.11	100.5	98.1	2.42	2.49
Fish	0	-	-	-	-	-	-
	5	4.87	4.82	97.4	96.4	1.99	2.02
	10	10.12	10.07	101.2	100.7	2.21	2.27
	30	29.47	28.99	98.3	96.7	1.87	1.91
	45	43.87	44.21	97.5	98.7	2.14	2.17
Honey	0	-	-	-	-	-	-
	5	4.93	4.86	98.6	97.2	2.36	2.31
	10	9.97	9.85	99.7	98.5	2.22	2.28
	30	30.28	29.92	101	99.8	2.14	2.17
	45	45.12	45.22	100.3	100.5	2.34	2.34
Milk	0	-	-	-	-	-	-
	5	5.12	5.07	102.4	101.4	2.25	2.15
	10	10.21	10.06	102.1	100.6	2.07	2.11
	30	28.87	29.26	96.3	97.6	2.25	2.23
	45	44.25	44.76	98.4	99.5	2.28	2.31
Municipal wastewater	0	-	-	-	-	-	-
	5	5.07	5.03	101.4	100.6	2.36	2.34
	10	10.03	10.11	100.3	101.1	2.27	2.31
	30	30.65	30.82	102.2	102.8	2.01	2.21
	45	45.51	45.64	101.2	101.5	2.41	2.38

Chapter Ten: Paper VIII

Pioneering electrochemical sensing platform of multi-elemental nanocomposites for simultaneously determining azithromycin and enrofloxacin residues in food and water samples

Wondimeneh Dubale Adane, Bhagwan Singh Chandravanshi, Merid Tessema

Electrochemica Acta

(Under Review)

Pioneering electrochemical sensing platform of multi-elemental nanocomposites for simultaneously determining azithromycin and enrofloxacin residues in food and water samples

Wondimeneh Dubale Adane[a], Bhagwan Singh Chandravanshi*[a], Merid Tessema**[a]

[a]Department of Chemistry, Addis Ababa University, P. O. Box 1176, Addis Ababa, Ethiopia

*Corresponding author. E-mail address: bscv2006@yahoo.com

**Corresponding author. E-mail address: tessemamerid@yahoo.com

Abstract

Herein, we introduce a pioneering electrochemical sensing platform for simultaneously determining the residues of antibacterial drugs, azithromycin (AZM) and enrofloxacin (ENF), in food and water samples. The sensor was developed by integrating thermally annealed gold-silver alloy nanoporous matrices (TA-Au-Ag-ANpM) with iron-doped polyaniline (Fe-dop-PANI) and nickel oxide nanoparticles (NiO-NPs). The surface morphology and elemental composition of TA-Au-Ag-ANpM/Fe-dop-PANI/NiO-NPs/GCE were exhaustively characterized using an array of analytical (FT-IR, XRD, SEM, and EDX), and electrochemical (EIS, CV, and SWV) techniques. The sensor exhibited exceptional performance over a wide linear range, from 0.8 pM–250 µM for AZM and 0.1 pM–550 µM for ENF. The LOD and LOQ values were found to be 0.053 pM and 0.18 pM for AZM, and 0.013 pM and 0.042 pM for ENF, respectively. Additionally, the sensor demonstrated outstanding selectivity, long-term stability, repeatability, and reproducibility. It also yielded an excellent recoveries of 96.4–102.8% and relative standard deviations between 1.13% and 1.36%, to detect AZM and ENF residues in chicken meat, egg, fish, river, and lake water samples. Generally, the developed sensor sets a new standard and represents a significant advancement in addressing the global antibiotic residue pollution problem in chicken meat, egg, fish, river, and lake water samples.

Keywords: Electrochemical sensor; Antibiotic residues; Azithromycin; Enrofloxacin; Food samples

1. Introduction

Antibiotics are widely used in combating infectious diseases in humans and animals, as well as for promoting growth and enhancing performance in livestock. They are administered to animals for various purposes, including controlling reproductive cycles, improving breeding performance, and preventing infections [1,2]. In humans, antibiotics are effectively prescribed for treating different infectious diseases, such as genital, abdominal, urinary tract, skin, and gastrointestinal infections, as well as diseases such as leprosy, tuberculosis, strep throat, bronchitis, pneumonia, arthritis, sinusitis, and typhoid [3]. The primary mechanisms of action of antibiotics involve inhibiting bacterial cell wall and protein synthesis, restricting DNA synthesis, disrupting RNA elongation, and eradicating microbial communities. Nevertheless, the indiscriminate and irresponsible use of antibiotics has spurred the development of antimicrobial-resistant bacteria, presenting a grave peril to worldwide health [4]. Additionally, antibiotic residues released into the environment from unused or expired medicines and animal excretion can accumulate in food products like milk, fish, eggs, meat, honey, and chicken, increasing the risk of antibiotic resistance in humans [2]. These residues exert selective pressure on bacteria, promoting the survival and dissemination of resistant strains, which presents a serious hazard to human health. The consequences of antibiotic resistance are severe, leading to prolonged illness, escalating healthcare costs, and increasing mortality rates and undermining the efficacy of medical procedures [5]. Therefore, developing an innovative analytical approach is decisive for addressing the increasing threat of antibiotic residues.

Azithromycin (AZM), a widely used broad-spectrum antibiotic, plays a vital role in treating various infections, such as enteric, genitourinary, dermal, and respiratory infections [6]. It is also recommended for the management of cat-scratch disease, tick-borne infections, Lyme disease, whooping cough, Legionnaires' disease, travelers' diarrhea, H. pylori infection, and prophylaxis of heart infection [7]. However, despite its therapeutic benefits, AZM is associated with adverse effects, such as rash, dizziness, headache, abdominal pain, diarrhea, vomiting, and nausea, in rare cases, serious complications such as liver damage or heart problems [8]. Studies have indicated the presence of AZM in high concentrations in aquatic environments, raising potential health concerns. The residues of AZM can enter the environment through various pathways, including human and animal waste, pharmaceutical wastewater, and the disposal of expired or unused

medications. These residues can harm beneficial bacteria, and contributing to the development of antibiotic-resistant bacteria (ARB) [9,10]. Therefore, it is imperative to develop accurate analytical devices for detecting AZM residues in food and water samples to address the potential health and environmental effects associated with their presence.

Enrofloxacin (ENF), a fluoroquinolone antibiotic widely used in veterinary medicine, is recognized for its broad antibacterial spectrum, potent bactericidal effects, rapid action, and extensive tissue distribution [11]. Despite its efficacy, the widespread use of ENF has raised a significant public health concerns due to the accumulation of residues in animal products and aquatic environments. The presence of these residues can result in the development of antibiotic-resistant bacteria and poses various health risks, including allergic reactions and carcinogenic mutations. Furthermore, excessive disposal of ENF into aquatic environments poses a threat to both the environment and aquatic organisms [12.13]. The maximum residue limits for ENF are established by various countries and organizations around the world, and they vary depending on the specific animal product. These limits typically range from 100 to 500 μg/kg [14]. Hence, the fabrication of an exceedingly sensitive sensing platform for detecting residues of ENF in animal-based products and their surrounding environment is vital for safeguarding food safety and public health.

Bimetallic alloy nanoparticles have gained considerable interest for electrochemical sensor development due to their outstanding sensitivity, enhanced detection capabilities, and robust stability [15]. Their specific surface morphology, size, and composition contribute to enhanced catalytic performance and synergistic properties, expanding their potential applications in cancer treatment, nanomedicine, catalysis, and DNA delivery [16]. Of particular interest are gold-silver alloy nanoparticles, which exhibit outstanding electrocatalytic activity, electrical conductivity, and optical properties, making them highly sought-after for various electrochemical sensing applications [17]. Furthermore, metal-doped polyaniline electrodes have made significant contributions to the advancement of electrochemical sensing. Doping polyaniline with metals not only enhances conductivity, stability, and sensitivity but also facilitates smooth charge transfer, extends sensor lifespan, and enables customizable detection to meet specific requirements. These characteristics make metal-doped polyaniline electrodes suitable for diverse applications, ranging from environmental pollutant monitoring to biomedical sensing of biomolecules and physiological

parameters [18,19]. Their selectivity, sensitivity, and versatility position them as ideal choices for fabricating cutting-edge electrochemical sensing platforms across various fields. Similarly, Nickel oxide nanoparticles (NiO-NPs) exhibit remarkable versatility, finding applications in numerous fields, particularly for the preparation of sensitivity, and selectivity electrochemical sensors [20,21]. Their nano-size provides a large surface area and increased reactivity, making them efficient catalysts for various electrochemical reactions. Additionally, NiO-NPs play critical roles in energy storage, organic synthesis catalysis, gas sensing, and environmental photocatalysis [22]. Herein, a novel multi-elemental electrochemical sensor was developed by integrating the benefits of the three nanocomposites for accurately and precisely detecting AZM and ENF residues in food and water samples.

Various techniques have been reported for the quantification of AZM and ENF in different matrices, including LC-MS/MS [23], UHPLC-MS/MS [24], spectrofluorometry [25], and flow injection chemiluminescence immunoassay [26]. Although these methods are sensitive and selective, they have several limitations, such as complex operational procedures, time-consuming sample preparation, lengthy analysis times, the need for skilled hands, and high equipment costs [27]. In contrast, voltammetric techniques are cost-effective, user-friendly, highly sensitive, and can be miniaturized. They also offer fast analysis and require minimal reagent volume [28]. Among electrochemical techniques, square wave voltammetry (SWV) stands out due to its rapid analysis time, minimal sample consumption, background discrimination, and high sensitivity [29]. This makes SWV an excellent choice for the efficient and accurate detection of AZM and ENF residues.

The objective of this study was to develop advanced multi-elemental nanocomposite electrochemical sensing platform, the first of its kind, by integrating TA-Au-Ag-ANpM with Fe-dop-PANI and NiO-NPs for simultaneously determining AZM and ENF residues in chicken meat, egg, fish, river, and lake water samples. The modifiers were selected by taking various factors into consideration. TA-Au-Ag-ANpM nanocomposites were preferred because of their significant surface areas and catalytic properties, which were crucial for the detection of target analytes. The addition of Fe-dop-PANI improved the electrical conductivity of the composite and enhanced the sensor selectivity by offering specific binding sites for the analyte molecules. The role of the NiO-NPs was to act as an electron mediator, facilitating the electrons transfer within the electrode

surface and the target analyte, thereby enhancing the stability and sensitivity of the sensor. TA-Au-Ag-ANpM/Fe-dop-PANI/NiO-NPs/GCE was extensively characterized using numerous analytical and electrochemical techniques. The sensor exhibited a remarkable capability in detecting the analytes over a broad dynamic range, down to the picomolar level. The integration of distinct nanocomposite modifiers within the sensor resulted in a synergistic effect, enhancing the sensitivity, selectivity, and stability. This was demonstrated by the enhanced and well-defined current responses to the ultra-trace analyte concentrations. Moreover, the sensor exhibited exceptional selectivity, reproducibility, and repeatability. Finally, the developed sensor was successfully applied to quantify AZM and ENF residues in the desired samples, revealing very good percentage recoveries while maintaining the relative standard deviation (RSD) values below 5%.

2. Experimental

2.1. Chemical and reagents

Sodium citrate, sodium borohydride, silver nitrate, and tetrachloroauric acid were obtained from Shanghai Sinopharm Chemical Reagent Co., Ltd. (China). Nitric acid, sulfuric acid, and sodium citrate were purchased from Merck Chemical (Germany). BDH Chemicals Ltd. (England), provided potassium hexacyanoferrate(III). Polyvinyl pyrrolidone PVP K15, MW ≈ 40,000) was obtained from the Research Lab. Fine Chem. Industries (Mumbai, India). All the remaining chemicals and antibiotic standards were obtained from Sigma-Aldrich (USA). All chemicals and reagents used were of analytical grade and were used without additional purification. Aqueous solutions were prepared using Milli-Q water (18.2 MΩ cm) obtained from a Millipore water purification system. To prepare a 0.01 M stock solution of AZM, 187.4 mg of the analyte was dissolved in 25 mL of distilled water. For ENF, 0.01 M stock solution was prepared by dissolving 89.8 mg of the analyte in 25 mL of dimethyl sulfoxide. The stock solutions were diluted with 0.1 M PBS (pH 7) to prepare working solutions for each analyte.

2.2. Apparatus and instruments

Voltammetric experiments were performed in 20-mL cells using a CHI 760D electrochemical analyzer (CH Instruments, USA). A conventional three-electrode system was

utilized, comprising a reference electrode (Ag/AgCl (3M KCl)), working electrode (either modified GCE or bare GCE), and counter electrode (platinum wire). The surface properties of the modified electrodes were characterized using scanning electron microscopy (SEM, CX-200plus, Coxem, Korea), and energy-dispersive X-ray spectroscopy (EDS) was used for elemental analysis. BRUKER ECOD 8 advance diffractometer with Cu Kα radiation (wavelength $\lambda = 0.15406$ nm) was used for analysis of X-ray diffraction (XRD) patterns of the nanocomposites. A PerkinElmer Spectrum 100 FT-IR spectrometer (PerkinElmer, USA) was used for Fourier transform infrared (FT-IR) spectral analysis. The pH measurements were conducted using a Senses Ion + MM150 pH meter (China).

2.3. Synthesis of TA-Au-Ag-ANpM

The synthesis of TA-Ag-NpM proceeded by initially mixing 0.1 M solutions of $AgNO_3$ and CTAB in a 1:1 volume ratio to form the precursor solution. The pH was then adjusted to a range of 10 to 11 using 0.1 M NaOH to facilitate the controlled formation of nanoporous structures during subsequent reduction steps. The reduction of Ag^+ (aq) and the formation of Ag nanoporous structures were initiated by gradually adding 10 mL of 0.1 M $NaBH_4$. The mixture was heated at 120 °C for 7 h to promote the formation of a stable nanoporous Ag matrix. The solution was cooled to room temperature, centrifuged to remove excess reactants, and washed thoroughly with ethanol to obtain the desired nanoporous Ag matrix. A critical part of the synthesis involved a controlled thermal treatment in an oven at 175 °C for 2 h. The annealing process played a pivotal role in consolidating the nanoporous Ag structure, enhancing the stability, and improving the properties. Finally, the synthesized TA-Ag-NpM was dispersed in distilled water and stored as a colloidal suspension.

The synthesis of TA-Au-Ag-ANpM was performed by modifying the galvanic replacement reaction method [30]. Initially, TA-Ag-NpM was collected by centrifugation from the colloidal suspension and then re-dispersed in distilled water. In a 100 mL flask, the dispersion was mixed with a 0.15 M polyvinyl pyrrolidone (PVP). The flask was then immersed in an oil bath set at 90 °C with continuous stirring, and 4 mL of 0.001 M $HAuCl_4$ solution was introduced at a rate of 3 mL/h. Finally, the synthesized TA-Au-Ag-ANpM was subjected to centrifugation, washed, and re-dispersed in 97% ethanol for subsequent use.

2.4. Preparation of Fe-dop-PANI and NiO-NPs

The synthesis of Fe-doped polyaniline (Fe-dop-PANI) was performed based on the procedure by El-Khodarya et al. [31], with some modifications. Initially, 50 mL of aniline monomer was added to 50 mL of distilled water, which serve as the base for the polymerization reaction. Iron ions were introduced by adding 10 mL of 0.1 M $FeCl_3$ dropwise with continuous stirring. Next, the incorporation of Fe ions into the polymer matrix was facilitated in an acidic medium by adding 5 mL of 0.1 M H_2SO_4 to the reaction vessel. Polymerization was initiated by gradually adding 10 mL of $(NH_4)_2S_2O_8$ (0.1 M), and the reaction proceeded under continuous stirring for 12 h at a controlled temperature with continuous monitoring of the pH. The color change from colorless to dark green indicated the formation of Fe-dop-PANI. The reaction was halted by introducing 0.5 M ascorbic acid (5 mL). Finally, the synthesized Fe-dop-PANI was collected by filtration, thoroughly washed and dried.

The synthesis of NiO-NPs was carried out by modifying the procedure of Khan et al. [32]. Initially, 0.15 g of $Ni(NO_3)_2$ was dissolved in 25 mL of distilled water. To this solution, 10 mL of 0.1 M NaOH was added to form a crystalline nickel oxide precursor. To control particle size and prevent agglomeration, 12 mL of 0.15 M polyvinylpyrrolidone (PVP) was introduced. The reduction reaction was initiated by adding 15 mL of 0.1 M $NaBH_4$, and the mixture was heated at 90 °C for 3 h under controlled conditions to regulate the morphology and size of the nanoparticles. The color change from pale to black indicated the formation of NiO-NPs. Finally, the synthesized NiO-NPs were centrifuged, thoroughly washed, and dried.

2.5. Fabrication of TA-Au-Ag-ANpM/Fe-dop-PANI/NiO-NPs/GCE

Before the modification, the surface of the GCE was polished with 0.3 and 0.05 µm alumina slurries and then rinsed with distilled water. Subsequently, the electrode was sonicated in ethanol/water (1:1) and electrochemically activated in 0.1 M H_2SO_4 by conducting ten potential scans from -0.4 to +1.2 V at a scan rate of 100 mVs^{-1}. To fabricate the TA-Au-Ag-ANpM/Fe-dop-PANI/NiO-NPs nanocomposite dispersion, 5.0 mL of TA-Au-Ag-ANpM, 6 mL of Fe-dop-PANI, and 4 mL of NiO-NPs dispersions were mixed and vigorously stirred for 25 min at room temperature. The nanocomposite mixture was then heated in a water bath at 15 °C for 45 min.

Subsequently, it was subjected to ultrasonication, centrifugation, and dried. The dried nanocomposite was ultrasonically re-dispersed in deionized water for 40 min, resulting in a 20 mL nanocomposites dispersion mixture for subsequent use.

TA-Au-Ag-ANpM/Fe-dop-PANI/NiO-NPs/GCE was prepared by drop-casting 10 µL of the TA-Au-Ag-ANpM/Fe-dop-PANI/NiO-NP nanocomposite dispersion at the surface of the activated GCE, followed by drying at room temperature. Similar procedures were applied for the preparation of the other modified electrodes.

3. Results and discussion

3.1. Analytical characterizations

The FT-IR spectrum of NiO-NPs (Fig. 1A(a)) exhibits peaks at 3478 cm^{-1} (COOH group), 568 cm^{-1} (Ni-O symmetric stretching vibrations and implying crystallinity), 450 cm^{-1} (Ni-O asymmetric stretching vibrations and showing lattice structure changes), and 1383 cm^{-1} (a complex combination of bands indicating crystallinity and orientation). In the FT-IR spectrum of Fe-doped PANI (Fig. 1A(b)), the characteristic peaks at 3235 cm^{-1}, 1488 cm^{-1}, and 1570 cm^{-1} indicate the vibrations of the polymer backbone, and illustrate its structural integrity. The successful doping of Fe was confirmed by the presence of distinctive Fe-O and Fe-N stretching peaks (diagnostic markers) at 693 cm^{-1} and 495 cm^{-1}, respectively. The FT-IR spectrum of TA-Ag-NpM (Fig. 1A(c)) showed reduced Ag-O stretching vibrations at 572 cm^{-1}, suggesting partial breaking of the Ag-O bonds during thermally annealing. The reduced stretching vibrations of C-O and C=O suggest the restructuring of oxygen-related functional groups on the nanoporous surface. The peak at 1754 cm^{-1} indicates the introduction of COOH groups onto the TA-Ag-NpM surface. The FT-IR of TA-Au-Ag-ANpM (Fig. 1A(d)) exhibited characteristic peaks associated with Au and Ag nanoporous matrices, including Au-O at 540 cm^{-1} and Au-Ag at 860 cm^{-1}, confirming alloying. Silver-related stretching vibrations at 568 cm^{-1} (Ag-O), 1078 cm^{-1} (C-O), and 2856 and 2929 cm^{-1} (C-H) suggest the presence of silver atoms and stabilizing alkyl chains. The peaks at 1629 cm^{-1} and 3459 cm^{-1} indicate the presence of C=O and O-H on the nanoporous structure. The FT-IR spectrum of TA-Au-Ag-ANpM/Fe-dop-PANI/NiO-NPs (Fig. 1A(e)) reveals characteristic peaks at 835 cm^{-1} for

Au-Ag alloy bonds, 694 cm^{-1} and 426 cm^{-1} for Fe-doped PANI, and 1384 cm^{-1} for Ni-O bonds, confirming the successful integration of individual nanocomposites in the sensor.

The XRD analysis of the NiO-NPs revealed distinct diffraction peaks at 2θ = 37.2°, 43.3°, 62.9°, and 75.1° (Fig. 1B(a)), corresponding to the (111), (200), (220), and (311) crystallographic planes of face-centered cubic (FCC) NiO, respectively [33]. The XRD analysis of Fe-dop-PANI (Fig. 1B(b)) revealed characteristic peaks associated with the crystallographic planes of both PANI and Fe dopant. The 2θ values in the range of 20-25° are attributed to the crystal planes of PANI [34]. Furthermore, the incorporation of Fe dopant introduced a broad peak at 2θ = 26.1°, indicating a potential alterations in the crystalline structure induced by Fe doping. The XRD diffraction peaks of TA-Ag-NpM at 2θ = 34.3°, 38.1°, 39.9°, 44.2°, and 57.7° (Fig. 1B(c)) were indexed to the (100), (111), (200), (220), and (311) planes, respectively, characteristic of FCC structured Ag metal crystals and consistent with previous reports [35]. In the XRD analysis of TA-Au-Ag-ANpM, a distinctive peak at 26.5° (Fig. 1B(d)) is attributed to the (111) crystal plane, indicating the formation of intermetallic alloy species. The amorphous structure of the nanoporous matrix was further confirmed by the characteristic peak at 23.9°, assigned to the (100) plane [36]. The XRD spectra of TA-Au-Ag-ANpM/Fe-dop-PANI/NiO-NPs contains all the characteristic peaks of the individual component nanocomposites (Fig. 1B(e)), thereby confirming the successful integration of each nanocomposite within the sensor.

The SEM image of the NiO-NPs (Fig. 1C(a)) reveals agglomerates of crystalline particles that are irregularly shaped, rough, and non-uniformly distributed. The EDX spectra of the NiO-NPs primarily consist of O (16.38%) and Ni (83.62%) (Fig. S1(d)), indicating a high degree of purity. SEM analysis of Fe-dop-PANI (Fig. 1C(b)) showed a rough surface, heterogeneously dispersed, non-uniformly sized and shaped, and porous structures. The elemental mapping of Fe-dop-PANI (Fig. S1(e)) indicated the presence of C (73.2%), O (14.4%), and Fe (12.4%), confirming the successful doping of Fe onto the PANI surface. The investigation of TA-Ag-NpM revealed a porous crystalline structure with baked agglomerated silver matrices of irregular shapes (Fig. 1C(c)). These matrices are non-uniformly distributed and possess rough surfaces. SEM image of the TA-Au-Ag-ANpM (Fig. 1C(d)) showed a uniform size distribution, and a porous structure with rough and irregular crystalline facets. The EDX spectra of TA-Ag-NpM (Fig. S1(f)) indicated the presence of C (43.18%), O (4.8%), Br (4.05%), and Ag (47.97%); those of TA-Au-Ag-ANpM

(Fig. S1(i)) contained C (38.7%), O (4.3%), Br (3.63%), Ag (42.99%), and Au (10.38%), confirming the successful incorporation of gold into TA -Ag-NpM. The SEM image of TA-Au-Ag-ANpM/Fe-doped-PANI/NiO-NPs (Fig. 1C(e)) revealed irregular shapes, a rough surface, non-uniform distribution, heterogeneous dispersion, and agglomeration of particles. The corresponding EDX spectra (Fig. 1C(f)) indicated the presence of C (18.81%), N (6.52%), O (7.38%), Fe (4.87%), Br (2.34%), Ni (27.65%), Ag (25.22%), and Au (7.21%). This finding further confirms the successful incorporation of each nanomaterial into the sensor, consistent with the XRD results.

Insert Fig. 1 Here

3.2. Electrochemical characterization

The electrodes were subjected to electrochemical impedance spectroscopy (EIS) analysis over a frequency range of 0.1 Hz to 100 kHz with 5 mM $[Fe(CN)_6]^{3-/4-}$ containing 0.1 M KCl (Fig. 2A). The experimental data were fitted to the Randles equivalent circuit model and presented in a Nyquist plot (inset Fig. 2A). The semicircular section of the EIS curve corresponds the rate-limiting step of the electrochemical reaction, whereas the diameter of the semicircle represents the charge transfer resistance (R_{ct}). The linear segment corresponds to the diffusion process, which becomes the rate-limiting step in the transportation of reactants and products to and from the electrode surface [37]. The R_{ct} values for the bare GCE, NiO-NPs/GCE, Fe-dop-PANI/NiO-NPs/GCE, TA-Au-Ag-ANpM/NiO-NPs/GCE, TA-Au-Ag-ANpM/Fe-dop-PANI/GCE, and TA-Au-Ag-ANpM/Fe-dop-PANI/NiO-NPs/GCE were determined to be 4724.3, 2639.1, 1772.5, 1197.6, 732.4, and 212.8 Ω, respectively. Notably, the lowest R_{ct} value was observed for the TA-Au-Ag-ANpM/Fe-dop-PANI/NiO-NPs/GCE, indicating a significant enhancement in the electroactive surface area, electron transfer capability, and conductivity due to the synergistic effect of the nanocomposite modifiers.

The voltammetric characteristics of both the bare and modified electrodes were evaluated using CV in the presence of a redox probe (5 mM $[Fe(CN)_6]^{3-/4-}$ containing 0.1 M KCl, scan rate: 50 mVs^{-1}) (Fig. 2B). The bare GCE displayed weak redox current and the highest peak-to-peak separation (ΔEp = 743 mV), attributed to its sluggish electrical conductivity (Fig. 2B(a)). In contrast, the NiO-NPs/GCE (Fig. 2B(b)) and Fe-dop-PANI/NiO-NPs/GCE (Fig. 2B(c)) exhibited

well-defined redox current responses and lower ΔEp values (ΔEp = 441 mV and ΔEp = 400 mV, respectively) due to the substantial conductivity, electrocatalytic, and electron transfer abilities of the NiO-NPs and Fe-dop-PANI. Moreover, the voltammetric response increased significantly for TA-Au-Ag-ANpM/NiO-NPs/GCE (Fig. 2B(d)) and TA-Au-Ag-ANpM/Fe-dop-PANI/GCE (Fig. 2B(e)), accompanied by reduced ΔEp values (364 mV and 341 mV, respectively). Notably, the current response at the surface of the TA-Au-Ag-ANpM/Fe-dop-PANI/NiO-NPs/GCE (Fig. 2B(f)) reached its maximum value with a decrease in ΔEp to 317 mV, underscoring the synergistic enhancement of the overall performance of the sensor by the modifiers, which aligns with the findings from the EIS analysis.

Insert Fig. 2 Here

The electroactive surface area of an electrode crucially influences electrochemical reactions, affecting catalytic efficiency and electrode sensitivity. Herein, the electroactive surface area was probed at various modification stages using CV and computed using the Randles-Sevcik equation (1) [38].

$$I_p = 2.69 \times 10^5 n^{3/2} A D^{1/2} C v^{1/2} \quad (1)$$

where I_p = peak current, A = electrode surface area, n = number of electrons, D = diffusion coefficient, C = concentration of $[Fe(CN)_6]^{3-/4-}$, and v = scan rate. The regression equations for Ipa vs. $v^{1/2}$ are given as: Ipa (μA) = $4.3v^{1/2}$ $(mVs^{-1})^{1/2}$ + 28.8 (R^2 = 0.992) for the bare GCE (Fig. S2(A and B)) and Ipa (μA) =$10.6v^{1/2}$ $(mVs^{-1})^{1/2}$ + 69.3 (R^2 = 0.991) for TA-Au-Ag-ANpM/Fe-dop-PANI/NiO-NPs/GCE (Fig. S2(C and D)). The electroactive surface areas, determined from the slopes of the plots, were 0.039 cm^2 for the bare GCE and 0.161 cm^2 for the sensor. TA-Au-Ag-ANpM/Fe-dop-PANI/NiO-NPs/GCE exhibited a fourfold higher surface area than the bare GCE, indicating that the synergistic effect of the constitute nanocomposites enhanced the electroactive part of the developed sensor.

3.3. Electrochemical behavior of AZM and ENF

The voltammetric properties of 25 μM AZM and ENF were investigated at bare and modified GCEs using SWV and CV at a scan rate of 100 mVs^{-1} and a potential range of 0.5–1.4 V. No CV

currents were observed from the blank solutions, indicating the absence of the analytes or their being below the detection limit. The absence of cathodic peaks in the reverse CV scan indicates the electro-oxidations of AZM and ENF were irreversible reactions. Weak current responses at the bare GCE indicated slow electron transfer kinetics and poor electrical conductivity. In contrast, the NiO-NPs/GCE exhibited enhanced current responses due to the improved electrical conductivity of NiO-NPs. The Fe-dop-PANI/NiO-NP/GCE showed higher current responses, benefiting from the combined effects of the conductive polymer and iron dopants in Fe-dop-PANI. The TA-Au-Ag-ANpM/Fe-dop-PANI/GCE demonstrated improved electrical conductivity due to the alloying of Au and Ag, and the annealed nanoporous matrices further facilitated conductivity by enhancing the electroactive area and reducing the distance electrons travel [39]. The highest CV responses were observed at the TA-Au-Ag-ANpM/Fe-dop-PANI/NiO-NPs/GCE (Fig. 3A), indicating the synergistic effects of the constituent nanocomposites.

SWV was employed to further investigate the voltammetric characteristics of AZM and ENF (Fig. 3B). The bare GCE displayed the lowest anodic current response, which was attributed to its weak catalytic activity and adsorption capacity. Conversely, the TA-Au-Ag-ANpM/Fe-dop-PANI/NiO-NPs/GCE exhibited the highest oxidation current due to the synergistically strong electron transfer kinetics, enhanced conductivity, and increased surface area due to the precursor modifiers, consistent with the CV results. The observed ΔEp (408 mV) between AZM and ENF provided adequate differentiation for the simultaneous determination of the analytes. Thus, TA-Au-Ag-ANpM/Fe-dop-PANI/NiO-NPs/GCE was effectively utilized for the detection of AZM and ENF residues in food and water samples.

Insert Fig. 3 Here

3.4. Optimization of experimental conditions

3.4.1. Effect of electrolyte solution

The shape of the voltammogram and the current response are significantly influenced by the type of supporting electrolyte solution used during the electrochemical measurements. Therefore, it is essential to choose the appropriate supporting electrolyte before conducting any voltammetric analysis. The effect of various supporting electrolytes, including Britton-Robinson, phosphate,

citrate-phosphate, citrate, acetate buffer solutions, and sulfuric acid, were exhaustively assessed using SWV. The current response of phosphate buffer solution (PBS) was well-defined and sufficiently high for both analytes, confirming its superiority as an optimal medium (Fig. S3). Therefore, PBS was selected as the appropriate supporting electrolyte solution to simultaneously determine the residues of AZM and ENF in food and water samples.

3.4.2. Effect of pH

The effect of PBS pH on the current responses of 25 µM AZM and ENF was evaluated within the pH range of 3.0 to 8.0 at the TA-Au-Ag-ANpM/Fe-dop-PANI/NiO-NPs/GCE (Fig. 4A). The responses of the analytes gradually increased with increasing pH, reaching their maximum at pH 6.0 (Figs. 4B(a) and 4C(a)). However, above pH 6.0, a decline in responses was observed. Consequently, pH 6.0 was selected as the optimal value for future experiments. The oxidation potentials of AZM and ENF exhibited a similar trend, shifting towards less positive values with increasing pH, indicating the involvement of protons in the electrode reactions. The relationship between Epa and pH revealed linear equations illustrated as Epa (V) = 0.92 – 0.05pH (R^2 = 0.991) (Fig. 4B(b)) and Epa (V) =1.34 – 0.057pH (R^2 = 0.993) (Fig. 4C(b)) for AZM and ENF, respectively. The slope values of 0.05 V/pH for AZM and 0.057 V/pH for ENF are close to the theoretical Nernstian value of 0.059 V/pH, indicating the participation of an equal number of protons and electrons in the electro-oxidation of the analytes, in line with previous reports [7,40].

Insert Fig. 4 Here

3.4.3. Effect of scan rate

The effect of scan rate on the current responses of 25 µM AZM and ENF in 0.1 M PBS (pH 6) was investigated using SWV in the scan rate range of 25–300 mVs^{-1}. The absence of cathodic responses during the reverse scan and the progressive shift of the anodic peak towards more positive potentials with increasing scan rate suggest the irreversibility of the electrode processes (Fig. 5A). The linear increase in anodic currents with the square root of the scan rate indicates predominantly diffusion-controlled electrode processes, formulated as Ipa (µA) = $0.44\nu^{1/2}$ $(mVs^{-1})^{1/2}$ – 0.22 (R^2 = 0.995) and Ipa (µA) = $0.88\nu^{1/2}$ $(mVs^{-1})^{1/2}$ + 0.88 (R^2 = 0.991) for AZM and ENF, respectively (Fig. 5B(a) and (b)). Furthermore, the linear correlation between log Ipa and log *v*

yielded slopes of 0.45 and 0.52 for AZM and ENF, respectively (Fig. 5C(a) and (b)), closely aligned with the theoretical value of 0.5. This confirms the prevalence of diffusion-controlled electro-reactions of the analytes. Equation (2) was applied to determine the number of electrons involved in the electrode reaction [3].

$$E_p = E^0 + \frac{2.303RT}{\alpha nF}\log\frac{RTk^0}{\alpha nF} + \frac{2.303RT}{\alpha nF}\log\nu \quad (2)$$

where, E^0 = formal potential, k^0 = heterogeneous rate constant, F = Faraday constant, T = temperature, n = number of electrons, ν = scan rate, and R = universal gas constant. Epa showed a strong correlation with log ν for both AZM and ENF, which was applied to calculate αn from the slope of each plot (2.303RT/αnF). The resulting αn values were 0.467 for AZM and 2.022 for ENF. In the context of irreversible electrode reactions, the transfer coefficient (α) conventionally has a value of 0.5 [27]. The number of electrons (n) involved in the electro-oxidation of AZM and ENF were calculated to be 0.934 (≈1) and 4.044 (≈4), respectively, consistent with previous findings [7,40]. The schematic illustration depicting the electro-oxidation of AZM and ENF is given in Fig. 5D.

Insert Fig. 5 Here

3.4.4. Optimization of SWV parameters

To examining the effect of experimental parameters on the current responses of 25 µM AZM and ENF, three instrumental parameters, i.e. frequency, amplitude, and step potential, were studied. Initially, the influence of frequency, within the range of 20–100 Hz, was explored while maintaining step potential and amplitude constant. The peak current exhibited a progressive increase in frequency, reaching its peak at 60 Hz (Fig. S4(a)). Consequently, 60 Hz was designated as the optimum frequency for succeeding experiments. Next, the effect of amplitude was investigated in the range of 40–100 mV, by keeping the step potential and frequency constant. The anodic current increased up to 80 mV for both analytes before declining (Fig. S4(b)). Hence, 80 mV was selected as the optimal amplitude for succeeding experimentations. Finally, the effect of step potential was examined in the range of 2–14 mV by keeping other parameters constant,

revealed an increasing anodic current response for the analytes, peaking at 10 mV (Fig. S4(c)). Consequently, 10 mV was selected as the optimum value for following works.

3.5. Simultaneous determination of AZM and ENF

The linear range, LOD, and LOQ of AZM and ENF were determined using SWV under the optimized experimental conditions (Fig. 6A). The current response exhibited a linear correlation with the concentrations of the analytes, indicating the suitability of the sensor for real-sample analysis. Specifically, the anodic current demonstrated a linear relationship with concentrations ranging from 0.8 pM to 250 µM for AZM and from 0.1 pM to 550 µM for ENF. The corresponding linear regression equations were found to be Ipa (µA) = 0.46C (µM) + 10.09 (R^2 = 0.996) for AZM (Fig. 6B(a)) and Ipa (µA) = 1.11C (µM) + 21.25 (R^2 = 0.995) for ENF (Fig. 6B(b)). The LOD (3σ/m, S/N = 3, n = 5) and LOQ (10σ/m, S/N = 3, n = 5) values were calculated to be 0.053 pM and 0.18 pM for AZM, and 0.013 pM and 0.042 pM for ENF, respectively. Compared to previously reported sensors, TA-Au-Ag-ANpM/Fe-dop-PANI/NiO-NPs/GCE demonstrated outstanding performance, featuring a picomolar LOD and an extensive linear range, surpassing those of prior ones (Table 1). This represents a substantial advancement and a noteworthy contribution to the scientific community.

Insert Fig. 6 Here

Table 1: Comparison of the developed method with recently reported sensors.

Electrodes	Targets	Matrices	Linear range (μM)	LOD (μM)	Ref.
TiO_2 NPs/SPCI	AZM	Urine and tap water	0.05–50	0.93	[41]
$Zn_3V_2O_8$/P-rGO	AZM	Blood serum, urine, and wastewater	0.099–450	0.0067	[8]
MIP Bth/3-TBA	AZM	Urine, plasma and tears	13.33 nM–66.67	0.85 nM	[42]
PET/ITO/VO_2	AZM	Pharmaceuticals and water	1.0–80	0.02	[43]
APB-PDA-COFs/AuNPs	ENF	Milk and water	0.05–10 and 10–120	0.041	[44]
MWCNTs/MIPs/GCE	ENF	Marine environment	2.8 pM–28	0.9 pM	[45]
APT-BDD	ENF	Pharmaceuticals and urine	0.07–2.78	0.016	[46]
MIP-ECL based on MPA-Cu NCs	ENF	Environmental water	0.1 nM–1.0	27 pM	[13]
TA-Au-Ag-ANpM/Fe-dop-PANI/NiO-NPs/GCE	AZM	Food and water	0.8 pM–250	0.053 pM	This work
	ENF		0.1 pM–550	0.013 pM	

3.6. Repeatability, reproducibility, stability and selectivity

The reproducibility, repeatability, storage stability and selectivity of the TA-Au-Ag-ANpM/Fe-dop-PANI/NiO-NPs/GCE were examined by SWV while simultaneously quantifying 20 μM AZM and ENF. To assess the reproducibility, nine electrodes were prepared under identical conditions, yielding RSD values of 1.96% for AZM and 2.45% for ENF, indicating exceptional reproducibility. Repeatability was determined by conducting ten replicate SWV measurements with a single sensor, resulting in RSD values of 2.12% for AZM and 2.28% for ENF, demonstrating outstanding repeatability. The stability of the developed electrode was assessed by monitoring its responses weekly for two months, with storage at 4 °C after each weekly use. TA-Au-Ag-ANpM/Fe-dop-PANI/NiO-NPs/GCE exhibited long-term stability, displaying only a 6.15% decrease in the current response for AZM and a 5.98% decrease for ENF over the entire storage period. Finally, the selectivity was examined by subjecting the sensor to potentially interfering substances in the presence of 20 μM AZM and ENF. The current response of the sensor

for the target analytes was not affected in the presence of 300-fold excess concentrations of antibiotics (rifampicin, metronidazole, norfloxacin, tinidazole, ciprofloxacin, vancomycin, chloramphenicol, ceftriaxone, and erythromycin), 600-times larger amount of common interferents (fructose, glucose, sucrose, ascorbic acid, urea, dopamine, uric acid, folic acid, and lactose), and 1200 times higher concentrations of inorganic species (HCO^{3-}, Fe^{3+}, NO_3^-, Ca^{2+}, K^+, SO_4^{2-}, Cu^{2+}, Mg^{2+}, CO_3^2, and Cl^-) (Table S1), demonstrating the excellent anti-interference capability of the developed device.

3.7. Real sample analysis

The applicability of TA-Au-Ag-ANpM/Fe-dop-PANI/NiO-NPs/GCE for real-sample analysis was evaluated by performing spiking experiments using the standard addition method. The real samples were spiked with known concentrations of AZM and ENF standards (0, 5, 15, 25, and 40 µM), and their percentage recoveries were determined (Table 2). Before spiking the analyte standards, the initial responses of the unspiked original samples were recorded, showing no detectable current response, indicating that AZM and ENF residues were either absent or below the detection limit. The percentage recoveries in spiked chicken meat, egg, fish, river, and lake water samples found between 96.4% to 102.6% for AZM and 96.8% to 102.8% for ENF. The lowest RSD values ranging from 1.13% to 1.37% for AZM and 1.19% to 1.36% for ENF demonstrate the high efficiency and reliability of TA-Au-Ag-ANpM/Fe-dop-PANI/NiO-NPs/GCE in detecting AZM and ENF residues in real-time applications.

Table 2: Summary of results from triplicate spiking experiments.

Samples	Spiked (µM)	Found (µM) ± SD		Recovery (%)		RSD (%)	
		AZM	ENF	AZM	ENF	AZM	ENF
Chicken meat	0	-	-	-	-	-	-
	5	4.97 ± 0.11	5.02 ± 0.13	99.4	100.4	1.27	1.24
	15	15.21 ± 1.09	15.11 ± 1.04	101.4	100.7	1.13	1.19
	25	25.47 ± 1.48	24.25 ± 1.36	101.9	97	1.25	1.21
	40	38.54 ± 2.14	41.12 ± 2.25	96.4	102.8	1.28	1.25
Egg	0	-	-	-	-	-	-
	5	5.13 ± 0.17	5.07 ± 0.15	102.6	101.4	1.32	1.36
	15	14.76 ± 0.98	14.52 ± 0.95	98.4	96.8	1.37	1.34
	25	25.14 ± 1.42	24.62 ± 1.39	100.6	98.5	1.29	1.33
	40	38.96 ± 2.18	40.28 ± 2.21	97.4	100.7	1.32	1.28
Fish	0	-	-	-	-	-	-
	5	5.05 ± 0.14	4.86 ± 0.11	101	97.2	1.25	1.29
	15	14.79 ± 0.99	14.94 ± 1.01	98.6	99.6	1.31	1.27
	25	25.22 ± 1.42	25.14 ± 1.39	100.9	100.6	1.25	1.22
	40	40.15 ± 2.19	40.06 ± 2.15	100.4	100.2	1.27	1.25
River water	0	-	-	-	-	-	-
	5	4.83 ± 0.12	5.12 ± 0.17	96.6	102.4	1.32	1.36
	15	14.75 ± 0.98	14.86 ± 0.99	98.3	99.1	1.35	1.31
	25	24.97 ± 1.39	24.83 ± 1.34	99.9	99.3	1.36	1.36
	40	40.11 ± 2.18	38.94 ± 2.17	100.3	97.4	1.29	1.32
Lake water	0	-	-	-	-	-	-
	5	5.13 ± 0.16	5.09 ± 0.14	102.6	101.8	1.29	1.32
	15	14.87 ± 0.98	15.04 ± 0.11	99.1	100.3	1.32	1.28
	25	24.85 ± 1.37	24.79 ± 1.35	99.4	99.2	1.33	1.33
	40	40.11 ± 2.14	40.16 ± 2.17	100.3	100.4	1.28	1.33

5. Conclusion

In this study, a pioneering electrochemical sensor comprising TA-Au-Ag-ANpM, Fe-dop-PANI, and NiO-NPs nanocomposites, the first of its kind, was developed for simultaneously determining AZM and ENF residues in chicken meat, egg, fish, river, and lake water samples. The surface morphology and elemental composition of the developed sensor were examined using several analytical and voltammetric techniques. The TA-Au-Ag-ANpM/Fe-dop-PANI/NiO-NPs/GCE exhibited exceptional performance, demonstrating a picomolar LOD and a wider linear range, surpassing those of previously reported sensors, attributable to its enhanced electrical conductivity, larger electroactive surface area, and high electrocatalytic activity. Furthermore, the sensor demonstrated resistance to potentially interfering substances, and displayed remarkable selectivity and specificity. It also exhibited outstanding repeatability, reproducibility, and long-term stability. In general, TA-Au-Ag-ANpM/Fe-dop-PANI/NiO-NPs/GCE represents a significant advancement and noteworthy contribution to the scientific community, offering promise for ensuring food safety and public health. It is poised as an ideal tool for pharmaceuticals, food producers, and regulatory bodies.

Data availability statement

All the data are included in the manuscript. There are no additional data with the authors.

CRediT authorship contribution statement

Wondimeneh Dubale Adane: Conceptualization, Methodology, Software, Resources, Formal analysis, Investigation, Writing-original draft. **Bhagwan Singh Chandravanshi**: Conceptualization, Writing-review & editing, Supervision. **Merid Tessema:** Conceptualization, Writing-review & editing, Supervision.

Declaration of competing interest

We wish to confirm that there are no known conflicts of interest related to this publication and that this research has not received specific funding from any public, commercial or non-profit sector funding body.

Acknowledgements

The authors gratefully acknowledge the Department of Chemistry, Addis Ababa University, Addis Ababa, Ethiopia for providing laboratory facilities.

References

[1] X. Wang, Y. Xie, L. Lin, Recent development of microfluidic biosensors for the analysis of antibiotic residues, TrAC, Trends Anal. Chem. 157 (2022) 116797. https://doi.org/10.1016/j.trac.2022.116797.

[2] M. Majdinasab, R.K. Mishra, X. Tang, J.L. Marty, Detection of antibiotics in food: new achievements in the development of biosensors, TrAC, Trends Anal. Chem. 127 (2020) 115883. https://doi.org/10.1016/j.trac.2020.115883.

[3] W.D. Adane, B.S. Chandravanshi, M. Tessema, Highly sensitive and selective electrochemical sensor for the simultaneous determination of tinidazole and chloramphenicol in food samples (egg, honey and milk), Sens. Actuators B Chem. 390 (2023) 134023. https://doi.org/10.1016/j.snb.2023.134023.

[4] D.G.J. Larsson, C.F. Flach, Antibiotic resistance in the environment, Nat. Rev. Microbiol 20 (2022) 257–269. https://doi.org/10.1038/s41579-021-00649-x.

[5] P. Dadgostar, Antimicrobial resistance: implications and costs, Infect. Drug Resist. 12 (2019) 3903–3910. https://doi.org/10.2147/IDR.S234610.

[6] M.J. Parnham, V.E. Haber, E.J. Giamarellos-Bourboulis, G. Perletti, G.M. Verleden, R., Vos, Azithromycin: mechanisms of action and their relevance for clinical applications, Pharmacol. Ther. 143 (2014) 225–245. https://doi.org/10.1016/j.pharmthera.2014.03.003.

[7] F. Pogăcean, C. Varodi, L. Măgeruşan, S.R.I. Stefan-van, S. Pruneanu, Highly sensitive electrochemical detection of azithromycin with graphene-modified electrode, Sensors 22 (2022) 6181. https://doi.org/10.3390/s22166181.

[8] T.S.K. Sharma, K.Y. Hwa, Architecting hierarchal $Zn_3V_2O_8$/P-rGO nanostructure: electrochemical determination of anti-viral drug azithromycin in biological samples using SPCE, Chem. Eng. J. 439 (2022) 135591. https://doi.org/10.1016/j.cej.2022.135591.

[9] P. Rebelo, J.G. Pacheco, M.N.D.S. Cordeiro, A. Melo, C. Delerue-Matos, Azithromycin electrochemical detection using a molecularly imprinted polymer prepared on a disposable screen-printed electrode, Anal. Methods 12 (2020) 1486–1494. https://doi.org/10.1039/C9AY02566A.

[10] C. Vatovec, J. Kolodinsky, P. Callas, C. Hart, K. Gallagher, Pharmaceutical pollution sources and solutions: survey of human and veterinary medication purchasing, use, and disposal, J. Environ. Manage. 285 (2021) 112106. https://doi.org/10.1016/j.jenvman.2021.112106.

[11] A. Gallegos-Tabanico, J. Jimenez-Canale, S.G. Hernandez-Leon, A.J. Burgara-Estrella, J.C. Encinas-Encinas, J.A. Sarabia-Sainz, Development of an electrochemical sensor conjugated with molecularly imprinted polymers for the detection of enrofloxacin, Chemosensors 10 (2022) 448. https://doi.org/10.3390/chemosensors10110448.

[12] C. Aymard, H. Kanso, M.J. Serrano, R. Pagán, T. Noguer, G. Istamboulie, Development of a new dual electrochemical immunosensor for a rapid and sensitive detection of enrofloxacin in meat samples, Food Chem. 370 (2022) 131016. https://doi.org/10.1016/j.foodchem.2021.131016.

[13] D. Wang, S. Jiang, Y. Liang, X. Wang, X. Zhuang, C. Tian, F. Luan, L. Chen, Selective detection of enrofloxacin in biological and environmental samples using a molecularly imprinted electrochemiluminescence sensor based on functionalized copper nanoclusters, Talanta 236 (2022) 122835. https://doi.org/10.1016/j.talanta.2021.122835.

[14] G. Shen, Y. Ma, H. Zhang, F. Wang, F. Yang, H. Ye, R. Li, C. Wang, Y. Tang, Novel fluorescence strategy based on g-quadruplex structure-switching aptamer for enrofloxacin detection in food and environmental samples, Food Chem. 441 (2024) 138393. https://doi.org/10.1016/j.foodchem.2024.138393.

[15] P. Veerakumar, C. Koventhan, S.M. Chen, Copper-palladium alloy nanoparticles immobilized over porous carbon for voltammetric determination of dimetridazole, J. Alloys Compd. 931 (2022) 167474. https://doi.org/10.1016/j.jallcom.2022.167474.

[16] G. Das, S. Seo, I.J. Yang, L.T.H. Nguyen, H.S. Shin, J.K. Patra, Sericin mediated gold/silver bimetallic nanoparticles and exploration of its multi-therapeutic efficiency and photocatalytic degradation potential, Environ. Res. 229 (2023) 115935. https://doi.org/10.1016/j.envres.2023.115935.

[17] L. Feng, G. Gao, P. Huang, K. Wang, X. Wang, T. Luo, C. Zhang, Optical properties and catalytic activity of bimetallic gold-silver nanoparticles, Nano Biomed. Eng. 2 (2010) 258–267. https://doi.org/10.5101/nbe.v2i4.p258-267.

[18] Md.M. Rahman, T. Mahtab, M.Z.B. Mukhlish, M.O. Faruk, M.M. Rahman, Enhancement of electrical properties of metal doped polyaniline synthesized by different doping techniques, Polym. Bull. 78 (2021) 5379–5397. https://doi.org/10.1007/s00289-020-03389-9.

[19] T.A. Hamdalla, M.M. Aljohani, A.M. Alsharari, Synthesis and characterization of PANI/$ZnFe_2O_4$ nRs with different doping concentrations for potential applications in various fields, J. Spectrosc. 2023 (2023) 1–10. https://doi.org/10.1155/2023/1679035.

[20] S.U. Akond, K. Barman, A. Mahanta, S.K. Jasimuddin, Electrochemical sensor for detection of p-nitrophenol based on nickel oxide nanoparticles/α-cyclodextrin functionalized reduced graphene oxide, Electroanalysis 33 (2021) 900–908. https://doi.org/10.1002/elan.202060450.

[21] M. Khairy, H.A. Ayoub, C.E. Banks, Non-enzymatic electrochemical platform for parathion pesticide sensing based on nanometer-sized nickel oxide modified screen-printed electrodes, Food Chem. 255 (2018) 104–111. https://doi.org/10.1016/j.foodchem.2018.02.004.

[22] A. Singh, V. Goyal, J. Singh, H. Kaur, S. Kumar, K.M., Batoo, J. Gaur, M. Pal, M. Rawat, S. Hussain, Structurally and morphologically engineered single-pot biogenic synthesis of NiO nanoparticles with enhanced photocatalytic and antimicrobial activities, J. Clean. Prod. 343 (2022) 131026. https://doi.org/10.1016/j.jclepro.2022.131026.

[23] Y. Zhang, V. Bala, Y.S Chhonker, W.N. Aldhafiri, L.N. John, C.M. Bjerum, C.L. King, O. Mitja, M. Marks, D.J. Murry, A simple, high-throughput and validated LC–MS/MS method for the determination of azithromycin in human plasma and its application to a clinical pharmacokinetic study, Biomed. Chromatogr. 36 (2022) e5443. https://doi.org/10.1002/bmc.5443.

[24] N. Cai, X. Wu, J. Lin, J. Zou, J.L. Yi, X. Luo, UHPLC–MS/MS method for the determination of azithromycin in human plasma of pediatric patients, Biomed. Chromatogr. 36 (2022) e5415. https://doi.org/10.1002/bmc.5415.

[25] M.G. Arriagada, D. Pino, P. Richter, I.M. Toral, First-derivative spectrofluorometric determination of enrofloxacin and ciprofloxacin in cow milk using rotating sportive extraction, J. Chil. Chem. Soc. 66 (2021) 5035–5040. https://doi.org/10.4067/S0717-97072021000105035.

[26] Y. Pei, L. Zeng, C. Wen, K. Wu, A. Deng, J. Li, Detection of enrofloxacin by flow injection chemiluminescence immunoassay based on cobalt hydroxide nanozyme, Microchim. Acta. 188 (2021) 194. https://doi.org/10.1007/s00604-021-04846-6.

[27] W.D. Adane, B.S. Chandravanshi, M. Tessema, A simple, ultrasensitive and cost-effective electrochemical sensor for the determination of ciprofloxacin in various types of samples, Sens. Bio-Sens. Res. 39 (2023) 100547. https://doi.org/10.1016/j.sbsr.2022.100547

[28] W.D. Adane, B.S. Chandravanshi, M. Tessema, A novel electrochemical sensor for the detection of metronidazole residues in food samples, Chemosphere 359 (2024) 142279. https://doi.org/10.1016/j.chemosphere.2024.142279.

[29] T. Williams, R. Shum, D. Rappleye, Review-concentration measurements in molten chloride salts using electrochemical methods, J. Electrochem. Soc. 168 (2021) 123510. https://doi.org/10.1149/1945-7111/ac436a.

[30] K. Yu, X. Sun, L. Pan, T. Liu, A. Liu, G. Chen, Y. Huang, Hollow Au–Ag alloy nanorices and their optical properties, Nanomaterials 7 (2017) 255. https://doi.org/10.3390/nano7090255.

[31] S.A. El-Khodarya, G.M. El-Enanyb, M. El-Okrc, M. Ibrahim, Modified iron doped polyaniline/sulfonated carbon nanotubes for all symmetric solid-state supercapacitor, Synth. Met. 233 (2017) 41–51. http://dx.doi.org/10.1016/j.synthmet.2017.09.002.

[32] M.I. Khan, M. Nawaz, M.B. Tahir, T. Iqbal, M. Pervaiz, M. Rafique, F. Aziz, U. Younas, H. Alrobei, Synthesis, characterization and antibacterial activity of NiO NPs against pathogen, Inorg. Chem. Commun. 122 (2020) 108300. https://doi.org/10.1016/j.inoche.2020.108300.

[33] S. Kailasa, B.G. Rani, M.S. Bhargava Reddy, N. Jayarambabu, P. Munindra, S. Sharma, K. Venkateswara Rao, NiO nanoparticles decorated conductive polyaniline nanosheets for amperometric glucose biosensor, Mater. Chem. Phys. 242 (2020) 122524. https://doi.org/10.1016/j.matchemphys.2019.122524.

[34] S. Bhadra, D. Khastgir, Determination of crystal structure of polyaniline and substituted polyanilines through powder x-ray diffraction analysis, Polym. Test. (2008) 851–857. https://doi.org/10.1016/j.polymertesting.2008.07.002.

[35] M. Al-Ansari, N. Alkubaisi, K. Gopinath, V. Karthika, A. Arumugam, M. Govindarajan, Facile and cost-effective Ag nanoparticles fabricated by lilium lancifolium leaf extract: antibacterial and antibiofilm potential, J. Clust. Sci. 30 (2019) 1081–1089. https://doi.org/10.1007/s10876-019-01569-w.

[36] H. Zhao, M. Guo, F. Li, Y. Zhou, G. Zhu, Y. Liu, Q. Ran, F. Nie, V. Dubovyk, Fabrication of gallic acid electrochemical sensor based on interconnected super-P carbon black@mesoporous silica nanocomposite modified glassy carbon electrode, J. Mater. Res. Technol. 24 (2023) 2100–2112. https://doi.org/10.1016/j.jmrt.2023.03.129.

[37] W.D. Adane, B.S. Chandravanshi, N. Getachew, M. Tessema, A cutting-edge electrochemical sensing platform for the simultaneous determination of the residues of antimicrobial drugs, rifampicin and norfloxacin, in water samples, Anal. Chim. Acta 1312 (2024) 342746. https://doi.org/10.1016/j.aca.2024.342746.

[38] W.D. Adane, B.S. Chandravanshi, M. Tessema, Hypersensitive electrochemical sensor based on thermally annealed gold–silver alloy nanoporous matrices for the simultaneous determination of sulfathiazole and sulfamethoxazole residues in food samples, Food Chem. 456 (2024) 140071. https://doi.org/10.1016/j.foodchem.2024.140071.

[39] Y. Tong, X. Yan, J. Liang, S.X. Dou, Metal-based electrocatalysts for methanol electro-oxidation: progress, opportunities, and challenges, Small 17 (2021) 1904126. https://doi.org/10.1002/smll.201904126.

[40] N. Karuppusamy, V. Mariyappan, S.M. Chen, R.A. Ramachandran, Novel electrochemical sensor for the detection of enrofloxacin based on a 3D flower-like metal tungstate-incorporated reduced graphene oxide nanocomposite, Nanoscale (2022) 1250–1263. https://doi.org/10.1039/D1NR06343J.

[41] F. Sopaj, F. Loshaj, A. Contini, E. Mehmeti, A. Veseli, Preparation of an efficient and selective voltammetric sensor based on screen printed carbon ink electrode modified with TiO_2 nanoparticles for azithromycin quantification, Results Chem. 6 (2023) 101123. https://doi.org/10.1016/j.rechem.2023.101123.

[42] I.A. Stoian, B.C. Iacob, C.L. Dudaș, L. Barbu-Tudoran, D. Bogdan, I.O. Marian, E. Bodoki, R. Oprean, Biomimetic electrochemical sensor for the highly selective detection of azithromycin in biological samples, Biosens. Bioelectron. 155 (2020) 112098. https://doi.org/10.1016/j.bios.2020.112098.

[43] E.M. Guerra, D.T. Cestarolli, Azithromycin electrochemical detection using a VO_2 thin film, J. Alloys Compd. 885 (2021) 160997. https://doi.org/10.1016/j.jallcom.2021.160997.

[44] S. Lu, S. Wang, P. Wu, D. Wang, J. Yi, L. Li, P. Ding, H. Pan, A composite prepared from covalent organic framework and gold nanoparticles for the electrochemical determination of enrofloxacin, Adv. Powder Technol. 32 (2021) 2106–2115. https://doi.org/10.1016/j.apt.2021.04.025.

686 **Figures**

687

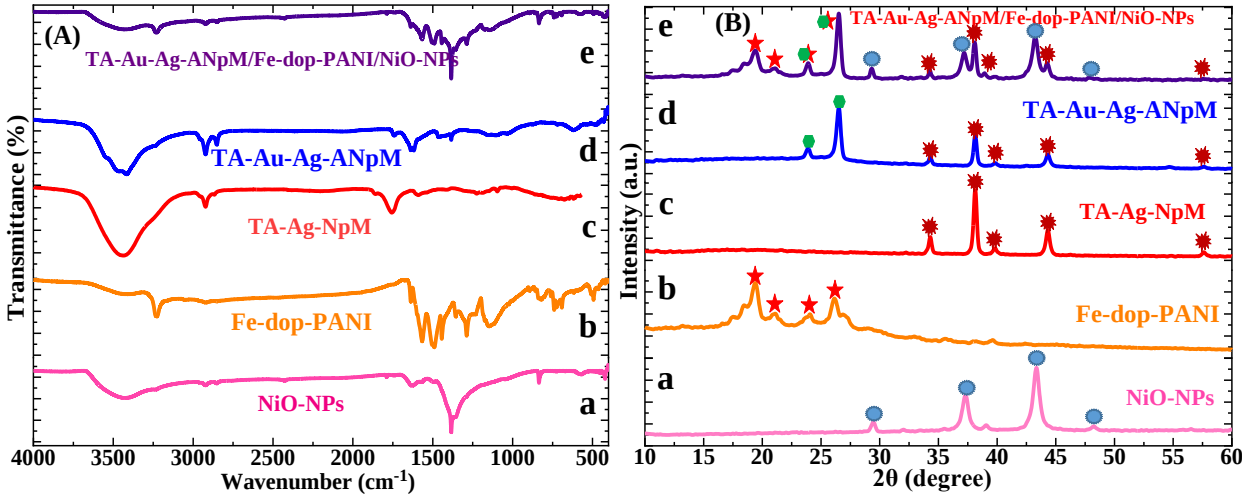

688

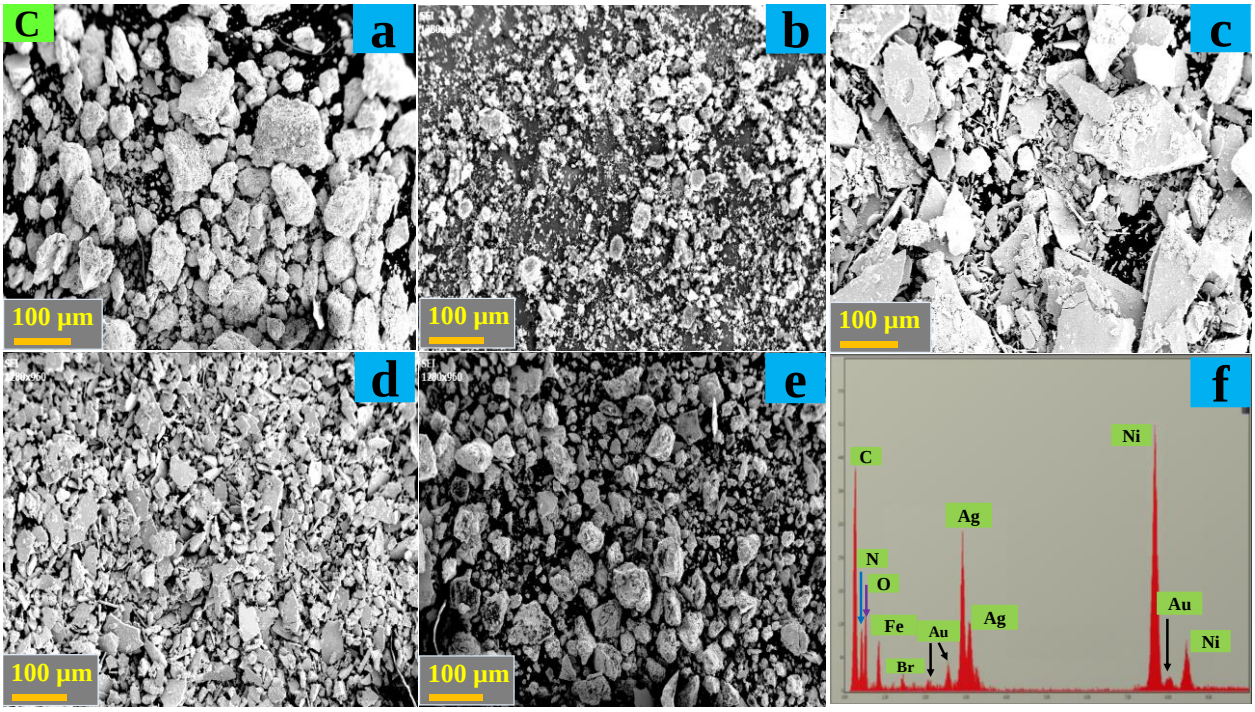

689 **Fig. 1.**

690

691

692

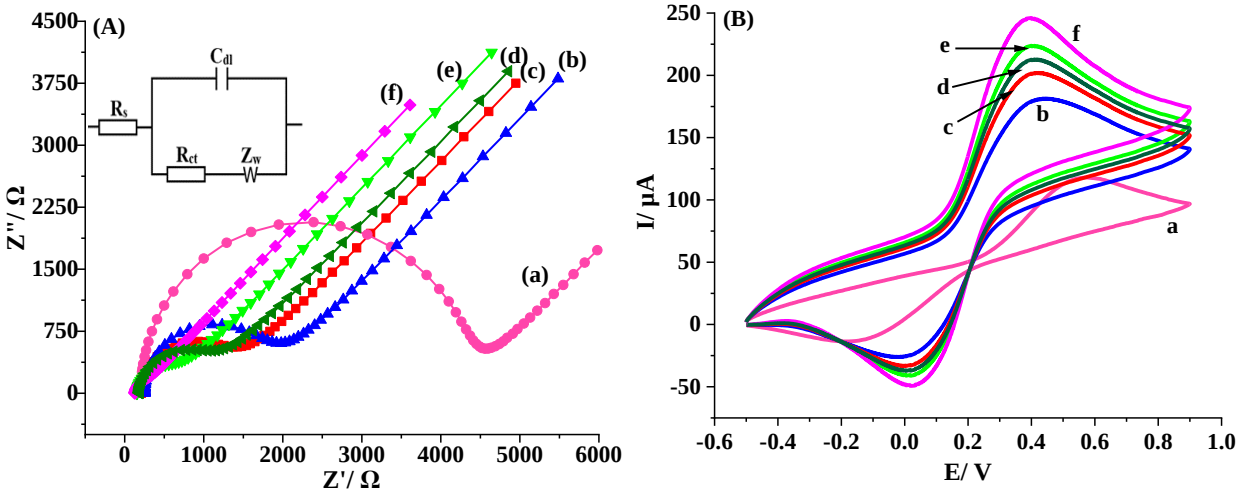
(A)
Cdl
Rs
Rct
Zw
(a)
(b)
(c)
(d)
(e)
(f)
Z''/ Ω
Z'/ Ω
(B)
a
b
c
d
e
f
I/ µA
E/ V

Fig. 2.

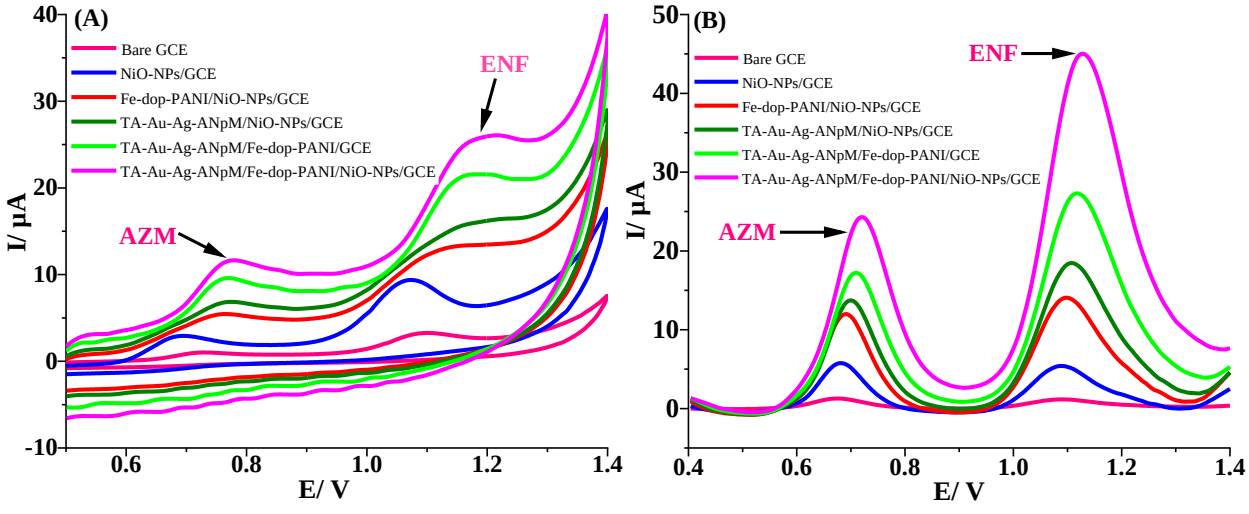
(A)
Bare GCE
NiO-NPs/GCE
Fe-dop-PANI/NiO-NPs/GCE
TA-Au-Ag-ANpM/NiO-NPs/GCE
TA-Au-Ag-ANpM/Fe-dop-PANI/GCE
TA-Au-Ag-ANpM/Fe-dop-PANI/NiO-NPs/GCE
AZM
ENF
I/ µA
E/ V
(B)
Bare GCE
NiO-NPs/GCE
Fe-dop-PANI/NiO-NPs/GCE
TA-Au-Ag-ANpM/NiO-NPs/GCE
TA-Au-Ag-ANpM/Fe-dop-PANI/GCE
TA-Au-Ag-ANpM/Fe-dop-PANI/NiO-NPs/GCE
AZM
ENF
I/ µA
E/ V

Fig. 3.

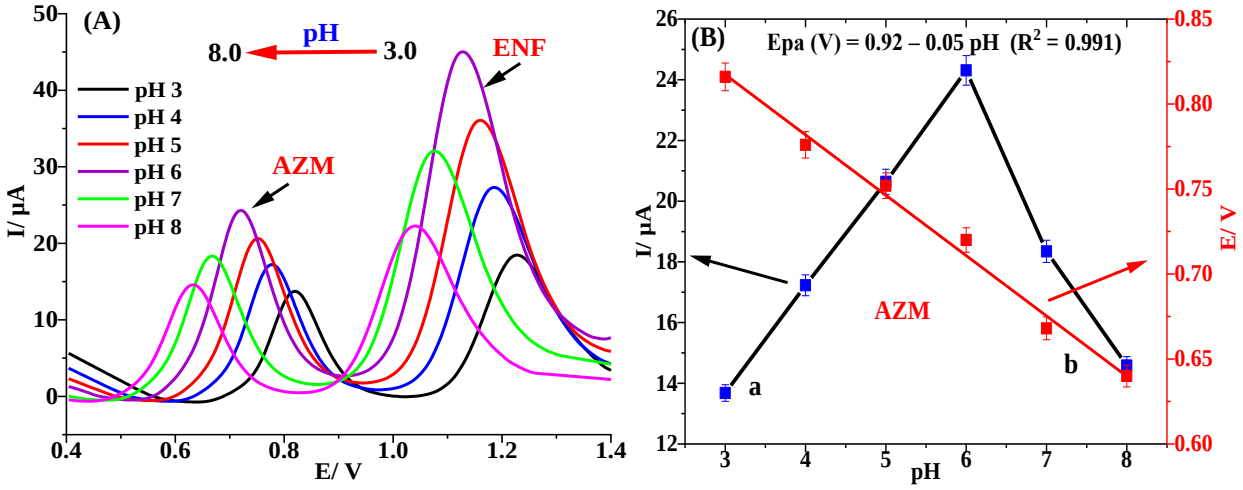
(A)
pH
8.0
3.0
ENF
AZM
pH 3
pH 4
pH 5
pH 6
pH 7
pH 8
I/ µA
E/ V
(B)
Epa (V) = 0.92 – 0.05 pH (R2 = 0.991)
AZM
a
b
I/ µA
E/ V
pH

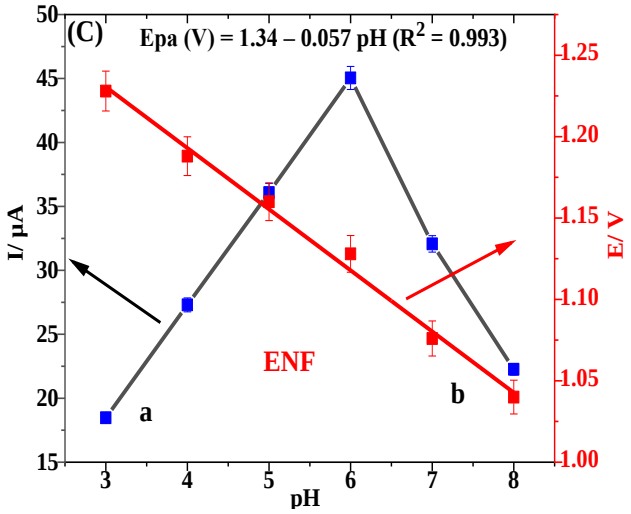
(C)
Epa (V) = 1.34 – 0.057 pH (R2 = 0.993)
ENF
a
b
I/ µA
E/ V
pH

Fig. 4.

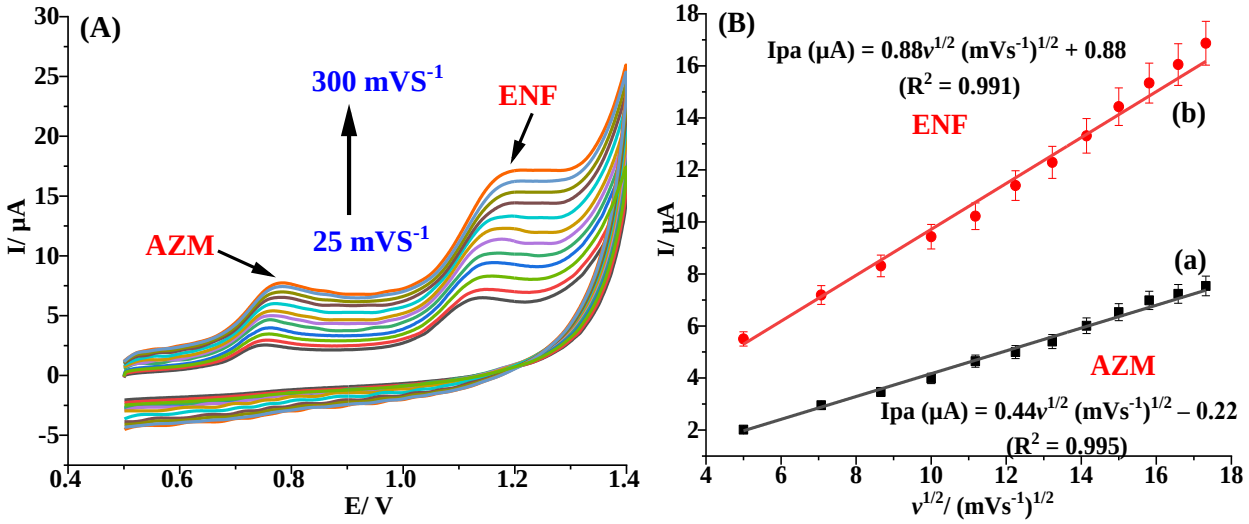
(A)
300 mVS-1
25 mVS-1
ENF
AZM
I/ µA
E/ V
(B)
Ipa (µA) = 0.88v1/2 (mVs-1)1/2 + 0.88
(R2 = 0.991)
ENF
(b)
(a)
AZM
Ipa (µA) = 0.44v1/2 (mVs-1)1/2 – 0.22
(R2 = 0.995)
I/ µA
v1/2/ (mVs-1)1/2

710

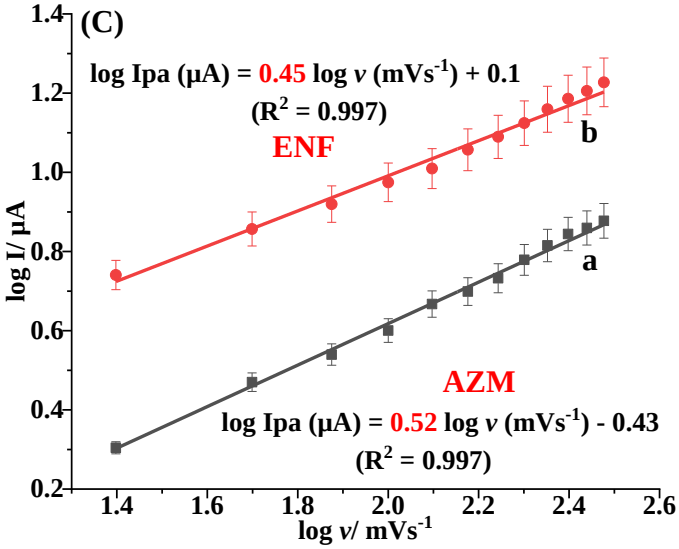
(C)
log Ipa (µA) = 0.45 log v (mVs-1) + 0.1
(R2 = 0.997)
ENF
b
a
AZM
log Ipa (µA) = 0.52 log v (mVs-1) - 0.43
(R2 = 0.997)
log I/ µA
log v/ mVs-1

711

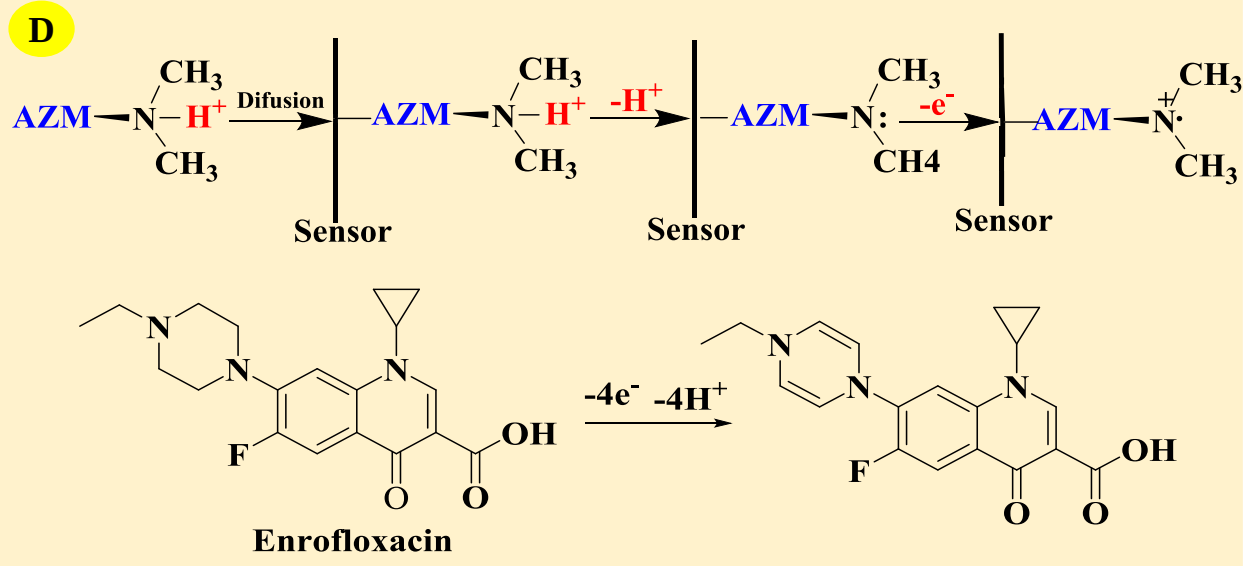

712

713 **Fig. 5.**

714

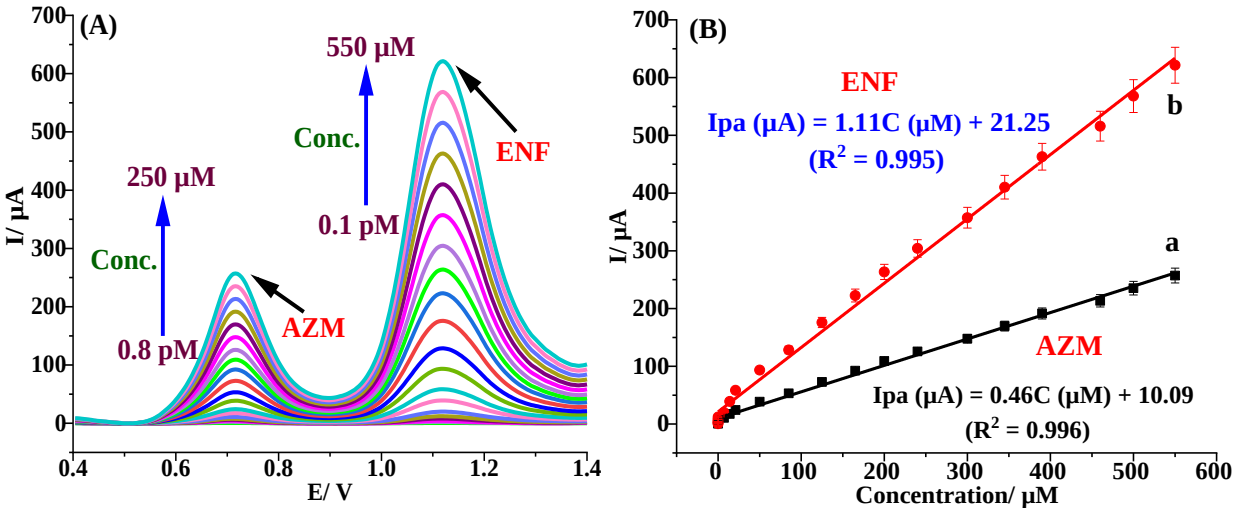

715

716 **Fig. 6.**

717

718

719

Figure captions

Fig. 1. (A) FT-IR spectra, (B) XRD diffraction patterns, (C) SEM images of NiO-NPs (a), Fe-dop-PANI (b), TA-Ag-NpM (c), TA-Au-Ag-ANpM (d), TA-Au-Ag-ANpM/Fe-dop-PANI/NiO-NPs (e), and (C) EDX spectra of TA-Au-Ag-ANpM/Fe-dop-PANI/NiO-NPs (f).

Fig. 2. Nyquist plots (A) and CVs (B) of bare GCE (a), NiO-NPs/GCE (b), Fe-dop-PANI/NiO-NPs/GCE (c), TA-Au-Ag-ANpM/NiO-NPs/GCE (d), TA-Au-Ag-ANpM/Fe-dop-PANI/GCE (e), and TA-Au-Ag-ANpM/Fe-dop-PANI/NiO-NPs/GCE (f).

Fig. 3. (A) CVs and (B) SWVs of 25 µM AZM and ENF in 0.1 M PBS (pH 6) at the bare GCE and different modified electrodes at a scan rate of 100 mVs^{-1}.

Fig. 4. SWV of 25 µM AZM and ENF at different pH of PBS (A), Ipa (µA) *vs.* pH (B(a) and C(a)) and Epa (V) *vs.* pH (B(b) and C(b)) for AZM and ENF, respectively.

Fig. 5. CVs of 25 µM AZM and ENF at different scan rate (A), plots of Ipa *vs.* $v^{1/2}$ (B), and log Ipa *vs.* log *v* (C), and schematic illustration for the electro-oxidation of AZM and ENF (D).

Fig. 6. SWVs of different concentrations of AZM and ENF (A), and Ipa *vs.* conc. (B).

Supplementary Material

Pioneering electrochemical sensing platform of multi-elemental nanocomposites for simultaneously determining azithromycin and enrofloxacin residues in food and water samples

Wondimeneh Dubale Adane[a], Bhagwan Singh Chandravanshi*[a], Merid Tessema**[a]
[a]Department of Chemistry, Addis Ababa University, P. O. Box 1176, Addis Ababa, Ethiopia
*Corresponding author. E-mail address: bscv2006@yahoo.com
**Corresponding author. E-mail address: tessemamerid@yahoo.com

Sample preparation

Chicken meat samples

Chicken meat samples were purchased from a local supermarket in Addis Ababa, Ethiopia, and homogenized before extraction. To extract the target analyte, 5.0 g of the homogenized meat sample was mixed with 20 mL of 0.1 M PBS solution. The meat sample and PBS solution were thoroughly mixed using a vortex mixer to ensure complete dispersion of the sample in the solvent. Subsequently, the mixture was subjected to ultrasonic treatment for 45 min. This step aimed at facilitating the efficient extraction of the desired components from the meat matrix, thereby enhancing the quality and accuracy of our analysis. Then after, the mixture was centrifuged at 4,000 rpm for 15 min. This centrifugation step was performed to separate the constituents, and as a result, a clear solution containing the extracted analyte was collected. Finally, the sample was spiked with appropriate concentrations of AZM and ENF standard solutions.

Egg samples

Egg samples were obtained from the Elfora Agro-Industries Plc poultry farm in Debre Zeit, Ethiopia, and stored at 4 ^{o}C until analysis. The whole egg was homogenized at room temperature with continuous stirring, and 5.0 g egg homogenate was transferred to a 15 mL polypropylene centrifuge tube, and 10 mL acetonitrile was added. The mixture was ultrasonically extracted for 15 min and centrifuged at 2240 relative centrifugal force (RCF) for 10 min, then the supernatant

was transferred to another 15 mL polypropylene centrifuge tube. Then after 1.0 mL of 4.0 M ammonium acetate buffer (pH 6.75) was added and mixed by vortexing. 20 mL of dichloromethane was added to the mixture and vortexed for 10 min and centrifuged at 2240 RCF for 10 min; the supernatant was collected and evaporated at 40 ^{o}C. The extractant was re-dissolved with 2.0 mL of 4.0 M phosphate buffer (pH 7.0) and filtered through a 150 mm membrane filter before analysis.

Fish samples

Fish samples were collected from a local supermarket in Addis Ababa, Ethiopia and stored in a deep freezer until analysis. Approximately 2.0 g of the homogenized fish sample was weighed into a 50 mL falcon tube, followed by the addition of 5 mL of water and 5 mL of acetonitrile. The mixture was vortexed for 5 min to ensure thorough mixing. Subsequently, 5.0 g of $MgSO_4$ and 2.0 g of NaCl were added to the falcon tube and manually shaken for 2 min to promote solid-phase extraction. The resulting mixture was centrifuged at 4000 rpm for 15 min to separate the supernatant from the solid phase. The collected supernatant was carefully transferred to another falcon tube. After 5 min vortexing, the mixture was centrifuged again at 10,000 rpm for 10 min, resulting in a clear solution of the analytes of interest. Finally, to quantify the concentrations of AZM and ENF in the samples, the samples were spiked with appropriate concentrations (0, 5, 15, 25, and 40 µM) of AZM and ENF standard solutions.

River and lake water samples

800 mL of river water samples were collected from Kebena River in Addis Ababa, Ethiopia, and lake water samples of the same volume were obtained from Lake Hawassa in Hawassa, Ethiopia. Both water samples were subjected to a uniform preparation procedure and were stored at 4 °C until analysis. The samples were filtered thrice using a 150 mm filter paper, diluted with a phosphate buffer solution, and mixed with standard solutions of the analytes. No further pretreatment was performed before analysis.

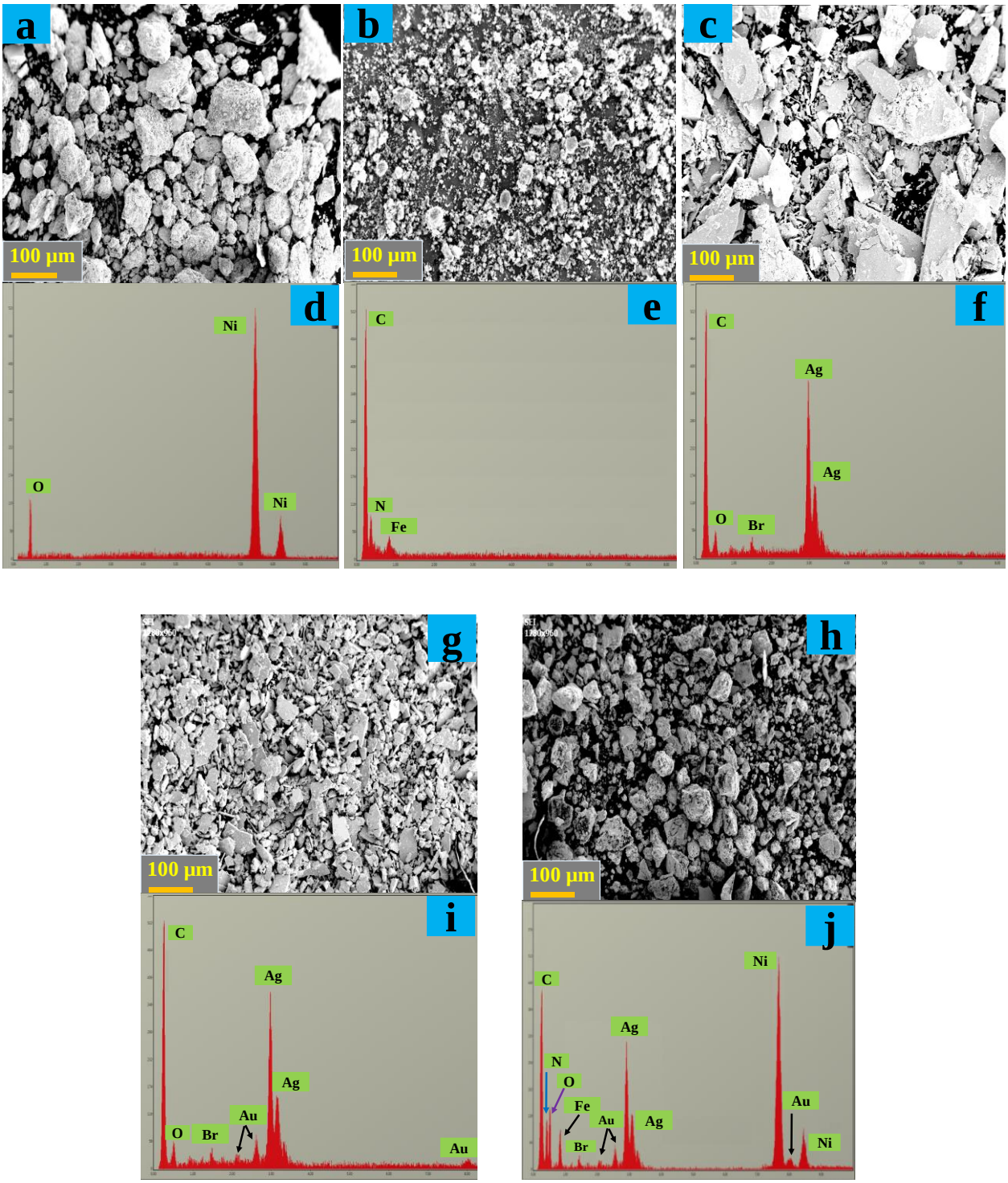

Fig. S1. (A) SEM images and EDX spectrum of NiO-NPs (a and d), Fe-dop-PANI (b and e), TA-Ag-NpM (c and f), TA-Au-Ag-ANpM (g and i), TA-Au-Ag-ANpM/Fe-dop-PANI/NiO-NPs (h and j).

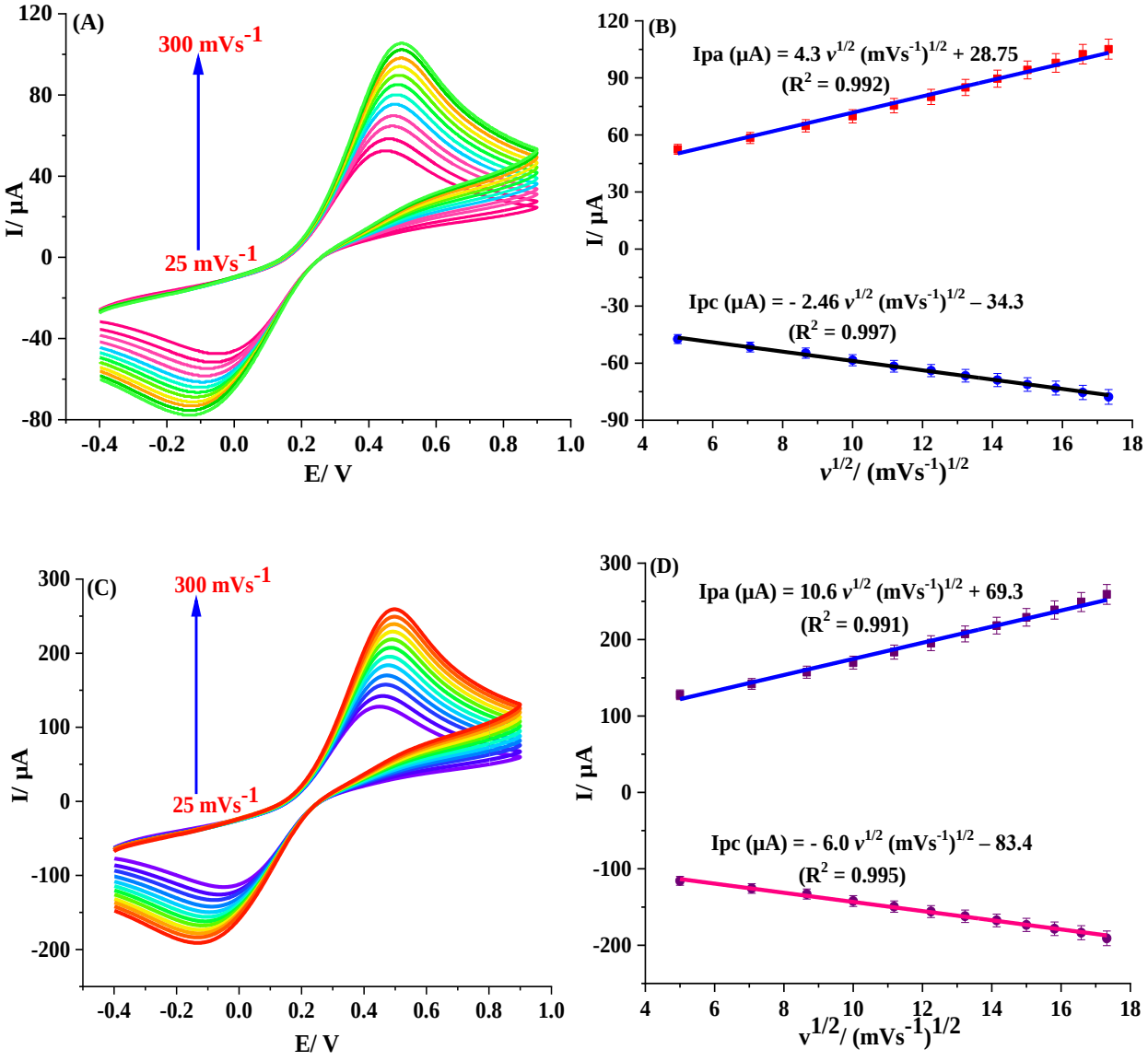

Fig. S2. CVs of bare GCE (A) and TA-Au-Ag-ANpM/Fe-dop-PANI/NiO-NPs/GCE (C) in a redox probe solution of 5 mM $[Fe(CN)_6]^{3-/4-}$ containing 0.1 M KCl at different scan rates, and plots of Ipa *vs.* $v^{1/2}$ (B and D).

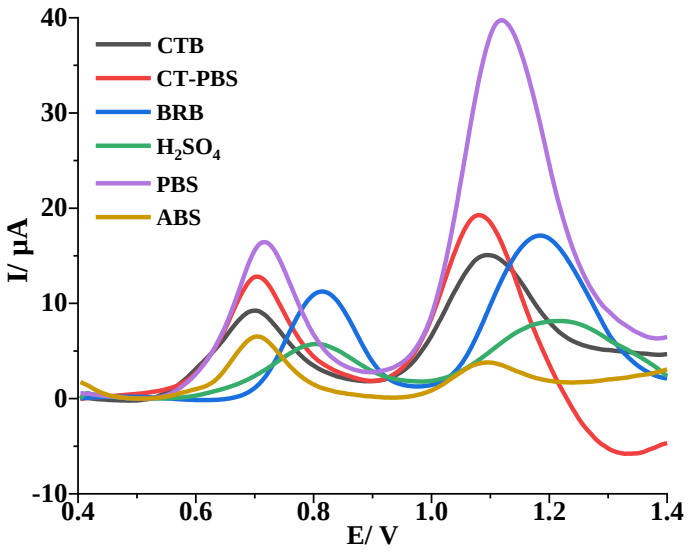

Fig. S3. SWVs of 25 µM AZM and ENF in different electrolyte solutions.

Optimization of the nanocomposites mixture ratio and volume of drop-cast species

In the pursuit of optimal performance for a specific application, the optimization of the mixing ratio of nanocomposites is a pivotal step in the development of an intended electrochemical sensors. The optimal proportions of TA-Au-Ag-ANpM, Fe-dop-PANI, and NiO-NPs were found to be 5:6:4, yielding the highest current response for the detection of 25 µM AZM and ENF, as illustrated in Fig. SM1 (a). The enhanced performance at a 5:6:4 ratio can be attributed to the synergistic effects (high electrical conductivity, catalytic activity, and electroactive surface area) of the three nanocomposites. These synergistic properties gives the sensor enhanced sensitivity to the target analytes. Consequently, a 5:6:4 ratio for TA-Au-Ag-ANpM, Fe-dop-PANI, and NiO-NPs was chosen as the optimum value for developing the proposed sensor in subsequent experiments.

To ensure the effective modification of the GCE surface, it is important to optimize the drop-cast volume of the TA-Au-Ag-ANpM/Fe-dop-PANI/NiO-NPs dispersion mixture. The volume affects the thickness and uniformity of the modified layer, which can affect the electrode performance. To determine the optimal drop-cast amount, various volumes of the dispersion mixture were tested by examining the current response of the modified electrode for simultaneously detecting 25 µM AZM and ENF. As shown in Fig. SM1 (b), the highest current

response was achieved with a drop-cast volume of 10 µL. Therefore, 10 µL of the TA-Au-Ag-ANpM/Fe-dop-PANI/NiO-NPs dispersion mixture was selected as the optimal volume for preparing the TA-Au-Ag-ANpM/Fe-dop-PANI/NiO-NPs/GCE for subsequent experiments.

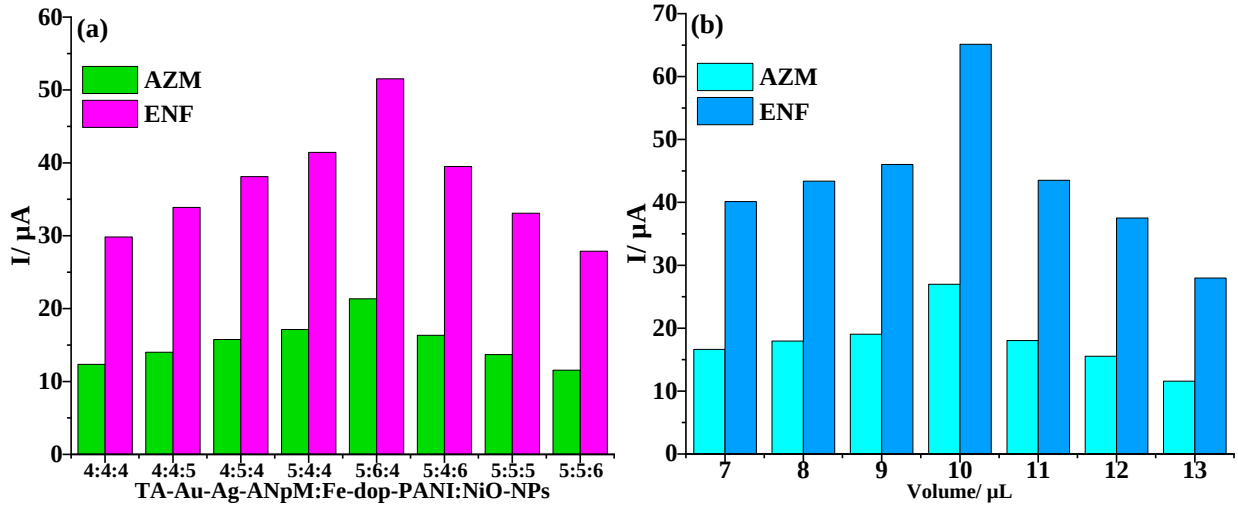

Fig. SM1. The optimization of the nanocomposite mixture ratio and drop-cast volume.

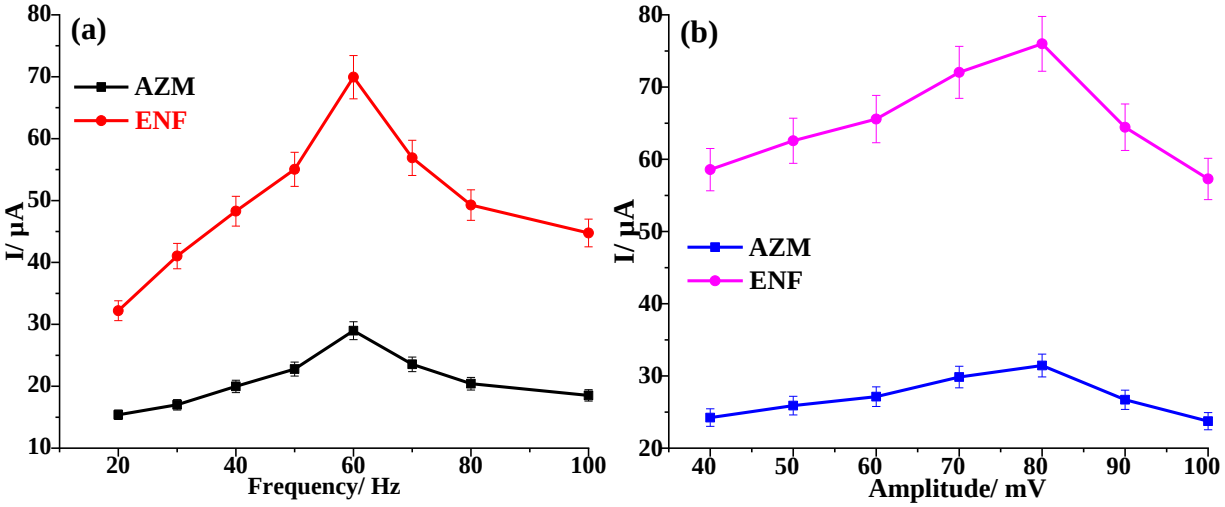

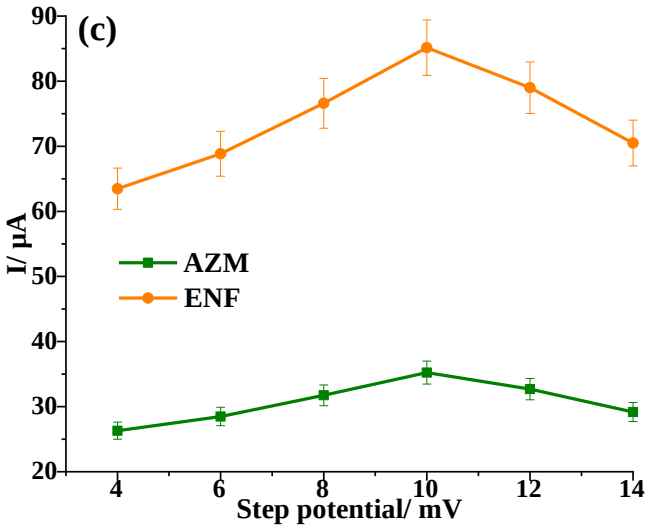

Fig. S4. The effect of SWV parameters: frequency (a), amplitude (b), and step potential (c) on the anodic current responses of 25 µM AZM and ENF.

Table S1: The effect of co-existing interferents on the current response of the sensor.

Interferents	Conc. (µM)	Relative Percentage Error (%)		Interferents	Conc. (µM)	Relative Percentage Error (%)	
		AZM	ENF			AZM	ENF
Rifampicin	300	3.67	3.71	Dopamine	600	2.24	2.21
Metronidazole	300	3.56	3.51	Uric Acid	600	2.33	2.38
Norfloxacin	300	3.46	3.52	Folic Acid	600	2.12	2.17
Tinidazole	300	3.75	3.69	Lactose	600	2.28	2.19
Ciprofloxacin	300	3.64	3.64	HCO_3^-	1200	1.14	1.14
Vancomycin	300	3.83	3.78	Fe^{3+}	1200	1.08	1.05
Chloramphenicol	300	3.62	3.68	NO_3^-	1200	0.98	0.92
Ceftriaxone	300	3.45	3.41	Ca^{2+}	1200	0.87	0.81
Erythromycin	300	3.74	3.74	K^+	1200	1.09	0.96
Fructose	600	2.13	2.16	SO_4^{2-}	1200	1.05	1.05
Glucose	600	2.21	2.17	Cu^{2+}	1200	0.97	0.95
Sucrose	600	2.35	2.35	Mg^{2+}	1200	0.86	0.83
Ascorbic Acid	600	2.17	2.14	CO_3^{2-}	1200	1.27	1.24
Urea	600	2.43	2.49	Cl^-	1200	1.08	1.16

Conclusions and Recommendations

In this study, eight pioneering electrochemical sensors were successfully developed for the simultaneous and individual determination of selected antibiotic residues in food, water, and environmental samples. The sensors were meticulously designed using innovative materials such as TA-Au-Ag-ANpM, Au-Ag-ANCCs, Fe-dop-PANI, NiO-NPs, ZnO-NPs, *f*-MWCNTs, *r*-GO, poly(L-histidine), poly(L-serine), poly(glycine), polyethylene oxide (PEO), and ChCl to improve sensitivity, selectivity, and stability. The integration of the modifiers results in sensors with superior electrochemical properties, characterized by low limits of detection and quantification, and wide linear ranges. These attributes are crucial for accurately identifying trace amounts of antibiotics, which is essential given the growing concern over antibiotic residues contaminating food and water.

The surface morphology, elemental composition, and electrochemical properties of the developed sensors were characterized using an array of analytical techniques including UV–Vis spectroscopy, FT-IR, XRD, EDX, SEM, EIS, and CV. The developed sensors include: ChCl/CPE for CPRO with a LOD of 0.36 nM and a LOQ of 1.2 nM; a ChCl/GCE for the simultaneous detection of TIN with a LOD of 0.90 nM and a LOQ of 3.0 nM, and CAP with a LOD of 0.27 nM and a LOQ of 0.89 nM; a TA-Au-Ag-ANpM/*r*-GO/poly(glycine)/GCE for MTZ with a LOD of 0.0312 pM and a LOQ of 0.104 pM; a Au–Ag-ANCCs/*f*-MWCNTs-CPE/ChCl for RAMP with a LOD of 2.7 pM and a LOQ of 8.85 pM, and NFX with a LOD of 0.14 nM and a LOQ of 0.47 nM; a TA-Au-Ag-ANpM/*f*-MWCNTs-CPE/poly(l-serine) for SFT with a LOD of 0.53 pM and a LOQ of 1.75 pM, and SFM with a LOD of 0.41 pM and a LOQ of 1.35 pM; a Au-Ag-ANCCs/*r*-GO/poly(L-histidine)/GCE for VAN with a LOD of 0.11 pM and a LOQ of 0.36 pM, and CFT with a LOD of 0.017 pM and a LOQ of 0.057 pM; an ultra-performance multi-elemental nanocomposite electrochemical sensor integrating gold-silver-alloy nanocoral clusters with ZnO-NPs-CPE and PEO for NFT with a LOD of 0.26 pM and a LOQ of 0.88 pM, and FZD with a LOD of 0.023 pM and a LOQ of 0.076 pM; and a TA-Au-Ag-ANpM/Fe-dop-PANI/NiO-NPs/GCE for AZM with a LOD of 0.053 pM and a LOQ of 0.18 pM, and ENF with a LOD of 0.013 pM and a LOQ of 0.042 pM. These detection limits were significantly lower, and the detection ranges were broader than those of recently reported sensors, highlighting the superior performance of the developed sensors. The exceptional performance of these sensors were further demonstrated by

their remarkable repeatability, reproducibility, long-term stability, and extraordinary selectivity against potentially interfering substances. Practical applications of these sensors in detecting antibiotic residues in food samples (such as chicken meat, fish, honey, eggs, and milk) and environmental water samples (including river, lake, and hospital wastewater) showed very high percentage recoveries, ranging from 93% to 104%, and RSD below 5%. For instance, the sensor for SFT and SFM demonstrated recoveries of 95.6–102.4% in honey, beef, and egg samples, with RSD below 5%. Similarly, the sensor for AZM and ENF yielded recoveries of 96.4–102.8% in chicken meat, egg, fish, river, and lake water samples, with RSD between 1.13% and 1.36%.

Overall, these studies highlight significant advancements in the field of electrochemical sensing technology. The newly developed sensors are not only efficient, sensitive, and selective but also cost-effective and environmentally friendly, making them highly suitable for real-world applications. They provide a robust solution to the pressing issue of antibiotic residue pollution, which poses a substantial threat to human health, environmental sustainability, and the global economy. By ensuring the effective monitoring and control of antibiotic residues in various matrices, these sensors contribute to enhancing food safety, protecting public health, and preserving environmental integrity.

Moving forward, it is recommended that further research be conducted to refine and optimize the developed sensors for broader applications and real-world implementation. Collaboration with industry stakeholders and regulatory bodies can facilitate the integration of these sensors into existing monitoring systems, thereby ensuring their widespread adoption and impact. Additionally, ongoing efforts should focus on enhancing the robustness and versatility of sensors to accommodate a diverse range of antimicrobial compounds and sample matrices. This will strengthen their utility in addressing the evolving challenges and emerging contaminants in food and water safety.

Overall, the findings and recommendations presented in this dissertation underscore the vital role of advanced electrochemical sensing technologies in safeguarding public health and enhancing food and water quality assurance measures. We hope that the insights gained from this research will inspire further innovation and collaboration in the field, ultimately leading to tangible improvements in antimicrobial drug residue detection and mitigation strategies.